frontiers | Research Topics

The insights of multi-omics into the microenvironment after tumor metastasis: a paradigm shift in molecular targeting modeling and immunotherapy for advanced cancer patients

Edited by
Chao Wang, Xinhua Xiao, Qi Wang, Divya Gopinath and Hailin Tang

Published in
Frontiers in Immunology
Frontiers in Oncology

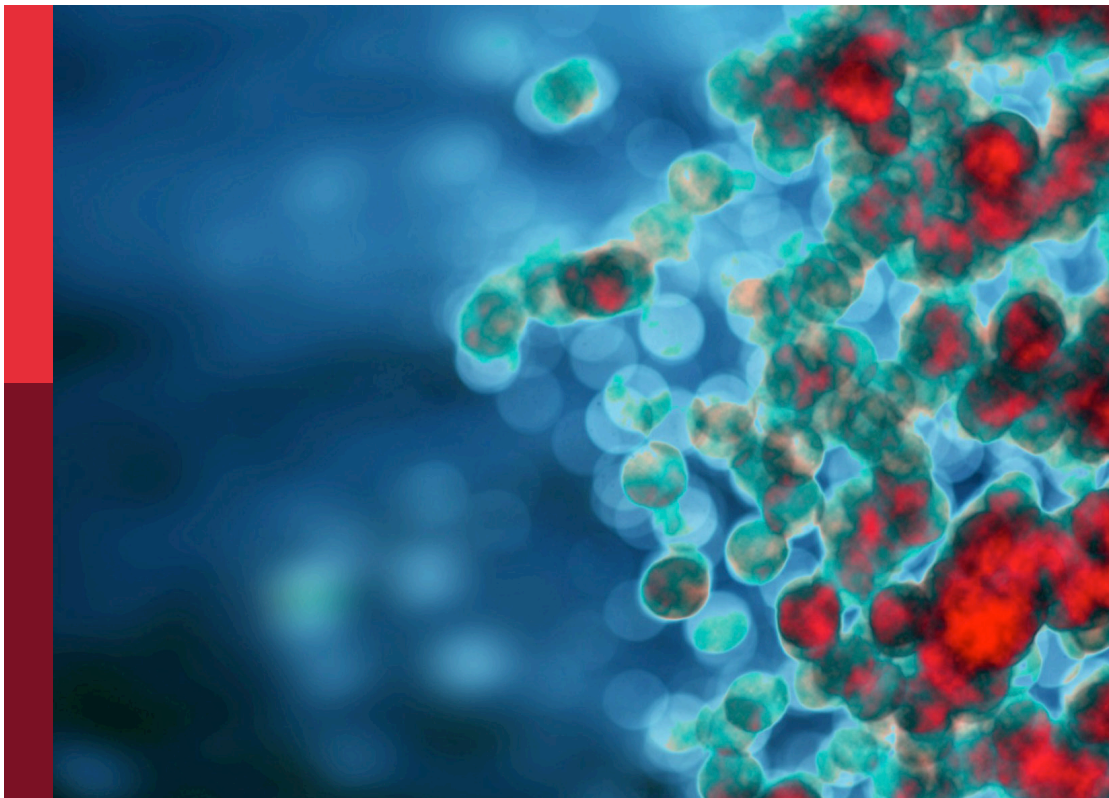

FRONTIERS EBOOK COPYRIGHT STATEMENT

The copyright in the text of individual articles in this ebook is the property of their respective authors or their respective institutions or funders. The copyright in graphics and images within each article may be subject to copyright of other parties. In both cases this is subject to a license granted to Frontiers.

The compilation of articles constituting this ebook is the property of Frontiers.

Each article within this ebook, and the ebook itself, are published under the most recent version of the Creative Commons CC-BY licence. The version current at the date of publication of this ebook is CC-BY 4.0. If the CC-BY licence is updated, the licence granted by Frontiers is automatically updated to the new version.

When exercising any right under the CC-BY licence, Frontiers must be attributed as the original publisher of the article or ebook, as applicable.

Authors have the responsibility of ensuring that any graphics or other materials which are the property of others may be included in the CC-BY licence, but this should be checked before relying on the CC-BY licence to reproduce those materials. Any copyright notices relating to those materials must be complied with.

Copyright and source acknowledgement notices may not be removed and must be displayed in any copy, derivative work or partial copy which includes the elements in question.

All copyright, and all rights therein, are protected by national and international copyright laws. The above represents a summary only. For further information please read Frontiers' Conditions for Website Use and Copyright Statement, and the applicable CC-BY licence.

ISSN 1664-8714
ISBN 978-2-8325-7338-9
DOI 10.3389/978-2-8325-7338-9

Generative AI statement
Any alternative text (Alt text) provided alongside figures in the articles in this ebook has been generated by Frontiers with the support of artificial intelligence and reasonable efforts have been made to ensure accuracy, including review by the authors wherever possible. If you identify any issues, please contact us.

About Frontiers

Frontiers is more than just an open access publisher of scholarly articles: it is a pioneering approach to the world of academia, radically improving the way scholarly research is managed. The grand vision of Frontiers is a world where all people have an equal opportunity to seek, share and generate knowledge. Frontiers provides immediate and permanent online open access to all its publications, but this alone is not enough to realize our grand goals.

Frontiers journal series

The Frontiers journal series is a multi-tier and interdisciplinary set of open-access, online journals, promising a paradigm shift from the current review, selection and dissemination processes in academic publishing. All Frontiers journals are driven by researchers for researchers; therefore, they constitute a service to the scholarly community. At the same time, the *Frontiers journal series* operates on a revolutionary invention, the tiered publishing system, initially addressing specific communities of scholars, and gradually climbing up to broader public understanding, thus serving the interests of the lay society, too.

Dedication to quality

Each Frontiers article is a landmark of the highest quality, thanks to genuinely collaborative interactions between authors and review editors, who include some of the world's best academicians. Research must be certified by peers before entering a stream of knowledge that may eventually reach the public - and shape society; therefore, Frontiers only applies the most rigorous and unbiased reviews. Frontiers revolutionizes research publishing by freely delivering the most outstanding research, evaluated with no bias from both the academic and social point of view. By applying the most advanced information technologies, Frontiers is catapulting scholarly publishing into a new generation.

What are Frontiers Research Topics?

Frontiers Research Topics are very popular trademarks of the *Frontiers journals series*: they are collections of at least ten articles, all centered on a particular subject. With their unique mix of varied contributions from Original Research to Review Articles, Frontiers Research Topics unify the most influential researchers, the latest key findings and historical advances in a hot research area.

Find out more on how to host your own Frontiers Research Topic or contribute to one as an author by contacting the Frontiers editorial office: frontiersin.org/about/contact

The insights of multi-omics into the microenvironment after tumor metastasis: a paradigm shift in molecular targeting modeling and immunotherapy for advanced cancer patients

Topic editors

Chao Wang — Shanghai Jiao Tong University, China
Xinhua Xiao — Guangzhou Medical University, China
Qi Wang — Affiliated Hospital of Jiangsu University, Jiangsu University, China
Divya Gopinath — Ajman University, United Arab Emirates
Hailin Tang — Sun Yat-sen University Cancer Center (SYSUCC), China

Citation

Wang, C., Xiao, X., Wang, Q., Gopinath, D., Tang, H., eds. (2026). *The insights of multi-omics into the microenvironment after tumor metastasis: a paradigm shift in molecular targeting modeling and immunotherapy for advanced cancer patients*. Lausanne: Frontiers Media SA. doi: 10.3389/978-2-8325-7338-9

Table of contents

06 Editorial: The insights of multi-omics into the microenvironment after tumor metastasis: a paradigm shift in molecular targeting modeling and immunotherapy for advanced cancer patients
Xuejian Liu, Qi Wang, Yang Ma, Xinhua Xiao, Xue Zhao, Hailin Tang, Divya Gopinath and Chao Wang

10 Unveiling purine metabolism dysregulation orchestrated immunosuppression in advanced pancreatic cancer and concentrating on the central role of NT5E
Junqian Zhang, Xiaobo Zhang, Ruixin Wu and Chang-Sheng Dong

27 Neutrophil-to-lymphocyte ratio predicts a poor prognosis for penile cancer with an immunosuppressive tumor microenvironment
Xingliang Tan, Yanjun Wang, Yiqi Yu, Runhao Zheng, Jing Li, Shaohua Chen, Qingling Xie, Shengjie Guo, Chichen Zhang, Xinpei Deng, Zhicheng Liu, Yi Tang, Hang Li, Weicheng Wu, Juexiao Chen, Qianghua Zhou, Wensu Wei, Kai Yao and Zhiming Wu

40 Unraveling the immune evasion mechanisms in the tumor microenvironment of head and neck squamous cell carcinoma
Xuri Zhao, Yaping Zhu, Youya He, Weiyan Gu, Qi Zhou, Bei Jin, Shenguo Chen and Haisheng Lin

49 Splenic volume as a predictor of survival in cancer patients treated with immune checkpoint inhibitors
Yunhua Zhang, Xin Fu, Lilong Zhang, Qing Zhou and Weixing Wang

60 Radiation therapy induced intestinal barrier damage and repair process - differences in salivary metabolites and monitoring of intestinal barrier function
Zhang Jingjing, Wang Kun, Qiao Yanyu, Zhang Mengjie, Chen Yunqing, Tian Yulong, Jiao Xuelong, Tan Xiaojie, Jiang Haitao and Hou Feng

69 Machine learning-based integration of DCE-MRI radiomics for STAT3 expression prediction and survival stratification in breast cancer
Dong Pan, Cheng-Yan Zhang, Ya-Fei Wang, Shuang Liu and Xiong-Zhi Wu

84 Analysis of immune cell infiltration in the tumor microenvironment of cervical cancer and its impact on immunotherapy
Fei Qin, Lu Huan, Xia Shi, Yuanyuan Hua and Yi Wu

101 The impact of sarcopenia on prognosis and fruquintinib efficacy in advanced colorectal cancer: a retrospective and mendelian randomization study
Yao Wang, Du Meilu, Shi Qi, Tang Yufei, Gao Song, Han Susu, Wen Haotian, Zhu Tingting, Wang Chao, Hou Fenggang and Yin Xiaoling

115 Correction: The impact of sarcopenia on prognosis and fruquintinib efficacy in advanced colorectal cancer: a retrospective and mendelian randomization study
Frontiers Production Office

117 Integrating proteomics and machine learning reveals characteristics and risks of lymph node-independent distant metastasis in colorectal cancer
Chenxiao Zheng, Baiwang Zhu, Yanyu Chen, Numan Shahid, Yiwang Hu, Hajar Mansoor Ahmed Ali Husain, Binbin Ou, Qiongying Zhang, Haobo Jin, Yating Zheng, Peng Li, Yifei Pan and Xiaodong Zhang

136 Targeting GABA signaling in the tumor microenvironment: implications for immune cell regulation and immunotherapy resistance
Yuanqing Zhao, Jin Xu, Ke Yang and Li Bao

147 Analysis of standard vs dose-escalated stereotactic body radiation therapy in localized prostate cancer: a comparative evaluation of survival outcomes
Bichun Xu, Xianzhi Zhao, Tingting Wei, Yiyin Liang, Weiwei Zhang, Liang Chen, Zuping Lian and Huojun Zhang

158 Diagnostic value of thyroid-related serological indicators and pan-immune-inflammation value for differentiated thyroid carcinoma
Yicheng Wen, Xin Yi, Jixin Shi, Peng Wan, Huan Wang, Li Tian and Huixia Liu

167 Integrating single-cell omics and materials science for uveal melanoma: from mechanistic insights to precision therapeutics
Shouyong Fu and Changfei Li

183 Integrating deep learning features from mammography with SHAP values for a machine learning model predicting over 5-year recurrence of breast ductal carcinoma *In Situ* post-lumpectomy
Yupeng Sha, Quan Yuan, Yi Du, Shuqi Yang, Ming Niu, Xiaoshuan Liang, Shanshan Sun, Tong Li, Shu Gong and Jiguang Han

196 Stemness- and hypoxia-based prognostic stratification index reveals G6PD as a regulator of hypoxia-driven stemness in hepatocellular carcinoma
Mingwei Gao, Yuechuan Liu, Jianhui Wu, Peiru Zhang, Jin Liu, Kun Guo, Binwen Sun, Sunbin Ling and Liming Wang

216 Multi-omics analysis of the tumor microenvironment after metastasis: advancing toward personalized immunotherapy and molecular targeted strategies
Qing Gao, Huqiang Wu, Li Duan, Guanhua Lv and Dongmei Quan

230 AI-based non-invasive profiling of the tumor immune microenvironment using longitudinal CT radiomics predicts immunotherapy response in lung cancer
Guangjie Liu, Xiaoyan Zhang, Yutong He, Di Liang, Shaonan Xie, Ning Zhang, Nan Geng, Liwen Zhang, Yajie Huang, Fang Liu and Qingyi Liu

242 Development and validation of a novel sodium-overload related genes signature for prognostic prediction in breast cancer: integrating bioinformatics and experimental approaches
Qizhen Feng, Wenlin Yang, Guohao Su, Fei Wu and Chungen Xing

260 Targeting the CCL28-STAT3-PLAC8 axis to suppress metastasis and remodel tumor microenvironment in colorectal cancer
Yao Yang, Qixin Jiang, Zhe Zhu, Shun Zhang, Tao Du, Shuzheng Song and Xiaohua Jiang

272 Antibody-drug conjugates as immuno-oncology agents in colorectal cancer: targets, payloads, and therapeutic synergies
Yihan Wang, Kai Lu, Yang Xu, Shengshan Xu, Hongyu Chu and Xuedong Fang

frontiers | Frontiers in Oncology

TYPE Editorial
PUBLISHED 16 December 2025
DOI 10.3389/fonc.2025.1749178

Check for updates

OPEN ACCESS

EDITED AND REVIEWED BY
Peter Brossart,
University of Bonn, Germany

*CORRESPONDENCE
Xue Zhao
15821277930@163.com
Hailin Tang
tanghl@sysucc.org.cn
Divya Gopinath
d.gopinath@ajman.ac.ae
Chao Wang
18766851283@163.com

†These authors have contributed equally to this work

RECEIVED 18 November 2025
REVISED 27 November 2025
ACCEPTED 01 December 2025
PUBLISHED 16 December 2025

CITATION
Liu X, Wang Q, Ma Y, Xiao X, Zhao X, Tang H, Gopinath D and Wang C (2025) Editorial: The insights of multi-omics into the microenvironment after tumor metastasis: a paradigm shift in molecular targeting modeling and immunotherapy for advanced cancer patients.
Front. Oncol. 15:1749178.
doi: 10.3389/fonc.2025.1749178

COPYRIGHT
© 2025 Liu, Wang, Ma, Xiao, Zhao, Tang, Gopinath and Wang. This is an open-access article distributed under the terms of the Creative Commons Attribution License (CC BY). The use, distribution or reproduction in other forums is permitted, provided the original author(s) and the copyright owner(s) are credited and that the original publication in this journal is cited, in accordance with accepted academic practice. No use, distribution or reproduction is permitted which does not comply with these terms.

Editorial: The insights of multi-omics into the microenvironment after tumor metastasis: a paradigm shift in molecular targeting modeling and immunotherapy for advanced cancer patients

Xuejian Liu[1†], Qi Wang[2†], Yang Ma[3,4,5,6†], Xinhua Xiao[7†], Xue Zhao[8*], Hailin Tang[9*], Divya Gopinath[10,11*] and Chao Wang[12*]

[1]Department of Radiology, Xinjiang 474 Hospital, Urumqi, China, [2]Department of Gastroenterology, Affiliated Hospital of Jiangsu University, Jiangsu University, Zhenjiang, China, [3]Department of General Surgery, Pancreatic Disease Center, Ruijin Hospital, Shanghai Jiao Tong University School of Medicine, Shanghai, China, [4]Shanghai Key Laboratory of Pancreatic Neoplasms Translational Research, Research Institute of Pancreatic Diseases, Shanghai Jiao Tong University School of Medicine, Shanghai, China, [5]State Key Laboratory of Systems Medicine for Cancer, Shanghai, China, [6]Institute of Translational Medicine, Shanghai Jiao Tong University, Shanghai, China, [7]Department of Hematology and Oncology, Women and Children's Medical Center, Guangzhou Medical University, Guangzhou, China, [8]Department of General Practice, Changshou Community Health Service Center of Putuo District, Shanghai, China, [9]State Key Laboratory of Oncology in South China, Guangdong Provincial Clinical Research Center for Cancer, Sun Yat-sen University Cancer Center, Guangzhou, China, [10]Basic Medical and Dental Sciences Department, College of Dentistry, Ajman University, Ajman, United Arab Emirates, [11]Centre of Medical and Bio-allied Health Sciences Research, Ajman University, Ajman, United Arab Emirates, [12]Department of Oncology, Ruijin Hospital, Shanghai Jiao Tong University School of Medicine, Shanghai, China

KEYWORDS

immunotherapy, metastasis, microenvironment, multi-omics, tumor

Editorial on the Research Topic

The insights of multi-omics into the microenvironment after tumor metastasis: a paradigm shift in molecular targeting modeling and immunotherapy for advanced cancer patients

Understanding the complex interplay within the tumor microenvironment (TME) following metastasis, using multi-omics technologies, is essential for revolutionizing treatments for advanced cancer. The post-metastatic TME is an intricate system of diverse cellular and molecular components (1). Integrating genomic, epigenomic, proteomic, and metabolomic data provides a panoramic view of the mechanisms driving tumor metastasis and therapy resistance. This holistic perspective facilitates the identification of molecular signatures and metabolic changes that are critical for developing precision medicine strategies (2–4). Such comprehensive analyses can yield innovative molecular targeting models and immunotherapeutic approaches, with the

ultimate aim of transforming the therapeutic landscape for patients with advanced cancer (5).

This Research Topic aims to explore the transformative potential of multi-omics for understanding and treating advanced cancer. By dissecting the molecular intricacies and immune cell interactions within the post-metastatic tumor microenvironment (TME), this Research Topic seeks to advance therapeutic strategies that target both tumor cells and their surrounding milieu (6). These strategies are designed to enhance the efficacy of immunotherapy, improve patient survival rates, and increase quality of life. Driving this shift toward customized treatments represents an emerging frontier in oncology (7). To gather further insights into the intersection of immunotherapy, multi-omics, and the TME, we welcome contributions on key themes, including high-quality reviews on immunotherapy applications, investigations into the dynamic changes of the post-metastatic TME, multi-omics-guided optimization of immunotherapy, and biomarker validation for personalized medicine. This Research Topic, titled "Multi-Omics Insights into the Post-Metastatic Microenvironment: A Paradigm Shift for Molecular Targeting and Immunotherapy," was curated by five guest editors and comprises 20 articles (5 reviews and 15 original research studies). Together, these works provide a novel, comprehensive perspective on the multi-omics-based dissection of the post-metastatic TME and propose potential precision strategies to overcome the challenges of advanced cancer.

A series of studies in this Research Topic examine the molecular regulatory mechanisms of the metastatic tumor microenvironment (TME) and the development of targeted immunotherapies to address the core challenges of immune escape and therapy resistance in advanced cancers. Gao et al. reviewed multi-omics findings on the cellular composition, signaling pathways, immune landscape, and metabolic rewiring within the metastatic TME, providing a comprehensive framework for using integrative omics data to guide personalized immunotherapeutic and targeted strategies. In colorectal cancer (CRC), Wang et al. reframed antibody-drug conjugates (ADCs) as immuno-oncology agents, demonstrating that payloads which induce immunogenic cell death or pyroptosis can convert the "cold" microsatellite-stable (MSS) CRC TME into an immunologically "hot" state, thereby synergizing with checkpoint inhibitors to overcome therapeutic resistance. Complementing this, Yang et al. identified the CCL28-STAT3-PLAC8 axis in CRC, showing that CCL28 activates STAT3 signaling to upregulate PLAC8, which in turn drives epithelial-mesenchymal transition (EMT) and metastasis; PLAC8 was also identified as an independent prognostic factor in CRC patients. Beyond CRC, Zhao et al. summarized the immunomodulatory role of γ-aminobutyric acid (GABA) in the TME, detailing how it regulates tumor-associated macrophages, CD8+ T cells, and dendritic cells to promote immune escape and immunotherapy resistance across multiple cancer types. In head and neck squamous cell carcinoma (HNSCC), Zhao et al. proposed a "Trinity" immune evasion network comprising metabolic reprogramming, stromal cell dysfunction, and epigenetic remodeling. Based on single-cell sequencing data, they further advanced a "lineage plasticity-driven immune adaptation" paradigm, offering novel insights into the immune escape mechanisms of HNSCC. Collectively, these studies delineate the complex regulatory networks of the metastatic TME and propose actionable immunotherapeutic strategies, laying a solid mechanistic foundation for transforming the treatment of advanced cancers.

Another group of studies focuses on constructing prognostic models and validating key biomarkers for advanced cancers by leveraging multi-omics data and machine learning to enhance prognostic precision and identify potential therapeutic targets. In breast cancer, Feng et al. identified 753 differentially expressed sodium-overload-related genes (DESORGs), built a prognostic ridge regression model centered on IFNG, and validated NR1H3 as a protective biomarker. For hepatocellular carcinoma (HCC), Gao et al. developed a stemness- and hypoxia-related prognostic index (SHRPI) using random forest and Cox regression analyses. They identified G6PD as a key regulator of hypoxia-driven cancer stemness, demonstrating that it interacts with HIF-1α to form a positive feedback loop under hypoxic conditions; they also proposed BI2536 as a promising therapeutic for high-SHRPI patients. In colorectal cancer (CRC), Zheng et al. established a lymph node-independent metastasis gene (LIMG) signature using data-independent acquisition mass spectrometry (DIA-MS) and machine learning, pinpointing ITGA11 as a key driver of early metastasis. For cervical cancer, Qin et al. integrated transcriptomic, mutational, and clinical data from The Cancer Genome Atlas (TCGA) and Gene Expression Omnibus (GEO) to construct a prognostic model. This model included high-risk biomarkers (EZH2, PCNA, BIRC5) and protective factors (CD34, ROBO4, CXCL12), and predicted greater sensitivity to Afuresertib and Venetoclax in high-risk patients. Additionally, Wang et al. combined a retrospective study with Mendelian randomization analysis, revealing that sarcopenia is associated with a poor prognosis in advanced CRC patients treated with fruquintinib and identifying the SYK gene as a key mediator of this treatment-associated sarcopenia. Collectively, these studies establish reliable prognostic tools and pinpoint critical molecular targets, thereby laying a foundation for personalized risk stratification and targeted therapy in advanced cancers.

A significant portion of the included studies is dedicated to developing non-invasive diagnostic and predictive tools and to optimizing clinical regimens, addressing the need to minimize invasive procedures and improve therapeutic efficacy. In lung cancer, Liu et al. developed a radiomics framework that integrated longitudinal CT tumor growth kinetics with deep learning to derive an Immune Evasion Score (IES). This score non-invasively predicts PD-L1 expression (AUC = 0.85), CD8+ T-cell exclusion, and immunotherapy response with high accuracy. For breast ductal carcinoma *in situ* (DCIS), Sha et al. created an interpretable Gradient Boosting Machine (GBM) model that combines mammographic deep learning features with clinicopathological data, achieving an AUC of 0.918 for predicting recurrence more than five years after lumpectomy; the mammographic signature, Ki-67 index, and histological grade were key predictors. In a related study, Pan et al. used a DCE-MRI radiomics model based on logistic regression to predict STAT3

expression in breast cancer. They found that high radiomics scores correlated with elevated STAT3 expression, longer overall survival, and an enhanced immune response, offering a non-invasive method for assessing STAT3-related tumor microenvironment features. For differentiated thyroid carcinoma (DTC), Wen et al. evaluated serological indicators and the pan-immune-inflammation value (PIV), demonstrating that a panel including TSH, FT4, Tg, and PIV achieved an AUC of 0.860 for diagnosis, underscoring PIV's potential as a novel immune-inflammatory biomarker. In localized prostate cancer, Xu et al. used propensity score matching to compare high-dose and standard-dose stereotactic body radiotherapy (SBRT), finding that dose escalation did not significantly improve overall, cancer-specific, or biochemical progression-free survival, despite providing better local control. In CRC patients receiving neoadjuvant radiotherapy, Zhang et al. investigated radiation-induced intestinal barrier damage, observing impaired mucosal structure, elevated inflammatory factors in tissue and serum, and altered salivary metabolites. These findings inform the optimal timing for post-radiotherapy surgery. Another study by Zhang et al., combining retrospective analysis with meta-analysis, established that a high baseline spleen volume and an increase in volume during immune checkpoint inhibitor (ICI) therapy are independent predictors of poor overall and progression-free survival in HCC patients, providing a simple, imaging-based prognostic indicator for ICI therapy. Collectively, these non-invasive tools and optimized strategies help bridge the translational gap between basic research and clinical application, enhancing the accuracy of decision-making and the safety of interventions for advanced cancers.

A unique study in this Research Topic investigates precision therapy for uveal melanoma (UM) by integrating single-cell omics with materials science to address the disease's high metastatic potential and poor prognosis. Fu et al. employed single-cell RNA sequencing (scRNA-seq), single-cell ATAC-seq (scATAC-seq), and spatial transcriptomics to characterize UM's tumor heterogeneity, immunosuppressive tumor microenvironment (TME), and key molecular drivers—including novel macrophage subsets, senescent endothelial cells, and non-canonical immune checkpoints. Building on these omics insights, the authors integrated advances from materials science and biomedical engineering, demonstrating how engineered nanocarriers, biodegradable implants, and advanced gene therapy vectors could facilitate targeted drug delivery and genetic modulation tailored to the eye's unique anatomy and immune privilege. The study further cataloged validated molecular targets for UM and proposed an interdisciplinary framework combining targeted therapies, immunomodulation, minimally invasive devices, and engineered delivery systems. This integrative approach transcends conventional oncology research boundaries, presenting a new paradigm for developing precision therapies for cancers with significant metastatic potential and unique anatomical constraints, while providing a blueprint for bench-to-bedside translation in UM.

The studies in this Research Topic collectively demonstrate the transformative power of multi-omics technologies in deciphering the metastatic tumor microenvironment (TME). By identifying novel molecular pathways and prognostic signatures and by developing non-invasive diagnostic tools and precision therapies, these works significantly advance our understanding of metastatic mechanisms and their clinical translation. Key advancements include the integration of multi-omics data with machine learning for robust modeling, the discovery of context-specific therapeutic targets, and cross-disciplinary synergy with materials science for targeted drug delivery. Notably, several studies highlight the critical role of the immunosuppressive TME in therapy resistance, underscoring the necessity for combination strategies that target both malignant cells and their microenvironment.

Future research should prioritize the large-scale validation of candidate biomarkers and targets, the development of real-time monitoring tools for the metastatic tumor microenvironment (TME), and clinical trials for multi-targeted combination therapies (8, 9). Furthermore, addressing the inter- and intratumoral heterogeneity of metastatic lesions is essential for advancing personalized medicine (10). We anticipate that the insights from this Research Topic will catalyze innovation in molecular targeting and immunotherapy, ultimately improving outcomes for patients with advanced cancer.

Author contributions

XL: Writing – original draft, Writing – review & editing. QW: Writing – original draft, Writing – review & editing. YM: Writing – original draft, Writing – review & editing. XX: Writing – original draft, Writing – review & editing. XZ: Writing – original draft, Writing – review & editing. HT: Writing – original draft, Writing – review & editing. DG: Writing – original draft, Writing – review & editing. CW: Writing – original draft, Writing – review & editing.

Funding

The author(s) declared that financial support was received for this work and/or its publication. This work was financially supported by the National Natural Science Foundation of China (NSFC) Project under Grant Number 82573219 (CW) and the Shanghai Putuo District Health System Scientific and Technological Innovation Project under Grant Number ptkwws202422 (XZ).

Acknowledgments

We would like to express our sincere thanks to all the authors who submitted their study to the present Research Topic and the reviewers who evaluated the manuscripts. Their efforts help us to communicate current knowledge under this topic to a worldwide audience.

Conflict of interest

The author(s) declared that this work was conducted in the absence of any commercial or financial relationships that could be construed as a potential conflict of interest.

The authors CW, QW, HT, XX and DG declared that they were an editorial board member of Frontiers, at the time of submission. This had no impact on the peer review process and the final decision.

Generative AI statement

The author(s) declared that generative AI was not used in the creation of this manuscript.

Any alternative text (alt text) provided alongside figures in this article has been generated by Frontiers with the support of artificial intelligence and reasonable efforts have been made to ensure accuracy, including review by the authors wherever possible. If you identify any issues, please contact us.

Publisher's note

All claims expressed in this article are solely those of the authors and do not necessarily represent those of their affiliated organizations, or those of the publisher, the editors and the reviewers. Any product that may be evaluated in this article, or claim that may be made by its manufacturer, is not guaranteed or endorsed by the publisher.

References

1. Shi X, Wang X, Yao W, Shi D, Shao X, Lu Z, et al. Mechanism insights and therapeutic intervention of tumor metastasis: latest developments and perspectives. *Signal Transduct Target Ther*. (2024) 9:192. doi: 10.1038/s41392-024-01885-2

2. Boxer E, Feigin N, Tschernichovsky R, Darnell NG, Greenwald AR, Hoefflin R, et al. Emerging clinical applications of single-cell RNA sequencing in oncology. *Nat Rev Clin Oncol*. (2025) 22:315–26. doi: 10.1038/s41571-025-01003-3

3. Zhang H, Fan J, Kong D, Sun Y, Zhang Q, Xiang R, et al. Immunometabolism: crosstalk with tumor metabolism and implications for cancer immunotherapy. *Mol Cancer*. (2025) 24:249. doi: 10.1186/s12943-025-02460-1

4. Xie J, Liu M, Deng X, Tang Y, Zheng S, Ou X, et al. Gut microbiota reshapes cancer immunotherapy efficacy: Mechanisms and therapeutic strategies. *Imeta*. (2024) 3:e156. doi: 10.1002/imt2.156

5. Zhou Z, Lu ZR. Molecular imaging of the tumor microenvironment. *Adv Drug Delivery Rev*. (2017) 113:24–48. doi: 10.1016/j.addr.2016.07.012

6. Xie J, Liu W, Deng X, Wang H, Ou X, An X, et al. Paracrine orchestration of tumor microenvironment remodeling induced by GLO1 potentiates lymph node metastasis in breast cancer. *Adv Sci (Weinh)*. (2025) 12:e00722. doi: 10.1002/advs.202500722

7. Li Z, Li J, Bai X, Huang X, Wang Q. Tumor microenvironment as a complex milieu driving cancer progression: a mini review. *Clin Transl Oncol*. (2025) 27:1943–52. doi: 10.1007/s12094-024-03697-w

8. Deng X, Yan Y, Zhan Z, Xie J, Tang H, Zou Y, et al. A glimpse into the future: Integrating artificial intelligence for precision HER2-positive breast cancer management. *iMetaOmics*. (2024) 1:e19. doi: 10.1002/imo2.19

9. Bejarano L, Jordao MJC, Joyce JA. Therapeutic targeting of the tumor microenvironment. *Cancer Discov*. (2021) 11:933–59. doi: 10.1158/2159-8290.CD-20-1808

10. Hu X, Deng X, Xie J, Tang H, Zou Y. Heterogeneous PD-L1 expression in metastases impacts immunotherapy response. *EBioMedicine*. (2023) 97:104816. doi: 10.1016/j.ebiom.2023.104816

frontiers | Frontiers in Immunology

TYPE Original Research
PUBLISHED 01 April 2025
DOI 10.3389/fimmu.2025.1569088

Check for updates

OPEN ACCESS

EDITED BY
Hailin Tang,
Sun Yat-sen University Cancer Center (SYSUCC), China

REVIEWED BY
Qihang Yuan,
Dalian Medical University, China
Jian Liu,
Qingpu Branch of Zhongshan Hospital affiliated to Fudan University, China
Longbin Wang,
Deutsches Zentrum für Neurodegenerative Erkrankungen, Germany

*CORRESPONDENCE
Ruixin Wu
szy_wuruixin@shutcm.edu.cn
Chang-Sheng Dong
csdong@shutcm.edu.cn

†These authors have contributed equally to this work

RECEIVED 31 January 2025
ACCEPTED 07 March 2025
PUBLISHED 01 April 2025

CITATION
Zhang J, Zhang X, Wu R and Dong C-S (2025) Unveiling purine metabolism dysregulation orchestrated immunosuppression in advanced pancreatic cancer and concentrating on the central role of NT5E. *Front. Immunol.* 16:1569088. doi: 10.3389/fimmu.2025.1569088

COPYRIGHT
© 2025 Zhang, Zhang, Wu and Dong. This is an open-access article distributed under the terms of the Creative Commons Attribution License (CC BY). The use, distribution or reproduction in other forums is permitted, provided the original author(s) and the copyright owner(s) are credited and that the original publication in this journal is cited, in accordance with accepted academic practice. No use, distribution or reproduction is permitted which does not comply with these terms.

Unveiling purine metabolism dysregulation orchestrated immunosuppression in advanced pancreatic cancer and concentrating on the central role of NT5E

Junqian Zhang[1†], Xiaobo Zhang[2†], Ruixin Wu[3*] and Chang-Sheng Dong[4*]

[1]Henan Key Laboratory of Cancer Epigenetics; Cancer Institute, The First Affiliated Hospital, and College of Clinical Medicine of Henan University of Science and Technology, Luoyang, China, [2]Department of Hepatobiliary Surgery, The First Affiliated Hospital, and College of Clinical Medicine of Henan University of Science and Technology, Luoyang, China, [3]Preclinical Department, Shanghai Municipal Hospital of Traditional Chinese Medicine, Shanghai University of Traditional Chinese Medicine, Shanghai, China, [4]Cancer Institute of Traditional Chinese Medicine/Department of Oncology, Longhua Hospital, Shanghai University of Traditional Chinese Medicine, Shanghai, China

Background: The dismal efficacy of immunotherapy for Pancreatic cancer (PC) can be predominantly ascribed to its distinctive cold-tumor properties. The by-products of purine metabolic reprogramming are extensively engaged in tumor immune modulation, influencing the functions and recruitment of immune cells and molding an immune microenvironment that is propitious for tumor growth.

Methods: We harnessed single-cell transcriptomics and spatial transcriptomics to concurrently analyze the purine metabolism (PM) features of the PC microenvironment. We quantitatively appraised the PM traits of diverse cell subsets via scoring algorithms such as AUCell and Ucell. Moreover, cell development and cell-cell interaction analysis elucidated the alterations in TME induced by PM dysregulation. Additionally, we defined the PM disorder characteristics of PC patients and utilized this to assess the immune phenotypes and prognoses of the patient population. Also, we identified the crucial intermediate genes that impact PM reprogramming and the establishment of an immunosuppressive environment within the TME of PC, and validated them through spatial sectioning and cell co-culture experiments.

Results: Multi - dimensional transcriptome data elucidated the unique heterogeneity of PM in the PC microenvironment, which manifested that tumor cells and fibroblasts demonstrating higher PM scores in the TME. Cellchat analysis revealed that malignant cells with elevated PM expression were concomitantly associated with frequent interactions with CAFs as well as high expression of ligand-receptor pairs and transcription factors. Spatial data further corroborated this finding. Furthermore, the newly constructed PM disorder criteria indicated that patients with high PM levels were associated with a lack of response to immunotherapy and an immunosuppressive microenvironment. Finally, this study identified the singular role of NT5E in the

immunosuppression resulting from PM reprogramming in PC. CCK8 and invasion experiments following the co-culture model demonstrated that intervention targeting NT5E could reverse the augmented malignancy of PC induced by co-cultured CAFs. NT5E is potentially a key target for reversing the "stiff-cancer" characteristics of PC.

Conclusion: This study demonstrates that PM metabolic disorders could impinge upon tumor immunotherapy and exacerbate the immunosuppression engendered by the progression of PC fibrosis. Therapeutic strategies targeting PM or NT5E may offer a ray of hope for patients with advanced PDAC.

KEYWORDS

purine metabolism, immunotherapy, CAFs, NT5E, pancreatic cancer

1 Introduction

Among all solid tumors, PC exhibits one of the gravest prognoses. It is characterized by highly intricate genomic features. The prevalence of KRAS mutations exceeds 90%, and mutations in genes like TP53, SMAD4, and CDKN2A are also rather common. Moreover, pancreatic ductal adenocarcinoma (PDAC) tissue is replete with a substantial amount of dense stroma, which consists of cancer-associated fibroblasts (CAFs), extracellular matrix (ECM), vascular endothelial cells, and immune cells (1–3). This structure assumes a pivotal role in tumor development. Functioning as a formidable "barrier," it impedes the infiltration of immune cells into tumor cells, thereby hampering the immune system from exerting its normal anti-tumor function (4). Simultaneously, it exerts immunosuppressive effects, capable of suppressing the activity of immune cells and establishing an "immune-privileged zone" for tumor cells (5–7). This dense stroma is also intricately associated with treatment resistance, severely undermining the efficacy of diverse treatment modalities and enabling tumor cells to elude drug-mediated attacks (5). Immune Checkpoint Blockade (ICB) has demonstrated limited efficacy in the treatment of PDAC. PDAC is characterized by typical immune-cold tumor features, which represent one of the primary factors contributing to the meager efficacy of ICB (8–10). CAFs, being one of the principal cell components within the PDAC microenvironment, constitute 50%-80% of the tumor stroma (11, 12). Among them, iCAF plays a significant role in immunosuppression. It predominantly secretes immunosuppressive factors such as IL-6, IL-10, and CXCL12. These factors can recruit Tregs and M2-type macrophages into the tumor microenvironment while suppressing the functions of effector T cells (Teff), thus significantly attenuating the efficacy of ICB (12–14).

Tumor metabolic reprogramming constitutes a fundamental and pivotal mechanism through which cancer cells adapt to the dynamic changes within the tumor microenvironment (TME), thereby ensuring their survival and proliferation. This process is of utmost significance in the pathogenesis and progression of PDAC (15). PDAC cells display remarkable metabolic remodeling, and aberrations in glucose, glutamine, and lipid metabolism have been extensively investigated (16). Owing to their rapid proliferation, tumor cells have an escalated demand for purines. This renders the purine metabolic pathway hyperactive and transforms it into a potential crucial target for tumor therapy. In the realm of tumor treatment, intervention strategies targeting purine metabolism have exhibited certain promise. By inhibiting key enzymes involved in purine synthesis, such as phosphoribosyl pyrophosphate synthetase (PRPS), the purine supply to tumor cells can be disrupted, and their proliferation can be inhibited (17) Certain antimetabolic drugs, like methotrexate, exert their anti-tumor effects in accordance with this principle (17). Furthermore, purine metabolites are intricately involved in the regulation of the tumor immune response. Tumor cells can manipulate the functions and recruitment of immune cells by releasing purine metabolites, thereby creating an immune microenvironment that is permissive to tumor growth and progression (18). In recent years, there has been a growing interest in understanding the role of purine metabolism in the immune regulation of PDAC.

The purine metabolism pathway primarily encompasses the synthesis and degradation of adenine and guanine nucleotides. The products of this pathway serve multiple essential functions. Not only do they act as the fundamental building blocks for DNA and RNA synthesis, providing the necessary material basis for the rapid proliferation of tumor cells, but they also play a central role in energy metabolism (e.g., ATP and GTP) and signal transduction processes (e.g., cAMP and cGMP) (19). PDAC cells often upregulate the purine synthesis pathway to enhance their proliferative capacity. For instance, the overexpression of genes such as PRPS2, ATIC, PPAT, and IMPDH1 enables tumor cells to rapidly synthesize purines, thereby meeting the high demands of their continuous proliferation (20). Concurrently, this process also promotes immunosuppression. In the PDAC microenvironment, extracellular ATP secreted by tumor cells can be hydrolyzed into adenosine via the CD39/CD73 cascade. As a crucial immune-

regulatory molecule, adenosine acts on effector T cells through A2AR, inhibiting their proliferation and cytotoxicity and preventing effector T cells from effectively fulfilling their anti-tumor function (20, 21). Moreover, adenosine can induce the differentiation of M2-type macrophages, which further promotes the formation of an immunosuppressive tumor microenvironment, allowing tumor cells to evade immune surveillance and continue to survive and progress (21–23).

Consequently, delving deeply into the molecular mechanism of purine metabolism in Pancreatic cancer (PC) is of utmost significance for elucidating the pathogenesis of PC, identifying novel therapeutic targets, and developing more efficacious combination treatment strategies. To this end, this study employed the most comprehensive spatial transcriptomics and single-cell transcriptomics technologies to analyze the purine metabolism characteristics of the PC microenvironment and sought to identify the key factors regulating these relationships. It is anticipated that through precise intervention in the purine metabolic pathway, the immunosuppressive microenvironment of PC can be disrupted, and the efficacy of immunotherapy can be enhanced.

2 Methods

2.1 Data acquisition and standardized processing

In the present study, the sequencing data of TCGA-PDAC along with the corresponding clinical data were all retrieved from the UCSC Xena website (https://xenabrowser.net/). The GEO database was harnessed to obtain single-cell sequencing data of PC patients, encompassing one normal pancreatic tissue sample sourced from GSE165399 and two PC patient tissue samples from GSE154778. To guarantee the accuracy and consistency of the data, the "limma" and "sva" R packages were employed to carry out batch calibration and integration on the sequencing gene expression datasets. The "harmony" algorithm was utilized to integrate single-cell sequencing samples, thereby eliminating potential batch effects. The GeneCards database was utilized to amass the "purine metabolism" gene set, which was subsequently applied for scoring and gene screening in the ensuing research.

2.2 Identification of cell sub-populations in PC single-cell data and determination of purine metabolism criteria

The "Seurat" R package was utilized to conduct pre-processing on the scRNA-seq data. The "PercentageFeatureSet" function was employed to assess the proportion of low-quality genes within the dataset. Each cell was requisite to express a gene count ranging from 200 to 10,000, and the mitochondrial content was required to be less than 20%. Subsequent to the aforementioned screening, the "NormalizeData" function was used to standardize the scRNA-seq data. The standardized data was then converted into a Seurat object, and the "FindVariableFeatures" function was utilized to identify highly variable genes. The "RunPCA" tool was employed to scale and execute principal component analysis on this set of highly variable genes. To more effectively present the data characteristics, the data underwent dimensionality reduction and visualization through algorithms. The "FindAllMarkers" and "FindMarkers" algorithms were utilized to perform Wilcoxon tests, meticulously compare different cell types, and annotate diverse cell sub-populations in accordance with these marker genes. To evaluate the purine metabolism characteristics of the single-cell sequencing data of PC, five commonly-used algorithms were adopted, namely "AddModuleScore", "ssGSEA", "AUCell", "UCell", and "singscore". Bubble plots were utilized to visualize the purine metabolism characteristics of each individual cell.

2.3 Inference of cell developmental trajectories and analysis of cell-cell interactions

The "Monocle" R package was utilized to meticulously analyze the pseudo-time trajectories of tumor cells. The "PLOT_CELL_TRACTURE" function was employed to precisely order and visualize different cell sub-populations in accordance with the pseudo- time sequence. The "CellChat" package was used to construct a ligand-receptor-level regulatory network grounded in the PC microenvironment. The "netVisualDiffInteraction" algorithm was utilized to compare the intensity of cell-cell communication.

2.4 Processing of PC spatial sections and annotation of spatial cell sub – populations

PDAC_GSE203612 and PDAC_GSE211895 were loaded from the GEO database as validations for the spatial transcriptome sections. The "SCTransform" within the Seurat package was utilized to standardize the UMI counts. "RunPCA" was employed for dimensionality reduction and unsupervised clustering analysis. With the assistance of the "SpatialFeaturePlot" function, the visualization of subgroups and genes was accomplished. "stLearn" developed based on "Scanpy" was utilized for spatial transcriptome data analysis to determine the gene expression characteristics of cells in disparate regions and unearth the interactions and spatial distribution patterns of cells within the tumor microenvironment. "RCTD" was utilized in this study to discriminate the gene expression characteristics of different cell types such as tumor cells, immune cells, and stromal cells.

2.5 Establishment of PM criteria and evaluation of clinical characteristics

The TCGA cohort was randomly partitioned into a training set and a validation set. The R software package "survival" was utilized to perform univariate Cox regression analysis to screen out genes

that were statistically significant with respect to the prognosis of PDAC patients. Subsequently, Lasso and multivariate step-wise regression analyses were carried out to ascertain the most critical combination of factors influencing the prognosis. A PM score was computed and assigned to each PDAC patient, and patients were classified into high- risk and low-risk groups based on the median PM score. The Kaplan-Meier method was employed to understand the survival status of patients, and the ROC curve was introduced to gauge the prediction performance of the model. A column-line graph was constructed to calculate the 1, 3, 5 years overall survival rates of PDAC patients, with risk scores, age, and clinical stages incorporated as independent prognostic factors.

2.6 Correlation analysis between PM score and immune characteristics

The R package "Estimate" was utilized to estimate the abundances of tumor mesenchymal and immune cells in PC patients and concurrently evaluate tumor purity. The results of seven methods for evaluating immune infiltration were procured from the TIMER 2.0 database. ssGSEA was utilized to score specific characteristic gene sets to understand the activity levels of different immune cell types within the samples. Additionally, the tumor stem cell index obtained from prior studies was used to quantify the stem cell characteristics of tumor samples. To evaluate the likelihood of immune escape in tumor samples, we adopted the TIDE calculation framework (http://tide.dfci.harvard.edu/) to assess the immune escape status of tumor samples. Moreover, "ggplot2" was utilized to present the data of PM score and TMB in the form of scatter plots and line graphs.

2.7 Cell culture and establishment of co-culture system

In this study, the PC cells (PANC-1) utilized in the experiment were procured from the American Type Culture Collection (ATCC), and the human pancreatic tumor fibroblasts (immortalized) were obtained from the Chinese Academy of Sciences. Both types of cells were cultured in PRMI1640 medium supplemented with 10% high-quality fetal bovine serum. Subsequent to operations such as passage and stable transfection, the aforementioned cells were co-cultured in a transwell mold to observe the survival-related effects of inter-cellular signaling factors on the two types of cells.

2.8 sh-NT5E cell transfection

The sh-LY6D knockdown plasmid from GenePharma Company was selected. The cells to be treated were inoculated in a 6-well plate. When the cell confluence reached 50%, Lipofectamine 3000RNAiMAX was utilized for the transfection procedure.

2.9 CCK-8 cell viability measurement experiment

The cells were prepared into a homogeneous suspension and precisely inoculated into a 96- well plate at a density of 5×10^3 cells per well and incubated for 24 hours. Subsequently, 10 μL of CCK-8 labeling agent was added to each well. After the addition of the labeling agent, to avert the influence of light on the reagent, the 96-well plate was placed in a 37°C environment and incubated in the dark for an additional 2 hours. Thereafter, a microplate reader was used to continuously measure the absorbance values at 450nm, and the alteration in absorbance was employed to mirror the cell viability.

2.10 Cell invasion experiment

The PANC-1 cells were pre-treated with starvation to render the cells in a relatively quiescent state. Post-treatment, the cell suspension was added to the upper chamber containing Costar, and a serum-containing medium was added to the lower chamber. Subsequently, it was placed in an incubator for 48 hours to afford the cells sufficient time for invasion activities. After the experiment, the cells were fixed with 4% paraformaldehyde, stained with crystal violet, and then subjected to counting and analysis.

2.11 Statistical analysis

All data calculation steps involved in this article were carried out using the 64-bit R version 4.2 and its accompanying publicly available R packages. The specific statistical verification rules were defined during the development process of the R packages. In this study, an asterisk (*) represents $P < 0.05$, which is considered to be statistically significant.

3 Results

3.1 Comparison of purine metabolism characteristics in the PC microenvironment via multiple algorithms

Following quality control and dimensionality reduction of paired samples from three PC patients, the present study clustered into the subsequent key cell clusters: mononuclear macrophages, plasma cells, epithelial cells, T/NK cells, B cells, endothelial cells, fibroblasts, plasma cells, and pancreatic stellate cells (Figures 1A–E). The cellular composition within the PC microenvironment across different patients exhibited relative equilibrium, and the specifically-expressed marker genes of diverse cell clusters are presented in (Figures 1F, G). To comprehensively analyze the purine metabolism characteristics in the PC microenvironment, the current study utilized five single-cell

10.3389/fimmu.2025.1569088

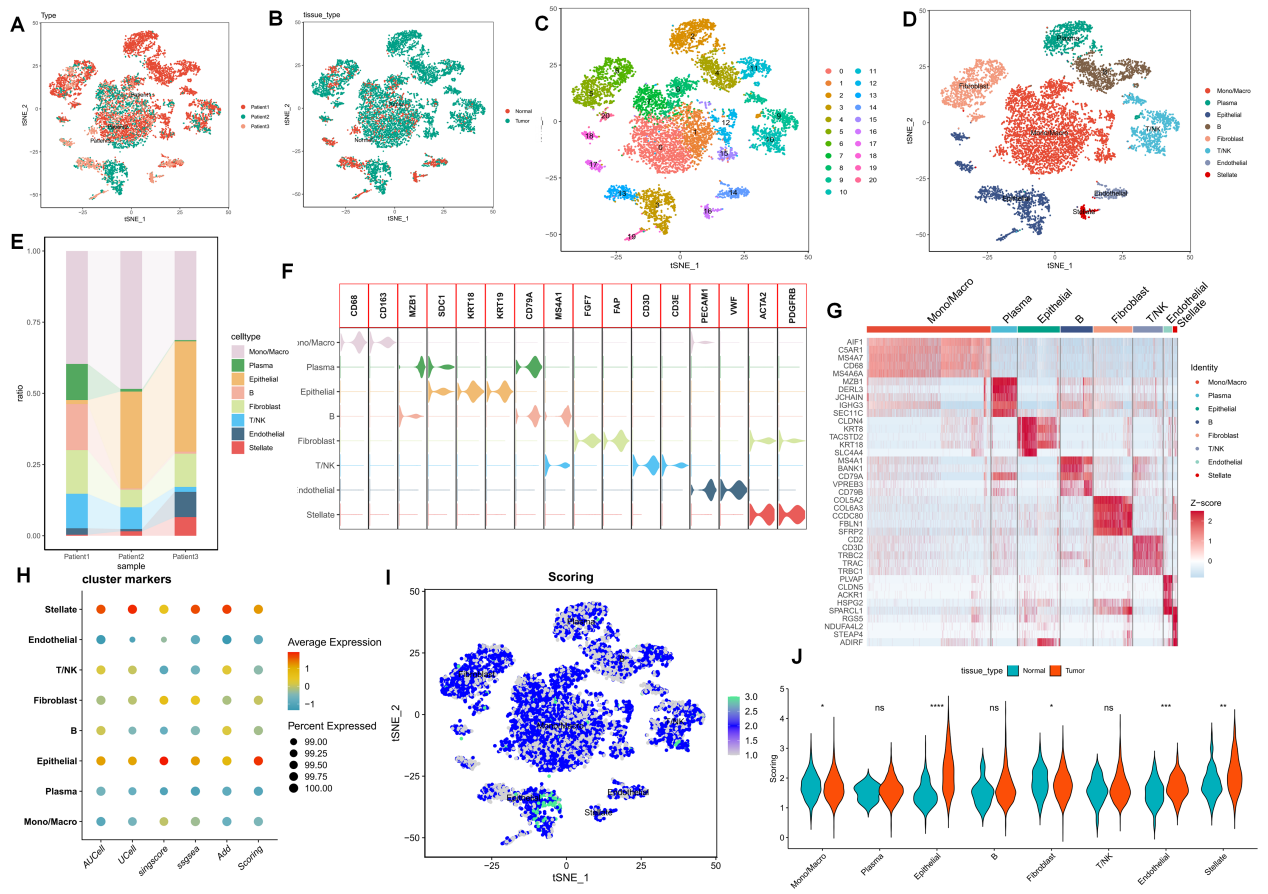

FIGURE 1
(A-E) The UMAP plot elucidates the clustering pattern of the samples. **(F, G)** The expression profiles of specifically-expressed marker genes within diverse cell clusters are presented. **(H)** Five single-cell scoring tools are employed to quantitatively assess the PM characteristics of distinct cell clusters. **(I, J)** A comparison of PMscores between tumor samples and normal samples is conducted. p values < 0.05 (*p < 0.05) were considered significant, where **p < 0.01, ***p < 0.001, and ****p < 0.0001, ns (non- significant).

scoring tools, namely AddModuleScore, UCell, GSVA, AUCell, and singscore, for assessment. The scores assigned to different cells demonstrated variability. Overall, endothelial cells and stellate cells within the PC cell microenvironment manifested higher purine metabolism scores, which we hereinafter referred to as PMscore (Figure 1H). Subsequently, a comparison of PMscores between tumor and normal samples was conducted. The findings revealed disparities in endothelial cells, epithelial cells, stellate cells, and macrophages, with epithelial and stellate cells showing distinct differences between normal and cancerous samples (Figures 1I, J).

3.2 Imbalance in cell differentiation and interaction induced by abnormal purine metabolism

To gain a more lucid understanding of the impact of purine metabolism on the development of microenvironment cells, this study initially performed cell trajectory analysis on distinct epithelial cell clusters subsequent to dimensionality reduction. The epithelial cell states were classified into five distinct states, with cluster 18 representing the endpoint of cell differentiation (Figure 2A). Subsequently, the expression of purine-metabolism-related genes displaying the highest differential expression at various developmental stages of these cell clusters was depicted in a heat map. The results indicated that different purine-metabolism genes also underwent changes during the process of cell differentiation (Figure 2B). Further, epithelial cells were segregated into a PMS low group and a PMS high group based on the median PMS of epithelial cells in tumor tissues, and common signaling pathways were contrasted (Figure 2C). It was discerned that common signaling pathways such as the TNF signaling pathway and the HIF-1 signaling pathway exhibited significant differences between fibroblasts and stellate cells in different PMS groups, suggesting that this might represent a pivotal factor influencing the crosstalk among these three cell groups. Consequently, our focus shifted to cell-cell interactions. The results indicated that epithelial cells with high PMS received an increased number of signals from fibroblasts and stellate cells. Correspondingly, these cells transmitted more signals to fibroblasts, stellate cells, and T cells (Figure 2D). The ligand-receptor relationships within this process were presented, with the NECTIN3-NECTIN2 signal and the WNT7B-FZD1 emerging as the most prominent ligand-receptor relationships in the interaction between these two cell groups (Figures 2E, F). To further enrich the potential cell-mechanism network, we identified two transcription factors, CTNNB1 and LEF1, which may be implicated

10.3389/fimmu.2025.1569088

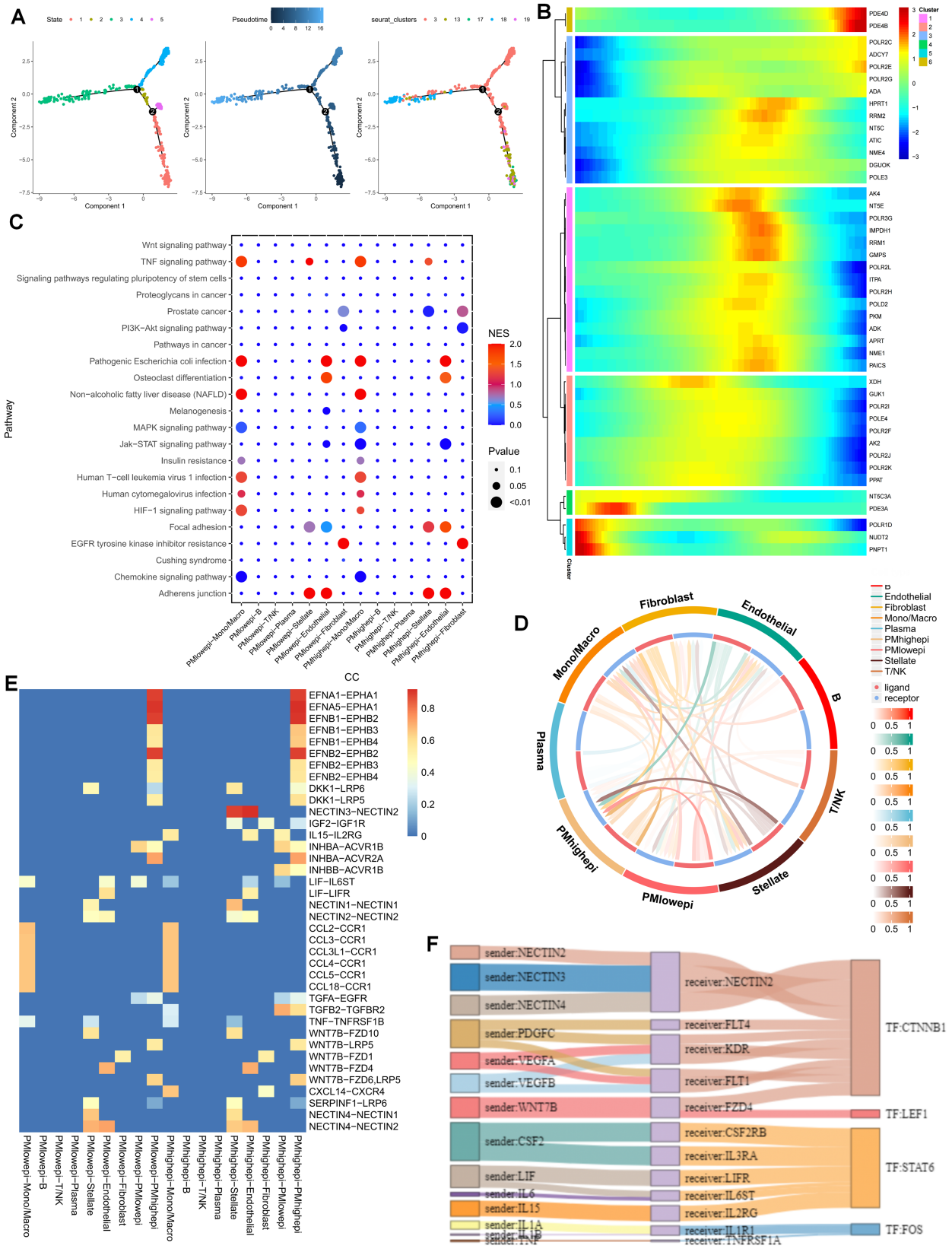

FIGURE 2
(A) Cell trajectory analysis was executed on epithelial cell clusters. **(B)** A heatmap illustrates that different purine-metabolism genes are also in a dynamic state during the process of cell differentiation. **(C)** A comparison of common signaling pathways between the PMS low group and the PMS high group is carried out. **(D)** A comparison of cell-cell interactions between the PMS low group and the PMS high group is performed. **(E, F)** A comparison of ligand-receptor relationships between the PMS low group and the PMS high group is presented.

in regulating the interaction between these two cell groups and could potentially serve as a crucial means of restoring the purine metabolism imbalance in the PC microenvironment in the future (Figures 2E, F).

3.3 Unveiling cell disorders resulting from purine metabolism imbalance from a spatial perspective

As previously mentioned, the PDAC tumor microenvironment experiences alterations in cell communication and differentiation in the presence of purine-metabolism imbalance. To more precisely delineate this characteristic, we utilized spatial transcriptome sections to outline this aspect. Initially, six distinct cell sub-populations were identified in the PC spatial sections, primarily facilitated by the joint annotation of single-cell data (Figures 3A, B). Genes of utmost significance in purine metabolism exhibited varying expressions at different spatial locations. Genes such as PKM and GUK1 demonstrated substantial differences across different clusters, indicating their potential involvement in the tandem interaction between spatial spots (Figure 3C). To comprehensively assess the metabolic disorders within the tumor microenvironment, we further employed the "scMetabolism" R package to analyze the metabolic activities in different regions. The results revealed a close association between Cluster 6 and purine-metabolism activity (Figure 3D). Additionally, we observed that this region was concomitantly accompanied by active sphingolipid metabolism and taurine metabolism (Figures 3E, F). From a spatial perspective, upon further examination of the developmental trajectories of cell sub-populations, cells in region 6 with pronounced purine metabolism were found to be undergoing differentiation towards region 3 and region 8 (Figures 3G–I). We further utilized the RCTD algorithm to map cells onto the spatial framework. The results indicated that epithelial cells with high PMS were diffusely distributed within the tumor microenvironment of PC, a characteristic associated with the unique "stiff-cancer" phenotype of PC, suggesting that high purine metabolism may offer a direction for overcoming this phenotype (Figure 3J). Subsequently, we quantitatively analyzed the relationships between different cell clusters using spatial-location interaction. The results corroborated previous findings, with

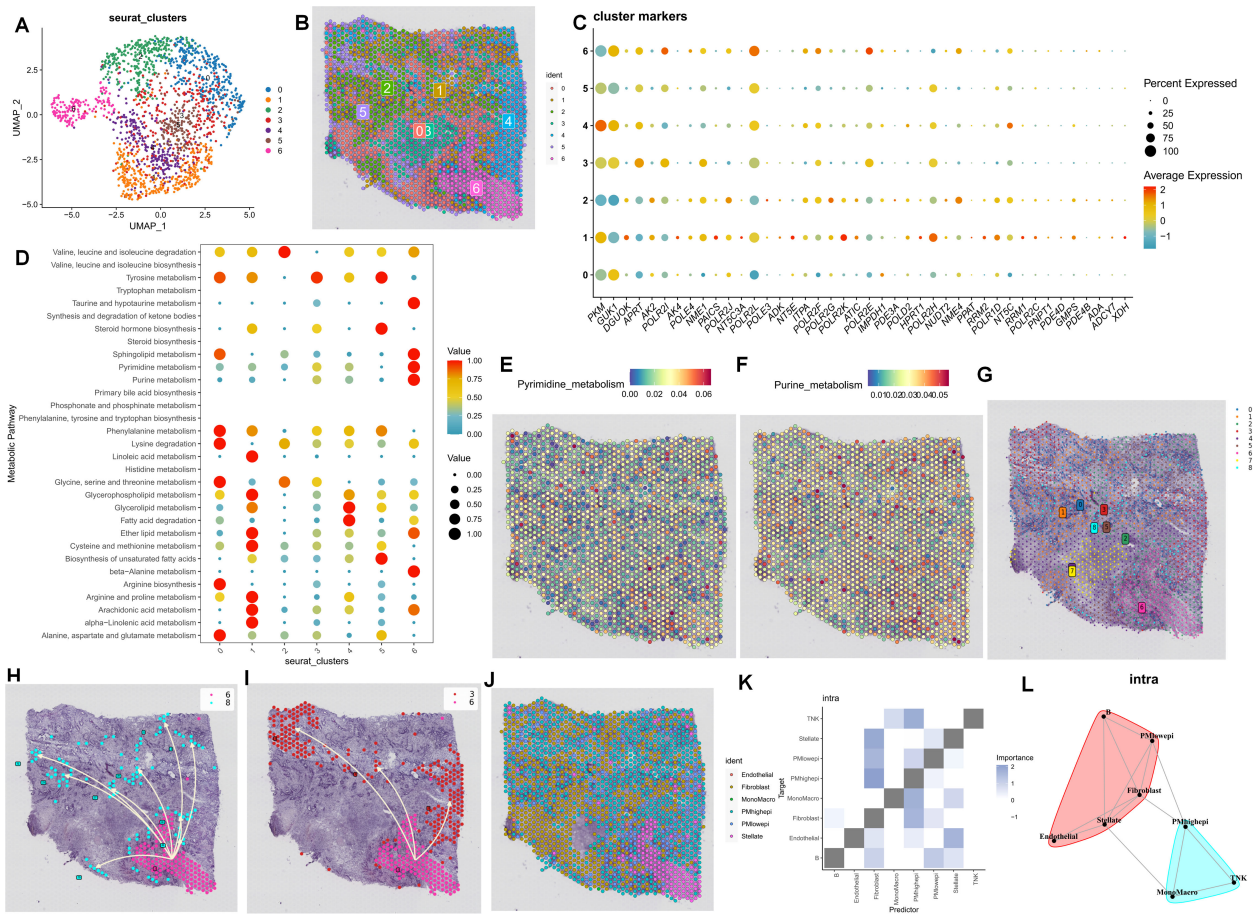

FIGURE 3
(A, B) Six distinct cell sub-populations were identified through the joint annotation of spatial transcriptome sections and single-cell data. **(C)** The expression patterns of the most significant genes in purine metabolism at various spatial spots are shown. **(D)** The metabolic activities in different regions are analyzed. **(E, F)** Heatmaps depicting sphingolipid metabolism and taurine metabolism in spatial sections are presented. **(G-I)** The developmental trajectories of cell sub-populations from a spatial perspective are investigated. **(J-L)** Spatial-location interaction is utilized to quantitatively analyze the relationships between different cell clusters.

10.3389/fimmu.2025.1569088

epithelial cells having high PMS showing a significant correlation with fibroblasts (Figures 3K, L).

3.4 Construction of the purine-metabolism disorder index PMS for observing the clinical characteristics of the PDAC population

The foregoing clues suggest that purine metabolism may instigate disorders within the PDAC tumor microenvironment. Consequently, we constructed a purine-metabolism disorder index to investigate the purine-metabolism disorder characteristics of the PC patient population. The purine-metabolism gene set was intersected with the differential genes of epithelial cells exhibiting high and low PMS expressions. Subsequently, lasso regression analysis was performed on the 40 genes obtained following univariate COX regression analysis (Figures 4A, B). Taking into account over-fitting and other relevant factors, and narrowing the gene range for predicting OS, a 5-gene signature was constructed through Lasso-Cox regression analysis. Based on PMS, with the median serving as the cut-off point, patients were categorized into a low-PMS group and a high-PMS group. The risk plot demonstrated that, within both the training and validation groups, the OS of patients in the high-PMS group was inferior to that of patients in the low-PMS group (Figures 4C–F). Moreover, the AUC curve in this study indicated that the classification criterion based on purine-metabolism disorder could effectively predict the prognosis of PC patients (Figure 4G). This performance was further accentuated in the risk plot, which presented the detailed survival outcomes of each patient in the training set and the validation cohort (Figures 4H, I).

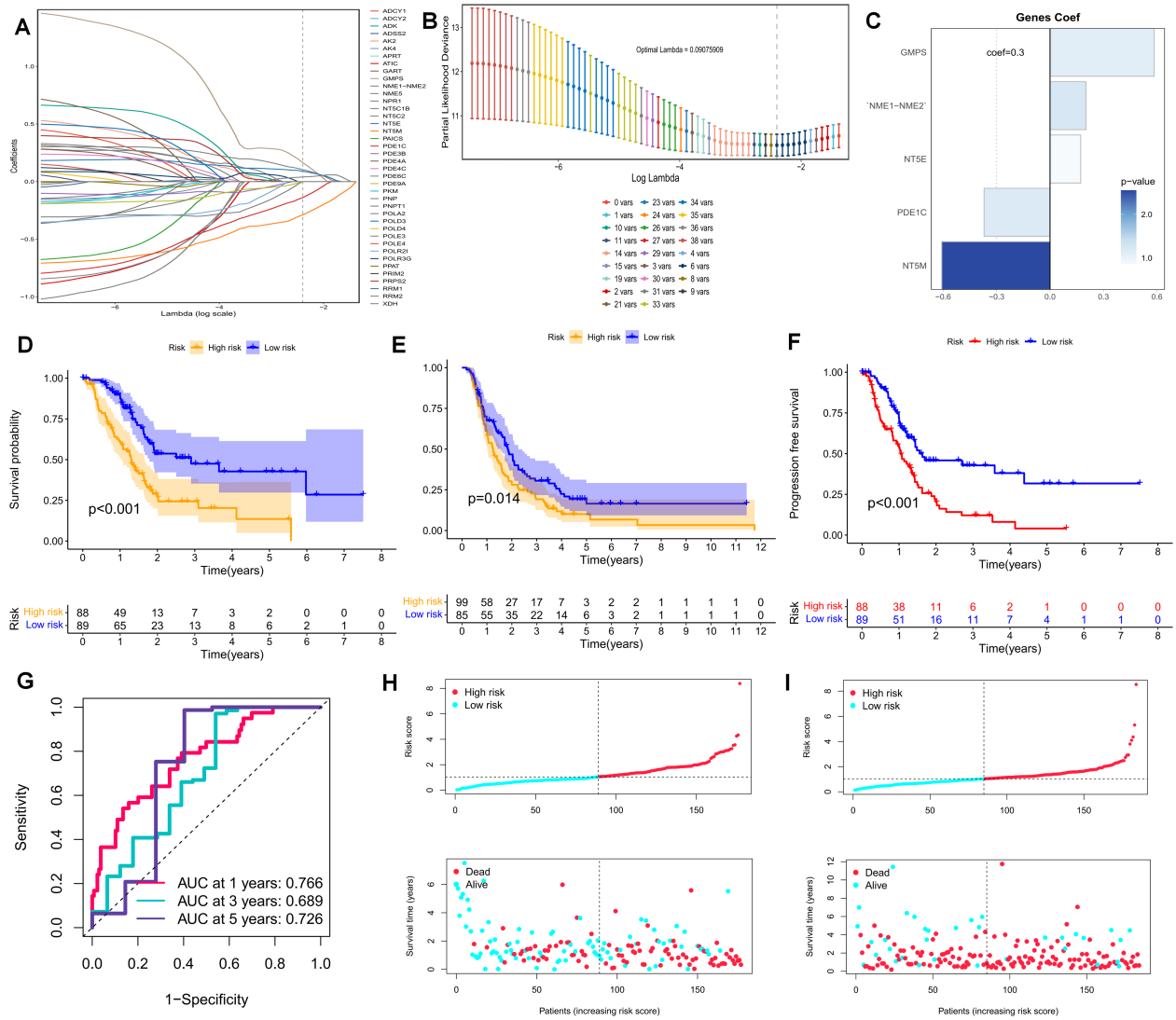

FIGURE 4
(A, B) Lasso regression analysis was performed on the 40 genes obtained subsequent to univariate COX regression analysis. **(C)** The Coef values of the model-building genes are determined. **(D, F)** The discrimination of PMS and the prognoses of patients in the validation set and the training set are evaluated. **(F)** The PFS of patients in the training set is analyzed. **(G)** The standard classification based on purine-metabolism disorder can effectively predict the AUC curve of pancreatic cancer patients. **(H, I)** The risk plots of each patient in the training set and the validation cohort are presented.

10.3389/fimmu.2025.1569088

Through a comprehensive comparison of univariate and multivariate Cox analyses, PMS was identified as an independent prognostic indicator for PDAC patients, with the area under the curve (AUC) of PMS being considerably higher than that of other clinicopathological features (Figures 5A, B). A nomogram developed for predicting the survival rates of PDAC patients at different time intervals demonstrated that PMS could yield accurate predictions (Figures 5C, D). Additionally, the DCA curve and C-index value indicated that the current nomogram constructed based on PMS provided the highest net benefit, representing an optimization of traditional models in the

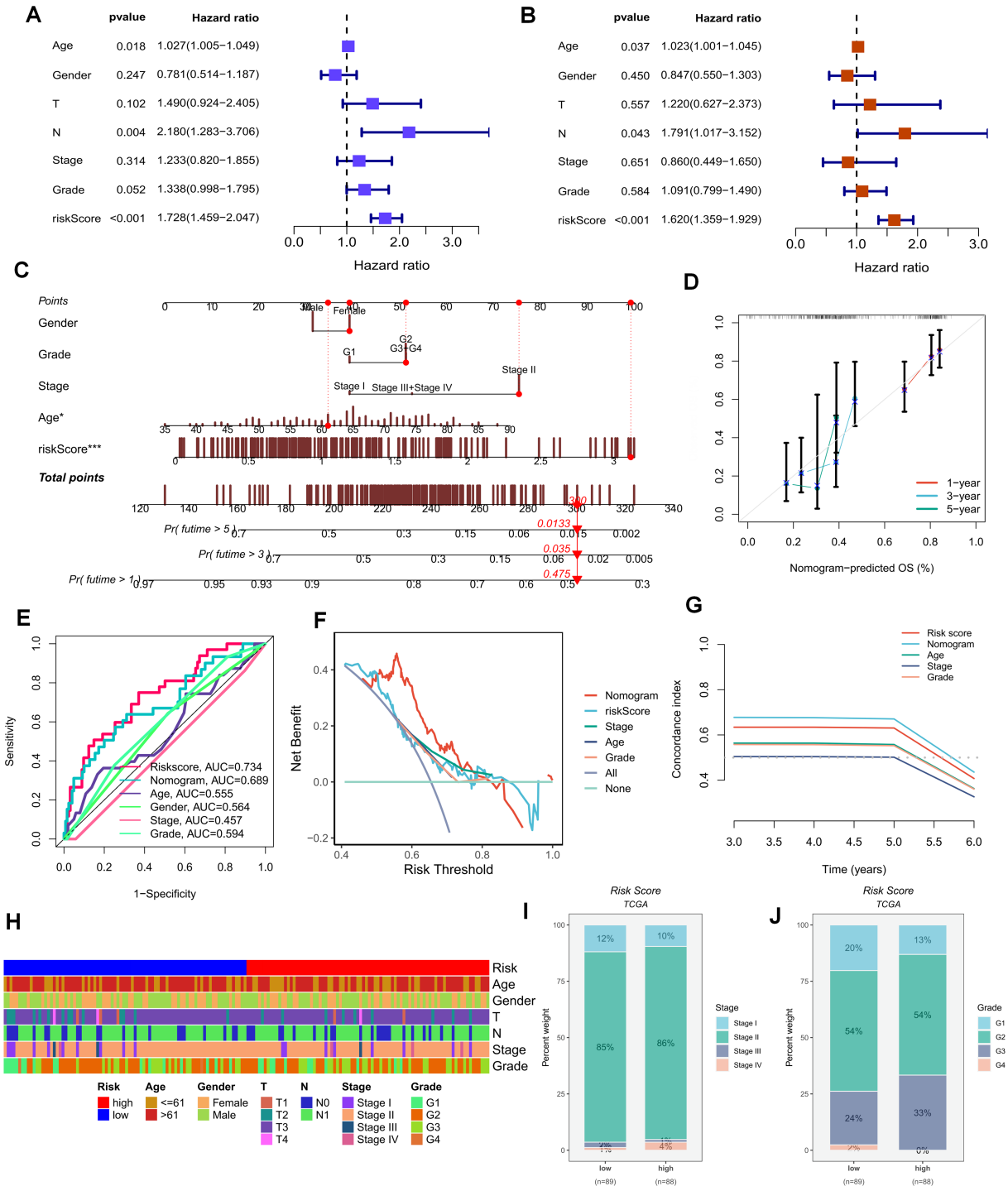

FIGURE 5
(A, B) Univariate and multivariate Cox analyses demonstrate that PMS can be utilized as an independent prognostic indicator for PAAD patients. **(C, D)** Nomograms for predicting the survival rates of PAAD patients at different time intervals are constructed. **(E–G)** The DCA curve and C-index value reveal the current nomogram constructed based on PMS. **(H)** The differences in clinical parameters between the groups of people with high and low risk scores. **(I, J)** The correlations between the risk scores and the clinical and pathological stages of the tumors.

10.3389/fimmu.2025.1569088

context of clinical decision-making (Figures 5E-G). Simultaneously, the current PMS was found to be strongly associated with clinical-stage characteristics. Specifically, patients with high PMS were frequently in the advanced stage of PDAC (Figures 5E–G).

3.5 Influence of purine-metabolism disorder on immune infiltration in PDAC patients

As previously stated, purine-metabolism disorder may disrupt the cell-composition components of the PDAC tumor microenvironment. The TME has been established as a critical determinant of patients' clinical outcomes and immunotherapy responses. Hence, this study delved deeper into the immune-cell infiltration in different PMS populations. The reliability of this aspect was enhanced through cross-validation using multiple immune-infiltration algorithms. Specifically, the low-PMS population typically exhibited heightened activation of immune-effector cells, including T cells, NK cells, and B cells (Figure 6A). Subsequently, we depicted the immune-checkpoint genes, immune scores, immune-cell infiltration, and tumor-microenvironment scores in different PMS groups via a heat map (Figure 6B). The results indicated that patients in the low-PMS group had reduced immune activation, suggesting the presence of an immunosuppressive microenvironment in this subset of patients (Figure 6B). Consequently, we considered the potential impact of immune-checkpoint molecules on patients with purine-metabolism disorders, observing that the expression levels of

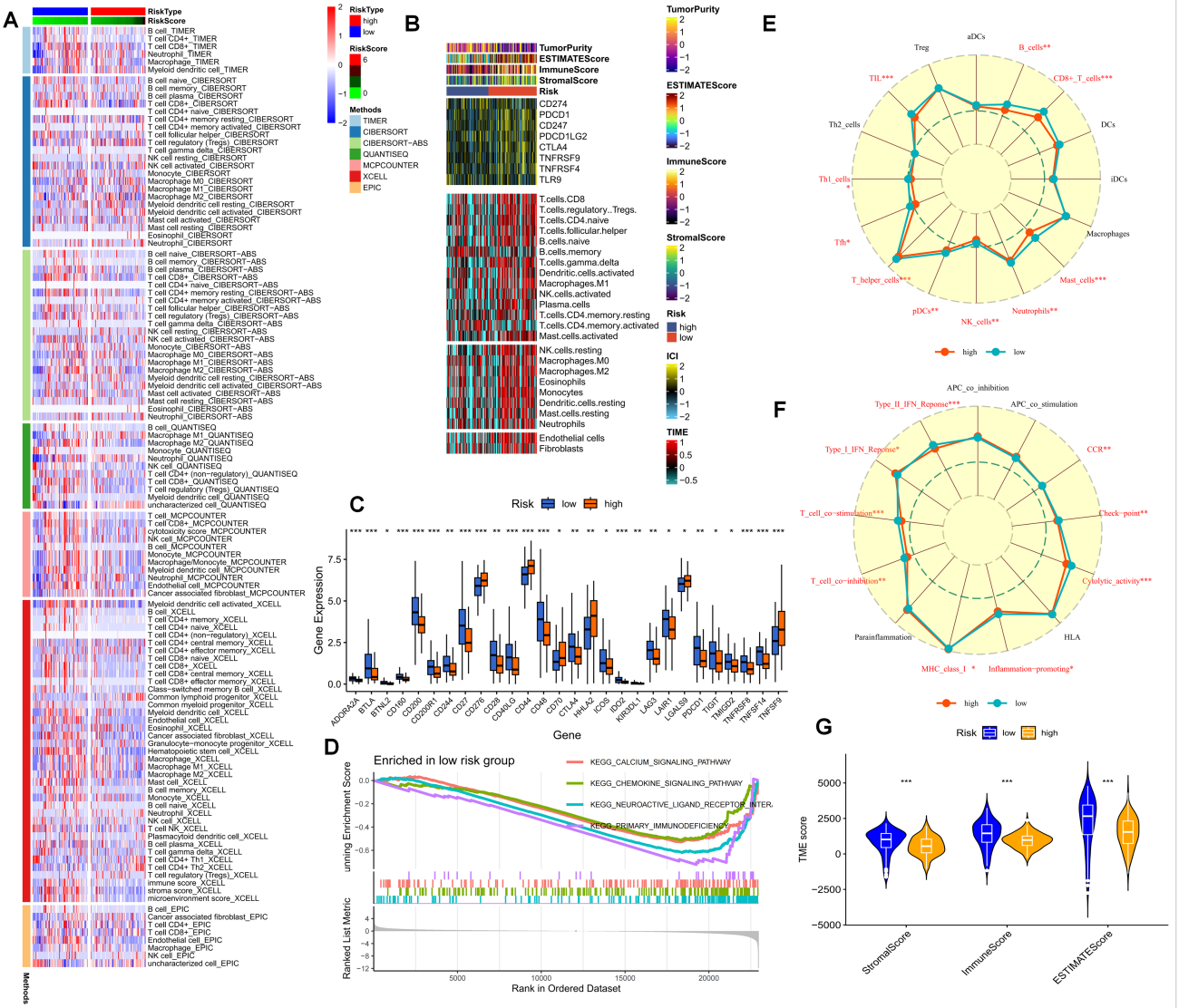

FIGURE 6
(A) The immune-cell infiltration in different PMS populations is examined. **(B)** A heatmap portrays the immune-checkpoint genes, immune scores, immune-cell infiltration, and tumor-microenvironment scores in different PMS groups. **(C)** The expression levels of immune-checkpoint molecules in the PMS low group and the PMS high group are compared. **(D)** GSEA results further indicate that high PMS is accompanied by the inhibition of immune pathways. **(E-G)** The ssGSEA method is employed to evaluate the enrichment scores of different immune-cell subsets and functions. p values < 0.05 (*p < 0.05) were considered significant, where **p < 0.01, ***p < 0.001, and ****p < 0.0001).

the vast majority of immune checkpoints were elevated in the high-PMS group (Figure 6C). Additionally, GSEA results indicated that high PMS was associated with the inhibition of immune pathways (Figure 6D). More specifically, we employed the ssGSEA method to evaluate the enrichment scores of different immune-cell subsets and functions, aiming to gain a more in-depth understanding of the relationship between the risk score and immune-related functions. The results suggested that the immune-cell infiltration scores and immune-pathway scores in the high-PMS group were significantly lower compared to those in the low-PMS group (Figures 6E–G). Overall, the above results indicated that the low-PMS group often displayed more immune-activation characteristics, as further corroborated by the immune scores, suggesting that modulating purine-metabolism disorders may provide crucial evidence for enhancing immunotherapy (Figures 6E–G).

3.6 Association of high PMS population with low response to immunotherapy

The current study posits that a higher TMB generally implies that tumor cells harbor a greater number of gene mutations, rendering them more readily recognizable by the immune system. We analyzed the distribution of the most prevalent mutated genes in PDAC patients across risk-score subgroups (Figure 7A). The high-PMS population was frequently associated with a greater number of mutations in KRAS, TP53, and SMAD4 (Figure 7A). Additionally, this subgroup exhibited more TMB mutations, with the TMB mutation level being significantly higher than that of the low-PMS population (Figure 7B). Accordingly, patients were divided into four groups based on the median TMB and PMS values. The results indicated that the OS of patients with high PMS and high TMB was relatively poor, which we attribute to the more pronounced immunosuppression in high-PMS patients (Figures 7C–E). Moreover, PMS exhibited substantial and meaningful associations with numerous key stages of the tumor-immune cycle (Figure 7F). Subsequently, we conducted a correlation analysis involving model genes and classic immune-related genes to explore the differences in immune responses among different subgroups (Figures 7G–H). The TIDE prediction score is currently regarded as a reliable metric for evaluating the reactivity of immune-checkpoint blockade (ICB). Consequently, we conducted a PMS-correlation analysis of the TIDE score and the immune-exhaustion score. The current research findings revealed that individuals in the high-PMS group exhibited higher Immune Exclusion and lower Immune Dysfunction scores, although the difference in TIDE scores between the two groups was not particularly significant (Figures 7G–H).

3.7 Identification of key representative genes influenced by purine-metabolism disorder in immunotherapy

Following preliminary screening, the present study identified two key representative genes, GMPS and NT5E, both of which were highly expressed in the PC population relative to the normal population (Figures 8A, B). On spatial sections, the expression of GMPS was diffusely distributed within the tumor area, and the population with high GMPS expression typically demonstrated a poorer response to immunotherapy (Figures 8C, D). Additionally, the prognosis of the population with high expression of these cells was also significantly unfavorable (Figure 8E). To elucidate this phenomenon from the perspective of crosstalk within the PDAC immune microenvironment, it was predominantly observed that cells with high GMPS expression were significantly associated with MDSC cells (Figures 8F–I). When focusing on NT5E, we found that NT5E+ cells were more malignant in terms of both prognosis and response to immunotherapy (Figures 8J–P). From a spatial analysis, it was observable that NT5E+ cells frequently engaged in more interactions with fibroblasts. In terms of spatial distribution, NT5E+ cells were diffusely distributed throughout the PC microenvironment alongside tumor-associated fibroblasts (Figure 8J). The cell-cell interactions based on spatial sections also indicated a significant interaction between the two (Figures 8K–P). Based on these results, our study posits that NT5E+ cells may play a pivotal role in the dysregulated microenvironment of PDAC fibroblasts following purine-metabolism disorder, with this role being more evident in the formation of an immunosuppressive microenvironment and a reduced response to immunotherapy (Figures 8K–P).

3.8 NT5E as an intermediate mediator in the purine-metabolic reprogramming of the PC TME and the formation of an immunosuppressive environment

To further reinforce the conclusions drawn above, we verified the relationships among tumor cells, fibroblasts, T cells, and NT5E expression in an additional spatial-transcriptome section. Following dimensionality reduction and clustering of the spatial sections, a total of 17 spatial cell clusters were obtained. Tumor cells were predominantly located in C1, C4, C5, C9, and C10, while fibroblasts were mainly distributed in C2, C3, C6, C9, C11, C12, and C15 (Figures 9A–G). By comparing the spatial positions, it was evident that NT5E was predominantly expressed on tumor cells, with fibroblasts interspersed among tumor cells, creating a typical “stiff-cancer” environment in PC, characterized by a scarcity of CD8 T cells (Figures 9C, H). By further analyzing the relationship between NT5E and tumor immunity from the bulk RNA-seq data, we can conclude that NT5E has the closest relationship with the infiltration of neutrophils, macrophages, and fibroblasts. Additionally, NT5E is also closely related to immune factors such as CCL13 and CCL18. This indicates that NT5E may play a mediating role in the tumor immune microenvironment of PC (Supplementary Figures 1A, B). These findings support the hypotheses presented in previous sections, namely, that the disorder and reprogramming of purine metabolism are predominantly manifested in tumor cells and fibroblasts, and that NT5E, a PM-disorder gene, indicates a poor prognosis for tumor patients. Consequently, we postulate that NT5E serves as an intermediate mediator in the purine-metabolic reprogramming of the PC TME

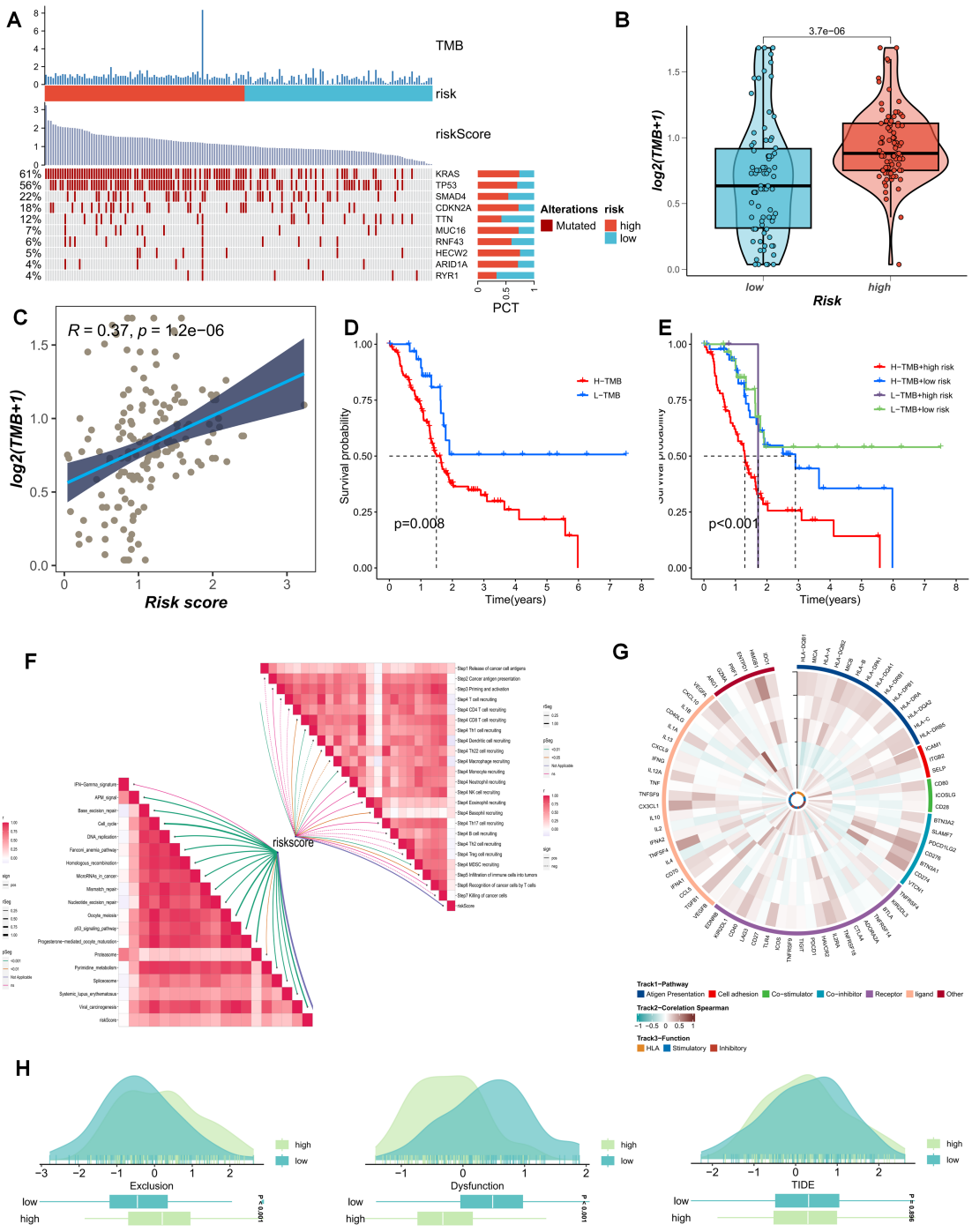

FIGURE 7
(A) The distribution of common mutated genes in PAAD patients across risk-score subgroups is analyzed. **(B)** The TMB mutation levels in the PMS low group and the PMS high group are compared. **(C)** The correlation between PMS score and TMB is explored. **(D, E)** The survival outcomes of patients divided into four groups according to the median TMB value and PMS value are investigated. **(F)** The association between PMS and the tumor-immune cycle is analyzed. **(G-H)** Correlation analysis of model genes and classic immune-related genes is conducted to study the differences in immune responses between different subgroups.

and the formation of an immunosuppressive environment. To this end, we verified the co-culture model system. After stably transfecting and knocking down NT5E in PC cells PANC-1, they were co-cultured with pancreatic-cancer-associated fibroblasts (Figure 9I). The results suggested that knocking down NT5E could attenuate the growth and invasion capabilities of tumor cells; however, when co-cultured with CAFs, this trend was mitigated, indicating that the inter-cellular signal communication between CAFs and tumor cells plays a significant role in the malignant progression of PC (Figures 9K–L). In fact, our study further analyzed the significance of NT5E in the four immunotherapy

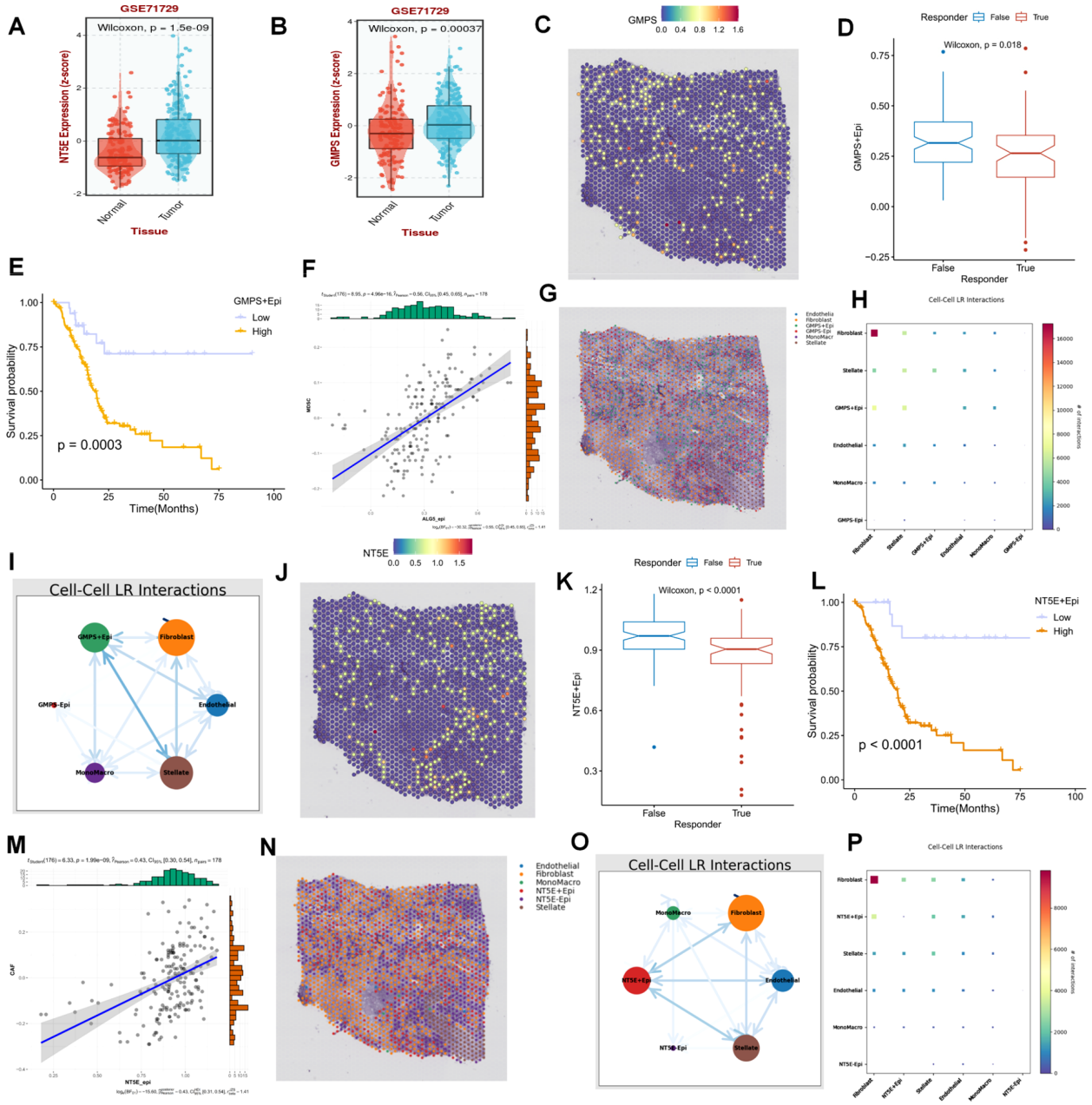

FIGURE 8
(A, B) Two key representative genes, GMPS and NT5E, were identified. **(C)** The expression of GMPS on spatial sections is visualized. **(D)** The population with high GMPS expression exhibits a poorer response to immunotherapy. **(E)** The prognosis of the population with high-expressing GMPS cells is significantly adverse. **(F-I)** Cells with high GMPS expression are significantly correlated with MDSC cells. **(J)** The expression of NT5E on spatial sections is presented. **(K)** The population with high NT5E expression shows a poorer response to immunotherapy. **(L)** The prognosis of the population with high-expressing NT5E cells is significantly unfavorable. **(M-P)** Cells with high NT5E expression are significantly associated with MDSC cells.

datasets of GSE67501, GSE136961, GSE140901, and GSE165252. The results showed that NT5E could effectively distinguish the effects of immunotherapy. This indicates that the level of NT5E expression has a significant impact on the response of pancreatic cancer patients to immunotherapy. From another perspective, it also confirms the prominent role of NT5E in the immune microenvironment (Supplementary Figures 1C–F).

4 Discussion

Within the highly distinctive immunosuppressive microenvironment of PC, fibroblasts assume a role of utmost significance and centrality. PC, widely renowned as a "cold tumor", which possess less infiltration of effector immune cells such as T cells, making it difficult for them to effectively recognize and attack tumor cells, owes this designation to its

10.3389/fimmu.2025.1569088

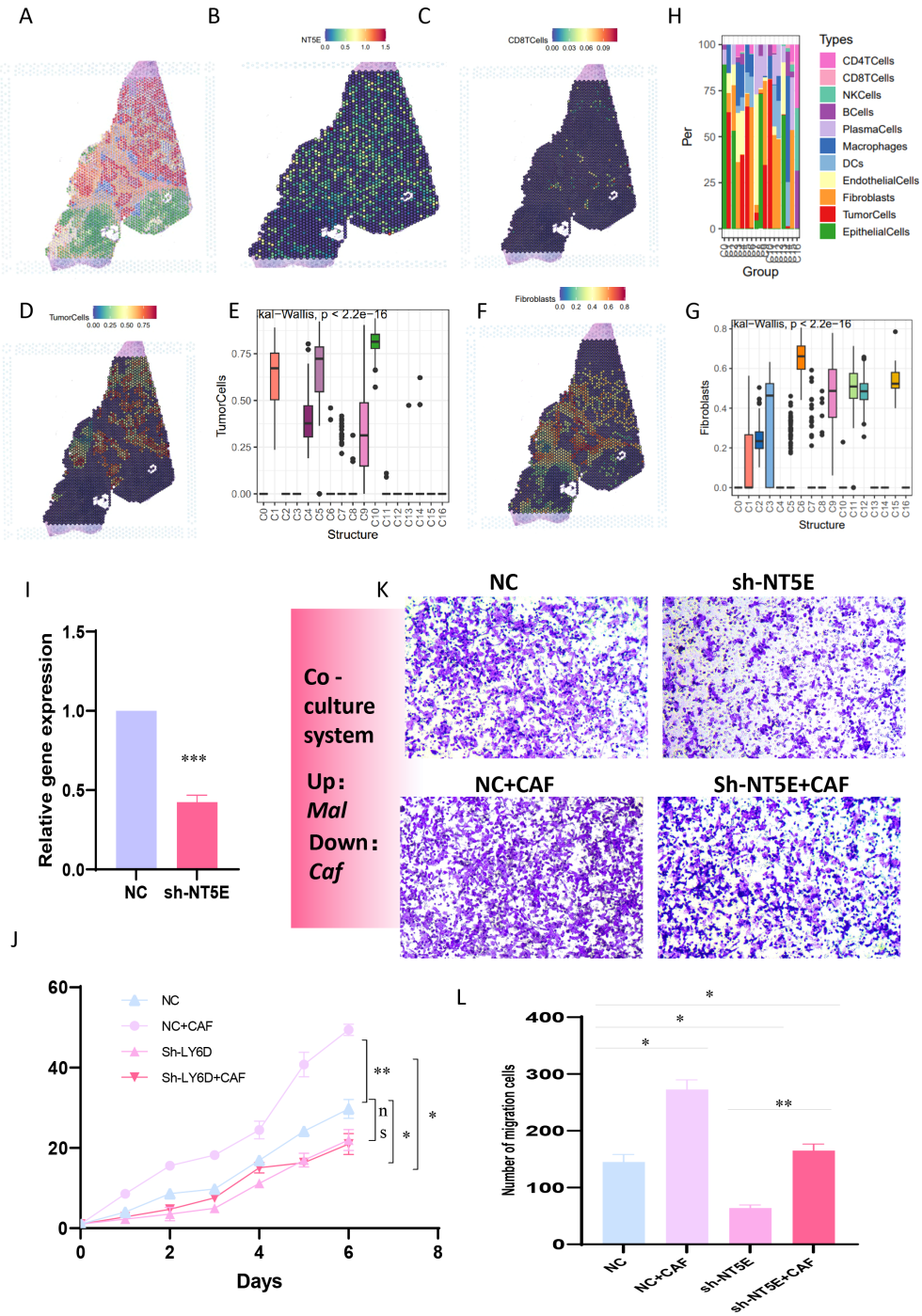

FIGURE 9
(A-G) The relationships among tumor cells, fibroblasts, T cells, and NT5E expression in spatial transcriptome sections are explored. **(H)** A bar chart depicts the cell distribution relationships within different spatial clusters. **(I)** Pancreatic cancer cells PANC-1 with stably transfected and knocked-down NT5E are prepared. **(K, L)** Transwell experiments are conducted to compare the invasion ability of pancreatic cancer cells in the co-culture system. **(L)** CCK-8 experiments are carried out to compare the survival ability of pancreatic cancer cells in the co-culture system. p values < 0.05 (*p < 0.05) were considered significant, where **p < 0.01, ***p < 0.001, and ****p < 0.0001, ns (non- significant).

uniquely fibrotic microenvironment. The establishment of its immunosuppressive characteristics is intricately intertwined with the functional remodeling of cancer-associated fibroblasts (CAFs) (10). Notably, CAFs not only erect a physical barrier through the secretion of extracellular matrix (ECM) proteins, thereby impeding the infiltration of T-cells, but also release immunosuppressive factors such as TGF-β and IL-6, thereby constructing a multi-level immune-escape network (12, 24). Among these, TGF-β has the capacity to inhibit the activities of immune cells including T cells and NK cells, while simultaneously promoting the differentiation of regulatory T cells (Tregs), thus giving rise to an immunosuppressive microenvironment (25). Moreover, VEGF can stimulate tumor angiogenesis, forging a vascular network

that is conducive to the survival and metastasis of tumor cells, providing tumor cells with the means to evade the body's immune surveillance (26–28).

This investigation has unearthed the existence of substantial NECTIN3-NECTIN2 and WNT7B-FZD1 signal interactions between epithelial cells with high PMS and fibroblasts, suggesting that CAFs might reshape the immunosuppressive niche through purine-metabolism reprogramming. Epithelial cells with high PMS receive an increased quantity of signals from fibroblasts and stellate cells and, concurrently, transmit more signals to fibroblasts, stellate cells, and T cells. One of the consequences of this metabolic reprogramming is to drive the formation of the "stiff-cancer" phenotype characteristic of PC. Tumor cells and CAFs synergistically promote ECM deposition through a "metabolic symbiosis" relationship. For example, the high-purine-metabolism region (Cluster6) undergoes co-activation with sphingolipid metabolism and taurine metabolism and may influence ECM remodeling by modulating the activity of PKM (29). In response to this, the spatial-transcriptome data obtained from this study have revealed that epithelial cells with high PMS are diffusely distributed within the tumor area, which exhibits a high degree of correlation with the stiff-cancer characteristics of PC, suggesting that abnormal purine metabolism may serve as a potential driver for stromal sclerosis. In terms of pathway activation, common signaling pathways such as the TNF signaling pathway and the HIF-1 signaling pathway exhibit marked differences between fibroblasts and stellate cells in different PMS groups, implying that these pathways, particularly the hypoxic environment, may exacerbate the fibrosis of PC and initiate a vicious cycle (30). The transcription factors CTNNB1 and LEF1 may be involved in regulating the interaction between these two groups of cells, signifying their latent importance in maintaining the balance of cell-cell interactions and the homeostasis of purine metabolism. Within the intricate tumor microenvironment, when perturbations arise in cell-cell interactions and purine metabolic processes, the expression profiles and functional activities of CTNNB1 and LEF1 are prone to undergo alterations. Subsequently, through their reciprocal interplay and the orchestrated regulation of downstream target genes, these two transcription factors strive to reinstate the homeostasis of both cell-cell interactions and purine metabolism.

Studies have demonstrated that the inhibition of the activities of certain key signaling pathways within fibroblasts can reduce the production of extracellular matrix and promote the infiltration of immune cells (25).As previously elaborated, patients in the high-PMS group are frequently accompanied by an immunosuppressive microenvironment, characterized by low immune-cell infiltration scores and immune-pathway scores, as well as high expression levels of the majority of immune checkpoints. This microenvironment inhibits the functions of immune cells, making it arduous for them to effectively attack tumor cells, thereby reducing the efficacy of immunotherapy. Nevertheless, this also offers novel perspectives for enhancing the effectiveness of immunotherapy. Through the optimized regulation of purine metabolism, it is anticipated to break through the immunosuppressive microenvironment, enhance the activity of immune cells, and thereby improve the sensitivity of immunotherapy (21). It is worth noting that with respect to the phenomenon that the overall survival (OS) of patients with high PMS and high tumor mutational burden (TMB) is relatively poor, it is possible that the immunosuppressive microenvironment generated by high PMS nullifies the potential immune-activation advantage conferred by high TMB. Although high TMB implies that tumor cells carry more gene mutations and are, in theory, more readily recognizable by the immune system, the immunosuppressive environment obstructs the effective attack of immune cells on tumor cells, enabling tumor cells to evade the body's immune surveillance and clearance, ultimately leading to a dismal prognosis for patients (31–33).

GMPS (GMP synthase), the rate-limiting enzyme in *de novo* purine synthesis, has a high expression level associated with tumor-cell proliferation and chemoresistance. Recent research has revealed that GMPS can influence the activity of the RAS-MAPK signaling pathway by regulating the level of GTP, thereby facilitating the progression of KRAS-mutant tumors (34). NT5E (CD73), functioning as an ectonucleotidase, catalyzes the conversion of AMP to adenosine and represents a core molecule in tumor immunosuppression (35, 36). This study has determined that high GMPS expression is positively correlated with MDSCs infiltration, and NT5E+ cells are spatially co-located with CAFs, suggesting that the two entities shape the inhibitory microenvironment through "metabolic-immune" synergy. NT5E is more likely to act as an intermediate mediator in the purine-metabolic reprogramming of the pancreatic-cancer tumor microenvironment (TME) and the formation of an immunosuppressive environment. From the perspective of spatial distribution, NT5E is predominantly expressed on tumor cells, with fibroblasts interspersed among tumor cells. This distribution pattern gives rise to a typical "stiff-cancer" environment in PC, resulting in a scarcity of CD8 T cells and being conducive to the formation of an immunosuppressive environment. In terms of function, NT5E may be involved in purine-metabolism reprogramming, influencing the metabolic states of tumor cells and their surrounding cells, and thus regulating cell-cell communication and interaction (37). Significantly, in the verification experiment of the co-culture model system, knocking down NT5E can reduce the growth and invasion capabilities of tumor cells, yet when co-cultured with CAF, this downward trend is alleviated. This indicates that NT5E plays a vital role in the inter-cellular signal communication between tumor cells and CAF, promotes the malignant progression of PC, and thus emerges as a key intermediate mediator in the purine-metabolic reprogramming and the formation of an immunosuppressive environment.

In summary, this study has not only comprehensively analyzed the characteristics of purine metabolism in the pancreatic-cancer microenvironment but also delved deeply into the impacts of abnormal purine metabolism on cell differentiation, interaction, and the efficacy of immunotherapy, and identified key representative genes GMPS and NT5E, particularly clarifying the intermediate-mediating role of NT5E in the purine-metabolic reprogramming of the pancreatic-cancer TME and the formation of an immunosuppressive environment. However, this study still has certain limitations. The current small sample size may affect the generality of the conclusions. Additionally, in the future, it could integrate organoid models and spatial metabolomics to dynamically analyze the spatiotemporal

evolution laws of the metabolic-immune network, thereby providing a novel paradigm for surmounting the treatment dilemma of PC.

Data availability statement

The original contributions presented in the study are included in the article/Supplementary Material. Further inquiries can be directed to the corresponding authors.

Author contributions

JZ: Conceptualization, Writing – original draft, Writing – review & editing. XZ: Conceptualization, Investigation, Writing – review & editing. RW: Formal Analysis, Project administration, Writing – original draft. C-SD: Funding acquisition, Resources, Supervision, Writing – original draft, Writing – review & editing.

Funding

The author(s) declare that financial support was received for the research and/or publication of this article. 2024 Shanghai University of Traditional Chinese Medicine and Shanghai Institute of Traditional Chinese Medicine Science and Technology Development Project: Research on the Clinical Efficacy and Mechanism of Tiao-Yuan-Jie-Du (Tonifying Yuan Qi and Detoxification) Theory in Anti cancer Treatment (No. 24YJS08); The Third Traditional Chinese Medicine Heritage Talent Project of Shanghai Traditional Chinese Medicine Hospital (No. SZYCC(2023–2024)-ZYCCXM03).

Conflict of interest

The authors declare that the research was conducted in the absence of any commercial or financial relationships that could be construed as a potential conflict of interest.

Generative AI statement

The author(s) declare that no Generative AI was used in the creation of this manuscript.

Publisher's note

All claims expressed in this article are solely those of the authors and do not necessarily represent those of their affiliated organizations, or those of the publisher, the editors and the reviewers. Any product that may be evaluated in this article, or claim that may be made by its manufacturer, is not guaranteed or endorsed by the publisher.

Supplementary material

The Supplementary Material for this article can be found online at: https://www.frontiersin.org/articles/10.3389/fimmu.2025.1569088/full#supplementary-material

SUPPLEMENTARY FIGURE 1
(A, B) Immuno-correlation analysis of NT5E, controlling for immune factors and infiltration of immune cells. **(C-F)** Evaluation of the therapeutic efficacy of NT5E in common cell cohorts for tumor immunotherapy.

References

1. Hu ZI, O'Reilly EM. Therapeutic developments in pancreatic cancer. *Nat Rev Gastroenterol Hepatol.* (2024) 21:7–24. doi: 10.1038/s41575-023-00840-w

2. Voutsadakis IA, Digklia A. Pancreatic adenocarcinomas without KRAS, TP53, CDKN2A and SMAD4 mutations and CDKN2A/CDKN2B copy number alterations: a review of the genomic landscape to unveil therapeutic avenues. *Chin Clin Oncol.* (2023) 12:2. doi: 10.21037/cco-22-108

3. Wang Q, Wang H, Ding Y, Wan M, Xu M. The role of adipokines in pancreatic cancer. *Front Oncol.* (2022) 12:926230. doi: 10.3389/fonc.2022.926230

4. Zhang M, Zhang F, Wang J, Liang Q, Zhou W, Liu J. Comprehensive characterization of stemness-related lncRNAs in triple-negative breast cancer identified a novel prognostic signature related to treatment outcomes, immune landscape analysis and therapeutic guidance: a silico analysis with *in vivo* experiments. *J Transl Med.* (2024) 22:423. doi: 10.1186/s12967-024-05237-0

5. Li Z, Li J, Bai X, Huang X, Wang Q. Tumor microenvironment as a complex milieu driving cancer progression: a mini review. *Clin Transl Oncol.* (2024) 1–10. doi: 10.1007/s12094-024-03697-w

6. Chakkera M, Foote JB, Farran B, Nagaraju GP. Breaking the stromal barrier in pancreatic cancer: Advances and challenges. *Biochim Biophys Acta Rev Cancer.* (2024) 1879:189065. doi: 10.1016/j.bbcan.2023.189065

7. Tang Y, Tian W, Xie J, Zou Y, Wang Z, Li N, et al. Prognosis and dissection of immunosuppressive microenvironment in breast cancer based on fatty acid metabolism-related signature. *Front Immunol.* (2022) 13:843515. doi: 10.3389/fimmu.2022.843515

8. Springfeld C, Ferrone CR, Katz MHG, Philip PA, Hong TS, Hackert T, et al. Neoadjuvant therapy for pancreatic cancer. *Nat Rev Clin Oncol.* (2023) 20:318–37. doi: 10.1038/s41571-023-00746-1

9. Sherman MH, Beatty GL. Tumor microenvironment in pancreatic cancer pathogenesis and therapeutic resistance. *Annu Rev Pathol.* (2023) 18:123–48. doi: 10.1146/annurev-pathmechdis-031621-024600

10. Liu J, Mroczek M, Mach A, Stępień M, Aplas A, Pronobis-Szczylik B, et al. Genetics, genomics and emerging molecular therapies of pancreatic cancer. *Cancers (Basel).* (2023) 15:779. doi: 10.3390/cancers15030779

11. Raaijmakers K, Adema GJ, Bussink J, Ansems M. Cancer-associated fibroblasts, tumor and radiotherapy: interactions in the tumor micro-environment. *J Exp Clin Cancer Res.* (2024) 43:323. doi: 10.1186/s13046-024-03251-0

12. Wen L, He C, Guo Y, Zhou N, Meng X, Chen Y, et al. Strategies for specific multimodal imaging of cancer-associated fibroblasts and applications in theranostics of cancer. *Mater Today Bio.* (2025) 30:101420. doi: 10.1016/j.mtbio.2024.101420

13. Hu HH, Chen DQ, Wang YN, Feng YL, Cao G, Vaziri ND, et al. New insights into TGF-β/Smad signaling in tissue fibrosis. *Chem Biol Interact.* (2018) 292:76–83. doi: 10.1016/j.cbi.2018.07.008

14. Glaviano A, Lau HS, Carter LM, Lee EHC, Lam HY, Okina E, et al. Harnessing the tumor microenvironment: targeted cancer therapies through modulation of epithelial-mesenchymal transition. *J Hematol Oncol.* (2025) 18:6. doi: 10.1186/s13045-024-01634-6

15. Yamazaki M, Ishimoto T. Targeting cancer-associated fibroblasts: eliminate or reprogram? *Cancer Sci.* (2025) 116:613–21. doi: 10.1111/cas.v116.3

16. Li J, Zhang W, Chen L, Wang X, Liu J, Huang Y, et al. Targeting extracellular matrix interaction in gastrointestinal cancer: Immune modulation, metabolic reprogramming, and therapeutic strategies. *Biochim Biophys Acta Rev Cancer.* (2024) 1879:189225. doi: 10.1016/j.bbcan.2024.189225

17. Qiao J, Yu Z, Zhou H, Wang W, Wu H, Ye J. The pentose phosphate pathway: from mechanisms to implications for gastrointestinal cancers. *Int J Mol Sci*. (2025) 26. doi: 10.3390/ijms26020610

18. Yang L, Zhang Y, Yang L. Adenosine signaling in tumor-associated macrophages and targeting adenosine signaling for cancer therapy. *Cancer Biol Med*. (2024) 21:995–1011. doi: 10.20892/j.issn.2095-3941.2024.0228

19. Wu D, Yang S, Yuan C, Zhang K, Tan J, Guan K, et al. Targeting purine metabolism-related enzymes for therapeutic intervention: A review from molecular mechanism to therapeutic breakthrough. *Int J Biol Macromol*. (2024) 282:136828. doi: 10.1016/j.ijbiomac.2024.136828

20. Gardani CFF, Diz FM, Dondé LB, Rockenbach L, Laufer S, Morrone FB. The potential role of purinergic signaling in cancer therapy: perspectives on anti-CD73 strategies for prostate cancer. *Front Immunol*. (2024) 15:1455469. doi: 10.3389/fimmu.2024.1455469

21. Fathi M, Zarei A, Moghimi A, Jalali P, Salehi Z, Gholamin S, et al. Combined cancer immunotherapy based on targeting adenosine pathway and PD-1/PDL-1 axis. *Expert Opin Ther Targets*. (2024) 28:757–77. doi: 10.1080/14728222.2024.2405090

22. Han Y, Dong C, Hu M, Wang X, Wang G. Unlocking the adenosine receptor mechanism of the tumor immune microenvironment. *Front Immunol*. (2024) 15:1434118. doi: 10.3389/fimmu.2024.1434118

23. Shen G, Wang Q, Li Z, Xie J, Han X, Wei Z, et al. Bridging chronic inflammation and digestive cancer: the critical role of innate lymphoid cells in tumor microenvironments. *Int J Biol Sci*. (2024) 20:4799–818. doi: 10.7150/ijbs.96338

24. Liu C, Xie J, Lin B, Tian W, Wu Y, Xin S, et al. Pan-cancer single-cell and spatial-resolved profiling reveals the immunosuppressive role of APOE+ Macrophages in immune checkpoint inhibitor therapy. *Adv Sci (Weinh)*. (2024) 11:e2401061. doi: 10.1002/advs.202401061

25. Zhang Z, Wang R, Chen L. Drug delivery system targeting cancer-associated fibroblast for improving immunotherapy. *Int J Nanomed*. (2025) 20:483–503. doi: 10.2147/IJN.S500591

26. Shukla S, Dalai P, Agrawal-Rajput R. Metabolic crosstalk: Extracellular ATP and the tumor microenvironment in cancer progression and therapy. *Cell Signal*. (2024) 121:111281. doi: 10.1016/j.cellsig.2024.111281

27. Wang Q, Liu Y, Li Z, Tang Y, Long W, Xin H, et al. Establishment of a novel lysosomal signature for the diagnosis of gastric cancer with *in-vitro* and *in-situ* validation. *Front Immunol*. (2023) 14:1182277. doi: 10.3389/fimmu.2023.1182277

28. Xie J, Yang A, Liu Q, Deng X, Lv G, Ou X, et al. Single-cell RNA sequencing elucidated the landscape of breast cancer brain metastases and identified ILF2 as a potential therapeutic target. *Cell Prolif*. (2024) 57:e13697. doi: 10.1111/cpr.v57.11

29. Liu J, Zhang B, Huang B, Zhang K, Guo F, Wang Z, et al. A stumbling block in pancreatic cancer treatment: drug resistance signaling networks. *Front Cell Dev Biol*. (2024) 12:1462808. doi: 10.3389/fcell.2024.1462808

30. Shi Y, Gilkes DM. HIF-1 and HIF-2 in cancer: structure, regulation, and therapeutic prospects. *Cell Mol Life Sci*. (2025) 82:44. doi: 10.1007/s00018-024-05537-0

31. Wang J, Yang J, Narang A, He J, Wolfgang C, Li K, et al. Consensus, debate, and prospective on pancreatic cancer treatments. *J Hematol Oncol*. (2024) 17:92. doi: 10.1186/s13045-024-01613-x

32. Budczies J, Kazdal D, Menzel M, Beck S, Kluck K, Altbürger C, et al. Tumor mutational burden: clinical utility, challenges and emerging improvements. *Nat Rev Clin Oncol*. (2024) 21:725–42. doi: 10.1038/s41571-024-00932-9

33. Holder AM, Dedeilia A, Sierra-Davidson K, Cohen S, Liu D, Parikh A, et al. Defining clinically useful biomarkers of immune checkpoint inhibitors in solid tumors. *Nat Rev Cancer*. (2024) 24:498–512. doi: 10.1038/s41568-024-00705-7

34. Ballut L, Violot S, Kumar S, Aghajari N, Balaram H. GMP synthetase: allostery, structure, and function. *Biomolecules*. (2023) 13:1379. doi: 10.3390/biom13091379

35. Zhan J, Huang L, Niu L, Lu W, Sun C, Liu S, et al. Regulation of CD73 on NAD metabolism: Unravelling the interplay between tumor immunity and tumor metabolism. *Cell Commun Signal*. (2024) 22:387. doi: 10.1186/s12964-024-01755-y

36. Kurago Z, Guo G, Shi H, Bollag RJ, Groves MW, Byrd JK, et al. Inhibitors of the CD73-adenosinergic checkpoint as promising combinatory agents for conventional and advanced cancer immunotherapy. *Front Immunol*. (2023) 14:1212209. doi: 10.3389/fimmu.2023.1212209

37. Iser IC, Vedovatto S, Oliveira FD, Beckenkamp LR, Lenz G, Wink MR. The crossroads of adenosinergic pathway and epithelial-mesenchymal plasticity in cancer. *Semin Cancer Biol*. (2022) 86:202–13. doi: 10.1016/j.semcancer.2022.06.012

frontiers | Frontiers in Immunology

TYPE Original Research
PUBLISHED 16 April 2025
DOI 10.3389/fimmu.2025.1568825

Check for updates

OPEN ACCESS

EDITED BY
Qi Wang,
Jiangsu University, China

REVIEWED BY
Xiongbin Kang,
Bielefeld University, Germany
Jianing Lin,
Karolinska Institutet (KI), Sweden
Jianzhong Ai,
Sichuan University, China

*CORRESPONDENCE
Qianghua Zhou
zhouqh1@sysucc.org.cn
Wensu Wei
weiws@sysucc.org.cn
Kai Yao
yaokai@sysucc.org.cn
Zhiming Wu
wuzhim@sysucc.org.cn

†These authors have contributed equally to this work

RECEIVED 30 January 2025
ACCEPTED 02 April 2025
PUBLISHED 16 April 2025

CITATION
Tan X, Wang Y, Yu Y, Zheng R, Li J, Chen S, Xie Q, Guo S, Zhang C, Deng X, Liu Z, Tang Y, Li H, Wu W, Chen J, Zhou Q, Wei W, Yao K and Wu Z (2025) Neutrophil-to-lymphocyte ratio predicts a poor prognosis for penile cancer with an immunosuppressive tumor microenvironment.
Front. Immunol. 16:1568825.
doi: 10.3389/fimmu.2025.1568825

COPYRIGHT
© 2025 Tan, Wang, Yu, Zheng, Li, Chen, Xie, Guo, Zhang, Deng, Liu, Tang, Li, Wu, Chen, Zhou, Wei, Yao and Wu. This is an open-access article distributed under the terms of the Creative Commons Attribution License (CC BY). The use, distribution or reproduction in other forums is permitted, provided the original author(s) and the copyright owner(s) are credited and that the original publication in this journal is cited, in accordance with accepted academic practice. No use, distribution or reproduction is permitted which does not comply with these terms.

Neutrophil-to-lymphocyte ratio predicts a poor prognosis for penile cancer with an immunosuppressive tumor microenvironment

Xingliang Tan[1,2,3†], Yanjun Wang[1,2,3†], Yiqi Yu[4†], Runhao Zheng[1,2,3†], Jing Li[5], Shaohua Chen[6], Qingling Xie[7], Shengjie Guo[1,2,3], Chichen Zhang[1,2,3], Xinpei Deng[1,2,3], Zhicheng Liu[1,2,3], Yi Tang[1,2,3], Hang Li[4], Weicheng Wu[4], Juexiao Chen[4], Qianghua Zhou[1,2,3*], Wensu Wei[1,2,3*], Kai Yao[1,2,3*] and Zhiming Wu[1,2,3*]

[1]Department of Urology, Sun Yat-sen University Cancer Center, Guangzhou, China, [2]State Key Laboratory of Oncology in Southern China, Guangzhou, China, [3]Guangdong Provincial Clinical Research Center for Cancer, Guangzhou, China, [4]Zhongshan School of Medicine, Sun Yat-Sen University, Guangzhou, China, [5]Department of Urology, Affiliated Cancer Hospital and Institute of Guangzhou Medical University, Guangzhou, China, [6]Department of Urology, Guangxi Medical University Cancer Center, Nanning, China, [7]Department of Urology, The Fifth Affiliated Hospital of Guangzhou Medical University, Guangzhou Medical University, Guangzhou, China

Background: Chronic inflammation related to poor genital hygiene is a well-recognized pathogenic trigger for penile cancer (PC). The neutrophil-to-lymphocyte ratio (NLR) is a simple, reproducible systemic inflammatory marker and has been reported to indicate unfavorable outcomes. However, previous studies were limited by small sample sizes, confounding prognostic factors and a lack of high-quality evidence demonstrating the significance of the NLR in PC.

Methods: A large multicenter cohort of 582 PC patients who underwent radical inguinal lymphadenectomy with definitive pN stage information was assessed. Univariate and multivariate Cox regression analyses were performed to investigate the prognostic value of inflammation-related markers. Propensity score matching (PSM) was used to minimize confounding prognostic clinicopathological features. Immunofluorescence was used to assess the immunosuppressive tumor microenvironment (TME).

Results: A high preoperative NLR (≥ 3.0) was associated with advanced pT, pN, and pathological grade and lymphovascular invasion in PC patients. After PSM to eliminate interference from clinical factors, pN and the NLR were found to be independent prognostic indicators (both $p<0.001$). PC patients with high NLRs had shorter progression-free survival (PFS) and poorer cisplatin-based chemotherapy and PD-1 immunotherapy response. We also found that the NLR is associated with proinflammatory cytokine secretion and increased N2 tumor-associated neutrophils (TANs) infiltration and $CD8^+$ T-cell exhaustion in TME. N2 TANs induced neutrophil extracellular trap formation might contribute to tumor progression and resistance in high-NLR PC patients.

Conclusions: The NLR is an effective, simple and independent prognostic indicator for PC. A high NLR is associated with an immunosuppressive TME and poor outcomes.

KEYWORDS

cancer, neutrophil-to-lymphocyte ratio, tumor-associated neutrophils, neutrophil extracellular traps, propensity score matching

1 Background

Penile cancer (PC) is a physically and mentally devastating malignancy in males and is particularly prevalent in developing countries with poor economic and hygienic conditions (1, 2). According to the Global Cancer Observatory, the worldwide age-standardized incidence rate of PC was 0.80 cases per 100,000 person-years in 2018, with an expected increase of over 56% by 2040 (1). The prediction of PC prognosis is mainly based on the tumor–node–metastasis (TNM) staging system and pathological characteristics (3, 4). Lymph node metastasis is recognized as a key risk factor in PC, with dramatic decreases in 5-year overall survival (OS) rates of 79.7–31.8% for pN1–pN3 patients and 93.6% for pN0 patients (5–7); however, molecular signatures for individualized prognosis assessment are lacking. Although several markers (8–11), including squamous cell carcinoma antigen (SCC-Ag) expression, HER2 overexpression, and EGFR amplification, have been reported to be correlated with survival, their low sensitivity has limited their clinical application; thus, prognostic indicators, especially for preoperative assessment, are still lacking.

Human papilloma virus infection, chronic irritation, and inflammation are key factors in PC tumorigenesis and progression (12). Chronic inflammation is responsible for cancer incidence and controlling inflammation is a potential strategy to stop the development of cancer (13). The neutrophil-to-lymphocyte ratio (NLR) has been recognized as an indicator of systemic inflammation associated with advanced disease, poor outcomes and chemotherapy resistance in a series of solid tumors (14–17). The NLR serves as a simple, reproducible and economical marker that is related to lymph node metastasis, immunotherapy response, and survival in PC patients (16, 18–21). The high level of NLR is associated with tumor-associated neutrophils (TANs), mediating the suppressive immune microenvironment, and is related to poor outcomes. However, previous studies have not only ignored the dominant influence of lymph node metastasis and other confounding factors on NLR-based prognostic assessment but have also been limited by small sample sizes, the use of single-center cohorts, a lack of standardized inguinal lymph node dissection and the use of inappropriate statistical methods (18–20, 22). In addition, the relationship between the peripheral NLR and the inflammatory microenvironment of tumors remains unclear.

In our study, we addressed these limitations by conducting a multicenter, large-scale, propensity score matching (PSM) analysis of 582 PC patients with clear pN stage information to demonstrate that the NLR serves as an independent predictor of survival in PC patients. Additionally, we investigated the correlations between the NLR and the levels of serum inflammatory cytokines, secreted proteins and tumor-infiltrating immune cells (TIICs). We found that a high preoperative NLR affected the immunosuppressive tumor microenvironment (TME) by increasing N2-type tumor-associated neutrophil (TAN) infiltration, which induced the formation of neutrophil extracellular traps (NETs) to promote tumor progression, contributing to a poor prognosis in PC patients.

Abbreviations: BMI, body mass index; CRP, C-reactive protein; CSS, cancer-specific survival; ELISA:enzyme-linked immunosorbent assay; IHC, immunohistochemistry; HE, hematoxylin and eosin; LMR, lymphocyte-monocyte ratio; LVI, lymphovascular invasion; mIF, immunofluorescence; MPO, myeloperoxidase; NETs:neutrophil extracellular traps; NLR, neutrophil-to-lymphocyte ratio; OS, overall survival; PC, penile cancer; PFS, progression-free survival; PSCC, penile squamous cell carcinoma; PSM, propensity score matching; ROC, receiver operating characteristic; rILND, radical inguinal lymphadenectomy; SAA, serum amyloid A; SCC-Ag, squamous cell carcinoma antigen; TAN, tumor-associated neutrophil; TIICs, tumor-infiltrating immune cells; TME, tumor microenvironment; TNM, tumor-node-metastasis.

2 Methods

2.1 Patient cohorts and research ethics

This retrospective study was conducted on 582 pathologically confirmed PSCC patients between January 2010 and December 2023 from four centers; this cohort included 495 (85.1%) patients from Sun Yat-sen University Cancer Center (SYSUCC), and the detailed information is listed in Table 1. The inclusion criteria were as follows: 1. Naive patients who underwent bilateral and radical inguinal lymphadenectomy (rILND) with classical boundaries (23, 24). 2. Clear pN stage information individually determined by experienced pathologists on the basis of the 8th edition of the AJCC TNM Staging System for Penile Cancer (2). 3. Reliable preoperative routine blood, blood chemistry and inflammatory secreted proteins and cytokines. 4. Clear clinical outcome data. Our study received approval from the ethics committee of Sun Yat-sen University Cancer Center (Approval number: G2023-098-01),

10.3389/fimmu.2025.1568825

TABLE 1 Clinicopathological characteristics of 582 penile cancer patients.

Variables (n = 582)	
Institution	
SYSUCC	495 (85.1%)
ACHIGMU	41 (7.0%)
GMUCC	36 (6.2%)
FAHGMU	10 (1.7%)
Age (years)	
> 55	290 (49.8%)
≤ 55	292 (50.2%)
Body mass index (kg/m^2)	
> 23	266 (45.7%)
≤ 23	274 (47.1%)
Unknown	42 (7.2%)
pT stage	
pTa/Tis	26 (4.4%)
pT1	209 (35.9%)
pT2	124 (21.3%)
pT3	187 (32.1%)
pT4	14 (2.4%)
pTx	22 (3.7%)
pN stage	
pN0	312 (53.6%)
pN1	75 (12.8%)
pN2	55 (9.4%)
pN3	140 (24.0%)
Grade	
G1	284 (48.7%)
G2	212 (36.4%)
G3/4	64 (10.9%)
Gx	22 (3.7%)
Pathologic high-risk factors	
Lymphovascular invasion	62 (10.6%)
Perineural invasion	89 (15.2%)
Extranodal extension	105 (18.0%)
Inflammatory indicators (Median, IQR)	
NLR (n = 582)	2.56 (1.82-3.75)
LMR (n = 582)	3.69 (2.63-5.00)
CRP (n = 559)	2.40 (0.88-9.56)
SAA (n = 412)	6.75 (3.60-23.03)
Perioperative therapy	
Cisplatin-based chemotherapy	205 (35.2%)
Chemotherapy + anti-PD-1 immunotherapy	107 (18.3%)
Clinical Outcomes	
Progression	162 (27.8%)
Death due to disease	124 (21.3%)

SYSUCC, Sun Yat-sen University Cancer Center; ACHIGMU, Affiliated Cancer Hospital and Institute of Guangzhou Medical University; FAHGMU, Fifth Affiliated Hospital of Guangzhou Medical University; GMUCC, Guangxi Medical University Cancer Center.

and informed consent was waived by the institutional review board due to the retrospective nature of the investigation.

2.2 Propensity score matching and cutoff values

PSM was performed with a 1:1 matching ratio, using the "nearest" method and a caliper of 0.2. The matched variables included age, pT stage, pN stage, histological grade, body mass index (BMI), and the presence of lymphovascular invasion (LVI), which were significantly different between the high and low NLR groups. For the PSM population, we used the chi-square test and absolute standardized difference test to assess the balance of the variables between the two groups. The primary endpoints for this analysis were cancer-specific survival (CSS) and progression-free survival (PFS). A receiver operating characteristic (ROC) curve was generated to determine the optimal cutoff values of continuous variables, including the NLR, lymphocyte–monocyte ratio (LMR), C-reactive protein (CRP), and serum amyloid A (SAA).

2.3 Evaluation of tumor immune microenvironment scores

To determine the composition of inflammatory immune cells and immune microenvironment heterogeneity across groups classified according to the NLR, 16 fresh tumor tissue samples (9 from the high NLR group and 7 from the low NLR group) were subjected to mRNA-seq. The Immune Cell Abundance Identifier (ImmuCellAI) tool was used to estimate the abundance of 24 immune cell types from the mRNA-seq matrix and provided a comprehensive landscape of inflammatory immune cells for high- and low-NLR tumors (25).

2.4 Laboratory assessments of inflammatory markers

The NLR and LMR and CRP, SAA and SCC-Ag levels were assessed before surgery. SAA detection was only conducted after

2017, so data on SAA were collected from only 412 patients. Serum proinflammatory cytokines (26), including interleukin-6 (IL-6) and IL-8, and anti-inflammatory cytokines (IL-4 and IL-10) were detected in 116 PC patients via enzyme-linked immunosorbent assay (ELISA) (Human ELISA Kit, Beyotime, #PI618, #PI330, #PI640 and #PI528). The specific steps are described in the kit instructions.

2.5 Hematoxylin and eosin staining and immunohistochemistry

A total of 167 PC patients with well-preserved, 4-μm paraffin-embedded tumor sections were included in the analysis. HE-stained samples were used to evaluate the proportion of TIICs. CD4+ T cells (CD4, CST, #25229), CD8+ T cells (CD8α, CST, #98941) and tumor-associated neutrophils (TANs) (CD66b, Abcam, #ab300122) were detected via IHC staining according to standard pathologic procedures previously described (27, 28). Five fields of view at high-magnification (400×) were randomly selected to count the absolute cell number of immune cells stained with each antibody. Pathological diagnosis and IHC staining were performed by two independent pathologists.

2.6 Flow cytometry and multiplex immunofluorescence

A total of 42 fresh tumor tissues were obtained and prepared as single-cell suspensions for subsequent flow cytometry. In brief, N2 TANs were identified according to dual positivity for CXCR2 (anti-CXCR2 antibody, Abcam, ab89254) and CD66b (anti-CD66b antibody, Abcam, ab48589) (29, 30). Flow cytometry was restricted to sorting double-positive cells, and the percentage of N2-phenotype cells among all TANs (CD66b+) was calculated. Multiplex immunofluorescence was performed with a Cellcook kit according to the manufacturer's instructions. The antibodies against the following targets were used: pan-CK (CST, #67306), CD66b (Abcam, ab48589), CXCR2 (Abcam, ab89254), myeloperoxidase (MPO) (CST, #14569), TGF-β (CST, #3709), TIM3 (CST, #75743) and (citH3) (CST, #97272). The visualization of NETs was performed according to MPO and citH3 staining (31). CD66b/CXCR2 and TIM3/CD8 were colocalized in N2 TANs and exhausted CD8+ T cells, respectively. The spatial distance between immune cells was analyzed via Halo software (Indica labs) and multiplex IHC modules.

2.7 Statistical analysis

Statistical analysis was conducted via SPSS software (Ver. 25.0). All the results are presented as the means ± SDs, and the differences between two groups were assessed via Student's t test or one-way ANOVA. Pearson correlation analysis was used to detect correlations between variables. Survival analysis, including PFS and CSS analysis, was performed using Kaplan–Meier survival curves, and multivariate analysis was performed via the forward method. A p value < 0.05 was considered to indicate statistical significance.

3 Results

3.1 Baseline characteristics

A total of 582 penile squamous cell carcinoma (PSCC) patients from four centers were enrolled in our study, and the mean follow-up time was 41.1 ± 31.4 months (Table 1). All patients underwent bilateral radical dissection of inguinal lymph nodes (13.12 ± 5.42 nodes per patient) (23). Among the patients, 46.4% of patients had positive nodes, and 12.8%, 9.4% and 24.0% of patients had clear pN1, pN2 and pN3 stage disease, respectively. Among these patients, 105 (18.0%) had extranodal extension (Table 1). Among pN+ patients, cisplatin-based chemotherapy combined with anti-PD-1 immunotherapy was administered to 205 patients (35.2%) and 107 patients (18.3%). Ultimately, 162 patients (27.8%) exhibited disease progression, and 124 patients died (21.3%) from PSCC; the 5-year PFS and 5-year CSS rates were 68.5% (95% CI: 0.64–0.73) and 75.0% (95% CI: 0.71–0.79), respectively, in our cohort.

3.2 Cutoff values of inflammatory markers and SCC-Ag

Preoperative inflammatory indicators, including the NLR and LMR and the levels of CRP, SAA, and SCC-Ag were assessed; the median values are listed in Table 1. The optimal cutoff values on the basis of the ROC curves were 3.5 for the LMR, 2.2 for CRP, 11.3 for SAA and 2.7 for SCC-Ag (Supplementary Figure S1). Although the cutoff value for the NLR was 2.75 in our cohort, the threshold was recalibrated to 3.0 to maintain consistency with previous literature and improve reproducibility and clinical practicality (Figure 1A) (20, 21). In total, a high NLR (NLR≥ 3) was detected in 38.8% of patients, and the NLR has a sensitivity of 63.7% and a specificity of 67.9% for predicting survival (Figure 1A).

3.3 Inflammatory markers and clinical outcomes

To further explore the clinical significance of inflammatory indicators in survival, Kaplan–Meier survival analysis was performed (Supplementary Table S1). Univariate analysis revealed that advanced pT, pN, and pathological grade; LVI/PNI; high NLR; high CRP, SAA and SCC-Ag levels; and low LMR were associated with poor CSS and PFS (Supplementary Table S1 and Supplementary Figure S2). More importantly, we found that a high NLR in was associated with a poor response to cisplatin-

10.3389/fimmu.2025.1568825

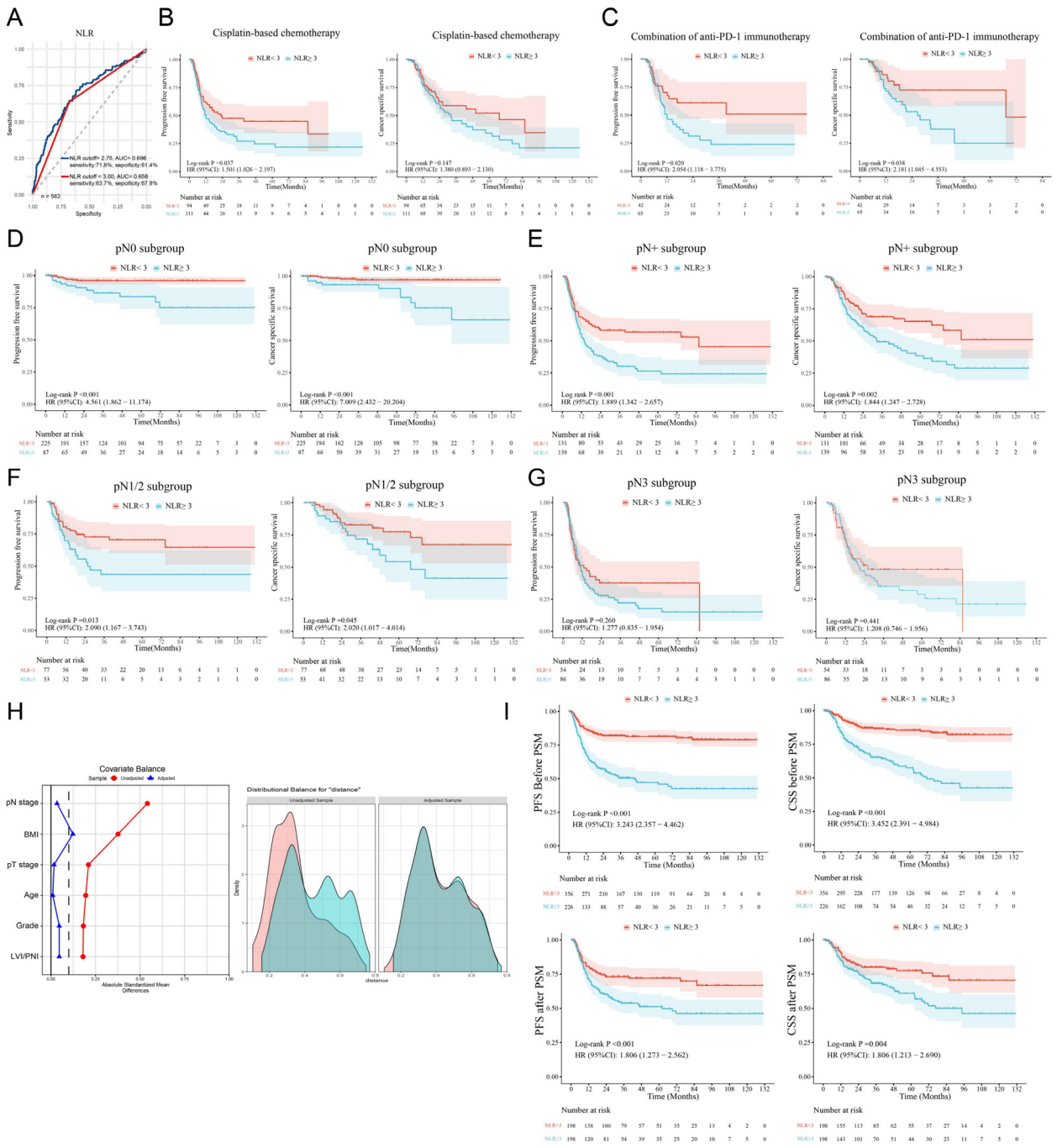

FIGURE 1
A high NLR is associated with a poor PSCC prognosis. **(A)** ROC curves indicated that the best cutoff value of the NLR for determining cancer-specific survival in PSCC patients was 2.75 in our cohort (blue line). The red line shows that the AUC was 0.658 when the cutoff value of the NLR was 3.00. **(B, C)** Subgroup analysis was performed on patients treated with therapeutic agents, and survival analysis revealed that high NLRs were related to poor response to chemotherapy and immunotherapy. **(D–G)** Survival analysis was performed for the pN0, pN+, pN1-N2 and pN3 subgroups. **(H)** PSM was used to adjust for confounding clinicopathological effects in the high/low NLR groups. **(I)** Differences in survival between the high- and low-NLR groups before and after PSM. NLR, neutrophil–lymphocyte ratio; ROC, receiver operating characteristic curve; AUC, area under the curve; PFS, progression-free survival; CSS, cancer-specific survival; PSM, propensity score matching; HR, hazard ratio; CI, confidence interval; LVI, lymphovascular invasion; PNI, perineural invasion; PSCC, penile squamous cell carcinoma.

based chemotherapy and anti-PD-1 immunotherapy in PSCC patients (Figures 1B, C). Further multivariate analysis revealed that only pN stage was an independent unfavorable prognostic factor (Supplementary Table S2). Similarly, our study indicated that lymph node metastasis was a radical and recognized prognostic factor for predicting clinical outcomes (7); thus, it might be a confounding factor in survival analysis based on the NLR that has been ignored in previous NLR studies.

3.4 Subgroup analysis and propensity score matching for the NLR

To control the confounding influence of lymph node metastasis in prognosis analysis, we first conducted subgroup analysis between different pN stages. We found that, in both the pN0 subgroup and the pN+ subgroup, PSCC patients with high preoperative NLRs had shorter PFS and CSS than those with low NLRs did (both $p < 0.01$) (Figures 1D, E). In patients with pN1/N2-stage disease and a low metastatic burden, the NLR was also associated with poor outcomes (Figure 1F), but the differences between patients with advanced (pN3-stage) disease were not statistically significant (Figure 1G).

Subsequently, the chi-square test demonstrated that a high NLR was significantly correlated with age, body mass index (BMI), pT stage, pN stage, pathological grade and LVI/PNI (Table 2). To balance the above confounding factors, we constructed a 1:1 cohort (high NLR versus low NLR, with 198 patients in each group) via the PSM method. The baseline characteristics were comparable between the two groups (Table 2**).** PSM analysis confirmed that the covariates were well balanced, as evidenced by absolute standard differences of less than 0.1 for all included factors (Figure 1H). To our surprise, the survival differences between the high- and low-NLR groups persisted; notably, PFS and CSS were significantly longer in the low-NLR group (Figure 1I). After the clinicopathological factors were adjusted via PSM, univariate and multivariate analyses revealed that pN stage and a high NLR were both independent prognostic indicators in terms of PFS (HR: 1.64; 95% CI: 1.15–2.34) and CSS (HR: 1.56; 95% CI: 1.04–2.34) (Table 3).

3.5 A high NLR is associated with increased systemic inflammation and TAN infiltration

To investigate the correlation between the preoperative NLR and the level of systemic inflammation, Pearson correlation analysis was performed, which revealed that the NLR was positively corelated with the levels of the inflammatory proteins CRP and SAA but negatively correlated with the LMR (Figures 2A, B). In addition, the levels of the proinflammatory cytokines IL-6 and IL-8 were significantly elevated in the high NLR group (n=59), whereas the levels of the anti-inflammatory cytokines IL-4 and IL-10 were significantly reduced (Figure 2C). These findings indicate that PC patients with a high NLR have a greater degree of systemic inflammation.

To further explore the tumor inflammatory immune microenvironment in patients grouped according to the NLR. Sixteen tumors were subjected to mRNA-seq to analyze immune cell subtypes via ImmuCellAI (Supplementary Figure S3) (25). Although there was no significant difference in the proportion of tumor-infiltrating immune cells (TIICs) between the high-NLR and low-NLR groups, the high-NLR group presented more tumor-associated neutrophils (TANs) and less infiltration of antitumor CD8+ T cells (Figure 2D). Moreover, paraffin-embedded tumor samples from 167 tumor tissues were used to verify the findings (Figures 2E, F). Notably, a high NLR was significantly correlated with an increased $CD66^+$ TAN/CD8+ T-cell ratio (Figure 2F) (18). These results suggest that the preoperative NLR in PC patients is associated with a proinflammatory microenvironment in tumors, especially those with an immunosuppressive phenotype.

TABLE 2 Association between the NLR and clinicopathological features before and after propensity score matching.

Variables	Before PSM					After PSM				
	Total (n=582)	NLR<3 (n=356)	NLR≥3 (n=226)	χ^2	P value	Total (n=396)	NLR<3 (n=198)	NLR≥3 (n=198)	χ^2	P value
Age, n (%)				5.187	**0.023**				0.010	0.920
≤ 55	292 (50.17)	192 (53.93)	100 (44.25)			191 (48.23)	96 (48.48)	95 (47.98)		
> 55	290 (49.83)	164 (46.07)	126 (55.75)			205 (51.77)	102 (51.52)	103 (52.02)		
BMI, n (%)				9.473	**0.009**				1.803	0.406
≤ 23	274 (47.08)	161 (45.22)	113 (50.00)			198 (50)	102 (51.52)	96 (48.48)		
> 23	266 (45.7)	160 (44.94)	106 (46.90)			188 (47.47)	93 (46.97)	95 (47.98)		
MD	42 (7.22)	35 (9.83)	7 (3.10)			10 (2.53)	3 (1.52)	7 (3.54)		
pT stage, n (%)				12.653	**0.013**				1.799	0.773
pTa/ Tis/pT1	235 (40.38)	158 (44.38)	77 (34.07)			150 (37.88)	74 (37.37)	76 (38.38)		
pT2	124 (21.31)	80 (22.47)	44 (19.47)			82 (20.71)	44 (22.22)	38 (19.19)		
pT3	187 (32.13)	102 (28.65)	85 (37.61)			136 (34.34)	68 (34.34)	68 (34.34)		
pT4	14 (2.41)	5 (1.40)	9 (3.98)			12 (3.03)	4 (2.02)	8 (4.04)		
pTx	22 (3.78)	11 (3.09)	11 (4.87)			16 (4.04)	8 (4.04)	8 (4.04)		

(Continued)

TABLE 2 Continued

Variables	Before PSM					After PSM				
	Total (n=582)	NLR<3 (n=356)	NLR≥3 (n=226)	χ^2	P value	Total (n=396)	NLR<3 (n=198)	NLR≥3 (n=198)	χ^2	P value
pN stage, n (%)				46.373	**<0.001**				1.159	0.763
pN0	312 (53.61)	225 (63.20)	87 (38.50)			175 (44.19)	88 (44.44)	87 (43.94)		
pN1	75 (12.89)	46 (12.92)	29 (12.83)			58 (14.65)	29 (14.65)	29 (14.65)		
pN2	55 (9.45)	31 (8.71)	24 (10.62)			50 (12.63)	28 (14.14)	22 (11.11)		
pN3	140 (24.05)	54 (15.17)	86 (38.05)			113 (28.54)	53 (26.77)	60 (30.30)		
Grade, n (%)				11.724	**0.020**				3.287	0.511
G1	284 (48.8)	189 (53.09)	95 (42.04)			179 (45.2)	92 (46.46)	87 (43.94)		
G2	212 (36.43)	127 (35.67)	85 (37.61)			152 (38.38)	78 (39.39)	74 (37.37)		
G3	61 (10.48)	28 (7.87)	33 (14.60)			47 (11.87)	20 (10.10)	27 (13.64)		
G4	3 (0.52)	1 (0.28)	2 (0.88)			2 (0.51)	0 (0.00)	2 (1.01)		
Gx	22 (3.78)	11 (3.09)	11 (4.87)			16 (4.04)	8 (4.04)	8 (4.04)		
LVI/PNI, n (%)				5.178	**0.023**				0.230	0.631
No	463 (79.55)	294 (82.58)	169 (74.78)			306 (77.27)	151 (76.26)	155 (78.28)		
Yes	119 (20.45)	62 (17.42)	57 (25.22)			90 (22.73)	47 (23.74)	43 (21.72)		

PSM, propensity score matching; MD, missing data; LVI, lymphovascular invasion; PNI, perineural invasion; NLR, neutrophil–lymphocyte ratio.
The bold-faced values represent P-values that indicate statistical significance.

TABLE 3 Univariate and multivariate analyses of clinicopathological factors associated with survival after PSM.

Variables	PFS after PSM				CSS after PSM			
	Univariate analysis		Multivariate analysis		Univariate analysis		Multivariate analysis	
	HR (95% CI)	P value	HR (95% CI)	P value	HR (95% CI)	P value	HR (95% CI)	P value
Age (>55 vs. ≤55)	0.85 (0.60-1.19)	0.350	1.21 (0.85-1.73)	0.283	0.95 (0.64-1.40)	0.790	1.42 (0.95-2.13)	0.087
BMI (>23 vs. ≤23)	1.03 (0.92-1.14)	0.640	1.09 (0.97-1.23)	0.152	1.03 (0.93-1.15)	0.564	1.11 (0.98-1.25)	0.087
pT stage[a]	1.17 (1.07-1.27)	**<0.001**	1.12 (0.95-1.31)	0.179	1.14 (1.03-1.26)	0.013	1.07 (0.89-1.28)	0.495
pN stage[a]	2.22 (1.90-2.58)	**<0.001**	2.22 (1.89-2.60)	**<0.001**	2.22 (1.86-2.65)	**<0.001**	2.28 (1.89-2.75)	**<0.001**
Pathological grade[a]	1.13 (1.04-1.24)	0.006	0.99 (0.85-1.17)	0.929	1.10 (0.99-1.23)	0.084	0.97 (0.81-1.17)	0.759
LVI/PNI (Yes vs. No)	1.55 (1.06-2.27)	0.023	1.12 (0.76-1.66)	0.562	1.66 (1.09-2.55)	**0.019**	1.25 (0.81-1.94)	0.320
NLR (≥ 3.0 vs. < 3.0)	1.81 (1.27-2.56)	**<0.001**	1.64 (1.15-2.34)	**0.006**	1.81 (1.21-2.69)	**0.004**	1.56 (1.04-2.34)	**0.030**

[a]pT, pN and pathological grade used linear trends to compare different subgroups. PSM, propensity score matching; PFS, progression-free survival; CSS, cancer-specific survival; HR, hazard ratio; 95% CI, 95% confidence interval; LVI, lymphovascular invasion; PNI, perineural invasion; NLR, neutrophil–lymphocyte ratio.
The bold-faced values represent P-values that indicate statistical significance.

More importantly, survival analysis revealed that high infiltration of CD66$^+$ TANs was associated with poor PFS and CSS (Figure 3A), whereas enrichment of CD8+ T cells was correlated with better CSS but was not significantly correlated with PFS (Figure 3B). Both the CD66$^+$ TAN ratio and the CD66$^+$ TAN/CD8+ T-cell ratio indicated the presence of an immunosuppressive phenotype and predicted a poor immunotherapy response and clinical outcomes (Figures 3C, D).

3.6 The proinflammatory response leads to TAN N2 polarization and NET formation, inducing CD8+ T-cell depletion

Accumulating evidence indicates that N2 TANs are critical components that stimulate immunosuppression, tumor progression and metastasis and can be induced by the proinflammatory cytokine IL-8 (30, 32–35). To assess the

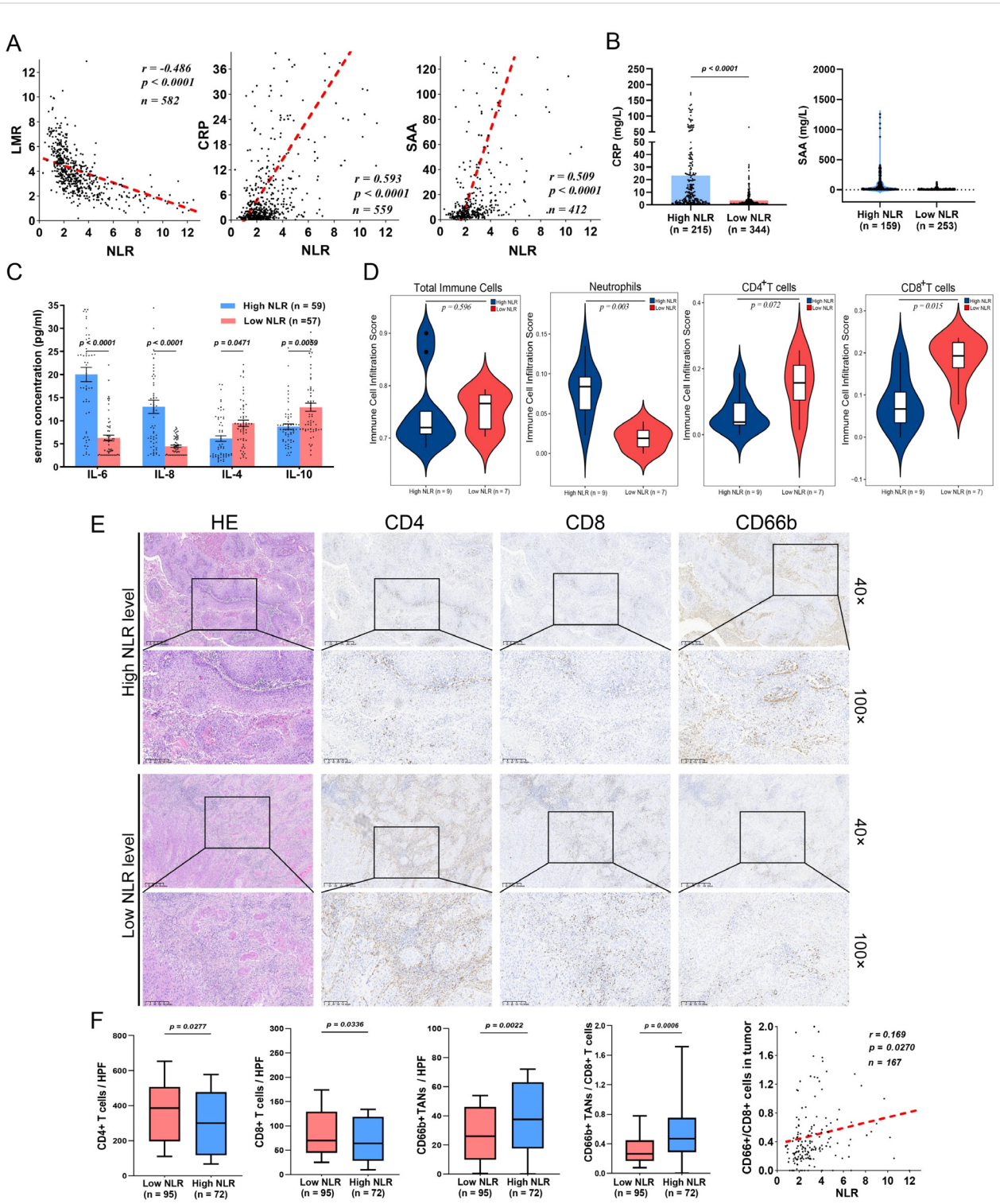

FIGURE 2
A high preoperative NLR is associated with TAN infiltration and a decrease in CD8+ T cells in the TME. **(A)** In PSCC patients, the NLR is negatively correlated with LMR and positively correlated with proinflammatory CRP and SAA protein expression. **(B)** CRP and SAA were evaluated in the high-NLR groups. **(C)** The NLR is related to high proinflammatory cytokine secretion (IL-6 and IL-8) and low levels of anti-inflammatory cytokines (IL-4 and IL-10) in PSCC. **(D)** Immune infiltration scores determined by ImmuCellAI indicated that the infiltration of TANs was increased, whereas the infiltration of CD8+ T cells was decreased in the high-NLR groups. **(E)** IHC assays showing the expression patterns of TANs ($CD66^+$), $CD4^+$ T cells and $CD8^+$ T cells in the TME. **(F)** $CD4^+$ T cells and $CD8^+$ T cells were abundant in the low NLR subgroup, whereas TAN infiltration and the TANs/$CD8^+$ T-cell ratio were increased and positively correlated with the high NLR subgroup. CRP, C-reactive protein; IHC, immunohistochemistry; LMR, lymphocyte–monocyte ratio; NLR, neutrophil–lymphocyte ratio; TANs, tumor-associated neutrophils; TME, tumor microenvironment; SAA, serum amyloid A; PSCC, penile squamous cell carcinoma.

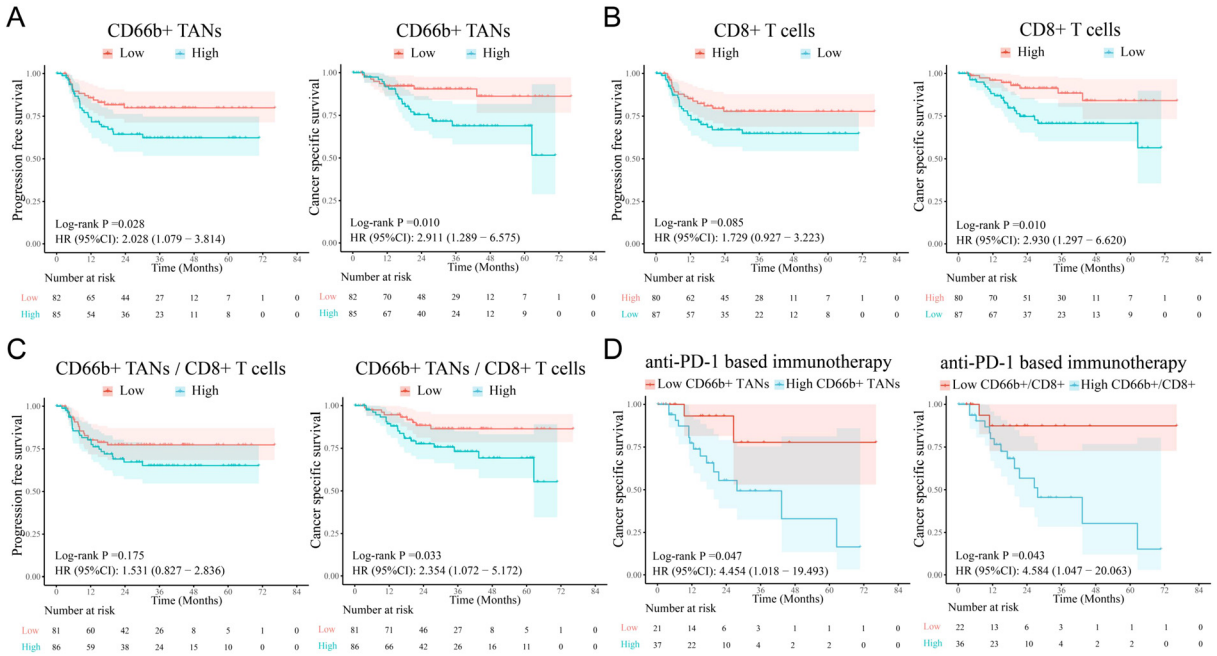

FIGURE 3
The infiltration levels of TANs and CD8$^+$ T cells are correlated with survival in PSCC patients. **(A)** Survival analysis revealed that high TAN infiltration in tumors was associated with poor PFS and CSS in PSCC patients. **(B, C)** A reduction in the number of CD8$^+$ T cells and an increase in the CD66b$^+$/CD8$^+$ T-cell ratio were related to poor survival, although the differences in PFS were not significant. **(D)** Increases in CD66b$^+$ TANs and the CD66b$^+$/CD8$^+$ ratio were associated with poor immunotherapy response. TANs, tumor-associated neutrophils; PFS, progression-free survival; CSS, cancer-specific survival.

polarization of TANs, flow cytometric analysis was performed; the results revealed that the proportion of N2 TANs (CXCR2$^+$CD66$^+$) was significantly greater in patients with high NLRs and was associated with advanced pT and pN stages (Figures 4A, B). Through mIF staining, we discovered that in tumors from high-NLR patients, N2 TANs formed many NETs through NETosis (36); these NETs were identified via CitH3 and MPO staining and also exhibited high expression of the prometastatic cytokine TGF-β (Figure 4D). Previous studies have also indicated that NETs can impair antitumor T-cell responses by increasing CD8+ T-cell exhaustion (37, 38). We found that exhausted CD8$^+$ T cells were enriched in high-NLR tumors, which was consistent with N2 TAN infiltration (Figure 4E). Spatial distance analysis revealed that exhausted CD8+ T cells were in close proximity to N2 TANs in the high-NLR group (Figure 4F). Survival analysis revealed that a closer average distance between these cells was associated with a poorer prognosis (Figure 4G). These results suggest that N2 TANs mediate the formation of NETs, which might induce the exhaustion of neighboring CD8+ T cells, thereby promoting the formation of an immunosuppressive microenvironment. This could be the underlying reason for the poor response to immunotherapy and the unfavorable prognosis in patients with high NLRs.

4 Discussion

Penile cancer (PC) is more prevalent in underdeveloped regions with poor access to education and medical resources (2). Although PC can be cured in more than 80% of patients with early-stage disease, PC progresses to a life-threatening disease when lymphatic metastasis occurs; up to 40% of newly diagnosed cases in China exhibit lymph node metastasis (1, 39). Definitive TNM staging is the most commonly used method to predict prognosis, but there is a lack of available personalized molecular markers to address intratumor heterogeneity. To enhance therapeutic efficacy, it was great challenges to explore the heterogeneity and complexity of the TME in PC (40). Although previous studies indicate that IDO1, RAB20 and HOXD11 are related to a poor PC prognosis (27, 28, 41); the disadvantages of high cost, high time consumption and poor repeatability for genetic testing of these markers make their clinical application more difficult. The NLR is an economical, simple and widely used inflammatory marker that is related to immunotherapy resistance, regional lymph node metastasis and poor outcomes in patients with PC (16). The preoperative NLR, as an ideal indicator, is beneficial for predicting survival before surgery and can be used to guide treatment and follow-up precisely. However, previous studies of the NLR in PC patients lacked high-

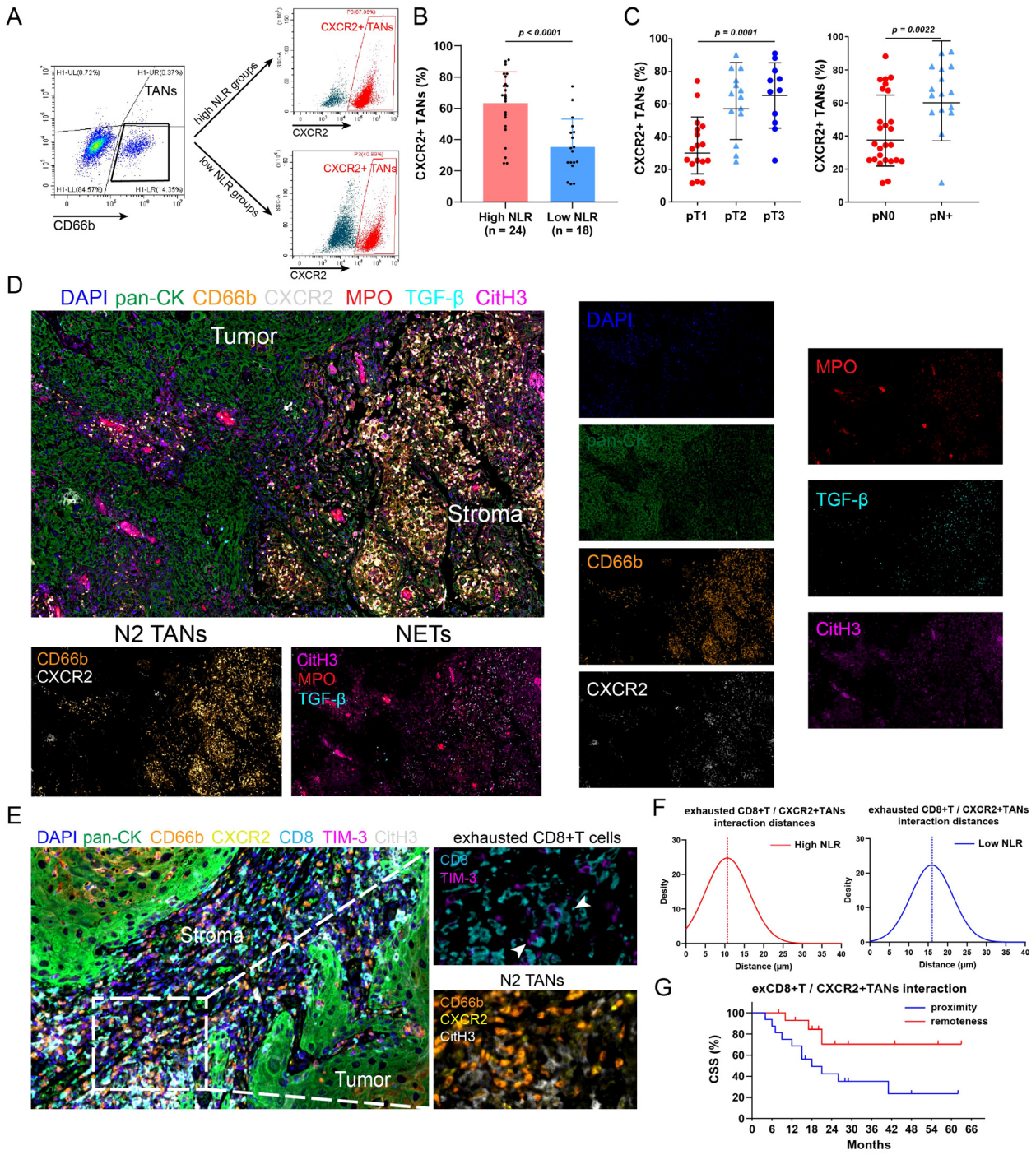

FIGURE 4
N2 TANs induce NET formation and CD8+ T cell exhaustion in tumors with high NLRs. **(A)** Flow cytometry was conducted to detect N2 TANs ($CXCR2^{+}CD66^{+}$) in tumors with different NLRs. **(B)** PSCC patients with high NLRs had increased N2-weighted TAN infiltration in tumors. **(C)** The abundance of N2 TANs in PSCC was associated with advanced pT stage and lymph node metastasis. **(D)** Immunofluorescence staining revealed the tumor and stroma regions in PSCC tumors (400×). In patients with high NLRs, TANs exhibit the N2 phenotype ($CXCR2^{+}$), promote NET formation (marked by CitH3, MPO) and secrete the protumor cytokine TGF-β. **(E)** Multiple immunofluorescence assays revealed the spatial relationship between N2 TANs and exhausted CD8+ T cells ($CD8^{+}TIM\text{-}3^{+}$) (1000×). **(F)** The relative distance between N2 TANs and exhausted CD8+ T cells was shorter in patients with high NLRs than in those with low NLRs, indicating that NET formation could mediate the dysfunction of CD8+ T cells. **(G)** A close relationship between N2 TANs and exhausted CD8+ T cells was associated with poor survival (12 patients in the proximity group, 15 patients in the remoteness group). TANs, tumor-associated neutrophils; NETs, neutrophil extracellular traps; ex, exhausted; NLR, neutrophil–lymphocyte ratio.

quality prognostic evidence, and the relationships between the NLR and the inflammatory TME and the underlying mechanism warrant additional exploration.

In previous studies, it was highly challenging to obtain a large cohort of PC patients with standardized baseline treatment initially. Owing to the surgical timing and boundary of inguinal lymph node dissection remaining controversial in PC (4), the surgical patterns are not consistent. To ensure data quality, all PC patients in our study underwent concurrent lymphadenectomy to obtain clear pN stage information, and prognostic bias attributed to insufficient surgical treatment was ruled out (23). More importantly, most studies did not account for the notably greater proportion of pN+ patients in the high NLR group, which might lead to overestimation of the prognostic value of the NLR. In addition, given the rare nature of this disease, existing studies have focused on small sample sizes and single-center cohorts.

Since 2010, a total of 582 PC patients from four centers were enrolled in our study. The results underscore the significant correlation between a high NLR and adverse clinical characteristics such as pT stage, pN stage, grade, and lymphovascular and perineural invasion. Similar to previous findings, PC patients with high NLRs presented a systemic hyperinflammatory status associated with shorter PFS and CSS (16, 19, 20, 22). Importantly, our study represents the first use of PSM and stratified analysis to control for the prognostic bias of pN stage and revealed that the NLR is also an independent unfavorable prognostic indicator for both PFS (HR: 1.64, 95% CI: 1.15–2.34) and CSS (HR: 1.56, 95% CI: 1.04–2.34). Interestingly, high NLR level patients were also associated with poor chemotherapy and immunotherapy response. Therefore, through rigorous enrollment and reasonable statistical methods, we demonstrated that the preoperative NLR is a simple and reliable marker for PC prognosis evaluation and is particularly suitable for wide use in underdeveloped regions. Besides, preoperative NLR level is an available marker to predict response especially in the neoadjuvant therapy phase, and is also beneficial for postoperative treatment decisions.

Although the NLR reflects the balance between systemic inflammation and adaptive immunity, the dynamic changes in cytokines, secreted proteins and the inflammatory TME in PC remain unclear. Wang et al. reported that IL1RN and PRRX1 is the prognostic biomarker correlated with immune infiltrates in colorectal cancer (42). The increase in the NLR was consistent with the trends in the levels of CRP and the proinflammatory cytokines IL-6, IL-2 and TNF-α (43). Similarly, we found that a high NLR was associated with high SAA, CRP and serum IL-6 and IL-8 levels in PC patients, indicating a direct link between the NLR and the inflammatory immune microenvironment.

To further characterize the inflammatory microenvironment in high-NLR patients, comprehensive sequencing, IHC and mIF were performed, and the results revealed an immunosuppressive phenotype due to the enrichment of TANs and decreased enrichment of CD8+ T cells. It was reported that IL-6 and IL-8 recruit and induce the migration of macrophages and neutrophils into the TME to amplify inflammatory signaling and promote malignant progression (44). In addition, IL-8 plays a dominant role in the polarization of TANs toward N2, which is widely associated with immunosuppression and metastasis (32, 33, 44–46). Our results proved that the preoperative NLR is strongly related to the N2-weighted TAN/CD8+ T-cell ratio in the TME. In PC patients, a high-NLR was related to increased IL-8 secretion, TAN enrichment, N2 phenotype differentiation, reduced CD8+ T-cell infiltration. The imbalance in the TAN/CD8+ T-cell ratio is a key feature that explains the poor prognosis and immunotherapy resistance of high-NLR patients. On the other hand, N2 TANs can induce NET formation by forming web-like DNA structures and releasing reactive oxygen species, cytokines and granular proteins to promote tumor dissemination and metastasis (47, 48). NETs facilitate tumor progression and poor outcomes through various mechanisms. For example, the release of matrix metalloproteinase-9 and neutrophil elastase promotes degradation of the extracellular matrix, creating a more permissive environment for tumor cell invasion (49). Second, NETs induce TGF-β and VEGF secretion to increase tumor angiogenesis, which supplies nutrients and oxygen, further supporting their growth and metastatic potential (50). Moreover, NETs mediate epithelial–mesenchymal transition by continuously secreting protumor cytokines to promote the acquisition of mesenchymal and invasive properties by tumor cells (51). We found that many NETs formed around N2 TANs in PC tissues with high NLRs. We also found that oversecretion of TGF-β by N2 TANs induced CD8+ T-cell depletion and might facilitate metastasis by inducing angiogenesis. Our results preliminarily revealed that in PC patients with high NLRs, the proinflammatory immune microenvironment might promote tumor progression and was associated with poor prognosis. Further understanding of the detailed mechanisms is urgently needed to improve current treatments and outcomes.

Finally, the study has several limitations. First, it was a retrospective observational study with inherent bias and limited by the small sample sizes of patients performing with mRNA-seq. The clinical significance of the NLR needs to be validated in other centers, especially in cohorts from different areas with different races. Second, a prospective study design is essential to validate the predictive role of the NLR in guiding treatment decision making and follow-up strategies. Besides, PSM methods excluded substantial portions of the whole cohort, potentially distorting the true effects of covariates. Although we highlight the relationship between the NLR and the suppressive immune microenvironment, the associated molecular pathways and interventions need to be further explored.

5 Conclusion

In summary, we used PSM to demonstrate that the NLR is an independent unfavorable prognostic indicator in a high-quality and large multicenter cohort of PC patients. A high preoperative NLR is associated with a systematic inflammatory response that suppresses the immune response by promoting N2 TAN infiltration, NET formation and CD8+ T-cell exhaustion and ultimately mediates immunotherapy resistance and poor outcomes.

Data availability statement

The raw data supporting the conclusions of this article will be made available by the authors, without undue reservation.

Ethics statement

The studies involving humans were approved by Sun Yat-sen University Cancer Center ethics committee. The studies were conducted in accordance with the local legislation and institutional requirements. The participants provided their written informed consent to participate in this study.

Author contributions

XT: Conceptualization, Data curation, Formal Analysis, Funding acquisition, Writing – original draft, Writing – review & editing. YW: Conceptualization, Data curation, Investigation, Writing – original draft. YY: Data curation, Formal Analysis, Writing – original draft. QZ: Data curation, Investigation, Writing – original draft. JL: Data curation, Writing – original draft. SC: Data curation, Writing – original draft. QX: Data curation, Writing – original draft. CZ: Investigation, Writing – original draft. XD: Investigation, Writing – original draft. RZ: Investigation, Writing – original draft. ZL: Software, Writing – original draft. YT: Validation, Writing – original draft. HL: Visualization, Writing – original draft. WCW: Visualization, Writing – original draft. JC: Visualization, Writing – original draft. WSW: Data curation, Investigation, Writing – review & editing. ZW: Conceptualization, Writing – review & editing. KY: Conceptualization, Funding acquisition, Project administration, Resources, Writing – review & editing. SG: Conceptualization, Project administration, Writing – review & editing.

Funding

The author(s) declare that financial support was received for the research and/or publication of this article. This study was supported by the GuangDong Basic and Applied Basic Research Foundation (No. 2024A1515013007) to Kai Yao and the Beijing Xisike Clinical Oncology Research Foundation (No. Y-Gilead2024-ZD-0239) to Kai Yao. This study was also supported by the Postdoctoral Fellowship Program (Grade B) of China Postdoctoral Science Foundation (No. GZB20240901) to Xingliang Tan, and the 76th China Postdoctoral Science Foundation (No. 2024M763799) to Xingliang Tan.

Acknowledgments

We appreciate Keming Chen for providing pathological assistance.

Conflict of interest

The authors declare that the research was conducted in the absence of any commercial or financial relationships that could be construed as a potential conflict of interest.

Generative AI statement

The author(s) declare that no Generative AI was used in the creation of this manuscript.

Publisher's note

All claims expressed in this article are solely those of the authors and do not necessarily represent those of their affiliated organizations, or those of the publisher, the editors and the reviewers. Any product that may be evaluated in this article, or claim that may be made by its manufacturer, is not guaranteed or endorsed by the publisher.

Supplementary material

The Supplementary Material for this article can be found online at: https://www.frontiersin.org/articles/10.3389/fimmu.2025.1568825/full#supplementary-material

References

1. Fu L, Tian T, Yao K, Chen XF, Luo G, Gao Y, et al. Global pattern and trends in penile cancer incidence: population-based study. *JMIR Public Health Surveill.* (2022) 8: e34874. doi: 10.2196/34874

2. Brouwer OR, Albersen M, Parnham A, Protzel C, Pettaway CA, Ayres B, et al. European association of urology-american society of clinical oncology collaborative guideline on penile cancer: 2023 update. *Eur Urol.* (2023) 83:548–60. doi: 10.1016/j.eururo.2023.02.027

3. Amin MB, Greene FL, Edge SB, Compton CC, Gershenwald JE, Brookland RK, et al. The Eighth Edition AJCC Cancer Staging Manual: Continuing to build a bridge from a population-based to a more "personalized" approach to cancer staging. *CA Cancer J Clin.* (2017) 67:93–9. doi: 10.3322/caac.21388

4. Cindolo L, Spiess PE, Bada M, Chipollini JJ, Nyirády P, Chiodini P, et al. Adherence to EAU guidelines on penile cancer translates into better outcomes: a multicenter international study. *World J Urol.* (2019) 37:1649–57. doi: 10.1007/s00345-018-2549-3

5. Yao K, Chen Y, Ye Y, Wu Z, Chen D, Han H, et al. Lymph node mapping in patients with penile cancer undergoing pelvic lymph node dissection. *J Urol.* (2021) 205:145–51. doi: 10.1097/JU.0000000000001322

6. Tan X, Chen D, Guo S, Wang Y, Zou Y, Wu Z, et al. Molecular stratification by BCL2A1 and AIM2 provides additional prognostic value in penile squamous cell carcinoma. *Theranostics.* (2021) 11:1364–76. doi: 10.7150/thno.51725

7. Joshi SS, Handorf E, Strauss D, Correa AF, Kutikov A, Chen DYT, et al. Treatment trends and outcomes for patients with lymph node-positive cancer of the penis. *JAMA Oncol*. (2018) 4:643–9. doi: 10.1001/jamaoncol.2017.5608

8. Tan X, Wang Y, Wu Z, Zhou Q, Tang Y, Liu Z, et al. The role of Her-2 in penile squamous cell carcinoma progression and cisplatin chemoresistance and potential for antibody-drug conjugate-based therapy. *Eur J Cancer*. (2023) 194:113360. doi: 10.1016/j.ejca.2023.113360

9. Sanchez DF, Soares F, Alvarado-Cabrero I, Cañete S, Fernández-Nestosa MJ, Rodríguez IM, et al. Pathological factors, behavior, and histological prognostic risk groups in subtypes of penile squamous cell carcinomas (SCC). *Semin Diagn Pathol*. (2015) 32:222–31. doi: 10.1053/j.semdp.2014.12.017

10. Yan R, Ma H, Jiang L, Guo S, Shi Y, Sheng X, et al. First-line programmed death receptor-1 (PD-1) inhibitor and epidermal growth factor receptor (EGFR) blockade, combined with platinum-based chemotherapy, for stage IV penile cancer. *BJU Int*. (2023) 131:198–207. doi: 10.1111/bju.v131.2

11. Zhou QH, Deng CZ, Chen JP, Huang KB, Liu TY, Yao K, et al. Elevated serum LAMC2 is associated with lymph node metastasis and predicts poor prognosis in penile squamous cell carcinoma. *Cancer Manag Res*. (2018) 10:2983–95. doi: 10.2147/CMAR.S171912

12. Thomas A, Necchi A, Muneer A, Tobias-MaChado M, Tran ATH, Van Rompuy AS, et al. Penile cancer. *Nat Rev Dis Primers*. (2021) 7:11. doi: 10.1038/s41572-021-00246-5

13. Shen G, Wang Q, Li Z, Xie J, Han X, Wei Z, et al. Bridging chronic inflammation and digestive cancer: the critical role of innate lymphoid cells in tumor microenvironments. *Int J Biol Sci*. (2024) 20:4799–818. doi: 10.7150/ijbs.96338

14. Hold GL, Rao H-L, Chen J-W, Li M, Xiao Y-B, Fu J, et al. Increased intratumoral neutrophil in colorectal carcinomas correlates closely with Malignant phenotype and predicts patients' Adverse prognosis. *PloS One*. (2012) 7. doi: 10.1371/journal.pone.0030806

15. Liu K, Zhao K, Wang L, Sun E. The prognostic values of tumor-infiltrating neutrophils, lymphocytes and neutrophil/lymphocyte rates in bladder urothelial cancer. *Pathol - Res Pract*. (2018) 214:1074–80. doi: 10.1016/j.prp.2018.05.010

16. Saputra HM, Hidayatullah F, Kloping YP, Renaldo J, Chung E, Hakim L. Prognostic value of neutrophil-to-lymphocyte ratio (NLR) in penile cancer: A systematic review and meta-analysis. *Ann Med Surg*. (2022) 81. doi: 10.1016/j.amsu.2022.104335

17. García-Escobar A, Vera-Vera S, Tébar-Márquez D, Rivero-Santana B, Jurado-Román A, Jiménez-Valero S, et al. Neutrophil-to-lymphocyte ratio an inflammatory biomarker, and prognostic marker in heart failure, cardiovascular disease and chronic inflammatory diseases: New insights for a potential predictor of anti-cytokine therapy responsiveness. *Microvasc Res*. (2023) 150:104598. doi: 10.1016/j.mvr.2023.104598

18. Kasuga J, Kawahara T, Takamoto D, Fukui S, Tokita T, Tadenuma T, et al. Increased neutrophil-to-lymphocyte ratio is associated with disease-specific mortality in patients with penile cancer. *BMC Cancer*. (2016) 16. doi: 10.1186/s12885-016-2443-6

19. Azizi M, Peyton CC, Boulware DC, Chipollini J, Juwono T, Pow-Sang JM, et al. Prognostic value of neutrophil-to-lymphocyte ratio in penile squamous cell carcinoma patients undergoing inguinal lymph node dissection. *Eur Urol Focus*. (2019) 5:1085–90. doi: 10.1016/j.euf.2018.06.008

20. Jindal T, Pawar P, Agarwal S, Jain P, Meena M, Sarwal A, et al. The use of preoperative neutrophil–lymphocyte ratio and lymphocyte–monocyte ratio in predicting survival and groin node involvement of patients with squamous cell carcinoma of penis. *Urol Ann*. (2021) 13(4):391–396. doi: 10.4103/UA.UA_112_20

21. El Zarif T, Nassar AH, Pond GR, Zhuang TZ, Master V, Nazha B, et al. Safety and efficacy of immune checkpoint inhibitors in advanced penile cancer: report from the Global Society of Rare Genitourinary Tumors. *JNCI: J Natl Cancer Institute*. (2023) 115(12):1605–1615. doi: 10.1200/JCO.2023.41.6_suppl.5

22. Hu C, Bai Y, Li J, Zhang G, Yang L, Bi C, et al. Prognostic value of systemic inflammatory factors NLR, LMR, PLR and LDH in penile cancer. *BMC Urol*. (2020) 20. doi: 10.1186/s12894-020-00628-z

23. Tan X, Cai T, Wang Y, Wu Z, Zhou Q, Guo S, et al. Regional lymph node mapping in patients with penile cancer undergoing radical inguinal lymph node dissection - a retrospective cohort study. *Int J Surg*. (2024) 110:2865–73. doi: 10.1097/JS9.0000000000001160

24. Yao K, Tu H, Li Y-H, Qin Z-K, Liu Z-W, Zhou F-J, et al. Modified technique of radical inguinal lymphadenectomy for penile carcinoma: morbidity and outcome. *J Urol*. (2010) 184:546–52. doi: 10.1016/j.juro.2010.03.140

25. Miao YR, Zhang Q, Lei Q, Luo M, Xie GY, Wang H, et al. ImmuCellAI: A unique method for comprehensive T-cell subsets abundance prediction and its application in cancer immunotherapy. *Adv Sci (Weinh)*. (2020) 7:1902880. doi: 10.1002/advs.201902880

26. Czajkowski M, Wierzbicki PM, Kotulak-Chrząszcz A, Małkiewicz B, Sosnowski R, Kmieć Z, et al. Pro-inflammatory cytokine gene expression in penile cancer: preliminary studies. *Medicina (Kaunas)*. (2023) 59. doi: 10.3390/medicina59091623

27. Tan X, Yuan G, Wang Y, Zou Y, Luo S, Han H, et al. RAB20 Promotes Proliferation via G2/M Phase through the Chk1/cdc25c/cdc2-cyclinB1 Pathway in Penile Squamous Cell Carcinoma. *Cancers (Basel)*. (2022) 14. doi: 10.3390/cancers14051106

28. Tan X, Liu Z, Wang Y, Wu Z, Zou Y, Luo S, et al. miR-138-5p-mediated HOXD11 promotes cell invasion and metastasis by activating the FN1/MMP2/MMP9 pathway and predicts poor prognosis in penile squamous cell carcinoma. *Cell Death Dis*. (2022) 13:816. doi: 10.1038/s41419-022-05261-2

29. Strieter RM, Burdick MD, Mestas J, Gomperts B, Keane MP, Belperio JA. Cancer CXC chemokine networks and tumour angiogenesis. *Eur J Cancer*. (2006) 42:768–78. doi: 10.1016/j.ejca.2006.01.006

30. Jamieson T, Clarke M, Steele CW, Samuel MS, Neumann J, Jung A, et al. Inhibition of CXCR2 profoundly suppresses inflammation-driven and spontaneous tumorigenesis. *J Clin Invest*. (2012) 122:3127–44. doi: 10.1172/JCI61067

31. Mahiddine K, Blaisdell A, Ma S, Créquer-Grandhomme A, Lowell CA, Erlebacher A. Relief of tumor hypoxia unleashes the tumoricidal potential of neutrophils. *J Clin Invest*. (2019) 130:389–403. doi: 10.1172/JCI130952

32. Peng H-H, Liang S, Henderson AJ, Dong C. Regulation of interleukin-8 expression in melanoma-stimulated neutrophil inflammatory response. *Exp Cell Res*. (2007) 313:551–9. doi: 10.1016/j.yexcr.2006.10.030

33. Waugh DJJ, Wilson C. The interleukin-8 pathway in cancer. *Clin Cancer Res*. (2008) 14:6735–41. doi: 10.1158/1078-0432.CCR-07-4843

34. Masucci MT, Minopoli M, Carriero MV. Tumor associated neutrophils. Their role in tumorigenesis, metastasis, prognosis and therapy. *Front Oncol*. (2019) 9:1146. doi: 10.3389/fonc.2019.01146

35. Shaul ME, Fridlender ZG. Neutrophils as active regulators of the immune system in the tumor microenvironment. *J Leukoc Biol*. (2017) 102:343–9. doi: 10.1189/jlb.5MR1216-508R

36. Mowery YM, Luke JJ. NETosis impact on tumor biology, radiation, and systemic therapy resistance. *Clin Cancer Res*. (2024) 30:3965–7. doi: 10.1158/1078-0432.CCR-24-1363

37. Taifour T, Attalla SS, Zuo D, Gu Y, Sanguin-Gendreau V, Proud H, et al. The tumor-derived cytokine Chi3l1 induces neutrophil extracellular traps that promote T cell exclusion in triple-negative breast cancer. *Immunity*. (2023) 56:2755–2772.e8. doi: 10.1016/j.immuni.2023.11.002

38. Teijeira Á, Garasa S, Gato M, Alfaro C, Migueliz I, Cirella A, et al. CXCR1 and CXCR2 chemokine receptor agonists produced by tumors induce neutrophil extracellular traps that interfere with immune cytotoxicity. *Immunity*. (2020) 52:856–871.e8. doi: 10.1016/j.immuni.2020.03.001

39. Zekan DS, Dahman A, Hajiran AJ, Luchey AM, Chahoud J, Spiess PE. Prognostic predictors of lymph node metastasis in penile cancer: a systematic review. *Int Braz J Urol*. (2021) 47:943–56. doi: 10.1590/s1677-5538.ibju.2020.0959

40. Li Z, Li J, Bai X, Huang X, Wang Q. Tumor microenvironment as a complex milieu driving cancer progression: a mini review. *Clin Transl Oncol*. (2024). doi: 10.1007/s12094-024-03697-w

41. Zhou QH, Han H, Lu JB, Liu TY, Huang KB, Deng CZ, et al. Up-regulation of indoleamine 2,3-dioxygenase 1 (IDO1) expression and catalytic activity is associated with immunosuppression and poor prognosis in penile squamous cell carcinoma patients. *Cancer Commun (Lond)*. (2020) 40:3–15. doi: 10.1002/cac2.12001

42. Wang Q, Huang X, Zhou S, Ding Y, Wang H, Jiang W, et al. IL1RN and PRRX1 as a prognostic biomarker correlated with immune infiltrates in colorectal cancer: evidence from bioinformatic analysis. *Int J Genomics*. (2022) 2022:2723264. doi: 10.1155/2022/2723264

43. Wang Y, Li C, Niu L, Fu M, Tian J, An X. Difference in serum miRNA expression between immunoglobulin-sensitive and -insensitive incomplete Kawasaki disease patients. *Exp Ther Med*. (2021) 21:162. doi: 10.3892/etm.2020.9593

44. Eruslanov EB, Bhojnagarwala PS, Quatromoni JG, Stephen TL, Ranganathan A, Deshpande C, et al. Tumor-associated neutrophils stimulate T cell responses in early-stage human lung cancer. *J Clin Invest*. (2014) 124:5466–80. doi: 10.1172/JCI77053

45. Fridlender ZG, Sun J, Kim S, Kapoor V, Cheng G, Ling L, et al. Polarization of tumor-associated neutrophil phenotype by TGF-beta: "N1" versus "N2" TAN. *Cancer Cell*. (2009) 16:183–94. doi: 10.1016/j.ccr.2009.06.017

46. Ke M, Zhu H, Lin Y, Zhang Y, Tang T, Xie Y, et al. Actin-related protein 2/3 complex subunit 1B promotes ovarian cancer progression by regulating the AKT/PI3K/mTOR signaling pathway. *J Transl Int Med*. (2024) 12:406–23. doi: 10.2478/jtim-2024-0025

47. Stojkov D, Gigon L, Peng S, Lukowski R, Ruth P, Karaulov A, et al. Physiological and pathophysiological roles of metabolic pathways for NET formation and other neutrophil functions. *Front Immunol*. (2022) 13:826515. doi: 10.3389/fimmu.2022.826515

48. Sorvillo N, Cherpokova D, Martinod K, Wagner DD. Extracellular DNA NET-works with dire consequences for health. *Circ Res*. (2019) 125:470–88. doi: 10.1161/CIRCRESAHA.119.314581

49. Mekori YA, Baram D. Heterotypic adhesion-induced mast cell activation: biologic relevance in the inflammatory context. *Mol Immunol*. (2002) 38:1363–7. doi: 10.1016/S0161-5890(02)00089-5

50. Mousset A, Lecorgne E, Bourget I, Lopez P, Jenovai K, Cherfils-Vicini J, et al. Neutrophil extracellular traps formed during chemotherapy confer treatment resistance via TGF-β activation. *Cancer Cell*. (2023) 41:757–775.e10. doi: 10.1016/j.ccell.2023.03.008

51. Demkow U. Neutrophil extracellular traps (NETs) in cancer invasion, evasion and metastasis. *Cancers (Basel)*. (2021) 13. doi: 10.3390/cancers13174495

frontiers | Frontiers in Immunology

TYPE Review
PUBLISHED 14 May 2025
DOI 10.3389/fimmu.2025.1597202

Check for updates

OPEN ACCESS

EDITED BY
Qi Wang,
Jiangsu University, China

REVIEWED BY
Qiong Lu,
Central South University, China
Hyundeok Kang,
Flowtrials, United States
Shengshan Xu,
Jiangmen Central Hospital, China

*CORRESPONDENCE
Shenguo Chen
61604884@qq.com
Haisheng Lin
linhs669306@163.com

†These authors have contributed equally to this work and share first authorship

RECEIVED 20 March 2025
ACCEPTED 23 April 2025
PUBLISHED 14 May 2025

CITATION
Zhao X, Zhu Y, He Y, Gu W, Zhou Q, Jin B, Chen S and Lin H (2025) Unraveling the immune evasion mechanisms in the tumor microenvironment of head and neck squamous cell carcinoma.
Front. Immunol. 16:1597202.
doi: 10.3389/fimmu.2025.1597202

COPYRIGHT
© 2025 Zhao, Zhu, He, Gu, Zhou, Jin, Chen and Lin. This is an open-access article distributed under the terms of the Creative Commons Attribution License (CC BY). The use, distribution or reproduction in other forums is permitted, provided the original author(s) and the copyright owner(s) are credited and that the original publication in this journal is cited, in accordance with accepted academic practice. No use, distribution or reproduction is permitted which does not comply with these terms.

Unraveling the immune evasion mechanisms in the tumor microenvironment of head and neck squamous cell carcinoma

Xuri Zhao†, Yaping Zhu†, Youya He†, Weiyan Gu, Qi Zhou, Bei Jin, Shenguo Chen* and Haisheng Lin*

Department of Stomatology, Taizhou Hospital of Zhejiang Province Affiliated to Wenzhou Medical University, Taizhou, Zhejiang, China

Head and neck squamous cell carcinoma (HNSCC) is a highly aggressive malignancy characterized by a complex tumor microenvironment (TME) that plays a pivotal role in tumor initiation, progression, and immune evasion. Recent advancements have highlighted the intricate interplay between immune cell infiltration patterns, immune checkpoint dysregulation, and metabolic reprogramming in driving HNSCC immune escape. Despite these insights, significant challenges remain, including the incomplete understanding of specific immune evasion pathways and the lack of personalized therapeutic strategies. To address these gaps, this review introduces a novel "Trinity" regulatory network of immune evasion in HNSCC, encompassing: (1) metabolic reprogramming-mediated immune checkpoint modulation, (2) stromal cell-driven immune dysfunction, and (3) epigenetic remodeling fostering immune tolerance. This framework provides a theoretical foundation for the development of multi-targeted combination therapies and offers innovative strategies to overcome immune evasion. Additionally, this review systematically synthesizes the current understanding of the relationship between the HNSCC microenvironment and immune escape, with a focus on emerging immunotherapeutic approaches such as PD-1/PD-L1 inhibitors and CAR-T cell therapy. Leveraging cutting-edge single-cell sequencing and spatial transcriptomics, we elucidate the spatiotemporal heterogeneity of the HNSCC immune landscape and propose a new paradigm of "lineage plasticity-driven immune adaptation." These insights not only advance our understanding of HNSCC biology but also pave the way for the development of precision immunotherapies aimed at improving patient survival and quality of life. By integrating multidisciplinary perspectives, this work underscores the importance of targeting the TME to achieve durable clinical responses and overcome immunotherapy resistance in HNSCC.

KEYWORDS

head and neck squamous cell carcinoma, tumor microenvironment, immune escape, immunotherapy, immune checkpoint, metabolic reprogramming

1 Introduction

Head and neck squamous cell carcinoma (HNSCC) is a prevalent malignant tumor with rising incidence and mortality rates globally (1). The tumor microenvironment (TME)—comprising immune cells, fibroblasts, vasculature, microbiota, and extracellular matrix—plays a decisive role in tumor initiation, progression, and resistance to therapy. Immune evasion within this complex ecosystem has emerged as a key hallmark of HNSCC (2, 3). A central driver of these processes is immune evasion, a critical strategy by which tumors circumvent host immune surveillance. In HNSCC, diverse TME-associated factors—including cytokines, immunosuppressive cells, and intricate intercellular communication networks—are closely linked to immune evasion.

Within the HNSCC TME, immune cell infiltration patterns profoundly influence tumor progression and immune evasion. Studies demonstrate that CD8+ T cells and regulatory T cells (Tregs) play dual roles in immune surveillance and suppression. High CD8+ T cell infiltration correlates with favorable prognosis, whereas elevated Treg levels are associated with immunosuppression, potentially enabling tumor cells to evade immune attack (4). Tumor-associated macrophages (TAMs) further contribute to immune escape in pan-cancer (5) not to mention HNSCC; their M2-polarized phenotype promotes tumor growth, metastasis, and suppression of antitumor immunity (6).

Metabolic reprogramming in HNSCC represents another crucial axis of immune evasion. Tumor cells alter metabolic pathways to exploit nutrients for proliferation while impairing immune cell function. For instance, excessive lactate production by tumor cells induces localized acidosis, thereby inhibiting T cell activation and proliferation (7). Hypoxic conditions within the TME further exacerbate immune escape by undermining immune surveillance (8).

Immune checkpoint dysregulation is a hallmark of HNSCC immune evasion. Tumor cells upregulate PD-L1 and other checkpoint molecules to suppress T cell activity and evade immune detection (9), and it is even closely related to cell death (Li, 10). Although immune checkpoint inhibitors (e.g., PD-1/PD-L1 blockers) have emerged as a cornerstone of HNSCC therapy, their clinical efficacy remains limited to a subset of patients, reflecting the complexity and heterogeneity of the TME in modulating treatment responses (11).

Despite progress in dissecting individual mechanisms—such as immune checkpoint overexpression, T cell exhaustion, and stromal remodeling—the field lacks an integrated framework to explain how these factors collectively drive immune escape. To address this, we propose a "Trinity" model involving three interlinked pathways: (1) metabolic reprogramming, (2) stromal cell-driven immune dysfunction, and (3) epigenetic remodeling.

This review is the first to systematically integrate and elucidate the spatiotemporal heterogeneity of the HNSCC immune microenvironment, proposing a novel paradigm of "lineage plasticity-driven immune adaptation." And we synthesize current knowledge on HNSCC immune escape mechanisms and provide new theoretical and practical insights based on the "Trinity" network. By innovatively synthesizing the network regulation of immune metabolism, checkpoint interactions, and cellular crosstalk, this work provides fresh insights into the multifaceted mechanisms of immune evasion in HNSCC. Furthermore, it establishes a theoretical foundation for developing precision combination therapies targeting TME-specific vulnerabilities.

Abbreviations: HNSCC, Head and neck squamous cell carcinoma; TME, Tumor microenvironment; Tregs, Regulatory T cells; TAMs, Tumor-associated macrophages; NK cell, Natural killer cell; PD-L1, Programmed death-ligand 1; CSCs, Cancer stem-like cells; MDSCs, Myeloid derived suppressor cells; TMB, Tumor mutational burden; CAF, Cancer associated fibroblasts; ICIs, Immune checkpoint inhibitors; LDH, Lactate dehydrogenase; LCN2, Lipocalin-2; HDAC, Histone deacetylase; PGE2, Prostaglandin E2; HLA, Human leukocyte antigen; LncRNAs, Long non-coding RNAs.

2 Immune infiltration patterns in the HNSCC microenvironment

2.1 Cellular heterogeneity of immune infiltration landscapes

The HNSCC microenvironment exhibits highly heterogeneous and complex immune cell infiltration patterns (12) (Figure 1). Key infiltrating immune populations include CD8+ T cells, CD4+ T cell subsets (Th1/Th2/Th17), natural killer (NK) cells, macrophages, and dendritic cells, collectively forming a dynamic immune network that governs tumor progression and therapeutic responses (13). CD8+ T cells, as central antitumor effectors, demonstrate prognostic significance linked to their infiltration density and spatial organization (14). However, tumor-derived immunosuppressive factors such as IL-10 and TGF-β drive CD8+ T cell dysfunction and exhaustion, facilitating immune escape (15). TAMs further contribute to this immunosuppressive milieu. While M1-polarized TAMs exhibit antitumor activity, M2-polarized TAMs dominate the HNSCC microenvironment, promoting tumor progression via ARG1-mediated L-arginine depletion (impairing TCR signaling) and IL-10/VEGF-driven immunosuppressive angiogenesis (16, 17).

2.2 Tumor-immune cell crosstalk

Bidirectional interactions between tumor and immune cells critically shape HNSCC progression and therapeutic resistance. Programmed death-ligand 1 (PD-L1), overexpressed in ~50% of HNSCC cases, mediates immune evasion through dual mechanisms: membrane-bound PD-L1 engages PD-1 on T cells to induce exhaustion, while extracellular vesicle (EV)-encapsulated PD-L1 systemically suppresses T cell activity (18). Spatial proteomic analyses reveal PD-L1 enrichment at invasive fronts, particularly on cancer stem-like cells (CSCs), where PD-1/PD-L1 interactions impair immune synapse formation (19). Spatial proteomic analyses reveal PD-L1 enrichment at invasive fronts, particularly on CSCs, where PD-1/PD-L1 interactions impair immune synapse formation (20). Tumor-derived IL-6 and TGF-β synergistically reinforce immunosuppression: IL-6

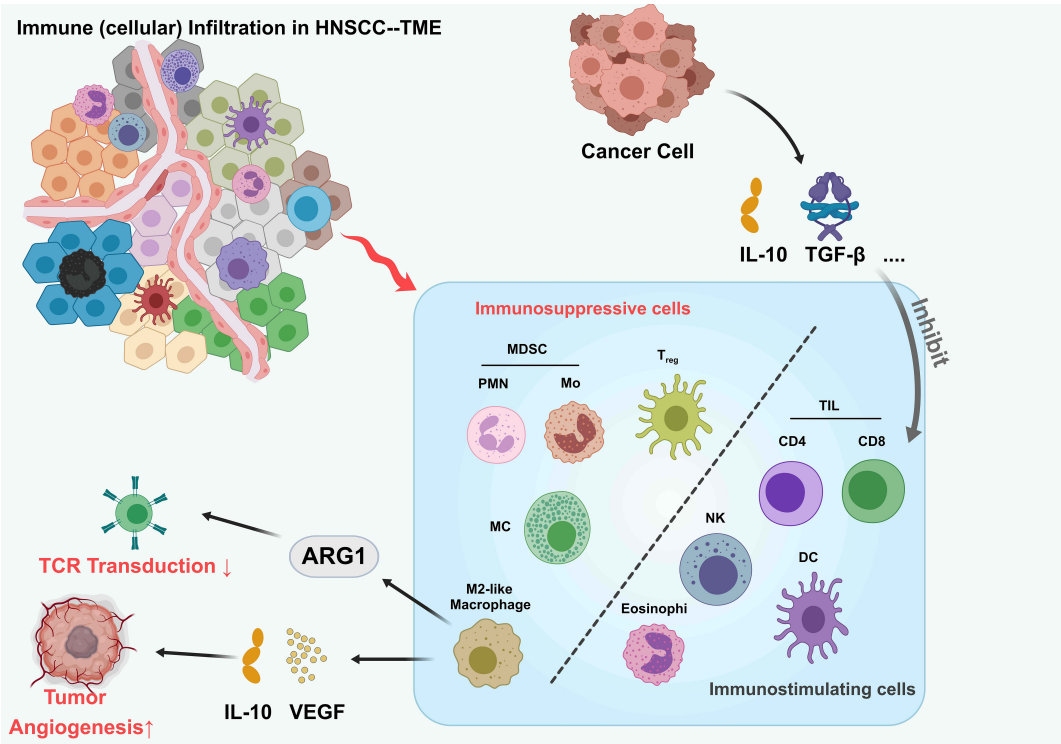

FIGURE 1
Tumor immune infiltrating microenvironment of HNSCC. The tumor microenvironment (TME) in head and neck squamous cell carcinoma (HNSCC), highlighting interactions between immune cells and cancer cells. Tumor cells secrete immunosuppressive cytokines (IL-10, TGF-β) that recruit myeloid-derived suppressor cells (MDSCs; PMN and Mo subsets), regulatory T cells (Treg), M2-like macrophages, and eosinophils. These cells inhibit tumor-infiltrating lymphocytes (TILs), including CD4+, CD8+ T cells, natural killer (NK) cells, and dendritic cells (DCs), suppressing antitumor immunity. ARG1 expression in MDSCs and M2-like macrophages further dampens T cell receptor (TCR) signaling. Additionally, VEGF secretion by tumor cells promotes angiogenesis. This balance between immunosuppressive and immunostimulatory cells shapes the TME, influencing tumor progression.

activates STAT3 to upregulate B7-H3 expression, while TGF-β drives Treg differentiation and confers CD8+ T cells with stem-like exhausted epigenetic states (21). Myeloid-derived suppressor cells (MDSCs) exacerbate immune evasion through peroxynitrite-mediated antigen modification, impairing TCR recognition (22).

2.3 Multilayered regulation of microenvironmental niches

Immune infiltration patterns are modulated by tumor-intrinsic mutations, cytokine networks, and physicochemical stressors. High tumor mutational burden (TMB) inversely correlates with immune infiltration, suggesting genomic instability shapes immune evasion (23). NOTCH1 mutations disrupt CD8+ T cell/Treg balance, while PIK3CA-activating mutations recruit MDSCs via CXCL12/CXCR4 signaling (24). In addition, the hypoxic state in the tumor microenvironment also suppresses the function of immune cells, leading to immune escape (25). The study also found that tumor-associated fibroblasts (CAFs) play an important role in the HNSCC microenvironment (26–28). CAFs alter the infiltration pattern of immune cells and promote tumor growth and metastasis by secreting a variety of cytokines and growth factors (29). Hypoxia-driven HIF-1α activation reprograms Treg metabolism to enhance adenosine production via CD39/CD73 upregulation, while extracellular acidosis (pH 6.5–6.8) inhibits NFAT nuclear translocation, blunting T cell activation (30). CAFs emerge as central stromal orchestrators, secreting TGF-β superfamily ligands to polarize M2 macrophages and LOXL2-mediated collagen crosslinking to form T cell-excluding physical barriers (31).

2.4 Spatial heterogeneity and immune desert/excluded phenotypes

In recent years, the breakthrough of single-cell spatial analysis technology has enabled the detailed analysis of the spatial structure of HNSCC immune microenvironment. Spatial transcriptomic studies have shown that HNSCC has a characteristic “Immune Desert” and “Immune Excluded” phenotype (32). The immune desert region showed substantial loss of effector T cells and dendritic cells, forming a “cold tumor” characteristic without immune monitoring. CD8+ T cells and TAMs were abundant in the immune rejection region, but these cells showed a state of functional inactivation, and their spatial distribution was highly coexisting with the remodeled ECM region (33). This spatial heterogeneity suggests that tumor cells establish hierarchical immune escape mechanisms through physical barrier construction and immunosuppressive signal diffusion.

Pseudotemporal analysis reveals spatial dynamics of T cell exhaustion, with CD8+ T cells transitioning from TCF1+ progenitor states at tumor margins to TIM-3+ terminally exhausted populations in cores—a process governed by TOX/OX40-driven epigenetic reprogramming (34, 35).

Current research paradigms are shifting from targeting oncogenic drivers toward remodeling the immunosuppressive niche. Deciphering the stromal barriers in immune deserts and metabolic suppression networks in excluded zones will enable spatiotemporally precise combination strategies (e.g., ECM degradation coupled with checkpoint blockade). This therapeutic evolution—from tumor eradication to immune ecosystem reconstruction—holds promise for overcoming the spatial limitations of current immunotherapies and achieving durable clinical responses.

3 Dynamic expression and regulatory networks of immune checkpoints

3.1 Spatiotemporal regulation of the PD-1/PD-L1 axis

The PD-1/PD-L1 signaling axis, a central hub of immune evasion in HNSCC, exhibits marked spatiotemporal heterogeneity in its expression dynamics (Figure 2). Single-cell spatial analyses reveal that PD-L1 is specifically overexpressed in CD44+EpCAM+ cancer stem-like subpopulations at invasive tumor fronts, where it induces T cell inactivation through dual mechanisms: membrane-bound signaling and exosome-mediated delivery (36). This expression pattern correlates with HPV status (37), HPV+ tumors upregulate PD-L1 transcription via NF-κB/p65 signaling driven by E6/E7 oncoproteins, whereas HPV− tumors primarily rely on EGFR/MAPK pathways (15). PD-L1 is expressed in approximately 50% of HNSCC tumors, with higher prevalence in HPV+ cases (18). IFN-γ-induced PD-L1 regulation exhibits biphasic dynamics: acute stimulation rapidly upregulates expression via JAK/STAT signaling, while chronic exposure leads to persistent hypermethylation-associated expression (38). Despite the approval of PD-1/PD-L1 inhibitors for recurrent/metastatic HNSCC, clinical response rates remain modest (15–20%), attributed to spatial heterogeneity, the absence of tertiary lymphoid structures, CXCL13+CD8+ T cell exhaustion, and tumor mutational burden (39). These findings underscore the limitations of monotherapy and emphasize the need for combinatorial strategies targeting complementary immunosuppressive pathways.

3.2 Multidimensional regulation of synergistic immune checkpoints

CTLA-4, a critical early immune checkpoint, sculpts immunosuppressive niches via two mechanisms: (1) competitive B7 ligand binding in lymph nodes to inhibit naïve T cell priming, and (2) IDO+ dendritic cell-mediated Treg expansion within tumors (40). Preclinical evidence suggests that dual CTLA-4/PD-1 blockade

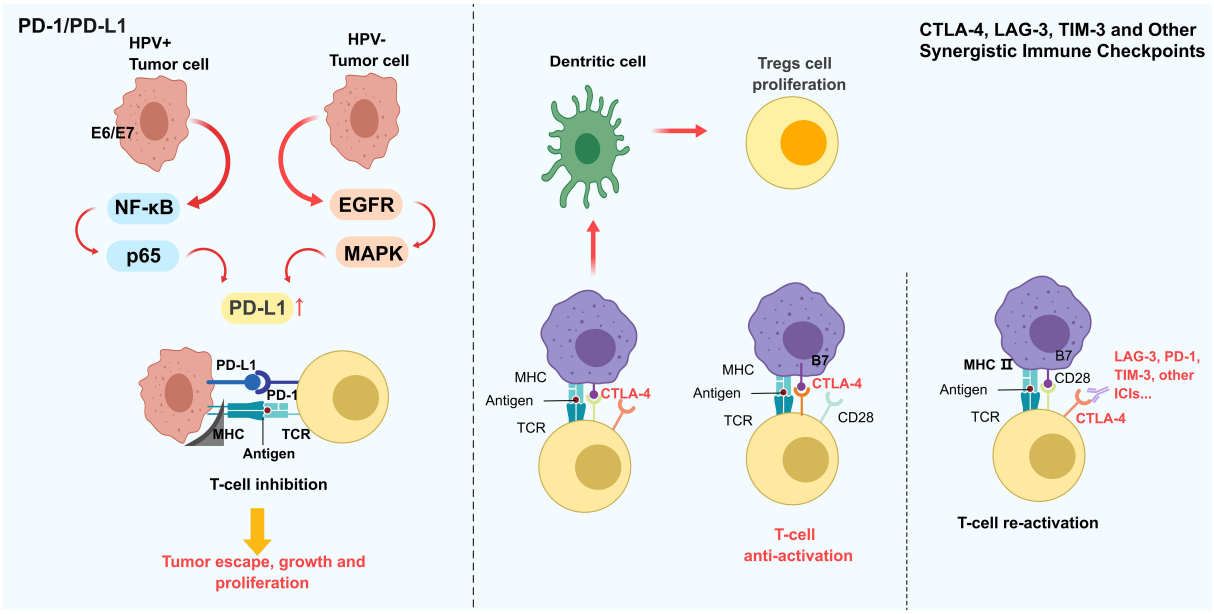

FIGURE 2
Dynamic expression and interaction patterns of different HNSCC immune checkpoints. The PD-1/PD-L1 axis as a central immune evasion mechanism in HNSCC, regulated by HPV status: HPV+ tumors upregulate PD-L1 via NF-κB/p65 signaling, while HPV− tumors rely on EGFR/MAPK pathways. PD-L1 binds to PD-1 on T cells, inducing T cell inhibition and promoting tumor escape. Other checkpoints, including CTLA-4, LAG-3, and TIM-3, further suppress T cell function by blocking co-stimulatory signals (e.g., CD28-B7) and enhancing Treg proliferation. This synergistic suppression creates a pro-tumorigenic microenvironment. The figure emphasizes the need for combination therapies targeting multiple checkpoints to overcome limitations of PD-1/PD-L1 monotherapy, which often face modest responses due to spatial heterogeneity and T cell exhaustion.

enhances antitumor immunity. However, TIM-3 overexpression exacerbates PD-1-driven T cell exhaustion by suppressing IL-2 secretion in CD4+ T cells, while LAG-3 amplifies CTLA-4 suppression via MHC class II-dependent pathways (41). TIM-3 and LAG-3 further promote immune escape by impairing T cell function through distinct mechanisms (42). Despite these advances, clinical efficacy remains constrained by the redundancy of immune evasion mechanisms, necessitating rational combinations of checkpoint inhibitors and microenvironmental modulators.

3.3 Precision targeting strategies for immune checkpoints

Immune checkpoint inhibitors (ICIs), including anti-PD-1 antibodies such as pembrolizumab and nivolumab, are approved therapies for HNSCC, but anti-CTLA-4 antibodies are still under investigation and not yet considered standard of care (40, 43–47). Additionally, the metabolic reprogramming observed in HNSCC, including upregulation of glycolytic pathways and lactate production, contributes to an acidic microenvironment that suppresses T cell function and reduces the efficacy of ICIs (48). Macrophage reprogramming, such as depleting M2-polarized TAMs or blocking CSF-1/IL-10 signaling, reverses immunosuppression and synergizes with PD-1 blockade (49). Furthermore, epigenetic changes in tumor cells and immune cells can lead to a loss of PD-L1 expression or promote immune exhaustion, rendering T cells unresponsive to checkpoint blocked. Emerging therapeutic strategies targeting these resistance mechanisms aim to restore T cell function, such as by reprogramming TAMs or targeting key metabolic enzymes like lactate dehydrogenase (LDH), which has shown promise in enhancing the antitumor efficacy of ICIs. Moreover, combination therapies that incorporate epigenetic modulators to reverse immune evasion mechanisms are being actively explored as a way to overcome resistance to current therapies. These combined approaches hold potential for improving the overall success rates of immunotherapies in HNSCC and other solid tumors.

The PD-1/PD-L1 axis and synergistic checkpoints play pivotal roles in HNSCC immune evasion. Understanding their spatiotemporal regulation, compensatory networks, and microenvironmental interactions is key to developing next-generation immunotherapies. Rational combinations of checkpoint inhibitors with metabolic modulators, stromal disruptors, or epigenetic therapies hold promise for transforming immune "cold" HNSCC into responsive ecosystems, ultimately improving clinical outcomes.

4 Metabolic reprogramming and its impact on immune evasion

4.1 Hallmarks of tumor metabolic reprogramming

HNSCC exhibits spatially heterogeneous metabolic reprogramming that supports tumor survival and immune evasion. The classical "Warburg effect" (aerobic glycolysis) not only fuels ATP production but also generates an acidic microenvironment via lactate accumulation, especially in hypoxia in multiple cancers (50–52), directly suppressing CD8+ T cell cytotoxicity (53). Single-cell metabolomics reveals compartmentalized metabolic in HNSCC: glucose-dependent metabolism dominates at invasive margins, while core regions favor glutamine metabolism, creating dynamic gradients of metabolites (54). Lipid metabolism also facilitates immune escape, tumor cells utilize FABP4-mediated lipid droplet storage for energy reserves and secrete lipocalin-2 (LCN2) to polarize macrophages toward an M2 immunosuppressive phenotype (55). These reprogrammed pathways reshape the TME, depleting nutrients and altering metabolite profiles to suppress immune cell activity (10).

4.2 Immunosuppressive roles of metabolic by-products

Tumor-derived metabolites reinforce immune evasion through signaling and epigenetic remodeling. Lactate acts beyond metabolism —via GPR81 signaling, it induces dendritic cell tolerization and inhibits $CD8^+$ T cell effector function by hyperacetylating the IFN-γ promoter through HDAC inhibition (38). Acidosis (pH 6.5–6.8) further impairs T cell proliferation and cytotoxicity (15). Additionally, lipid-derived mediators such as prostaglandin E2 (PGE2) promote M2 macrophage polarization and Treg expansion, consolidating the immunosuppressive niche (56).

4.3 Metabolic targeting strategies

Targeting tumor metabolism has emerged as a promising approach to enhance immunotherapy. Inhibiting glycolysis or lipid metabolism can restore T-cell function; for instance, targeting HK2 can reverse impaired glucose uptake in $PD\text{-}1^+$ $CD8^+$ T cells (53). Combination strategies are also under investigation: the adenosine receptor antagonist AB928, when paired with anti-PD-1 therapy, significantly improved responses in HPV-negative HNSCC by promoting TLS formation and increasing $CXCR3^+$ T cell infiltration (57). Thus, metabolic interventions may overcome immune resistance and broaden treatment options. Continued research into how metabolic rewiring facilitates immune escape could yield novel therapeutic targets and optimize existing immunotherapies (58).

5 Current advances in immunotherapy

5.1 Clinical use of PD-1/PD-L1 inhibitors

PD-1/PD-L1 inhibitors have made significant progress in the treatment of HNSCC. In recent years, anti-PD-1 monoclonal antibodies such as pembrolizumab and nivolumab have been approved by the FDA and EMA for the treatment of patients with recurrent or metastatic HNSCC. By blocking the interaction between PD-1 and its ligand PD-L1, these drugs restore the anti-

tumor activity of T cells, thereby enhancing the immune system 's attack on tumor cells. However, their overall clinical efficacy remains limited—approximately 60% of patients do not respond, and only 20–30% achieve durable progression-free survival (47).

Emerging evidence suggests that this limited efficacy is largely attributable to TME factors, including immune exclusion, upregulation of immunosuppressive cytokines, and downregulation of human leukocyte antigen (HLA) expression (40). For example, increased infiltration of MDSCs and regulatory T cells has been associated with resistance to anti-PD-1 therapy. To address these challenges, combination therapies are being actively explored. Clinical trials have demonstrated that combining PD-1/PD-L1 inhibitors with chemotherapy or radiotherapy can synergistically enhance antigen release and immune priming. In KEYNOTE-048, for instance, pembrolizumab plus chemotherapy significantly improved overall survival compared to chemotherapy alone in PD-L1–positive HNSCC. Preclinical models also support combinations with anti-angiogenic agents, epigenetic modulators (e.g., DNMT or HDAC inhibitors), or metabolic modulators targeting lactate dehydrogenase (LDH) and adenosine pathways.

Future directions include rational selection of patients based on biomarkers (TMB, PD-L1 expression, and TLS formation) and spatiotemporal profiling of immune infiltration to guide individualized therapy.

5.2 Current status and challenges of CAR-T cell therapy

CAR-T cell therapy is an emerging immunotherapeutic approach that has achieved significant success in hematological tumors, but its use in solid tumors such as HNSCC remains challenging. CAR-T cells are genetically engineered to express specific antigen receptors, thereby enhancing the recognition and killing ability of tumor cells. However, the tumor microenvironment of HNSCC is often highly immunosuppressive, which can limit the effectiveness of CAR-T cell therapy (59–61).

In HNSCC, CAFs secrete IL-6, TGF-β, and ECM-modifying proteins such as LOXL2, which restrict T cell trafficking and promote Treg polarization. Additionally, tumor antigen heterogeneity and antigen loss variants further compromise CAR-T targeting. CAFs showed inhibitory effects on CD8 + T cells, further limiting the antitumor activity of CAR-T cells (Qin, 9).

To overcome these obstacles, researchers are exploring multiple strategies, including optimizing the manufacturing process of CAR-T cells, combining other immunotherapies or targeted therapies, and developing novel CAR-T cell designs to improve their efficacy in solid tumors (62). These improvements are expected to overcome the limitations of existing treatments and enhance the clinical application of CAR-T therapy in HNSCC.

5.3 Exploration of other immunotherapy strategies

Beyond PD-1/PD-L1 inhibitors and CAR-T cell therapy, several alternative and adjunctive immune-therapeutic strategies are under rapid development in HNSCC. For example, interventions directed at the tumor microenvironment, such as by modulating the function of TAMs or CAFs, may effectively enhance antitumor immune responses (63, 64). In addition, cancer vaccines and immunomodulators are being developed to improve the immune response to tumors by activating the patient 's immune system (65). Combination regimens involving radiotherapy have shown synergistic effects, where ionizing radiation increases tumor antigen release and upregulates immune checkpoint molecules, thereby sensitizing tumors to PD-1 blockade (Chen, 66).

However, these strategies face several challenges: Lack of validated biomarkers to guide patient selection; Heterogeneity in immune phenotypes among HPV+ vs. HPV− tumors; Incomplete understanding of immune escape mechanisms in immune-desert tumors; Need for robust clinical data to confirm long-term efficacy and safety (67).

6 Future directions

6.1 Rational combination therapies

In the treatment of HNSCC, monotherapies often yield suboptimal outcomes, underscoring the need for rational combination strategies. Studies demonstrate that multimodal approaches can overcome immune evasion mechanisms in the TME, thereby enhancing therapeutic efficacy (47). Combining immune checkpoint inhibitors with chemotherapy, radiotherapy, or targeted therapies can amplify antitumor immune responses. Additionally, cancer stem cells significantly contribute to metastasis and immune evasion, making CSC-targeting approaches a critical component of combination regimens (19).

Specific combinations, such as PD-1/PD-L1 inhibitors co-administered with other immunomodulators (TGF-β blockers or CSF-1R inhibitors), show promise in reshaping the immunosuppressive TME. For instance, dual PD-1/CTLA-4 blockade has yielded improved response rates and survival outcomes in HNSCC patients (15).

Future clinical trials could explore that sequential or adaptive regimens that tailor dosing intervals and drug sequencing to dynamic TME changes, and combinations with epigenetic therapies or metabolic modulators to restore tumor immunogenicity and T cell function. This comprehensive approach may bolster the durability of immunotherapy responses and overcome primary or acquired resistance (68, 69). These strategies aim to comprehensively reshape the immunosuppressive TME, offering new avenues for improving immunotherapy outcomes.

6.2 Development of personalized treatment strategies

Personalized therapy has become essential for optimizing HNSCC treatment outcomes. With the advent of omics technologies, clinicians can now profile tumor genetics, proteomics, and immunophenotypes to tailor individualized regimens. For instance, TMB and TME characteristics have been identified as predictive biomarkers for immunotherapy response (70). Integrating genomic profiling of tumor samples allows for precision immunotherapy selection, targeting specific mutations and expression patterns (71).

In addition to genetic and molecular data, clinical features such as HPV status and comorbidities also inform personalized treatment. PD-L1 expression levels can guide therapeutic decisions regarding PD-1/PD-L1 inhibitors (72) (18). Moving forward, prospective clinical trials should incorporate longitudinal biomarker analysis—such as monitoring circulating tumor DNA (ctDNA) or single-cell transcriptomic changes—to refine therapy choices in real time.

6.3 Discovery and application of biomarkers

Biomarker development is central to early diagnosis, prognostication, and treatment monitoring in HNSCC. Recent high-throughput methods, including single-cell RNA sequencing and bioinformatics-driven integrative analyses, have revealed numerous biomarkers correlated with tumor progression and immune evasion (73). For instance, dysregulated long non-coding RNAs (lncRNAs) may predict immunotherapy responses and disease trajectory (74).

Future research should focus on multiparametric biomarker panels, integrating immune cell composition, cytokine profiles, and metabolic signatures to stratify patients more accurately. In addition to that, TAM and CAF phenotypes, as their polarization states strongly impact patient prognosis and therapy responsiveness (75, 76). By combining multi-biomarker analyses with functional TME characterization, we can drive the evolution of precision medicine. Large-scale clinical trials, employing adaptive designs and real-time biomarker assessment, will accelerate the translation of these findings into standard-of-care practices.

7 Conclusion

The immune escape mechanisms in HNSCC represent a pivotal focus in tumor biology and immunotherapy research. As our understanding of the TME expands, it has become clear that tumor cells do not exist in isolation but engage in dynamic interactions with immune cells, stromal components, and the extracellular matrix. These interactions play a profound role in influencing tumor growth, metastasis, and therapeutic responses.

This review emphasizes the critical role of immune cell infiltration patterns and checkpoint dysregulation in the progression of HNSCC. While high infiltration of CD8+ T cells is generally correlated with favorable clinical outcomes, TAMs and Tregs are frequently associated with tumor progression and poor prognosis. However, inconsistencies in study outcomes, influenced by variations in sample selection, methodologies, and analytical approaches, pose significant challenges to integrating findings. Addressing these discrepancies is crucial for advancing HNSCC immunotherapy.

Recent advances in immunotherapy, particularly immune checkpoint inhibitors, have demonstrated considerable clinical benefits. By restoring immune activity through PD-1/PD-L1 or CTLA-4 blockade, these therapies have shown promise in improving patient survival and quality of life. Nevertheless, their efficacy remains variable, highlighting the urgent need for strategies to identify the appropriate patient populations and develop personalized treatment regimens.

Looking ahead, the complexity of the TME offers numerous opportunities for future research. Investigating the intricate interactions between tumor cells and immune cells, and exploring methods to modulate the TME, such as targeting immunosuppressive cytokines or employing genetic editing to alter tumor cell immunophenotypes, holds great potential for enhancing the efficacy of immunotherapy. Additionally, a deeper understanding of these mechanisms could inform the development of combination therapies, further improving patient outcomes.

In conclusion, the immune escape mechanisms in HNSCC reflect the intricate interplay between tumors and their microenvironment. Future research should focus on clarifying these complex interactions and identifying biomarkers for personalized treatment strategies. Multidisciplinary collaboration, integrating basic research with clinical trials, will be essential in driving the development of more effective therapies. These advances not only offer hope for improved HNSCC outcomes but also provide valuable insights for immunotherapy across a range of other malignancies, setting the stage for broader clinical applications.

Author contributions

XZ: Writing – original draft, Writing – review & editing. YZ: Writing – original draft. YH: Writing – original draft. WG: Writing – review & editing. QZ: Writing – review & editing. BJ: Writing – review & editing. SC: Writing – review & editing. HL: Writing – review & editing.

Funding

The author(s) declare that financial support was received for the research and/or publication of this article. This study was supported by Taizhou Hospital of Zhejiang Province affiliated to Wenzhou Medical University.

Acknowledgments

The figures were drawn with the help of medpeer (medpeer.cn). The DeepSeek (https://chat.deepseek.com) was used for manuscript text polishing, with full responsibility for content accuracy and integrity remaining with the authors.

Conflict of interest

The authors declare that the research was conducted in the absence of any commercial or financial relationships that could be construed as a potential conflict of interest.

Generative AI statement

The author(s) declare that no Generative AI was used in the creation of this manuscript.

Publisher's note

All claims expressed in this article are solely those of the authors and do not necessarily represent those of their affiliated organizations, or those of the publisher, the editors and the reviewers. Any product that may be evaluated in this article, or claim that may be made by its manufacturer, is not guaranteed or endorsed by the publisher.

References

1. Bray F, Laversanne M, Sung H, Ferlay J, Siegel RL, Soerjomataram I, et al. Global cancer statistics 2022: GLOBOCAN estimates of incidence and mortality worldwide for 36 cancers in 185 countries. *CA Cancer J Clin*. (2024) 74:229–63. doi: 10.3322/caac.21834

2. Li Z, Li J, Bai X, Huang X, Wang Q. Tumor microenvironment as a complex milieu driving cancer progression: a mini review. *Clin Transl Oncol*. (2024) 27(5):1943–52. doi: 10.1007/s12094-024-03697-w

3. Yang L, Wang Q, He L, Sun X. The critical role of tumor microbiome in cancer immunotherapy. *Cancer Biol Ther*. (2024) 25:2301801. doi: 10.1080/15384047.2024.2301801

4. Zhang L, Wang WQ, Chen JH, Feng J, Liao YZ, Zou Y, et al. Tumor-infiltrating immune cells and survival in head and neck squamous cell carcinoma: a retrospective computational study. *Sci Rep*. (2024) 14:6390. doi: 10.1038/s41598-024-56738-3

5. Yang S, Liu H, Zheng Y, Chu H, Lu Z, Yuan J, et al. The role of PLIN3 in prognosis and tumor-associated macrophage infiltration: A pan-cancer analysis. *J Inflammation Res*. (2025) 18:3757–77. doi: 10.2147/JIR.S509245

6. Evrard D, Szturz P, Tijeras-Raballand A, Astorgues-Xerri L, Abitbol C, Paradis V, et al. Macrophages in the microenvironment of head and neck cancer: potential targets for cancer therapy. *Oncol*. (2019) 88:29–38. doi: 10.1016/j.oraloncology.2018.10.040

7. Yang Y, Cai Z, Huang K, Li M, Wang X, Lin Y, et al. A composite score based on immune-related gene prognostic index and m(6)A risk score of head and neck squamous cell carcinoma. *Front Genet*. (2023) 14:1061569. doi: 10.3389/fgene.2023.1061569

8. Zandi M, Shafaati M, Hosseini F. Mechanisms of immune evasion of monkeypox virus. *Front Microbiol*. (2023) 14:1106247. doi: 10.3389/fmicb.2023.1106247

9. Zhang J, Liu Y, Xia L, Zhen J, Gao J, Atsushi T. Constructing heterogeneous single-cell landscape and identifying microenvironment molecular characteristics of primary and lymphatic metastatic head and neck squamous cell carcinoma. *Comput Biol Med*. (2023) 165:107459. doi: 10.1016/j.compbiomed.2023.107459

10. Wang G, Shen X, Jin W, Song C, Dong M, Zhou Z, et al. Elucidating the role of S100A10 in CD8(+) T cell exhaustion and HCC immune escape via the cPLA2 and 5-LOX axis. *Cell Death Dis*. (2024) 15:573. doi: 10.1038/s41419-024-06895-0

11. Guo Z, Li K, Liu P, Zhang X, Lv J, Zeng X, et al. Targeted therapy for head and neck squamous cell carcinoma microenvironment. *Front Med (Lausanne)*. (2023) 10:1257898. doi: 10.3389/fmed.2023.1257898

12. Cillo AR, Kürten CHL, Tabib T, Qi Z, Onkar S, Wang T, et al. Immune landscape of viral- and carcinogen-driven head and neck cancer. *Immunity*. (2020) 52:183–199.e189. doi: 10.1016/j.immuni.2019.11.014

13. Shen G, Wang Q, Li Z, Xie J, Han X, Wei Z, et al. Bridging chronic inflammation and digestive cancer: the critical role of innate lymphoid cells in tumor microenvironments. *Int J Biol Sci*. (2024) 20:4799–818. doi: 10.7150/ijbs.96338

14. Zhu C, Wu Q, Yang N, Zheng Z, Zhou F, Zhou Y. Immune infiltration characteristics and a gene prognostic signature associated with the immune infiltration in head and neck squamous cell carcinoma. *Front Genet*. (2022) 13:848841. doi: 10.3389/fgene.2022.848841

15. Meliante PG, Barbato C, Zoccali F, Ralli M, Greco A, de Vincentiis M, et al. Programmed cell death-ligand 1 in head and neck squamous cell carcinoma: molecular insights, preclinical and clinical data, and therapies. *Int J Mol Sci*. (2022) 23(23):15384. doi: 10.3390/ijms232315384

16. DePeaux K, Delgoffe GM. Metabolic barriers to cancer immunotherapy. *Nat Rev Immunol*. (2021) 21:785–97. doi: 10.1038/s41577-021-00541-y

17. Ma B, Li H, Zheng M, Cao R, Yu R. A novel autophagy-related subtypes to distinguish immune phenotypes and predict immunotherapy response in head and neck squamous cell carcinoma. *Biomol BioMed*. (2023) 23:997–1013. doi: 10.17305/bb.2023.9094

18. Outh-Gauer S, Morini A, Tartour E, Lépine C, Jung AC, Badoual C. The microenvironment of head and neck cancers: papillomavirus involvement and potential impact of immunomodulatory treatments. *Head Neck Pathol*. (2020) 14:330–40. doi: 10.1007/s12105-020-01147-x

19. Qin Z, Zhang W, Liu S, Wang Y, Peng X, Jia L. PVT1 inhibition stimulates anti-tumor immunity, prevents metastasis, and depletes cancer stem cells in squamous cell carcinoma. *Cell Death Dis*. (2023) 14:187. doi: 10.1038/s41419-023-05710-6

20. Hänggi K, Ruffell B. Cell death, therapeutics, and the immune response in cancer. *Trends Cancer*. (2023) 9:381–96. doi: 10.1016/j.trecan.2023.02.001

21. Philip M, Fairchild L, Sun L, Horste EL, Camara S, Shakiba M, et al. Chromatin states define tumour-specific T cell dysfunction and reprogramming. *Nature*. (2017) 545:452–6. doi: 10.1038/nature22367

22. Molinier-Frenkel V, Castellano F. Immunosuppressive enzymes in the tumor microenvironment. *FEBS Lett*. (2017) 591:3135–57. doi: 10.1002/1873-3468.12784

23. Li D, Ma D, Hou Y. Pyroptosis patterns influence the clinical outcome and immune microenvironment characterization in HPV-positive head and neck squamous cell carcinoma. *Infect Agent Cancer*. (2023) 18:30. doi: 10.1186/s13027-023-00507-w

24. Pickering CR, Zhou JH, Lee JJ, Drummond JA, Peng SA, Saade RE, et al. Mutational landscape of aggressive cutaneous squamous cell carcinoma. *Clin Cancer Res*. (2014) 20:6582–92. doi: 10.1158/1078-0432.ccr-14-1768

25. Liao TT, Chen YH, Li ZY, Hsiao AC, Huang YL, Hao RX, et al. Hypoxia-induced long noncoding RNA HIF1A-AS2 regulates stability of MHC class I protein in head and neck cancer. *Cancer Immunol Res*. (2024) 12:1468–84. doi: 10.1158/2326-6066.CIR-23-0622

26. Zhao H, Jiang E, Shang Z. 3D co-culture of cancer-associated fibroblast with oral cancer organoids. *J Dent Res*. (2021) 100:201–8. doi: 10.1177/0022034520956614

27. Raudenska M, Balvan J, Hanelova K, Bugajova M, Masarik M. Cancer-associated fibroblasts: Mediators of head and neck tumor microenvironment remodeling. *Biochim Biophys Acta Rev Cancer*. (2023) 1878:188940. doi: 10.1016/j.bbcan.2023.188940

28. Li C, Guo H, Zhai P, Yan M, Liu C, Wang X, et al. Spatial and single-cell transcriptomics reveal a cancer-associated fibroblast subset in HNSCC that restricts infiltration and antitumor activity of CD8+ T cells. *Cancer Res*. (2024) 84:258–75. doi: 10.1158/0008-5472.can-23-1448

29. Liu S, Wang R, Fang J. Exploring the frontiers: tumor immune microenvironment and immunotherapy in head and neck squamous cell carcinoma. *Discov Oncol*. (2024) 15:22. doi: 10.1007/s12672-024-00870-z

30. Veglia F, Tyurin VA, Blasi M, De Leo A, Kossenkov AV, Donthireddy L, et al. Fatty acid transport protein 2 reprograms neutrophils in cancer. *Nature*. (2019) 569:73–8. doi: 10.1038/s41586-019-1118-2

31. Hutton C, Heider F, Blanco-Gomez A, Banyard A, Kononov A, Zhang X, et al. Single-cell analysis defines a pancreatic fibroblast lineage that supports anti-tumor immunity. *Cancer Cell*. (2021) 39:1227–1244.e1220. doi: 10.1016/j.ccell.2021.06.017

32. Punovuori K, Bertillot F, Miroshnikova YA, Binner MI, Myllymäki SM, Follain G, et al. Multiparameter imaging reveals clinically relevant cancer cell-stroma interaction dynamics in head and neck cancer. *Cell*. (2024) 187:7267–7284.e7220. doi: 10.1016/j.cell.2024.09.046

33. Cheng J, Xiao Y, Peng T, Zhang Z, Qin Y, Wang Y, et al. ETV7 limits the antiviral and antitumor efficacy of CD8(+) T cells by diverting their fate toward exhaustion. *Nat Cancer*. (2025) 6:338–56. doi: 10.1038/s43018-024-00892-0

34. Belk JA, Daniel B, Satpathy AT. Epigenetic regulation of T cell exhaustion. *Nat Immunol*. (2022) 23:848–60. doi: 10.1038/s41590-022-01224-z

35. Zeng S, Hu H, Li Z, Hu Q, Shen R, Li M, et al. Local TSH/TSHR signaling promotes CD8(+) T cell exhaustion and immune evasion in colorectal carcinoma. *Cancer Commun (Lond)*. (2024) 44:1287–310. doi: 10.1002/cac2.12605

36. Sim F, Leidner R, Bell RB. Immunotherapy for head and neck cancer. *Hematol Oncol Clin North Am*. (2019) 33:301–21. doi: 10.1016/j.hoc.2018.12.006

37. Liu L, Xie Y, Yang H, Lin A, Dong M, Wang H, et al. HPVTIMER: A shiny web application for tumor immune estimation in human papillomavirus-associated cancers. *Imeta*. (2023) 2:e130. doi: 10.1002/imt2.130

38. Krupar R. The tumor microenvironment-relay station for prognosis and therapy response. *Pathol (Heidelb)*. (2022) 43:141–7. doi: 10.1007/s00292-022-01159-0

39. Li HS, Tang R, Shi HS, Qin ZJ, Zhang XY, Sun YF, et al. Ultra-high dose rate radiotherapy overcomes radioresistance in head and neck squamous cell carcinoma. *Signal Transduct Target Ther*. (2025) 10:82. doi: 10.1038/s41392-025-02184-0

40. Morris LGT. Loss of human leukocyte antigen and immune escape in head and neck cancer. *Laryngoscope*. (2024) 134:160–5. doi: 10.1002/lary.30761

41. Wong SK, Beckermann KE, Johnson DB, Das S. Combining anti-cytotoxic T-lymphocyte antigen 4 (CTLA-4) and -programmed cell death protein 1 (PD-1) agents for cancer immunotherapy. *Expert Opin Biol Ther*. (2021) 21:1623–34. doi: 10.1080/14712598.2021.1921140

42. Ai L, Xu A, Xu J. Roles of PD-1/PD-L1 pathway: signaling, cancer, and beyond. *Adv Exp Med Biol*. (2020) 1248:33–59. doi: 10.1007/978-981-15-3266-5_3

43. Masarwy R, Kampel L, Horowitz G, Gutfeld O, Muhanna N. Neoadjuvant PD-1/PD-L1 inhibitors for resectable head and neck cancer: A systematic review and meta-analysis. *JAMA Otolaryngol Head Neck Surg*. (2021) 147:871–8. doi: 10.1001/jamaoto.2021.2191

44. Gilardi M, Saddawi-Konefka R, Wu VH, Lopez-Ramirez MA, Wang Z, Soto F, et al. Microneedle-mediated Intratumoral Delivery of Anti-CTLA-4 Promotes cDC1-dependent Eradication of Oral Squamous Cell Carcinoma with Limited irAEs. *Mol Cancer Ther*. (2022) 21:616–24. doi: 10.1158/1535-7163.mct-21-0234

45. Okuyama K, Naruse T, Yanamoto S. Tumor microenvironmental modification by the current target therapy for head and neck squamous cell carcinoma. *J Exp Clin Cancer Res*. (2023) 42:114. doi: 10.1186/s13046-023-02691-4

46. Xiao Y, Mao L, Yang QC, Wang S, Wu ZZ, Wan SC, et al. CD103 blockade impair anti-CTLA-4 immunotherapy in oral cancer. *Oncol*. (2023) 138:106331. doi: 10.1016/j.oraloncology.2023.106331

47. Meci A, Goyal N, Slonimsky G. Mechanisms of resistance and therapeutic perspectives in immunotherapy for advanced head and neck cancers. *Cancers (Basel)*. (2024) 16(4):703. doi: 10.3390/cancers16040703

48. Yang Z, Chu B, Tu Y, Li L, Chen D, Huang S, et al. Dual inhibitors of DNMT and HDAC remodels the immune microenvironment of colorectal cancer and enhances the efficacy of anti-PD-L1 therapy. *Pharmacol Res*. (2024) 206:107271. doi: 10.1016/j.phrs.2024.107271

49. Tiyamanee W, Konnai S, Okagawa T, Nojima Y, Ganbaatar O, Maekawa N, et al. Molecular characterization of immunoinhibitory factors PD-1/PD-L1 in sheep. *Vet Immunol Immunopathol*. (2023) 261:110609. doi: 10.1016/j.vetimm.2023.110609

50. Pouysségur J, Marchiq I, Parks SK, Durivault J, Ždralević M, Vucetic M. Warburg effect' controls tumor growth, bacterial, viral infections and immunity - Genetic deconstruction and therapeutic perspectives. *Semin Cancer Biol*. (2022) 86:334–46. doi: 10.1016/j.semcancer.2022.07.004

51. Qiu C, Wang W, Xu S, Li Y, Zhu J, Zhang Y, et al. Construction and validation of a hypoxia-related gene signature to predict the prognosis of breast cancer. *BMC Cancer*. (2024) 24:402. doi: 10.1186/s12885-024-12182-0

52. Zhang J, Ouyang F, Gao A, Zeng T, Li M, Li H, et al. ESM1 enhances fatty acid synthesis and vascular mimicry in ovarian cancer by utilizing the PKM2-dependent warburg effect within the hypoxic tumor microenvironment. *Mol Cancer*. (2024) 23:94. doi: 10.1186/s12943-024-02009-8

53. Tan S, Yang Y, Yang W, Han Y, Huang L, Yang R, et al. Exosomal cargos-mediated metabolic reprogramming in tumor microenvironment. *J Exp Clin Cancer Res*. (2023) 42:59. doi: 10.1186/s13046-023-02634-z

54. Ju SH, Lee SE, Kang YE, Shong M. Development of metabolic synthetic lethality and its implications for thyroid cancer. *Endocrinol Metab (Seoul)*. (2022) 37:53–61. doi: 10.3803/enm.2022.1402

55. Mobet Y, Liu X, Liu T, Yu J, Yi P. Interplay between m(6)A RNA methylation and regulation of metabolism in cancer. *Front Cell Dev Biol*. (2022) 10:813581. doi: 10.3389/fcell.2022.813581

56. Wiggs A, Molina S, Sumner SJ, Rushing BR. A review of metabolic targets of anticancer nutrients and nutraceuticals in pre-clinical models of triple-negative breast cancer. *Nutrients*. (2022) 14(10):1990. doi: 10.3390/nu14101990

57. Mao Y, Xia Z, Xia W, Jiang P. Metabolic reprogramming, sensing, and cancer therapy. *Cell Rep*. (2024) 43:115064. doi: 10.1016/j.celrep.2024.115064

58. Huang K, Han Y, Chen Y, Shen H, Zeng S, Cai C. Tumor metabolic regulators: key drivers of metabolic reprogramming and the promising targets in cancer therapy. *Mol Cancer*. (2025) 24:7. doi: 10.1186/s12943-024-02205-6

59. Hu C, Liu M, Li Y, Zhao Y, Sharma A, Liu H, et al. Recent advances and future perspectives of CAR-T cell therapy in head and neck cancer. *Front Immunol*. (2023) 14:1213716. doi: 10.3389/fimmu.2023.1213716

60. Summers SE, Salih V, Foey AD. ErbB- and MUC1-targeted CAR-T cell immunotherapy of oral squamous cell carcinoma. *Front Dent Med*. (2023) 4:1116402. doi: 10.3389/fdmed.2023.1116402

61. Wang HQ, Fu R, Man QW, Yang G, Liu B, Bu LL. Advances in CAR-T cell therapy in head and neck squamous cell carcinoma. *J Clin Med*. (2023) 12(6):2173. doi: 10.3390/jcm12062173

62. Wondergem NE, Nijenhuis D, Poell JB, Leemans CR, Brakenhoff RH, van de Ven R. At the crossroads of molecular biology and immunology: molecular pathways for immunological targeting of head and neck squamous cell carcinoma. *Front Health*. (2021) 2:647980. doi: 10.3389/froh.2021.647980

63. Chen S, Yang Y, He S, Lian M, Wang R, Fang J. Review of biomarkers for response to immunotherapy in HNSCC microenvironment. *Front Oncol*. (2023) 13:1037884. doi: 10.3389/fonc.2023.1037884

64. Liao T, Chen X, Qiu F, Zhang X, Wu F, Zhao Z, et al. Regulation of cancer-associated fibroblasts for enhanced cancer immunotherapy using advanced functional nanomedicines: an updated review. *J Nanobiotechnol*. (2025) 23:166. doi: 10.1186/s12951-025-03217-0

65. Wu SY, Lin KC, Lawal B, Wu ATH, Wu CZ. MXD3 as an onco-immunological biomarker encompassing the tumor microenvironment, disease staging, prognoses, and therapeutic responses in multiple cancer types. *Comput Struct Biotechnol J*. (2021) 19:4970–83. doi: 10.1016/j.csbj.2021.08.047

66. Chen X, Chen L, Kürten CHL, Jabbari F, Vujanovic L, Ding Y, et al. An individualized causal framework for learning intercellular communication networks that define microenvironments of individual tumors. *PloS Comput Biol*. (2022) 18:e1010761. doi: 10.1371/journal.pcbi.1010761

67. Stouten I, van Montfoort N, Hawinkels L. The tango between cancer-associated fibroblasts (CAFs) and immune cells in affecting immunotherapy efficacy in pancreatic cancer. *Int J Mol Sci*. (2023) 24(10):8707. doi: 10.3390/ijms24108707

68. Charap AJ, Enokida T, Brody R, Sfakianos J, Miles B, Bhardwaj N, et al. Landscape of natural killer cell activity in head and neck squamous cell carcinoma. *J Immunother Cancer*. (2020) 8(2):e001523. doi: 10.1136/jitc-2020-001523

69. Liu Z, Zuo L, Zhou Z, Liu S, Ba Y, Zuo A, et al. Targeting immunosenescence for improved tumor immunotherapy. *MedComm (2020)*. (2024) 5:e777. doi: 10.1002/mco2.777

70. Li Y, Ji L, Zhang Y, Zhang J, Reuben A, Zeng H, et al. The combination of tumor mutational burden and T-cell receptor repertoire predicts the response to immunotherapy in patients with advanced non-small cell lung cancer. *MedComm (2020)*. (2024) 5:e604. doi: 10.1002/mco2.604

71. de Klerk LK, Goedegebuure RSA, van Grieken NCT, van Sandick JW, Cats A, Stiekema J, et al. Molecular profiles of response to neoadjuvant chemoradiotherapy in oesophageal cancers to develop personalized treatment strategies. *Mol Oncol*. (2021) 15:901–14. doi: 10.1002/1878-0261.12907

72. Dang K, Zhang W, Jiang S, Lin X, Qian A. Application of lectin microarrays for biomarker discovery. *ChemistryOpen*. (2020) 9:285–300. doi: 10.1002/open.201900326

73. Li Y, Tam WW, Yu Y, Zhuo Z, Xue Z, Tsang C, et al. The application of Aptamer in biomarker discovery. *Biomark Res*. (2023) 11:70. doi: 10.1186/s40364-023-00510-8

74. Pan X, Li C, Feng J. The role of LncRNAs in tumor immunotherapy. *Cancer Cell Int*. (2023) 23:30. doi: 10.1186/s12935-023-02872-3

75. Kondoh N, Mizuno-Kamiya M, Umemura N, Takayama E, Kawaki H, Mitsudo K, et al. Immunomodulatory aspects in the progression and treatment of oral Malignancy. *Jpn Dent Sci Rev*. (2019) 55:113–20. doi: 10.1016/j.jdsr.2019.09.001

76. Li Z, Wang Q, Huang X, Fu R, Wen X, Zhang L. Multi-omics analysis reveals that ferroptosis-related gene CISD2 is a prognostic biomarker of head and neck squamous cell carcinoma. *J Gene Med*. (2024) 26:e3580. doi: 10.1002/jgm.3580

frontiers | Frontiers in Immunology

TYPE Original Research
PUBLISHED 30 May 2025
DOI 10.3389/fimmu.2025.1598484

Check for updates

OPEN ACCESS

EDITED BY
Qi Wang,
Jiangsu University, China

REVIEWED BY
Xiaocui Liang,
Wuhan Hospital of Traditional Chinese and Western Medicine, China
Chong Jin,
Taizhou Central Hospital, China
Volkan Aslan,
Gulhane Training and Research Hospital, Türkiye

*CORRESPONDENCE
Qing Zhou
qingzhou@whu.edu.cn
Weixing Wang
wangwx@whu.edu.cn

†These authors have contributed equally to this work

RECEIVED 23 March 2025
ACCEPTED 12 May 2025
PUBLISHED 30 May 2025

CITATION
Zhang Y, Fu X, Zhang L, Zhou Q and Wang W (2025) Splenic volume as a predictor of survival in cancer patients treated with immune checkpoint inhibitors. *Front. Immunol.* 16:1598484. doi: 10.3389/fimmu.2025.1598484

COPYRIGHT
© 2025 Zhang, Fu, Zhang, Zhou and Wang. This is an open-access article distributed under the terms of the Creative Commons Attribution License (CC BY). The use, distribution or reproduction in other forums is permitted, provided the original author(s) and the copyright owner(s) are credited and that the original publication in this journal is cited, in accordance with accepted academic practice. No use, distribution or reproduction is permitted which does not comply with these terms.

Splenic volume as a predictor of survival in cancer patients treated with immune checkpoint inhibitors

Yunhua Zhang[1,2,3†], Xin Fu[4†], Lilong Zhang[2,3,5], Qing Zhou[1,2,3*] and Weixing Wang[2,3,5*]

[1]Department of Ultrasound Imaging, Renmin Hospital of Wuhan University, Wuhan, Hubei, China, [2]Hubei Key Laboratory of Digestive System Disease, Renmin Hospital of Wuhan University, Wuhan, Hubei, China, [3]General Surgery Laboratory, Renmin Hospital of Wuhan University, Wuhan, Hubei, China, [4]Department of Anesthesiology, Renmin Hospital of Wuhan University, Wuhan, Hubei, China, [5]Department of General Surgery, Renmin Hospital of Wuhan University, Wuhan, Hubei, China

Objective: This investigation seeks to examine the association between spleen volume and prognosis in cancer patients undergoing immune checkpoint inhibitor (ICI) treatment.

Methods: We performed a retrospective analysis involving 61 patients diagnosed with hepatocellular carcinoma (HCC) who received ICIs at our institution. We evaluated the relationship between baseline splenic volume and its changes during ICI therapy concerning overall survival (OS) and progression-free survival (PFS) using a log-rank test. To identify relevant literature, we searched databases such as PubMed, EMBASE, the Cochrane Library, and Google Scholar up until February 20, 2024. The primary metrics assessed were hazard ratios (HR) for both OS and PFS, with pooled estimates and corresponding 95% confidence intervals (CIs) calculated.

Results: Within our study population, findings demonstrated a significantly decreased OS (HR: 2.02, 95% CI: 1.08–3.77, $p = 0.027$) and PFS (HR: 1.84, 95% CI: 1.05–3.21, $p = 0.032$) in HCC patients with a high baseline spleen volume, compared to individuals with lower spleen volumes. Additionally, HCC patients who experienced an increase in spleen volume during ICI therapy exhibited significantly poorer OS (HR: 2.27, 95% CI: 1.17–4.41, $p = 0.016$) and PFS (HR: 2.40, 95% CI: 1.30–4.41, $p = 0.005$) than those whose spleen volume decreased. The meta-analysis results revealed that subjects with higher spleen volumes had a significantly reduced OS (HR: 1.74, 95% CI: 1.12–2.72, $p = 0.014$) and PFS (HR: 1.35, 95% CI: 1.15–1.58, $p < 0.001$) compared to counterparts with lower volumes. Furthermore, the data clearly highlighted that patients with increases in splenic volume faced significantly poorer clinical outcomes, as indicated by reduced OS (HR: 1.83, 95% CI: 1.36–2.46, $p < 0.001$) and PFS (HR: 1.70, 95% CI: 1.28–2.25, $p < 0.001$) relative to those with decreases in splenic size.

Conclusion: A higher baseline spleen volume and an increase in spleen volume during ICI therapy were predictors of a poor prognosis in cancer patients treated with ICI.

KEYWORDS

immune checkpoint inhibitors, cancer, splenic volume, prognosis, hepatocellular carcinoma

1 Introduction

Immune checkpoints, which encompass both stimulatory and inhibitory signals, regulate the immune response and protect neoplastic cells from immune detection (1–3). In recent years, oncology has experienced notable progress, highlighted by the emergence of immune checkpoint inhibitors (ICIs) and various immunotherapeutic approaches (4–7). The use of ICIs has become vital in treating various cancers, offering a distinct survival advantage compared to traditional treatments, including chemotherapy and radiation (4–7). While conventional chemotherapy primarily targets cancerous cells to disrupt their cycle, ICIs consist of antibodies that target PD-1, PD-L1, or CTLA-4. This mechanism interrupts critical regulatory signals that inhibit immune activity in the tumor microenvironment (TME) (4–8). As a result, ICIs reduce immune suppression, allowing tumor-specific T cells to trigger an antitumor response by leveraging the patient's immune capabilities against the cancer (4–7).

The efficacy of ICI treatment varies significantly among different cancer types, typically ranging from 10% to 40%. Most patients ultimately experience progression despite an initial favorable response (9, 10). Furthermore, the negative effects associated with immune responses triggered by ICI treatment can be severe or even life-threatening (11). Consequently, early identification of patients unlikely to benefit from ICI therapy has become a critical focus in oncology, aimed at preventing ineffective therapy and reducing the risk of adverse reactions (12, 13). At present, intra-tumoral PD-L1 assays are commonly employed as biomarkers to inform ICI treatment (14, 15). However, the clinical predictive value of PD-L1 in practice is limited due to its heterogeneous expression across tumor tissues (16). Additional immune-related biomarkers, such as tumor mutation burden, are also used for companion diagnostics (17–20). Nevertheless, the individual effectiveness of these markers in predicting treatment outcomes is restricted (17, 18). Moreover, establishing standardized criteria for the quantification of these biomarkers presents significant challenges. Thus, the discovery of new prognostic markers that can improve outcomes for cancer patients receiving ICIs is critically important.

The spleen is the largest lymphoid organ in humans, containing diverse populations of immune cells. Previous studies suggest that individuals with splenomegaly may experience splenic dysfunction along with alterations in the immune microenvironment. This abnormal enlargement could potentially affect the efficacy of ICIs, influenced by imbalances in the immune microenvironment. However, the predictive effect of baseline spleen volume or changes in spleen volume on the efficacy of ICI in cancer patients remains controversial. This study aims to offer valuable insights by systematically consolidating all existing evidence, thereby improving our comprehension of the clinical significance of spleen volume in forecasting the prognosis of cancer patients treated with ICIs. To the best of our knowledge, this represents the first meta-analysis examining the role of spleen volume in predicting prognosis in cancer patients receiving ICI.

2 Methods

2.1 Study cohort and data collection

The institutional review board approved this study. Due to its retrospective nature, informed consent was not required. We conducted a retrospective analysis of patients with hepatocellular carcinoma (HCC) who received immunotherapy and angiogenesis blockade therapy at our institution between December 2020 and June 2022. The immunotherapy treatments included anti-PD-1 and anti-PD-L1 agents. Eligible patients had diagnosed HCC, with a baseline computed tomography (CT) scan performed within four weeks before the start of treatment. Patients were included if they had at least one measurable lesion, as defined by RECIST version 1.1. Exclusion criteria included prior immunotherapy exposure and the absence of a pretreatment CT scan.

Comprehensive data were collected from patient medical records, encompassing demographic details (age, sex), Eastern Cooperative Oncology Group performance status (ECOG PS), hepatitis etiology, liver cirrhosis, Barcelona Clinic Liver Cancer (BCLC) classification, Child–Pugh classification, tumor count, macrovascular invasion, treatment line, modified albumin-bilirubin grade, and AFP levels. Tumor progression was assessed according to RECIST version 1.1. Follow-up CT imaging was performed every one to three months after the initiation of treatment. Progression-free survival (PFS) was defined as the

duration from the start of ICI therapy to death or disease progression, while overall survival (OS) was measured from the start of ICI therapy until death.

2.2 Spleen volume estimation

Spleen volume was assessed using CT imaging, following the method outlined in a previous study (21). The spleen's maximal width (W) was determined by measuring the largest diameter across any transverse section, while the thickness at the hilum (Th) was defined as the distance between the inner and outer borders of the spleen on a plane perpendicular to the width and intersecting the hilum. Additionally, the spleen length (L) was recorded from abdominal CT scans. Spleen volume was calculated using the following formula: Spleen volume = 30 + 0.58 (W × L × Th).

2.3 Search strategy and inclusion/exclusion criteria

An electronic search was initiated on February 1, 2025, across several bibliographic databases, including PubMed, EMBASE, and the Cochrane Library. The search incorporated a range of key terms such as "immune checkpoint inhibitors" [Mesh], "PD-1 inhibitors," "PD-L1 inhibitors," "CTLA-4 inhibitors," "splenomegaly" [Mesh], "splenic volume," "spleen volume," and "enlarged spleen," with a focus on all relevant fields. Only studies published in English involving human participants were included. Detailed search strategies are outlined in Supplementary Material 1. In addition, grey literature was sourced from Google Scholar, and reference lists of eligible studies were manually reviewed. All search results, both electronic and manual, were consolidated in Covidence software for streamlined data management, in accordance with Cochrane collaboration guidelines.

Inclusion criteria were as follows: (i) studies involving cancer patients, (ii) administration of ICIs as the therapeutic approach, (iii) evaluation of the association between baseline spleen volume (categorized into high and low groups) and changes in spleen volume and prognosis, and (iv) documentation of at least one outcome measure, including OS or PFS. Exclusion criteria included studies utilizing methodologies such as animal models, literature reviews, case reports, or conference abstracts and studies lacking hazard ratios (HRs) for evaluating outcomes based on published or text data. In cases of overlapping patient cohorts, preference was given to studies that provided comprehensive data and adhered to rigorous research methodologies.

2.4 Data extraction and quality assessment

During the data collection phase, we extracted key details such as author information, year of publication, study period, country, cancer type, treatment regimens, sample size, and gender, along with splenic volume-related parameters (including measurement tool and calculation method). HRs and their respective 95% confidence intervals (CIs) were primarily obtained from multivariate analyses. In cases where these were unavailable, data were derived from univariate analyses or extracted from survival curves using Engauge Digitizer software (22).

To evaluate the quality of the included observational studies, the Newcastle-Ottawa Scale (NOS) was used, with studies scoring six or more points classified as high quality (23). The quality assessment considered nine criteria across three domains: patient selection, study comparability, and outcome evaluation. All aspects of the process, including literature retrieval, screening, data extraction, and quality assessment, were independently performed by two researchers, with any disagreements resolved through discussions with the senior author.

Two independent reviewers conducted the screening and data extraction processes to reduce bias and ensure accuracy. Any discrepancies were resolved through discussion or consultation with a third reviewer.

2.5 Statistical methods

The Cox proportional-hazards model and the Kaplan-Meier method were used to assess survival curves across different groups. Meta-analysis was conducted using Stata version 18.0, with results visually represented through forest plots. Heterogeneity was assessed using Cochran's Q test and the I^2 statistic, with significant variation defined as a p-value < 0.1 or an I^2 value > 50%. In cases of significant heterogeneity, a random-effects model based on the DerSimonian-Laird approach was applied; otherwise, a fixed-effects model using the Inverse Variance method was used. Publication bias was evaluated through Egger's regression test (24) and Begg's test (25). Sensitivity analyses were performed to test the robustness of the findings by sequentially excluding individual studies (26). Additionally, subgroup analyses were conducted based on different body composition assessment techniques. Statistical significance was set at a two-tailed p-value of < 0.05.

3 Results

3.1 Patient characteristics

Table 1 outlines the characteristics of the patient cohort. The median age was 61.3 years, with a range from 42.5 to 83.2 years. Within the cohort, 38 patients (62.3%) were male. The ECOG PS was 0 in 39 patients (63.93%) and 1 in 22 patients (36.07%). Viral

TABLE 1 Patient characteristics.

Factors	Overall (n=61)
Age	61.3 (42.5-83.2)
Males	38 (62.30%)
ECOG PS	
0	39 (63.93%)
1	22 (36.07%)

(Continued)

10.3389/fimmu.2025.1598484

TABLE 1 Continued

Factors	Overall (n=61)
Etiology	
Viral	48 (78.69%)
Other	13 (21.31%)
Liver cirrhosis	
Yes	41 (67.21%)
No	20 (32.79%)
BCLC stage	
Early	3 (4.92%)
Intermediate	26 (42.62%)
Advanced	32 (52.46%)
Child-Pugh class	
A	51 (83.61%)
B	10 (16.39%)
Tumor number	
< 3	46 (75.41%)
≥ 3	15 (24.59%)
Macrovascular invasion	
Yes	18 (29.51%)
No	43 (70.49%)
Treatment line	
First-line	35 (57.38%)
Later-line	26 (42.62%)
mALBI grade	
1	28 (45.90%)
2	33 (54.10%)
AFP (ng/mL)	
≥ 400	34 (55.74%)
< 400	27 (44.26%)

Data shown are means with range or numbers with percentage.
ECOG PS, Eastern Cooperative Oncology Group performance status; BCLC, Barcelona Clinic Liver Cancer; AFP, α-fetoprotein; mALBI grade, modified albumin-bilirubin grade.

infections were present in 48 individuals (78.69%), and liver cirrhosis was identified in 41 patients (67.21%). The distribution of Barcelona Clinic Liver Cancer stages was as follows: early stage (n=3, 4.92%), intermediate stage (n=26, 42.62%), and advanced stage (n=32, 52.46%).

3.2 Relationship between baseline splenic volume, changes in splenic volume, and prognosis

The median basal splenic volume of all patients was 198 mL (range: 118–369). We divided the cohort into two groups based on the cutoff value for the median pretreatment splenic volume. Survival curves revealed significantly shorter OS (HR: 2.02, 95% CI: 1.08–3.77, p = 0.027, Figure 1A) and PFS (HR: 1.84, 95% CI: 1.05–3.21, p = 0.032; Figure 1B) in HCC patients with high baseline spleen volume compared to those with low spleen volume. Additionally, we also found that HCC patients with an increase in spleen volume during ICI treatment exhibited worse OS (HR: 2.27, 95% CI: 1.17–4.41, p = 0.016; Figure 1C) and PFS (HR: 2.40, 95% CI: 1.30–4.41, p = 0.005; Figure 1D) compared to those with a decrease in spleen volume. Therefore, data from our center indicate that HCC patients with high baseline spleen volume or an increase in spleen volume during ICI treatment have a worse prognosis.

3.3 Search results and included studies

The initial search strategy, combined with manual screening, identified 365 potentially relevant articles. After removing 40 duplicates, 287 articles were excluded based on title and abstract screening for non-compliance with the selection criteria. A full-text evaluation of the remaining 38 articles resulted in the exclusion of 29 that did not meet the required standards. Ultimately, 9 studies (27–35) were included in the final analysis (Figure 2).

3.4 Study characteristics

Table 2 summarizes the key features of the studies analyzed in this research. A total of 1,024 participants were included, of whom 77.34% were male, with individual study sample sizes ranging from 45 to 276. Geographically, three studies were conducted in China, two in Germany, and one each in Brazil, France, Japan, and Turkey. To evaluate spleen volume, all studies employed either computed tomography (CT) or magnetic resonance imaging (MRI). These studies were exclusively retrospective in design, with NOS scores ranging from 6 to 8, indicating a low likelihood of bias (Table 1).

3.5 Baseline spleen volume and overall survival and progression-free survival

In this investigation, we analyzed data from nine studies involving a total of 917 patients to assess the impact of pre-treatment spleen volumes on OS and PFS in cancer patients receiving ICIs. The results indicated that individuals with high spleen volume experienced significantly reduced OS (HR: 1.74, 95% CI: 1.12–2.72, p = 0.014, Figure 3A) and PFS (HR: 1.35, 95% CI: 1.15–1.58, p < 0.001, Figure 3B) compared to those with low spleen volume. The analysis of OS using the Cochran Q test and I^2 statistics (I^2 = 59.8%, p = 0.015) revealed considerable heterogeneity across the studies. Consequently, we employed a random-effects model for these analyses. In contrast, the evaluation of PFS studies did not show significant heterogeneity (I^2 = 35.7%, p = 0.144); thus, a fixed-effects model was considered appropriate.

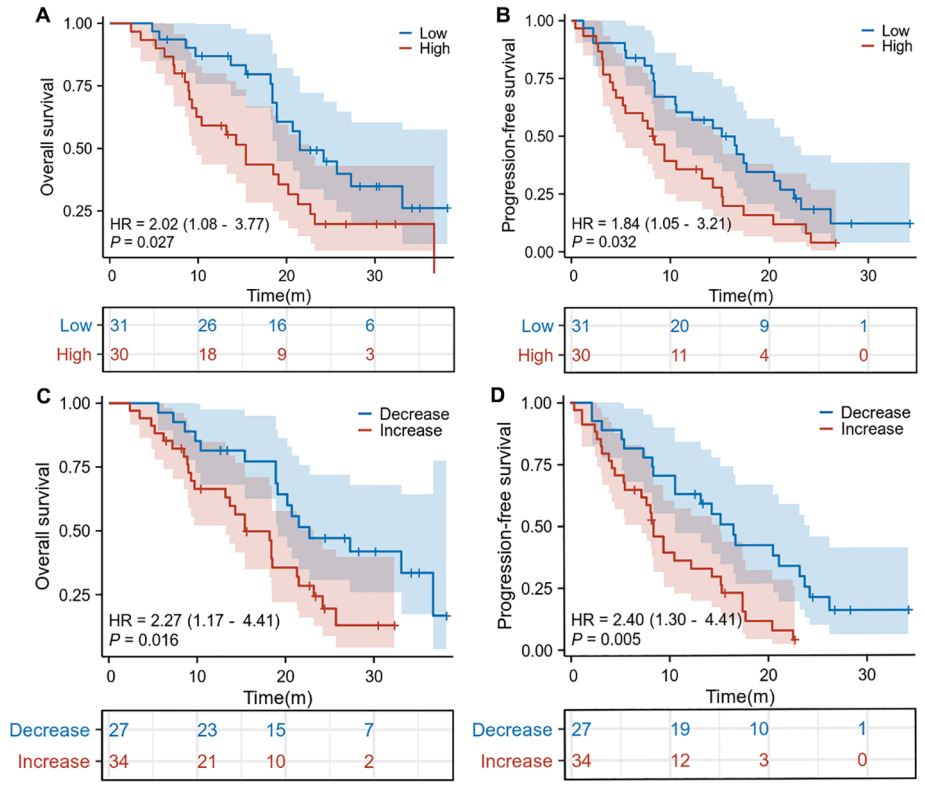

FIGURE 1
The Kaplan-Meier curve of overall survival **(A)** and progression-free survival **(B)** in the pretreatment high splenic volume and low splenic volume in our cohorts. The Kaplan-Meier curve of overall survival **(C)** and progression-free survival **(D)** according to the relative change compared to baseline splenic volume in our cohorts. HR, hazard ratio; CI, confidence interval.

The assessment of potential publication bias was performed using funnel plots, along with Begg's and Egger's tests. The results showed no significant bias concerning OS (Egger's test: $p = 0.913$; Begg's test: $p = 0.711$; Supplementary Figure S1A) or PFS (Egger's test: $p = 0.651$; Begg's test: $p = 0.902$; Supplementary Figure S1B). Our sensitivity analysis, which systematically excluded each study one at a time, demonstrated the consistent stability and robustness of the pooled HRs for both OS and PFS (Figures 4A, B).

3.6 Changes in splenic volume and overall survival and progression-free survival

An analysis was further conducted to investigate the correlation between changes in splenic volume and OS as well as PFS among cancer patients, incorporating data from seven studies with a total of 829 subjects. Notably, these studies exhibited minimal heterogeneity for both OS ($I^2 = 12.5\%$, $p = 0.334$) and PFS ($I^2 = 0$, $p = 0.420$), supporting the use of a fixed-effects model for the analysis. The results clearly indicated that patients with increases in splenic volume faced significantly worse outcomes, with reduced OS (HR: 1.83, 95% CI: 1.36–2.46, $p < 0.001$, Figure 5A) and PFS (HR: 1.70, 95% CI: 1.28–2.25, $p < 0.001$, Figure 5B) compared to those with decreases in splenic volume.

Publication bias was assessed using funnel plots, along with Begg's and Egger's tests. The findings showed no significant bias for OS (Egger's test: $p = 0.753$; Begg's test: $p = 0.548$; Supplementary Figure S2A) or PFS (Egger's test: $p = 0.129$; Begg's test: $p = 0.308$; Supplementary Figure S2B). Additionally, sensitivity analysis, which sequentially excluded individual studies, reaffirmed the stability and robustness of the pooled HRs (Figures 6A, B).

4 Discussion

In our queue, we found that a higher baseline spleen volume and an increase in spleen volume during ICI therapy were predictors of a poor prognosis in HCC cancer patients treated with ICI. Considering the controversies between different studies, we further included nine studies for meta-analysis and the conclusions were consistent with the findings of our cohort.

The spleen plays a vital role in regulating hematopoiesis and immune responses, making it a key focus for assessing the effectiveness of immunotherapy across various cancer types (36).

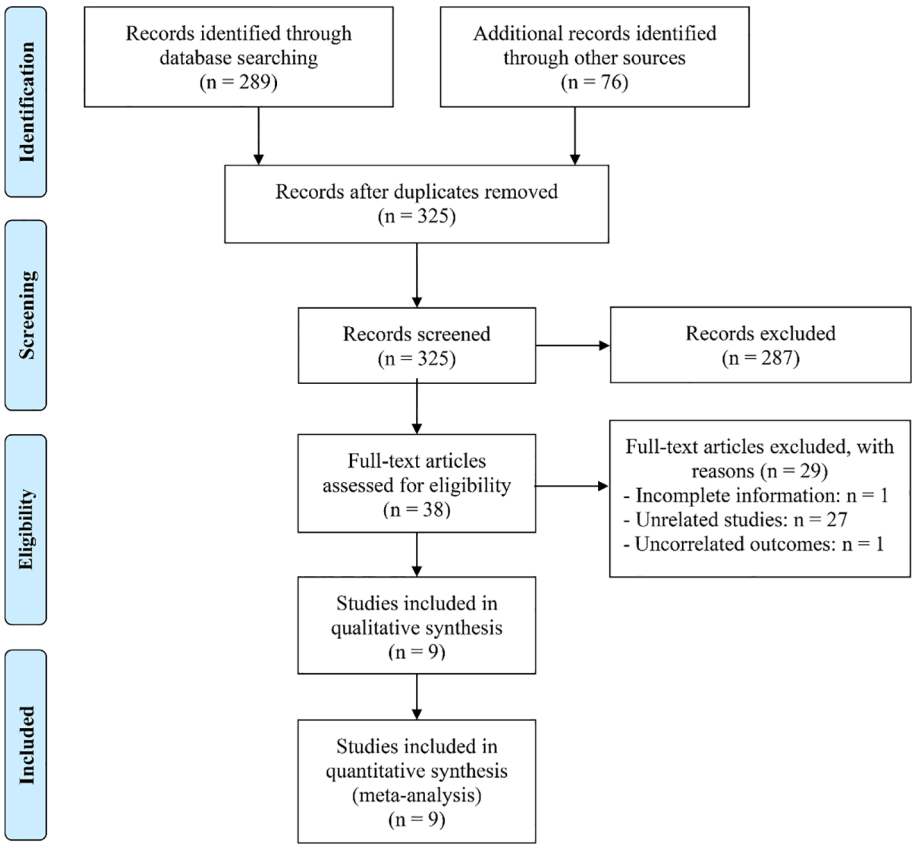

FIGURE 2
The flow diagram of identifying eligible studies.

TABLE 2 Main characteristics of the studies included.

Study	Study period	Country	Sample size	Gender (male/female)	Treatment	Cancer type	Tool	Calculation method	NOS
Hatanaka et al., 2024 (34)	09/2020-07/2022	Japan	164	135/29	Atezo/bev	HCC	CT	30 + 0.58 (W × L × Th)	8
Mo et al., 2024 (35)	03/2016-12/2022	China	168	136/32	Atezo/bev or bevacizumab +sintilimab or camrelizumab	HCC	CT	30 + 0.58 (W × L × Th)	8
Oliveira et al., 2023 (33)	09/2019-03/2021	Brazil	50	32/18	Nivolumab or pembrolizumab or ipilimumab+nivolumab	Melanoma	CT or MRI	Fully automated AI-based splenic segmentation	7
Duwe et al., 2023 (32)	01/2012-05/2022	Germany	65	50/15	ICIs	UC, RCC	CT or MRI	Fully automated AI-based splenic segmentation	6
Xiao et al., 2022 (30)	08/2018-10/2020	China	161	144/17	ICIs	PLC	CT	Maximum diameter of the spleen	7
Yang et al., 2021 (28)	06/2015-05/2020	China	45	31/14	Nivolumab	PA	CT or MRI	30 + 0.58 (W × L × Th)	6

(Continued)

10.3389/fimmu.2025.1598484

TABLE 2 Continued

Study	Study period	Country	Sample size	Gender (male/female)	Treatment	Cancer type	Tool	Calculation method	NOS
Müller et al., 2022 (29)	05/2016-10/2021	Germany	50	40/10	Atezo/bev or pembrolizumab or nivolumab	HCC	CT	Fully automated AI-based splenic segmentation	6
Galland et al., 2021 (27)	01/2014-06/2020	France	276	193/83	Anti-PD-1/PD-L1	NSCLC	CT	30 + 0.58 (W × L × Th)	8
Aslan et al., 2023 (31)	09/2010-09/2021	Turkey	45	31/14	Nivolumab	RCC	CT	30 + 0.58 (W × L × Th)	6

Atezo/bev: atezolizumab+bevazizumab; ICIs, immune checkpoint inhibitors; PD-1, programmed cell death protein 1; PD-L1, programmed cell death ligand 1; HCC, hepatocellular carcinoma; UC, urothelial carcinoma; RCC, renal cell carcinoma; PLC, primary liver cancer; PA, pancreatic adenocarcinoma; NSCLC, non small cell lung cancer; CT, computed tomography; MRI, magnetic resonance imaging; W × L × Th, maximal width of the spleen × maximal thickness of the spleen × length of the spleen.

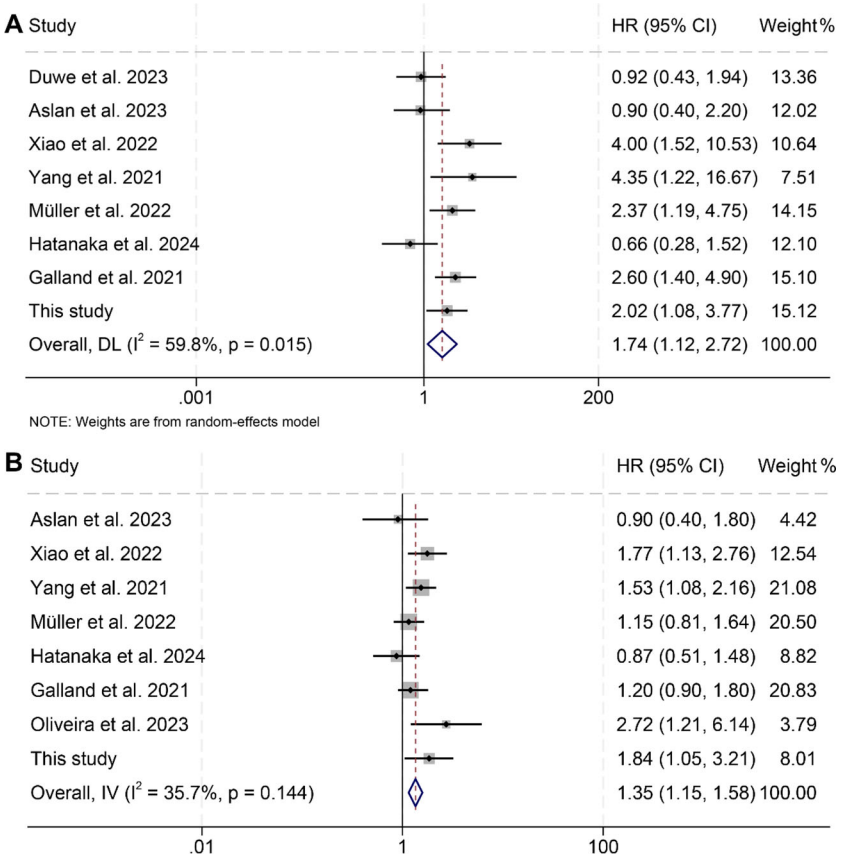

FIGURE 3
Forest plots illustrating the relationship between spleen volume and overall survival **(A)** and progression-free survival **(B)**. HR, hazard ratio; CI, confidence interval; DL, DerSimonian and Laird; IV, inverse-variance model.

In animal models, a significant accumulation of myeloid-derived suppressor cells (MDSCs) has been noted in the spleen, resulting in splenomegaly (37, 38). Additionally, certain clinical studies have shown a correlation between MDSC levels and splenic volume (39). Measuring splenic volume is both quick and straightforward in clinical settings.

Recent studies have identified an increase in MDSCs as a significant factor contributing to resistance against immunotherapy (40). This heterogeneous group consists of immature, immunosuppressive myeloid progenitor cells. The prevalence of MDSCs is heightened in the spleen, bloodstream of cancer patients, and within the TME across various malignancies.

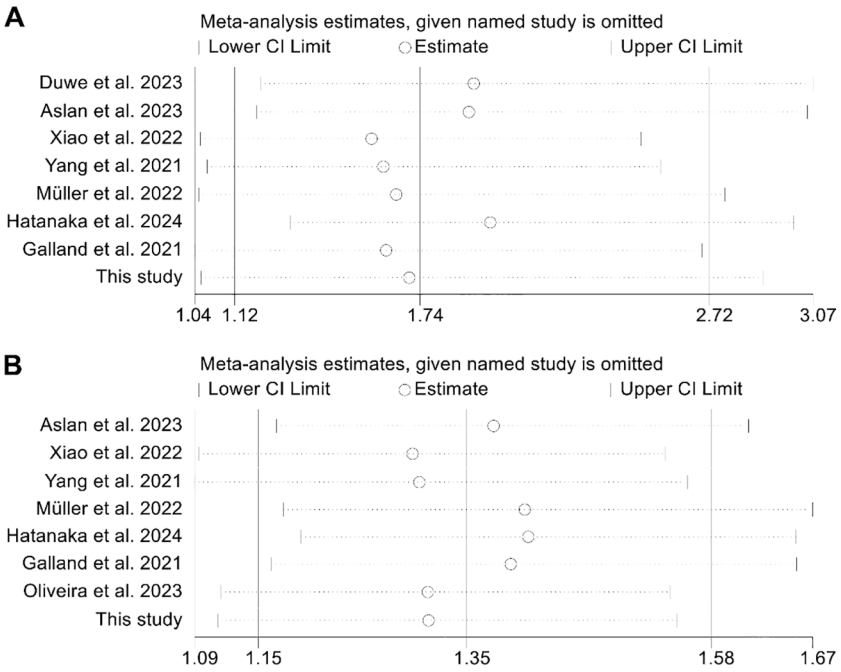

FIGURE 4
Sensitivity analysis of the relationship between spleen volume and overall survival **(A)** and progression-free survival **(B)**. HR, hazard ratio; CI, confidence interval.

Their elevation in these areas is influenced by chemokines, growth factors, and cytokines secreted by tumors (41, 42). MDSCs are known for their role in fostering immunotherapy resistance by suppressing the functions of natural killer cells and T cells, as well as by activating immunosuppressive regulatory T cells. These pathological cells create an immunosuppressive environment through the excessive production of interleukin-10, transforming growth factor-β, arginase, and nitric oxide within the TME.

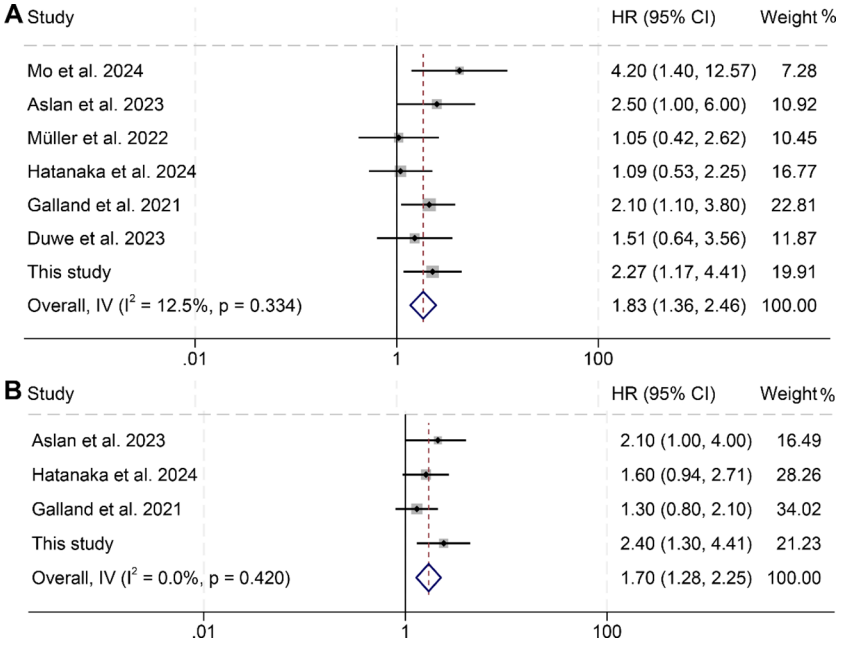

FIGURE 5
Forest plots illustrating the relationship between changes in splenic volume and overall survival **(A)** as well as progression-free survival **(B)**. HR, hazard ratio; CI, confidence interval; IV, inverse-variance model.

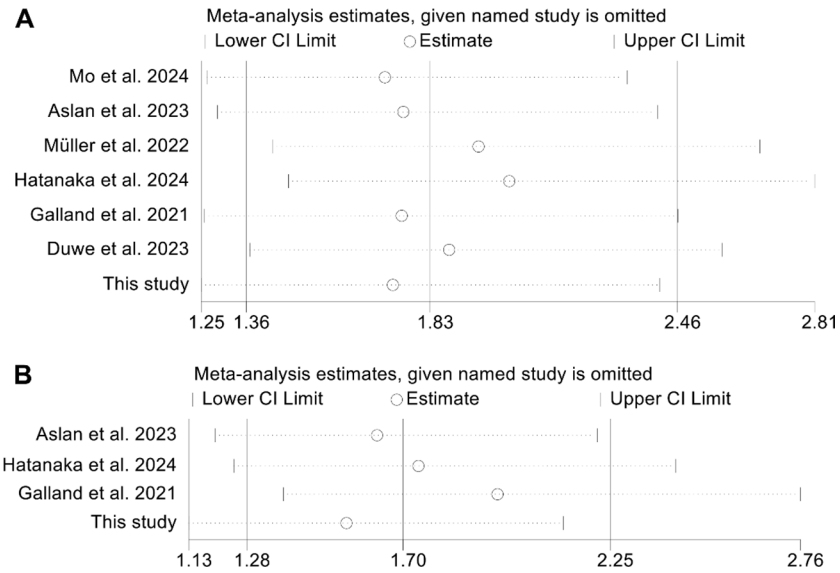

FIGURE 6
Sensitivity analysis of the relationship between changes in splenic volume and overall survival **(A)** and progression-free survival **(B)**. HR, hazard ratio; CI, confidence interval.

Additionally, they promote tumor progression by expressing surface receptors that inhibit T cell activity (41, 43–46). Research shows that targeting and inactivating Tregs or MDSCs can restore the anticancer efficacy of ICIs (47–49). Furthermore, a study involving RCC indicated that combining MDSC-targeted therapy with IL-2 treatment enhances the response to immunotherapy (50). So far, the mechanism by which splenomegaly affects the curative effect of ICI has not been reported. We suggest that the relationship between splenomegaly and MDSCs may partly explain our conclusions.

Splenomegaly serves as a valuable predictor due to the straightforward, accessible, non-invasive, and cost-effective imaging methods available for assessing spleen size. Previous research indicated that high-affinity neoantigens are associated with improved OS in individuals diagnosed with HCC (51). However, the analysis of neoantigens was performed through whole-exome sequencing, a method that is both expensive and not readily available in clinical settings. Additionally, the expression of PD-L1 has been linked to the effectiveness of ICIs (52). Nonetheless, PD-L1 levels were assessed using immunohistochemistry, a technique that is invasive and not easily accessible in clinical practice. Another investigation found that immune-related adverse events could predict the effectiveness of ICIs (53). While these adverse events do not occur in every patient, spleen size can be reliably measured through imaging techniques for all individuals. Therefore, we believe that the assessment of spleen volume is a very meaningful indicator to predict the efficacy of ICI treatment.

The single-center cohort predominantly consisted of HCC patients with underlying cirrhosis, mainly of viral etiology, which is commonly associated with portal hypertension and resultant splenomegaly. Baseline splenomegaly in these patients may partly reflect the presence and severity of portal hypertension, a factor that could have independently contributed to poorer survival outcomes. We intentionally chose not to exclude these patients or set a mean baseline splenic volume cutoff in order to preserve the real-world clinical scenario, despite the potential confounding effect. Importantly, our meta-analysis, which incorporated a larger and more diverse patient cohort, supports the overall conclusions drawn from our findings. Nonetheless, future studies with more detailed stratification are warranted to further delineate the specific impact of portal hypertension and related factors on patient outcomes.

This meta-analysis has certain limitations that must be acknowledged. First, it is crucial to recognize that all studies included were retrospective cohort designs, which may restrict their statistical validity. Second, the limited number of studies analyzed hindered our ability to perform subgroup analyses for specific cancer types and ICIs. Third, the cut-off values for the same diagnostic criteria varied among the studies. Finally, due to the limited sample size in our single-center data, multivariate analysis was not performed. Therefore, to draw more robust conclusions, there is an urgent need for a global, multicenter study to explore the impact of splenic volume on the outcomes of cancer patients receiving ICIs.

5 Conclusion

A higher baseline spleen volume and an increase in spleen volume during ICI therapy were predictors of a poor prognosis in cancer patients treated with ICI.

Data availability statement

The original contributions presented in the study are included in the article/Supplementary Material. Further inquiries can be directed to the corresponding author/s.

Ethics statement

The studies involving humans were approved by Ethics Committee of Renmin Hospital of Wuhan University. The studies were conducted in accordance with the local legislation and institutional requirements. The participants provided their written informed consent to participate in this study.

Author contributions

YZ: Methodology, Writing – original draft, Investigation, Conceptualization, Formal Analysis, Resources, Data curation, Visualization. XF: Writing – original draft, Conceptualization, Formal Analysis, Software, Data curation, Methodology, Investigation, Visualization. LZ: Methodology, Investigation, Resources, Writing – original draft, Visualization. QZ: Visualization, Validation, Project administration, Conceptualization, Supervision, Writing – review & editing. WW: Validation, Conceptualization, Writing – original draft, Supervision, Project administration, Visualization.

Funding

The author(s) declare that no financial support was received for the research and/or publication of this article.

Acknowledgments

The authors thank all the medical staff who contributed to the maintenance of the medical record database.

Conflict of interest

The authors declare that the research was conducted in the absence of any commercial or financial relationships that could be construed as a potential conflict of interest.

Generative AI statement

The author(s) declare that no Generative AI was used in the creation of this manuscript.

Publisher's note

All claims expressed in this article are solely those of the authors and do not necessarily represent those of their affiliated organizations, or those of the publisher, the editors and the reviewers. Any product that may be evaluated in this article, or claim that may be made by its manufacturer, is not guaranteed or endorsed by the publisher.

Supplementary material

The Supplementary Material for this article can be found online at: https://www.frontiersin.org/articles/10.3389/fimmu.2025.1598484/full#supplementary-material

References

1. Hanahan D, Weinberg RA. Hallmarks of cancer: the next generation. *Cell*. (2011) 144:646–74. doi: 10.1016/j.cell.2011.02.013

2. Yuan Q, Deng D, Pan C, Ren J, Wei T, Wu Z, et al. Integration of transcriptomics, proteomics, and metabolomics data to reveal HER2-associated metabolic heterogeneity in gastric cancer with response to immunotherapy and neoadjuvant chemotherapy. *Front Immunol*. (2022) 13:951137. doi: 10.3389/fimmu.2022.951137

3. Pardoll DM. The blockade of immune checkpoints in cancer immunotherapy. *Nat Rev Cancer*. (2012) 12:252–64. doi: 10.1038/nrc3239

4. Larkin J, Chiarion-Sileni V, Gonzalez R, Grob JJ, Rutkowski P, Lao CD, et al. Five-year survival with combined nivolumab and ipilimumab in advanced melanoma. *N Engl J Med*. (2019) 381:1535–46. doi: 10.1056/NEJMoa1910836

5. Ansell SM, Lesokhin AM, Borrello I, Halwani A, Scott EC, Gutierrez M, et al. PD-1 blockade with nivolumab in relapsed or refractory Hodgkin's lymphoma. *N Engl J Med*. (2015) 372:311–9. doi: 10.1056/NEJMoa1411087

6. Larkin J, Chiarion-Sileni V, Gonzalez R, Grob JJ, Cowey CL, Lao CD, et al. Combined nivolumab and ipilimumab or monotherapy in untreated melanoma. *N Engl J Med*. (2015) 373:23–34. doi: 10.1056/NEJMoa1504030

7. Cheng W, Fu D, Xu F, Zhang Z. Unwrapping the genomic characteristics of urothelial bladder cancer and successes with immune checkpoint blockade therapy. *Oncogenesis*. (2018) 7:2. doi: 10.1038/s41389-017-0013-7

8. Li Z, Liu Y, Huang X, Wang Q, Fu R, Wen X, et al. F. Nucleatum enhances oral squamous cell carcinoma proliferation via E-cadherin/β-Catenin pathway. *BMC Health*. (2024) 24:518. doi: 10.1186/s12903-024-04252-3

9. Ribas A, Wolchok JD. Cancer immunotherapy using checkpoint blockade. *Science*. (2018) 359:1350–5. doi: 10.1126/science.aar4060

10. O'Donnell JS, Teng MWL, Smyth MJ. Cancer immunoediting and resistance to T cell-based immunotherapy. *Nat Rev Clin Oncol*. (2019) 16:151–67. doi: 10.1038/s41571-018-0142-8

11. Dolladille C, Ederhy S, Sassier M, Cautela J, Thuny F, Cohen AA, et al. Immune checkpoint inhibitor rechallenge after immune-related adverse events in patients with cancer. *JAMA Oncol*. (2020) 6:865–71. doi: 10.1001/jamaoncol.2020.0726

12. Zhang L, Feng J, Kuang T, Chai D, Qiu Z, Deng W, et al. Blood biomarkers predict outcomes in patients with hepatocellular carcinoma treated with immune checkpoint Inhibitors: A pooled analysis of 44 retrospective sudies. *Int Immunopharmacol*. (2023) 118:110019. doi: 10.1016/j.intimp.2023.110019

13. Zhao J, Li D, Xie S, Deng X, Wen X, Li J, et al. Nomogram for predicting prognosis of patients with metastatic melanoma after immunotherapy: A Chinese population-based analysis. *Front Immunol*. (2022) 13:1083840. doi: 10.3389/fimmu.2022.1083840

14. Ren J, Wang A, Liu J, Yuan Q. Identification and validation of a novel redox-related lncRNA prognostic signature in lung adenocarcinoma. *Bioengineered*. (2021) 12:4331–48. doi: 10.1080/21655979.2021.1951522

15. Havel JJ, Chowell D, Chan TA. The evolving landscape of biomarkers for checkpoint inhibitor immunotherapy. *Nat Rev Cancer*. (2019) 19:133–50. doi: 10.1038/s41568-019-0116-x

16. Zhou KI, Peterson B, Serritella A, Thomas J, Reizine N, Moya S, et al. Spatial and Temporal Heterogeneity of PD-L1 Expression and Tumor Mutational Burden in Gastroesophageal Adenocarcinoma at Baseline Diagnosis and after Chemotherapy. *Clin Cancer Res*. (2020) 26:6453–63. doi: 10.1158/1078-0432.CCR-20-2085

17. Jørgensen JT. Companion and complementary diagnostics: clinical and regulatory perspectives. *Trends Cancer*. (2016) 2:706–12. doi: 10.1016/j.trecan.2016.10.013

18. Schalper KA, Carleton M, Zhou M, Chen T, Feng Y, Huang SP, et al. Elevated serum interleukin-8 is associated with enhanced intratumor neutrophils and reduced clinical benefit of immune-checkpoint inhibitors. *Nat Med*. (2020) 26:688–92. doi: 10.1038/s41591-020-0856-x

19. Wang Y, Wang J, Liu J, Zhu H. Immune-related diagnostic markers for benign prostatic hyperplasia and their potential as drug targets. *Front Immunol*. (2024) 15:1516362. doi: 10.3389/fimmu.2024.1516362

20. Pang ZQ, Wang JS, Wang JF, Wang YX, Ji B, Xu YD, et al. JAM3: A prognostic biomarker for bladder cancer via epithelial-mesenchymal transition regulation. *Biomol Biomed*. (2024) 24:897–911. doi: 10.17305/bb.2024.9979

21. Prassopoulos P, Daskalogiannaki M, Raissaki M, Hatjidakis A, Gourtsoyiannis N. Determination of normal splenic volume on computed tomography in relation to age, gender and body habitus. *Eur Radiol*. (1997) 7:246–8. doi: 10.1007/s003300050145

22. Deng J, Huang Y, Yu K, Luo H, Zhou D, Li D. Changes in the gut microbiome of patients with esophageal cancer: A systematic review and meta-analysis based on 16S gene sequencing technology. *Microb Pathog*. (2024) 193:106784. doi: 10.1016/j.micpath.2024.106784

23. Lilong Z, Kuang T, Li M, Li X, Hu P, Deng W, et al. Sarcopenia affects the clinical efficacy of immune checkpoint inhibitors in patients with gastrointestinal cancers. *Clin Nutr*. (2024) 43:31–41. doi: 10.1016/j.clnu.2023.11.009

24. Egger M, Davey Smith G, Schneider M, Minder C. Bias in meta-analysis detected by a simple, graphical test. *Bmj*. (1997) 315:629–34. doi: 10.1136/bmj.315.7109.629

25. Begg CB, Mazumdar M. Operating characteristics of a rank correlation test for publication bias. *Biometrics*. (1994) 50:1088–101. doi: 10.2307/2533446

26. Zhang L, Xia Z, Li Z, Zhang J, Wang K, Wang W. Influence of body fat tissue on outcomes in patients undergoing hepatectomy or liver transplantation: a systematic review and meta-analysis. *Int J Surg*. (2025) 111:1167–81. doi: 10.1097/JS9.0000000000001864

27. Galland L, Lecuelle J, Favier L, Fraisse C, Lagrange A, Kaderbhai C, et al. Splenic volume as a surrogate marker of immune checkpoint inhibitor efficacy in metastatic non small cell lung cancer. *Cancers (Basel)*. (2021) 13(12):3020. doi: 10.3390/cancers13123020

28. Yang SH, Lu LC, Kao HF, Chen BB, Kuo TC, Kuo SH, et al. Negative prognostic implications of splenomegaly in nivolumab-treated advanced or recurrent pancreatic adenocarcinoma. *Oncoimmunology*. (2021) 10:1973710. doi: 10.1080/2162402X.2021.1973710

29. Müller L, Gairing SJ, Kloeckner R, Foerster F, Weinmann A, Mittler J, et al. Baseline splenic volume outweighs immuno-modulated size changes with regard to survival outcome in patients with hepatocellular carcinoma under immunotherapy. *Cancers*. (2022) 14(15):3574. doi: 10.3390/cancers14153574

30. Xiao LS, Hu CY, Cui H, Li RN, Hong C, Li QM, et al. Splenomegaly in predicting the survival of patients with advanced primary liver cancer treated with immune checkpoint inhibitors. *Cancer Med*. (2022) 11:4880–8. doi: 10.1002/cam4.v11.24

31. Aslan V, Karabörk Kılıç AC, Özet A, Üner A, Günel N, Yazıcı O, et al. The role of spleen volume change in predicting immunotherapy response in metastatic renal cell carcinoma. *BMC Cancer*. (2023) 23:1045. doi: 10.1186/s12885-023-11558-y

32. Duwe G, Müller L, Ruckes C, Fischer ND, Frey LJ, Börner JH, et al. Change in splenic volume as a surrogate marker for immunotherapy response in patients with advanced urothelial and renal cell carcinoma-evaluation of a novel approach of fully automated artificial intelligence based splenic segmentation. *Biomedicines*. (2023) 11 (9):2482. doi: 10.3390/biomedicines11092482

33. Oliveira Taveira M, de Barros ESMJ, Vieira Barbosa Pinto PN. Imaging-calculated splenic volume is associated with response in melanoma patients treated with immunotherapy. *Immunotherapy*. (2023) 15:343–51. doi: 10.2217/imt-2022-0222

34. Hatanaka T, Saito N, Kakizaki S, Hiraoka A, Tada T, Kariyama K, et al. Factors affecting an increase in spleen volume and association of spleen volume variation with the clinical outcomes of atezolizumab and bevacizumab treatment for hepatocellular carcinoma: A retrospective analysis. *Oncology*. (2024) 103(2):94–106. doi: 10.1159/000541002

35. Mo Z, Lv L, Mai Q, Li Q, He J, Zhang T, et al. Prognostic model for unresectable hepatocellular carcinoma treated with dual PD-1 and angiogenesis blockade therapy. *J Immunother Cancer*. (2024) 12(1):e008191. doi: 10.1136/jitc-2023-008191

36. Wang Q, Huang X, Zhou S, Ding Y, Wang H, Jiang W, et al. IL1RN and PRRX1 as a prognostic biomarker correlated with immune infiltrates in colorectal cancer: evidence from bioinformatic analysis. *Int J Genomics*. (2022) 2022:2723264. doi: 10.1155/2022/2723264

37. Bronte V, Pittet MJ. The spleen in local and systemic regulation of immunity. *Immunity*. (2013) 39:806–18. doi: 10.1016/j.immuni.2013.10.010

38. Ramudo L, Yubero S, Manso MA, Vicente S, De Dios I. Signal transduction of MCP-1 expression induced by pancreatitis-associated ascitic fluid in pancreatic acinar cells. *J Cell Mol Med*. (2009) 13:1314–20. doi: 10.1111/j.1582-4934.2008.00529.x

39. Limagne E, Euvrard R, Thibaudin M, Rébé C, Derangère V, Chevriaux A, et al. Accumulation of MDSC and th17 cells in patients with metastatic colorectal cancer predicts the efficacy of a FOLFOX-bevacizumab drug treatment regimen. *Cancer Res*. (2016) 76:5241–52. doi: 10.1158/0008-5472.CAN-15-3164

40. Wang Q, Wang H, Ding Y, Wan M, Xu M. The role of adipokines in pancreatic cancer. *Front Oncol*. (2022) 12:926230. doi: 10.3389/fonc.2022.926230

41. Gabrilovich DI. Myeloid-derived suppressor cells. *Cancer Immunol Res*. (2017) 5:3–8. doi: 10.1158/2326-6066.CIR-16-0297

42. Liu C, Liu R, Wang B, Lian J, Yao Y, Sun H, et al. Blocking IL-17A enhances tumor response to anti-PD-1 immunotherapy in microsatellite stable colorectal cancer. *J Immunother Cancer*. (2021) 9(1):e001895. doi: 10.1136/jitc-2020-001895

43. Pastaki Khoshbin A, Eskian M, Keshavarz-Fathi M, Rezaei N. Roles of myeloid-derived suppressor cells in cancer metastasis: immunosuppression and beyond. *Arch Immunol Ther Exp (Warsz)*. (2019) 67:89–102. doi: 10.1007/s00005-018-0531-9

44. Veglia F, Sanseviero E, Gabrilovich DI. Myeloid-derived suppressor cells in the era of increasing myeloid cell diversity. *Nat Rev Immunol*. (2021) 21:485–98. doi: 10.1038/s41577-020-00490-y

45. Ye B, Wang Q, Zhu X, Zeng L, Luo H, Xiong Y, et al. Single-cell RNA sequencing identifies a novel proliferation cell type affecting clinical outcome of pancreatic ductal adenocarcinoma. *Front Oncol*. (2023) 13:1236435. doi: 10.3389/fonc.2023.1236435

46. Li Z, Li J, Bai X, Huang X, Wang Q. Tumor microenvironment as a complex milieu driving cancer progression: a mini review. *Clin Transl Oncol*. (2024) 27(5):1943–52. doi: 10.1007/s12094-024-03697-w

47. Highfill SL, Cui Y, Giles AJ, Smith JP, Zhang H, Morse E, et al. Disruption of CXCR2-mediated MDSC tumor trafficking enhances anti-PD1 efficacy. *Sci Transl Med*. (2014) 6:237ra67. doi: 10.1126/scitranslmed.3007974

48. Taylor NA, Vick SC, Iglesia MD, Brickey WJ, Midkiff BR, McKinnon KP, et al. Treg depletion potentiates checkpoint inhibition in claudin-low breast cancer. *J Clin Invest*. (2017) 127:3472–83. doi: 10.1172/JCI90499

49. Gide TN, Wilmott JS, Scolyer RA, Long GV. Primary and acquired resistance to immune checkpoint inhibitors in metastatic melanoma. *Clin Cancer Res*. (2018) 24:1260–70. doi: 10.1158/1078-0432.CCR-17-2267

50. Haka AS, Volynskaya Z, Gardecki JA, Nazemi J, Lyons J, Hicks D, et al. *In vivo* margin assessment during partial mastectomy breast surgery using raman spectroscopy. *Cancer Res*. (2006) 66:3317–22. doi: 10.1158/0008-5472.CAN-05-2815

51. Liu T, Tan J, Wu M, Fan W, Wei J, Zhu B, et al. High-affinity neoantigens correlate with better prognosis and trigger potent antihepatocellular carcinoma (HCC) activity by activating CD39(+)CD8(+) T cells. *Gut*. (2021) 70:1965–77. doi: 10.1136/gutjnl-2020-322196

52. Khemlina G, Ikeda S, Kurzrock R. The biology of Hepatocellular carcinoma: implications for genomic and immune therapies. *Mol Cancer*. (2017) 16:149. doi: 10.1186/s12943-017-0712-x

53. Lu L, Xing K, Wei W, Ling Y, Li P, Li S, et al. Immune-related adverse events predict responses to PD-1 blockade immunotherapy in hepatocellular carcinoma. *Int J Cancer*. (2021) 149(9):959–66. doi: 10.1002/ijc.v149.4

frontiers | Frontiers in Immunology

TYPE Original Research
PUBLISHED 12 June 2025
DOI 10.3389/fimmu.2025.1590219

Check for updates

OPEN ACCESS

EDITED BY
Hailin Tang,
Sun Yat-sen University Cancer Center (SYSUCC), China

REVIEWED BY
Quan Wang,
Air Force Military Medical University, China
Namuunaa Juramt,
Harvard Medical School, United States
Radoslaw Pach,
Jagiellonian University, Poland

*CORRESPONDENCE
Hou Feng
houfshan0717@163.com
Jiang Haitao
jianght67122@sina.com

†These authors have contributed equally to this work and share first authorship

RECEIVED 09 March 2025
ACCEPTED 12 May 2025
PUBLISHED 12 June 2025

CITATION
Jingjing Z, Kun W, Yanyu Q, Mengjie Z, Yunqing C, Yulong T, Xuelong J, Xiaojie T, Haitao J and Feng H (2025) Radiation therapy induced intestinal barrier damage and repair process - differences in salivary metabolites and monitoring of intestinal barrier function. *Front. Immunol.* 16:1590219. doi: 10.3389/fimmu.2025.1590219

COPYRIGHT
© 2025 Jingjing, Kun, Yanyu, Mengjie, Yunqing, Yulong, Xuelong, Xiaojie, Haitao and Feng. This is an open-access article distributed under the terms of the Creative Commons Attribution License (CC BY). The use, distribution or reproduction in other forums is permitted, provided the original author(s) and the copyright owner(s) are credited and that the original publication in this journal is cited, in accordance with accepted academic practice. No use, distribution or reproduction is permitted which does not comply with these terms.

Radiation therapy induced intestinal barrier damage and repair process - differences in salivary metabolites and monitoring of intestinal barrier function

Zhang Jingjing[1†], Wang Kun[2†], Qiao Yanyu[1†], Zhang Mengjie[3], Chen Yunqing[1], Tian Yulong[2], Jiao Xuelong[2], Tan Xiaojie[2], Jiang Haitao[2*] and Hou Feng[1*]

[1]Department of Pathology Department, Affiliated Hospital of Qingdao University, Qingdao, China, [2]Department of Gastrointestinal Surgery, Affiliated Hospital of Qingdao University, Qingdao, China, [3]Department of Gynaecology, Affiliated Hospital of Qingdao University, Qingdao, China

Purpose: Colorectal cancer (CRC) is still one of the most common malignant tumors, with gradual increase in its annual morbidity and mortality. But most cases are diagnosed in the late stage. For stage II-III cancer, clinical guidelines recommend surgery following neoadjuvant radiation therapy at ≥6 weeks after the last radiotherapy is completed. However, radiotherapy may impair intestinal mucosal barrier function, especially the biological and immune barriers, accompanied by perioperative complications. This study was conducted to investigate the changes, repair patterns, and potential mechanisms in patients after radiotherapy.

Methods: This study detected inflammatory factors in postoperative intestinal mucosal tissue and serum, as well as metabolites in saliva samples, and collected hematoxylin-eosin (HE)-stained pathological images in CRC patients who had received and did not receive radiotherapy.

Results: The results showed that after radiotherapy, there were significantly impaired intestinal mucosal tissue structure; obviously elevated inflammatory factors in intestinal mucosal tissue and blood; as well as upregulation/downregulation of metabolites in saliva samples.

Conclusion: In conclusion, findings in this study may provide potential reference for predicting the recovery of intestinal mucosa and selecting the optimal timing for surgery after radiotherapy. In addition, this study will benefit the understanding and reduction of perioperative complications caused by intestinal barrier damage.

KEYWORDS

rectal cancer, radiotherapy, damage and repair, intestinal mucosal barrier, biological barrier, immune barrier, salivary metabolites

Introduction

Colorectal cancer (CRC), as one of the most common malignant tumors, presents a rising incidence rate in recent decades (1). In 2020, CRC ranked among the top ten newly diagnosed cancers worldwide, with 1,944,826 cases (10.0%) reported (2). In China, the morbidity and mortality of digestive malignancies are still increasing (3), significantly compromising public health and life expectancy, while also imposing substantial economic and social burdens on families and society (4). Patients with advanced gastrointestinal cancers may still experience poor prognosis, despite advancements in cancer screening. The early stages of gastric, colorectal, and liver cancers in China account for a relatively low percentage of total cases, with most being diagnosed at more progressive stages (5). For patients with advanced CRC, neoadjuvant therapy radiotherapy may offer oncological benefits (6). Radiation therapy can have certain side effects on the intestinal tissue of patients, namely the occurrence of radiation-induced enteritis, which damages the intestinal mucosal barrier function of patients. However, radiotherapy can damage the intestinal mucosal barrier, especially the biological and immune barriers, potentially leading to bacterial translocation, which is closely associated with perioperative complications such as infection and anastomotic fistulae (7, 8). According to existing Guidelines (9), surgery should be performed wait at ≥6 weeks following radiotherapy. In our previous research, damage to the intestinal barrier, caused by radiotherapy, might be recovered in some cases within 8 to 12 weeks; however, it was impossible to restore to the normal status around three months post-treatment. Our previous research found that radiation therapy can cause changes in the oral microbiota of patients with rectal cancer (10). Therefore, this study was performed to analyze the damage to the barrier function and related biological changes of intestinal mucosa caused by radiotherapy. This study aims to assess improvement and recovery of intestinal mucosal barrier function through preoperative colonoscopy biopsy specimens and saliva analysis, with an expectation to provide valuable insights for non-invasive monitoring to reduce perioperative complications resulting from radiotherapy, and to facilitate the recovery of intestinal barrier function in CRC patients.

Materials and methods

Materials and grouping situation

This study postoperatively collected intestinal tissue samples from patients who underwent radical surgery for CRC at our Center between 2023 and 2024. Patients who underwent surgery without prior radiotherapy and those who had surgery 60 to 90 days following radiotherapy were categorized into four distinct groups: Group 1 (no radiotherapy), Group 2 (surgery 60 ± 3 days post-radiotherapy), Group 3 (surgery 75 ± 3 days post-radiotherapy), and Group 4 (surgery 90 ± 3 days post-radiotherapy). Meanwhile, 24 saliva samples were collected from these CRC patients, comprising 13 patients who did not receive preoperative radiotherapy and 11 patients who underwent surgery following radiotherapy. Exclusion criteria: patients with medical history of inflammatory bowel disease and autoimmune diseases, and those with history of chemotherapy and targeted therapy; patients who had received immunosuppressive drugs, hormones, or antibiotics within the two weeks prior to surgery. Furthermore, hematoxylin-eosin (HE)-stained pathological images were taken from 50 postoperative pathological slides of patients who underwent radical surgery for CRC at our Center within the past year. There were no statistically significant differences in gender, age and other baseline data among groups.

Observation of intestinal mucosal damage

All samples were selected from normal intestinal mucosal tissue located more than 5cm away from the tumor and fixed in a 4% paraformaldehyde solution for 48 hours. After being dehydrated with ethanol, soaked in xylene, embedded in paraffin, and sectioned, the pathological results of intestinal histology were observed under the light microscope after staining with HE and the repair of intestinal mucosal damage was summarized and analyzed.

Western blotting was used to detect IFN - γ and TGF - β in intestinal mucosal tissue

Dilute the sample with the prepared cell lysis buffer to the same concentration, and take an equal amount of sample buffer from a test tube with a protein mass of 70ug for later use. Before loading the samples onto the gel, they were heat treated at 95-100°C, and then cooled on ice for 5 minutes. The electrophoresis conditions included 20 min of constant voltage at 80V for the stacking gel and 80 min at 100V for the separating gel. The gel was taken out and soaked in the transfer buffer for 15 min. Filter paper and PVDF (Polyvinylidene Fluoride) membrane were prepared and placed in the transfer buffer and deionized water, respectively. The gel was then sandwiched between the filter paper, PVDF membrane, and filter paper, and the electrodes were placed on the layer. After removing air bubbles at each layer, the upper electrode was placed on the sandwich material, and a constant current of 200 mA was applied for 1h. The PVDF membrane was blocked with a 5% skimmed milk blocking solution at room temperature for 1 hour, after which the solution was discarded without washing. The membrane was then incubated with an appropriate amount of primary antibodies (INF-γ, CST, USA; TGF-β, CST, USA) against β-actin (Immunoway, USA) at a dilution of 1:4000, along with the blocking solution, on a shaker at 4°C overnight. The membrane was washed four times with PBST (Phosphate Buffered Saline Tween 20), with each wash lasting 5 minutes. Subsequently, a secondary antibody (horseradish peroxidase-conjugated antibody, Jackson, USA) at a dilution of 1:5000 was added to the membrane and incubated on a shaker at room temperature for 1 to 2 hours. Subsequently, thoroughly wash the membrane with PBST for 5 minutes, repeating this process five times. After applying the

developer to the PVDF membrane, incubate it at room temperature for 1 minute, using a developer volume EP calculated at 0.1 mL/cm². Next, wrap the film with plastic film while minimizing bubble formation during the procedure. The film should then be rapidly exposed to X-ray film in a darkroom and processed using an automatic film processor. Prior to the appearance of the optimal frequency band, it is essential to continuously adjust the exposure time.

The ELISA method is used to detect the inflammatory factors IL-1 β and IL-1 β in the blood IL-6, IL-17, INF-γ

We collected data from 80 patients who underwent radical CRC surgery at our center within the past year (excluding patients with incomplete records). Group 1 comprised patients who underwent surgery within 8–12 weeks post-radiotherapy (n=57), while Group 2 consisted of patients who underwent surgery without prior radiotherapy (n=23). Take about 2ml of blood sample, centrifuge at 3000rpm for 15 minutes on a centrifuge, and transfer the supernatant obtained to a 2.5ml EP(Eppendorf) tube for further use. All operations are performed on ice. According to the detailed instructions of the kit (Jingmei, Jiangsu, China), ELISA was used to detect the levels of inflammatory factors IL-1 β, IL-6, IL-17, and INF - γ.

Non-targeted Metabolomics for Detecting Changes in Salivary Metabolites

Sample preparation and extraction

The sample stored at -80°C refrigerator was thawed on ice and vortexed for 10 s. A 150 μL extract solution (ACN (Acetonitrile): Methanol = 1:4, V/V) containing internal standard was added into 50 μL sample. Then the sample was vortex for 3 min and centrifuged at 12000 rpm for 10 min (4°C). A 150 μL aliquots of the supernatant was collected and placed in -20°C for 30 min, and then centrifuged at 12000 rpm for 3 min (4°C). 120 μL aliquots of supernatant were transferred for LC-MS analysis.

HPLC conditions (T3)

All samples were collected by LC-MS system according to machine orders. The analysis conditions are as follows: UPLC: Column, Waters ACQUITY UPLC HSS T3 C18 (1.8 μ m, 2.1 mm * 100 mm); column temperature 40 °C; flow rate, 0.4 mL/min; injection volume, 2 μ L; solvent system, water (0.1% formic OPLS acid): acetonitrile (0.1% formic acid; elute the column with 5% mobile phase B (0.1% formic acid acetonitrile solution) at 0 minutes, then linearly gradient to 90% mobile phase B within 11 minutes, maintain for 1 minute, and then return to 5% mobile phase C within 0.1 minutes, maintain for 1.9 minutes.

Analytical method

The original data file acquisited by LC-MS was converted into mzML format by ProteoWizard software. Peak extraction, peak alignment and retention time correction were respectively performed by XCMS program. The "SVR" method was used to correct the peak area. The peaks with detetion rate lower than 50% in each group of samples were discarded. After that, metabolic identification information was obtained by searching the laboratory's self-built database, integrated public database, AI database and metDNA.

1. PCA.

Unsupervised Principal Component Analysis (PCA) is conducted using the statistical function `prcomp` in R. It is essential to perform unit variance scaling on the data prior to executing unsupervised PCA.

2. Hierarchical Cluster Analysis and Pearson Correlation Coefficients.

The results of the Hierarchical Cluster Analysis (HCA) for samples and metabolites are presented in a heatmap alongside a dendrogram. In contrast, the Pearson correlation coefficient (PCC) between samples is calculated using the cor function in R and is represented solely by the heatmap. Both HCA and PCC analyses are conducted using the R package 'Complex Heatmap'. For HCA, the normalized signal intensity of metabolites is visualized on a unit variance scale.

3. Selected differential metabolites.

For the two analyses, differential metabolites were identified based on a VIP threshold (VIP > 1) and a P-value threshold ($P < 0.05$, Student's t-test). The VIP values were derived from the OPLS-DA (Orthogonal Partial Least Squares-Discriminant Analysis) results, which also included score and permutation graphs generated using the R package MetaboAnalystR. Before conducting OPLS-DA, the data were subjected to logarithmic transformation (log2) and mean centering. To prevent overfitting, a permutation test with 200 permutations was performed.

Statistical analysis

Statistical analysis was conducted using SPSS 26.0 software. Normal distribution and mean square deviation measurement data are represented as mean ± standard deviation. When testing intestinal tissue samples, independent sample t-test is used for comparison between the two groups. The comparison between three groups undergoing surgery at different times after radiotherapy was conducted using one-way analysis of variance. Independent sample t-test was used to compare serum inflammatory factors between patients who received radiotherapy and those who did not. The median (quartiles) is used for comparison between groups that do not meet the above criteria. * $p< 0.05$; **$p < 0.01$; △$p > 0.05$.

Result

Post-radiotherapy intestinal mucosal damage and repair pattern

After radiotherapy, HE staining showed obvious damage to the intestinal mucosa, intestinal mucosal destruction, inflammatory cell

infiltration, and original structure changes. Moreover, with the prolongation of the time after radiotherapy, there was gradually reduced intestinal mucosal damage. But different degrees of damage persisted in about 12 weeks after radiotherapy. This pattern of change was revealed in HE-stained tissue sections. Figures 1A–D are the more representative HE-stained slices of the postoperative intestinal mucosa of patients from the four groups. In Figure A, it was observed with mild proctitis, with intact epithelial structure, and a small amount of chronic inflammatory cells infiltrating the mesenchymal stroma. in Figure B, there were severe active chronic proctitis, with ulcer formation and granulomatous tissue hyperplasia, as well as apoptotic crypts. Moreover, in this figure partially, there existed active chronic proctitis with ulcer formation and granulomatous tissue proliferation, crypt apoptosis in some parts of the surface epithelium with reparative changes, interstitial fibrosis, massive lymphocytes and plasma cells, capillary dilatation, as well as congestion with hemorrhage. In Figure C, there was active chronic proctitis with crypt apoptosis, proliferative interstitial fibrous tissue with fibrosis and infiltration of lymphocytes and plasma cells, swelling of endothelial cells of small submucosal arteries, and formation of occlusive vasculitis. In addition, in Figure D, there were intestinal mucosa with moderate inflammation and erosion, infiltration of inflammatory cells in the interstitium, and surface epithelial loss.

Patterns of INF-γ and TGF-β changes in intestinal mucosa

As shown in Figure 2, the levels of INF-γ and TGF-β in the postoperative intestinal mucosal tissue were significantly elevated within the 8–12 week range after radiotherapy compared to the non-radiotherapy group. Over time, INF-γ and TGF-β levels gradually returned to the normal range, and did not completely normalize within the 8–12 week period. However, there was no longer statistically significant difference in INF-γ and TGF-β levels by 90 days post-radiotherapy. Independent sample t-tests and one-way ANOVA were respectively employed for comparisons between the non-radiotherapy group and various post-radiotherapy intervals, as well as those among the different post-radiotherapy intervals.

Post-radiotherapy changes in serum levels of IL-1β, IL-6, IL-17, and INF-γ in patients 8–12 weeks

As displayed in Figure 3, compared with patients who did not receive preoperative radiotherapy, patients who received preoperative radiotherapy had higher serum levels of IL-1 β, IL-6,

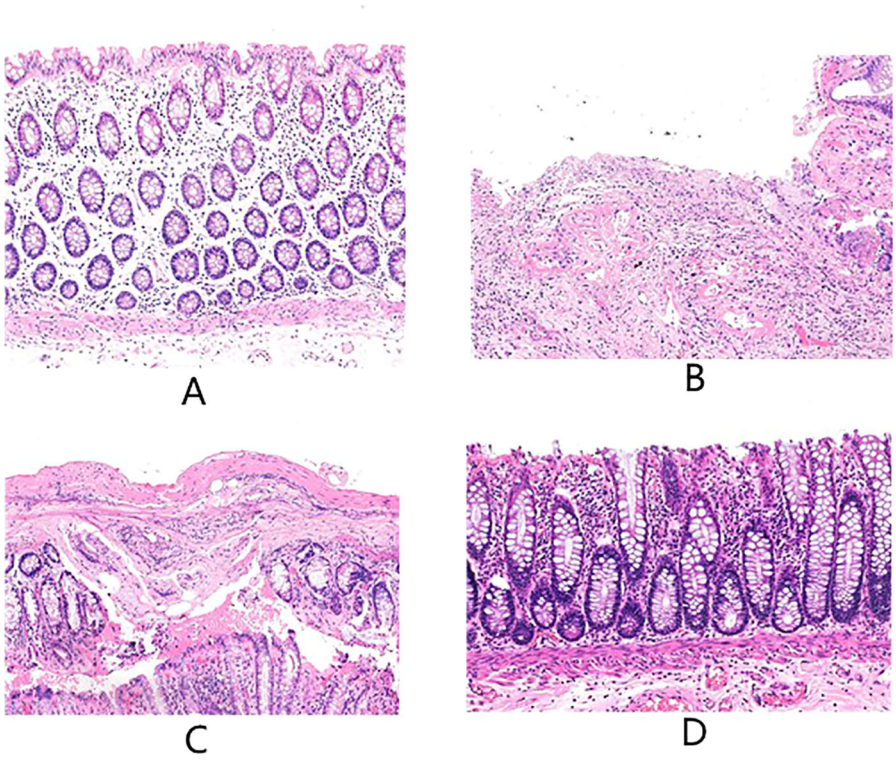

FIGURE 1
The above are the more representative pictures of HE stained slices of normal tissue intestinal mucosa distal to the tumor in the postoperative period of patients with rectal cancer who underwent surgery in our center, **(A-D)** are 60 days ± 3 days, 75 days ± 3 days, and 90 days ± 3 days after no radiotherapy versus radiotherapy, respectively.

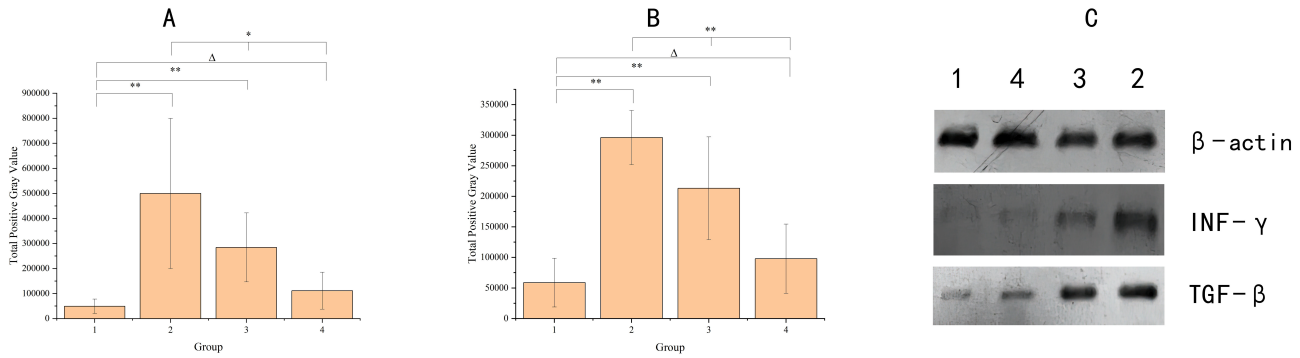

FIGURE 2
The graph shows the cytokine levels in the intestinal mucosal tissues of the four groups of samples. Panel **(A)** indicates INF-γ, Panel **(B)** indicates TGF-β, X-axis groups, where group 1 (no radiotherapy group), group 2 (60 ± 3 days after radiotherapy), group 3 (75 ± 3 days after radiotherapy), and group 4 (90 ± 3 days after radiotherapy). y-axis indicates the total grayscale values of the WB detection bands for each cytokine. Where * denotes $p < 0.05$; ** denotes $p < 0.01$; Δ denotes $p > 0.05$. Panel **(C)** shows the electrophoretic images of cytokines detected by protein blotting, with different cytokines indicated on the right side and different groups labeled on the top.

IL-17, and INF-γ. However, no statistically significant differences were observed in the levels of IL-1 β, IL-6, and INF-γ. IL-17 levels showed statistically significant differences.

Differential metabolites in saliva

This study continued to examine the differences of metabolites in saliva by non-targeted metabolomics, and the results are shown in Figure 4. Specifically, Figure 4A is the main component analysis map, and Figure 4B is the clustering heat map of differential metabolites. There was significant difference of differential metabolites between the radiotherapy group (RG) and the non-radiotherapy group (NRG). Figure 4C is a volcano plot of differential metabolites, with red dots indicating upregulated metabolites and green dots indicating downregulated metabolites. There were more up-regulated/down-regulated differential metabolites in CRC patients after radiotherapy compared with those without radiotherapy. Figure D shows the bar chart of the multiplicity of difference, with red representing the up-regulation of metabolite content, and green indicating the down-regulation of metabolite content. This study detected the top-20 metabolites in the multiplicity of difference in the comparison between groups, all of which were up-regulated. Among them, most metabolites were amino acids and their metabolites, including 3-hydroxyquinidine, prolyl-valyl-aspartic acid, glycine-glycine-phenylalanine, Lysyl alanyl-alanine, prolyl-prolinyl-leucine, valine-lysinyl-glutamic acid, and prolyl-serinyl-isoleucine.

Discussion

CRC remains one of the most prevalent gastrointestinal malignancies. Advances in awareness and early screening have improved patient staging of CRC, however, many patients are still diagnosed in the intermediate to advanced stages (11, 12). For individuals with stage II-III CRC, preoperative radiotherapy is widely recognized as an effective treatment. It significantly reduces the likelihood of recurrence and metastasis, and increases the success rate of anal preservation in patients with lower CRC (13). However, radiotherapy is a double-edged sword, which presents challenges, such as radiation-induced enteritis, even with anti-oncological benefits. This condition complicates pelvic radiotherapy for both patients and surgeons. Patients may experience complications such as abdominal adhesions, intestinal edema, increased fragility, and impaired healing, ultimately making surgical procedures more difficult and risky. Moreover, it compromises the intestinal mucosal barrier, potentially resulting in bacterial translocation, increased postoperative systemic inflammatory responses, and elevated risks of anastomotic fistulas. This radiation damage also restricts the feasible dose of radiotherapy, significantly decreasing the quality of life for treated cancer patients (14–16).

In patients with CRC, the first priority is usually oncological outcomes, with insufficient attention given to maintaining the integrity of the intestinal barrier. However, it cannot be ignored that radiotherapy can cause damage to the intestinal mucosa and the resultant complications. The intestinal barrier comprises mechanical, chemical, biological, and immune components.

Radiotherapy has been documented to disrupt this barrier, manifesting as intestinal edema, villous atrophy, compromised tight junctions, as well as reduced absorptive and barrier functions (17–19). Zhao et al. demonstrated an correlation of the mechanical barrier disruption with decreased levels of Claudin family proteins and tight junction protein NO-1 (20). Moreover, our previous research revealed that damage to the intestinal mucosal immune barrier function might alter the proportion of CD4+and CD8+T lymphocyte subsets; decrease the content of secretory immunoglobulin A; as well as elevate levels of pro-inflammatory cytokines IL-1β, IL-6, and IL-17 in intestinal tissue. Previous studies in patients with inflammatory bowel disease have found that strengthening the intestinal mucosal barrier function is closely related to the IL-17RA pathway (21). It can be inferred that

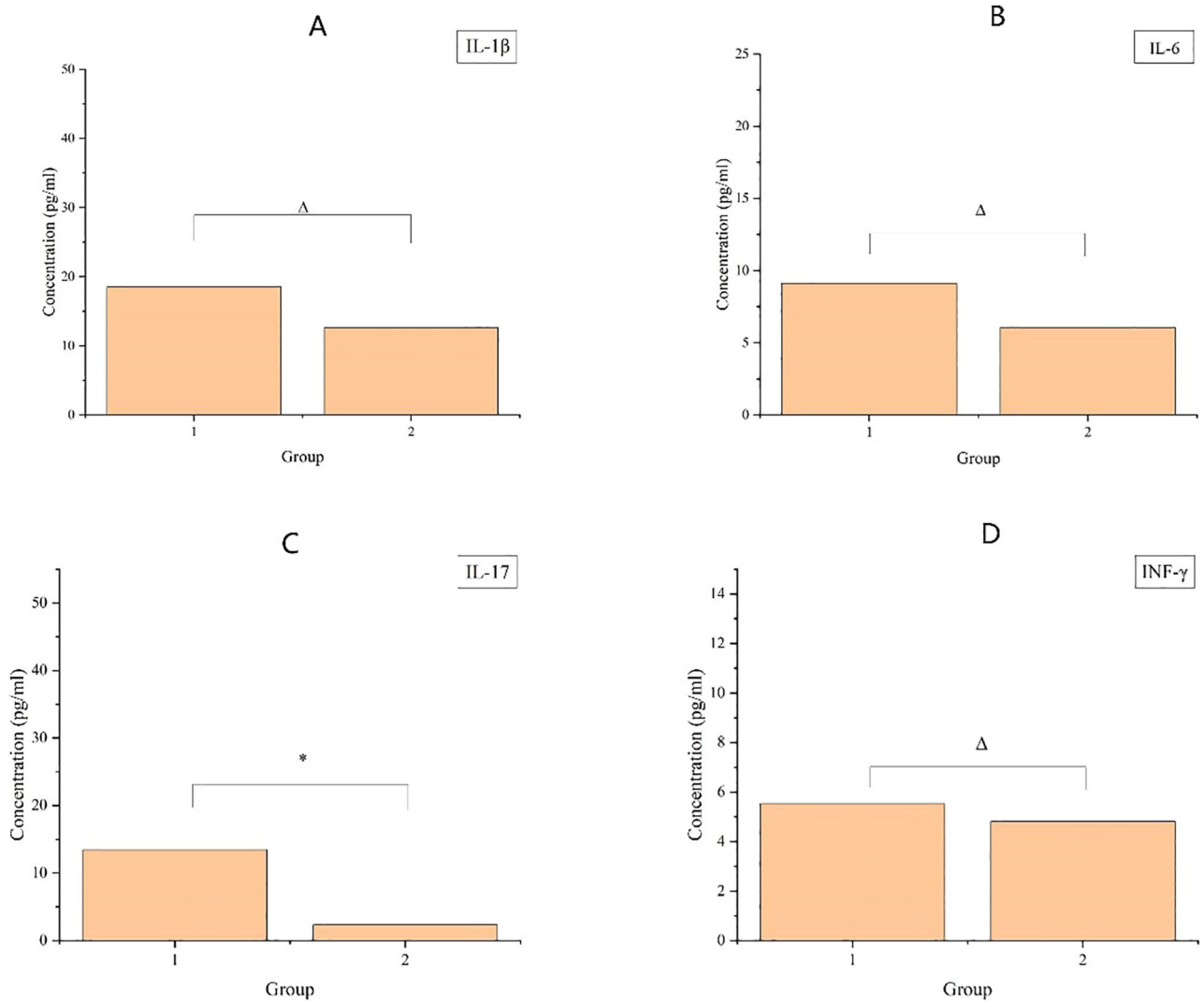

FIGURE 3
The upper graph demonstrates the cytokine content in patients' serum, where **(A-D)** denote the four inflammatory factors, IL-1β, IL-6, IL-17, and INF-γ, respectively, with vertical coordinates denoting the content, and horizontal coordinates denoting the groups, Group 1 (8–12 weeks after radiotherapy) and Group 2 (no radiotherapy group). Where * indicates $p < 0.05$; ** indicates $p < 0.01$; Δ indicates $p > 0.05$.

there was a compromise in the immune barrier and an onset of radiation-induced enterocolitis. Notably, alterations in oral flora composition and abundance were found in irradiated CRC patients compared to non-irradiated individuals, suggesting a connection to the intestinal mucosal biological barrier. Given the known association between oral microbiota and systemic diseases, Jiaming Zhang et al. found correlations between altered oral and intestinal flora in thyroid cancer patients (22, 23), while Xiaoxiao Li et al. summarized numerous studies on the interplay between gastrointestinal malignancies and oral microbiota (24).

In our study, HE staining revealed that in CRC patients undergoing resection shortly after radiotherapy exhibited, the intestinal mucosa was observed with severe active chronic proctitis, characterized by ulceration, granulomatous tissue formation, crypt apoptosis, reparative changes in surface epithelium, interstitial fibrosis, as well as lymphocyte and plasma cell infiltration, alongside capillary dilation and hemorrhage. All these changes might be recovered over time, culminating in improved tissue architecture and reduced inflammatory response. However, the intestinal mucosa of these patients did not return to normal levels at least 12 weeks post-radiotherapy, suggesting the possibility of recovery, but no complete recovery potentially.

Meanwhile, increased levels of INF-γ and TGF-β were noted in the intestinal mucosa, with time-dependent amelioration. INF-γ serves as a significant immunomodulatory protein with diverse functions, including promotion of intestinal barrier damage, with elevated levels under conditions such as infections, inflammation, tumors, etc. (25). TGF-β, a multifunctional cytokine from the TGF-β superfamily, regulates several cellular processes and is integral to the repair of intestinal barrier damage and colitis (26).

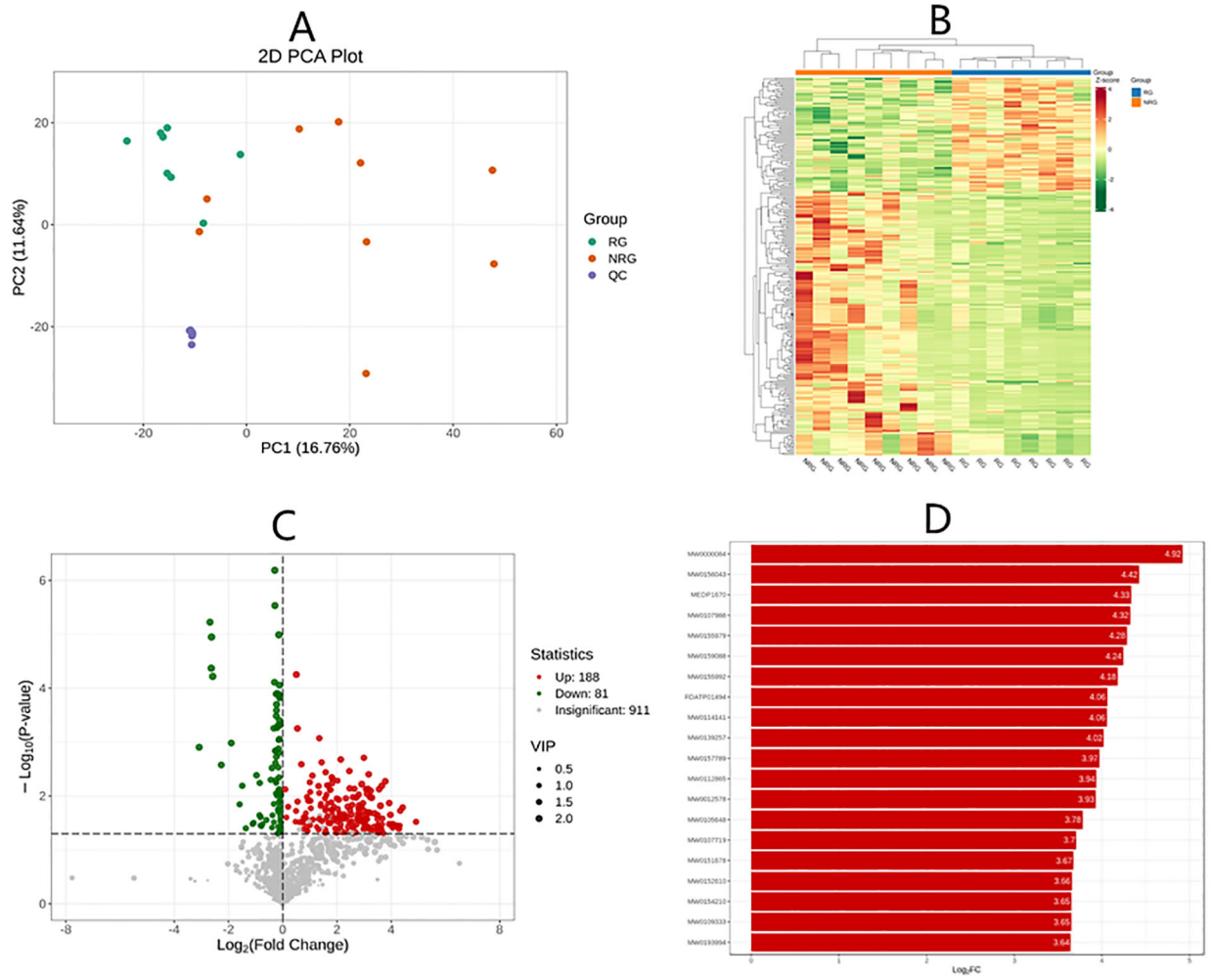

FIGURE 4
Panel **(A)** is the grouped principal component analysis, PC1 represents the first principal component, PC2 represents the second principal component, and the percentage represents the variance explained by the principal component to the data set; each point in the figure represents a sample, and samples in the same group are represented by the same color, and Group is the subgroup. Panel **(B)** is the differential metabolite clustering heatmap, the horizontal is the information of the samples, the vertical is the information of the differential metabolites, and Group is the subgroup. Group is the grouping, and different colors are the colors filled with different values obtained from the normalization of different relative contents (red for high content, green for low content). Panel **(C)** is the differential metabolite volcano plot, each point represents a metabolite, where green points represent down-regulated differential metabolites and red points represent up-regulated differential metabolites; the horizontal coordinate represents the relative content of a metabolite in the two groups of samples Under VIP + FC + P-value screening condition: the vertical coordinate represents the significance level of difference (-log1010P-value), and the size of the dots represents the VIP value. Panel **(D)** is the bar chart of differential metabolites, and the horizontal coordinate is the log22FC of the differential metabolites, i.e., the value of the multiplicity of difference of differential metabolites logarithmically based on the base of 2, and the vertical coordinate is the differential metabolites. The vertical coordinate is the differential metabolite. Red color represents up-regulation of metabolite content and green color represents down-regulation of metabolite content.

Therefore, in addition to presence of radiation enteritis, increased INF-γ and TGF-β levels in post-radiotherapy patients may reveal dysfunction of the intestinal mucosal immune barrier, which gradually repairs over time.

We also studied the levels of inflammatory factors (i.e., IL-1β, IL-6, IL-17, and INF-γ) in the serum of CRC patients. All the four cytokines were significantly elevated, especially IL-17. IL-17 is a cytokine produced by activated CD4+T cells, which participates in the body's immune defense and inflammatory response (27). This may reinforce our previous findings regarding increased CD4+ T lymphocyte proportions and correlating IL-17 levels in intestinal tissues post-radiotherapy, likely tied to declined barrier function and release of inflammatory mediators. Monitoring intestinal inflammation and repair of barrier damage via serum markers could pave the way for a succinct understanding of inflammatory responses and the recovery of intestinal mucosal integrity.

Furthermore and noticeably, radiotherapy can inflict substantial damage on the intestinal mucosal barrier, significantly affecting mechanical and immune functions, which, while partially reversible over time, may not normalize within the commonly recommended surgical time-frame of 8–12 weeks post-radiotherapy. Therefore,

extending the waiting period for surgery could potentially mitigate the risk of intestinal barrier damage, contingent upon patients' overall conditions. In addition, elevated IL-17 serum levels could also serve as a predictor to assess the recovery status of the intestinal mucosal barrier prior to surgery, helping to determining the optimal surgical timing.

Non-targeted metabolomics analyses unveiled shifts in salivary metabolites among patients post-radiotherapy, with the majority of upregulated metabolites falling within the category of amino acids and their derivatives. These metabolites have been found to exert roles of intestinal barrier repair, inflammation, and gastrointestinal tumor development (28, 29). For instance, butyric acid can enhance tight junction integrity in intestinal epithelial cells, maintaining mucosal barrier function—a process impaired in inflammatory bowel disease due to reductions in butyric acid-producing bacteria (30–32).

Changes in oral microbiota and their metabolites exhibit potential association with various systemic diseases and tumors (33–35). Dong et al. discovered alterations in the oral microbiota of mice with colon cancer after radiotherapy, which might affect tumor development and prognosis (36). Previous studies have found that chronic inflammation of the intestine may be associated with the occurrence of tumors (37). Our previous research also noted changes in the oral microbiota of patients who underwent surgery after radiotherapy and those who underwent surgery directly without radiotherapy, which were associated with upregulation of various intestinal metabolites (10). Thus, intestinal mucosal barrier damage may have a relationship with altered salivary metabolites, offering potential insights into predicting patient responses to radiotherapy and oncological outcomes.

In view of the above discussion, damage to the intestinal barrier can manifest through mechanical, biological, and immune mechanisms, and can be assessed via biopsy pathology alongside metabolite and inflammatory marker analyses. Intestinal barrier function may be assessed in a non-invasive manner of monitoring changes in oral microbiota metabolites and inflammatory factors in the bloodstream. This exploratory study may lay groundwork for future non-invasive monitoring strategies, despite the deficiency of limited sample size that imposed challenges in accurately identifying indices and ranges. Advancements in artificial intelligence and large-sample analyses may further facilitate the determination of comprehensive standards for monitoring specific saliva substance levels alongside routine biochemical markers. It can eventually benefit dynamic management of patients undergoing various radiotherapy regimens, ultimately reducing complications associated with intestinal barrier damage and enhancing surgical outcomes.

Conclusion

Radiotherapy can cause serious damage to the intestinal mucosa and its barrier function, as well as to the immune and biological barrier functions, as evidenced by changes in histopathology, intestinal mucosa and saliva metabolites. It is possible to noninvasively detect the recovery of intestinal mucosal barrier function after radiotherapy-induced injury.

Data availability statement

The original contributions presented in the study are included in the article/Supplementary Material. Further inquiries can be directed to the corresponding authors.

Ethics statement

The studies involving humans were approved by The Ethics Committee of Qingdao University Affiliated Hospital. The studies were conducted in accordance with the local legislation and institutional requirements. The human samples used in this study were acquired from primarily isolated as part of your previous study for which ethical approval was obtained. Written informed consent for participation was not required from the participants or the participants' legal guardians/next of kin in accordance with the national legislation and institutional requirements.

Author contributions

JZ: Data curation, Investigation, Resources, Writing – original draft, Writing – review & editing. KW: Conceptualization, Funding acquisition, Methodology, Writing – original draft, Writing – review & editing. YQ: Software, Validation, Writing – original draft, Writing – review & editing. MZ: Data curation, Visualization, Writing – original draft. YC: Data curation, Resources, Writing – original draft. YT: Data curation, Formal analysis, Writing – original draft. XJ: Formal analysis, Validation, Writing – original draft. XT: Project administration, Supervision, Writing – original draft. HJ: Funding acquisition, Methodology, Writing – original draft, Writing – review & editing. FH: Methodology, Resources, Writing – original draft, Writing – review & editing.

Funding

The author(s) declare that financial support was received for the research and/or publication of this article. Chinese International Medical Exchange Foundation -Academician Li Jieshou Intestinal Barrier Research Fund Project (LJS 2020C3) and Qingdao University (QDU)(QDFY+X202103).

Conflict of interest

The authors declare that the research was conducted in the absence of any commercial or financial relationships that could be construed as a potential conflict of interest.

Generative AI statement

The author(s) declare that no Generative AI was used in the creation of this manuscript.

Publisher's note

All claims expressed in this article are solely those of the authors and do not necessarily represent those of their affiliated organizations, or those of the publisher, the editors and the reviewers. Any product that may be evaluated in this article, or claim that may be made by its manufacturer, is not guaranteed or endorsed by the publisher.

Supplementary material

The Supplementary Material for this article can be found online at: https://www.frontiersin.org/articles/10.3389/fimmu.2025.1590219/full#supplementary-material

References

1. Yang Y, Wang HY, Chen YK, Chen JJ, Song C, Gu J. Current status of surgical treatment of rectal cancer in China. *Chin Med J (Engl)*. (2020) 133:2703–11. doi: 10.1097/CM9.0000000000001076

2. Bray F, Laversanne M, Sung H, Ferlay J, Siegel RL, Soerjomataram I, et al. Global cancer statistics 2022: GLOBOCAN estimates of incidence and mortality worldwide for 36 cancers in 185 countries. *CA Cancer J Clin*. (2024) 74:229–63. doi: 10.3322/caac.21834

3. Zheng RS, Chen R, Han BF, Wang SM, Li L, Sun KX, et al. Cancer incidence and mortality in China, 2022. *Zhonghua Zhong Liu Za Zhi*. (2024) 46:221–31. doi: 10.3760/cma.j.cn112152-20240119-00035

4. Gu J, Chen N. Current status of rectal cancer treatment in China. *Colorectal Dis*. (2013) 15:1345–50. doi: 10.1111/codi.12269

5. Huang J, Lucero-Prisno DE 3rd, Zhang L, Xu W, Wong SH, Ng SC, et al. Updated epidemiology of gastrointestinal cancers in East Asia. *Nat Rev Gastroenterol Hepatol*. (2023) 20:271–87. doi: 10.1038/s41575-022-00726-3

6. Kasi A, Abbasi S, Handa S, Al-Rajabi R, Saeed A, Baranda J, et al. Total neoadjuvant therapy vs standard therapy in locally advanced rectal cancer: A systematic review and meta-analysis. *JAMA Netw Open*. (2020) 3:e2030097. doi: 10.1001/jamanetworkopen.2020.30097

7. Yang J, Luo Y, Tian T, Dong P, Fu Z. Effects of neoadjuvant radiotherapy on postoperative complications in rectal cancer: A meta-analysis. *J Oncol*. (2022) 2022:8197701. doi: 10.1155/2022/8197701

8. Nejdfors P, Ekelund M, Weström BR, Willén R, Jeppsson B. Intestinal permeability in humans is increased after radiation therapy. *Dis Colon Rectum*. (2000) 43:1582–1587; discussion 1587-8. doi: 10.1007/BF02236743

9. Vendrely V, Rivin Del Campo E, Modesto A, Jolnerowski M, Meillan N, Chiavassa S, et al. Rectal cancer radiotherapy. *Cancer Radiother*. (2022) 26:272–8. doi: 10.1016/j.canrad.2021.11.002

10. Wang K, Zhang J, Zhang Y, Xue J, Wang H, Tan X, et al. The recovery of intestinal barrier function and changes in oral microbiota after radiation therapy injury. *Front Cell Infect Microbiol*. (2024) 13:1288666. doi: 10.3389/fcimb.2023.1288666

11. Baidoun F, Elshiwy K, Elkeraie Y, Merjaneh Z, Khoudari G, Sarmini MT, et al. Colorectal cancer epidemiology: recent trends and impact on outcomes. *Curr Drug Target*. (2021) 22:998–1009. doi: 10.2174/1389450121999201117115717

12. Arnold M, Sierra MS, Laversanne M, Soerjomataram I, Jemal A, Bray F. Global patterns and trends in colorectal cancer incidence and mortality. *Gut*. (2017) 66:683–91. doi: 10.1136/gutjnl-2015-310912

13. Li Y, Wang J, Ma X, Tan L, Yan Y, Xue C, et al. A review of neoadjuvant chemoradiotherapy for locally advanced rectal cancer. *Int J Biol Sci*. (2016) 12:1022–31. doi: 10.7150/ijbs.15438

14. Ooi BS, Tjandra JJ, Green MD. Morbidities of adjuvant chemotherapy and radiotherapy for resectable rectal cancer: an overview. *Dis Colon Rectum*. (1999) 42:403–18. doi: 10.1007/BF02236362

15. Russell JC, Welch JP. Operative management of radiation injuries of the intestinal tract. *Am J Surg*. (1979) 137:433–42. doi: 10.1016/0002-9610(79)90111-9

16. Qin Q, Huang Q, Zhong Q, Fan X, Chen D, Wang L. Clinical risk factors for late intestinal toxicity after radiotherapy: a systematic review protocol. *Syst Rev*. (2013) 2:39. doi: 10.1186/2046-4053-2-39

17. Ren H, Wu Q, Sun Z, Fang M, Liu J, Luo J. Research progress and treatment of radiation enteritis and gut microbiota. *Radiat Oncol J*. (2023) 41:61–8. doi: 10.3857/roj.2023.00346

18. Salvo Romero E, Alonso Cotoner C, Pardo Camacho C, Casado Bedmar M, Vicario M. The intestinal barrier function and its involvement in digestive disease. *Rev Esp Enferm Dig*. (2015) 107:686–96. doi: 10.17235/reed.2015.3846/2015

19. Takiishi T, Fenero CIM, Câmara NOS. Intestinal barrier and gut microbiota: Shaping our immune responses throughout life. *Tissue Barriers*. (2017) 5:e1373208. doi: 10.1080/21688370.2017.1373208

20. Zhao Z, Cheng W, Qu W, Wang K. Arabinoxylan rice bran (MGN-3/Biobran) alleviates radiation-induced intestinal barrier dysfunction of mice in a mitochondrion-dependent manner. *BioMed Pharmacother*. (2020) 124:109855. doi: 10.1016/j.biopha.2020.109855

21. Liang J, Dai W, Liu C, Wen Y, Chen C, Xu Y, et al. Gingerenone A Attenuates Ulcerative Colitis via Targeting IL-17RA to Inhibit Inflammation and Restore Intestinal Barrier Function. *Adv Sci (Weinh)*. (2024) 11(28):e2400206. doi: 10.1002/advs.202400206

22. Zhang J, Zhang F, Zhao C, Xu Q, Liang C, Yang Y, et al. Dysbiosis of the gut microbiome is associated with thyroid cancer and thyroid nodules and correlated with clinical index of thyroid function. *Endocrine*. (2019) 64:564–74. doi: 10.1007/s12020-018-1831-x

23. Jiao J, Zheng Y, Zhang Q, Xia D, Zhang L, Ma N. Saliva microbiome changes in thyroid cancer and thyroid nodules patients. *Front Cell Infect Microbiol*. (2022) 12:989188. doi: 10.3389/fcimb.2022.989188

24. Li X, Zhu S, Zhang T, Chen X. Association between oral microflora and gastrointestinal tumors (Review). *Oncol Rep*. (2021) 46:160. doi: 10.3892/or.2021.8111

25. Woznicki JA, Saini N, Flood P, Rajaram S, Lee CM, Stamou P, et al. TNF-α synergises with IFN-γ to induce caspase-8-JAK1/2-STAT1-dependent death of intestinal epithelial cells. *Cell Death Dis*. (2021) 12:864. doi: 10.1038/s41419-021-04151-3

26. Li J, Niu C, Ai H, Li X, Zhang L, Lang Y, et al. TSP50 attenuates DSS-induced colitis by regulating TGF-β Signaling mediated maintenance of intestinal mucosal barrier integrity. *Adv Sci (Weinh)*. (2024) 11:e2305893. doi: 10.1002/advs.202305893

27. Rovedatti L, Kudo T, Biancheri P, Sarra M, Knowles CH, Rampton DS, et al. Differential regulation of interleukin 17 and interferon gamma production in inflammatory bowel disease. *Gut*. (2009) 58:1629–36. doi: 10.1136/gut.2009.182170

28. Scott SA, Fu J, Chang PV. Dopamine receptor D2 confers colonization resistance via microbial metabolites. *Nature*. (2024) 628:180–5. doi: 10.1038/s41586-024-07179-5

29. Fu Y, Lyu J, Wang S. The role of intestinal microbes on intestinal barrier function and host immunity from a metabolite perspective. *Front Immunol*. (2023) 14:1277102. doi: 10.3389/fimmu.2023.1277102

30. Li G, Lin J, Zhang C, Gao H, Lu H, Gao X, et al. Microbiota metabolite butyrate constrains neutrophil functions and ameliorates mucosal inflammation in inflammatory bowel disease. *Gut Microbes*. (2021) 13:1968257. doi: 10.1080/19490976.2021.1968257

31. Recharla N, Geesala R, Shi XZ. Gut microbial metabolite butyrate and its therapeutic role in inflammatory bowel disease: A literature review. *Nutrients*. (2023) 15:2275. doi: 10.3390/nu15102275

32. Parada Venegas D, de la Fuente MK, Landskron G, González MJ, Quera R, Dijkstra G, et al. Short chain fatty acids (SCFAs)-mediated gut epithelial and immune regulation and its relevance for inflammatory bowel diseases. *Front Immunol*. (2019) 10:277. doi: 10.3389/fimmu.2019.00277

33. Jia H, Shen X, Guan Y, Xu M, Tu J, Mo M, et al. Predicting the pathological response to neoadjuvant chemoradiation using untargeted metabolomics in locally advanced rectal cancer. *Radiother Oncol*. (2018) 128:548–56. doi: 10.1016/j.radonc.2018.06.022

34. Yang Y, Misra BB, Liang L, Bi D, Weng W, Wu W, et al. Integrated microbiome and metabolome analysis reveals a novel interplay between commensal bacteria and metabolites in colorectal cancer. *Theranostics*. (2019) 9:4101–14. doi: 10.7150/thno.35186

35. Zheng Y, Fang Z, Xue Y, Zhang J, Zhu J, Gao R, et al. Specific gut microbiome signature predicts the early-stage lung cancer. *Gut Microbes*. (2020) 11:1030–42. doi: 10.1080/19490976.2020.1737487

36. Dong J, Li Y, Xiao H, Zhang S, Wang B, Wang H, et al. Oral microbiota affects the efficacy and prognosis of radiotherapy for colorectal cancer in mouse models. *Cell Rep*. (2021) 37:109886. doi: 10.1016/j.celrep.2021.109886

37. Chen Y, Liang J, Chen S, Lin N, Xu S, Miao J, et al. Discovery of vitexin as a novel VDR agonist that mitigates the transition from chronic intestinal inflammation to colorectal cancer. *Mol Cancer*. (2024) 23(1):196. doi: 10.1186/s12943-024-02108-6

frontiers | Frontiers in Immunology

TYPE Original Research
PUBLISHED 25 June 2025
DOI 10.3389/fimmu.2025.1619186

Check for updates

OPEN ACCESS

EDITED BY
Qi Wang,
Jiangsu University, China

REVIEWED BY
Yue Li,
Shanghai Jiao Tong University, China
Jiayi Tan,
Cedars Sinai Medical Center, United States
Namuunaa Juramt,
Brigham and Women's Hospital and Harvard Medical School, United States

*CORRESPONDENCE
Xiong-Zhi Wu
wuxiongzhi@163.com

†These authors have contributed equally to this work

RECEIVED 27 April 2025
ACCEPTED 28 May 2025
PUBLISHED 25 June 2025

CITATION
Pan D, Zhang C-Y, Wang Y-F, Liu S and Wu X-Z (2025) Machine learning-based integration of DCE-MRI radiomics for STAT3 expression prediction and survival stratification in breast cancer. *Front. Immunol.* 16:1619186. doi: 10.3389/fimmu.2025.1619186

COPYRIGHT
© 2025 Pan, Zhang, Wang, Liu and Wu. This is an open-access article distributed under the terms of the Creative Commons Attribution License (CC BY). The use, distribution or reproduction in other forums is permitted, provided the original author(s) and the copyright owner(s) are credited and that the original publication in this journal is cited, in accordance with accepted academic practice. No use, distribution or reproduction is permitted which does not comply with these terms.

Machine learning-based integration of DCE-MRI radiomics for STAT3 expression prediction and survival stratification in breast cancer

Dong Pan[1,2,3†], Cheng-Yan Zhang[4,5,6†], Ya-Fei Wang[5,6], Shuang Liu[1,2,3] and Xiong-Zhi Wu[1,2,3,5,6*]

[1]Tianjin NanKai Hospital, Tianjin Medical University, Tianjin, China, [2]Tianjin Key Laboratory of Acute Abdomen Disease Associated Organ Injury and ITCWM Repair, Tianjin, China, [3]Institute of Integrative Medicine for Acute Abdominal Diseases, Tianjin, China, [4]Department of Gastroenterology, Shanxi Province Cancer Hospital/Shanxi Hospital Affiliated to Cancer Hospital, Chinese Academy of Medical Sciences/Cancer Hospital Affiliated to Shanxi Medical University, Taiyuan, China, [5]Tianjin Medical University Cancer Institute and Hospital, National Clinical Research Center for Cancer, Tianjin, China, [6]Tianjin's Clinical Research Center for Cancer, Tianjin, China

Objective: To explore the association between signal transducer and activator of transcription 3 (STAT3) expression, tumor immune microenvironment, and overall survival (OS) in breast cancer, and to develop a non-invasive radiomics model for early risk stratification using dynamic contrast-enhanced magnetic resonance imaging (DCE-MRI).

Methods: Data from 1,008 patients with breast cancer in The Cancer Genome Atlas were analyzed to evaluate the prognostic significance of STAT3 expression using Kaplan-Meier survival analysis and Cox regression models. Functional enrichment and immune cell infiltration analyses were performed to assess tumor immune microenvironment characteristics. Additionally, DCE-MRI data from 101 patients in The Cancer Imaging Archive were used to extract radiomic features from early- and delayed-phase images. A STAT3 predictive model was developed using six machine learning algorithms. Model performance was assessed using receiver operating characteristic (ROC) and related diagnostic statistical indicators.

Results: Low STAT3 expression was significantly associated with poorer OS (hazard ratio [HR] = 1.927, $p < 0.001$). GSEA revealed that high STAT3 expression enhanced epithelial apoptosis and TNF-α/NFκB signaling while suppressing pro-tumorigenic pathways, which was associated with an immunosuppressive microenvironment, whereas low STAT3 correlated with T-cell exhaustion. DIA confirmed elevated STAT3 in tumor versus normal tissue ($p < 0.05$). The logistic regression-derived radiomics model for STAT3 expression prediction exhibited consistent discriminative performance, with area under curve (AUC) values of 0.861 (95% CI: 0.749 - 0.947) in the development cohort and 0.742 (95% CI: 0.588 - 0.884) in the validation cohort. High radiomics-derived scores were positively correlated with elevated STAT3 expression, longer OS ($p = 0.034$), and immune-related gene signatures indicative of a heightened immune response.

10.3389/fimmu.2025.1619186

Conclusion: Radiomics analysis of DCE-MRI images in this study offered a non-invasive method for predicting STAT3 expression and characterization of the tumor immune microenvironment. This approach can offer valuable insights into breast cancer prognosis and support the development of personalized therapies.

KEYWORDS

breast cancer, immune microenvironment, prognosis, STAT3, machine learning

1 Introduction

Breast cancer remains the most prevalent malignancy and leading cause of cancer-related mortality among women worldwide (1). Although significant progress has been made in primary treatments (surgery, chemotherapy, and radiotherapy), 10%–20% of early-stage patients still experience recurrence and metastasis within five years (2). This underscores the critical need for more precise prognostic tools to enable early intervention and personalized therapy. While current prognostic markers including TNM staging, molecular subtypes, and treatment modalities (3–5) could provide valuable information, they are limited by subjectivity, poor reproducibility, and the invasive nature of tissue sampling, which may not fully represent tumor heterogeneity, highlighting the necessity for objective, non-invasive methods to enhance the accuracy of prognostic assessments (6).

Signal transducer and activator of transcription 3 (STAT3) is a key transcription factor that plays a dual role in immune regulation and tumor progression, making it a compelling target for cancer research (7, 8). Unlike immune checkpoint markers such as PD-L1, which primarily modulate T-cell activity, STAT3 drives oncogenic processes directly by promoting tumor cell survival, proliferation, and metastasis (9, 10). Its activation upregulates key mediators like cyclin D1, c-myc, and Bcl-2, enabling breast cancer progression, while also enhancing metastatic potential through matrix metalloproteinases (MMPs) (11–13). Given its central role in both immune evasion and tumor aggressiveness, STAT3 inhibition offers a broader therapeutic strategy compared to pathway-specific targets like PD-L1 (14). This study focuses on STAT3 to elucidate its tumor-intrinsic mechanisms and explore its potential as a multifaceted therapeutic target in breast cancer.

Radiomics provides a powerful framework for non-invasively linking imaging phenotypes to molecular characteristics (15). Dynamic contrast-enhanced magnetic resonance imaging (DCE-MRI), known for its superior soft tissue resolution, provides detailed and quantifiable data, making it increasingly valuable in breast cancer diagnosis and treatment. The integration of radiomics with DCE-MRI images has emerged as a transformative strategy for the non-invasive diagnosis and prognosis of breast cancer, aiding in tumor identification, characterization, staging, and treatment planning. This approach advances personalized medicine by quantifying tumor heterogeneity, offering tailored therapies, and prognostic insights However, current radiomics research primarily focuses on macroscopic tumor features, with limited investigation of underlying molecular mechanisms.

While radiogenomic correlations have been well characterized in malignancies such as lung adenocarcinoma (16), hepatocellular carcinoma (17), head and neck squamous cell carcinoma (18), glioma (19), gastrointestinal tumor (20), and pancreatic cancer (21), no study has been reported in breast cancer regarding non-invasive biomarkers for STAT3 pathway activation and its clinical implications. To address this gap, we aimed to develop a non-invasive radiomics approach using DCE-MRI to predict STAT3 expression and assess tumor immune status. Our approach integrates bioinformatics with machine learning (ML), employing six distinct classifiers to construct predictive models from early- and delayed-phase MRI radiomic features. By systematically optimizing model performance, we aim to establish a robust, imaging-based tool for prognostic stratification and personalized therapeutic decision-making in breast cancer.

2 Materials and methods

2.1 Study sample

The study incorporated multi-modal data from established public repositories. From The Cancer Genome Atlas Breast Invasive Carcinoma collection (TCGA-BRCA) (22), we obtained RNA-seq and clinical data for 1,070 breast cancer patients, applying stringent quality controls that excluded: (a) 20 samples with inadequate sequencing quality; (b) 30 patients with OS <30 days, to reduce non-cancer-related mortality bias; and (c) 12 male patients, resulting in a final cohort of 1,008 cases with complete molecular and clinical profiles. To establish a robust normal tissue reference, 80 female breast samples from GTEx (23) were acquired and integrated after batch effect correction using the "limma" package (Additional file 1).

For radiogenomic analysis, DCE-MRI data from The Cancer Imaging Archive (TCIA) database (24) were analyzed. TCGA and TCIA breast cancer cohorts were matched using patient IDs and DICOM metadata to ensure consistent patient populations. Exclusion criteria included: (a) missing gene expression data (n = 5); (b) incomplete MRI sequences (n = 16); (c) prior treatments (n =

4); and (d) suboptimal image quality, including SNR < 20 dB, presence of motion artifact or incomplete image coverage (n = 7), yielding 101 patients with matched imaging-genomic data. All molecular profiles (including tumor/normal samples) were accessed via Xena (25), while immune-related gene sets were sourced from ImmPORT (26) (Additional file 2). The integrated study design is summarized in Figure 1A, and the follow-up research process is shown in Figure 1B. As this research utilized exclusively de-identified, publicly available data, institutional review board approval was waived.

2.2 Digital image analysis of STAT3 expression

STAT3 expression was quantified using standardized IHC with a validated anti-STAT3 antibody on FFPE tumor sections, following established protocols with appropriate controls. Digital image analysis was performed using QuPath, with tumor and stromal compartments annotated by pathologists. Expression levels were assessed through integrated and average optical density measurements. Methodological rigor was ensured through technical reproducibility testing, molecular correlation with transcriptomic data, and clinically relevant threshold determination. Complete details are provided in the Methods section.

2.3 Association between STAT3 expression and prognostic outcomes in patients

We employed the minimum *p*-value method to establish the optimal STAT3 expression cutoff, stratifying patients into low (n = 431) and high (n = 577) expression groups. Survival outcomes were compared using Kaplan-Meier analysis ("survminer" package) with log-rank testing (95% CIs). A 10-year landmark analysis was implemented as it represents a clinically meaningful timeframe for breast cancer outcomes while maintaining adequate statistical power, capturing both early immunoediting and late immune escape phases relevant to STAT3 biology.

2.4 Assessment of clinical prognostic factors through cox regression and subgroup analyses

Prognostic analyses were conducted using a two-stage approach: (1) univariate Cox regression ("survival" package) identified significant clinical risk factors, which were then (2) incorporated into multivariate models adjusting for potential confounders. Subgroup analyses evaluated STAT3-prognosis associations across key clinical strata including: age, gender, menopausal status, prior malignancy history, clinical stage at diagnosis, surgical procedures for breast carcinoma and axillary lymph nodes, tumor histological type, pathological TNM stage, and radiation therapy administration.

2.5 Functional analysis by Gene Set Enrichment Analysis

Gene Set Enrichment Analysis (GSEA) was performed to investigate pathway associations with STAT3 expression in breast cancer. We conducted differential pathway analysis comparing high versus low STAT3 expression groups, examining Hallmark, Kyoto Encyclopedia of Genes and Genomes (KEGG), and Gene Ontology (GO) terms. The corresponding gene sets for Hallmark, KEGG, and GO pathways were obtained from the GSEA database for this analysis. Significance of enriched pathways was determined using a nominal p-value < 0.05 and an FDR-adjusted q-value threshold of < 0.25 to account for multiple testing. Pathways meeting these criteria were considered statistically significant.

2.6 Immune microenvironment and treatment predictions in breast cancer

To explore the TIME, RNA-seq data from all patients were analyzed using the CIBERSORTx database (27) to evaluate immune cell infiltration. Spearman correlation analysis was used to examine the association between STAT3 expression levels and immune cell infiltration in breast cancer, providing insights into the immune landscape and its potential implications for treatment predictions.

2.7 Construction and evaluation of the radiomic model

An experienced radiologist performed semi-automated 3D tumor segmentation using 3D Slicer on early- and delayed-phase MRI from 101 patients, generating paired volumes of interest (VOIs) per case. Inter-reader consistency was assessed in a 30-case subset by a senior radiologist.

Image preprocessing (bias field correction, resampling) was performed using PyRadiomics (v3.01) and SimpleITK (v2.2.0). Radiomic features (first-order, morphological, texture, and high-order statistics) were extracted from segmented VOIs. To mitigate batch effects, ComBat harmonization (Batch=6) was applied using scanner model information from DICOM metadata, followed by Z-score normalization. Subsequently, patients were divided into development/validation sets (6: 4) by STAT3 expression, balanced via Chi-square/Fisher's tests. Features were screened in the development cohort, retaining only features with ICC > 0.70. Following redundancy reduction (r > 0.90), LASSO regression with 50% discount cross-validation selected optimal features.

The predictive models were developed using six ML algorithms (LR, SVM, KNN, RF, DT, XGBoost) to generate radiomics scores via SPSS (v26). To prevent overfitting with limited samples, we optimized

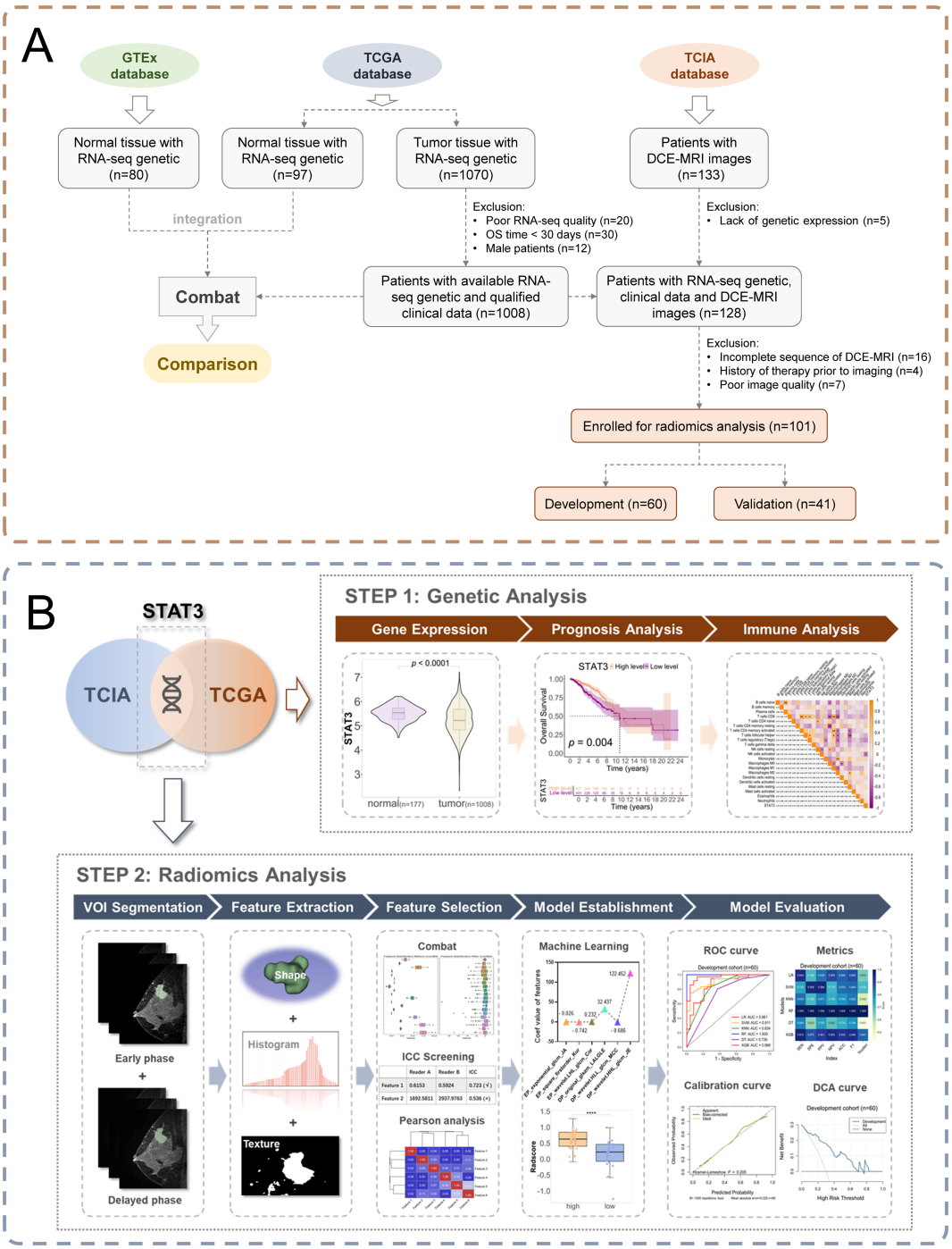

FIGURE 1
Study workflow. **(A)** Patient enrollment flow chart; **(B)** Schematic diagram of the workflow of an imaging histology study.

the scikit-learn framework and hyperparameters via grid search (detailed in Additional file 3). Model discrimination was assessed through receiver operating characteristic (ROC) analysis with area under curve (AUC). The Youden index-derived cutoff optimized Rad-score classification, followed by comprehensive evaluation using sensitivity, specificity, positive predictive value (PPV), negative predictive value (NPV), and F1-score. The best-performing model in the validation cohort was selected for clinical application. The optimal model identified in the validation cohort was further subjected to bootstrap resampling (n = 1,000 iterations) to evaluate its robustness. Additional validation included Hosmer-Lemeshow testing, calibration curves, and decision curve analysis (DCA) to assess clinical utility

2.8 Integrated analysis of radiomics, STAT3 expression, survival, and immune correlations

Our radiomics model was employed to calculate RAD-scores for patients stratified by STAT3 expression levels (high vs low) across development and validation cohorts. Using the Youden index, we established RAD-score thresholds to categorize patients into high-RAD and low-RAD groups. Survival outcomes were then analyzed through Kaplan-Meier curves generated with the "survminer" package, with statistical significance assessed via log-rank testing. To investigate potential immune correlates, we performed Spearman correlation analysis between RAD-scores and immune-related genes from the ImmPORT database.

2.9 Statistical analyses

For comparative analyses, categorical variables were evaluated using Chi-square or Fisher's exact test, while continuous variables were analyzed with t-tests (normal distribution) or Mann-Whitney U-tests (non-normal distribution). STAT3 expression thresholds were determined using the minimum p-value method. RAD-score cutoffs were established based on imaging histology scores corresponding to the Youden index.

A p-value ≤ 0.05 was considered statistically significant. All statistical analyses were performed using SPSS (v26), and R (v4.3.2). Figures were generated with GraphPad Prism (v8.0.0).

3 Results

3.1 Baseline characteristics of patients

This study analyzed a cohort of 1,008 breast cancer patients from TCGA along with 80 normal breast tissue samples from GTEx for comparative analysis. We determined the optimal STAT3 expression cutoff value to be 5.089 by using the minimum p-value method, which stratified patients into low-expression (n = 431, ≤ 5.089) and high-expression (n = 577, > 5.089) groups. Baseline clinical characteristics are presented in Table 1, revealing statistically significant differences between groups for breast carcinoma surgical procedure (p = 0.015) and tumor histological type (p = 0.007), while other clinical indicators showed no significant variation. Comparative analysis of the combined GTEx and TCGA datasets demonstrated significantly lower STAT3 expression in tumor tissues compared to normal breast specimens (p < 0.001, Figure 2A).

3.2 STAT3 expression levels and ten-year survival

K-M analysis revealed significantly better survival outcomes in the high STAT3 expression group compared to the low-expression cohort (p = 0.004, Figure 2B). Landmark analysis demonstrated this survival advantage was particularly pronounced within the first 10 years (p = 0.001), though the difference attenuated beyond this timeframe (p = 0.383, Figure 2C). Cox regression analyses confirmed STAT3's independent prognostic value, with low expression associated with worse overall survival in both univariate (Hazard ratio [HR] = 1.596, 95% CI: 1.160–2.196, p = 0.004, Figure 3A) and multivariate models (adjusted HR = 1.927, 95% CI: 1.369–2.712, p < 0.001, Figure 3B). Subgroup analyses identified particularly strong protective associations in non-metastatic patients (HR = 0.525, 95% CI: 0.351–0.786, p = 0.002) and those receiving radiotherapy (HR = 0.633, 95% CI: 0.433–0.925, p = 0.018) (Additional file 4).

3.3 GSEA analysis of STAT3 expression and functional pathways

To elucidate the biological mechanisms underlying the survival advantage observed in patients with high STAT3 expression, we performed GSEA to identify differentially regulated pathways. High STAT3 expression was positively associated with epithelial apoptotic processes (Figure 4A), suggesting enhanced tumor suppression through regulated cell death, and with TNF-α signaling via NFκB (Figure 4B), indicating robust anti-tumor immunity. The folate biosynthesis pathway (Figure 4C) was also enriched, potentially linking metabolic factors to improved prognosis. Conversely, low STAT3 expression correlated with pro-tumorigenic pathways including mRNA 3'-UTR binding (Figure 4D) and epithelial-mesenchymal transition (Figure 4E), consistent with increased metastatic potential. Notably, T-cell receptor signaling enrichment in low-STAT3 tumors (Figure 4F) may reflect T-cell exhaustion, suggesting compromised immune surveillance.

3.4 STAT3 expression and immune reaction in patients with breast cancer

Consistent with STAT3's established immunomodulatory functions (7, 28, 29), we systematically evaluated its association with tumor immune infiltration patterns. Correlation analyses revealed a complex relationship between STAT3 expression and immune cell profiles. Elevated STAT3 levels demonstrated significant negative correlations with cytotoxic immune effectors, including CD8+ T lymphocytes and natural killer (NK) cells, suggesting impairment of antitumor immunity in high-STAT3 tumors. Conversely, STAT3 expression showed positive correlations with immunosuppressive populations, particularly monocytes, M2-polarized macrophages, and tumor-associated neutrophils. Mechanistically, these findings suggest STAT3 promotes an immunosuppressive niche through recruitment of regulatory myeloid cells and subsequent release of immunosuppressive mediators, establishing a self-perpetuating inhibitory microenvironment (Figure 4G).

TABLE 1 Baseline table of STAT3 gene high and low expression groups in breast cancer.

Variables	Total (n = 1008)	High expression (n = 577)	Low expression (n = 431)	*P*-value
Age				0.102
< 45	152 (15.1)	75 (13.0)	77 (17.9)	
45 ~ 60	412 (40.9)	241 (41.8)	171 (39.7)	
> 60	444 (44.0)	261 (45.2)	183 (42.4)	
Menopause status				0.886
Premenopausal	217 (21.5)	126 (21.8)	91 (21.1)	
Postmenopausal	647 (64.2)	366 (63.4)	281 (65.2)	
Perimenopausal	35 (3.5)	22 (3.8)	13 (3.0)	
Unknown	109 (10.8)	63 (10.9)	46 (10.7)	
Prior malignancy diagnoses				1
Yes	60 (6.0)	34 (5.9)	26 (6.0)	
No	948 (94.0)	543 (94.1)	405 (94.0)	
Clinical stage at diagnosis				0.158
I/II	742 (73.6)	435 (75.4)	307 (71.2)	
III/IV/Unknown	266 (26.4)	142 (24.6)	124 (28.8)	
Breast carcinoma surgical procedure				0.015
BCS	237 (23.5)	133 (23.1)	104 (24.1)	
Mastectomy	471 (46.7)	252 (43.7)	219 (50.8)	
Unknown	300 (29.8)	192 (33.3)	108 (25.1)	
Axillary lymph node surgical procedure				0.108
Axillary lymph node dissection	533 (52.9)	289 (50.1)	244 (56.6)	
Sentinel node biopsy alone	250 (24.8)	149 (25.8)	101 (23.4)	
Unknown	225 (22.3)	139 (24.1)	86 (20.0)	
Histological type of tumor				0.007
Ductal	710 (70.4)	384 (66.6)	326 (75.6)	
Lobular	192 (19.0)	126 (21.8)	66 (15.3)	
mixed/others	106 (10.5)	67 (11.6)	39 (9.0)	
Pathologic T stage				0.889
T1/T2	845 (83.8)	485 (84.1)	360 (83.5)	
T3/T4/Tx	163 (16.2)	92 (15.9)	71 (16.5)	
Pathologic N stage				0.055
N0/N1/NX	828 (82.1)	486 (84.2)	342 (79.4)	
N2/N3	180 (17.9)	91 (15.8)	89 (20.6)	
Pathologic M stage				0.444
M0	835 (82.8)	483 (83.7)	352 (81.7)	
cM0 (i+)/M1/Mx	173 (17.2)	94 (16.3)	79 (18.3)	
Radiation therapy				0.54

(Continued)

TABLE 1 Continued

Variables	Total (n = 1008)	High expression (n = 577)	Low expression (n = 431)	*P*-value
Yes	524 (52.0)	308 (53.4)	216 (50.1)	
No	383 (38.0)	211 (36.6)	172 (39.9)	
Unknown	101 (10.0)	58 (10.1)	43 (10.0)	

BCS, breast-conserving surgery; ALND, axillary lymph node dissection; SNB, sentinel node biopsy.

3.5 Quantitative analysis of STAT3 protein expression in breast cancer tissues using DIA

We utilized the DIA software QuPath for both qualitative and quantitative anal-yses of IHC-stained images from the HPA database. By integrating the regions of in-terest delineated by pathologists, facilitated by QuPath, we distinguished between distinct compartments within breast cancer (tumor and stromal regions) and normal breast tissue (breast and stromal components). Furthermore, we identified cells within STAT3-positive (STAT3+) and STAT3-negative (STAT3-) breast cancer subtypes, as well as across various sectors of normal breast tissue (Figure 5A). Semi-quantitative anal-ysis demonstrated a statistically significant difference in Integrated Optical Density (IOD) and Average Optical Density (AOD) between breast cancer and normal tissues (IOD: $p = 0.004$; AOD: $p < 0.001$, Figure 5B). The positive rate of STAT3+ cells in tumor re-gions was significantly higher compared to region of normal breast tissue ($p = 0.048$, Figure 5C). The number and density of STAT3+ cells in tumor tissues were found to be higher compared to those in normal tissues, however, no statistically significant dif-ference was observed (number: $p = 0.113$, Figure 5D; density: $p = 0.125$, Figure 5E). Notably, in breast cancer tissues, the number of STAT3+ cells within the tumor regions were sig-nificantly greater than that observed in the stromal regions ($p < 0.0001$, Figure 5F).

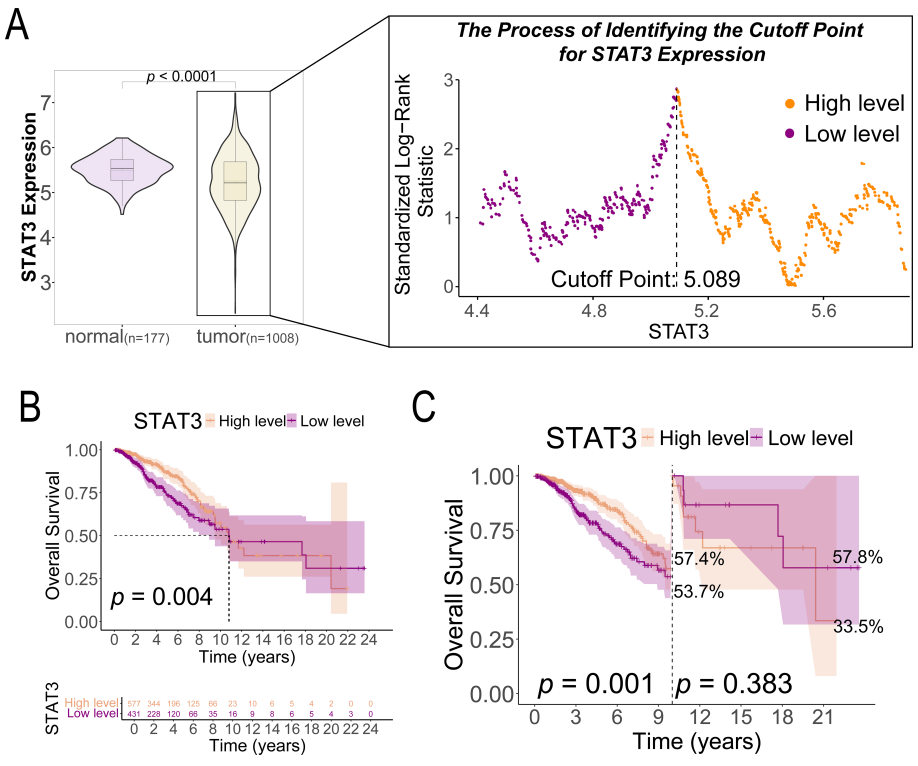

FIGURE 2
STAT3 gene expression in breast cancer tissues (n = 1008) and normal tissues (n = 177) and its prognostic implications in patients with breast cancer. **(A)** The cutoff value of STAT3 gene expression based on the highest Youden index; **(B)** K-M survival curves comparing OS between high and low STAT3 gene expression groups in patients with breast cancer (n = 1008); **(C)** Landmark analysis of OS between high and low STAT3 gene expression groups in patients with breast cancer (n = 1008).

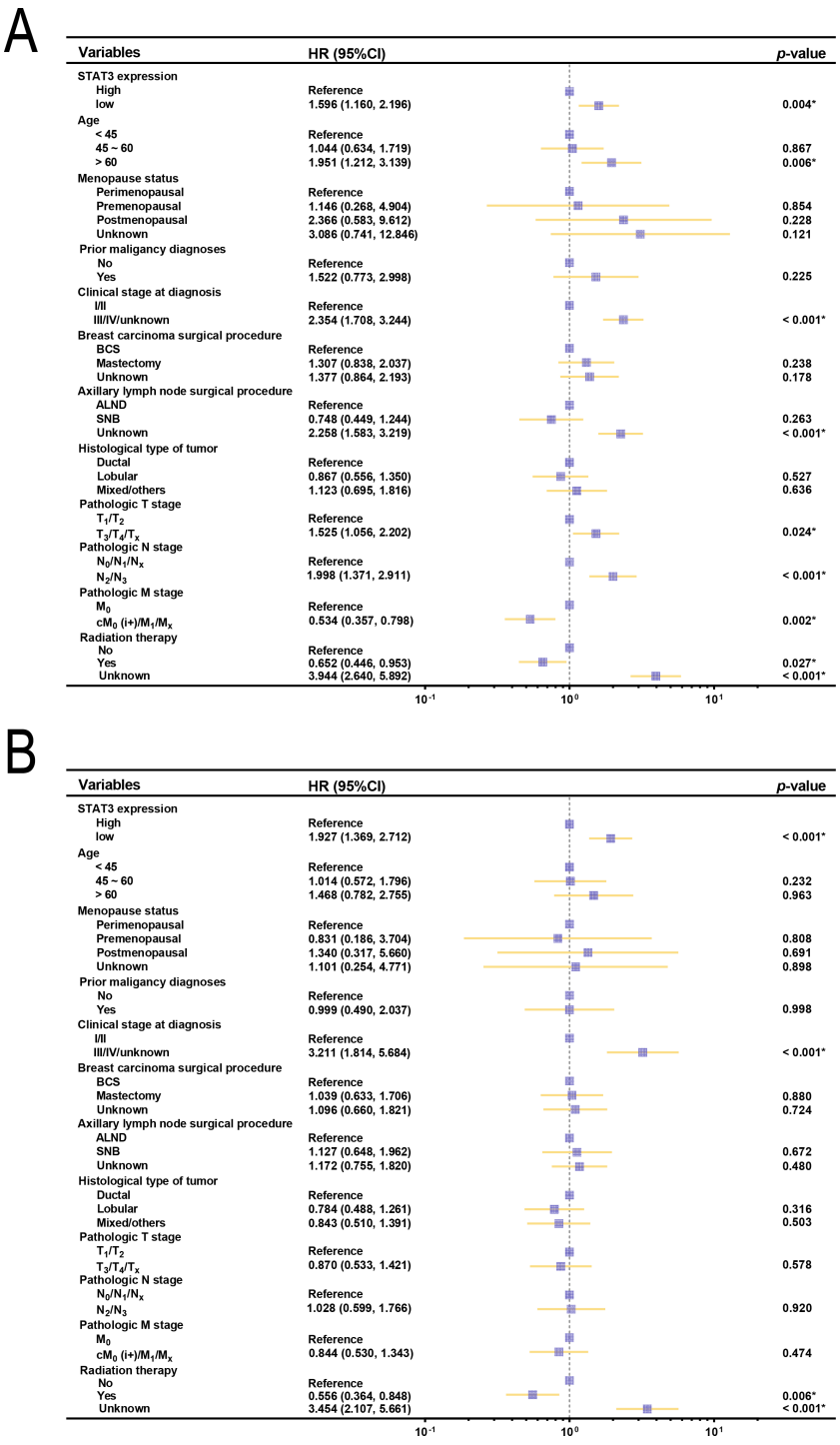

FIGURE 3
Forest plots of OS and clinical characteristics in patients with breast cancer (n = 1008). **(A)** Forest plot of univariate analysis examining the relationship between OS and clinical characteristics in patients with breast cancer; **(B)** Forest plot of multivariate analysis between OS and clinical characteristics in patients with breast cancer. BCS, breast-conserving surgery; ALND, axillary lymph node dissection; SNB, sentinel node biopsy.

3.5 Screening radiomics features and performance evaluation of models

The study cohort comprised 101 patients, randomly divided into development (n = 60) and validation (n = 41) sets at a 6:4 ratio, with balanced clinical characteristics and STAT3 expression between groups ($p > 0.05$, Additional file 5). From multiphase MRI, 3,100 radiomic features were initially extracted. Following combat analysis (Figure 6A), quality control (ICC ≥ 0.70, Additional file 6), Pearson correlation analysis, and LASSO regression with 5-fold cross-validation (optimal λ

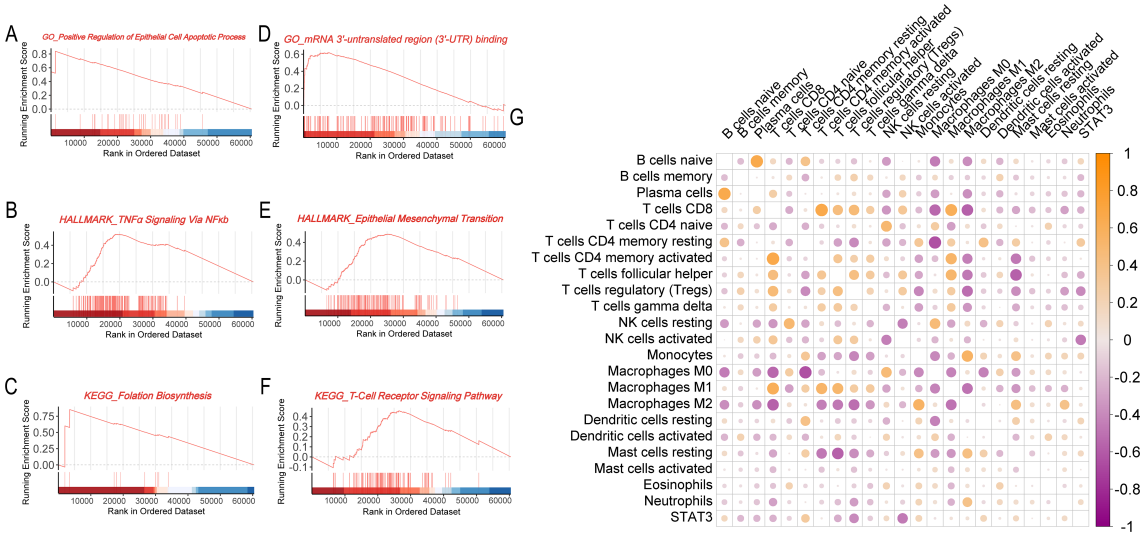

FIGURE 4
Biological and immunological functions of the STAT3 gene in breast cancer. **(A–C)** GSEA enrichment analysis for the STAT3 high expression group (**A**, GO analysis; **B**, Hallmark pathway analysis; **C**, KEGG pathway analysis); **(D–F)** GSEA enrichment analysis for the STAT3 low expression group (**D**, GO analysis; **E**, Hallmark pathway analysis; **F**, KEGG pathway analysis); **(G)** Correlation matrix showing the relationship between STAT3 gene expression and immune cell infiltration levels in breast cancer tissues.

= 0.081), six robust features (three each from early- and delayed-phase images) were identified at last (Figure B). The weight coefficients of each selected features inherently represent their importance were shown in Additional file 7, and the clinical and biological interpretations were detailed in Additional file 8.

The analysis revealed that while the RF model showed significantly higher AUC than LR in the training cohort ($p = 0.029$), other models demonstrated only marginal improvements over LR (Additional file 9). Notably, both LR and DT models maintained consistent performance across development and validation cohorts ($p > 0.05$), indicating acceptable generalizability, whereas other models exhibited varying degrees of overfitting. When comparing the two stable models (Additional file 9), LR demonstrated superior discriminative ability in both cohorts (development: 0.861, 95% CI [0.749 - 0.947], Figure 6C; validation: 0.742, 95% CI [0.588 - 0.884], Figure 6D, p = 0.209) compared to DT (development: 0.730, 95% CI [0.615 - 0.837], Figure 6C; validation: 0.571, 95% CI [0.376 - 0.746], Figure 6D, p = 0.089). Based on this robust performance and stability across datasets, we selected the LR model as the optimal predictive model for our study. The performance matrix analysis (Figures 6E, F) further confirmed that the LR model achieved the highest specificity (92.3%), PPV (94.1%), and Youden index (0.495) in the validation cohort. Bootstrap validation confirmed LR model stability (mean AUC = 0.822, 95%CI: 0.780–0.847, Additional file 10). Calibration analysis showed excellent fit in both cohorts ($p = 0.412$ development, $p = 0.088$ validation; Figures 6G, H). DCA demonstrated clinical utility across probability thresholds of 0%-70% (development, Figure 6I) and 20% - 50% (validation, Figure 6J). These results validate the LR model's accuracy, reliability, and clinical applicability for breast cancer stratification.

The Rad-score was calculated using the LR-based model and compared between STAT3-low and STAT3-high expression groups in both the development and validation cohorts. Significant RAD-score differences were observed between STAT3 expression groups in both development (median [IQR]: 0.222 [-0.070, 0.465] vs 0.628 [0.405, 0.844], $p < 0.001$, Figures 6K–L) and validation cohorts (0.258 [-0.069, 0.452] vs 0.582 [0.430, 0.789], $p = 0.018$, Figures 6M, N).

3.6 Relationship between RAD-scores and patient survival

The prognostic value of RAD-scores was evaluated by analyzing their association with OS in the 101-patient cohort. Using the Youden index-derived cutoff (0.523), patients were stratified into high (n = 47) and low (n = 54) RAD-score groups. K-M analysis demonstrated significantly improved OS in the high-RAD group ($p = 0.034$, Figure 7A), confirming the model's prognostic capability.

3.7 Relationship between RAD-scores and tumor immune-related genes

Our analysis revealed significant immunogenomic correlations with RAD-scores in breast cancer. A strong positive association was observed between RAD-scores and STAT3 expression (r = 0.47, $p < 0.01$, Figure 7B), with similar correlation patterns for immune-related genes. Specifically, RAD-scores showed significant positive correlations with:

- T-cell related genes (TSC1, FOXP1, LEF1, SEMA4A, RELB, PSEN1, EIF2AK4, RORA, IFNW1, IL4R, KMT2A, BCL6; $p < 0.05$, Figure 7C)

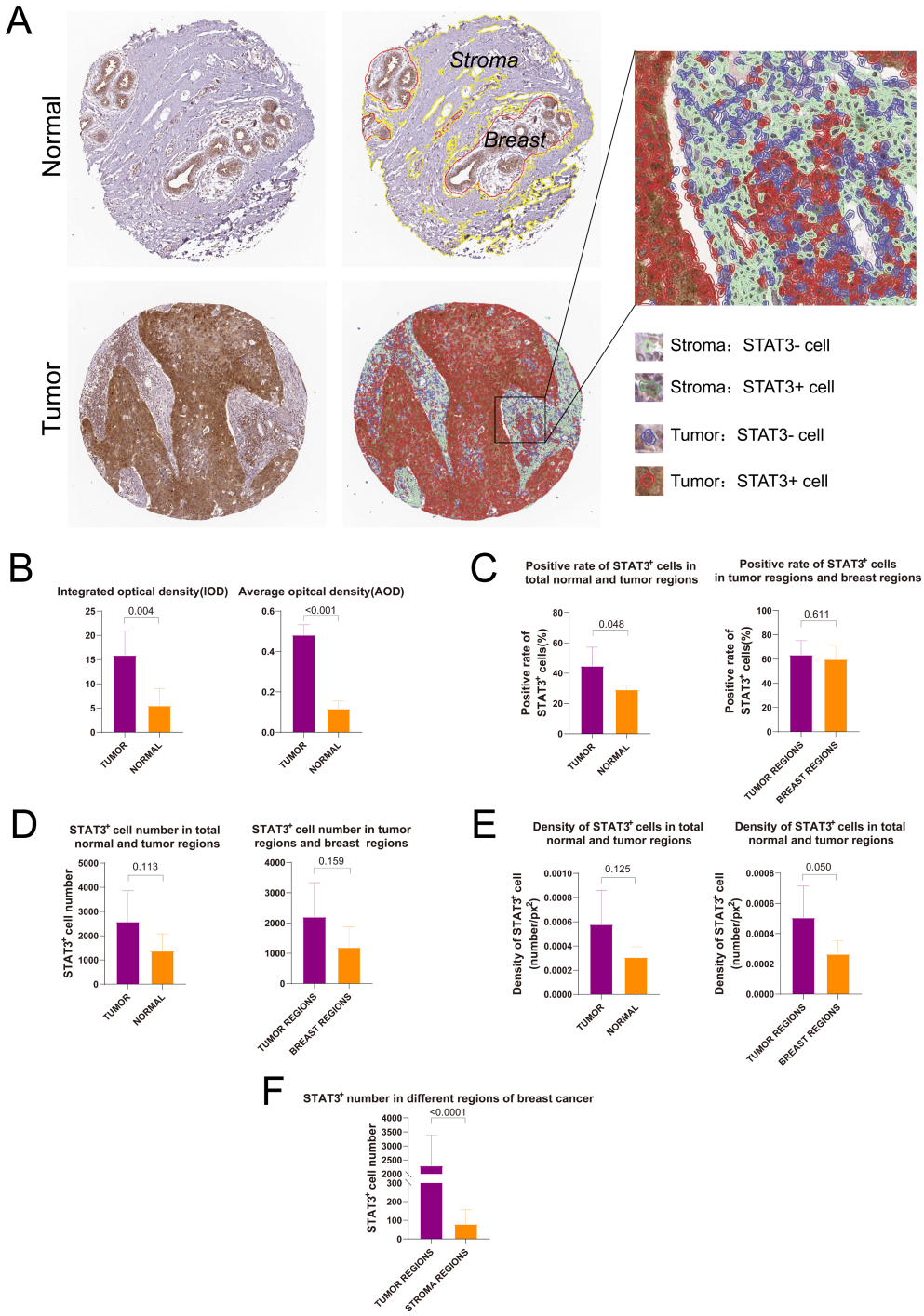

FIGURE 5
Digital image analysis of immunohistochemical staining images in HPA database. **(A)** Results of tissue segmentation and cell recognition of breast cancer and normal breast tissue; **(B)** Integrated optical density and average optical density of STAT3+ cells in breast cancer and normal breast tissues; **(C)** Rate of STAT3+ cells in breast cancer and normal breast tissues; **(D)** Number of STAT3+ cells in breast cancer and normal breast tissues; **(E)** Density of STAT3+ cells in breast cancer and normal breast tissues; **(F)** Comparison of the number of STAT3+ cells in different regions.

- NK-cell markers (STAT5B, AXL, PBX1, IFNW1, RABL3; $p < 0.05$, Figure 7D)
- B-cell associated genes (NOTCH2, BCL2, MLH1, LEF1, ZBTB1, BLNK, PIK3R1; $p < 0.05$, Figure 7E)

4 Discussion

Breast cancer biomarker research remains in nascent stages, with no single prognostic marker achieving universal clinical

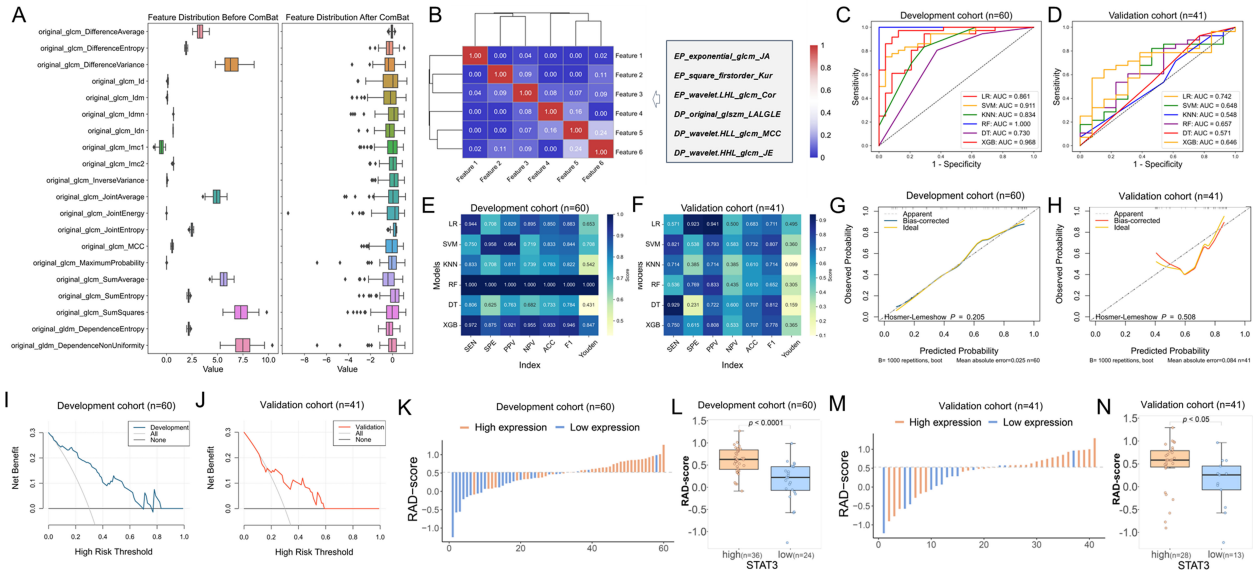

FIGURE 6
Radiomics model construction and efficacy evaluation results. **(A)** The box diagram of eigenvalue distribution before and after Combat with 20 random features; **(B)** Cluster heatmap of the correlation of selected features; **(C, D)** ROC curves showing the performance of all radiomics models in the development and validation cohorts; **(E, F)** Metric heatmap analysis of diagnostic efficacy parameters for all radiomics models in the development and validation cohorts; **(G, H)** Calibration curves depicting the agreement between predicted and observed outcomes based on LR model in the development and validation cohorts; **(I, J)** DCA curves evaluating the clinical utility of the LR model in the development and validation cohorts; **(K)** Waterfall plot illustrating the distribution of radiomics scores (RAD-scores) in the development cohort; **(L)** Box plot showing the differences in distribution of RAD-scores between high and low STAT3 expression groups in the development cohort; **(M)** Waterfall plot of RAD-scores in the validation cohort; **(N)** Box plot comparing RAD-score distributions between high and low STAT3 expression groups in the validation cohort.

adoption. Among emerging candidates, STAT3 has emerged as a critical regulator in breast cancer progression, particularly in triple-negative subtypes, demonstrating strong prognostic value and immunotherapy response associations (10, 30). These characteristics position STAT3 expression status as a crucial determinant for personalized treatment strategies.

Our study findings demonstrate the complex role of STAT3 in breast cancer, particularly its complex relationship with immune regulation and patient prognosis, which aligns with existing literature that emphasizes the importance of STAT3 as a prognostic factor and potential biomarker for immunotherapy responses in breast cancer (31, 32), and this phenomenon may contribute to the diminished ten-year survival rates observed in these patients, reflecting the complex interplay between STAT3 expression patterns and immune activity Additionally, our study developed a novel radiomics approach using DCE-MRI to non-invasively predict STAT3 expression, bridging imaging and genomic analysis in precision oncology.

Our study revealed higher STAT3 mRNA levels in normal tissues compared to breast cancer tissues, challenging the conventional oncogenic view of STAT3 (33). This paradox underscores the complexity of its role in cancer biology, necessitating evaluation of multiple factors, including mRNA/protein expression, activation states (e.g., phosphorylation), and context-dependent signaling pathway interactions. Notably, STAT3 expression correlated significantly with immune modulation, particularly through suppressed NK cell activity—a key anti-tumor mechanism—potentially facilitating immune evasion via impaired IFN-γ and TNF-α production (34, 35). While our CIBERSORTx analysis identified these immune correlates, the computational nature of deconvolution warrants validation through flow cytometry or spatial transcriptomics in future studies.

The GSEA analysis revealed enrichment of immune-suppressive pathways and exhaustion markers in low-STAT3 tumors, suggesting STAT3 deficiency may drive immune evasion through both immunosuppressive cell recruitment and T-cell dysfunction. This aligns with evidence that STAT3 loss promotes TGF-β-mediated suppression and PD-L1 upregulation, while impairing T-cell metabolic fitness through oxidative stress (36, 37). The combined effects of tumor cell p-STAT3 hyperactivation and STAT3 mRNA deficiency likely create a dual immunosuppressive axis, though future studies should dissect cell-type-specific effects using spatial transcriptomics.

The prognostic paradox of low STAT3 mRNA associating with poorer survival may reflect compensatory hyperactivation through post-transcriptional modifications. Growing evidence suggests STAT3's functional activity is primarily regulated through phosphorylation status rather than mRNA abundance (38). While moderate STAT3 activity maintains normal T-cell function (39), its deficiency may drive T-cell exhaustion, evidenced by enriched TCR signaling pathways as a compensatory mechanism. This aligns with studies demonstrating that STAT3 activation (p-STAT3), not total STAT3 mRNA levels, drives tumor progression and poor survival, likely via cell-autonomous and immune-mediated mechanisms

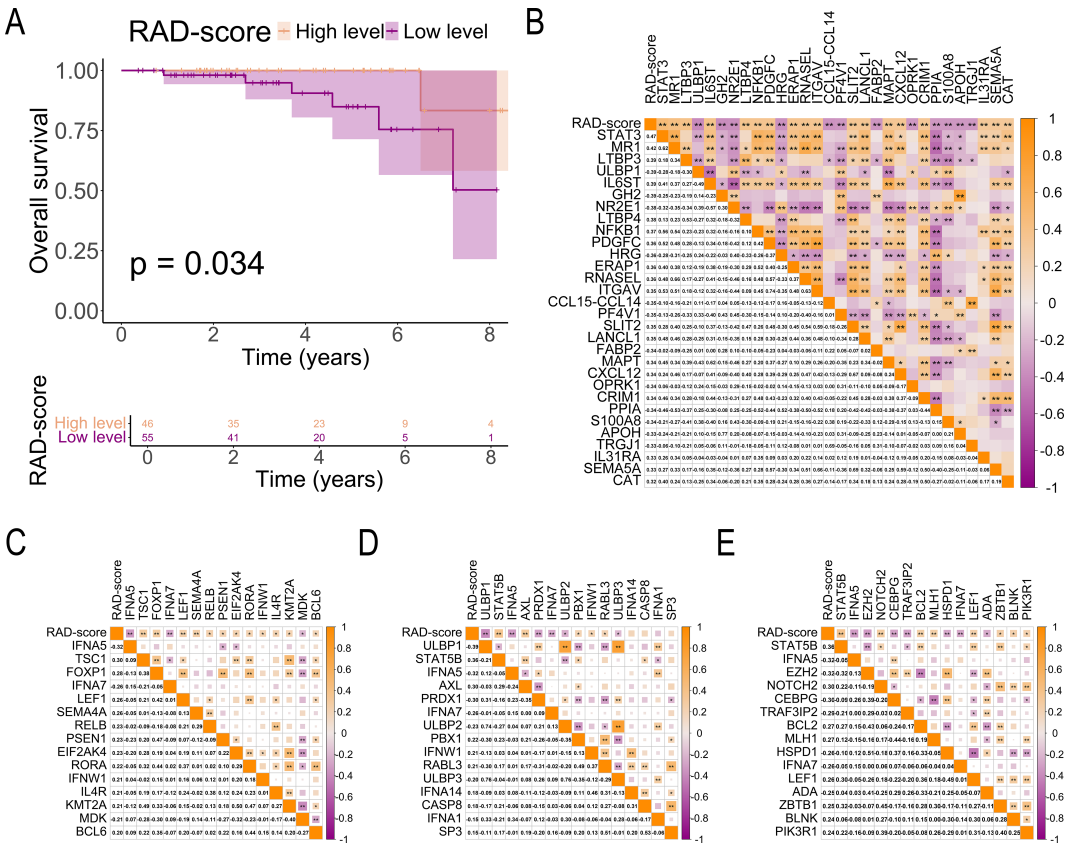

FIGURE 7
Association of RAD-score With Prognosis and Immune-Related Genes. **(A)** K-M curves comparing survival outcomes between high and low RAD-score groups in patients with breast cancer; **(B)** Correlation matrix illustrating the relationship between RAD-scores and immune cell-related gene expression in breast cancer tissues; **(C–E)** Correlation matrix between RAD-score and immune cell-related gene expression in breast cancer tissues (**C**, T cell-related genes; **D**, NK cell-related genes; **E**, B cell-related genes). The symbols "*" and "**" indicate statistical significance levels of $p < 0.05$ and $p < 0.01$, respectively.

(40). Although our study identifies a correlation between low STAT3 expression and T cell exhaustion, the downstream mechanisms remain unclear. Prior work suggests STAT3 may regulate key exhaustion-related genes, such as PD-1 and TOX (41), and modulate T cell metabolism (42). While our data do not functionally validate these targets, the observed exhaustion signature aligns with potential STAT3-dependent regulation. Further studies could clarify these mechanistic links.

Contrary to previous reports of STAT3 upregulation in breast cancer (11, 12), our integrated TCGA/GTEx analysis demonstrated higher constitutive expression in normal tissues, with survival analysis showing no significant prognostic impact of mRNA levels alone. This dichotomy suggests STAT3's physiological role in normal tissue homeostasis (43) versus its cancer-specific hyperactivation through post-transcriptional mechanisms (44). Critically, tumor progression appears driven not by transcriptional overexpression but by dysregulated activation states, particularly phosphorylation-mediated signaling (45, 46). These findings redefine STAT3's oncogenic paradigm, emphasizing that malignant progression depends more on post-transcriptional activation than mRNA abundance, with important implications for targeted therapeutic strategies.

Recent advances in medical imaging and computer science have established radiomics as a powerful tool for breast cancer research (47). Multisequence, multiparametric breast MRI enables extraction of high-throughput radiomic features that provide novel biological insights, predict disease progression, and guide personalized treatment strategies. The emerging field of radiomics has demonstrated particular promise by correlating multimodal imaging data (MRI/CT) with genomic profiles to improve prognostic predictions (48–50). This approach has revealed significant associations between imaging features (tumor morphology, texture) and molecular characteristics, including gene expression patterns in the tumor microenvironment (51, 52). Given the established association between high STAT3 expression and poor prognosis (53), we hypothesized that integrating STAT3 expression profiles with advanced radiomic analysis could enhance prognostic accuracy.

In this study, we developed a novel MRI-based radiomics model to predict prognosis and immunotherapeutic characteristics based on STAT3 expression. Leveraging MRI's superior soft-tissue resolution and multiphasic contrast enhancement capabilities, so the signal intensity and texture features of these images correlate with tumor heterogeneity and may also serve as predictors of its biological

behavior (54). We identified six statistically significant radiomic features associated with STAT3 expression: one first-order feature (Square_Firstorder_Kurtosis), two texture features, and three wavelet-transformed higher-order features. Notably, the two most predictive features (regression coefficients > 10) derived from delayed-phase images included: (1) wavelet.HHL_glcm_JointEnergy (Coef = 122.452), reflecting tumor texture uniformity, and (2) original_glszm_LargeAreaLowGrayLevelEmphasis (Coef = 32.437), characterizing tissue distribution patterns (55). Through comprehensive evaluation of multiple machine learning classifiers, the LR-based model demonstrated superior generalizability in the validation cohort compared to alternative approaches. Despite comparable AUC to other models, LR was selected for its lower performance variance and higher specificity—a clinical priority to minimize costly false positives in molecular profiling. This finding supports the selection of the LR model as a robust, non-invasive tool for characterizing STAT3 expression levels, offering potential clinical utility for tumor phenotyping.

Our study advances previous research by uniquely integrating STAT3 expression analysis with advanced radiomics, revealing new relationships between molecular processes and imaging phenotypes. The identified features not only capture subvisual tumor heterogeneity but also demonstrate significant associations with gene expression and survival outcomes. Future directions include multi-omics integration for enhanced predictive modeling, prospective clinical validation, and investigation of radiomic-immune microenvironment correlations. While clinical translation requires further validation, our findings demonstrate radiomics' potential as a non-invasive tool for STAT3 expression profiling and prognostic assessment in breast cancer, representing a significant step toward precision oncology.

However, several limitations should be acknowledged in this study. First, this study focused on OS due to data availability constraints in public repositories. Future work should integrate disease-free survival and treatment-response metrics through prospective collaborations with clinical centers. Second, potential biases may exist as all DCE-MRI data were obtained from public repositories, and although ComBat harmonization was applied, residual variability across scanners may persist. Third, the smaller sample size (particularly in the TCIA cohort) may limit generalizability, warranting external validation in larger multicenter cohorts - an effort we are actively pursuing through expanded collaborations. Lastly, incomplete immunohistochemical data precluded molecular subtype analyses, potentially masking subtype-specific radiomic-STAT3 relationships. These limitations highlight the need for prospective multicenter studies with standardized protocols.

5 Conclusions

This study establishes STAT3 as a key prognostic biomarker in breast cancer and demonstrates the clinical potential of our validated DCE-MRI radiomics model for noninvasive STAT3 assessment. These findings advance precision oncology by enabling imaging-based prediction of tumor biology and treatment response, supporting personalized therapeutic strategies.

Data availability statement

The data used in this study are openly accessible from various public sources, including the UCSC Xena Database (https://xena.ucsc.edu/), The Cancer Imaging Archive (TCIA) for the TCGA-BRCA collection (https://www.cancerimagingarchive.net/collection/tcga-brca/), The Human Protein At-las (HPA) (https://www.proteinatlas.org/), ImmPort Shared Data (https://www.immport.org/shared/home), and the GTEx Database (https://www.gtexportal.org/).

Ethics statement

No animal studies are presented in this manuscript" and human ethics statement "As the data for this research were acquired from publicly available databases and used solely for scientific research, ethical approval was not required.

Author contributions

DP: Methodology, Data curation, Software, Writing – original draft. C-YZ: Data curation, Methodology, Validation, Conceptualization, Supervision, Writing – review & editing. Y-FW: Writing – review & editing, Methodology, Software, Visualization, Data curation. SL: Supervision, Writing – review & editing, Methodology, Formal Analysis, Validation. X-ZW: Validation, Writing – review & editing, Project administration, Supervision, Funding acquisition.

Funding

The author(s) declare that financial support was received for the research and/or publication of this article. This research was supported by the National Natural Science Foundation of China (No.82174103).

Conflict of interest

The authors declare that the research was conducted in the absence of any commercial or financial relationships that could be construed as a potential conflict of interest.

Generative AI statement

The author(s) declare that no Generative AI was used in the creation of this manuscript.

Publisher's note

All claims expressed in this article are solely those of the authors and do not necessarily represent those of their affiliated organizations, or those of the publisher, the editors and the reviewers. Any product that may be evaluated in this article, or claim that may be made by its manufacturer, is not guaranteed or endorsed by the publisher.

Supplementary material

The Supplementary Material for this article can be found online at: https://www.frontiersin.org/articles/10.3389/fimmu.2025.1619186/full#supplementary-material

ADDITIONAL FILE 1
Box Plot Illustrating the Removal of Batch Effects from STAT3 Gene Expression Data in the TCGA and GTEx Databases. (File format:.tif).

ADDITIONAL FILE 2
Gene List Retrieved from the ImmPORT Database. (File format:.xlsx).

ADDITIONAL FILE 3
Hyperparameter optimization during machine learning models construction. (File format:.docx).

ADDITIONAL FILE 4
Forest Plot of Subgroup Cox Regression Analysis. (File format:.tif).

ADDITIONAL FILE 5
Comparison of the Characteristics of the Development and Validation Cohorts. (File format:.docx).

ADDITIONAL FILE 6
ICC Values for Radiomics Features. (File format:.xlsx).

ADDITIONAL FILE 7
Weighted Coef Values of Each Features. (File format:.docx).

ADDITIONAL FILE 8
Description of selected radiomic features and their clinical relevance. (File format:.docx).

ADDITIONAL FILE 9
DeLong's test between models within and across development validation cohorts. (File format:.tif).

ADDITIONAL FILE 10
ROC Curve Derived from Bootstrap Analysis. (File format:.tif).

References

1. Sung H, Ferlay J, Siegel RL, Laversanne M, Soerjomataram I, Jemal A, et al. Global cancer statistics 2020: GLOBOCAN estimates of incidence and mortality worldwide for 36 cancers in 185 countries. *CA Cancer J Clin*. (2021) 71:209–49. doi: 10.3322/caac.21660

2. Loibl S, André F, Bachelot T, Barrios CH, Bergh J, Burstein HJ, et al. Early breast cancer: ESMO Clinical Practice Guideline for diagnosis, treatment and follow-up. *Ann Oncol*. (2024) 35:159–82. doi: 10.1016/j.annonc.2023.11.016

3. Goldhirsch A, Winer EP, Coates AS, Gelber RD, Piccart-Gebhart M, Thürlimann B, et al. Personalizing the treatment of women with early breast cancer: highlights of the St Gallen International Expert Consensus on the Primary Therapy of Early Breast Cancer 2013. *Ann Oncol*. (2013) 24:2206–23. doi: 10.1093/annonc/mdt303

4. Li J, Chen Z, Su K, Zeng J. Clinicopathological classification and traditional prognostic indicators of breast cancer. *Int J Clin Exp Pathol*. (2015) 8:8500–5.

5. Pescia C, Guerini-Rocco E, Viale G, Fusco N. Advances in early breast cancer risk profiling: from histopathology to molecular technologies. *Cancers*. (2023) 15:5430. doi: 10.3390/cancers15225430

6. Vellan CJ, Islam T, De Silva S, Mohd Taib NA, Prasanna G, Jayapalan JJ. Exploring novel protein-based biomarkers for advancing breast cancer diagnosis: A review. *Clin Biochem*. (2024) 129:110776. doi: 10.1016/j.clinbiochem.2024.110776

7. Zou S, Tong Q, Liu B, Huang W, Tian Y, Fu X. Targeting STAT3 in cancer immunotherapy. *Mol Cancer*. (2020) 19:145. doi: 10.1186/s12943-020-01258-7

8. Santoni M, Miccini F, Cimadamore A, Piva F, Massari F, Cheng L, et al. An update on investigational therapies that target STAT3 for the treatment of cancer. *Expert Opin investigational Drugs*. (2021) 30:245–51. doi: 10.1080/13543784.2021.1891222

9. Li T, Guo H, Zhao X, Jin J, Zhang L, Li H, et al. Gastric cancer cell proliferation and survival is enabled by a cyclophilin B/STAT3/miR-520d-5p signaling feedback loop. *Cancer Res*. (2017) 77:1227–40. doi: 10.1158/0008-5472.Can-16-0357

10. van Pul KM, Vuylsteke R, de Beijer MTA, van de Ven R, van den Tol MP, Stockmann H, et al. Breast cancer-induced immune suppression in the sentinel lymph node is effectively countered by CpG-B in conjunction with inhibition of the JAK2/STAT3 pathway. *J immunotherapy Cancer*. (2020) 8:e000761. doi: 10.1136/jitc-2020-000761

11. Lin WH, Dai WG, Xu XD, Yu QH, Zhang B, Li J, et al. Downregulation of DPF3 promotes the proliferation and motility of breast cancer cells through activating JAK2/STAT3 signaling. *Biochem Biophys Res Commun*. (2019) 514:639–44. doi: 10.1016/j.bbrc.2019.04.170

12. Chang R, Song L, Xu Y, Wu Y, Dai C, Wang X, et al. Loss of Wwox drives metastasis in triple-negative breast cancer by JAK2/STAT3 axis. *Nat Commun*. (2018) 9:3486. doi: 10.1038/s41467-018-05852-8

13. Ma Q, Gao FF, He X, Li K, Gao Y, Xu XL, et al. Antitumor effects of saikosaponin b2 on breast cancer cell proliferation and migration. *Mol Med Rep*. (2019) 20:1943–51. doi: 10.3892/mmr.2019.10385

14. Lee H, Jeong AJ, Ye SK. Highlighted STAT3 as a potential drug target for cancer therapy. *BMB Rep*. (2019) 52:415–23. doi: 10.5483/BMBRep.2019.52.7.152

15. Liu Z, Duan T, Zhang Y, Weng S, Xu H, Ren Y, et al. Radiogenomics: a key component of precision cancer medicine. *Br J Cancer*. (2023) 129:741–53. doi: 10.1038/s41416-023-02317-8

16. Zhao W, Yang J, Ni B, Bi D, Sun Y, Xu M, et al. Toward automatic prediction of EGFR mutation status in pulmonary adenocarcinoma with 3D deep learning. *Cancer Med*. (2019) 8:3532–43. doi: 10.1002/cam4.2233

17. Taouli B, Hoshida Y, Kakite S, Chen X, Tan PS, Sun X, et al. Imaging-based surrogate markers of transcriptome subclasses and signatures in hepatocellular carcinoma: preliminary results. *Eur Radiol*. (2017) 27:4472–81. doi: 10.1007/s00330-017-4844-6

18. Xie Y, Wang M, Xia H, Sun H, Yuan Y, Jia J, et al. Development and validation of a CECT-based radiomics model for predicting IL1B expression and prognosis of head and neck squamous cell carcinoma. *Front Oncol*. (2023) 13:1121485. doi: 10.3389/fonc.2023.1121485

19. Hu LS, Ning S, Eschbacher JM, Gaw N, Dueck AC, Smith KA, et al. Multi-parametric MRI and texture analysis to visualize spatial histologic heterogeneity and tumor extent in glioblastoma. *PloS One*. (2015) 10:0141506. doi: 10.1371/journal.pone.0141506

20. Mao L, Chen H, Liang M, Li K, Gao J, Qin P, et al. Quantitative radiomic model for predicting Malignancy of small solid pulmonary nodules detected by low-dose CT screening. *Quantitative Imaging Med Surg*. (2019) 9:263–72. doi: 10.21037/qims.2019.02.02

21. Pandit H, Hong YK, Li Y, Rostas J, Pulliam Z, Li SP, et al. Evaluating the regulatory immunomodulation effect of irreversible electroporation (IRE) in pancreatic adenocarcinoma. *Ann Surg Oncol*. (2019) 26:800–6. doi: 10.1245/s10434-018-07144-3

22. Weinstein JN, Collisson EA, Mills GB, Shaw KR, Ozenberger BA, Ellrott K, et al. The Cancer Genome Atlas Pan-Cancer analysis project. *Nat Genet*. (2013) 45:1113–20. doi: 10.1038/ng.2764

23. GTEx Consortium. The genotype-tissue expression (GTEx) project. *Nat Genet*. (2013) 45:580–5. doi: 10.1038/ng.2653

24. Lingle W, Erickson BJ, Zuley ML, Jarosz R, Bonaccio E, Filippini J, et al. *The cancer genome atlas breast invasive carcinoma collection (TCGA-BRCA) (Version 3)*. The Cancer Imaging Archive (2016). doi: 10.7937/K9/TCIA.2016.AB2NAZRP

25. Goldman MJ, Craft B, Hastie M, Repečka K, McDade F, Kamath A, et al. Visualizing and interpreting cancer genomics data via the Xena platform. *Nat Biotechnol*. (2020) 38:675–8. doi: 10.1038/s41587-020-0546-8

26. Bhattacharya S, Andorf S, Gomes L, Dunn P, Schaefer H, Pontius J, et al. ImmPort: disseminating data to the public for the future of immunology. *Immunologic Res*. (2014) 58:234–9. doi: 10.1007/s12026-014-8516-1

27. Newman AM, Steen CB, Liu CL, Gentles AJ, Chaudhuri AA, Scherer F, et al. Determining cell type abundance and expression from bulk tissues with digital cytometry. *Nat Biotechnol*. (2019) 37:773–82. doi: 10.1038/s41587-019-0114-2

28. Ma JH, Qin L, Li X. Role of STAT3 signaling pathway in breast cancer. *Cell communication signaling: CCS*. (2020) 18:33. doi: 10.1186/s12964-020-0527-z

29. Siveen KS, Sikka S, Surana R, Dai X, Zhang J, Kumar AP, et al. Targeting the STAT3 signaling pathway in cancer: role of synthetic and natural inhibitors. *Biochim Biophys Acta*. (2014) 1845:136–54. doi: 10.1016/j.bbcan.2013.12.005

30. Taifour T, Attalla SS, Zuo D, Gu Y, Sanguin-Gendreau V, Proud H, et al. The tumor-derived cytokine Chi3l1 induces neutrophil extracellular traps that promote T cell exclusion in triple-negative breast cancer. *Immunity*. (2023) 56:2755–2772.e2758. doi: 10.1016/j.immuni.2023.11.002

31. Zhou J, Wan F, Wang L, Peng C, Huang R, Peng F. STAT4 facilitates PD-L1 level via IL-12R/JAK2/STAT3 axis and predicts immunotherapy response in breast cancer. *MedComm*. (2023) 4:e464. doi: 10.1002/mco2.464

32. Chuangchot N, Jamjuntra P, Yangngam S, Luangwattananun P, Thongchot S, Junking M, et al. Enhancement of PD-L1-attenuated CAR-T cell function through breast cancer-associated fibroblasts-derived IL-6 signaling via STAT3/AKT pathways. *Breast Cancer research: BCR*. (2023) 25:86. doi: 10.1186/s13058-023-01684-7

33. Kaminskiy Y, Melenhorst JJ. STAT3 role in T-cell memory formation. *Int J Mol Sci*. (2022) 23:2878. doi: 10.3390/ijms23052878

34. Thanapati S, Ganu M, Giri P, Kulkarni S, Sharma M, Babar P, et al. Impaired NK cell functionality and increased TNF-α production as biomarkers of chronic chikungunya arthritis and rheumatoid arthritis. *Hum Immunol*. (2017) 78:370–4. doi: 10.1016/j.humimm.2017.02.006

35. Wang R, Jaw JJ, Stutzman NC, Zou Z, Sun PD. Natural killer cell-produced IFN-γ and TNF-α induce target cell cytolysis through up-regulation of ICAM-1. *J leukocyte Biol*. (2012) 91:299–309. doi: 10.1189/jlb.0611308

36. Bai R, Hao L, Zhou G, Fu Q, Zhang P, Lin P, et al. The mechanism of TGF-β mediating BRD4/STAT3 signaling pathway to promote fibroblast proliferation and thus promote keloid progression. *Heliyon*. (2024) 10:e38188. doi: 10.1016/j.heliyon.2024.e38188

37. Xie C, Zhou X, Liang C, Li X, Ge M, Chen Y, et al. Apatinib triggers autophagic and apoptotic cell death via VEGFR2/STAT3/PD-L1 and ROS/Nrf2/p62 signaling in lung cancer. *J Exp Clin Cancer research: CR*. (2021) 40:266. doi: 10.1186/s13046-021-02069-4

38. Ishteyaque S, Singh G, Yadav KS, Verma S, Sharma RK, Sen S, et al. Cooperative STAT3-NFkB signaling modulates mitochondrial dysfunction and metabolic profiling in hepatocellular carcinoma. *Metabolism*. (2024) 152:155771. doi: 10.1016/j.metabol.2023.155771

39. McIlwain DR, Grusdat M, Pozdeev VI, Xu HC, Shinde P, Reardon C, et al. T-cell STAT3 is required for the maintenance of humoral immunity to LCMV. *Eur J Immunol*. (2015) 45:418–27. doi: 10.1002/eji.201445060

40. Pan YM, Wang CG, Zhu M, Xing R, Cui JT, Li WM, et al. STAT3 signaling drives EZH2 transcriptional activation and mediates poor prognosis in gastric cancer. *Mol cancer*. (2016) 15:79. doi: 10.1186/s12943-016-0561-z

41. Cao C, Xu M, Wei Y, Peng T, Lin S, Liu X, et al. CXCR4 orchestrates the TOX-programmed exhausted phenotype of CD8(+) T cells via JAK2/STAT3 pathway. *Cell Genomics*. (2024) 4:100659. doi: 10.1016/j.xgen.2024.100659

42. Sun Q, Zhao X, Li R, Liu D, Pan B, Xie B, et al. STAT3 regulates CD8+ T cell differentiation and functions in cancer and acute infection. *J Exp Med*. (2023) 220: e20220686. doi: 10.1084/jem.20220686

43. Clarkson RW, Boland MP, Kritikou EA, Lee JM, Freeman TC, Tiffen PG, et al. The genes induced by signal transducer and activators of transcription (STAT)3 and STAT5 in mammary epithelial cells define the roles of these STATs in mammary development. *Mol Endocrinol (Baltimore Md.)*. (2006) 20:675–85. doi: 10.1210/me.2005-0392

44. Hughes K, Watson CJ. The multifaceted role of STAT3 in mammary gland involution and breast cancer. *Int J Mol Sci*. (2018) 19:1695. doi: 10.3390/ijms19061695

45. Zhao Y, Hu Z, Li J, Hu T. EZH2 exacerbates breast cancer by methylating and activating STAT3 directly. *J Cancer*. (2021) 12:5220–30. doi: 10.7150/jca.50675

46. Rébé C, Ghiringhelli F. STAT3, a master regulator of anti-tumor immune response. *Cancers*. (2019) 11:1280. doi: 10.3390/cancers11091280

47. Conti A, Duggento A, Indovina I, Guerrisi M, Toschi N. Radiomics in breast cancer classification and prediction. *Semin Cancer Biol*. (2021) 72:238–50. doi: 10.1016/j.semcancer.2020.04.002

48. Tagliafico AS, Piana M, Schenone D, Lai R, Massone AM, Houssami N. Overview of radiomics in breast cancer diagnosis and prognostication. *Breast (Edinburgh Scotland)*. (2020) 49:74–80. doi: 10.1016/j.breast.2019.10.018

49. Zheng X, Yao Z, Huang Y, Yu Y, Wang Y, Liu Y, et al. Deep learning radiomics can predict axillary lymph node status in early-stage breast cancer. *Nat Commun*. (2020) 11:1236. doi: 10.1038/s41467-020-15027-z

50. LoGullo R, Horvat J, Reiner J, Pinker K. Multimodal, multiparametric and genetic breast imaging. *Der Radiologe*. (2021) 61:183–91. doi: 10.1007/s00117-020-00801-3

51. Fan M, Wang K, Zhang Y, Ge Y, Lü Z, Li L. Radiogenomic analysis of cellular tumor-stroma heterogeneity as a prognostic predictor in breast cancer. *J Trans Med*. (2023) 21:851. doi: 10.1186/s12967-023-04748-6

52. Su GH, Xiao Y, You C, Zheng RC, Zhao S, Sun SY, et al. Radiogenomic-based multiomic analysis reveals imaging intratumor heterogeneity phenotypes and therapeutic targets. *Sci Adv*. (2023) 9:eadf0837. doi: 10.1126/sciadv.adf0837

53. Aleskandarany MA, Agarwal D, Negm OH, Ball G, Elmouna A, Ashankyty I, et al. The prognostic significance of STAT3 in invasive breast cancer: analysis of protein and mRNA expressions in large cohorts. *Breast Cancer Res Treat*. (2016) 156:9–20. doi: 10.1007/s10549-016-3709-z

54. Mungai F, Verrone GB, Pietragalla M, Berti V, Addeo G, Desideri I, et al. CT assessment of tumor heterogeneity and the potential for the prediction of human papillomavirus status in oropharyngeal squamous cell carcinoma. *La Radiologia Med*. (2019) 124:804–11. doi: 10.1007/s11547-019-01028-6

55. Peng B, Wang K, Xu R, Guo C, Lu T, Li Y, et al. Preoperative computed tomography-based tumoral radiomic features prediction for overall survival in resectable non-small cell lung cancer. *Front Oncol*. (2023) 13:1131816. doi: 10.3389/fonc.2023.1131816

frontiers | Frontiers in Oncology

TYPE Original Research
PUBLISHED 03 July 2025
DOI 10.3389/fonc.2025.1608597

Check for updates

OPEN ACCESS

EDITED BY
Chao Wang,
Shanghai Jiao Tong University, China

REVIEWED BY
Lanlan Chen,
Charité University Medicine Berlin, Germany
Mingming Zhang,
Central South University, China

*CORRESPONDENCE
Yi Wu
306406@hospital.cqmu.edu.cn

RECEIVED 09 April 2025
ACCEPTED 16 June 2025
PUBLISHED 03 July 2025

CITATION
Qin F, Huan L, Shi X, Hua Y and Wu Y (2025) Analysis of immune cell infiltration in the tumor microenvironment of cervical cancer and its impact on immunotherapy. *Front. Oncol.* 15:1608597. doi: 10.3389/fonc.2025.1608597

COPYRIGHT
© 2025 Qin, Huan, Shi, Hua and Wu. This is an open-access article distributed under the terms of the Creative Commons Attribution License (CC BY). The use, distribution or reproduction in other forums is permitted, provided the original author(s) and the copyright owner(s) are credited and that the original publication in this journal is cited, in accordance with accepted academic practice. No use, distribution or reproduction is permitted which does not comply with these terms.

Analysis of immune cell infiltration in the tumor microenvironment of cervical cancer and its impact on immunotherapy

Fei Qin[1], Lu Huan[2], Xia Shi[1], Yuanyuan Hua[1] and Yi Wu[1]*

[1]Department of Gynecology and Obstetrics, The Second Affiliated Hospital of Chongqing Medical University, Chongqing, China, [2]Renji Hospital, School of Medicine, Chongqing University, Chongqing, China

Background: Cervical cancer remains a leading cause of cancer-related mortality among women worldwide. Despite advances in vaccination and early screening, late-stage diagnoses are common and associated with poor outcomes. This study aimed to identify novel prognostic biomarkers and therapeutic targets through a multi-omics approach, providing insights into the tumor immune microenvironment.

Methods: We integrated transcriptomic, mutational, and clinical data from The Cancer Genome Atlas (TCGA) and Gene Expression Omnibus (GEO) to construct a prognostic model. Differential gene expression, enrichment analysis, immune infiltration profiling, and drug response prediction were performed to explore molecular features and therapeutic relevance.

Results: Key high-risk biomarkers (EZH2, PCNA, BIRC5) and protective factors (CD34, ROBO4, CXCL12) were identified. The model effectively stratified patient survival in both cohorts and showed strong predictive performance. High-risk patients displayed distinct immune cell infiltration patterns and upregulated immune checkpoint expression, suggesting potential benefit from immunotherapy. Additionally, higher tumor mutational burden (TMB) was associated with improved survival. Drug sensitivity analysis indicated increased responsiveness of high-risk patients to agents such as Afuresertib and Venetoclax.

Conclusion: This study establishes a reliable prognostic model and identifies critical biomarkers associated with cervical cancer progression, offering valuable insights into personalized therapeutic strategies. The findings contribute to a more comprehensive understanding of the disease and provide a foundation for future clinical applications. Nevertheless, further large-scale validation is required to confirm these findings and enhance their clinical utility.

KEYWORDS

cervical cancer, multi-omics analysis, immune infiltration, tumor mutation burden, tumor microenvironment

1 Introduction

Cervical cancer presents a significant global public health issue for women, as it stands as the fourth most common gynecological malignancy, thereby representing a major health concern on an international level (1). In 2020, approximately 604,000 new instances of cervical cancer were reported, resulting in around 342,000 deaths worldwide attributed to this malignancy (2). The predominant contributors to cervical cancer are widely acknowledged to be persistent infection with human papillomavirus (HPV) and the failure to eliminate the virus effectively (3). The timely administration of the HPV vaccine has proven to be an efficient preventative measure against cervical cancer (4, 5). However, it is important to note that this vaccine does not eradicate existing HPV infections (6). Furthermore, current treatment modalities, which include a combination of established methods such as radiotherapy, chemotherapy, and surgical excision, are often hampered by undesirable side effects and show limited efficacy in managing advanced disease stages (7). Despite progress in vaccination and early detection techniques, the rate of cervical cancer remains alarmingly elevated, particularly among patients diagnosed at later stages, who exhibit poor survival rates. This underscores an urgent need for innovative diagnostic and therapeutic strategies to enhance patient outcomes.

Recent research underscores the complex interactions between cancer and the immune microenvironment, indicating that both immune cells and tumor cells participate in dynamic exchanges that significantly affect tumor progression (8–10). A disruption in these interactions plays a pivotal role in tumorigenesis, with all cancer types displaying a shared characteristic of evading immune detection (11). Within this changing context, immunotherapy has emerged as a notable breakthrough, especially following the sanctioning of programmed cell death protein 1 (PD-1) inhibitors for the treatment of recurrent or metastatic cancers (12). Specifically, the US Food and Drug Administration (FDA) approved pembrolizumab for patients with recurrent and advanced-stage cervical cancer in 2021 (13). Additionally, the European Medicines Agency (EMA) made a similar decision in 2022, endorsing Cemiplimab due to its significant effect on overall survival rates in cervical cancer patients, which revealed a median survival of 12.0 months versus 8.5 months, accompanied by a hazard ratio of 0.69 (14). This highlights the promise of immunotherapeutic approaches in addressing the immunological evasion tactics employed by tumors. However, existing analyses often focus on individual omics datasets, lacking a robust integration of multi-omics methodologies. Thus, there is an urgent need for a thorough examination of various omics dimensions —including genomics, transcriptomics, and proteomics—to enhance our understanding of the molecular characteristics and underlying mechanisms of cervical cancer. By leveraging multi-omics data, researchers aspire to identify novel prognostic biomarkers and therapeutic targets that could facilitate personalized treatment approaches and improve clinical outcomes for patients.

Despite growing interest in immune-related prognostic models for cervical cancer, existing studies still exhibit key limitations. For instance, Yao et al. (15) constructed a transcriptomics-based immune score but did not incorporate genomic mutations or drug sensitivity. Chen et al. (16) focused on immune subtypes and ICI scores but lacked interpretable modeling of individual gene contributions. Lin et al. (17) proposed a predictive signature for immunotherapy efficacy, yet omitted tumor mutational burden (TMB) and multi-omics integration. Similarly, Wang et al. (18) analyzed immune-related lncRNA pairs, but their work remained limited to transcriptomic data with no exploration of model transparency. In contrast, our study addresses these limitations by establishing a comprehensive and interpretable model that integrates multi-omics data and provides actionable insights into prognosis and therapy.

To address these gaps, we developed a comprehensive and interpretable prognostic model for cervical cancer by integrating transcriptomic, mutational, and clinical data from TCGA and GEO cohorts. Our approach incorporates SHapley Additive exPlanations (SHAP) to assess the contribution of each gene to risk prediction, thereby enhancing the transparency and biological interpretability of the model. Beyond model construction, we further examined the relationship between the SHAP-defined risk score and tumor immune cell infiltration, tumor mutational burden (TMB), and potential response to immune checkpoint inhibitors and chemotherapeutic agents. This integrative framework not only improves the accuracy of prognostic prediction but also provides valuable insights into individualized treatment strategies and potential therapeutic targets for cervical cancer patients.

2 Materials and methods

2.1 Data available source

The expression profiles along with clinicopathological parameters were sourced from The Cancer Genome Atlas (TCGA). Furthermore, the Gene Expression Omnibus (GEO) dataset GSE30759 was employed for our analysis (19, 20). Relevant URLs for online resources and analytical tools have been carefully included in the context to facilitate convenient access.

2.2 Data collection and differentially expressed genes

Gene expression, clinical, and mutation datasets were sourced from TCGA repository. Notably, the DEG analysis in this study utilized the paired tumor-normal tissue samples available in TCGA,

Abbreviations: DEG, Differentially expressed gene; TMB, tumor mutation burden; HPV, human papillomavirus; PD-1, programmed cell death protein 1; TCGA, The Cancer Genome Atlas; GEO, Gene Expression Omnibus; FPKM, Fragments Per Kilobase of transcript per Million mapped reads; MAF, Mutation Annotation Format; GO, Gene Ontology; KEGG, Genes and Genomes; LASSO, Least Absolute Shrinkage and Selection Operator; ICIs, Immune Checkpoint Inhibitors; GDSC, Genomics of Drug Sensitivity in Cancer; IC, Inhibitory Concentration; PCA, Principal Component Analysis; SHAP, SHapley Additive exPlanations; SNN, Shared Nearest Neighbor.

but did not incorporate normal tissue data from the Genotype-Tissue Expression (GTEx) project, which provides a broader reference for gene expression in healthy tissues. The expression data were available in Fragments Per Kilobase of transcript per Million mapped reads (FPKM) format and were $\log_2$-transformed using the formula $\log_2(\text{FPKM} + 1)$ prior to downstream analysis to stabilize variance and improve comparability. Clinical details, including patient demographics, tumor staging, treatment regimens, and survival data—were also extracted. Additionally, the GEO database, part of the National Center for Biotechnology Information (NCBI), was queried using the term "Cervical Cancer Survival" to obtain relevant datasets, notably GSE30759. GSE30759 was selected after stringent criteria, including a large sample size (n=292), consistent clinical staging (covering stages I-IV), and technical alignment with TCGA (Affymetrix GPL570 platform), to ensure cross-cohort comparability in gene expression profiling. Each dataset encompassed clinical sample information reflecting a range of disease states, and the GPL platform included gene probes associated with the expression matrix. Subsequently, the total sample count and staging for each dataset were compiled and cataloged. For the GSE30759 dataset, quantile normalization was performed using the normalizeBetweenArrays function in the limma package to ensure consistency in expression scale. Importantly, the TCGA and GEO datasets were used separately as the training and validation cohorts, respectively; thus, batch effect correction across datasets was not applied. This design avoids artificial variance introduced by inter-cohort integration and enables robust external validation. The limma R package was utilized to determine DEGs between tumor and normal tissue samples across both TCGA and GEO datasets. Statistical evaluations were performed using either t-tests or ANOVA, contingent on the distribution of the data. Genes were deemed significantly differentially expressed if they satisfied the criteria of $|\log_2 \text{fold change}| > 1$ and a p-value < 0.05.

2.3 Functional enrichment analysis

In order to investigate the biological functions associated with the DEGs identified, we conducted enrichment analyses utilizing Gene Ontology (GO) and the Kyoto Encyclopedia of Genes and Genomes (KEGG) pathways through the clusterProfiler R package. Significance was determined based on a p-value threshold of less than 0.05. The HALLMARK gene set utilized in our study was sourced from the MSigDB database, and the Gene Set Enrichment Analysis (GSEA) was executed on the differentially expressed genes distinguishing high-risk from low-risk groups, also employing the "clusterProfiler" package. For visualization purposes, the "GseaVis" R package was implemented.

2.4 Prognostic genes and model

A univariate Cox regression analysis was conducted utilizing the survival R package to pinpoint genes linked to prognosis. Genes exhibiting a p-value of less than 0.05 were designated as potential prognostic biomarkers. Subsequently, these candidates underwent further validation via multivariate Cox regression analysis to ascertain independent prognostic factors. To create a prognostic risk model, the Least Absolute Shrinkage and Selection Operator (LASSO) regression technique was employed, which aids in the selection of crucial prognostic genes while mitigating the risk of overfitting. The glmnet R package facilitated the construction of the model. The risk score for each patient was computed based on the following formula:

Risk Score=∑i=1n(Coefficient of Genei×Expression Level of Genei)\text{Risk Score = \sum_{i=1}^{n} (\text{Coefficient of Gene}_i \times \text{Expression Level of Gene}_i)Risk Score=i=1∑n(Coefficient of Genei×Expression Level of Genei).

Moreover, to determine whether the risk score was an independent prognostic factor, multivariate Cox regression analysis was conducted while adjusting for clinical covariates such as age, gender, and tumor stage.

2.5 Model interpretation with SHapley Additive exPlanations analysis

In order to determine the importance of a specific attribution within the ensemble tree framework, the concept of gain is frequently utilized. Gain quantifies the overall reduction in loss that can be attributed to all the splits associated with the given attribution (21). However, the limitations of gain were emphasized by Lundberg, Erion, and Lee (22). To address these issues, Lundberg (23) introduced the Shapley value to measure the importance of various predictors. This approach suggests that the relevance of a specific predictor might diminish, even when the models increasingly rely on it. Named after the economist who proposed it, the Shapley value provides an equitable method for distributing gains among multiple contributors based on their respective contributions (24).

2.6 Survival analysis, ROC curve, and nomogram construction

In order to develop the nomogram, a multivariate Cox proportional hazards regression analysis was executed, which integrated clinical parameters such as age, sex, tumor stage, tumor grade, and a calculated risk score. The model was fitted utilizing the "cph" function available in the "rms" package. The nomogram was constructed based on the regression coefficients obtained from the Cox model, aimed at forecasting overall survival (OS) at 1, 3, and 5 years. Each clinical variable was allocated a score reflecting its influence on the predictive model, and the total of these scores yielded an overall score that estimates the probability of survival. Additionally, Kaplan-Meier survival analysis was performed through the survival R package to evaluate the survival outcomes between high-risk and low-risk cohorts. Receiver Operating Characteristic (ROC) curves were generated, and the Area Under the Curve (AUC) was computed to evaluate the predictive accuracy of the model.

2.7 Immune cell infiltration analysis

The ESTIMATE R package (25) (https://r-forge.r-project.org/projects/estimate/, accessed on May 19, 2024) was employed to derive the sample matrix score, immune score, and tumor purity. Furthermore, immune cell infiltration and the tumor microenvironment (TME) were assessed utilizing the CIBERSORT (26), TIMER (27), and ssGSEA (28) algorithms. The relationship between the risk score and immune checkpoint expression was analyzed through the Tumor and Immune System Interaction Database (TISIDB) (http://cis.hku.hk/TISIDB, accessed on May 22, 2024). Additionally, various methods for analyzing immune infiltration were applied to investigate the composition and distribution of immune cells between high- and low-risk groups within TCGA datasets.

2.8 Tumor mutational burden analysis

TMB was assessed utilizing mutation data from TCGA and is characterized as the aggregate count of somatic mutations per megabase of genomic sequence. An evaluation of the correlation between TMB and patient outcomes was conducted. For each patient within both the training and validation cohorts, TMB was established from somatic mutation data, subsequently categorizing patients into high-risk and low-risk groups according to the median TMB value.

2.9 Drug sensitivity prediction, immune escape and immunotherapy response analysis

Data derived from TCGA were scrutinized to evaluate the mutation frequencies of genes within high-risk and low-risk patient cohorts. Subsequently, the TIDE (29) algorithm (http://tide.dfci.harvard.edu/, accessed on May 26, 2024) was employed to predict the response of risk scores to Immune Checkpoint Inhibitors (ICIs). In addition, the Genomics of Drug Sensitivity in Cancer (GDSC) database (https://www.cancerrxgene.org/, accessed on May 28, 2024) was leveraged to assess the sensitivity of individual samples to various chemotherapy agents, utilizing the pRRophetic package to analyze and compare the half-maximal inhibitory concentration (IC50) values of these pharmacological agents (30, 31) (https://github.com/paulgeeleher/pRRophetic, accessed on May 28, 2024).

2.10 Statistical analysis

Survival disparities across different risk categories were evaluated utilizing Kaplan-Meier (KM) survival analysis. Predictive models were constructed employing both LASSO regression and Cox regression methodologies. All data processing and statistical evaluations were conducted using R software (version 4.3.2), with a significance threshold established at $p < 0.05$. Additionally, significance levels were defined as follows: $p < 0.05$ (*), $p < 0.01$ (**), and $p < 0.001$ (***). A p-value < 0.05 was chosen for analyzing drug sensitivity.

2.11 Single-cell RNA-seq analysis and intercellular communication inference

Single-cell RNA sequencing data from cervical cancer samples were obtained from the GEO database (GSE168652) (32). Raw count data were processed using the Seurat R package (v4.3.0). Cells with fewer than 50 detected genes or over 5% mitochondrial gene expression were excluded. The data were log-normalized, and 1,500 highly variable genes were identified. Dimensionality reduction was performed via PCA and t-SNE, followed by clustering using a shared nearest neighbor (SNN) algorithm with a resolution of 0.5. Marker genes were identified using the Wilcoxon rank-sum test (logFC > 1, adjusted $p < 0.05$). Cell types were annotated using the SingleR package with the Human Primary Cell Atlas as a reference, supplemented by manual validation based on canonical markers. The expression patterns of key prognostic genes (EZH2, CXCL12, PCNA, BIRC5, et al.) were assessed across clusters using violin plots, dot plots, and feature scatter maps. To investigate intercellular communication, CellPhoneDB (v2.1.7) was employed to predict significant ligand–receptor interactions among cell types. Interaction frequency and strength were visualized, highlighting key immunomodulatory pathways such as LGALS9–CD44. All analyses were performed using standard functions in Seurat, SingleR, and CellPhoneDB.

3 Results

3.1 Differential gene expression highlights immune-related alterations in the tumor microenvironment and enrichment analysis

To investigate the molecular characteristics associated with immune cell infiltration in cervical cancer, we conducted differential gene expression analysis between tumor and normal cervical tissue samples. As shown in Figure 1, the circular heatmap demonstrated a distinct separation between the two groups. Tumor samples exhibited significantly elevated expression of multiple immune- and inflammation-related genes, including MMP9, TNF, and members of the S100A family. These genes were previously reported to be involved in immune activation, cytokine signaling, and remodeling of the tumor microenvironment. The observed clustering pattern suggested that cervical cancer tissues possessed a distinct transcriptional profile enriched in immune-associated pathways, which may contribute to the altered immune cell composition and influence the effectiveness of immunotherapy.

To further explore the biological significance of DEGs in the context of immune cell infiltration, we performed GO and KEGG enrichment analyses. GO analysis (Figures 2a–c) revealed that the

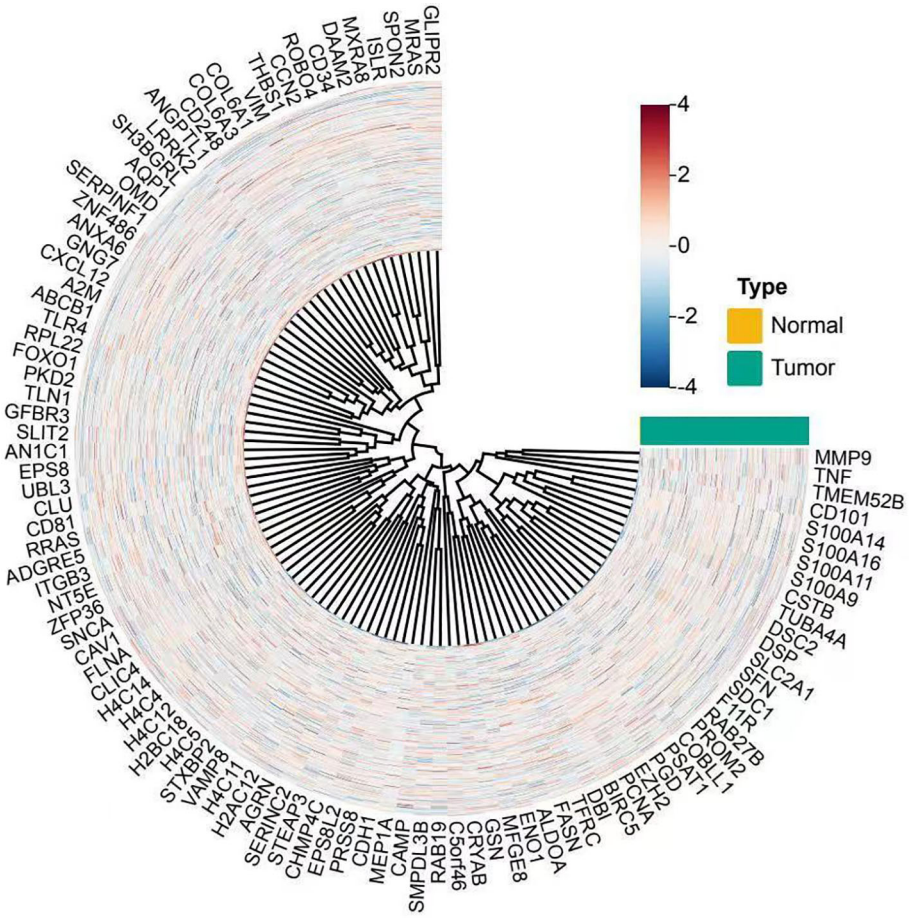

FIGURE 1
Circular heatmap showing differential gene expression between norml and tumor cervical tissue samples. Each spoke represents a gene, and each ring represents a sample. Samples are annotated by type, with normal tissues in yellow and tumor tissues in teal. Gene expression values are normalized and scaled (z-score), with red indicating higher and blue indicating lower expression levels. The clustering reveals distinct gene expression profiles between tumor and normal tissues, with upregulated genes such as MMP9, TNF, and S100A family prominently clustered in tumor samples.

DEGs were significantly enriched in immune-related biological processes such as nucleotide metabolic processes, pyridine-containing compound metabolism, and extracellular matrix organization. Many of these terms were also functionally clustered, as shown in the hierarchical dendrogram, suggesting coordinated regulation within immune and metabolic pathways. KEGG pathway analysis (Figure 2d) indicated significant enrichment in pathways associated with tumor progression and immune modulation, including the HIF-1 signaling pathway, ECM-receptor interaction, and proteoglycans in cancer. The Sankey diagram (Figure 2e) further illustrated that several core genes were involved in multiple immune- and microenvironment-associated pathways, highlighting their potential role in shaping the tumor immune landscape and influencing immunotherapy responsiveness. To further explore the biological significance of DEGs in the context of immune cell infiltration, we performed GO and KEGG enrichment analyses. GO analysis (Figures 2a–c) revealed that the DEGs were significantly enriched in immune-related biological processes such as nucleotide metabolic processes, pyridine-containing compound metabolism, and extracellular matrix organization. Many of these terms were also functionally clustered, as shown in the hierarchical dendrogram, suggesting coordinated regulation within immune and metabolic pathways. KEGG pathway analysis (Figure 2d) indicated significant enrichment in pathways associated with tumor progression and immune modulation, including the HIF-1 signaling pathway, ECM-receptor interaction, and proteoglycans in cancer. The Sankey diagram (Figure 2e) further illustrated that several core genes were involved in multiple immune- and microenvironment-associated pathways, highlighting their potential role in shaping the tumor immune landscape and influencing immunotherapy responsiveness.

3.2 Clustering analysis of risk groups and prognosis-related differential genes

The Principal Component Analysis (PCA) visualization reveals a prominent separation between high-risk and low-risk cohorts across the principal components, indicating inherent variability in

10.3389/fonc.2025.1608597

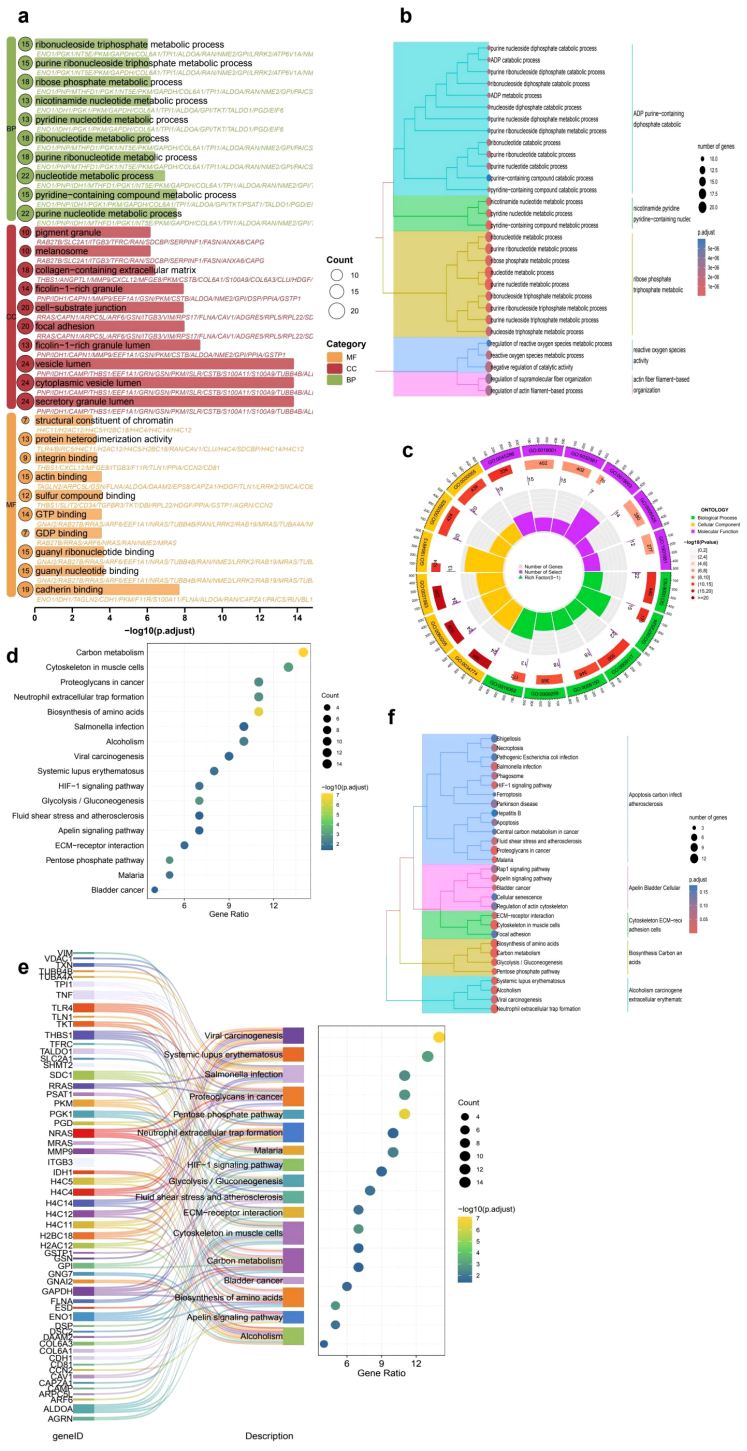

FIGURE 2
Functional enrichment analysis of differentially expressed genes (DEGs) in cervical cancer. **(a)** GO enrichment bubble plot displaying top significantly enriched terms across Biological Process (BP), Cellular Component (CC), and Molecular Function (MF) categories. Bubble size represents the number of genes, and color indicates the GO category. **(b)** Hierarchical clustering of enriched GO terms illustrating the relationship among biological processes. **(c)** Circular visualization of GO categories, highlighting the functional distribution and classification of enriched terms. **(d)** KEGG pathway enrichment analysis showing key tumor-related and immune-associated pathways such as ECM-receptor interaction, HIF-1 signaling, and proteoglycans in cancer. **(e)** Sankey plot linking DEGs to enriched KEGG pathways, demonstrating the multifunctional involvement of core genes in immune and metabolic processes. **(f)** Hierarchical clustering of KEGG pathways demonstrating modular associations among functionally related processes, including glycolysis/gluconeogenesis, neutrophil extracellular trap formation, and extracellular matrix remodeling, which may jointly influence tumor progression and immune dynamics.

gene expression profiles (Figure 3a). In a similar vein, both t-SNE and UMAP (Figures 3b, c) visualizations exhibit effective clustering, thereby reinforcing the notion that the model is capable of distinguishing between risk categories based on gene expression patterns. The prognostic evaluation uncovered numerous differentially expressed genes linked to survival outcomes. Notable genes such as ENO1, PGK1, NT5E, and RRAS displayed hazard ratios exceeding 1, implying potential risk correlations. In contrast, genes CAMP and MAN1C1 presented hazard ratios lower than 1, suggesting possible protective roles (Figure 3d).

3.3 Prognostic model

The datasets from TCGA and GEO have been classified into high-risk and low-risk categories utilizing a predetermined cutoff threshold. Simultaneously, TCGA serves as the training dataset, while GEO functions as the validation dataset. An examination of the TCGA dataset indicates a marked difference in overall survival rates between the high-risk and low-risk cohorts, with a p-value that is less than 0.001 (HR = 0.2, 95% CI: 0.11 - 0.36, p = 6.53e-08. Figure 3e). Similarly, the GEO dataset demonstrates a significant difference in survival outcomes between these two categories, yielding a p-value of 0.013 (HR = 0.34, 95% CI: 0.13 - 0.91, p = 0.0313. Figure 3f), thereby reinforcing the validity of the prognostic model.

3.4 Independent prognostic analysis and model performance evaluation

The univariate analysis highlights a notable correlation between the riskScore and patient prognosis (p = 0.006), with a calculated hazard ratio of 2.317 (Figure 4a). Additionally, the multivariate analysis corroborates the significance of both riskScore (p = 0.003) and T stage (p = 0.018) as independent prognostic indicators, each exhibiting hazard ratios of 3.100 and 3.741, respectively (Figure 4b). The time-dependent ROC analysis indicates that the predictive model consistently achieves an AUC of 0.809 (95% CI: 0.728–0.890) at one year, 0.800 (95% CI: 0.705–0.882) at three years, and 0.798 (95% CI: 0.694–0.875) at five years, reflecting its stable and dependable predictive capacity (Figure 4c). Furthermore, a comparative ROC analysis demonstrates that the risk model (AUC = 0.809) outperforms other clinical parameters, including Age (AUC = 0.577), Grade (AUC = 0.502), T stage (AUC = 0.692), and N stage (AUC = 0.500) (Figure 4d).

3.5 Clinical associations, nomogram construction, and predictive accuracy

The amalgamation of clinical parameters and prognostic indicators plays a pivotal role in evaluating patient outcomes. The clinical correlation heatmap illustrates the allocation of risk categories across a range of factors, including Age (≤65y, >65y), Grade (G1-G4, unknown), Stage (I-IV, unknown), T classification (T1-T4, unknown), M classification (M0, M1, unknown), and N classification (N0, N1, unknown). This stratification unveils notable associations between high-risk and low-risk groups with these clinical variables, highlighting their potential prognostic significance (Figure 4e). In addition, the nomogram functions as an advanced instrument that consolidates various prognostic factors to predict survival probabilities at intervals of 1, 3, and 5 years. Points are allocated based on individual risk profiles, thereby enhancing the precision of personalized predictions (Figure 4f). The robustness of this model is reinforced by calibration curves demonstrating a strong alignment between the predicted and actual survival rates, thereby affirming its credibility (Figure 4g). Furthermore, ROC curves reveal a high level of predictive accuracy, with AUC values recorded at 0.816, 0.873, and 0.842 for the 1-, 3-, and 5-year survival rates, respectively, showcasing the model's superior discrimination ability (Figure 4h).

3.6 SHAP analysis

The SHAP analysis offers critical insights into the significance of features and their contributions to the predictive capabilities of the model. The accompanying bar plot (Figure 5a) clearly illustrates that features such as CHMP4C, ATP13A2, and ALDOA exhibit the highest mean absolute SHAP values, thereby signifying their substantial impact on the model's predictions. Further examination through the bee plot (Figure 5b) delineates the relationship between varying feature values—especially for CHMP4C and ATP13A2—and their corresponding SHAP values, underscoring their pivotal roles in influencing the model's outcomes. The force plot (Figure 5c) provides a detailed breakdown of an individual prediction, revealing that VDAC1, with a SHAP value of 6.38, alongside DAAM2, which contributes a lesser amount of 0.46, exerts significant positive influences that drive the prediction closer to its final value of 11.6. In a similar vein, the waterfall plot (Figure 5d) conveys the cumulative impact of each feature, showcasing how elements such as TNF, TFRC, and ALDOA either positively or negatively affect the predicted outcome, thereby highlighting their critical importance in the decision-making process of the model.

3.7 Immune cell infiltration and functional alterations

Our investigation into the infiltration of immune cells and the functional variations between low- and high-risk cohorts revealed substantial differences in immune cell composition and associated processes (Figure 6a). In particular, we noted a significant enrichment of CD8+ T cells, M1 macrophages, and activated dendritic cells within one of the groups, indicating their pivotal involvement in tumor immunity. In contrast, M2 macrophages and naive B cells presented an opposing trend, which could suggest the existence of immunosuppressive mechanisms (Figure 6b). Additionally, we defined crucial immune functions that displayed

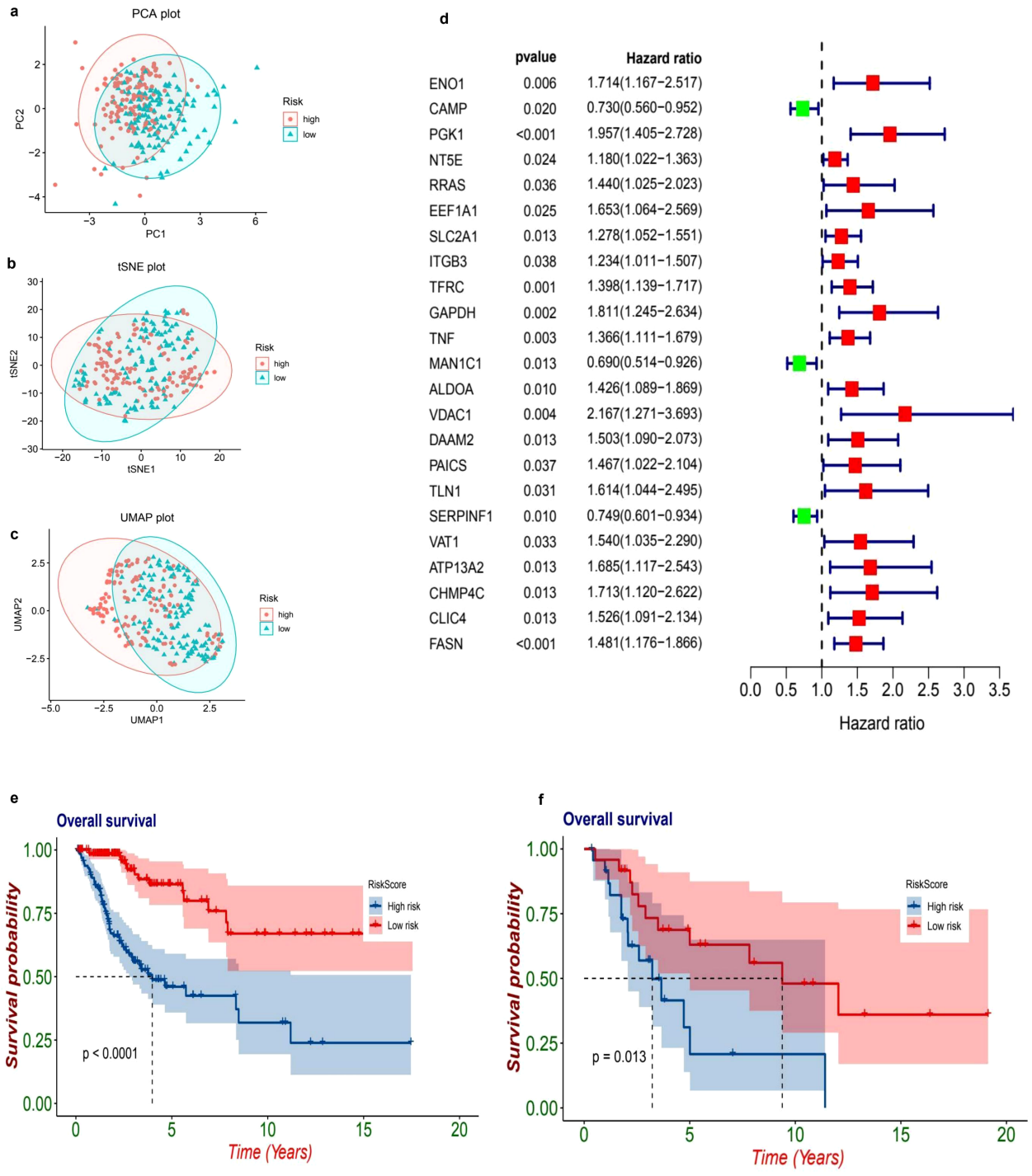

FIGURE 3
Risk stratification and survival analysis of patients based on gene expression profiles. The dimensionality reduction plots illustrate the distribution of patients based on their risk levels. In the first plot **(a)**, a Principal Component Analysis (PCA) is presented, showcasing how patients categorized as high-risk (marked in red) and low-risk (marked in blue) are distributed across the first two principal components, PC1 and PC2. Following this, the t-Distributed Stochastic Neighbor Embedding (t-SNE) plot **(b)** visualizes the separation of these high-risk and low-risk groups based on their gene expression profiles, highlighting distinct clusters. The Uniform Manifold Approximation and Projection (UMAP) plot **(c)** further emphasizes the clustering of high-risk and low-risk groups in a two-dimensional space, providing additional clarity on their separation. Moving to the forest plot **(d)**, this univariate Cox regression analysis presents hazard ratios (HR) and 95% confidence intervals (CI) for key genes linked to patient prognosis. In this plot, red squares indicate significant high-risk genes (with HR greater than 1), while green squares represent protective genes (with HR less than 1). The Kaplan-Meier survival curves **(e, f)** provide further insights into patient outcomes, with plot **(e)** comparing overall survival rates between high-risk (red) and low-risk (blue) patients, revealing a significant difference ($p < 0.001$) where high-risk patients show poorer survival outcomes. Lastly, plot **(f)** presents a subgroup survival analysis that reinforces the significant survival difference ($p = 0.024$) between the risk groups, further validating the prognostic value of the risk model.

10.3389/fonc.2025.1608597

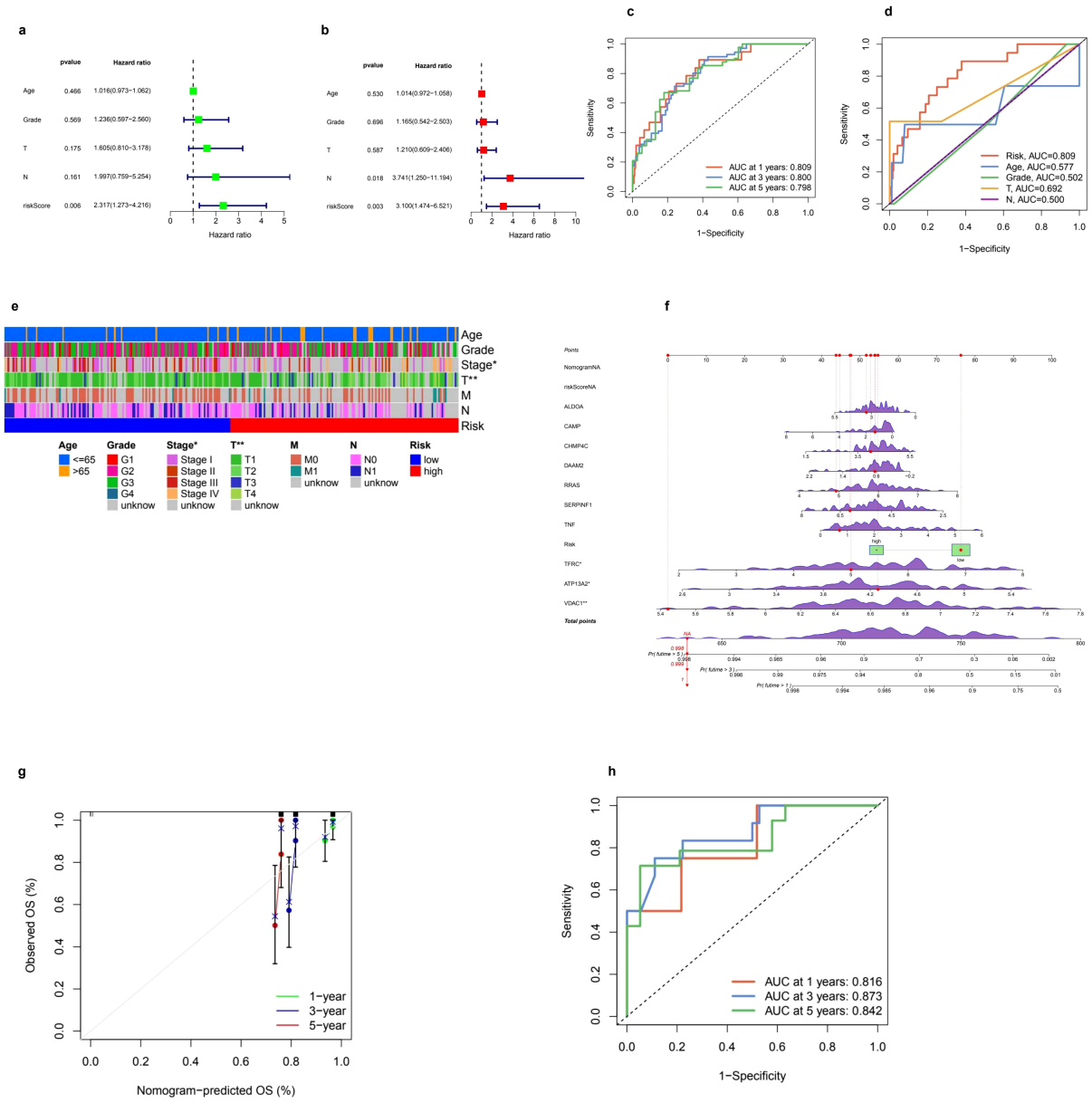

FIGURE 4
Prognostic model performance and clinical correlations. **(a, b)** Univariate and multivariate Cox regression analyses were conducted to evaluate clinical variables such as age, grade, TNM staging, and risk score in relation to overall survival (OS). The univariate analysis provided hazard ratios (HR) along with 95% confidence intervals (CI) for these variables. In the multivariate analysis, independent prognostic factors for OS were identified, confirming that the risk score remains a significant predictor even after adjusting for other clinical factors. **(c)** Additionally, receiver operating characteristic (ROC) curves were utilized to assess the prognostic performance of the model over time. The time-dependent ROC curves illustrated the model's predictive ability at 1, 3, and 5 years, accompanied by corresponding area under the curve (AUC) values. **(d)** Furthermore, ROC curves were compared to evaluate the predictive accuracy of the risk score against clinical parameters, highlighting the risk score's superior prognostic value. **(e)** A clinical heatmap was generated to visualize the distribution of clinical characteristics, including age, grade, and TNM stage, across low-risk and high-risk groups, with different colors representing various categorical clinical features. The mutation landscape of key prognostic genes was depicted through a waterfall plot, where red markers indicated significant mutations and green boxes highlighted key mutation hotspots. **(f)** Lastly, the calibration and validation of the nomogram were assessed, with a calibration plot illustrating the accuracy of the nomogram's predicted OS at 1, 3, and 5 years; **(g)** points closer to the diagonal line indicated better predictive performance. **(h)** The ROC curve for nomogram validation further demonstrated its discriminative power at the specified time points of 1, 3, and 5 years.

marked differences between the two groups. These included the co-stimulation and inhibition of antigen-presenting cells (APCs), cytolytic activity, pro-inflammatory responses, and checkpoint activation (Figure 6c). The distinct patterns observed in T cell co-stimulation and inhibition, alongside type I/II interferon responses and the activity of macrophages and neutrophils, suggest potential imbalances in immunoregulation that might correlate with our risk classification. These results underscore the complex interactions of

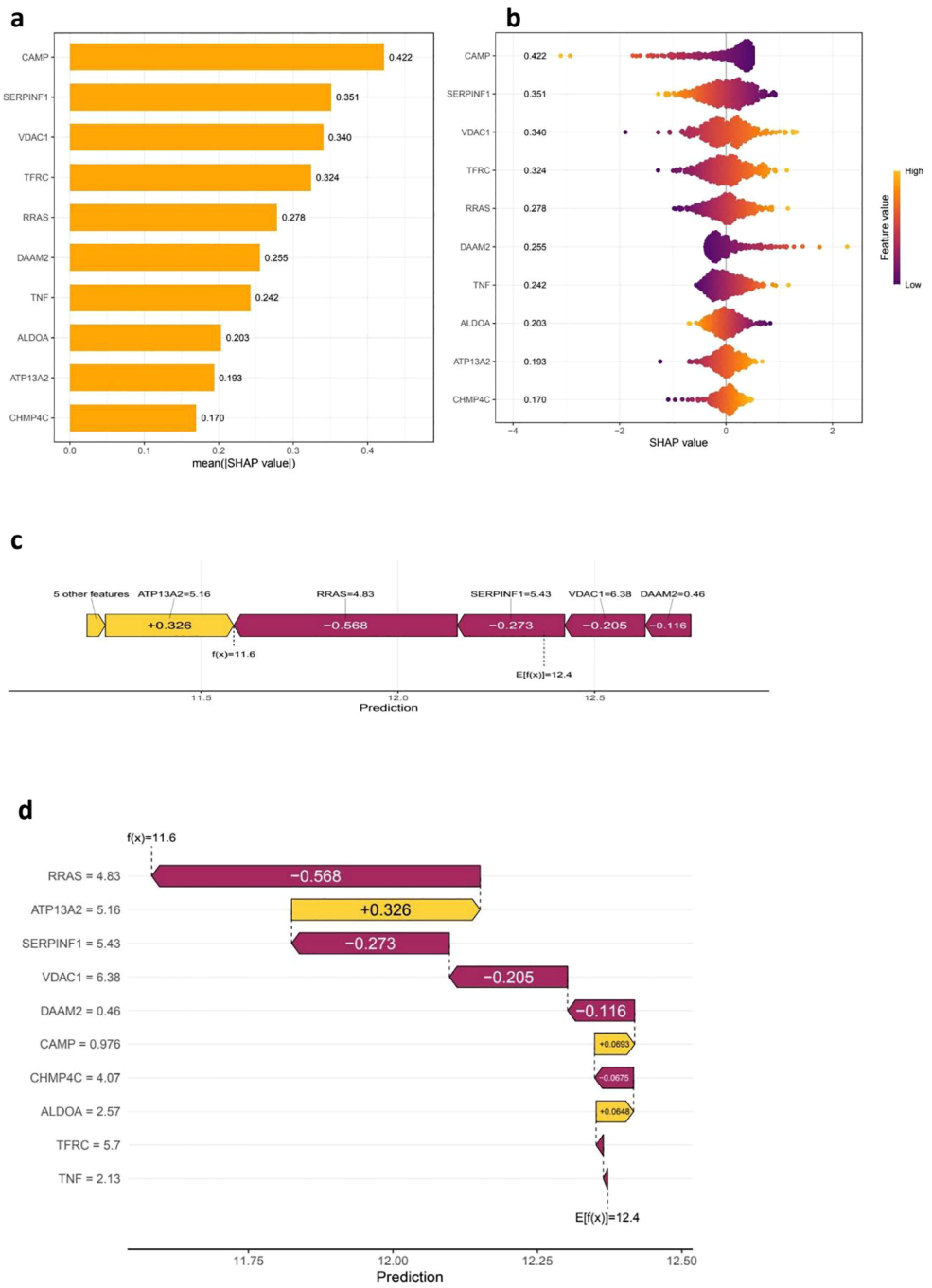

FIGURE 5
SHAP analysis for feature Importance and model interpretability. The **(a, b)** SHAP Summary Plots provide insights into feature importance by illustrating the mean absolute SHAP values, which reflect the overall contribution of each feature, or gene, to the model's predictions. Features with higher mean absolute SHAP values are deemed more influential, with CAMP, SERPINF1, and VDAC1 identified as the top contributors. Additionally, the SHAP value distribution plot reveals how each feature impacts the model's output, utilizing a color gradient to represent feature values—yellow indicates high values while purple signifies low values. This visualization highlights a clear trend in how the expression of these features influences risk predictions. Moving on to **(c, d)**, the SHAP Force and Waterfall Plots provide a closer look at individual predictions. The SHAP force plot illustrates how various features contribute to a specific patient's prediction, where positive SHAP values increase the prediction, while negative values decrease the predicted risk score. The SHAP waterfall plot further breaks down the cumulative contribution of individual features to the final prediction score, detailing the model's decision-making process and showcasing the relative impact of genes such as RRAS, ATP13A2, and SERPINF1 on the final outcome.

10.3389/fonc.2025.1608597

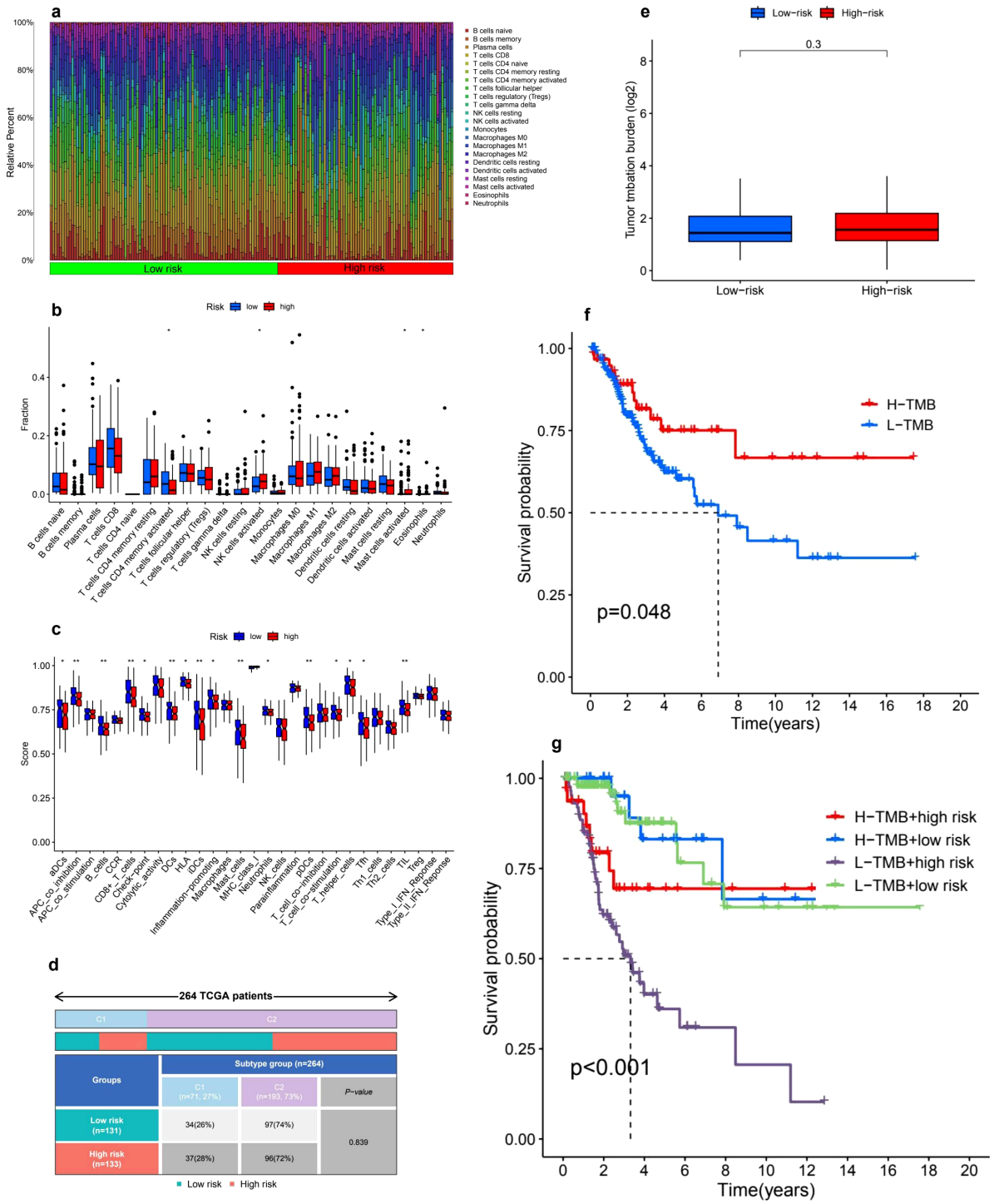

FIGURE 6
Tumor microenvironment and tumor mutation burden (TMB) analysis. **(a)** The analysis of immune cell infiltration distribution reveals notable differences between high-risk and low-risk groups, highlighting the relative abundance of various immune cell types. The color gradient effectively illustrates the diversity of immune cell populations across the samples. **(b)** A boxplot comparison of immune cell fractions between these two risk groups indicates significant differences in immune infiltration levels, with asterisks marking statistically significant differences ($p < 0.05$, $p < 0.01$, $p < 0.001$). **(c)** Furthermore, immune-related functional scores comparing different immune pathways between high-risk and low-risk patients uncover distinct patterns of immunological activity. **(d)** The distribution of risk groups among TCGA patient subtypes illustrates the proportions of low-risk and high-risk patients across various molecular subtypes. **(e)** In terms of tumor mutation burden (TMB), the comparison between the two risk groups shows no statistically significant difference ($p = 0.3$). **(f)** However, the Kaplan-Meier survival curve for high-TMB (H-TMB) and low-TMB (L-TMB) groups indicates that patients with higher TMB tend to experience better survival outcomes ($p = 0.048$). **(g)** Additionally, a combined survival analysis of TMB and risk groups reveals that the L-TMB + high-risk subgroup has the worst survival prognosis, while the H-TMB + low-risk subgroup demonstrates the best outcomes ($p < 0.001$).

immune responses and their relevance in comprehending tumor microenvironments.

3.8 Immune subtype analysis

An immune subtype assessment was performed involving 264 patients from the TCGA cohort, categorized into two distinct immune subtypes: C1 and C2 (Figure 6d). The breakdown of immune subtypes within the low-risk and high-risk stratifications is as follows: Subtype C1 encompassed 71 patients (27%), comprising 34 patients (26%) in the low-risk category and 37 patients (28%) in the high-risk category. Conversely, Subtype C2 included 193 patients (73%), with 97 patients (74%) belonging to the low-risk group and 96 patients (72%) classified as high-risk. The statistical evaluation indicated that there were no significant differences in the distribution of immune subtypes between the low-risk and high-risk groups (P-value = 0.839).

3.9 TMB analysis

The comparison of TMB between low-risk and high-risk groups revealed no significant differences. The TMB values, displayed on a log2-transformed scale, were similar across both groups, suggesting that TMB may not serve as a distinguishing factor for different risk classifications (Figure 6e). However, Kaplan-Meier survival analysis indicated that patients with high TMB (H-TMB) experienced significantly better overall survival compared to those with low TMB (L-TMB), with a P-value of 0.048 (Figure 6f). Furthermore, when TMB status was integrated with risk classification, survival analysis showed significant differences among the four subgroups: H-TMB with high risk, H-TMB with low risk, L-TMB with high risk, and L-TMB with low risk, yielding a P-value of less than 0.001 (Figure 6g).

3.10 Immune evasion and drug sensitivity

The Tumor Immune Dysfunction and Exclusion (TIDE) analysis indicated that individuals in the high-risk group had elevated TIDE scores, which points to a greater potential for immune evasion and suggests they may have a poorer response to ICIs. Conversely, the low-risk group, characterized by lower TIDE scores, appears to be more likely to benefit from ICIs, making them potentially better candidates for immunotherapy (Figure 7a). Furthermore, the analysis of drug sensitivity revealed notable differences in how the low-risk and high-risk groups responded to various medications. Specifically, the high-risk group demonstrated increased sensitivity to several drugs, including Afuresertib ($p = 0.00064$) (Figure 7b), Doramapimod ($p = 0.0003$) (Figure 7c), Navitoclax ($p = 0.0003$) (Figure 7d), Ribociclib ($p = 9.9e{-}07$) (Figure 7e) and Venetoclax ($p = 2.5e{-}06$) (Figure 7f), indicating that the response to these treatments varies significantly based on the risk group.

3.11 Single-cell validation of prognostic genes and cell–cell communication patterns

To validate our bulk RNA-seq findings, we reanalyzed the GSE168652 scRNA-seq dataset and identified three major cell populations: epithelial cells, keratinocytes, and monocytes (Figure 8a). Prognostic genes including EZH2, PCNA, and BIRC5 were specifically expressed in epithelial clusters, while CHMP4C, ATP13A2, and ALDOA showed broader expression patterns (Figures 8b–d), supporting their tumor-specific roles. CellPhoneDB-based communication analysis revealed strong interactions between monocytes and epithelial or keratinocyte cells (Figures 8e, f), with LGALS9–CD44 emerging as a key ligand–receptor pair (Figure 8g), suggesting potential immunoregulatory signaling. These single-cell results confirm the robustness of our signature genes, clarify their cellular origin, and reveal potential crosstalk within the tumor microenvironment that may influence immune response and therapeutic outcomes.

4 Discussion

Cervical cancer remains one of the most prevalent cancers among women worldwide, with annual statistics revealing more than 500,000 new cases and nearly 300,000 deaths attributed to the disease (33, 34). Our study employed comprehensive bioinformatics methods to analyze cervical cancer. Gene expression, clinical, and mutation data from TCGA and GEO were used to identify DEGs through the limma R package. Functional enrichment analysis (GO and KEGG) revealed key biological processes and pathways involved in cancer progression. A prognostic risk model was built using LASSO regression and validated with independent datasets. Notably, the validation cohort (GSE30759, n=292) was rigorously selected for its large sample size, consistent clinical staging (I-IV), and technical compatibility with TCGA (Affymetrix GPL570 platform), ensuring cross-cohort comparability. SHAP analysis transcended conventional model interpretation by quantifying the contribution of individual genes (CHMP4C, ATP13A2, ALDOA) to risk stratification, linking their expression to mechanistic pathways such as endosomal sorting (CHMP4C) and lysosomal function (ATP13A2), which may modulate immune evasion through impaired antigen presentation and exosome-mediated signaling. The model's predictive power was confirmed through survival analysis, ROC curves, and nomogram construction. Additionally, immune cell infiltration analysis highlighted significant differences in the tumor microenvironment between high- and low-risk groups, while TMB and drug sensitivity predictions offered potential therapeutic insights. Together, these findings provide a comprehensive understanding of the molecular, immune, and clinical factors influencing cervical cancer prognosis and treatment.

The findings of this study provide important insights into the DEGs in cervical cancer and their potential impact on patient prognosis. Our results are consistent with previous research, confirming the presence of several well-established DEGs while

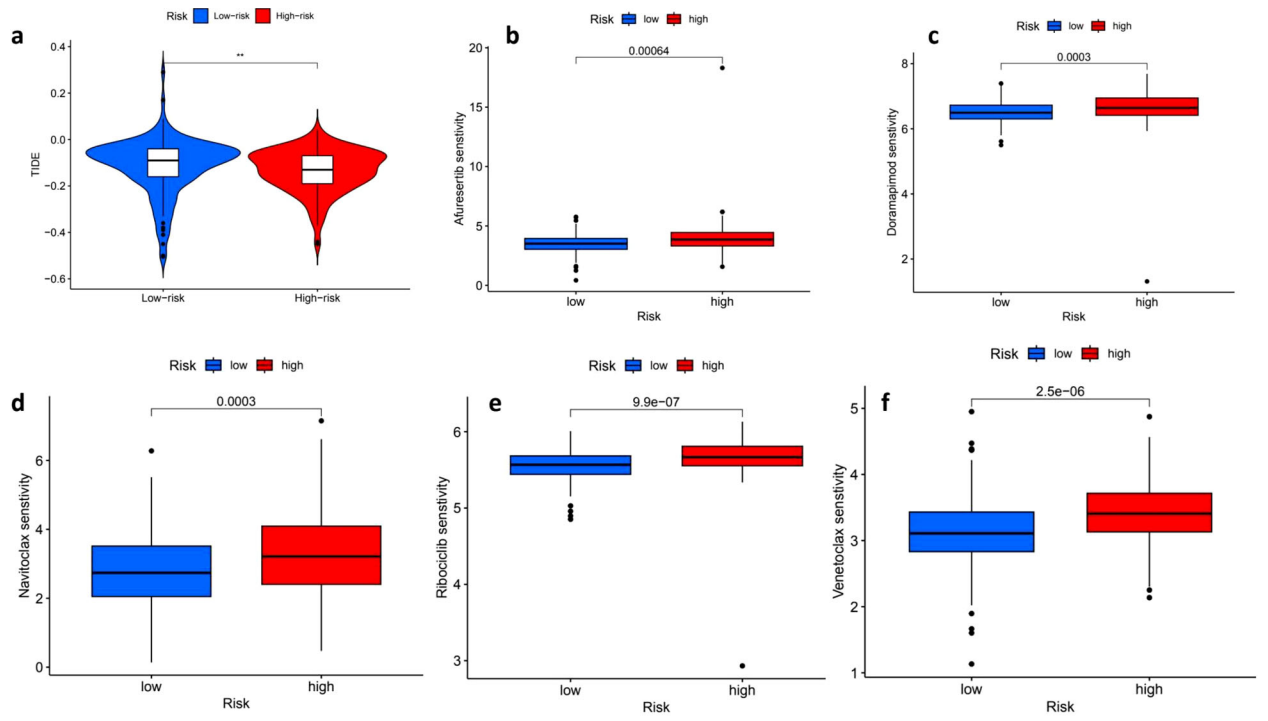

FIGURE 7
Tumor immune dysfunction and exclusion (TIDE) scores and drug sensitivity analysis. The distribution of Tumor Immune Dysfunction and Exclusion (TIDE) scores reveals a stark contrast between low-risk (blue) and high-risk (red) patients, with high-risk individuals exhibiting significantly elevated TIDE scores, which suggests a potential resistance to immune checkpoint blockade therapy ($p < 0.01$). In the context of drug sensitivity analysis across both high- and low-risk groups, several noteworthy findings emerged. For instance, the sensitivity to Alisertib was significantly greater in the high-risk group ($p = 0.00064$), while Doramapimod also demonstrated increased sensitivity among high-risk patients ($p = 0.0003$). Furthermore, a comparison of Navitoclax sensitivity indicated that high-risk patients had significantly higher drug sensitivity ($p = 0.0003$). Conversely, low-risk patients exhibited a higher sensitivity to Ribociclib, with a striking p-value of 9.9e-07. Lastly, the sensitivity to Venetoclax was significantly greater in high-risk patients as well, with a p-value of 2.5e-06, underscoring the complex dynamics of drug sensitivity in relation to patient risk stratification. ** means $p<0.01$.

also identifying new candidates that have not been widely reported in the literature. For example, genes like APOD, ACKR1, and SFRP4 have been recognized as significant in cervical cancer, and our analysis supports their involvement in tumor progression and patient survival, thereby reinforcing their potential as biomarkers in clinical practice. Furthermore, the prognostic model we developed demonstrated greater predictive power compared to those reported by Dong et al. (35, 36), primarily due to our larger sample size and the comprehensive integration of clinical and genomic data, highlighting the robustness of our findings. Multi-omics integration further revealed a molecular landscape characterized by dysregulated cancer metabolism (glycolysis/gluconeogenesis, pentose phosphate pathway) and immune response (HIF-1 signaling, systemic lupus erythematosus pathways), highlighting the interplay between metabolic reprogramming and immune evasion in tumor progression.

Our research identified several high-risk biomarkers, such as EZH2, PCNA, and BIRC5, alongside protective biomarkers like CD34, ROBO4, and CXCL12. Recognizing these biomarkers is crucial as they could assist in the early detection and tailored treatment strategies for patients with cervical cancer. Notably, EZH2 has been linked to tumor progression, and further exploration of its specific mechanisms may shed light on its role in cancer development and enhance our understanding of potential therapeutic targets (37). Moreover, the protective biomarkers could play a significant role in modulating the immune response, suggesting their relevance for immunotherapeutic approaches (33). The interplay of these biomarkers may enhance prognostic accuracy, highlighting the need for further research into their combined effects on predicting patient outcomes. Our established prognostic model demonstrated strong survival stratification capabilities across both the TCGA and GEO datasets, achieving impressive AUC values that underscore its reliability, with AUC values of 0.809 for 1-year, 0.800 for 3-year, and 0.798 for 5-year survival. This high level of accuracy underscores the model's potential application in clinical settings, enabling personalized treatment strategies based on individual risk assessments. Future discussions should focus on the practical application of this model in clinical decision-making, particularly regarding its integration with other clinical indicators to improve predictive performance (38).

As previously acknowledged, CCL5 and CXCL10 serve as crucial signaling bridges between NK cells, T cells, and tumor cells (39). CXCL9, produced by myeloid cells activated through the STING pathway, acts as an intermediary that stimulates the secretion of IFN in T cells, which in turn enhances the expression of CXCL9 in myeloid cells. Furthermore, Li (40) emphasized the

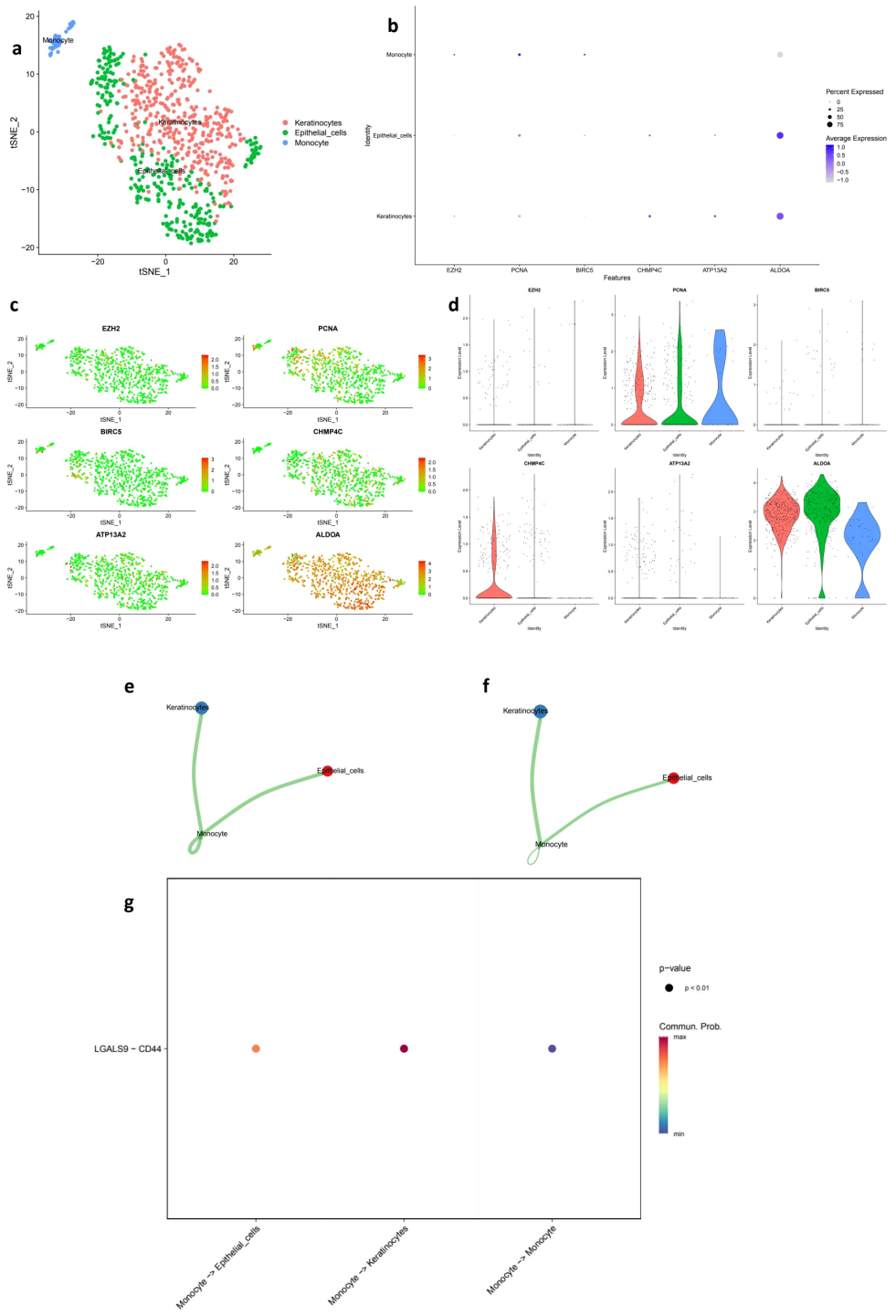

FIGURE 8
Single-cell transcriptomic validation and cell–cell communication analysis of prognostic genes. **(a)** t-SNE plot showing the clustering of single cells from the GSE168652 dataset into three major populations: keratinocytes, epithelial cells, and monocytes. **(b)** Dot plot of hub gene expression (EZH2, PCNA, BIRC5, CHMP4C, ATP13A2, ALDOA) across annotated cell types. Dot size represents the percentage of cells expressing each gene, and color indicates average expression level. **(c)** Feature plots illustrating the spatial distribution of hub gene expression across the t-SNE embedding. **(d)** Violin plots comparing the expression levels of hub genes among different cell populations. **(e)** Cell–cell communication frequency map showing the number of interactions among cell types, with stronger connectivity observed between monocytes and epithelial or keratinocyte populations. **(f)** Communication weight map reflecting the interaction intensity between cell types based on predicted ligand–receptor interactions. **(g)** Bubble plot displaying the statistically significant LGALS9–CD44 ligand–receptor interaction between monocytes and other cell types ($p < 0.01$), highlighting potential immunoregulatory mechanisms in the tumor microenvironment.

significant role of the STING pathway and the potential of MSA-2 in reshaping the immune microenvironment in cervical cancer. However, this study primarily focused on STING agonists and offered limited discussion on other immunotherapies. It also lacked comprehensive multi-omics analysis of immune infiltration and did not delve deeply into the mechanisms of adaptive immune escape. Therefore, gaining a thorough understanding of the interactions between immune microenvironments and therapeutic responses could aid in developing more effective clinical strategies tailored to individual patient profiles, particularly in relation to checkpoint inhibitor therapies (41). Our extensive study revealed a significant link between TMB and improved survival rates, highlighting TMB as a vital prognostic factor in cancer research. The correlation we found between TMB and immunogenicity indicates that patients with higher mutational loads are more likely to respond positively to immunotherapy. This underscores the importance of including TMB assessments in standard clinical practice to enhance patient outcomes. However, it is important to note that the overall TMB distribution did not show statistically significant differences between high-risk and low-risk groups. This finding highlights the intricate and complex nature of tumor biology, suggesting that TMB may serve as an independent prognostic factor, especially within certain risk subgroups, thereby increasing variations in survival outcomes when used in conjunction with risk stratification methods. Notably, high TMB correlated with improved survival ($p = 0.048$), and combined TMB-risk stratification identified subgroups with distinct outcomes, suggesting TMB may serve as an independent prognostic factor when integrated with risk scores (42, 43).

Drug sensitivity predictions revealed the responsiveness of high-risk patients to targeted therapies (Afuresertib, Venetoclax, Navitoclax), which correlates with the activation of PI3K-AKT pathways and BIRC5 overexpression in these subgroups. This highlights the potential of precision oncology approaches, where high-risk patients may derive clinical benefit from targeted agents, while low-risk patients with an immunologically "hot" tumor microenvironment could be prioritized for immune checkpoint inhibitors (ICIs). Additionally, the underexplored role of the STING pathway in reshaping the immune microenvironment provides a promising avenue for combinatorial therapies in low-risk subgroups.

In addition to TMB and immune features, our study also explored the therapeutic implications of risk stratification through drug sensitivity analysis. We found that the high-risk group exhibited significantly increased sensitivity to aurorasertib, doramapimod, navitoclax, ribociclib, and venetoclax. These compounds target mitotic checkpoints, cell cycle regulators, and apoptosis pathways—mechanistically aligning with our functional enrichment results that revealed upregulation of proliferation- and stress-related pathways in high-risk tumors. This suggests that these patients may benefit more from therapies targeting proliferative and anti-apoptotic processes, providing a rationale for integrating our model into personalized treatment planning. To further validate the cellular origin and biological relevance of key prognostic genes, single-cell transcriptomic analysis performed. EZH2, PCNA, and BIRC5 were predominantly expressed in epithelial clusters, supporting their tumor-intrinsic roles (44). Additionally, LGALS9–CD44 emerged as a key ligand–receptor axis mediating interactions between monocytes and epithelial cells, implicating Galectin-9 in immunosuppressive signaling through $CD8^+$ T cell inhibition (45). These observations are consistent with recent studies highlighting the role of tumor–immune crosstalk in modulating therapeutic responses (46, 47), and further underscore the translational potential of integrating single-cell analysis with risk modeling to inform immunotherapy strategies.

Notwithstanding these insights, a significant limitation is the lack of GTEx normal tissue data to complement TCGA's tumor-normal comparisons. GTEx, a comprehensive gene expression resource encompassing various healthy tissues, is extensively utilized to differentiate cancer-specific expression alterations from tissue-specific baselines, thereby enhancing the specificity of differential expression gene (DEG) analysis. For instance, biomarkers such as EZH2 (high-risk) and CD34 (protective) would benefit from validation against GTEx-derived normal cervical tissue expression to confirm their cancer-specific dysregulation. While our DEG analysis employed existing TCGA tumor-normal pairs, it will be crucial for future studies to integrate GTEx's larger and more diverse normal cohort in order to refine biomarker discovery and strengthen biological interpretability. This limitation underscores the necessity for multi-cohort validation that incorporates diverse normal tissue references to improve the generalizability of our findings. In addition to these considerations, another notable limitation arises from reliance on a single GEO dataset (GSE30759) for validation purposes, which may impact generalizability across varied populations or technical platforms. Although GSE30759 was chosen due to its substantial sample size and technical consistency with TCGA data, future investigations should aim to validate the model within multiple independent cohorts and among diverse clinical populations—including those representing different ethnic backgrounds or sequencing methodologies. Furthermore, the reliance of this study on computer simulation analysis, combined with the relatively limited sample size, imposes considerable limitations. And there may be batch effects between data sets, which may introduce variability and may also affect the reproducibility of our findings. In addition, the analysis flow of the study followed a conventional linear format and lacked novel algorithmic innovations or modular designs. While we currently lack the resources to implement advanced computational frameworks or perform wet laboratory validation, we are clearly committed to filling these gaps in future studies. Key steps will include: 1) validation with a larger multicenter dataset to mitigate batch effects and improve statistical power; 2) develop modular, open source libraries with adaptive machine learning algorithms to model gene-gene interactions; 3) Immunohistochemical staining of EZH2 and CXCL12 was performed in clinical tissue microarray to verify protein expression; 4) qPCR in paired normal tumor samples to validate the transcriptomics results; 5) perform functional experiments such as CRISPR-Cas9 knockout/overexpression experiments in cervical cancer cell lines to determine the role of

biomarkers in tumor progression. By integrating computational prediction and mechanistic validation, these efforts will improve the translational relevance of our results and pave the way for personalized treatment strategies for cervical cancer.

5 Conclusion

In conclusion, this study provides valuable insights into cervical cancer, revealing several findings with significant clinical implications. The prognostic risk model developed from genes such as CHMP4C, ATP13A2, and ALDOA serves as a promising tool for predicting patient outcomes. Furthermore, the observed differences in immune cell infiltration between high- and low-risk groups indicate the potential for immune-based therapies. The TMB emphasizes the importance of genetic mutations as key biomarkers for prognosis and response to therapy. Although these results are encouraging, it is essential to validate them in diverse populations. Future research should aim to deepen our understanding of changes in the immune microenvironment and investigate targeted therapies to improve patient survival. Additionally, integrating multi-omics data will enhance risk models and facilitate the development of personalized treatments for cervical cancer.

Data availability statement

The original contributions presented in the study are included in the article/supplementary material. Further inquiries can be directed to the corresponding author.

Author contributions

FQ: Project administration, Writing – review & editing, Investigation, Writing – original draft, Data curation. LH: Methodology, Writing – original draft, Formal Analysis, Software. XS: Formal Analysis, Software, Writing – original draft, Resources. YH: Writing – review & editing, Data curation, Visualization, Conceptualization. YW: Visualization, Writing – original draft, Project administration, Conceptualization, Validation, Writing – review & editing, Supervision.

Funding

The author(s) declare that no financial support was received for the research and/or publication of this article.

Acknowledgments

We express our gratitude to the TCGA and GEO databases for offering their platforms and to the contributors for sharing their valuable datasets.

Conflict of interest

The authors declare that the research was conducted in the absence of any commercial or financial relationships that could be construed as a potential conflict of interest.

Generative AI statement

The author(s) declare that no Generative AI was used in the creation of this manuscript.

Publisher's note

All claims expressed in this article are solely those of the authors and do not necessarily represent those of their affiliated organizations, or those of the publisher, the editors and the reviewers. Any product that may be evaluated in this article, or claim that may be made by its manufacturer, is not guaranteed or endorsed by the publisher.

References

1. Bhatla N, Aoki D, Sharma DN, Sankaranarayanan R. Cancer of the cervix uteri: 2021 update. *Int J gynaecology obstetrics: Off Organ Int Fed Gynaecology Obstetrics*. (2021) 155 Suppl 1:28–44. doi: 10.1002/ijgo.13865

2. Sung H, Ferlay J, Siegel RL, Laversanne M, Soerjomataram I, Jemal A, et al. Global cancer statistics 2020: GLOBOCAN estimates of incidence and mortality worldwide for 36 cancers in 185 countries. *CA: Cancer J Clin*. (2021) 71:209–49. doi: 10.3322/caac.21660

3. Zhang S, Batur P. Human papillomavirus in 2019: An update on cervical cancer prevention and screening guidelines. *Cleveland Clinic J Med*. (2019) 86:173–8. doi: 10.3949/ccjm.86a.18018

4. Okunade KS. Human papillomavirus and cervical cancer. *J obstetrics gynaecology: J Institute Obstetrics Gynaecology*. (2020) 40:602–8. doi: 10.1080/01443615.2019.1634030

5. Canfell K. Towards the global elimination of cervical cancer. *Papillomavirus Res (Amsterdam Netherlands)*. (2019) 8:100170. doi: 10.1016/j.pvr.2019.100170

6. Hancock G, Hellner K, Dorrell L. Therapeutic HPV vaccines. *Best Pract Res Clin obstetrics gynaecology*. (2018) 47:59–72. doi: 10.1016/j.bpobgyn.2017.09.008

7. Mayadev JS, Lin DC, Assenov Y, Plass C, Koeffler HP. Global challenges of radiotherapy for the treatment of locally advanced cervical cancer. *Int J gynecological cancer: Off J Int Gynecological Cancer Soc*. (2022) 32:436–45. doi: 10.1136/ijgc-2021-003001

8. Gajewski TF, Schreiber H, Fu YX. Innate and adaptive immune cells in the tumor microenvironment. *Nat Immunol*. (2013) 14:1014–22. doi: 10.1038/ni.2703

9. Koukourakis MI, Giatromanolaki A. Tumor microenvironment, immune response and post-radiotherapy tumor clearance. *Clin Trans oncology: Off Publ Fed Spanish Oncol Societies Natl Cancer Institute Mexico*. (2020) 22:2196–205. doi: 10.1007/s12094-020-02378-8

10. Qiao LY, Shen S, Liu M, Xia C, Kay JC, Zhang QL. Inflammation and activity augment brain-derived neurotrophic factor peripheral release. *Neuroscience*. (2016) 318:114–21. doi: 10.1016/j.neuroscience.2016.01.018

11. Hanahan D, Weinberg RA. Hallmarks of cancer: the next generation. *Cell*. (2011) 144:646–74. doi: 10.1016/j.cell.2011.02.013

12. Tewari KS, Monk BJ. New strategies in advanced cervical cancer: from angiogenesis blockade to immunotherapy. *Clin Cancer research: an Off J Am Assoc Cancer Res*. (2014) 20:5349–58. doi: 10.1158/1078-0432.ccr-14-1099

13. Monk BJ, Enomoto T, Kast WM, McCormack M, Tan DSP, Wu X, et al. Integration of immunotherapy into treatment of cervical cancer: Recent data and ongoing trials. *Cancer Treat Rev*. (2022) 106:102385. doi: 10.1016/j.ctrv.2022.102385

14. Tewari KS, Vergote I, Miller A, de Melo AC, Kim H, et al. Survival with cemiplimab in recurrent cervical cancer. *New Engl J Med*. (2022) 386:544–55. doi: 10.1056/NEJMoa2112187

15. Yao S, Zhao L, Chen S, Wang H, Gao Y, Shao N, et al. Cervical cancer immune infiltration microenvironment identification, construction of immune scores, assisting patient prognosis and immunotherapy. *Front Immunol*. (2023) 14:1135657. doi: 10.3389/fimmu.2023.1135657

16. Chen F, Shen L, Wang Y, Chen Y, Pan X, Liang X, et al. Signatures of immune cell infiltration for predicting immune escape and immunotherapy in cervical cancer. *Aging*. (2023) 15:1685–98. doi: 10.18632/aging.204583

17. Lin Y, Zhang R, Pan H, Li Y. A novel immune-related signature to predict prognosis and immune infiltration of cervical cancer. *Med Sci monitor: Int Med J Exp Clin Res*. (2023) 29:e938660. doi: 10.12659/msm.938660

18. Wang M, Li Z. Prediction of prognosis and immune landscape in cervical cancer based on heat shock protein-related genes. *Int J hyperthermia: Off J Eur Soc Hyperthermic Oncology North Am Hyperthermia Group*. (2023) 40:2259140. doi: 10.1080/02656736.2023.2259140

19. Teschendorff AE, Jones A, Fiegl H, Sargent A, Zhuang JJ, Kitchener HC, et al. Epigenetic variability in cells of normal cytology is associated with the risk of future morphological transformation. *Genome Med*. (2012) 4:24. doi: 10.1186/gm323

20. Zhuang J, Jones A, Lee S-H, Ng E, Fiegl H, Zikan M, et al. The dynamics and prognostic potential of DNA methylation changes at stem cell gene loci in women's cancer. *PloS Genet*. (2012) 8:e1002517. doi: 10.1371/journal.pgen.1002517

21. Bao S, Knoell DL. Zinc modulates cytokine-induced lung epithelial cell barrier permeability. *Am J Physiol Lung Cell Mol Physiol*. (2006) 291:L1132–1141. doi: 10.1152/ajplung.00207.2006

22. Barnett JB, Hamer DH, Meydani SN. Low zinc status: a new risk factor for pneumonia in the elderly? *Nutr Rev*. (2010) 68:30–7. doi: 10.1111/j.1753-4887.2009.00253.x

23. Aan de Stegge WB, Van Netten JJ, Bus SA. Does the skin heat up before it breaks down in diabetic foot ulceration? *Diabetes/metabolism Res Rev*. (2023) 39:e3621. doi: 10.1002/dmrr.3621

24. Argentiero A, Andriano A, Caradonna IC, de Martino G, Desantis V. Decoding the intricate landscape of pancreatic cancer: insights into tumor biology, microenvironment, and therapeutic interventions. *Cancers*. (2024) 16. doi: 10.3390/cancers16132438

25. Ren N, Liang B, Li Y. Identification of prognosis-related genes in the tumor microenvironment of stomach adenocarcinoma by TCGA and GEO datasets. *Bioscience Rep*. (2020) 40. doi: 10.1042/bsr20200980

26. Chen B, Khodadoust MS, Liu CL, Newman AM, Alizadeh AA. Profiling tumor infiltrating immune cells with CIBERSORT. *Methods Mol Biol (Clifton N.J.)*. (2018) 1711:243–59. doi: 10.1007/978-1-4939-7493-1_12

27. Li T, Fan J, Wang B, Traugh N, Chen Q, Liu JS, et al. TIMER: A web server for comprehensive analysis of tumor-infiltrating immune cells. *Cancer Res*. (2017) 77: e108–10. doi: 10.1158/0008-5472.can-17-0307

28. Jin Y, Wang Z, He D, Zhu Y, Chen X, Cao K, et al. Identification of novel subtypes based on ssGSEA in immune-related prognostic signature for tongue squamous cell carcinoma. *Cancer Med*. (2021) 10:8693–707. doi: 10.1002/cam4.4341

29. Jiang P, Gu S, Pan D, Fu J, Sahu A, Hu X, et al. Signatures of T cell dysfunction and exclusion predict cancer immunotherapy response. *Nat Med*. (2018) 24:1550–8. doi: 10.1038/s41591-018-0136-1

30. Liu C, Zhao J, Lu W, Dai Y, Hockings J, Zhou Y, et al. Individualized genetic network analysis reveals new therapeutic vulnerabilities in 6,700 cancer genomes. *PloS Comput Biol*. (2020) 16:e1007701. doi: 10.1371/journal.pcbi.1007701

31. Mulford AJ, Wing C, Dolan ME, Wheeler HE. Genetically regulated expression underlies cellular sensitivity to chemotherapy in diverse populations. *Hum Mol Genet*. (2021) 30:305–17. doi: 10.1093/hmg/ddab029

32. Li C, Guo L, Li S, Hua K. Single-cell transcriptomics reveals the landscape of intra-tumoral heterogeneity and transcriptional activities of ECs in CC. *Mol Ther Nucleic Acids*. (2021) 24:682–94. doi: 10.1016/j.omtn.2021.03.017

33. Bao H, Li X, Cao Z, Huang Z, Chen L, Wang M, et al. Identification of COPA as a potential prognostic biomarker and pharmacological intervention target of cervical cancer by quantitative proteomics and experimental verification. *J Trans Med*. (2022) 20:18. doi: 10.1186/s12967-021-03218-1

34. Abdul-Latif M, Tharmalingam H, Tsang Y, Hoskin PJ. Functional magnetic resonance imaging in cervical cancer diagnosis and treatment. *Clin Oncol (Royal Coll Radiologists (Great Britain))*. (2023) 35:598–610. doi: 10.1016/j.clon.2023.05.006

35. Ouyang D, Yang P, Cai J, Sun S, Wang Z. Comprehensive analysis of prognostic alternative splicing signature in cervical cancer. *Cancer Cell Int*. (2020) 20:221. doi: 10.1186/s12935-020-01299-4

36. Alldredge J, Kumar V, Nguyen J, Sanders BE, Gomez K, Jayachandran K, et al. Endogenous retrovirus RNA expression differences between race, stage and HPV status offer improved prognostication among women with cervical cancer. *Int J Mol Sci*. (2023) 24. doi: 10.3390/ijms24021492

37. Sajjad F, Jalal A, Jalal A, Gul Z, Mubeen H, Rizvi SZ, et al. Multi-omic analysis of dysregulated pathways in triple negative breast cancer. *Asia-Pacific J Clin Oncol*. (2024). doi: 10.1111/ajco.14095

38. Yang B, Wang Z, Deng Y, Xiao L, Zhang K. LncRNA LAMTOR5-AS1 sponges miR-210-3p and regulates cervical cancer progression. *J obstetrics gynaecology Res*. (2022) 48:3171–8. doi: 10.1111/jog.15439

39. Sokolowska O, Nowis D. STING signaling in cancer cells: important or not? *Archivum immunologiae therapiae experimentalis*. (2018) 66:125–32. doi: 10.1007/s00005-017-0481-7

40. Li T, Zhang W, Niu M, Wu Y, Deng X, Zhou J, et al. STING agonist inflames the cervical cancer immune microenvironment and overcomes anti-PD-1 therapy resistance. *Front Immunol*. (2024) 15:1342647. doi: 10.3389/fimmu.2024.1342647

41. Yu G, Pang Y, Merchant M, Kesserwan C, Gangalapudi V, Abdelmaksoud A, et al. Tumor mutation burden, expressed neoantigens and the immune microenvironment in diffuse gliomas. *Cancers*. (2021) 13. doi: 10.3390/cancers13236092

42. Merino DM, McShane LM, Fabrizio D, Funari V, Chen S-J, White JR, et al. Establishing guidelines to harmonize tumor mutational burden (TMB): in silico assessment of variation in TMB quantification across diagnostic platforms: phase I of the Friends of Cancer Research TMB Harmonization Project. *J immunotherapy Cancer*. (2020) 8. doi: 10.1136/jitc-2019-000147

43. Wu H, Wang H, Chen Y. Pan-cancer analysis of tumor mutation burden sensitive tumors reveals tumor-specific subtypes and hub genes related to immune infiltration. *J Cancer Res Clin Oncol*. (2023) 149:2793–804. doi: 10.1007/s00432-022-04139-2

44. Lang X, Huang C, Cui H. Prognosis analysis and validation of fatty acid metabolism-related lncRNAs and tumor immune microenvironment in cervical cancer. *J Immunol Res*. (2022) 2022:4954457. doi: 10.1155/2022/4954457

45. Yang R, Sun L, Li C-F, Wang Y-H, Yao J, Li H, et al. Galectin-9 interacts with PD-1 and TIM-3 to regulate T cell death and is a target for cancer immunotherapy. *Nat Commun*. (2021) 12:832. doi: 10.1038/s41467-021-21099-2

46. Chen R, Gan Q, Zhao S, Zhang D, Wang S, Yao L, et al. DNA methylation of miR-138 regulates cell proliferation and EMT in cervical cancer by targeting EZH2. *BMC Cancer*. (2022) 22:488. doi: 10.1186/s12885-022-09477-5

47. Wendel SO, Snow JA, Gu L, Banerjee NS, Malkas L, Wallace NA, et al. The potential of PCNA inhibition as a therapeutic strategy in cervical cancer. *J Med Virol*. (2023) 95:e29244. doi: 10.1002/jmv.29244

frontiers | Frontiers in Immunology

TYPE Original Research
PUBLISHED 16 July 2025
DOI 10.3389/fimmu.2025.1582308

Check for updates

OPEN ACCESS

EDITED BY
Antonio Mario Scanu,
University of Sassari, Italy

REVIEWED BY
Namuunaa Juramt,
Harvard Medical School, United States
Wenfeng He,
Macau University of Science and Technology, China

*CORRESPONDENCE
Wang Chao
pd362060@shsmu.edu.cn
Hou Fenggang
fghou555@126.com
Yin Xiaoling
yinxiaoling2015@163.com

†These authors have contributed equally to this work

RECEIVED 24 February 2025
ACCEPTED 10 June 2025
PUBLISHED 16 July 2025
CORRECTED 05 August 2025

CITATION
Wang Y, Meilu D, Qi S, Yufei T, Song G, Susu H, Haotian W, Tingting Z, Chao W, Fenggang H and Xiaoling Y (2025) The impact of sarcopenia on prognosis and fruquintinib efficacy in advanced colorectal cancer: a retrospective and mendelian randomization study. *Front. Immunol.* 16:1582308. doi: 10.3389/fimmu.2025.1582308

COPYRIGHT
© 2025 Wang, Meilu, Qi, Yufei, Song, Susu, Haotian, Tingting, Chao, Fenggang and Xiaoling. This is an open-access article distributed under the terms of the Creative Commons Attribution License (CC BY). The use, distribution or reproduction in other forums is permitted, provided the original author(s) and the copyright owner(s) are credited and that the original publication in this journal is cited, in accordance with accepted academic practice. No use, distribution or reproduction is permitted which does not comply with these terms.

The impact of sarcopenia on prognosis and fruquintinib efficacy in advanced colorectal cancer: a retrospective and mendelian randomization study

Yao Wang[1,2†], Du Meilu[1†], Shi Qi[1†], Tang Yufei[1], Gao Song[1], Han Susu[1], Wen Haotian[1], Zhu Tingting[1], Wang Chao[2*], Hou Fenggang[1*] and Yin Xiaoling[1*]

[1]Department of Oncology, Unit 3, Shanghai Municipal Hospital of Traditional Chinese Medicine, Shanghai, China, [2]Department of Oncology, Ruijin Hospital, Shanghai Jiao Tong University School of Medicine, Shanghai, China

Background: Reportedly, sarcopenia is associated with prognosis in advanced colorectal cancer (CRC) patients and can lead to reduced efficacy of targeted therapy. However, studies on the relationship between sarcopenia and the prognosis (or efficacy) of advanced CRC patients receiving fruquintinib targeted therapy remains scarce. Therefore, we conducted a comprehensive assessment of the relationship between nutritional status, inflammation, immune function, and cancer-related sarcopenia. We also investigated whether sarcopenia affects the therapeutic efficacy of fruquintinib targeted therapy.

Patients and methods: In this retrospective study, sarcopenia and several markers of nutritional status and immune function were assessed in advanced CRC patients with fruquintinib therapy at the hospital. We used drug target mendelian randomization (MR) analysis to investigate the impact of fruquintinib on sarcopenia.

Results: Advanced CRC patients with sarcopenia had a poorer prognosis compared to those without sarcopenia. Furthermore, sarcopenia showed a strong correlation with various markers of nutritional status, immune function indicators, inflammation markers, quality of life scores, and the prognostic nutrition index. MR studies suggest that the spleen tyrosine kinase (SYK) gene is a key factor in the occurrence of sarcopenia associated with the use of fruquintinib.

Conclusion: Sarcopenia could be a prognostic factor in patients with advanced CRC receiving fruquintinib targeted therapy.

KEYWORDS

sarcopenia, immune, nutrition, advanced colorectal cancer, fruquintinib, mendelian randomization study

Introduction

Colorectal cancer (CRC) poses significant health challenges worldwide, with alarming statistics reflecting its severity. The five-year survival rate for patients with metastatic CRC stands at approximately 14% (1), underscoring the dire prognosis for this condition. Epidemiological data indicates that CRC ranks as the third most common and lethal type of cancer globally. In 2020, it was estimated that there were over 1.9 million new cases and nearly 1 million deaths attributed to this malignancy (2), highlighting the urgent need for enhanced prevention, early detection, and effective treatment strategies (3).

The etiology of CRC is multifactorial, intricately linked to genetic, environmental, and lifestyle factors, making early diagnosis essential for improving patient outcomes (4–6). The low 5-year overall survival rate in CRC is primarily due to the metastasis of CRC (7, 8). The contemporary clinical management of CRC involves a multidisciplinary approach that integrates surgical intervention, chemotherapy, targeted therapy, and immunotherapy (9, 10). Patients with tumors frequently experience a state of metabolic dysregulation, which is typified by increased catabolic processes and diminished anabolic activity (11, 12). Sarcopenia, a syndrome characterized by the progressive loss of skeletal muscle mass and function, is increasingly recognized as a significant factor affecting the prognosis of cancer patients, particularly those with CRC (13, 14). Sarcopenia can lead to metabolic disorders, along with inflammatory reactions and immune dysfunction (15–17). Recently, fruquintinib, an innovative targeted therapy for advanced CRC, has shown promise as a third-line treatment option, offering potential survival benefits for these patients (18).

The prevalence of muscle wasting among advanced CRC patients, due to impaired digestive and absorptive capacity, raises concerns regarding its impact on the efficacy of targeted therapies. In a study of colorectal cancer patients, sarcopenia was found in 18.8% of the cohort and linked to poorer progression-free and overall survival (19). A prior study demonstrated the prognostic significance of baseline skeletal muscle index (SMI) in patients with metastatic CRC undergoing treatment with fruquintinib (20). However, the impact of sarcopenia on the therapeutic efficacy of fruquintinib, a widely utilized novel targeted therapy, remains uncertain. This study aims to investigate the impact of sarcopenia on patients with advanced CRC patients undergoing targeted therapy through a retrospective analysis. Addtionally, it seeks to identify key genes between fruquintinib and sarcopenia using MR analysis. Specifically, we hypothesize that sarcopenia serves as a prognostic factor in advanced CRC patients undergoing fruquintinib treatment, and identifying the key genes associated with fruquintinib-induced sarcopenia is crucial for elucidating its underlying mechanisms and optimizing therapeutic outcomes.

Methods

Patients and study design

In this retrospective study, patients treated for advanced CRC using fruquintinib, were selected from January 2021 to January 2024 at the Shanghai Municipal Hospital of Traditional Chinese Medicine.

Measurement of muscle mass

As previously outlined, sarcopenia assessment follows a method summarized below (21). Muscle mass was quantified through cross-sectional computed tomography (CT) imaging at the third lumbar (L3) level, measuring the skeletal muscle area using hounsfield units (HU) ranging from −29 to 150. We use the Slice Omatic 5.0 image analysis software to measure the L3 level. The SMI was calculated by normalizing the muscle area to height (cm^2/m^2), SMI is indicative of sarcopenia if less than 40.31 cm^2/m^2 in males and 30.88 cm^2/m^2 in females (22). Prior to fruquintinib treatment, CRC patients underwent standardized CT evaluations, categorizing them into sarcopenia groups (SG) and non-sarcopenia groups (NSG) based on SMI values, thus enabling precise assessment of sarcopenia's impact on treatment outcomes. Figure 1 demonstrates the comparison between CRC patients with sarcopenia (Figure 1A) and those without sarcopenia (Figure 1B), as visualized by CT scans at the L3 level, highlighting the skeletal muscle area.

Nutritional status assessment

We employed various traditional nutritional assessments, such as body mass index (BMI), SMI, albumin (ALB), prealbumin (PAB), retinol-binding protein (RBP) and the prognostic nutrition index (PNI).

Inflammatory status assessment

We assessed inflammatory markers, including interleukin-1β (IL-1β), interleukin-2 (IL-2), interleukin-6 (IL-6), interleukin-12 (IL-12), tumor necrosis factor-α (TNF-α), and interferon-γ (IFN-γ). These markers were measured using was conducted using a fully automated flow cytometer (NovoCyte D2060R).

Immune status assessment

We assessed immune markers, including the absolute counts of CD3, CD4, CD8, and natural killer (NK) cells. These immune markers were analyzed using a fully automated flow cytometer (BD FACSCanto II).

Statistical analysis was performed using SPSS (version 29). For continuous variables that followed a normal distribution, data are presented as mean ± standard deviation (SD), and group differences were analyzed using the t-test. For continuous variables that did not follow a normal distribution, data are presented as median (interquartile range), and group differences were analyzed using the Wilcoxon test. Categorical variables are described using frequency (percentage), and group differences were compared using the chi-square test or Fisher's exact test. To evaluate the relationships between variables, we used spearman correlation analysis, which measures the strength and direction of monotonic associations and is suitable for non-parametric data and ordinal variables.

Ethical consideration

The protocol for this investigation was approved by the Shanghai Municipal Hospital of Traditional Chinese Medicine (2021SHL-KY-04-03).

Study design of MR

To explore the causal relationship between fruquintinib and sarcopenia, we conducted a MR study. We validated the reliability of genetic variants as instrumental variables (IVs) by fulfilling three key MR assumptions. Firstly, we selected genome-wide significant variants ($P < 5\times10^{-8}$) strongly linked to the exposure, ensuring F-statistics > 10 to avoid weak instrument bias (20). Secondly, we screened IVs for associations with potential confounders (age, sex, BMI, smoking status, socioeconomic status) using PhenoScanner and multivariable MR adjustment. Thirdly, we confirmed that the IVs affect the outcome only through the exposure, with horizontal pleiotropy tests (MR-Egger intercept and MR-PRESSO) showing all $P > 0.05$ (23). In this study, gene expression quantitative trait loci (eQTLs) were employed as exposure variables, whereas indicators associated with left-hand grip strength, right-hand grip strength, appendicular muscle mass, and walking speedwere considered as outcome variables. Supplementary Figure S1 displays the study flowchart.

Sources

Three genes were identified from DrugBank and seven from the DGIdb database for fruquintinib. The SMILES structures of the compounds were retrieved from the PubChem database (https://pubchem.ncbi.nlm.nih.gov/). Target gene prediction using SwissTargetPrediction (http://www.swisstargetprediction.ch/) yielded 117 potential target genes. After merging and deduplicating results from the three databases, a final list of 111 target genes for fruquintinib was established.

The diagnosis of sarcopenia was referred to the criteria established by the European Working Group on Sarcopenia in Older People (EWGSOP) (24). This study includes 461,089 European samples with 9,851,867 single nucleotide polymorphisms (SNPs) associated with grip strength, including both left and right hand grip strength. For appendicular lean mass, 450,243 European samples and 18,071,518 SNPs were analyzed. Usual walking pace is associated with 459,915 European samples and 9,851,867 SNPs. A detailed description of the data used in this study is provided in Supplementary Table S1.

Statistical analysis of MR

To address horizontal pleiotropy in MR analyses, MR-PRESSO detected no outliers with Distortion test *P*-values < 0.05. Five methods—IVW, MR-Egger, Weighted Median, Simple Mode, and Weighted Mode (25)—were applied, prioritizing IVW results. Heterogeneity tests guided the use of random effects ($P < 0.05$) or fixed effects ($P > 0.05$) in IVW. The robustness of the results was ensured through sensitivity analyses, which included heterogeneity testing using mr_heterogeneity(), the application of MR-Egger regression to assess pleiotropy, and the implementation of a leave-one-out analysis (26). Causal effects were reported as odds ratios (OR) with 95% confidence intervals (CI). Analyses were

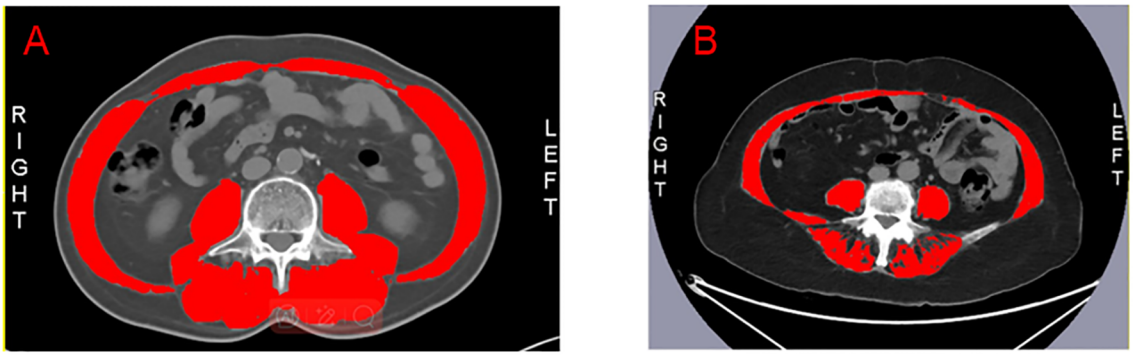

FIGURE 1
The red section represents the skeletal muscle at the L3 level. **(A)** The L3 level in patients with non-sarcopenia. **(B)** The L3 level in patients with sarcopenia.

performed using R packages "TwoSampleMR" (v 0.6.0) and "MRPRESSO" (v 1.0).

Results

Patients' characteristics

Of the 60 eligible patients, 31 were categorized into the sarcopenia group and 29 into the non-sarcopenia group. Table 1 details patients' background.

Comparison of nutritional, inflammatory, and immune indexes

Previous study found that sarcopenia correlates with the nutrition indicators (27). We assessed the relationship between nutritional markers such as albumin, prealbumin, retinol-binding protein, and sarcopenia in our study. Table 2 presents that compared to the NSG, patients in the SG had significantly lower levels of albumin, prealbumin, and retinol-binding protein. As a proinflammatory cytokine, IL-6, along with IL-6 signaling, plays a crucial role in the inflammatory microenvironment linked to CRC (28, 29). Furthermore, the progression of sarcopenia is associated with elevated serum levels of IL-6 (30). We found that IL-6 level was significantly higher in the SG than in the NSG ($P < 0.05$). Sarcopenia may impair myokine signaling, shift membrane-bound factors to a pro-inflammatory state, and reduce immune cell regeneration, leading to immune dysfunction (31). We compared absolute counts of CD3, CD4, CD8, and NK cells between the two groups. Our results revealed that, compared to the NSG, patients in the SG had a significant decrease in the absolute count of NK cells ($P < 0.01$). Thus, it is evident that tumor-associated sarcopenia may lead to alterations in the patient's nutritional, inflammatory, and immune status.

Correlation analysis

Subsequently, Our correlation analysis demonstrated a significant association between sarcopenia and several biomarkers, including albumin, prealbumin, retinol-binding protein, NK cells, BMI, and PNI. Based on these results, sarcopenia showed the strongest correlation with nutritional markers overall (Figure 2).

Efficacy for all patients

In SG the median progression-free survival (*PFS*) was 5.9 months (95% CI=0.3644-1.454, HR=1.655). In NSG the median PFS was 8.4 months (95% CI=0.71386-2.744, HR=0.6042). The median time to treatment failure (*TTF*) in SG was 59 days (95% Cl=0.4412-1.440, HR=1.571) while in NSG this value was 69 days (95% Cl=0.6943-2.267, HR=0.6364). Figure 3 demonstrates the Kaplan-Meier curves of PFS and TTF. In terms of PFS and TTF, no significant differences were observed between SG and NSG.

Safety analysis

According to reports, the main side effects of fruquintinib include hypertension, gastrointestinal reactions such as nausea, vomiting, and diarrhea, abnormal bleeding such as epistaxis and hematuria, as well as hand-foot syndrome and abnormalities in liver and kidney function (32–34). We analyzed the occurrence of adverse effects during fruquintinib targeted therapy in patients with and without sarcopenia (Figure 4). Our results indicated that patients in the SG presented the higher incidence of nausea than in the NSG ($P<0.05$). Patients in the SG exhibited higher levels of hypertension, hand-foot syndrome, and severity of symptoms compared to the NSG. Additionally, the SG had a higher incidence of diarrhea, and thrombocytopenia. However, there were no significant inter-group differences in these indicators.

MR results between the target genes of fruquintinib and left-hand grip strength

The relationship between the target genes of fruquintinib and left-hand grip strength are illustrated in Table 3. A p-value < 0.05 in MR analysis signifies a significant causal link. If the OR is > 1, it suggests that the gene is a risk factor for the outcome, meaning that an increase in the expression level of this gene is associated with a higher risk of the outcome. Conversely, if the OR is < 1, the gene is considered a protective factor, indicating that higher expression levels of this gene are associated with a decreased risk of the outcome. A total of 28 genes exhibited P-values < 0.05 between the target genes of fruquintinib and left-hand grip strength. The following drug target genes are correlated with an elevated risk (OR > 1) of adverse outcomes: FLT4, CA2, ZAP70, HDAC1, ADORA2A, SLC27A1, CDK7, CTSL, CTSK, CTSS, ADORA1, SYK, IMPDH2, IRAK4, MTOR.

MR results between the target genes of fruquintinib and right-hand grip strength

The relationship between the target genes of fruquintinib and right-hand grip strength are illustrated in Table 4. A total of 25 genes exhibited P-values < 0.05. The following drug target genes are associated with an increased risk of adverse outcomes: FLT4, CA2, ZAP70, HDAC1, PTK2B, PTGFR, ADORA2A, CDK7, CTSL, NAAA, CTSS, SYK, PTGER4, MTOR.

10.3389/fimmu.2025.1582308

TABLE 1 Patients' basic characteristics.

Variables	Total (n = 60)	Sarcopenia (n = 31)	Non-sarcopenia (n = 29)	*P*-Value
Sex, n (%)				0.76
Female	35 (58.33)	17 (54.84)	18 (62.07)	
Male	25 (41.67)	14 (45.16)	11 (37.93)	
Age, Mean ± SD (years)	64.47 ± 10.87	66.84 ± 8.9	61.93 ± 12.29	0.172
Hight, Median (Q1,Q3) (m)	1.63 (1.59, 1.71)	1.63 (1.6, 1.71)	1.63 (1.58, 1.7)	0.888
Weight, Median (Q1,Q3) (kg)	60 (55, 66)	57 (53.5, 65)	60 (55, 68)	0.029*
BMI, Mean ± SD (kg/m^2)	22.38 ± 2.91	21.08 ± 2.56	23.77 ± 2.64	< 0.001***
SMI, Mean ± SD (cm^2/m^2)	39.68 ± 8.77	33.73 ± 4.7	46.03 ± 7.59	< 0.001***
ECOG score, n (%)				0.07
0	12 (20)	3 (9.68)	9 (31.03)	
1	35 (58.33)	18 (58.06)	17 (58.62)	
2	6 (10)	4 (12.9)	2 (6.9)	
3	7 (11.67)	6 (19.35)	1 (3.45)	
Primary site, n (%)				0.408
Transverse colon	1 (1.67)	0 (0)	1 (3.45)	
Cecum and ileocecal region	3 (5)	2 (6.45)	1 (3.45)	
Descending colon	2 (3.33)	0 (0)	2 (6.9)	
Ascending colon	5 (8.33)	2 (6.45)	3 (10.34)	
Sigmoid colon	29 (48.33)	18 (58.06)	11 (37.93)	
Rectum	20 (33.33)	9 (29.03)	11 (37.93)	
Pulmonary metastasis, n (%)				0.846
No	48 (80)	24 (77.42)	24 (82.76)	
Yes	12 (20)	7 (22.58)	5 (17.24)	
Hepatic metastasis, n (%)				1
Yes	60 (100)	31 (100)	29 (100)	
Bone metastasis, n (%)				0.492
No	58 (96.67)	29 (93.55)	29 (100)	
Yes	2 (3.33)	2 (6.45)	0 (0)	
Brain metastasis, n (%)				1
No	59 (98.33)	30 (96.77)	29 (100)	
Yes	1 (1.67)	1 (3.23)	0 (0)	
Chemotherapy, n (%)				1
No	3 (5)	2 (6.45)	1 (3.45)	
Yes	57 (95)	29 (93.55)	28 (96.55)	
Surgery, n (%)				1
No	3 (5)	2 (6.45)	1 (3.45)	
Yes	57 (95)	29 (93.55)	28 (96.55)	

(Continued)

TABLE 1 Continued

Variables	Total (n = 60)	Sarcopenia (n = 31)	Non-sarcopenia (n = 29)	*P*-Value
Targeted therapy, n (%)				0.815
No	27 (45)	13 (41.94)	14 (48.28)	
Yes	33 (55)	18 (58.06)	15 (51.72)	
Immunotherapy, n (%)				0.053
No	55 (91.67)	26 (83.87)	29 (100)	
Yes	5 (8.33)	5 (16.13)	0 (0)	

BMI, Body Mass Index; SMI, Skeletal Muscle Index; ECOG, Eastern Cooperative Oncology Group performance status. *$P < 0.05$, ***$P < 0.001$.

MR results between the target genes of fruquintinib and muscle mass

The relationship between the target genes of fruquintinib and limb muscle mass are illustrated in Table 5. A total of 21 genes exhibited *P*-values < 0.05. The following drug target genes are associated with an increased risk of adverse outcomes: BAD, FLT4, CDC7, PDE8B, ZAP70, PTK2B, CDK7, CTSL, CTSK, CTSS, FNTA, MTOR.

MR results between the target genes of fruquintinib and walking speed

The relationship between the target genes of fruquintinib and walking speed are illustrated in Table 6. A total of 12 genes exhibited *P*-values < 0.05. The following drug target genes are associated with an increased risk of adverse outcomes: BAD, FGFR2, HSP90AA1, PDE8B, PTK2B, SYK, STAT3.

The intersection of MR results for drug target genes and the four outcome variables mentioned above was visualized, as shown in Supplementary Figure S2. Two genes, the BCL2 associated agonist of cell death (BAD) gene and the spleen tyrosine kinase (SYK) gene, were found to have a significant causal relationship with all four outcome variables (Table 7). The SYK gene is considered to be the most likely candidate gene associated with an increased risk of sarcopenia.

Figure 5 displays scatter plots of the associations between exposure factors and outcome variables obtained from five MR algorithms. The leave-one-out sensitivity analysis, shown in Figure 6, demonstrates that the removal of each SNP individually does not significantly affect the outcome variable, indicating that the results of this MR analysis are reliable and stable.

TABLE 2 Analysis of the inter-group differences for each diagnostic parameter.

Variables	Sarcopenia (n = 31)	Non-sarcopenia (n = 29)	*P*-Value
AlB (g/L)	34.78 ± 5.34	39.81 ± 5.14	<.001**
PAB (mg/L)	190.1 ± 67.00	258.34 ± 67.00	<.001**
RBP (mg/L)	28.19 ± 11.41	37.02 ± 9.83	0.002**
IL-1β (pg/mL)	3.23 (1.35~5.97)	3.6 (1.745~5.22)	0.559
IL-2 (pg/mL)	5.13 (3.27~8.08)	4.24 (2.93~7.355)	0.416
IL-6 (pg/mL)	8.13 (2.83~12.9)	4.52 (2.605~6.38)	0.031*
IL-12 (pg/mL)	3.67 (1.81~4.83)	2.36 (1.36~4.505)	0.277
TNF-α (pg/mL)	2.69 (1.91~5.63)	2.9 (1.875~4.875)	0.97
IFN-γ (pg/mL)	1.8 (0.9~2.9)	1.9 (0.85~4.4)	0.455
CD3 (/μL)	804 (538~1165)	891 (684~1152)	0.171
CD4 (/μL)	477 (245~668)	609 (340~808.5)	0.115
CD8 (/μL)	288 (173~434)	280 (219~441)	0.363
NK (/μL)	123 (78~177)	229 (159.5~323.5)	<.001**
PNI (g/dL)	40.54 ± 6.99	47.12 ± 5.85	0.219

ALB, Albumin; PAB, Prealbumin; RBP, Retinol-binding protein; IL-1β, Interleukin-1β; IL-2, Interleukin-2; IL-6, Interleukin-6; IL-12, Interleukin-12; TNF-α, Tumor Necrosis Factor-α; IFN-γ, Interferon-γ; CD3, Cluster of Differentiation 3; CD4, Cluster of Differentiation 4; CD8, Cluster of Differentiation 8; NK, Natural Killer Cell; PNI, Prognostic nutritional index. *$P < 0.05$, **$P < 0.01$.

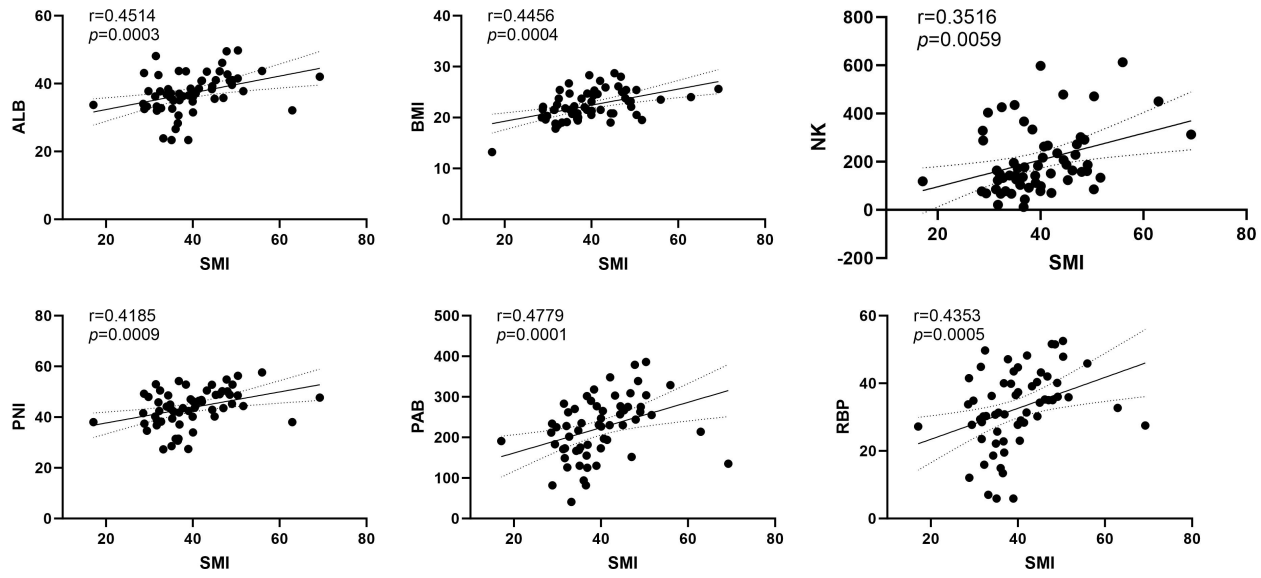

FIGURE 2
The correlation analysis between SMI and ALB, PAB, RBP, NK, BMI and PNI. ALB, Albumin (g/L); PAB, Prealbumin (mg/L); RBP, Retinol-binding protein (mg/L); NK, Natural Killer Cell (/μL); BMI, Body Mass Index (kg/m^2); PNI, Prognostic nutritional index (g/dL).

Discussion

This study provides significant insights into the relationship between sarcopenia and the clinical outcomes of fruquintinib targeted therapy in advanced CRC patients. Recently, poor baseline nutrition has been viewed as a predictor of cancer outcomes, particularly in gastrointestinal tumors (35, 36). A decline in SMI, BMI, and nutritional markers, including albumin, prealbumin, and the PNI, may serve as indicators for assessing the risk of sarcopenia (37–39). Moreover, the presence of sarcopenia can diminish the effectiveness of tumor-targeted therapies (40, 41). We observed that sarcopenic patients exhibited a significant decline in nutritional markers, including albumin, prealbumin, and retinol-binding protein, in comparison to non-sarcopenic patients (Table 2). Studies have shown that IL-6 levels correlate with muscle wasting and atrophy, which are key features of sarcopenia (42, 43). IL-6 is a cytokine that plays a significant role in inflammation and the immune response (44). In particular, IL-6 can suppress the function of NK cells, leading to a reduced ability to target and eliminate cancer cells (45, 46). Patients with sarcopenia exhibited increased concentrations of IL-6 and a significant decrease in NK cell counts, indicating a potential impairment in immune function (Table 2). Sarcopenic patients had a shorter duration of fruquintinib treatment and faced more adverse events, particularly gastrointestinal symptoms like nausea, and diarrhea. These symptoms can decrease appetite and food intake, worsening nutritional status and nutrient absorption, which in turn

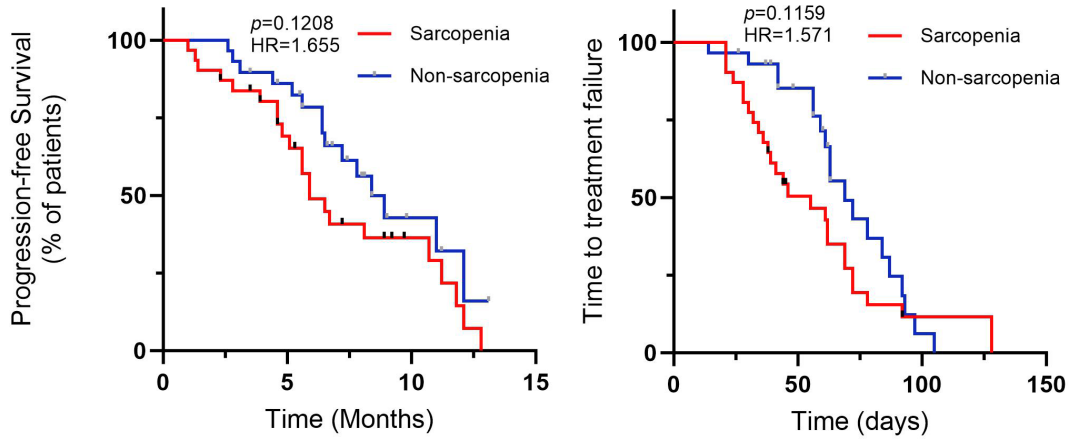

FIGURE 3
Profession-free survival (*PFS*), and time to treatment failure (*TTF*) for CRC patients with fruquintinib therapy.

10.3389/fimmu.2025.1582308

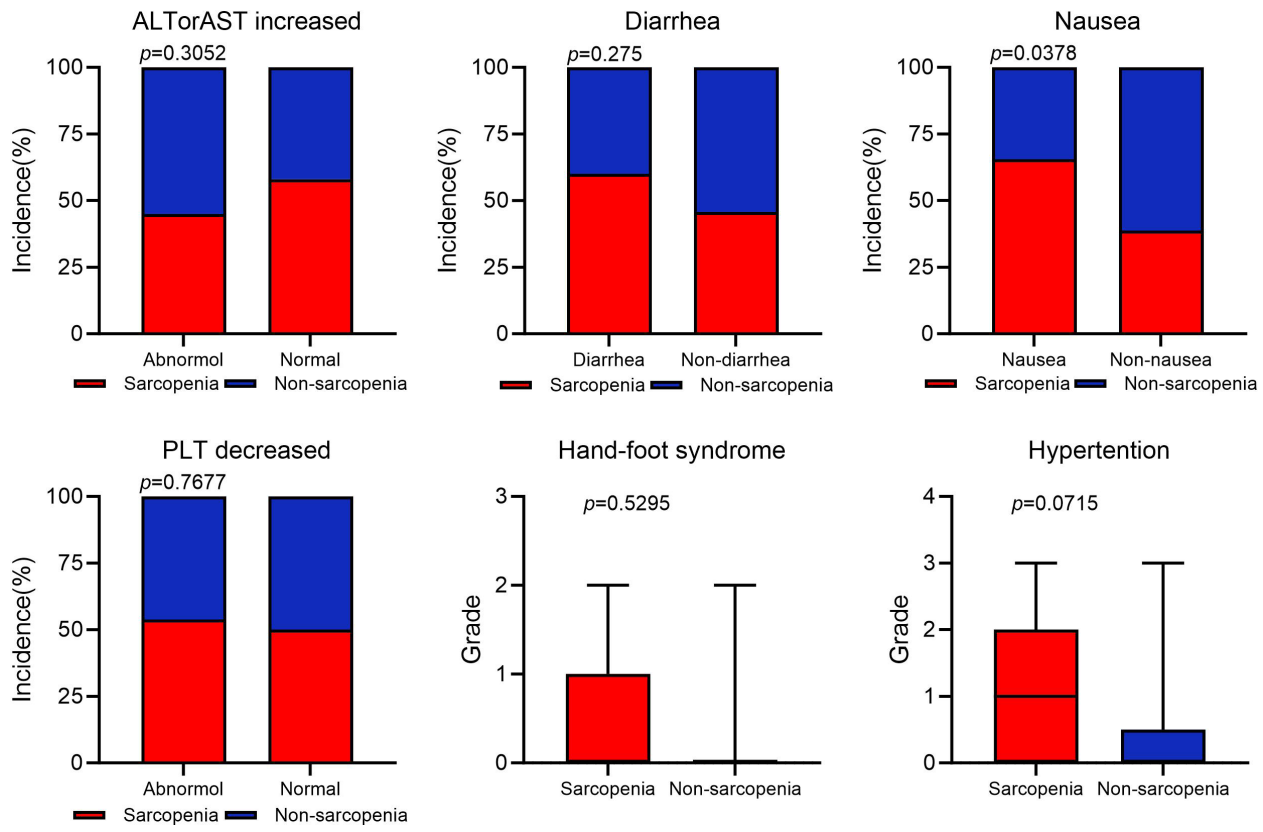

FIGURE 4
Adverse event occurrence statistics. AST, aspirate aminotransferase (U/L); ALT, alanine aminotransferase (U/L); PLT, platelet (x10^9^/L).

TABLE 3 MR results of exposure factors and outcomes (left hand grip strength).

exposure	outcome	method	nsnp	pval	OR(95% CI)	pleio_P
FLT4	Hand grip strength (left)	IVW	4	**0.002**	1.013 (1.005 to 1.021)	0.480
CA2		IVW	33	**<0.001**	1.007 (1.003 to 1.011)	0.826
ZAP70		IVW	12	**<0.001**	1.013 (1.008 to 1.019)	0.228
HDAC1		IVW	4	**0.047**	1.013 (1.000 to 1.026)	0.641
ADORA2A		IVW	3	**0.001**	1.017 (1.007 to 1.028)	0.845
SLC27A1		IVW	7	**0.020**	1.012 (1.002 to 1.021)	0.338
CDK7		IVW	3	**0.037**	1.017 (1.001 to 1.033)	0.337
CTSL		IVW	12	**0.040**	1.005 (1.000 to 1.009)	0.553
CTSK		IVW	26	**<0.001**	1.006 (1.003 to 1.009)	0.182
CTSS		IVW	27	**<0.001**	1.009 (1.007 to 1.012)	0.461
ADORA1		IVW	4	**0.037**	1.005 (1.000 to 1.009)	0.684
SYK		IVW	17	**0.037**	1.004 (1.000 to 1.009)	0.284
IMPDH2		IVW	12	**<0.001**	1.041 (1.031 to 1.051)	0.056
IRAK4		IVW	8	**0.028**	1.008 (1.001 to 1.015)	0.430
MTOR		IVW	4	**0.003**	1.009 (1.003 to 1.015)	0.737

0.95 1 1.05

pavl: Significance; OR, Odds ratio, with the 95% confidence interval of the odds ratio in parentheses; pleio_P: Test for horizontal pleiotropy.

aggravates sarcopenia by hindering muscle maintenance (Figure 4).This highlights the critical importance of monitoring sarcopenia in CRC patients undergoing targeted therapies, as it not only affects nutritional and immune status but also impacts treatment efficacy and toxicity.

One of the innovative aspects of this research is the identification of the SYK gene as a risk factor for sarcopenia development in patients treated with fruquintinib. The SYK is a non-receptor protein tyrosine kinase involved in immune signaling and tumor metastasis initiation (47). Meanwhile, the SYK is a cytoplasmic enzyme that links immune cell receptors to intracellular signaling, crucial for adaptive and inflammatory immune responses (48, 49). The SYK gene exhibits dual functionality, acting as both a promoter and a suppressor of tumorigenesis (50). SYK gain-of-function variants found in patients with immune deficiency and systemic inflammation boost immune signaling and elevate inflammatory cytokines. A SYK-S544Y knock-in

TABLE 4 MR results of exposure factors and outcomes (right hand grip strength).

exposure	outcome	method	nsnp	pval	OR(95% CI)	pleio_P
FLT4	Hand grip strength (right)	IVW	4	**0.010**	1.011 (1.003 to 1.019)	0.492
CA2		IVW	33	**<0.001**	1.008 (1.005 to 1.012)	0.877
ZAP70		IVW	12	**0.022**	1.009 (1.001 to 1.016)	0.219
HDAC1		IVW	4	**0.003**	1.019 (1.006 to 1.032)	0.962
PTK2B		IVW	16	**0.039**	1.004 (1.000 to 1.008)	0.879
PTGFR		IVW	9	**0.016**	1.011 (1.002 to 1.019)	0.610
ADORA2A		IVW	3	**0.011**	1.014 (1.003 to 1.025)	0.877
CDK7		IVW	3	**0.004**	1.023 (1.007 to 1.039)	0.574
CTSL		IVW	12	**0.036**	1.005 (1.000 to 1.009)	0.224
NAAA		IVW	59	**0.034**	1.003 (1.000 to 1.005)	0.237
CTSS		IVW	27	**<0.001**	1.008 (1.005 to 1.010)	0.441
SYK		IVW	17	**0.006**	1.006 (1.002 to 1.010)	0.689
PTGER4		IVW	21	**0.038**	1.005 (1.000 to 1.009)	0.261
MTOR		IVW	4	**<0.001**	1.012 (1.006 to 1.018)	0.623

pavl: Significance; OR, Odds ratio, with the 95% confidence interval of the odds ratio in parentheses; pleio_P: Test for horizontal pleiotropy.

TABLE 5 MR results of exposure factors and outcomes (limb muscle mass).

exposure	outcome	method	nsnp	pval	OR(95% CI)	pleio_P
BAD	Appendicular lean mass	IVW	3	**0.005**	1.033 (1.010 to 1.056)	0.782
FLT4		IVW	4	**0.013**	1.013 (1.003 to 1.024)	0.497
CDC7		IVW	23	**<0.001**	1.013 (1.008 to 1.017)	0.125
PDE8B		IVW	7	**<0.001**	1.026 (1.016 to 1.037)	0.292
ZAP70		IVW	13	**0.004**	1.015 (1.005 to 1.025)	0.749
PTK2B		IVW	16	**<0.001**	1.010 (1.005 to 1.015)	0.189
CDK7		IVW	3	**0.007**	1.027 (1.007 to 1.047)	0.305
CTSL		IVW	12	**0.015**	1.007 (1.001 to 1.013)	0.402
CTSK		IVW	26	**<0.001**	1.021 (1.016 to 1.027)	0.975
CTSS		IVW	29	**<0.001**	1.036 (1.027 to 1.045)	0.116
FNTA		IVW	8	**0.006**	1.024 (1.007 to 1.042)	0.265
MTOR		IVW	4	**<0.001**	1.064 (1.056 to 1.072)	0.913

pavl: Significance; OR, Odds ratio, with the 95% confidence interval of the odds ratio in parentheses; pleio_P: Test for horizontal pleiotropy.

mouse model mirrored human disease symptoms, which were partially relieved by SYK inhibitors (51). These findings emphasize the pivotal role of SYK in amplifying inflammatory and immune responses, and underscore the potential of targeting SYK as a fundamental therapeutic strategy for the management of related disorders. However, no studies have identified a correlation between the SYK gene and cancer-associated sarcopenia, indicating a need for further in-depth investigation in future research. Our study found that sarcopenia is closely related to inflammation and immune responses in advanced CRC patients treated with fruquintinib. We identified SYK as a risk gene for fruquintinib-induced sarcopenia through MR analysis. This discovery offers a novel perspective on the genetic basis of sarcopenia in cancer patients and may guide future precision medicine approaches. From a clinical perspective, our findings underscore the importance of early detection and management of sarcopenia, as addressing this condition may enhance the efficacy of treatments such as fruquintinib and mitigate associated adverse side effects. By improving nutritional status and enhancing immunity,

TABLE 6 MR results of exposure factors and outcomes (walking speed).

exposure	outcome	method	nsnp	pval	OR(95% CI)	pleio_P
BAD	Usual walking pace	IVW	3	**0.001**	1.025 (1.009 to 1.040)	0.924
FGFR2		IVW	5	**0.006**	1.007 (1.002 to 1.013)	0.852
HSP90AA1		IVW	8	**<0.001**	1.014 (1.006 to 1.022)	0.110
PDE8B		IVW	7	**0.007**	1.006 (1.002 to 1.010)	0.502
PTK2B		IVW	16	**<0.001**	1.009 (1.006 to 1.012)	0.688
SYK		IVW	17	**0.027**	1.004 (1.000 to 1.008)	0.292
STAT3		IVW	15	**<0.001**	1.013 (1.007 to 1.018)	0.064

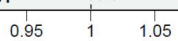

pavl: Significance; OR, Odds ratio, with the 95% confidence interval of the odds ratio in parentheses; pleio_P: Test for horizontal pleiotropy.

10.3389/fimmu.2025.1582308

TABLE 7 The significant results of the four outcome variables.

Exposure	Outcome	Id.exposure	Id.outcome	Method	Nsnp	Pval	Or
BAD	Hand grip strength (left)	eqtl-a-ENSG00000002330	ukb-b-7478	IVW	3	8.83E-10	0.946
	Hand grip strength (right)		ukb-b-10215	IVW	3	6.74E-04	0.970
	Appendicular lean mass		ebi-a-GCST90000025	IVW	3	0.005	1.033
	Usual walking pace		ukb-b-4711	IVW	3	0.001	1.025
SYK	Hand grip strength (left)	eqtl-a-ENSG00000165025	ukb-b-7478	IVW	17	0.037	1.004
	Hand grip strength (right)		ukb-b-10215	IVW	17	0.006	1.006
	Appendicular lean mass		ebi-a-GCST90000025	IVW	17	0.003	0.992
	Usual walking pace		ukb-b-4711	IVW	17	0.027	1.004

nutrition intervention can help alleviate symptoms and improve the prognosis for patients with CRC (52, 53). Thus, we can conclude that nutritional interventions and physical rehabilitation should be integrated into the standard care of CRC patients, especially those at risk for sarcopenia, to optimize outcomes.

This study has several limitations, including its retrospective design, which limits causal inference. Further prospective studies are needed to confirm these findings and explore the underlying mechanisms. Additionally, factors such as muscle strength, physical activity, and exercise interventions were not evaluated, and should be considered in future research. Further validation of the SYK gene in larger cohorts is also needed.

In conclusion, sarcopenia may be an important prognostic factor for patients with advanced colorectal cancer undergoing fruquintinib

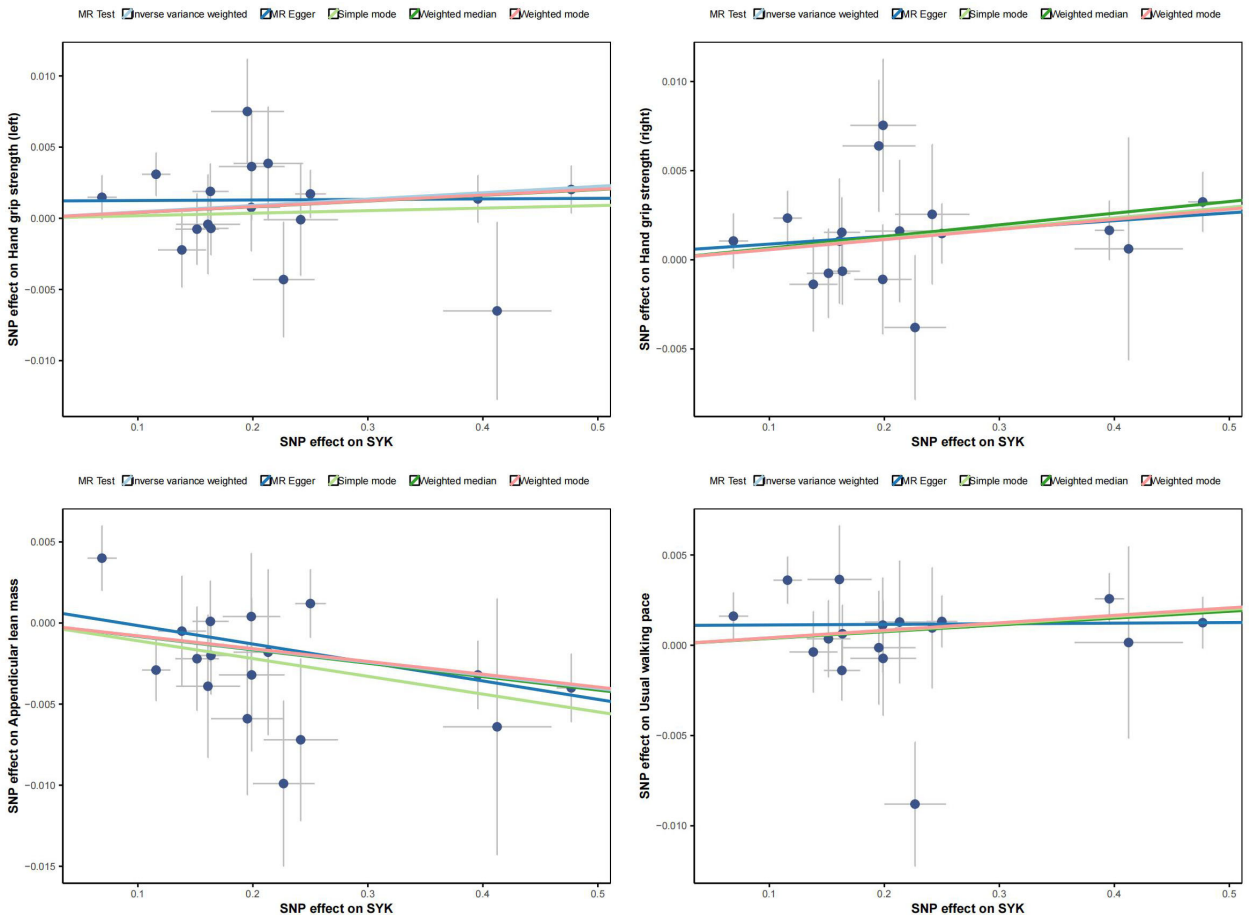

FIGURE 5
Scatter plot of exposure factors and outcomes.



FIGURE 6
Forest plot for the sequential exclusion of exposure factors and outcomes.

targeted therapy. Early identification and management of sarcopenia could potentially enhance treatment outcomes and reduce the risk of complications in these patients.

Data availability statement

The original contributions presented in the study are included in the article/Supplementary Material. Further inquiries can be directed to the corresponding authors.

Ethics statement

The studies involving humans were approved by Ethics Committee of Shanghai Municipal Hospital of Traditional Chinese Medicine. The studies were conducted in accordance with the local legislation and institutional requirements. Written informed consent for participation was not required from the participants or the participants' legal guardians/next of kin because Our study is a retrospective study and does not involve specific drug intervention protocols. Therefore, no written informed consent was required.

Author contributions

YW: Funding acquisition, Writing – original draft, Writing – review & editing. DM: Conceptualization, Investigation, Writing – review & editing. SQ: Conceptualization, Methodology, Writing – review & editing. TY: Data curation, Formal analysis, Writing – review & editing. GS: Data curation, Writing – review & editing. HS: Data curation, Methodology, Writing – review & editing. WH: Data curation, Methodology, Writing – review & editing. ZT: Data curation, Methodology, Project administration, Writing – review & editing. WC: Writing – review & editing, Data curation, Conceptualization. HF: Funding acquisition, Methodology, Writing – review & editing. YX: Conceptualization, Project administration, Resources, Software, Writing – original draft.

Funding

The author(s) declare that financial support was received for the research and/or publication of this article. This work was supported by the National Natural Science Foundation of China (82174188, 82405498) and Shanghai Municipal Health Commission Talent Program (2022YQ032).

Acknowledgments

The GWAS summary data were obtained from the online public platform (https://gwas.mrcieu.ac.uk/). The analyses of GWAS summary data were performed under application R version 4.0.2.

Conflict of interest

The authors declare that the research was conducted in the absence of any commercial or financial relationships that could be construed as a potential conflict of interest.

Generative AI statement

The author(s) declare that no Generative AI was used in the creation of this manuscript.

Correction note

A correction has been made to this article. Details can be found at: 10.3389/fimmu.2025.1671178.

Publisher's note

All claims expressed in this article are solely those of the authors and do not necessarily represent those of their affiliated organizations, or those of the publisher, the editors and the reviewers. Any product that may be evaluated in this article, or claim that may be made by its manufacturer, is not guaranteed or endorsed by the publisher.

Supplementary material

The Supplementary Material for this article can be found online at: https://www.frontiersin.org/articles/10.3389/fimmu.2025.1582308/full#supplementary-material

References

1. Fleischer JR, Schmitt AM, Haas G, Xu X, Zeisberg EM, Bohnenberger H, et al. Molecular differences of angiogenic versus vessel co-opting colorectal cancer liver metastases at single-cell resolution. *Mol Cancer*. (2023) 22:17. doi: 10.1186/s12943-023-01713-1

2. Sung H, Ferlay J, Siegel RL, Laversanne M, Soerjomataram I, Jemal A, et al. Global cancer statistics 2020: GLOBOCAN estimates of incidence and mortality worldwide for 36 cancers in 185 countries. *CA Cancer J Clin*. (2021) 71:209–49. doi: 10.3322/caac.21660

3. Wang Q, Huang X, Zhou S, Ding Y, Wang H, Jiang W, et al. IL1RN and PRRX1 as a prognostic biomarker correlated with immune infiltrates in colorectal cancer: evidence from bioinformatic analysis. *Int J Genomics*. (2022) 2022:2723264. doi: 10.1155/2022/2723264

4. Ying P, Chen C, Lu Z, Chen S, Zhang M, Cai Y, et al. Genome-wide enhancer-gene regulatory maps link causal variants to target genes underlying human cancer risk. *Nat Commun*. (2023) 14:5958. doi: 10.1038/s41467-023-41690-z

5. Lu L, Mullins CS, Schafmayer C, Zeißig S, Linnebacher M. A global assessment of recent trends in gastrointestinal cancer and lifestyle-associated risk factors. *Cancer Commun (Lond)*. (2021) 41:1137–51. doi: 10.1002/cac2.12220

6. Shen G, Wang Q, Li Z, Xie J, Han X, Wei Z, et al. Bridging chronic inflammation and digestive cancer: the critical role of innate lymphoid cells in tumor microenvironments. *Int J Biol Sci*. (2024) 20:4799–818. doi: 10.7150/ijbs.96338

7. Xia J, Ma N, Shi Q, Liu QC, Zhang W, Cao HJ, et al. XAF1 promotes colorectal cancer metastasis via VCP-RNF114-JUP axis. *J Cell Biol*. (2024) 223. doi: 10.1083/jcb.202303015

8. Biller LH, Schrag D. Diagnosis and treatment of metastatic colorectal cancer: A review. *Jama*. (2021) 325:669–85. doi: 10.1001/jama.2021.0106

9. Singh M, Morris VK, Bandey IN, Hong DS, Kopetz S. Advancements in combining targeted therapy and immunotherapy for colorectal cancer. *Trends Cancer*. (2024) 10:598–609. doi: 10.1016/j.trecan.2024.05.001

10. Shinji S, Yamada T, Matsuda A, Sonoda H, Ohta R, Iwai T, et al. Recent advances in the treatment of colorectal cancer: A review. *J Nippon Med Sch*. (2022) 89:246–54. doi: 10.1272/jnms.JNMS.2022_89-310

11. Feng L, Zhang W, Shen Q, Miao C, Chen L, Li Y, et al. Bile acid metabolism dysregulation associates with cancer cachexia: roles of liver and gut microbiome. *J Cachexia Sarcopenia Muscle*. (2021) 12:1553–69. doi: 10.1002/jcsm.12798

12. Halma MTJ, Tuszynski JA, Marik PE. Cancer metabolism as a therapeutic target and review of interventions. *Nutrients*. (2023) 15. doi: 10.3390/nu15194245

13. Souza BU, Souza NCS, Martucci RB, Rodrigues VD, Pinho NB, Gonzalez MC, et al. Factors associated with sarcopenia in patients with colorectal cancer. *Nutr Cancer*. (2018) 70:176–83. doi: 10.1080/01635581.2018.1412480

14. Xie H, Wei L, Gao S, Liu M, Liang Y, Yuan G, et al. Prognostic significance of sarcopenia diagnosed based on the anthropometric equation for progression-free survival and overall survival in patients with colorectal cancer. *Front Nutr*. (2023) 10:1076589. doi: 10.3389/fnut.2023.1076589

15. Nishikawa H, Asai A, Fukunishi S, Nishiguchi S, Higuchi K. Metabolic syndrome and sarcopenia. *Nutrients*. (2021) 13(10):3159. doi: 10.3390/nu13103519

16. Aluganti Narasimhulu C, Singla DK. Amelioration of diabetes-induced inflammation mediated pyroptosis, sarcopenia, and adverse muscle remodelling by bone morphogenetic protein-7. *J Cachexia Sarcopenia Muscle*. (2021) 12:403–20. doi: 10.1002/jcsm.12662

17. Nicholson T, Dhaliwal A, Quinlan JI, Allen SL, Williams FR, Hazeldine J, et al. Accelerated aging of skeletal muscle and the immune system in patients with chronic liver disease. *Exp Mol Med*. (2024) 56:1667–81. doi: 10.1038/s12276-024-01287-y

18. Li J, Qin S, Xu RH, Shen L, Xu J, Bai Y, et al. Effect of fruquintinib vs placebo on overall survival in patients with previously treated metastatic colorectal cancer: the FRESCO randomized clinical trial. *Jama*. (2018) 319:2486–96. doi: 10.1001/jama.2018.7855

19. Loeliger J, Edbrooke L, Daly RM, Stewart J, Bucci L, Puskas C, et al. Development and feasibility of an inpatient cancer-related sarcopenia pathway at a major cancer centre. *Int J Environ Res Public Health*. (2022) 19(7):4038. doi: 10.3390/ijerph19074038

20. Tang W, Li F, Zheng H, Zhao J, Wei H, Xiong X, et al. Prognostic Value of Baseline Skeletal Muscle Index in Colorectal Cancer Patients Treated with Fruquintinib: A multi-center real world analysis. *Int J Colorectal Dis*. (2024) 39:186. doi: 10.1007/s00384-024-04747-z

21. Aminianfar A, Hashemi R, Emami F, Heshmat R, Motlagh AD, Esmaillzadeh A. Associations between dietary total antioxidant capacity and sarcopenia: a cross-sectional study. *Nutr J*. (2024) 23:87. doi: 10.1186/s12937-024-00933-5

22. Sharma V, Fadel A, Tollefson MK, Psutka SP, Blezek DJ, Frank I, et al. Artificial intelligence-based assessment of pre-operative body composition is associated with early complications after radical cystectomy. *J Urol*. (2025) 213(2):2828–237. doi: 10.1097/JU.0000000000004292.

23. Du D, Jing Z, Zhang G, Dang X, Liu R, Song J. The relationship between central obesity and bone mineral density: a Mendelian randomization study. *Diabetol Metab Syndr*. (2022) 14:63. doi: 10.1186/s13098-022-00840-x

24. Cruz-Jentoft AJ, Baeyens JP, Bauer JM, Boirie Y, Cederholm T, Landi F, et al. Sarcopenia: European consensus on definition and diagnosis: Report of the European Working Group on Sarcopenia in Older People. *Age Ageing*. (2010) 39:412–23. doi: 10.1093/ageing/afq034

25. Mavromatis LA, Rosoff DB, Cupertino RB, Garavan H, Mackey S, Lohoff FW. Association between brain structure and alcohol use behaviors in adults: A mendelian randomization and multiomics study. *JAMA Psychiatry*. (2022) 79:869–78. doi: 10.1001/jamapsychiatry.2022.2196

26. Li Z, Huang X, Wang Q, Gopinath D. Causal association between microbiome and oral-oropharyngeal cancer: A mendelian randomization study. *Int Dent J*. (2025) 75(3):1897–1905. doi: 10.1016/j.identj.2025.01.017

27. Sugawara K, Yamashita H, Urabe M, Okumura Y, Yagi K, Aikou S, et al. Poor nutritional status and sarcopenia influences survival outcomes in gastric carcinoma patients undergoing radical surgery. *Eur J Surg Oncol*. (2020) 46:1963–70. doi: 10.1016/j.ejso.2020.04.044

28. Pucci M, Raimondo S, Urzì O, Moschetti M, Di Bella MA, Conigliaro A, et al. Tumor-derived small extracellular vesicles induce pro-inflammatory cytokine expression and PD-L1 regulation in M0 macrophages via IL-6/STAT3 and TLR4 signaling pathways. *Int J Mol Sci*. (2021) 22(22):12118. doi: 10.3390/ijms222212118

29. Jain SM, Deka D, Das A, Paul S, Pathak S, Banerjee A. Role of interleukins in inflammation-mediated tumor immune microenvironment modulation in colorectal cancer pathogenesis. *Dig Dis Sci*. (2023) 68:3220–36. doi: 10.1007/s10620-023-07972-8

30. Zanders L, Kny M, Hahn A, Schmidt S, Wundersitz S, Todiras M, et al. Sepsis induces interleukin 6, gp130/JAK2/STAT3, and muscle wasting. *J Cachexia Sarcopenia Muscle*. (2022) 13:713–27. doi: 10.1002/jcsm.12867

31. Nelke C, Dziewas R, Minnerup J, Meuth SG, Ruck T. Skeletal muscle as potential central link between sarcopenia and immune senescence. *EBioMedicine*. (2019) 49:381–8. doi: 10.1016/j.ebiom.2019.10.034

32. Li J, Wang Z, Zhong H, He Y, Zhang C, Niu Z, et al. A phase IV study to evaluate the safety of fruquintinib in Chinese patients in real-world clinical practice. *Oncologist*. (2024) 29:e1012–e9. doi: 10.1093/oncolo/oyae073

33. Li J, Guo W, Bai Y, Deng Y, Yang L, Chen Z, et al. Safety profile and adverse events of special interest for fruquintinib in chinese patients with previously treated metastatic colorectal cancer: analysis of the phase 3 FRESCO trial. *Adv Ther*. (2020) 37:4585–98. doi: 10.1007/s12325-020-01477-w

34. Tan S, Zhang S, Zhou N, Cai X, Yi C, Gou H. Efficacy and safety of fruquintinib dose-escalation strategy for elderly patients with refractory metastatic colorectal cancer: A single-arm, multicenter, phase II study. *Cancer Med*. (2023) 12:22038–46. doi: 10.1002/cam4.6786

35. Zhou J, Fang P, Li X, Luan S, Xiao X, Gu Y, et al. Prognostic value of geriatric nutritional risk index in esophageal carcinoma: A systematic review and meta-analysis. *Front Nutr*. (2022) 9:831283. doi: 10.3389/fnut.2022.831283

36. Cai H, Li J, Chen Y, Zhang Q, Liu Y, Jia H. Preoperative inflammation and nutrition-based comprehensive biomarker for predicting prognosis in resectable colorectal cancer. *Front Oncol*. (2023) 13:1279487. doi: 10.3389/fonc.2023.1279487

37. Meng Q, Tan S, Jiang Y, Han J, Xi Q, Zhuang Q, et al. Post-discharge oral nutritional supplements with dietary advice in patients at nutritional risk after surgery for gastric cancer: A randomized clinical trial. *Clin Nutr*. (2021) 40:40–6. doi: 10.1016/j.clnu.2020.04.043

38. Hayashi H, Shimizu A, Kubota K, Notake T, Masuo H, Yoshizawa T, et al. Combination of sarcopenia and prognostic nutritional index to predict long-term outcomes in patients undergoing initial hepatectomy for hepatocellular carcinoma. *Asian J Surg*. (2023) 46:816–23. doi: 10.1016/j.asjsur.2022.07.122

39. Yin M, Zhang H, Liu Q, Ding F, Hou L, Deng Y, et al. Determination of skeletal muscle mass by aspartate aminotransferase/alanine aminotransferase ratio, insulin and FSH in Chinese women with sarcopenia. *BMC Geriatr*. (2022) 22:893. doi: 10.1186/s12877-022-03491-9

40. Nishiyama A, Staub Y, Suga Y, Fujita M, Tanimoto A, Ohtsubo K, et al. Sarcopenia may influence the prognosis in advanced thyroid cancer patients treated with molecular targeted therapy. *In Vivo*. (2021) 35:401–10. doi: 10.21873/invivo.12271

41. Hiroshige T, Ogasawara N, Kumagae H, Ueda K, Chikui K, Uemura KI, et al. Sarcopenia and the therapeutic effects of androgen receptor-axis-targeted therapies in patients with castration-resistant prostate cancer. *In Vivo*. (2023) 37:1266–74. doi: 10.21873/invivo.13204

42. Riviati N, Legiran L, Saleh I, Indrajaya T, Ali Z, Irfannuddin, et al. Ophiocephalus striatus extract supplementation decreases serum IL-6 levels in older people with sarcopenia-A single-center experience. *Geriatr (Basel)*. (2024) 9:35. doi: 10.3390/geriatrics9020035

43. Dupont J, Vercauteren L, Amini N, Lapauw L, De Schaepdryver M, Poesen K, et al. Are inflammatory markers associated with sarcopenia-related traits in older adults with sarcopenia? - A cross-sectional analysis of the ENHANce study. *Exp Gerontol*. (2023) 178:112196. doi: 10.1016/j.exger.2023.112196

44. Orange ST, Leslie J, Ross M, Mann DA, Wackerhage H. The exercise IL-6 enigma in cancer. *Trends Endocrinol Metab*. (2023) 34:749–63. doi: 10.1016/j.tem.2023.08.001

45. Patel SA, Nilsson MB, Yang Y, Le X, Tran HT, Elamin YY, et al. IL6 mediates suppression of T- and NK-cell function in EMT-associated TKI-resistant EGFR-mutant NSCLC. *Clin Cancer Res*. (2023) 29:1292–304. doi: 10.1158/1078-0432.CCR-22-3379

46. Zhang R, Qi F, Zhao F, Li G, Shao S, Zhang X, et al. Cancer-associated fibroblasts enhance tumor-associated macrophages enrichment and suppress NK cells function in colorectal cancer. *Cell Death Dis*. (2019) 10:273. doi: 10.1038/s41419-019-1435-2

47. Biswas P, Dey D, Rahman A, Islam MA, Susmi TF, Kaium MA, et al. Analysis of SYK gene as a prognostic biomarker and suggested potential bioactive phytochemicals as an alternative therapeutic option for colorectal cancer: an in-silico pharmaco-informatics investigation. *J Pers Med*. (2021) 11:888. doi: 10.3390/jpm11090888

48. Mansueto MS, Reens A, Rakhilina L, Chi A, Pan BS, Miller JR. A reevaluation of the spleen tyrosine kinase (SYK) activation mechanism. *J Biol Chem*. (2019) 294:7658–68. doi: 10.1074/jbc.RA119.008045

49. Canton J, Blees H, Henry CM, Buck MD, Schulz O, Rogers NC, et al. The receptor DNGR-1 signals for phagosomal rupture to promote cross-presentation of dead-cell-associated antigens. *Nat Immunol*. (2021) 22:140–53. doi: 10.1038/s41590-020-00824-x

50. Buffard M, Naldi A, Freiss G, Deckert M, Radulescu O, Coopman PJ, et al. Comparison of SYK signaling networks reveals the potential molecular determinants of its tumor-promoting and suppressing functions. *Biomolecules*. (2021) 11:308. doi: 10.3390/biom11020308

51. Wang L, Aschenbrenner D, Zeng Z, Cao X, Mayr D, Mehta M, et al. Gain-of-function variants in SYK cause immune dysregulation and systemic inflammation in humans and mice. *Nat Genet*. (2021) 53:500–10. doi: 10.1038/s41588-021-00803-4

52. van Rooijen S, Carli F, Dalton S, Thomas G, Bojesen R, Le Guen M, et al. Multimodal prehabilitation in colorectal cancer patients to improve functional capacity and reduce postoperative complications: the first international randomized controlled trial for multimodal prehabilitation. *BMC Cancer*. (2019) 19:98. doi: 10.1186/s12885-018-5232-6

53. Ye J, Hu Y, Chen X, Chang C, Li K. Comparative effects of different nutritional supplements on inflammation, nutritional status, and clinical outcomes in colorectal cancer patients: A systematic review and network meta-analysis. *Nutrients*. (2023) 15:2772. doi: 10.3390/nu15122772

frontiers | Frontiers in Immunology

TYPE Correction
PUBLISHED 05 August 2025
DOI 10.3389/fimmu.2025.1671178

Check for updates

OPEN ACCESS

APPROVED BY
Frontiers Editorial Office,
Frontiers Media SA, Switzerland

*CORRESPONDENCE
Frontiers Production Office
production.office@frontiersin.org

RECEIVED 22 July 2025
ACCEPTED 22 July 2025
PUBLISHED 05 August 2025

CITATION
Frontiers Production Office (2025) Correction: The impact of sarcopenia on prognosis and fruquintinib efficacy in advanced colorectal cancer: a retrospective and mendelian randomization study. *Front. Immunol.* 16:1671178. doi: 10.3389/fimmu.2025.1671178

COPYRIGHT
© 2025 Frontiers Production Office. This is an open-access article distributed under the terms of the Creative Commons Attribution License (CC BY). The use, distribution or reproduction in other forums is permitted, provided the original author(s) and the copyright owner(s) are credited and that the original publication in this journal is cited, in accordance with accepted academic practice. No use, distribution or reproduction is permitted which does not comply with these terms.

Correction: The impact of sarcopenia on prognosis and fruquintinib efficacy in advanced colorectal cancer: a retrospective and mendelian randomization study

Frontiers Production Office*

Frontiers Media SA, Lausanne, Switzerland

KEYWORDS

sarcopenia, immune, nutrition, advanced colorectal cancer, fruquintinib, mendelian randomization study

A Correction on

The impact of sarcopenia on prognosis and fruquintinib efficacy in advanced colorectal cancer: a retrospective and mendelian randomization study

By Wang Y, Meilu D, Qi S, Yufei T, Song G, Susu H, Haotian W, Tingting Z, Chao W, Fenggang H and Xiaoling Y (2025) *Front. Immunol.* 16:1582308. doi: 10.3389/fimmu.2025.1582308

Due to a production mistake, there was a mistake in **Table 3** and **Table 5** as published. The tables were swapped. The corrected **Table 3** and **Table 5** appear below.

The publisher apologizes for the error and the original version of this article has been updated.

TABLE 3 MR results of exposure factors and outcomes (left hand grip strength).

exposure	outcome	method	nsnp	pval	OR(95% CI)	pleio_P
FLT4	Hand grip strength (left)	IVW	4	**0.002**	1.013 (1.005 to 1.021)	0.480
CA2		IVW	33	**<0.001**	1.007 (1.003 to 1.011)	0.826
ZAP70		IVW	12	**<0.001**	1.013 (1.008 to 1.019)	0.228
HDAC1		IVW	4	**0.047**	1.013 (1.000 to 1.026)	0.641
ADORA2A		IVW	3	**0.001**	1.017 (1.007 to 1.028)	0.845
SLC27A1		IVW	7	**0.020**	1.012 (1.002 to 1.021)	0.338
CDK7		IVW	3	**0.037**	1.017 (1.001 to 1.033)	0.337
CTSL		IVW	12	**0.040**	1.005 (1.000 to 1.009)	0.553
CTSK		IVW	26	**<0.001**	1.006 (1.003 to 1.009)	0.182
CTSS		IVW	27	**<0.001**	1.009 (1.007 to 1.012)	0.461
ADORA1		IVW	4	**0.037**	1.005 (1.000 to 1.009)	0.684
SYK		IVW	17	**0.037**	1.004 (1.000 to 1.009)	0.284
IMPDH2		IVW	12	**<0.001**	1.041 (1.031 to 1.051)	0.056
IRAK4		IVW	8	**0.028**	1.008 (1.001 to 1.015)	0.430
MTOR		IVW	4	**0.003**	1.009 (1.003 to 1.015)	0.737

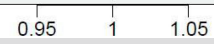

pavl: Significance; OR, Odds ratio, with the 95% confidence interval of the odds ratio in parentheses; pleio_P: Test for horizontal pleiotropy.

TABLE 5 MR results of exposure factors and outcomes (limb muscle mass).

exposure	outcome	method	nsnp	pval	OR(95% CI)	pleio_P
BAD	Appendicular lean mass	IVW	3	**0.005**	1.033 (1.010 to 1.056)	0.782
FLT4		IVW	4	**0.013**	1.013 (1.003 to 1.024)	0.497
CDC7		IVW	23	**<0.001**	1.013 (1.008 to 1.017)	0.125
PDE8B		IVW	7	**<0.001**	1.026 (1.016 to 1.037)	0.292
ZAP70		IVW	13	**0.004**	1.015 (1.005 to 1.025)	0.749
PTK2B		IVW	16	**<0.001**	1.010 (1.005 to 1.015)	0.189
CDK7		IVW	3	**0.007**	1.027 (1.007 to 1.047)	0.305
CTSL		IVW	12	**0.015**	1.007 (1.001 to 1.013)	0.402
CTSK		IVW	26	**<0.001**	1.021 (1.016 to 1.027)	0.975
CTSS		IVW	29	**<0.001**	1.036 (1.027 to 1.045)	0.116
FNTA		IVW	8	**0.006**	1.024 (1.007 to 1.042)	0.265
MTOR		IVW	4	**<0.001**	1.064 (1.056 to 1.072)	0.913

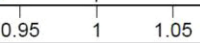

pavl: Significance; OR, Odds ratio, with the 95% confidence interval of the odds ratio in parentheses; pleio_P: Test for horizontal pleiotropy.

frontiers | Frontiers in Immunology

TYPE Original Research
PUBLISHED 21 July 2025
DOI 10.3389/fimmu.2025.1622528

Check for updates

OPEN ACCESS

EDITED BY
Chao Wang,
Shanghai Jiao Tong University, China

REVIEWED BY
Namuunaa Juramt,
Harvard Medical School, United States
Dulguun Juramt,
Charité University Medicine Berlin, Germany

*CORRESPONDENCE
Peng Li
lipenglimo@163.com
Yifei Pan
13506641535@139.com
Xiaodong Zhang
zhangxiaodong777@wmu.edu.cn

†These authors have contributed equally to this work and share last authorship

‡These authors share first authorship

RECEIVED 03 May 2025
ACCEPTED 25 June 2025
PUBLISHED 21 July 2025
CORRECTED 22 July 2025

CITATION
Zheng C, Zhu B, Chen Y, Shahid N, Hu Y, Ali Husain HMA, Ou B, Zhang Q, Jin H, Zheng Y, Li P, Pan Y and Zhang X (2025) Integrating proteomics and machine learning reveals characteristics and risks of lymph node-independent distant metastasis in colorectal cancer. *Front. Immunol.* 16:1622528. doi: 10.3389/fimmu.2025.1622528

COPYRIGHT
© 2025 Zheng, Zhu, Chen, Shahid, Hu, Ali Husain, Ou, Zhang, Jin, Zheng, Li, Pan and Zhang. This is an open-access article distributed under the terms of the Creative Commons Attribution License (CC BY). The use, distribution or reproduction in other forums is permitted, provided the original author(s) and the copyright owner(s) are credited and that the original publication in this journal is cited, in accordance with accepted academic practice. No use, distribution or reproduction is permitted which does not comply with these terms.

Integrating proteomics and machine learning reveals characteristics and risks of lymph node-independent distant metastasis in colorectal cancer

Chenxiao Zheng[1‡], Baiwang Zhu[1‡], Yanyu Chen[2], Numan Shahid[3], Yiwang Hu[1], Hajar Mansoor Ahmed Ali Husain[4], Binbin Ou[5], Qiongying Zhang[6], Haobo Jin[7], Yating Zheng[1], Peng Li[4*†], Yifei Pan[1*†] and Xiaodong Zhang[1,8*†]

[1]Department of Colorectal Anal Surgery, The First Affiliated Hospital of Wenzhou Medical University, Wenzhou, Zhejiang, China, [2]Clinical Medical College, Hangzhou Medical College, Hangzhou, Zhejiang, China, [3]Department of Hepato-Pancreato-Biliary (HPB) Surgery, King's College Hospital, Denmark Hill, London, United Kingdom, [4]Department of Hepatology, King's College Hospital, Denmark Hill, London, United Kingdom, [5]General Practice Department, Hangzhou Gongshu Hospital of Integrated Traditional and Western Medicine, Hangzhou, Zhejiang, China, [6]Department of Pathology, the First Affiliated Hospital of Wenzhou Medical University, Wenzhou, Zhejiang, China, [7]Laboratory Animal Centre, Wenzhou Medical University, Wenzhou, Zhejiang, China, [8]National Key Clinical Specialty (General Surgery), The First Affiliated Hospital of Wenzhou Medical University, Wenzhou, Zhejiang, China

Background: Metastatic colorectal cancer (mCRC) poses significant treatment challenges, especially liver metastasis (CRLM). A notable proportion of CRC has synchronous metastasis independent of lymph node metastasis (LNM). The biological traits of lymph node-independent metastasis in CRC are unclear, and early synchronous metastasis is hard to predict with current imaging or clinicopathological methods.

Method: We collected samples from 12 CRC patients with synchronous distant metastasis without LNM (T1-3N0M1). Data-Independent Acquisition Mass Spectrometry (DIA-MS), multi-omics data integration, and machine learning were used to develop a Lymph node-Independent Metastasis Genes (LIMGs) signature to predict synchronous distant metastasis risk in stage I-II CRC patients and validate it in multi-cohort. Immune microenvironment across risk subgroups was calculated by Estimating Relative Subsets of RNA Transcripts (CIBERSORT). Tumor Mutation Burden (TMB), Microsatellite Instability (MSI) score, immune functions and immune checkpoint gene expression were analyzed to evaluate immunotherapy response. Single cell RNA sequencing (scRNA-seq) analysis illustrated the expression profile of integrin α11 (ITGA11) in CRC. Immunohistochemistry (IHC) confirmed its expression pattern, while wound healing and transwell assays elucidated the role of ITGA11 in CRC metastasis.

Results: The LIMGs signature demonstrated strong predictive performance of lymph node-independent synchronous metastasis across cohorts. The high-risk subgroup exhibited enhanced extracellular matrix (ECM) remodeling, epithelial-mesenchymal transition (EMT) and correlated with immunosuppressive tumor

microenvironment (TME), lower TMB and MSI score, indicating worse immunotherapy response. Additionally, machine learning reveal ITGA11's pivotal role in lymph node-independent metastasis. IHC scores showing significant discriminatory ability of ITGA11 across different samples. Wound healing and transwell assays reveal that the knockdown of ITGA11 hinders the migration and invasion of CRC SW480 cells.

Conclusion: Our findings suggest that EMT-related signature LIMGs significantly affects lymph node-independent distant metastasis in CRC and effectively predicts non-LNM synchronous metastasis in stage I-II CRC patients. LIMG ITGA11 may promote early metastasis by enhancing migration and invasion. These offering insights into precise risk stratification and treatment for CRC patients.

KEYWORDS

colorectal cancer, proteomics, machine learning, synchronous metastasis, immune microenvironment, Itga11

Introduction

CRC currently ranks as the third most common cancer worldwide and the second leading cause of cancer-related deaths, with over 1,800,000 new cases and nearly 900,000 deaths annually worldwide (1). Metastatic colorectal cancer (mCRC) is one of the challenging aspects in the treatment of CRC, with the liver being the primary site for metastasis (CRLM). Synchronous metastases refer to metastasis detected before or at the time of CRC diagnosis (2). 15%–25% of CRC patients present with distant metastasis at diagnosis, and the vast majority (80%–90%) of CRLM are initially unresectable (3). Liver metastasis is also the leading cause of death in CRC patients, resulting in a significant social burden.

Traditionally, it has been believed that cancer progression involves sequential spread of the tumor to local lymph nodes followed by distant metastasis. However, a considerable number of mCRC patients do not exhibit early systemic spread. Among these, CRLM often occur without lymph node metastasis (LNM). Data indicate that approximately 23% of synchronous liver metastases originate from stage I-II (N0) CRC, and 44% of metachronous metastases arise from N0 CRC (4). A study on resection of CRLM showed that among over 12,000 patients, 37% had no LNM (5). Furthermore, there was no difference in the incidence of liver metastases between patients with and without LNM (6). At the molecular level, CRC metastasis are often proven to originate from a dominant clone within the primary tumor and sharing a high degree of consistency in mutated genes. In contrast, polyclonal origins are more commonly observed in LNM, with 65% of cases showing that LNM and distant metastases arise from independent subclones within the primary tumor (7). Moreover, LNM exhibits a high rate of inconsistency in mutations compared to the primary tumor (8), suggesting lymph nodes may not always be involved in distant metastasis. Animal models have further confirmed that CRC dissemination to the liver can occur independently of LNM, with direct hematogenous spread being a route for CRLM (9). This may imply that stage III and IV CRC may be considered as parallel progression from stage II disease rather than sequential progression.

An incidence model based on tumor size, time, and mutations shows that early metastasis in the majority (80%) of mCRC patients may occur before the primary tumor is clinically detectable (10). As disseminated tumor cells (DTCs) frequently colonize distant organs by the time of primary tumor detection, and they are undetectable with clinical imaging and patients remain asymptomatic regarding subclinical disease. Circulating tumor DNA (ctDNA) and circulating tumor cells (CTCs) show promise as biomarkers for micrometastasis but require enhanced sensitivity and clinical feasibility (11). Effective biomarkers based on tissue-based protein/RNA detection are needed, combining single-cell analysis, detection of ctDNA epigenetic modification, CTC, exosome, immune cell, cytokine may enable real-time predictive biomarker development.

Recent proteomic studies in CRC have revealed novel protein traits, molecular subtypes, and metastasis markers, underscoring molecular heterogeneity across clinicopathological subgroups (12). However, proteomic research on lymph node-independent distant metastasis in CRC remains limited. Epithelial-mesenchymal transition (EMT), which drives early CRC progression by diminishing cell-cell adhesion and apical polarity while enhancing invasion, is of particular interest (13). Here, we hypothesized that lymph node-independent distant metastasis in CRC arises from EMT-related micrometastasis and hematogenous routes. Our study aims to develop a predictive signature for direct distant metastasis risk in early-stage (I-II) CRC by integrating multi-omics data and

machine learning, thus refining risk stratification and guiding therapy. To this end, we analyzed 12 synchronous distant metastasis patients (T1-T3N0M1) using DIA-MS. Our findings identify EMT-linked LIMGs as key drivers of lymph node-independent metastasis, with high-risk samples exhibiting a more immunosuppressive tumor microenvironment that may facilitate early distant metastasis.

Materials and methods

Patients

For the DIA-MS analysis, the patient cohort was sourced from the Colorectal and Anal Surgery Department of the First Affiliated Hospital of Wenzhou Medical University, with the study having secured ethical approval (KY2022-183) from the hospital's Ethics Committee. Our study screened 271 mCRC patients who underwent simultaneous radical resection of primary tumors and distant metastases between 2018 and 2024. From them, 12 patients with a pathological stage of T1 - 3N0M1 were selected for specimen collection, as shown in Figure 1A. The inclusion criteria were age 18 - 80, clinical diagnosis of synchronous distant metastasis, having undergone radical surgery, histopathological confirmation of colorectal adenocarcinoma, and classification as T1 - 3N0M1 stage according to the 8th edition of the AJCC/UICC TNM staging system. Exclusion criteria included lymph node metastasis, an insufficient number of examined lymph nodes (< 12), a history of other primary malignancies, neoadjuvant therapy, and multiple distant metastases. A detailed overview of the clinicopathological characteristics of the study cohort is presented in Figure 1B and Supplementary Table S1.

Sample preparation

Formalin-fixed paraffinembedded (FFPE) samples of adjacent normal tissues, primary tumors, and distant metastases were collected from 12 CRC patients. Pathological examination by a pathologist confirmed the tumor areas and using hematoxylin-eosin-stained pathologic slides as reference. All pathological reports were cross diagnosed by two senior pathologists and reviewed by a third. To minimize specimen loss, the same type of tissue sections (4μm) from different patients were prepared and mixed into four composite samples for testing.

Protein extraction and peptide enzymatic digestion

For protein extraction, each sample was supplemented with an appropriate volume of SDT lysis buffer (4% SDS, 100 mM Tris-HCl, pH 7.6), followed by protein quantification using the BCA method. Subsequently, 15 μg of protein from each sample was mixed with 5× loading buffer, boiled for 5 minutes, and resolved via SDS-PAGE on a 4%–20% precast gradient gel under a constant voltage of 180 **V** for 45 minutes; the gel was stained with Coomassie Brilliant Blue R-250. To generate a quality control (QC) sample, equal amounts of protein from all samples were pooled into a "Pool sample." All samples, including the QC Pool sample, underwent trypsin digestion using the Filter-Aided Proteome Preparation (FASP) method, after which the resulting peptide fragments were desalted via C18 Cartridge columns, lyophilized, and reconstituted in 40 μL of 0.1% formic acid. Peptide concentrations were determined by measuring absorbance at 280 nm (OD280), and an appropriate quantity of iRT standard peptides was added to each sample prior to analysis by data-independent acquisition (DIA) mass spectrometry using an Astral high-resolution mass spectrometer.

DIA mass spectrometry analysis

Data-Independent Acquisition Mass Spectrometry (DIA-MS) analysis involved a two-step workflow: (1) chromatographic separation of samples using the Vanquish Neo system (Thermo Fisher) with nanoliter flow rates via nano-HPLC, followed by (2) DIA-MS analysis on the Astral high-resolution mass spectrometer (Thermo Scientific) in positive ion mode (parent ion scan range: 380–980 m/z). First-order mass spectrometry parameters included 240,000 resolutions at 200 m/z, 500% Normalized AGC Target, and 5 ms Maximum Injection Time (IT). DIA data acquisition utilized 299 scan windows (2 m/z isolation window, 25 eV HCD collision energy, 500% Normalized AGC Target, 3 ms IT for MS2). The raw DIA data were processed using DIA-NN software with trypsin digestion (max 1 missed cleavage site), carbamidomethyl (C) as fixed modification, and oxidation (M) and acetyl (N-terminal protein) as dynamic modifications. Database search results were filtered to retain only proteins with a False Discovery Rate (FDR) below 1% (14, 15).

Data resources

The RNA-seq, proteome datasets and clinical data for CRC patients were obtained from Gene Expression Omnibus (GEO) database, The Cancer Genomic Atlas (TCGA) database (https://portal.gdc.cancer.gov/), and Li et al.'s study cohort CCRC (16), totaling 1,479 samples across GSE39582 (n=585), CCRC (n=146), GSE38832 (n=122), and TCGA-COADREAD (n=626). Differential expression genes (DEGs) were identified using the limma package (Fold change < 0.67 or >1.5, $p < 0.05$). Overlaps of DEGs in primary tumors and distant metastases were visualized using the "Venn" tool. The CCRC cohort which containing N0M1 CRLM (n=23) and N0M0 (stage I-II, n=49) patients, was used as the training set, validated by GSE39582 and GSE38832, TCGA cohort were utilized for analyzing mutation frequency, TMB, MSI, CNVs and conducting survival analysis, while CRC_EMTAB8107 (n=7) was used for scRNA-seq data analysis.

10.3389/fimmu.2025.1622528

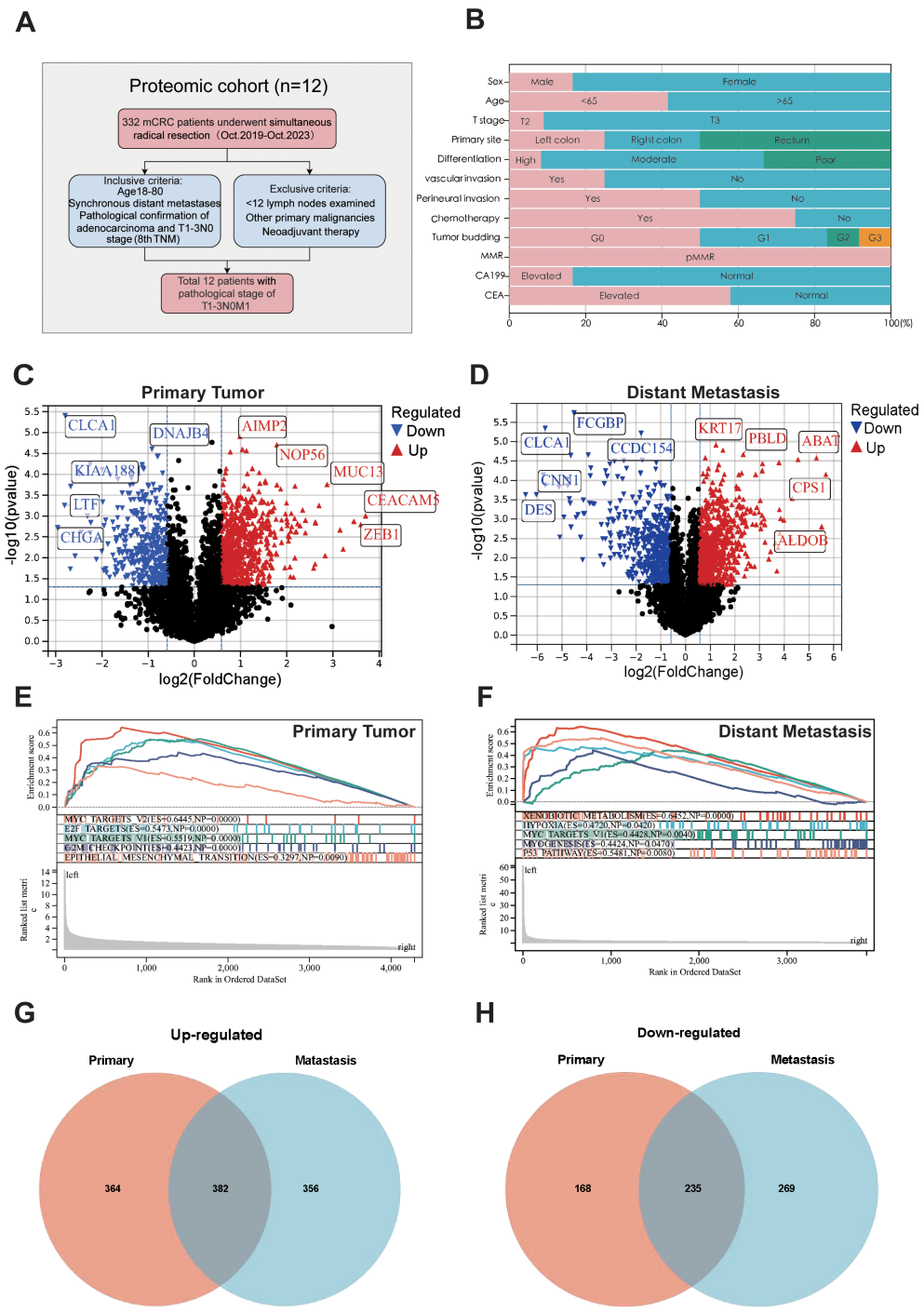

FIGURE 1
Sample selection and proteomics landscape of T1-T3N0M1 CRC. **(A)** Flow chart of the selection process. **(B)** Clinicopathological parameters are shown in histogram. Volcano plot of the differential expressed proteins in the primary tumors **(C)**, distant metastases **(D)** compared to adjacent normal tissues. GSEA analysis for the differential expressed protein in primary tumors **(E)** and distant metastases **(F)**. Venn plot of up-regulated **(G)** and down-regulated **(H)** proteins in primary tumors and distant metastases.

Protein-protein interaction network

The STRING database (http://string-db.org/) was employed to explore the interaction relationships among target proteins. Cytoscape software (version 3.10.0) and the GeneMANIA database (http://genemania.org/) were then used to construct a Protein - Protein Interaction (PPI) network, which helped identify the co - expression patterns and interactions of key proteins. By leveraging the Molecular Complex Detection (MCODE, version 2.0.3) plugin (https://apps.cytoscape.org/apps/mcode), we extracted potentially densely interconnected gene modules from the PPI network.

Biological function and pathway enrichment analysis

To unravel the biological functions and pathways associated with differentially expressed genes (DEGs) and the core cluster within the PPI network, we utilized the "ClusterProfiler" package and Gene Set Enrichment Analysis (GSEA) software, which can be accessed at https://www.gsea-msigdb.org/gsea/index.jsp. With these tools, we performed Kyoto Encyclopedia of Genes and Genomes (KEGG), Gene Ontology (GO), and GSEA analyses. To evaluate the correlation between gene expression levels and biological pathways or molecular mechanisms, we downloaded the h.all.v7.4.symbols.gmt subset from the Molecular Signatures Database (MSigDB), available at https://www.gsea-msigdb.org.

Machine learning identifies LIMGs prognostic biomarkers

Wilcoxon test identified differentially expressed genes between N0M0 (stage I-II) and N0M1 patients, Lasso regression eliminated redundant genes through ten-fold cross-validation using the glmnet package (17). Logistic analysis was used after Z-score transforming of the expression data to determine the odds ratio (OR) of potential hub genes and understand their contribution to the metastasis. Finally, 9 genes were identified as LIMGs. The diagnostic performance of LIMGs was validated using ten machine learning algorithms including Logistic, Support Vector Machine (SVM), Gradient Boosting Machine (GBM), Neural Network, Random Forest (RSF), XGboost, K-Nearest Neighbors (KNN), Adaptive Boosting (Adaboost), Light Gradient Boosting Machine (Light GBM), and Categorical Boosting (CatBoost). We applied them to the CCRC cohort for training, and further validated on external datasets (GSE39582, GSE38832), ROC curves generated by the pROC package were utilized to evaluate the accuracy of the model in diagnosing lymph node-independent distant metastasis of I-II stage CRC. For each patient, LIMG score was calculated for each sample and stratified them into subgroups based on the median score, Kaplan-Meier (KM) survival analysis and nomogram (rms package) assessed prognostic significance of LIMGs.

Mutation analysis and immune microenvironment

Based on the LIMGs Score, risk subgroups are classified in TCGA-COADREAD cohort. Utilizing the "mafTools" R package we analyzed the differences in somatic mutations, TMB between high-risk and low-risk groups, as well as mutation frequency in 9 LIMGs across all samples. The total count of non-synonymous somatic mutations per megabase across the entire genome was computed to assess the TMB. The CNV data and MSI score of CRC patients were downloaded using the TCGA bio links package. Using the CIBERSORT algorithm (18), we evaluated the abundance of 24 immune cell subsets in different risk subgroups. The immune-related functions and expression differences of immune checkpoint genes between subgroups calculated by ssGSEA package predicted immunotherapy response. Correlations between ITGA11 and immune cells were calculated using TIMER (19), QUANTISEQ (20), MCPcounter (21), EPIC (22), and CIBERSORT (23).

Drug sensitivity analysis

Based on Cancer Therapeutics Response Portal (CTRP, https://portals.broadinstitute.org/ctrp.v2.1/) and Genomics of Drug Sensitivity in Cancer (GDSC, https://www.cancerrxgene), the "Oncopredict" R package was used to conduct a half-maximal inhibitory concentration (IC50) analysis of drugs for high-risk and low-risk groups of CRC patients.

Single cell RNA sequencing analysis

We acquired a CRC dataset (CRC_EMTAB8107) from the Tumor Immune Single Cell Hub 2.0 (TISCH 2.0) database (http://tisch.compgenomics.org/) (24), comprising 23,176 cells from 7 tumor samples. Subsequent analyses included scRNA-seq for the ITGA11 and Cell-Cell Interaction (CCI) analysis and visualize the expression and distribution of ITGA11, and the interactions between target gene-enriched cell subpopulations and others.

Antibodies, plasmids, cell lines and culture

In this study, two antibodies were utilized: ITGA11 (#DF8992, Affinity Biosciences, USA) and GAPDH (#2118, Cell Signaling Technology, USA). The SW480 cell line (#CBP60019), authenticated by short tandem repeat (STR) profiling, was procured from the Chinese Academy of Sciences (CAS). Cells were cultured in RPMI 1640 medium (#C11875500BT, Gibco, USA) supplemented with 10% fetal bovine serum (FBS) and 10,000 U/ml penicillin-streptomycin (#15140122, Gibco, USA) in a humidified incubator with 5% CO_2. A knockdown plasmid targeting ITGA11 was synthesized by Miaoling Bioscience (Wuhan, China).

Immunohistochemical assay

Tissue specimens were fixed in 4% paraformaldehyde, embedded in paraffin, and sectioned into 4 μm-thick slices for slide preparation. After gradient deparaffinization and rehydration, antigen retrieval was performed using a microwave method with citrate buffer (100°C, four cycles of 7 minutes each). The slides were washed extensively with PBS and then blocked for 30 minutes to minimize nonspecific binding. The primary antibody was incubated

overnight at 4°C, followed by incubation with the secondary antibody at room temperature. Color development was achieved using DAB chromogen, and the sections were counterstained with hematoxylin.

Wound healing assay

Cells were plated in 6-well plates and grown to confluence. A sterile pipette tip scratched the monolayer, which was then washed with PBS to remove any dislodged cells. Culture medium with 1% (fetal bovine serum) FBS was added. Images of cell migration were taken at 0, 24, and 48 hours post-wounding. The wound closure area was calculated as: Migration Area (%) = (X0 - Xn)/X0 × 100, where X0 is the initial wound area and Xn is the area at a specific time.

Transwell assay

The invasive and metastatic potential of SW480 cells was assessed using a Matrigel-coated Transwell assay. Briefly, 3×10^4 cells were seeded in the upper chamber of a Transwell with serum-free medium, while the lower chamber contained 10% FBS-supplemented medium. After 24 hours of incubation at 37°C, cells in the upper chamber were fixed with methanol and stained with Giemsa for quantitative microscopic analysis of invasion and migration.

Western blot assay

Cell proteins were extracted using a lysis buffer (10 mM TRIS-HCl, pH 7.4, 1% SDS, 1 mM Na_3VO_4) and lysed via ultrasonic treatment. Protein concentration was quantified using a microspectrophotometer. Samples, mixed with loading buffer and a molecular weight marker, were loaded onto an 8% SDS-PAGE gel and subjected to electrophoresis at 80 **V** for 30 minutes, followed by 120 **V** for 90 minutes. Proteins were transferred to a PVDF membrane (25 **V**, 120 minutes) and blocked in buffer at 4°C for 3 hours. The membrane was then incubated overnight with primary antibodies at 4°C and for 3 hours with secondary antibodies. Protein bands were visualized using an ECF developer (RPN5785, GE Healthcare) and captured using a chemiluminescent imaging system (GE Healthcare).

Statistical analysis

All statistical analyses were conducted using R software (version 4.4.2). The Wilcoxon test compared variables between groups, the Chi-square test assessed categorical variable differences, Pearson correlation analyzed variable correlations, and KM survival analysis with log-rank test evaluated differences. Statistical significance was set at $p<0.05$: *: $p<0.05$; **: $p<0.01$; ***: $p<0.0001$; NS: non-significant.

Ethics approval

This study was conducted in accordance with the ethical standards outlined in the Helsinki Declaration and certified by the Ethics Committee of The First Affiliated Hospital of Wenzhou Medical University (KY2022-183). Given the retrospective nature of the study, informed consent was waived.

Results

Proteomic characteristics of T1-T3N0M1 patients

To identify the protein signatures and pathways associated with T1-T3N0M1 CRC, we used adjacent normal tissue as a control and analyzed the differentially expressed proteins in primary tumor and distant metastasis and conducted a comprehensive comparison of biological pathways and functions. Differential analysis revealed 746 upregulated and 403 downregulated proteins in primary tumors (Figure 1C), and 751 upregulated and 321 downregulated in distant metastases (Figure 1D). GSEA was performed to analyze the features of the proteins detected in primary tumors and distant metastases in terms of biological pathways and molecular mechanisms. Results showed enrichment in MYC targets V2, E2F targets, MYC targets V1, G2M Checkpoints, EMT pathway in primary tumors (Figure 1E). Xenobiotic metabolism, Hpoxia, MYC targets V1, Myogenesis, P53 pathway enrichment in distant metastases (Figure 1F). Analysis of GO and KEGG pathway of these proteins is provided in Supplementary Figure S1. Venn diagrams visualized the intersections of differentially expressed proteins among primary tumors and metastases (Figures 1G, H).

Construction of PPI networks and module identification for biomarker discovery

To construct a PPI network for biomarker identification, we uploaded 617 differentially expressed proteins shared between primary tumors and distant metastases into the STRING database. The resulting network was visualized using Cytoscape software and the MCODE plugin, enabling the identification of the five most functionally significant modules (Supplementary Figure S2). Among these, Cluster 2 emerged as a key module, comprising 40 nodes and 214 edges (Figure 2A). GO analysis reveals that Cluster2 is mainly enriched in ECM organization, cell adhesion, collagen-containing ECM, and ECM structural constituent (Figure 2B). The KEGG analysis indicates the enrichment of Focal adhesion, ECM-receptor interaction, and PI3K-Akt signaling pathway (Figures 2C, D). Hallmark pathway enrichment

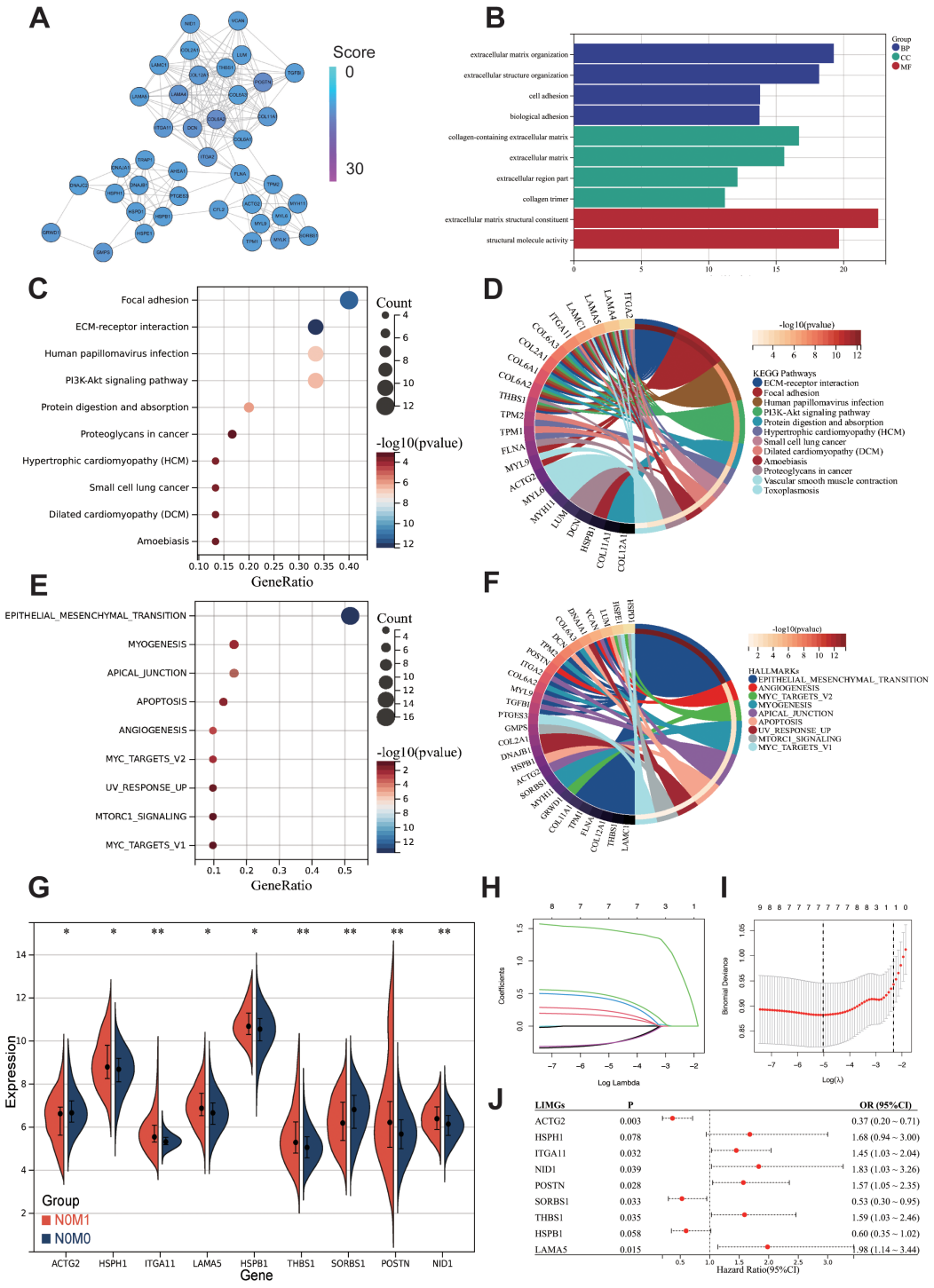

FIGURE 2
Preliminary screening of core biomarkers associated with lymph-node independent metastasis. **(A)** MCODE in Cytoscape identified a module consisting of 40 nodes from the PPI network. The GO **(B)**, KEGG **(C)** and Hallmark gene sets **(E)** enrichment analysis of the 40 genes from cluster2. Chord diagrams of KEGG **(D)**, and Hallmark gene sets **(F)** enrichments show associations of 40 genes across different biological aspects. Differentially expressed genes between N0M0 and N0M1 **(G)**. The Lasso regression path plot **(H)** and cross-validation plot **(I)** illustrate the gene selection process. The univariate logistic regression results of LIMGs **(J)**. Statistical signifificance: p<0.05; **: p<0.01; ***: p<0.0001; NS: non-signifificant.

analysis shows enrichment in EMT pathway, Myogenesis, Apical junction, Apoptosis, and Angiogenesis (Figures 2E, F).

Machine learning identifying LIMGs signature and constructing diagnostic model

To further identify core biomarkers and establish an accurate diagnostic model, we identified differentially expressed genes in Cluster2 between stage I-II and N0M1 CRC (Wilcoxon test, $p<0.05$) (Figure 2G), after eliminating redundant genes using Lasso regression (Figures 2H, I), 9 genes were selected as LIMGs (ACTG2, HSPH1, ITGA11, LAMA5, HSPB1, THBS1, SORBS1, POSTN, NID1). Univariate logistic regression highlighted the importance of LIMGs via OR (Figure 2J). Ten machine learning algorithms including Logistic, SVM, GBM, Neural Network, Random Forest, XGboost, KNN, Adaboost, Light GBM, and CatBoost were then applied to assess the diagnostic efficacy of LIMGs in the CCRC training set, ROC curves (Figure 3A), DCA (Figure 3D), confirmed robust diagnostic performance, with external validation in two cohorts (GSE39582, Figures 3B, E), (GSE38832, Figures 3C, F). The Neural Network model demonstrated consistent performance across cohorts, with diagnostic efficacy displayed by the confusion matrix (Figures 3G–I). Feature importance analysis of the top eight models in the training cohort identified ITGA11 as the key factor influencing lymph node-independent metastasis (Figure 3J).

LIMGs correlate with poor prognosis and clinicopathological features

The GSVA method scored GSE39582 (Figure 4A), GSE38832 (Figure 4B) and TCGA-COADREAD (Figure 4C) samples based on LIMGs expression, classifying risk subgroups by the median score. KM curves revealed significant survival difference between risk subgroups. KM curves for subgroups based on ITGA11 median expression revealed its significant impact on overall survival (OS), Disease-free survival (DFS), and Progression-free interval (PFI) (Figure 4D). To further explore the association between LIMGs and metastasis of patients, we employed the R package rms to integrate data on metastasis-free survival (MFS), survival status, and eight relevant features of CCRC cohort. A nomogram was constructed using the Cox method, and the prognostic significance of these features was assessed in 143 samples of CCRC cohort (Figure 4E). Kaplan-Meier curves (Figure 4F) and ROC curves for 1- and 3-years MFS (Figure 4G) underscored the predictive accuracy of LIMGs, highlighting its value in predicting metastasis. Further evaluation for the association between the LIMGs and other pathological characteristics reveals that higher LIMG score is significant associated with advance AJCC stage (Figure 5A), N stages, (Figure 5B), MSI status (Figures 5E, F), KRAS-WT (Figure 5G), and the left-sided colorectal cancer (Figure 5H) (all $p<0.05$). Furthermore, CRC is molecularly classifed into six subtypes by Marisa et al. (25) including C1 (downregulation of immune pathway), C2 (MSI subtype), C3 (KRAS mutant), C4 (chromosomal instability and stem-like), C5 (Wnt pathway upregulation) and C6 (derived from serrated tumors). We found that higer LIMG score correlated with C4-C6 molecular subtypes (Figure 5D). Additionally, no significant differences in LIMG score were observed across different T stages (Figure 5C), ages, sexes, vascular invasion statuses, histological types, and BRAF, TP53 mutation statuses (Supplementary Figure S3).

Analysis of LIMGs interaction and correlation with EMT

The hallmark enrichment revealed that LIMGs are mainly enriched in the EMT pathway (Figure 6A). EMT drives tumor invasion and metastasis through induction of stemness, modulation of the TME, angiogenesis promotion, and metabolic reprogramming. We investigated the correlation between LIMGs and the EMT pathway by 200 EMT-related genes from the MSigDB database v7.1. The correlation between LIMGs and EMT gene signatures was analyzed using Pearson correlation analysis on the GEPIA2 (http://gepia2.cancer-pku.cn/#index). The results indicated that ITGA11 has the strongest correlation with EMT (Figure 6D). Then we used GeneMANIA to analyze the interactions among LIMGs (Figure 6B) and the PPI network centered on ITGA11 (Figure 6C). The results of GO and KEGG enrichment analyses of LIMGs are shown in Supplementary Figure S4.

Mutation landscape and immune activity in different risk groups

To elucidate the distinct mutational patterns among different risk groups, we utilized the "mafTools" R package to analyze the distribution of top 20 somatic mutations between risk groups and mutation status in 9 LIMGs based on TCGA-COADREAD data. Our findings revealed that APC, TP53, TTN, and KRAS exhibited high mutation frequencies across different subgroups, with APC being identified as the most frequently mutated gene across subgroups (Figures 7A, C). LAMA5 showed the highest mutation frequencies among LIMGs (Figure 7B). Meanwhile, copy number variation (CNV) plays a crucial role in cancer occurrence and development. We found that the highest CNV in LIMGs was also found in LAMA5 (Figure 7F). Given the significance of TMB, MSI status, immune cell infiltration, immune functions, and immune checkpoint gene expression in immunotherapy response, we examined their relationship with LIMGs. Immune infiltration analysis by CIBERSORT revealed that the high-risk group had lower proportions of memory B cells, plasma cells, CD4+ T cells, NK cells, dentritic cells and eosinophils but higher proportions of M0 and M2 macrophages (Figure 7H). Moreover, the high-risk group exhibited greater immunological function, including higher levels of Type I and II IFN Response and APC co-stimulation.

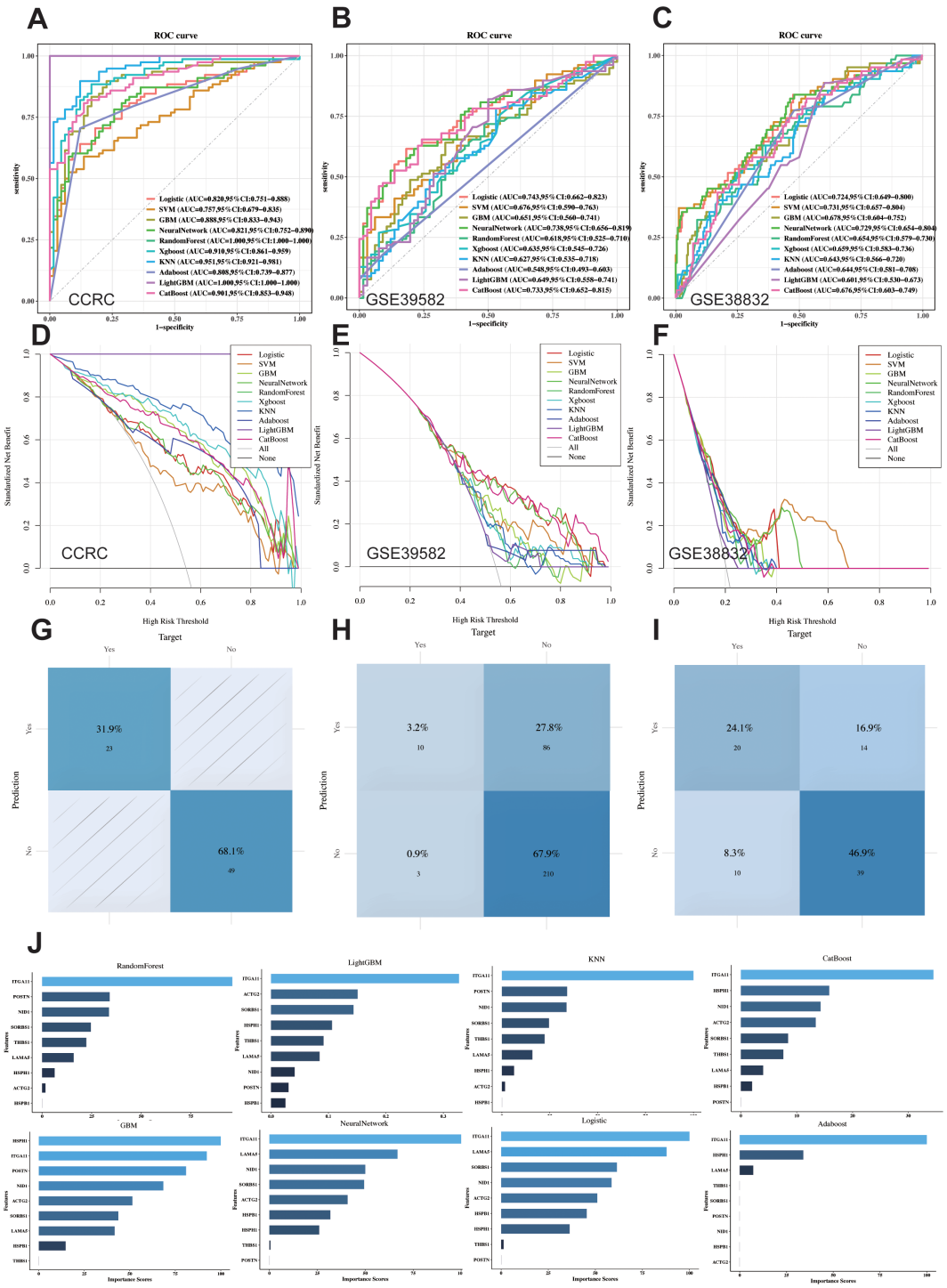

FIGURE 3
Ten Machine learning methods assess the diagnostic performance of LIMGs signature. ROC curves of ten machine learning methods (Logistic, SVM, GBM, Neural Network, RF, XGboost, KNN, Adaboost, Light GBM, and CatBoost) applied in CCRC training cohort **(A)** and external validation cohort GSE39582 **(B)** and GSE38832 **(C)**. Cost-benefit decision curves in training **(D)** and validation **(E, F)** cohorts. Classification confusion matrix of the Neural Network model in training **(G)** and validation cohort **(H, I)**. **(J)** The feature importance bar chart illustrates variable contributions to the top 8 models in training cohort.

(Figure 7I). The high-risk group also exhibited a significantly lower MSI proportion (Figure 7D) and lower TMB (Figure 7E). Conversely, the TMB and MSI status was higher in low-risk group, suggesting better immunotherapy response. Analysis of immune checkpoint expression showed higher expression of PDCD1 in low-risk group and higher expression of TIGIT, ICOS and CTLA4 in high-risk group (Figure 7G). Furthermore, the positive correlation between ITGA11 expression and various

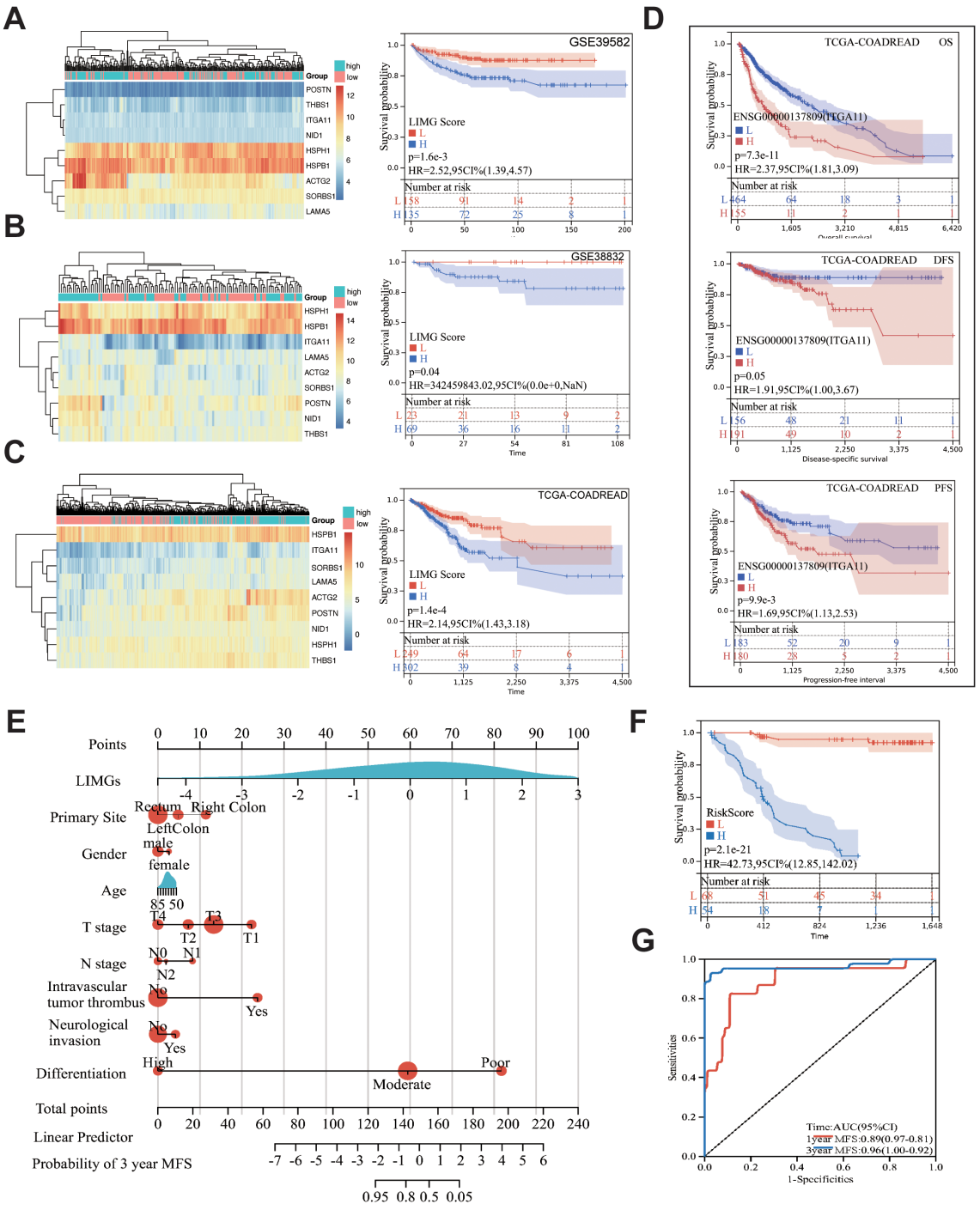

FIGURE 4
The correlation between the LIMGs and survival. Heatmaps of LIMGs expression and the KM curves stratified by high-risk and low-risk groups based on median LIMG Score in the GSE39582 **(A)**, GSE38832 **(B)**, and TCGA cohorts **(C)**. **(D)** KM curves for overall survival (OS), disease-free survival (DFS), and progression-free interval (PFI) in high-risk and low-risk groups stratified by the optimal cutoff value of ITGA11 expression in TCGA-COADREAD. **(E)** Nomogram for predicting Metastasis-free survival (MFS) was constructed using multivariate Cox regression. **(F)** KM curves compared high-risk vs. low-risk stratified by median risk score. **(G)** ROC curves evaluated 1-year/3-year MFS prediction accuracy of the Nomogram.

immune cells was calculated by five algorithms (TIMER, QUANTISEQ, MCPcounter, EPIC, CIBERSORT) (Figure 7J), specifically with high levels of CAFs and TAMs. This correlation may indicate poor prognosis in CRC patients with higher level of ITGA11+CAFs and ITGA11+TAMs. In summary, the high-risk group exhibited lower TMB, MSI status and immunosuppressive TME, suggesting less favorable immunotherapy outcomes compared to the low-risk group.

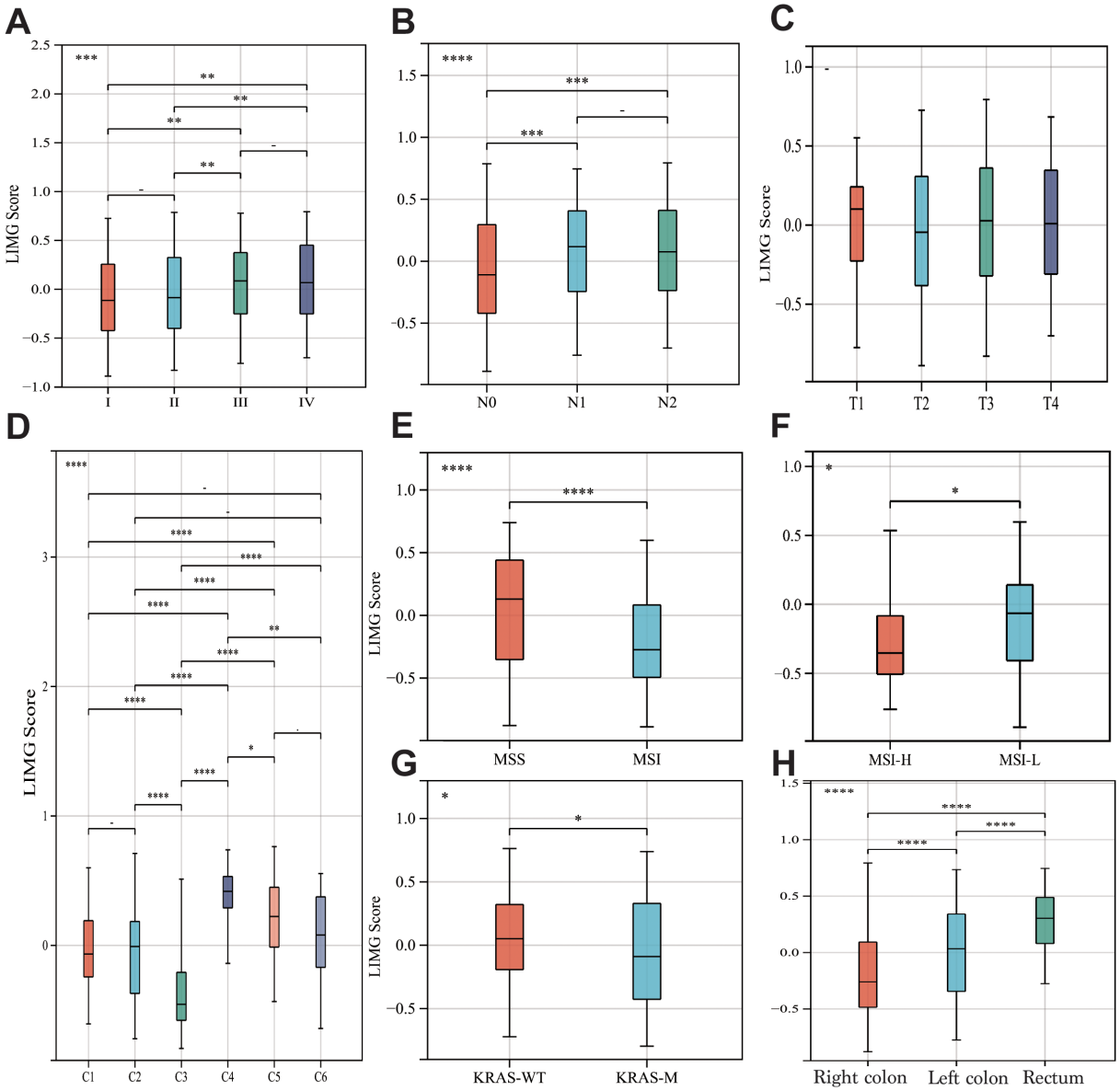

FIGURE 5
The correlation between LIMGs and clinicopathological features. The correlation between the LIMG Score and AJCC stage **(A)**, N stage **(B)**, T stage **(C)**, Molecular subtypes **(D)**, Microsatellite stability **(E, F)**, KRAS mutation status **(G)**, and tumor location **(H)**. Statistical significance: *: p<0.05; **: p<0.01; ***: p<0.001; ****: p<0.0001; NS, non-significant.

LIMGs associate with lower chemotherapy sensitivity

To predict drug sensitivity and identify potential therapeutic drugs for high-risk CRC patients, we calculated IC50 values for three commonly used CRC chemotherapy drugs (5-Fluorouracil, Oxaliplatin, Irinotecan) in different risk subgroups and assess the correlation between LIMG score and drug sensitivity. The results showed that high-risk patients had poorer sensitivity to 5-Fluorouracil (Figure 8A), Oxaliplatin (Figure 8B), and Irinotecan (Figure 8C), with IC50 values positively correlated with risk scores. Conversely, high risk patients exhibited higher sensitivity to Dasatinib (Figure 8D), Doramapimod (Figure 8E), and PRKDC inhibitor NU7441 (Figure 8F), with IC50 values negatively correlated with LIMG score.

ScRNA-seq analysis of ITGA11

To explore the expression and distribution of ITGA11 in the TME at the single-cell level, we conducted scRNA-seq analysis using the TISCH

10.3389/fimmu.2025.1622528

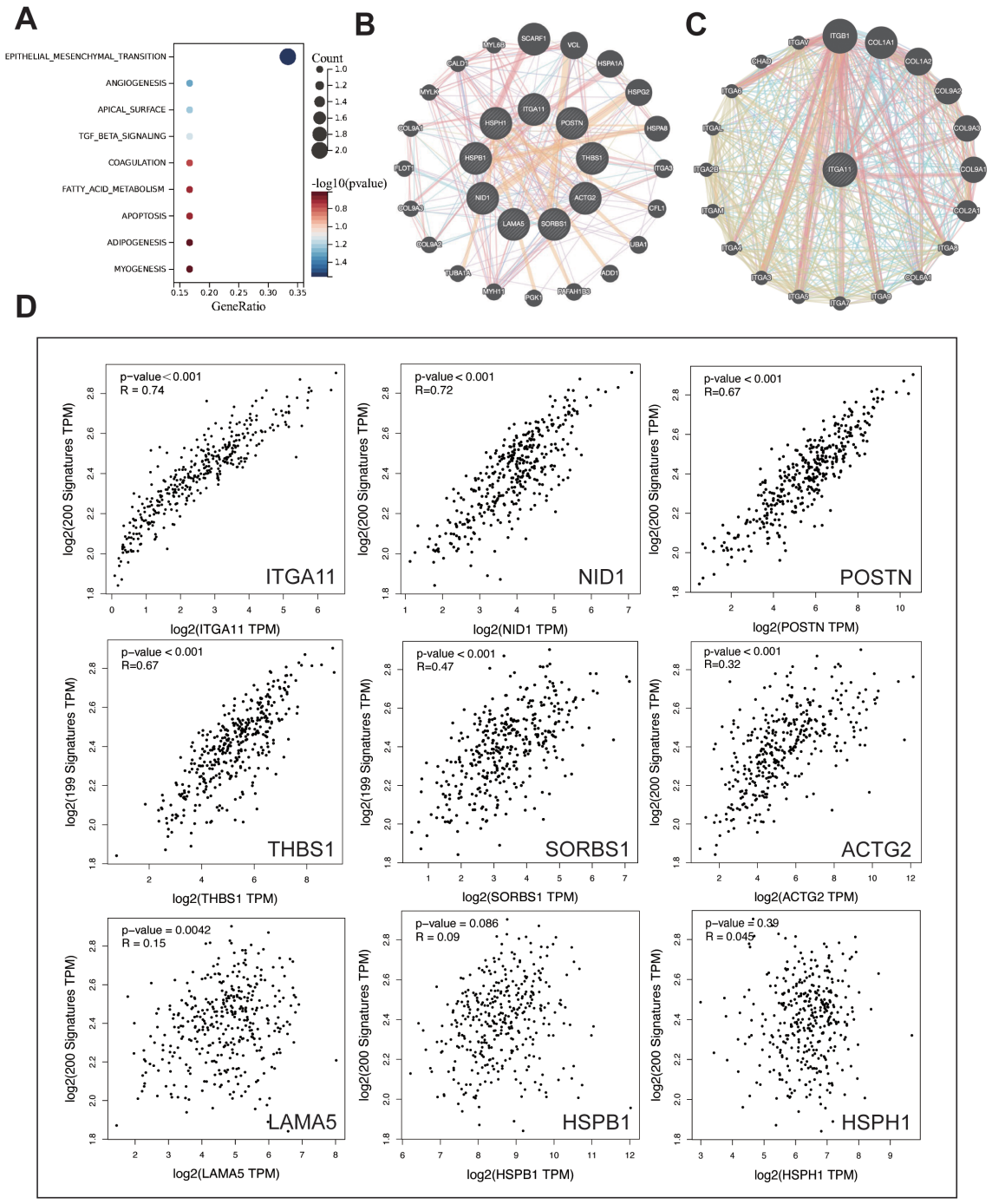

FIGURE 6
The enrichment and interaction analysis of LIMGs and correlation analysis between LIMGs expression and the EMT pathway. **(A)** Hallmark enrichment analysis plot of LIMGs. **(B)** Interactions among LIMGs. **(C)** The PPI network centered on ITGA11. **(D)** Correlation between LIMGs expression and the EMT pathway gene set.

2.0 database. Analysis of scRNA-seq data from the CRC_EMTAB8107 dataset revealed the identification of 20 cell clusters and 12 cell types within CRC tissues (Figure 9A). We observed a significant enrichment of ITGA11 in CAFs (Figure 9B), especially within clusters C3 and C10 (Figure 9F). The analysis of Cell-Cell Interactions (CCI) revealed that both C3 and C10 CAFs mainly interacted with C9 malignant cells and C19 endothelial cells (Figures 9D, E).

ITGA11 promotes migration and invasion of colorectal cancer cells

In this study, we unveiled the crucial role of LIMGs in distant metastasis of CRC, primarily associated with cell adhesion and EMT. Notably, LIMG ITGA11 is the gene most strongly correlated with EMT. Although ITGA11 overexpression has been reported in

10.3389/fimmu.2025.1622528

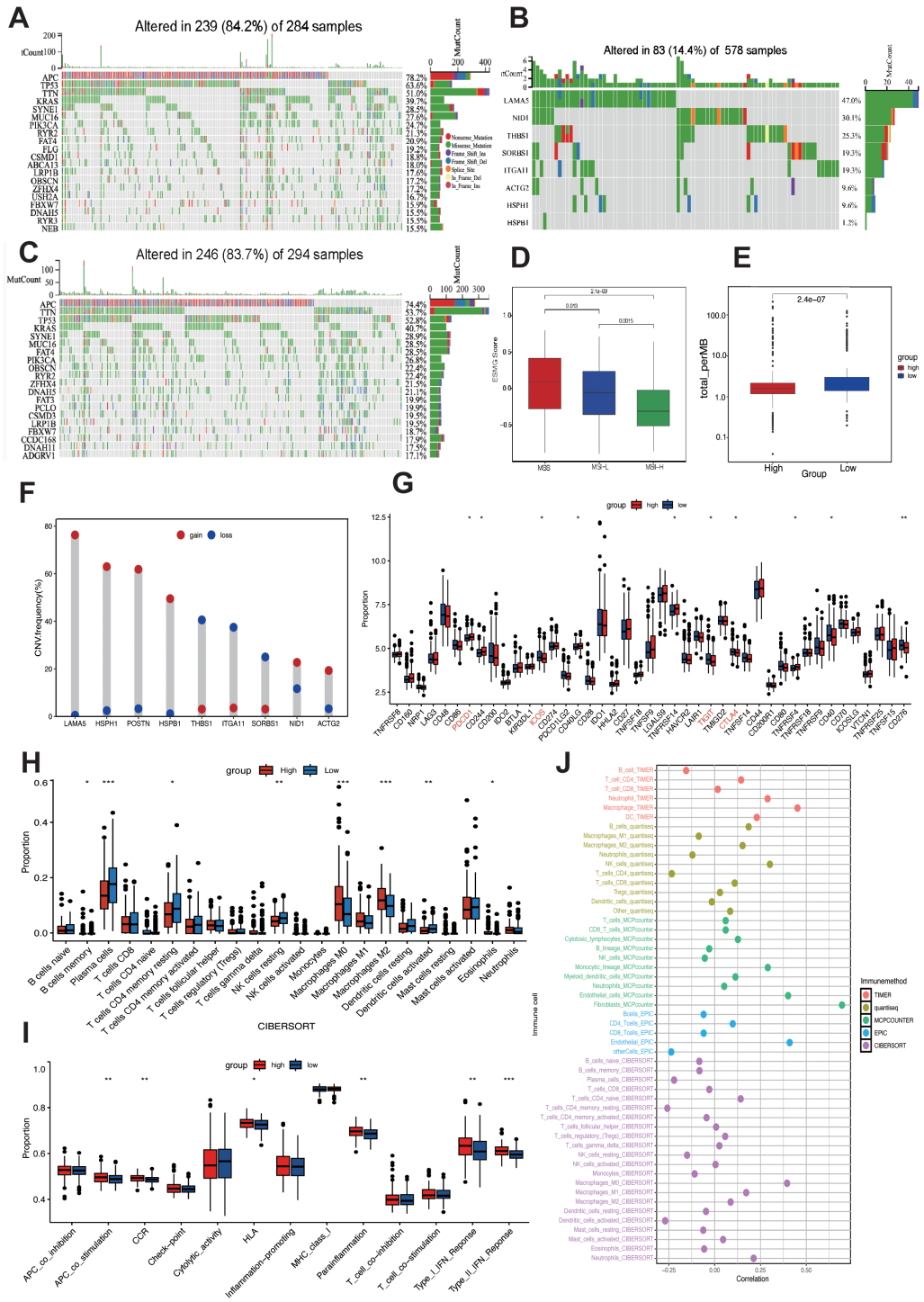

FIGURE 7
Mutation landscape and immune activity analysis. Top 20 mutated genes in high-risk **(A)** and low-risk **(C)** subgroups. **(B)** Mutation frequency of 9 LIMGs. **(D)** The LIMG Score of CRC patients with microsatellite instability-high (MSI-H), microsatellite instability-low (MSI-L) and microsatellite stability (MSS). **(E)** Comparison of TMB in high- and low- risk subgroups. **(F)** The CNV frequency of each LIMG signature genes. **(G)** Differentially expressed immunocheckpoint genes across risk subgroups. **(H)** Differences in immune cell infiltration across risk subgroups. **(I)** Immune-related functions in the high- and low- risk subgroups. **(J)** Correlation between ITGA11 expression and immune cells. Statistical significance: *:p<0.05; **: p<0.01; ***: p<0.0001; NS: non-significant.

several tumors, its impact on CRC cell migration and invasion remains unexplored. The radar chart illustrates the expression levels of LIMGs (Log2(FC)) based on our proteomics data (Supplementary Figure S5). The results reveal the expression across primary tumors, and distant metastasis for 9 LIMGs. Among them, ITGA11 showed higher expression in distant metastasis than in primary tumors. The IHC score further confirmed higher ITGA11 expression in both primary tumors

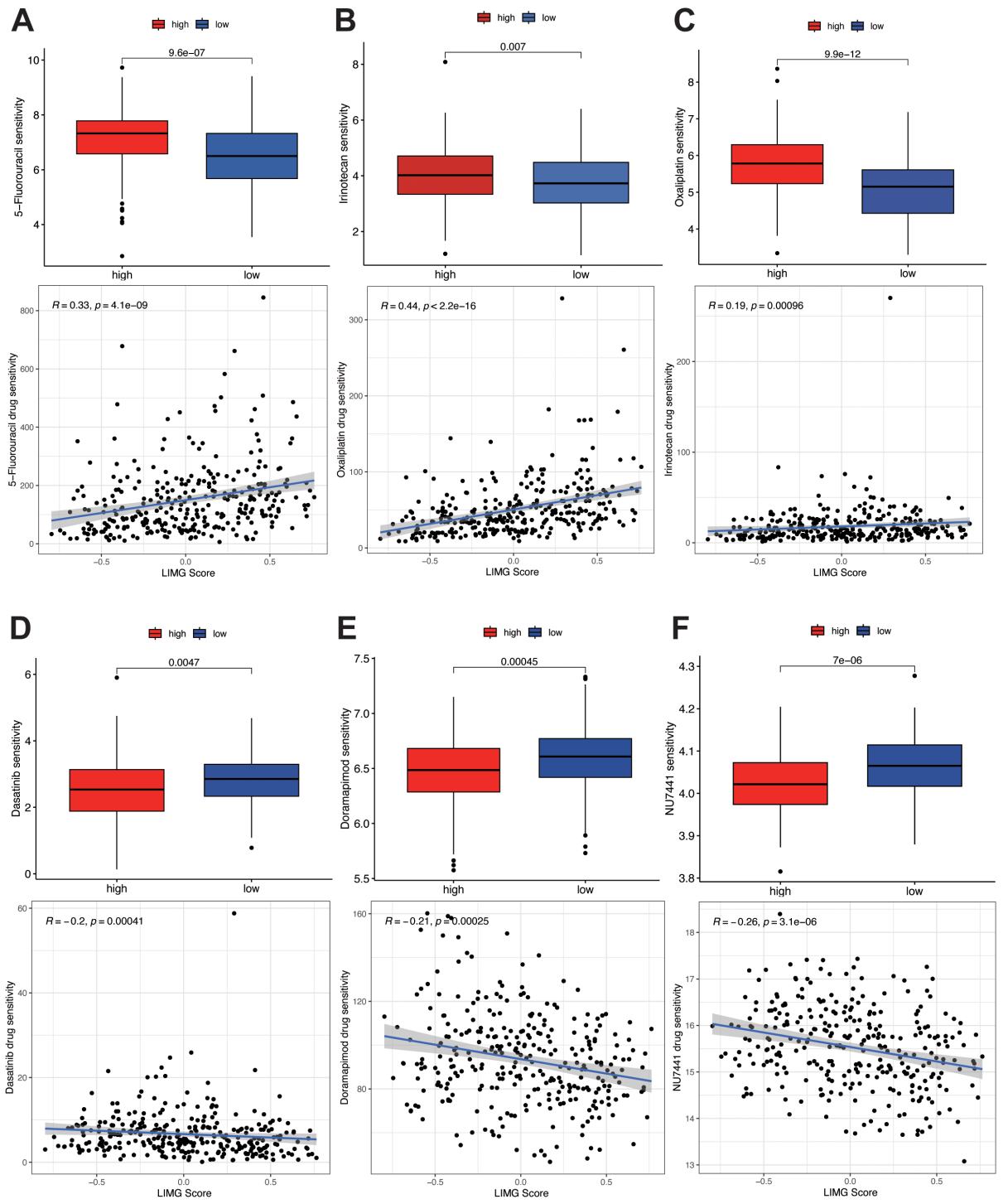

FIGURE 8
Drug sensitivity analysis. Sensitivity analysis of 5-fluorouracil **(A)**, oxaliplatin **(B)**, and irinotecan **(C)** in different risk groups. Sensitivity analysis of Dasatinib **(D)**, Doramapimod **(E)**, and PRKDC inhibitor NU7441 **(F)** in different risk groups.

and distant metastasis compared to normal tissues, with significantly higher levels in distant metastasis compared to primary tumors (Figure 10B, p<0.05). The ROC curve shows that ITGA11 significantly differentiates primary tumors from distant metastasis (Figures 10C–E). Furthermore, we achieved stable knockdown of ITGA11 in the human colon cancer cell line SW480 and subsequently evaluated the efficiency of this knockdown via Western blot analysis (Figure 10F). To assess the functional implications, we performed wound healing and transwell assays. The results of these assays demonstrated that ITGA11 knockdown significantly compromised the migratory ability of SW480 cells (Figure 10A; t - test, p < 0.05) and led to a

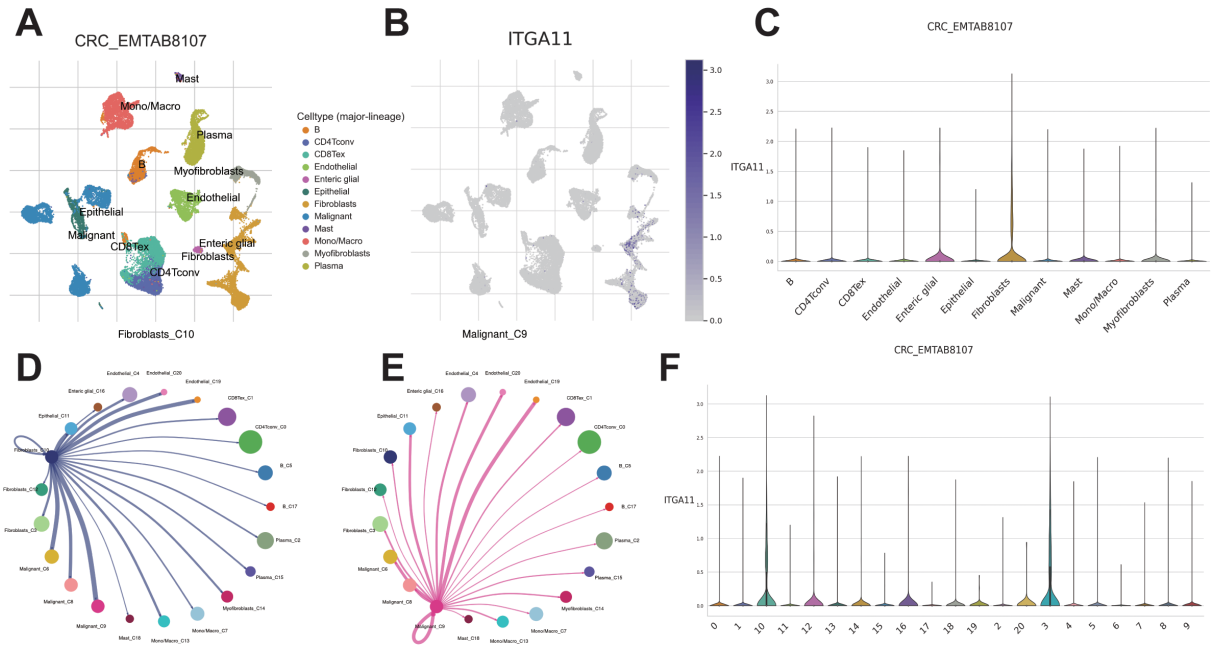

FIGURE 9
Single cell RNA sequencing analysis. **(A)** UMAP projection of all cells from CRC_EMTAB8107. **(B, C)** Expression distribution of ITGA11 across different cell types. CCI analysis between endothelial cluster C_4 **(D)** and fibroblast cluster C_12 **(E)**. **(F)** Expression distribution of ITGA11 across different cell clusters.

substantial decrease in the number of invading cells (Figure 10B; t -test, $p < 0.05$). Collectively, these findings underscore the pivotal role of ITGA11 in the migration and invasion processes of CRC.

Discussion

Approximately 20% of newly diagnosed CRC patients have synchronous distant metastasis and generally face a poor prognosis (26). While LNM signifies advanced disease, tumor cells may spread hematogenously before lymphatic metastasis. Previous reports indicate that about 18% of mCRC patients lack local lymph node involvement (27), and a novel CRC mouse model shows distant metastases can develop without prior lymph node involvement (9). Recurrence patterns in patients with CRLM undergoing liver transplantation without other metastasis suggest tumor cells may persist in circulation post-resection of primary and metastatic tumors. A more plausible explanation is that undetectable pre-operative metastasis account for most post-operative metastasis. Early hepatic metastases are often missed or undiagnosed by imaging, and by the time typical metastatic signs appear, radical surgery is usually no longer an option (28). Thus, identifying potential synchronous metastases or metastasis risks at early stage primary CRC is crucial (29).

The early occurrence of metastasis may stem from pre-existing, undetectable tumor dissemination prior to diagnosis or treatment. The primary tumor not only generates disseminated tumor cells but also establishes the pre-metastatic niche and modulates the immune response (30). Identifying the genetic traits of its stromal and extracellular matrix (ECM) components is vital for metastasis prediction (31). In cancer, EMT enables cancer cells to lose cell polarity and acquire a mesenchymal phenotype with enhanced stemness and migratory ability through complex interactions between fibers and proteins (13). Continuous remodeling of the ECM and actin cytoskeleton is closely associated with EMT, with integrins acting as physical linkers between the ECM and actin cytoskeleton, mediating mechanotransduction through interactions with major ECM components like collagen and fibronectin (31, 32). ITGA11, identified among LIMGs, shows the strongest correlation with EMT and high importance in various models predicting synchronous metastasis in CRC. ITGA11 promotes CAF invasion and CAF-induced tumor cell invasion, and associates with high-grade tumors and poor prognosis (33, 34). Mechanistically, ITGA11's pro-invasive activity may stem from its ligand-dependent interaction with PDGFRβ, promoting downregulated JNK activation and ECM changes, including increased deposition of a strongly co-expressed pro-invasive stromal protein (tenascin-C, TNC) (35). PDGFRα+ ITGA11+ CAFs are associated with lymphovascular invasion (LVI) and early metastasis in early-stage bladder cancer, promoting lymphangiogenesis by recognizing the ITGA11 receptor SELE on lymphatic endothelial cells. Additionally, CHI3L1 from the CAF aligns the surrounding stroma to facilitate cancer cell intravasation and promote early tumor metastasis (36). Laminin LAMA5, a glycoprotein in the ECM, has been identified as a specific molecular target in mCRC (37). It is a key component of the vascular basement membrane, forming a scaffold for endothelial cell adhesion in conjunction with collagen IV, and is linked to the angiogenesis and tumor growth in CRLM (31, 38). Notably, LAMA5 exhibits the highest mutation frequency and CNVs in LIMGs, it is reported that genetic

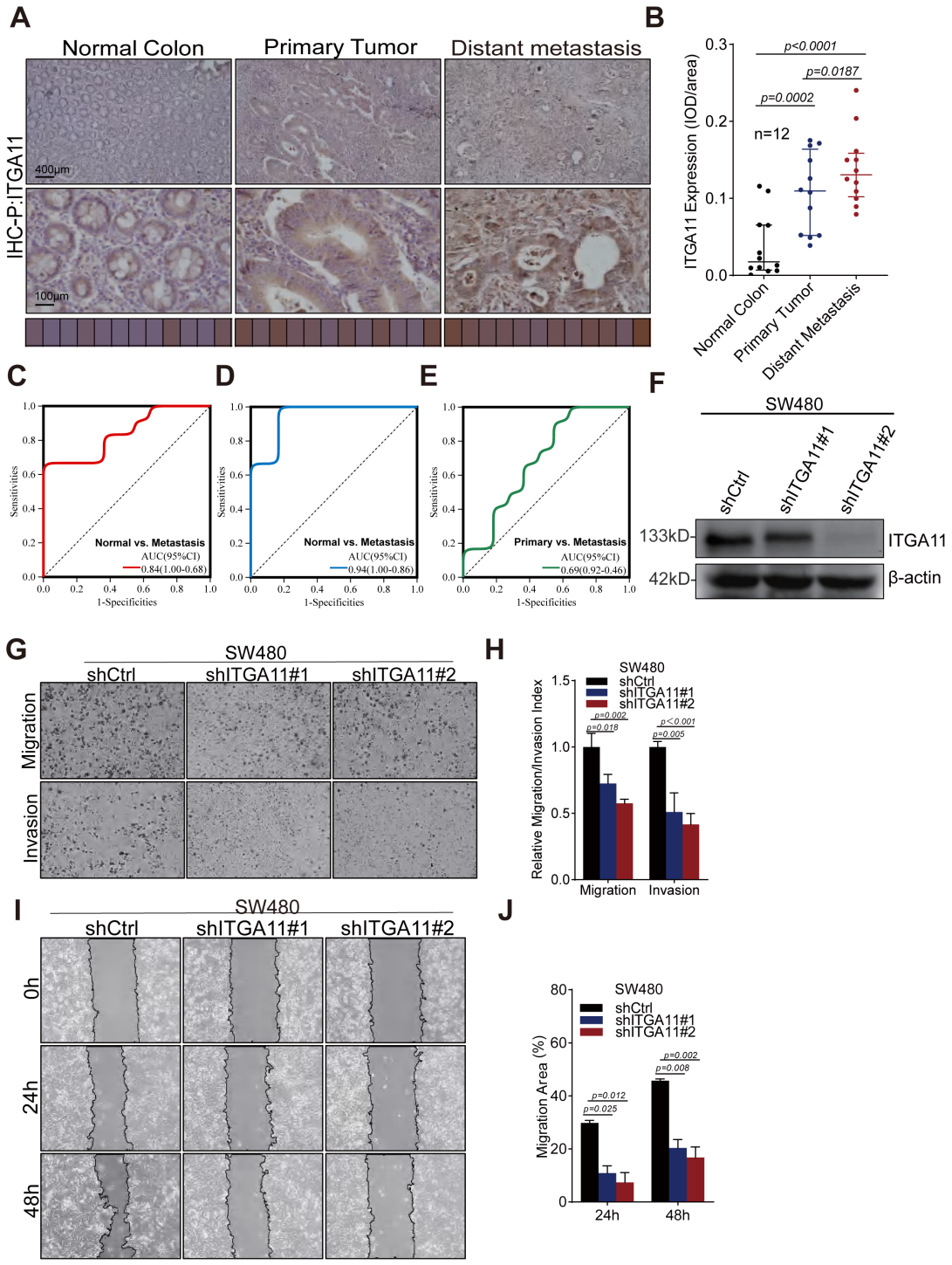

FIGURE 10
ITGA11 expression variation across tissues and its role in the migration and invasion of CRC cell. **(A)** Immunohistochemical analysis of ITGA11 expression in normal tissues, primary tumors, and distant metastases. **(B)** The Wilcoxon test indicated a significant difference (P<0.05) in ITGA11 expression across normal tissues, primary tumors, and distant metastases. **(C–E)** The ROC curves indicated that ITGA11 expression effectively differentiated normal tissues, primary tumors, and distant metastases. **(F)** The ITGA11 expression in human colon cancer cells SW480 was measured by western blotting. **(G, H)** Results of the transwell assay. **(I, J)** Results of the wound healing assay.

variant rs4925386 in chromosomal region 20q13.3 (LAMA5) significantly associated with CRC susceptibility (OR=0.93) (39). Periostin (POSTN), secreted by CAFs, accelerates angiogenesis, tumor invasion, and EMT via integrin interaction (40). Aberrant POSTN expression in CRC correlates strongly with peritoneal and distant organ metastasis. Meanwhile, POSTN+ CAFs significantly promote CRC cell migration and proliferation through hypoxia induced POSTN expression and secretion (41). The cbl-associated

protein (CAP), encoded by the sorbin and SH3 domain-containing 1 (SORBS1) gene, plays a role in actin cytoskeleton regulation, receptor tyrosine kinase signaling, and cell adhesion. Overexpression of SORBS1 inhibits the PI3K/AKT pathway, blocks EMT, and promotes M1 macrophage polarization (42). Conversely, SORBS1 silencing accelerates EMT, boosts Filopodium-like Protrusion (FLP) formation via JNK/c-Jun activation in cancer cells, and elevates chemosensitivity by enhancing p53 protein accumulation (43). Nidogen1 (NID1), directly induced by SNAIL/SNAI-1 transcription factor, promotes EMT. It connects laminin, collagen, and proteoglycans to cell receptors, regulating cell polarization, migration, and invasion (44). Actin gamma 2 (ACTG2) is aberrantly expressed in cancers (45), with low levels in CRC, its overexpression inhibits CRC cell proliferation, migration, and invasion (46). Thrombospondin-1 (THBS1) inhibits angiogenesis and immune activity (47), but has complex, contradictory roles in carcinogenesis. THBS1 expression correlates with CRC mesenchymal phenotype, immunosuppression, and poor prognosis, promoting metastasis by exhausting cytotoxic T cells and impairing angiogenesis, especially at metastatic sites (48).

Pathological analysis of early-stage CRC aids in risk identification and treatment guidance. Factors like T4 stage, poor differentiation, intestinal perforation, lymphovascular/perineural invasion, inadequate lymph node examined, and positive surgical margins heighten disease progression risk (49). Our study revealed no significant LIMG score differences in T stage, vascular invasion, and histological type. However, a higher LIMG score correlated with tumor location, MSI status, lower KRAS mutation frequency, and lower TMB. Study shows that synchronous CRLM exhibit poorer prognosis and biological traits than metachronous ones (2, 50), with synchronous CRLM showing lower TMB (51). Moreover, patients with LNM- mCRC typically have fewer high-risk pathological features than LNM+ mCRC (52), indicating clinicopathological factors may inadequately assess the lymph node-independent metastasis in CRC, potentially leading to misdiagnosis. LIMG Score variations across primary tumor sites may stem from tumor site-genomic alteration correlations in mCRC. Left-sided CRC is more prone to synchronous liver metastases (7.1% vs. 11.6%), which may be anatomically influenced by venous shunting (53). Molecularly, right-sided primary tumor-derived MSS-type mCRC has a higher median TMB, with oncogenic alterations like KRAS, BRAF, and PIK3CA enriched, while APC and TP53 are more enriched in left-sided tumors (54).

Immunotherapy benefits CRC patients but is limited by the complex immunosuppressive TME and tumor heterogeneity (55). Our study found that high-risk patients have lower infiltration of anti-tumor immune cells (memory B cells, plasma cells, CD4+ T cells, NK cells, DCs), while exhibiting higher levels of M2-type TAMs that promote tumor growth and immunosuppression. Plasma cells, as terminal effector B cells, eliminate tumor cells via antibody-dependent cell-mediated cytotoxicity (ADCC) (56), forming an immunological chain with DCs and participating in tertiary lymphoid structures (TLS) formation (57). Reduced plasma cell and DC infiltration may indicate weakened antibody-mediated anti-tumor effects, TLS deficiency, and inadequate immune surveillance, potentially with increased Bregs or M2-type TAMs, leading to insufficient $CD8^+$ T cell activation, further exacerbating immune escape, and diminished immunotherapy response.

Furthermore, we have identified ITGA11 as a critical factor in lymph node-independent metastasis in CRC, though its precise mechanism remains unclear. Our study demonstrated that knocking down ITGA11 significantly inhibits CRC cell migration and invasion. The mechanism behind ITGA11's involvement in lymph node-independent synchronous metastasis may encompass multiple pathways, with EMT being a potential key player, which we aim to explore further.

Study limitations are several. A notable drawback is the small sample size, stemming from our single - center study and the scarcity of specimens meeting our criteria. This challenge weakened our study's statistical power and robustness. Also, the heterogeneity of extensive stage II disease (N0), encompassing tumors confined to the serosa (T3) and those extending beyond it (T4), representing diverse histopathological risks. Additionally, even when an adequate number of lymph nodes are examined, there is a possibility of lymph node micrometastasis, as conventional histopathological examination cannot detect the presence of isolated tumor cells (ITCs) or micrometastases (MMs) within regional lymph nodes, and we did not perform ultra-staging for all these cases. Despite the limitations, we are committed to promoting multi - center, large - sample studies and employing multi - omics analysis in future research to better uncover the mechanisms underlying lymph node - independent distant metastasis and offer more reliable insights.

In summary, we integrated proteomics, multi-omics analysis, and machine learning to identify molecular features and developed an LIMGs signature based on nine genes, effectively predicting synchronous distant metastasis risk in stage I-II CRC patients. We also analyzed associations between the LIMG Score and pathological features, immune microenvironment and activity, and drug responses, offering insights into precise stratification and personalized therapy for CRC. Our findings also position ITGA11 as a crucial prognostic indicator for CRC metastasis.

Data availability statement

The datasets presented in this study can be found in online repositories. The names of the repository/repositories and accession number(s) can be found in the article/Supplementary Material.

Ethics statement

The studies involving humans were approved by Ethics Committee of The First Affiliated Hospital of Wenzhou Medical University (KY2022-183). The studies were conducted in accordance with the local legislation and institutional requirements. The ethics committee/institutional review board waived the requirement of written informed consent for participation from the participants or the participants' legal

guardians/next of kin because given the retrospective nature of the study, informed consent was waived.

Author contributions

BZ: Writing – original draft, Conceptualization, Investigation. CZ: Writing – original draft, Investigation, Formal Analysis, Methodology. YC: Conceptualization, Investigation, Writing – original draft, Methodology. NS: Writing – original draft, Validation. YH: Validation, Visualization, Writing – original draft. HH: Visualization, Writing – original draft. BO: Writing – original draft, Visualization. QZ: Writing – original draft, Investigation, Supervision, Conceptualization, Validation. HJ: Supervision, Writing – original draft, Project administration. YZ: Writing – original draft, Supervision, Validation. PL: Conceptualization, Writing – review & editing, Supervision, Writing – original draft, Investigation. YP: Conceptualization, Writing – original draft. XZ: Methodology, Conceptualization, Writing – review & editing, Formal Analysis, Writing – original draft, Project administration.

Funding

The author(s) declare that financial support was received for the research and/or publication of this article. This study is funded by Wenzhou Science and Technology Public Project (NO. Y20220184) and Wenzhou Science and Technology Public Project (NO. Y2020145).

Acknowledgments

The authors thank all participants in the study.

Conflict of interest

The authors declare that the research was conducted in the absence of any commercial or financial relationships that could be construed as a potential conflict of interest.

Generative AI statement

The author(s) declare that no Generative AI was used in the creation of this manuscript.

Correction note

This article has been corrected with minor changes. These changes do not impact the scientific content of the article.

Publisher's note

All claims expressed in this article are solely those of the authors and do not necessarily represent those of their affiliated organizations, or those of the publisher, the editors and the reviewers. Any product that may be evaluated in this article, or claim that may be made by its manufacturer, is not guaranteed or endorsed by the publisher.

Supplementary material

The Supplementary Material for this article can be found online at: https://www.frontiersin.org/articles/10.3389/fimmu.2025.1622528/full#supplementary-material

References

1. Sung H, Ferlay J, Siegel RL, Laversanne M, Soerjomataram I, Jemal A, et al. Global cancer statistics 2020: GLOBOCAN estimates of incidence and mortality worldwide for 36 cancers in 185 countries. *CA: A Cancer J Clin*. (2021) 71:209–49. doi: 10.3322/caac.21660

2. Adam R, de Gramont A, Figueras J, Kokudo N, Kunstlinger F, Loyer E, et al. Managing synchronous liver metastases from colorectal cancer: A multidisciplinary international consensus. *Cancer Treat Rev*. (2015) 41:729–41. doi: 10.1016/j.ctrv.2015.06.006

3. Ihnát P, Vávra P, Vra PZ. Treatment strategies for colorectal carcinoma with synchronous liver metastases: Which way to go? *World J Gastroenterol*. (2015) 21:7014–21. doi: 10.3748/wjg.v21.i22.7014

4. van Gestel YRBM, de Hingh IHJT, van Herk-Sukel MPP, van Erning FN, Beerepoot LV, Wijsman JH, et al. Patterns of metachronous metastases after curative treatment of colorectal cancer. *Cancer Epidemiol*. (2014) 38:448–54. doi: 10.1016/j.canep.2014.04.004

5. Siddiqui M, Nagtegaal I, Santiago I, Knijn N, Berho M, Mirnezami A, et al. Session 2: What causes liver metastases – lymph nodes or is it something else? *Colorectal Dis*. (2018) 20:39–42. doi: 10.1111/codi.14077

6. Knijn N, van Erning FN, Overbeek LIH, Punt CJ, Lemmens VE, Hugen N, et al. Limited effect of lymph node status on the metastatic pattern in colorectal cancer. *Oncotarget*. (2016) 7:31699–707. doi: 10.18632/oncotarget.9064

7. Naxerova K, Reiter JG, Brachtel E, Lennerz JK, van de Wetering M, Rowan A, et al. Origins of lymphatic and distant metastases in human colorectal cancer. *Science*. (2017) 357:55–60. doi: 10.1126/science.aai8515

8. Knijn N, Mekenkamp LJM, Klomp M, Vink-Börger ME, Tol J, Teerenstra S, et al. KRAS mutation analysis: a comparison between primary tumours and matched liver metastases in 305 colorectal cancer patients. *Br J Cancer*. (2011) 104:1020–6. doi: 10.1038/bjc.2011.26

9. Enquist IB, Good Z, Jubb AM, Fuh G, Wang X, Junttila MR, et al. Lymph node-independent liver metastasis in a model of metastatic colorectal cancer. *Nat Commun*. (2014) 5:3530. doi: 10.1038/ncomms4530

10. Hu Z, Ding J, Ma Z, Sun R, Seoane JA, Scott Shaffer J, et al. Quantitative evidence for early metastatic seeding in colorectal cancer. *Nat Genet*. (2019) 51:1113–22. doi: 10.1038/s41588-019-0423-x

11. Tivey A, Church M, Rothwell D, Dive C, Cook N. Circulating tumour DNA — looking beyond the blood. *Nat Rev Clin Oncol*. (2022) 19:600–12. doi: 10.1038/s41571-022-00660-y

12. Mani DR, Krug K, Zhang B, Satpathy S, Clauser KR, Ding L, et al. Cancer proteogenomics: current impact and future prospects. *Nat Rev Cancer*. (2022) 22:298–313. doi: 10.1038/s41568-022-00446-5

13. Bates RC, Mercurio A. The epithelial-mesenchymal tansition (EMT) and colorectal cancer progression. *Cancer Biol Ther*. (2005) 4:371–6. doi: 10.4161/cbt.4.4.1655

14. Elias JE, Gygi SP. Target-decoy search strategy for increased confidence in large-scale protein identifications by mass spectrometry. *Nat Methods*. (2007) 4:207–14. doi: 10.1038/nmeth1019

15. Deutsch EW, Lane L, Overall CM, Bandeira N, Baker MS, Pineau C, et al. Human proteome project mass spectrometry data interpretation guidelines 3.0. *J Proteome Res*. (2019) 18:4108–16. doi: 10.1021/acs.jproteome.9b00542

16. Li C, Sun YD, Yu GY, Cui JR, Lou Z, Zhang H, et al. Integrated omics of metastatic colorectal cancer. *Cancer Cell*. (2020) 38:734–747.e9. doi: 10.1016/j.ccell.2020.08.002

17. Engebretsen S, Bohlin J. Statistical predictions with glmnet. *Clin Epigenetics*. (2019) 11:123. doi: 10.1186/s13148-019-0730-1

18. Chen B, Khodadoust MS, Liu CL, Newman AM, Alizadeh AA. Profiling tumor infiltrating immune cells with CIBERSORT. In: von Stechow L, editor. *Cancer Systems Biology: Methods and Protocols*. Clifton, New Jersey: Springer (2018). p. 243–59. doi: 10.1007/978-1-4939-7493-1_12

19. Li T, Fan J, Wang B, Traugh N, Chen Q, Liu JS, et al. TIMER: A web server for comprehensive analysis of tumor-infiltrating immune cells. *Cancer Res*. (2017) 77: e108–10. doi: 10.1158/0008-5472.CAN-17-0307

20. Plattner C, Finotello F, Rieder D. Chapter Ten - Deconvoluting tumor-infiltrating immune cells from RNA-seq data using quanTIseq. In: Galluzzi L, Rudqvist NP, editors. *Methods in Enzymology*, vol. 636 Tumor Immunology and Immunotherapy – Integrated Methods Part B. Amsterdam, Netherlands; Boston, MA: Academic Press (2020). p. 261–85. doi: 10.1016/bs.mie.2019.05.056

21. Becht E, Giraldo NA, Lacroix L, Buttard B, Elarouci N, Petitprez F, et al. Estimating the population abundance of tissue-infiltrating immune and stromal cell populations using gene expression. *Genome Biol*. (2016) 17:218. doi: 10.1186/s13059-016-1070-5

22. Racle J, de Jonge K, Baumgaertner P, Speiser DE, Gfeller D. Simultaneous enumeration of cancer and immune cell types from bulk tumor gene expression data. *eLife*. (2017) 6:e26476. doi: 10.7554/eLife.26476

23. *Profiling Tumor Infiltrating Immune Cells with CIBERSORT* . SpringerLink.

24. Han Y, Wang Y, Dong X, Sun D, Liu Z, Yue J, et al. TISCH2: expanded datasets and new tools for single-cell transcriptome analyses of the tumor microenvironment. *Nucleic Acids Res*. (2023) 51:D1425–31. doi: 10.1093/nar/gkac959

25. Marisa L, de Reyniès A, Duval A, Selves J, Gaub MP, Vescovo L, et al. Gene expression classification of colon cancer into molecular subtypes: characterization, validation, and prognostic valu. *PloS Med*. (2013) 10(5):e1001453. doi: 10.1371/journal.pmed.1001453

26. Nitzkorski JR, Farma JM, Watson JC, Siripurapu V, Zhu F, Matteotti RS, et al. Outcome and natural history of patients with stage IV colorectal cancer receiving chemotherapy without primary tumor resection. *Ann Surg Oncol*. (2012) 19:379–83. doi: 10.1245/s10434-011-2028-1

27. Ahmed S, Leis A, Chandra-Kanthan S, Fields A, Zaidi A, Abbas T, et al. Regional lymph nodes status and ratio of metastatic to examined lymph nodes correlate with survival in stage IV colorectal cancer. *Ann Surg Oncol*. (2016) 23:2287–94. doi: 10.1245/s10434-016-5200-9

28. Hagness M, Foss A, Egge TS, Dueland S. Patterns of recurrence after liver transplantation for nonresectable liver metastases from colorectal cancer. *Ann Surg Oncol*. (2014) 21:1323–9. doi: 10.1245/s10434-013-3449-9

29. Veereman G, Robays J, Verleye L, Leroy R, Rolfo C, Van Cutsem E, et al. Pooled analysis of the surgical treatment for colorectal cancer liver metastases. *Crit Rev Oncology/Hematology*. (2015) 94:122–35. doi: 10.1016/j.critrevonc.2014.12.004

30. Zhao H, Achreja A, Iessi E, Logozzi M, Mizzoni D, Di Raimo R, et al. The key role of extracellular vesicles in the metastatic process. *Biochim Biophys Acta (BBA) - Rev Cancer*. (2018) 1869:64–77. doi: 10.1016/j.bbcan.2017.11.005

31. Gordon-Weeks A, Lim SY, Yuzhalin A, Lucotti S, Vermeer JAF, Jones K, et al. Tumour-derived laminin α5 (LAMA5) promotes colorectal liver metastasis growth, branching angiogenesis and notch pathway inhibition. *Cancers*. (2019) 11:630. doi: 10.3390/cancers11050630

32. Zeltz C, Gullberg D. The integrin–collagen connection – a glue for tissue repair? *J Cell Sci*. (2016) 129:1284. doi: 10.1242/jcs.188672

33. Yang X, Wei M, Huang Y, Yang X, Yuan Z, Huang J, et al. ITGA11, a prognostic factor associated with immunity in gastric adenocarcinoma. *IJGM*. (2024) 17:471–83. doi: 10.2147/IJGM.S444786

34. Iwai M, Tulafu M, Togo S, Kawaji H, Kadoya K, Namba Y, et al. Cancer-associated fibroblast migration in non-small cell lung cancers is modulated by increased integrin α11 expression. *Mol Oncol*. (2021) 15:1507–27. doi: 10.1002/1878-0261.12937

35. Primac I, Maquoi E, Blacher S, Heljasvaara R, Van Deun J, Smeland HY, et al. Stromal integrin α11 regulates PDGFRβ signaling and promotes breast cancer progression. *J Clin Invest*. (2019) 129:4609–28. doi: 10.1172/JCI125890

36. Zheng H, An M, Luo Y, Diao X, Zhong W, Pang M, et al. PDGFRα+ITGA11+ fibroblasts foster early-stage cancer lymphovascular invasion and lymphatic metastasis via ITGA11-SELE interplay. *Cancer Cell*. (2024) 42:682–700.e12. doi: 10.1016/j.ccell.2024.02.002

37. Bartolini A, Cardaci S, Lamba S, Oddo D, Marchiò C, Cassoni P, et al. BCAM and LAMA5 mediate the recognition between tumor cells and the endothelium in the metastatic spreading of KRAS-mutant colorectal cancer. *Clin Cancer Res*. (2016) 22:4923–33. doi: 10.1158/1078-0432.CCR-15-2664

38. Yousif LF, Di Russo J, Sorokin L. Laminin isoforms in endothelial and perivascular basement membranes. *Cell Adhesion Migration*. (2013) 7:101–10. doi: 10.4161/cam.22680

39. Houlston RS, Cheadle J, Dobbins SE, Tenesa A, Jones AM, Howarth K, et al. Meta-analysis of three genome-wide association studies identifies susceptibility loci for colorectal cancer at 1q41, 3q26.2, 12q13.13 and 20q13.33. *Nat Genet*. (2010) 42:973–7. doi: 10.1038/ng.670

40. Ueki A, Komura M, Koshino A, Wang C, Nagao K, Homochi M, et al. Stromal POSTN enhances motility of both cancer and stromal cells and predicts poor survival in colorectal cancer. *Cancers*. (2023) 15:606. doi: 10.3390/cancers15030606

41. Qin J, Hu S, Chen Y, Xu M, Xiao Q, Lou J, et al. Hypoxia promotes Malignant progression of colorectal cancer by inducing POSTN+ Cancer-associated fibroblast formation. *Mol Carcinogenesis*. (2025) 64:716–32. doi: 10.1002/mc.23882

42. Feng K, Di Y, Han M, Yan W, Wang Y. SORBS1 inhibits epithelial to mesenchymal transition (EMT) of breast cancer cells by regulating PI3K/AKT signaling and macrophage phenotypic polarization. *Aging*. (2024) 16:4789–810. doi: 10.18632/aging.205632

43. Song L, Chang R, Dai C, Wu Y, Guo J, Qi M, et al. SORBS1 suppresses tumor metastasis and improves the sensitivity of cancer to chemotherapy drug. *Oncotarget*. (2016) 8:9108–22. doi: 10.18632/oncotarget.12851

44. Miosge N, Holzhausen S, Zelent C, Sprysch P, Herken R. Nidogen-1 and nidogen-2 are found in basement membranes during human embryonic development. *Histochem J*. (2001) 33:523–30. doi: 10.1023/A:1014995523521

45. Beck AH, Lee CH, Witten DM, Gleason BC, Edris B, Espinosa I, et al. Discovery of molecular subtypes in leiomyosarcoma through integrative molecular profiling. *Oncogene*. (2010) 29:845–54. doi: 10.1038/onc.2009.381

46. Tang G, Wu D, Guo M, Li H. LncRNA MIR497HG inhibits colorectal cancer progression by the miR-3918/ACTG2 axis. *J Genet*. (2022) 101:27. doi: 10.1007/s12041-022-01367-w

47. Sweetwyne MT, Murphy-Ullrich JE. Thrombospondin1 in tissue repair and fibrosis: TGF-β-dependent and independent mechanisms. *Matrix Biol*. (2012) 31:178–86. doi: 10.1016/j.matbio.2012.01.006

48. Ramchandani D, Mittal V. Thrombospondin in tumor microenvironment. In: Birbrair A, editor. *Tumor Microenvironment: Extracellular Matrix Components – Part B*. Cham, Switzerland: Springer International Publishing (2020). p. 133–47. doi: 10.1007/978-3-030-48457-6_8

49. Amin MB, Greene FL, Edge SB, Compton CC, Gershenwald JE, Brookland RK, et al. The Eighth Edition AJCC Cancer Staging Manual: Continuing to build a bridge from a population-based to a more "personalized" approach to cancer staging. *CA: A Cancer J Clin*. (2017) 67:93–9. doi: 10.3322/caac.21388. Amin.

50. Cossu ML, Ginesu GC, Feo CF, Fancellu A, Pinna A, Vargiu I, et al. Surgical outcomes in patients with hepatic synchronous and metachronous colorectal metastases. *Annali Italiani di Chirurgia*. (2017) 88:497–504.

51. Wang HW, Yan XL, Wang LJ, Zhang MH, Yang CH, Wei-Liu , et al. Characterization of genomic alterations in Chinese colorectal cancer patients with liver metastases. *J Trans Med*. (2021) 19:313. doi: 10.1186/s12967-021-02986-0

52. Kuo YT, Tsai WS, Hung HY, Hsieh PS, Chiang SF, Lai CC, et al. Prognostic value of regional lymph node involvement in patients with metastatic colorectal cancer: palliative versus curative resection. *World J Surg Oncol*. (2021) 19:150. doi: 10.1186/s12957-021-02260-z

53. Holch JW, Ricard I, Stintzing S, Modest DP, Heinemann V. The relevance of primary tumour location in patients with metastatic colorectal cancer: A meta-analysis of first-line clinical trials. *Eur J Cancer*. (2017) 70:87–98. doi: 10.1016/j.ejca.2016.10.007

54. Yaeger R, Chatila WK, Lipsyc MD, Hechtman JF, Cercek A, Sanchez-Vega F , et al. Clinical sequencing defines the genomic landscape of metastatic colorectal cancer. *Cancer Cell*. (2018) 33:125–136.e3. doi: 10.1016/j.ccell.2017.12.004

55. Orhan A, Justesen TF, Raskov H, Qvortrup C, Gögenur I. Introducing neoadjuvant immunotherapy for colorectal cancer: advancing the frontier. *Ann Surgery*. (2025) 281:95. doi: 10.1097/SLA.0000000000006443

56. Laumont CM, Banville AC, Gilardi M, Hollern DP, Nelson BH. Tumour-infiltrating B cells: immunological mechanisms, clinical impact and therapeutic opportunities. *Nat Rev Cancer*. (2022) 22:414–30. doi: 10.1038/s41568-022-00466-1

57. Ghorbaninezhad F, Nour MA, Farzam OR, Saeedi H, Vanan AG, Bakhshivand M, et al. The tumor microenvironment and dendritic cells: Developers of pioneering strategies in colorectal cancer immunotherapy? *Biochim Biophys Acta (BBA) - Rev Cancer*. (2025) 1880:189281. doi: 10.1016/j.bbcan.2025.189281

frontiers | Frontiers in Immunology

TYPE Review
PUBLISHED 05 August 2025
DOI 10.3389/fimmu.2025.1645718

Check for updates

OPEN ACCESS

EDITED BY
Hailin Tang,
Sun Yat-sen University Cancer Center (SYSUCC), China

REVIEWED BY
Can Xu,
Hebei University, China
Hengrui Liu,
University of Cambridge, United Kingdom
Boxuan Zhou,
Shenzhen Hyzen Hospital, China

*CORRESPONDENCE
Li Bao
baoli1105@163.com

RECEIVED 12 June 2025
ACCEPTED 22 July 2025
PUBLISHED 05 August 2025

CITATION
Zhao Y, Xu J, Yang K and Bao L (2025) Targeting GABA signaling in the tumor microenvironment: implications for immune cell regulation and immunotherapy resistance.
Front. Immunol. 16:1645718.
doi: 10.3389/fimmu.2025.1645718

COPYRIGHT
© 2025 Zhao, Xu, Yang and Bao. This is an open-access article distributed under the terms of the Creative Commons Attribution License (CC BY). The use, distribution or reproduction in other forums is permitted, provided the original author(s) and the copyright owner(s) are credited and that the original publication in this journal is cited, in accordance with accepted academic practice. No use, distribution or reproduction is permitted which does not comply with these terms.

Targeting GABA signaling in the tumor microenvironment: implications for immune cell regulation and immunotherapy resistance

Yuanqing Zhao[1,2], Jin Xu[2,3], Ke Yang[1,2] and Li Bao[4]*

[1]Department of Laboratory Medicine, Clinical Laboratory Medicine Research Center, West China Hospital, Sichuan University, Sichuan Clinical Research Center for LaboratoryMedicine, Chengdu, Sichuan, China, [2]Department of Laboratory Medicine, Chengdu Shangjin Nanfu Hospital, Chengdu, Sichuan, China, [3]Medicine Research Center, West China Hospital, Sichuan University, Sichuan Clinical Research Center for Laboratory Medicine, Chengdu, Sichuan, China, [4]Department of Radiology, Key Laboratory of Birth Defects and Related Diseases of Women and Children of Ministry of Education, West China Second University Hospital, Sichuan University, Chengdu, China

As an important inhibitory neurotransmitter, γ-aminobutyric acid (GABA) not only plays a key role in the central nervous system, but also has attracted wide attention in the tumor immune microenvironment in recent years. Studies have shown that tumor cells can synthesize GABA and use it to remodel the tumor microenvironment, thereby promoting the occurrence, development and metastasis of tumors. Although previous studies have revealed the important role of GABA in tumor immune escape, there are still many unknown areas of its mechanism, especially the heterogeneous manifestations in different tumor types and tissue environments. This review summarizes the immunomodulatory mechanisms of GABA in tumor-associated macrophages, $CD8^+$ T cells and dendritic cells in the tumor immune microenvironment, and discusses its potential role in tumor immune escape and immunotherapy resistance, providing new ideas for the development of immunotherapeutic drugs targeting GABA receptors.

KEYWORDS

GABA signaling, tumor immunotherapy, tumor microenvironment, immune cell regulation, cancers

1 Introduction

Cancer remains a major global public health challenge, with incidence and mortality rates continuing to rise. According to the "Cancer Statistics, 2024" report, over 19 million new cancer cases were diagnosed worldwide in 2023, with certain tumor types such as breast cancer and lung cancer maintaining high incidence rates and showing significant

variability in five-year survival rates among patients (1). Reviewing the history of cancer treatments, based on the NIH's "Cancer Treatments: Past, Present, and Future" (2024), therapeutic approaches have evolved from traditional surgery and radiotherapy to chemotherapy, followed by targeted therapies and immunotherapies, greatly improving patient outcomes (2, 3). However, current treatments still face challenges posed by tumor heterogeneity and therapeutic resistance. Regarding cancer treatment strategies, recent research in "Different Strategies for Cancer Treatment: Targeting Cancer Cells or Their Neighbors?" (2025) highlights two primary approaches: direct targeting of tumor cells and modulation of the tumor microenvironment (4). The former achieves rapid tumor cell killing by targeting tumor-specific molecules but is prone to resistance development; the latter improves immune infiltration by regulating immune cells and stromal components, with complex mechanisms but considerable potential. Integrative treatment strategies that combine the advantages of both approaches are considered the future direction in oncology.

γ-Aminobutyric acid (GABA), a principal inhibitory neurotransmitter in the central nervous system, plays a critical role in modulating neuronal excitability, exerting calming and sedative effects (5). Traditionally recognized for its neurological functions, GABA has recently garnered attention in oncology due to its aberrant upregulation in a variety of solid tumors, where elevated GABA levels have been correlated with poor clinical outcomes (6). Emerging evidence indicates that tumor cells not only possess the capacity to synthesize GABA but also exploit it to modulate the tumor microenvironment, thereby promoting tumor progression and metastasis (7).

Within the landscape of tumor immune evasion, cancer cells deploy multifaceted mechanisms to escape host immune surveillance, ultimately undermining the efficacy of immunotherapy (8). A well-characterized strategy involves the upregulation of immune checkpoint molecules such as programmed death-ligand 1, which inhibits T cell activation and effector function (9). Beyond checkpoint pathways, GABA has been shown to reprogram tumor-associated macrophages toward an immunosuppressive M2 phenotype, thereby fostering an immune-permissive tumor microenvironment (10). Moreover, GABA signaling through $GABA_A$ receptors can directly impair the cytotoxic activity of $CD8^+$ T cells and reduce their production of interferon-gamma (IFN-γ). Simultaneously, GABA facilitates the infiltration and activity of regulatory T cells (Tregs), contributing to a multilayered immune evasion network (11).

Therefore, it is of great significance to further study the immunomodulatory role of GABA in the tumor microenvironment. A deeper understanding of how GABA mediates immune escape and resistance to immunotherapy may not only shed light on the biological underpinnings of cancer progression but also pave the way for innovative therapeutic strategies. This review aims to examine the emerging role of GABA in tumor immune evasion and immunotherapy resistance, and to explore its implications for the future of cancer immunotherapy.

2 Mechanisms and functions of GABA signaling

Recent studies have demonstrated that the role of GABA signaling within the tumor immune microenvironment shows significant heterogeneity across different cancer types and tissue contexts. For example, in glioblastoma, activation of the GABAB receptor on granulocytic myeloid-derived suppressor cells (gMDSCs) enhances L-arginine metabolism and NOS2 expression, promoting tumor growth; conversely, inhibition of GABABR prolongs survival in mouse models (12). In breast cancer, GABAergic signaling modulates tumor progression through distinct mechanisms: activation of the GABAA receptor δ subunit (GABRD) enhances GPT2-mediated metabolic reprogramming, promoting metastasis, while upregulation of the β3 subunit fosters clonal expansion and cell migration in triple-negative breast cancer (13). In pancreatic ductal adenocarcinoma (PDAC), GABA has been shown to promote proliferation via the GABAA receptor π subunit; paradoxically, some studies suggest it may suppress migration, indicating a complex bidirectional role. Moreover, in hepatocellular carcinoma (HCC), GABAergic signaling through distinct receptor subunits (such as α3, β3, π, θ) may exert context-dependent effects, with certain receptor profiles linked to tumor suppression (13). Recent studies have revealed significant differences in the expression of various GABA receptor subunits within immune cells. For example, the expression levels of the α3 and β2 subunits differ between T cells and tumor-associated macrophages (TAMs), which may lead to distinct responses to GABA signaling. Specifically, the α3 subunit may be involved in regulating immune cell activation and cytokine secretion, whereas the β2 subunit may influence cell polarization and immunosuppressive functions (10, 14). Selective modulation of different subunits not only helps to uncover the complex roles of GABA signaling in immune regulation but also provides a theoretical basis for the development of highly selective targeted drugs, thereby enabling precise immunotherapy strategies that improve efficacy while minimizing side effects. Collectively, these findings emphasize that the immunomodulatory effects of GABA are highly context-dependent and are shaped by tumor-intrinsic characteristics, tissue-specific microenvironments, and the composition of immune cell populations. GABA synthesis primarily depends on glutamate decarboxylase (GAD), which converts glutamate into GABA. GAD exists in two isoforms, GAD65(GAD2) and GAD67(GAD1), which play roles at the nerve terminals and in areas such as the cerebral cortex, respectively (15, 16). After synthesis, GABA undergoes metabolism via GABA transaminase (ABAT), which converts it into succinic semialdehyde, which is further transformed into

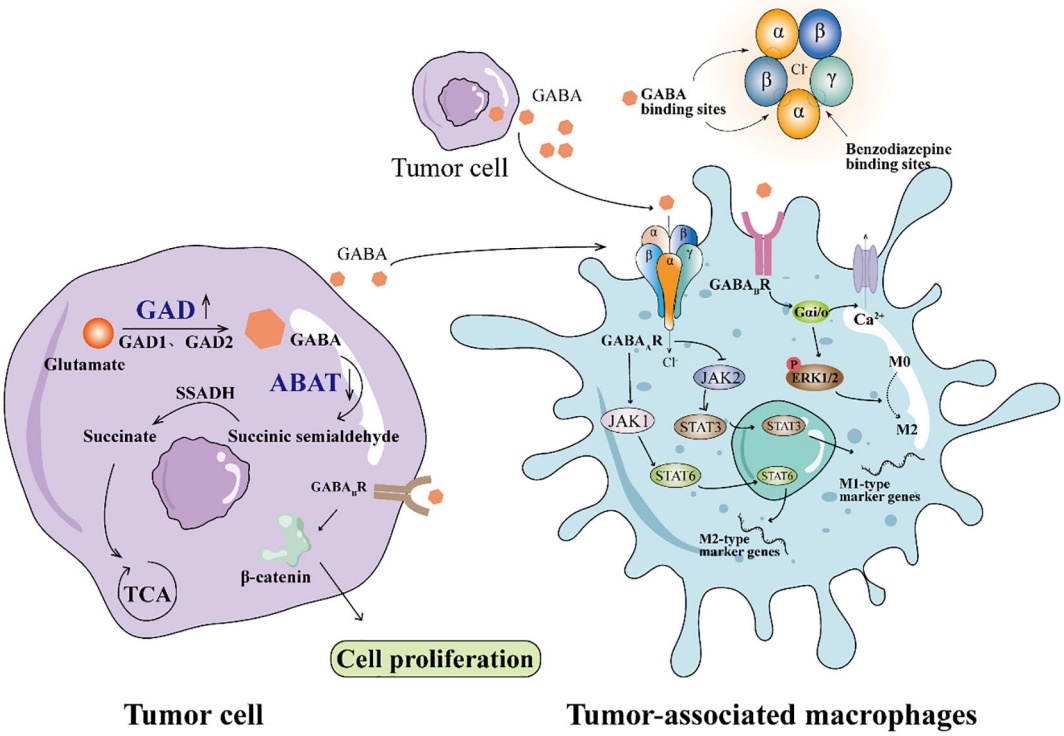

FIGURE 1
GABA signaling pathway in tumor microenvironment stimulates the polarization of macrophages to M2 type. Downregulation of GAD expression and downregulation of ABAT expression in tumor cells leads to GABA accumulation. GABA$_A$R on the surface of TAMs binds GABA from tumor cells to activate JAK1/STAT6 signaling and promote M2 polarization. GABA couples GABA$_B$R to Gαi, activates ERK1/2 signaling pathway, and promotes M2 polarization.

succinate by succinic semialdehyde dehydrogenase (SSADH), entering the tricarboxylic acid(TCA) cycle for energy metabolism (Figure 1). Previous studies have observed GAD1 upregulation and ABAT downregulation in tumor cells (6). Additionally, GABA is taken up by glial cells and neurons through GABA transporters (GAT) and is either converted back into glutamate or used for the synthesis of new GABA (17). The balance between GABA synthesis and metabolism is crucial for the proper function of the nervous system, and its dysregulation is closely associated with various neurological disorders, such as epilepsy and anxiety (18, 19).

The biological effects of GABA are primarily mediated through its receptors, including GABA$_A$, GABA$_B$, and GABA$_C$ receptors (20–22). GABA$_A$ receptors are ion channel receptors, and when GABA binds to them, Cl^- flow into the cell, causing hyperpolarization of the neuron and inhibiting neural activity, thus mediating rapid inhibitory synaptic transmission (23). GABA$_A$ receptors are drug targets, and benzodiazepines enhance their effects, providing sedative and anti-anxiety properties (24, 25). In contrast, GABA$_B$ receptors are G-protein coupled receptors, which regulate Ca^{2+} and K^+ channels to produce slower inhibitory effects, involved in long-term neural regulation, and play a broad role in learning, memory, and pain control (26, 27). GABA$_C$ receptors, primarily located in the retina (28), are ion channel receptors responsible for the rapid inhibitory transmission of visual information. These three receptor types each play a unique role in the nervous system, collectively maintaining the balance of neural function.

3 Role of GABA in tumor microenvironment

Tumor immune evasion refers to the ability of tumor cells to evade recognition and clearance by the host immune system, allowing the tumor to survive and develop under immune surveillance (29, 30). The primary function of the immune system is to maintain the health of the body by recognizing and attacking foreign substances, mutated cells, and tumor cells. However, tumor cells avoid this clearance by altering their surface characteristics or by modulating the immune environment. Tumor immune evasion is one of the major causes of cancer resistance and the progression of malignant tumors (31). Through immune evasion, tumor cells not only avoid detection by the immune system but may also accelerate tumor growth, metastasis, and the development of resistance to treatment. Studies have shown that GABA stimulates tumor cell proliferation by activating GABA$_B$ receptors (32). This process involves the inhibition of the GSK-3 signaling pathway, leading to the activation of β-catenin, which subsequently inhibit tumor cell proliferative capacity and impairs $CD8^+$ T cell infiltration into tumors (6, 33). Mohita et al. (34) found that GABA promotes

melanoma development by releasing a SNAR-dependent vesicle pathway. GABA signaling has an immunosuppressive effect in the tumor microenvironment, which makes GABA receptors a potential therapeutic target for cancer immunotherapy (35).

4 The influence of GABA on immune cells

4.1 The effect of GABA on TAM

Tumor-associated macrophages (TAMs) are important immune cells within the tumor microenvironment, primarily originating from circulating monocytes (36, 37). Tumors recruit these monocytes by secreting chemokines such as CCL2 and growth factors like CSF-1. These recruited monocytes differentiate into macrophages and become TAMs in response to local signals. The functional phenotype of TAMs is highly plastic and influenced by multiple signals within the tumor microenvironment. Pro-inflammatory stimuli such as IFN-γ and LPS drive TAMs toward an M1 phenotype, characterized by anti-tumor activity through the production of inflammatory cytokines and antigen presentation (38). In contrast, anti-inflammatory cytokines including IL-4 and IL-13 promote M2 polarization, which supports tumor progression by facilitating immune suppression, angiogenesis, and tissue remodeling. Increasing evidence suggests that GABA signaling can modulate TAM polarization. GABA binds to GABA receptors on macrophages, leading to downstream signaling changes that favor M2 polarization. Dong et al. (39) showed that macrophages activate the JAK1/STAT6 signaling pathway via GABA, which promotes the expression of Arg1, a gene related to M2. GABA aiso inhibited the NF-κB and JAK2/STAT3 signaling pathways, and decreased the expression of iNos related to M1 (Figure 1). This finding is consistent with previous research, and Zhang et al. (40) also confirmed that GABA can significantly reduce the nuclear localization of p65 in the NF-κB signaling pathway.

The changes in $GABA_A$ receptor ($GABA_AR$) expression may form the basis for macrophage polarization. During the differentiation of monocytes into the M0 macrophage phenotype, the expression of the $GABA_AR$ β2 subunit increases significantly, while the expression of the $GABA_AR$ α4 subunit shows no significant change. When M0 macrophages polarize to the M1 phenotype, the expression of the $GABA_AR$ α4 subunit and GAD1 decreases, while the β2 subunit expression returns to monocyte levels, and the expression of GAT2 increases significantly (41). These changes diminish the response of $GABA_AR$ to GABA, thereby relieving GABA's anti-inflammatory suppression and supporting the pro-inflammatory function of M1 macrophages. GABA Transporters(GAT) belongs to the SLC6A family, which includes GAT1–4 and is responsible for transporting GABA from the synaptic cleft or extracellular environment to the cell to maintain GABA homeostasis.Xia et al. (42) GAT2 deficiency in macrophages can increase intracellular betaine content, leading to hypoxanthine and S-adenosylmethionine accumulation (SAM), and the intracellular betaine/SAM/hypoxanthine metabolic pathway affects the methylation of the transcription factor KID3. It inhibits the formation of NLRP3-ASC-Caspase-1 complex and increases the intracellular OXPHOS level, thereby inhibiting the production of IL-1β in M1 macrophages. Liu et al. (43) found that GABA receptor agonists can promote the polarization of macrophages towards the M2 phenotype. Sun et al. (44) found that GABA-related genes can be used to judge the prognosis of glioma. Dou et al. (45) found that GABA secreted by oral squamous cell carcinoma (OSCC) promotes macrophage polarization toward the M2 phenotype by activating the $GABA_B$ R1 and its downstream ERK and Ca^{2+} signaling pathways, which promoted EMT of OSCC *in vivo*(Figure 1). These results suggest that GABA may play a role in tumor immune escape by regulating the polarization of macrophages in the tumor microenvironment.

4.2 The effect of GABA on T cell

$CD8^+$ T cells are a major subset of cytotoxic T lymphocytes, which express CD8 coreceptors and recognize antigens through MHC class I molecules. In the tumor microenvironment, $CD8^+$ T cells are the core effector cells of anti-tumor immunity, and their activity is positively correlated with the prognosis of patients. Tharp et al. (46) found that in the fibrotic tumor microenvironment, TAMs initiate collagen biosynthesis through TGF-β signaling, creating a metabolic environment that depletes arginine and secretes proline and ornithine, thereby inhibiting $CD8^+$ T cell antitumor responses. Previous studies have found that PMVK expression is increased in tumor tissues (47). Zhou et al. (11) observed in hepatocellular carcinoma cells that PMVK activity is negatively correlated with $CD8^+$ T cell infiltration and immune evasion. Their study demonstrated that PMVK promotes the conversion of glutamate to GABA by phosphorylating threonine 576 at the C-terminus of GAD1, thereby increasing GABA synthesis. Furthermore, PMVK directly binds to and stabilizes ACAT1 protein, facilitating the acetylation of GABA to generate 4-Ac-GABA. 4-Ac-GABA binds to the α3 subunit of the $GABA_AR$ on the surface of $CD8^+$ T cells, inhibiting AKT1 phosphorylation, which subsequently reduces the expression of $CD8^+$ T cell activation markers such as IFN-γ and granzyme B, and decreases their infiltration into the tumor microenvironment (Figure 2). Immunofluorescence conducted by Sparrow et al. (48) confirmed the presence of $GABA_AR$ subunits on the surface of both mouse and human T cells. Mouse T cells predominantly express the α2, α3, α5, β2, β3, γ1, and δ subunits, whereas human T cells highly express the α1, α5, β1, π, ρ1, and ρ2 subunits, with the ρ2 subunit being enriched on the surface of human T cells. Activation of $GABA_AR$ by benzodiazepines or neurosteroids significantly inhibited the proliferation of both mouse and human T cells, and this effect was reversed by $GABA_A$ receptor antagonists. These findings indicate that $GABA_A$ receptors play a crucial role in regulating T

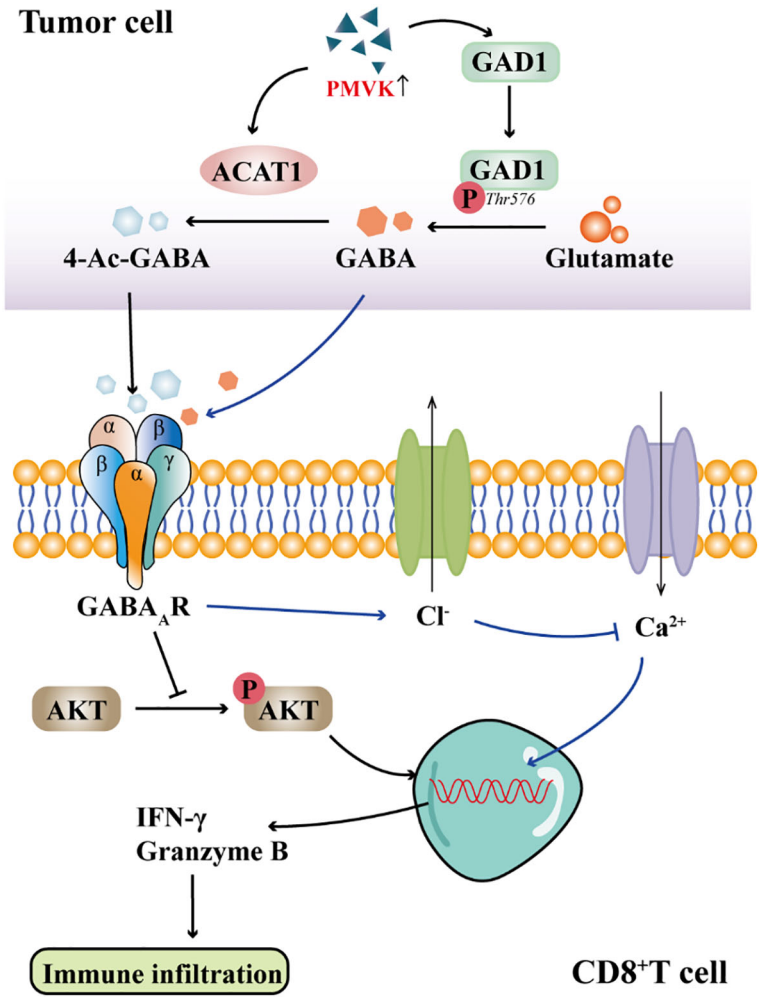

FIGURE 2
GABA signaling inhibits CD8+T cell immune infiltration. GABAAR on the membrane of CD8+T cells binds to 4-Ac-GABA from tumor cells, inhibits the phosphorylation of AKT and prevents the production of IFN-γ and Granzyme B, thereby affecting T cell activation and immune infiltration. Activation of $GABA_AR$ results in Cl^- efflux, inhibition of Ca^{2+} influx, and ultimately inhibition of T cell activation.

cell function; their activation can suppress T cell proliferation and immune activity, thereby potentially contributing to the regulation of immune responses and tumor immune evasion.

The enhancement of Ca^{2+} signaling can accelerate the activation process of T cells, thereby improving their responsiveness to tumor cells. Zhang et al. (40) implanted sustained-release GABA particles into $muMt^{-/-}$ mice and found that tumor growth in the mice was significantly increased. Further investigation revealed that GABA might regulate $CD8^+$ T cell function by binding to the $GABA_AR$ on the surface of T cells, inhibiting Ca^{2+} influx.Consistent with these findings, Tian et al. (49) also discovered that GABA activates $GABA_AR$ on the surface of T cells, leading to the opening of Cl^- channels, Cl^- efflux, and membrane depolarization, which in turn inhibits Ca^{2+} influx (Figure 2). Ca^{2+} influx is a critical step for the activation of naïve T cells and the function of effector T cells. Activation of GABA receptors primarily causes T cells to arrest in the G_0/G_1 phase, preventing their entry into the proliferative cycle and thereby inhibiting clonal expansion. Although the expression of $GABA_AR$ subunits has been identified in T cells, the specific role of these subunits in regulating T cell function is not well defined. The effects of different subunits on T cell activity, polarization and immune escape may be different, and further studies are needed to clarify.

4.3 The effect of GABA on DCs

Dendritic cells (DCs) are key antigen-presenting cells that bridge innate and adaptive immunity. They capture and internalize foreign antigens, process them into peptide fragments, and present these peptides bound to major histocompatibility complex (MHC) molecules to T cell receptors (50). This process activates and directs T cells to mount a targeted immune response against specific pathogens or abnormal cells. Dendritic cells promote the recognition and elimination of tumor cells by activating $CD8^+$ cytotoxic T cells and $CD4^+$ helper T cells (51). In addition, Dcs regulate the immune microenvironment, influencing the development of immune tolerance and immune evasion. Tumor cells and their surrounding stroma secrete various

immunosuppressive factors, such as TGF-β、IL-10 and VEGF, which inhibit the maturation and activation of dendritic cells, reducing their antigen-presenting capacity (52). In addition, metabolic products in the tumor microenvironment, such as lactate, can also suppress DCs function (53). Studies have shown that GABA receptors are not only present on T cells, B cells, and macrophages, but their expression profile also includes DCs (54). GABA is synthesized from glutamate catalyzed by GAD, which is expressed in DCs, indicating that DCs have the ability to produce GABA. At the same time, DCs express GATs on their surface, such as GAT1 and GAT3, enabling them to uptake extracellular GABA (55). Bekić et al. (56) found that in DCs, activation of the $GABA_BR$ induces a conformational change that couples with intracellular Gαi proteins, thereby activating G protein-coupled signaling pathways and inhibiting adenylate cyclase activity. This leads to a reduction in intracellular cAMP levels. The lowered cAMP levels promote the transition of DCs from an "immature" to a "mature" phenotype, increasing the expression of MHC II, CD86, and CD40, as well as the secretion of pro-inflammatory cytokines such as IL-1β, which in turn induces T cell differentiation toward the Th1 phenotype. This study reveals that monocyte-derived DCs may promote T cell proliferation and Th1 polarization through the $GABA_BR$/cAMP signaling pathway. Similarly, Huang et al. (57) also demonstrated that inhibiting the expression of $GABA_BR$ in DCs can suppress IL-6 production and hinder the differentiation of DCs into Th17 cells. Recent studies have further confirmed the regulatory role of GABA on dendritic cells (DCs) within the tumor microenvironment (TME). For example, one study demonstrated that tumor cells synthesize GABA through the expression of GAD1 and activate the β-catenin signaling pathway via GABA_B receptors, thereby inhibiting the recruitment of $CD103^+$ DCs and the infiltration of T cells into the tumor, ultimately promoting immune evasion and tumor progression (6). These findings indicate that GABA not only exerts effects in *in vitro* monocyte-derived DC cultures but also modulates anti-tumor immune responses by affecting DC function within the tumor microenvironment. In summary, while the role of GABA in regulating T cells and macrophages has been relatively well studied, its effects on dendritic cells—especially within the tumor microenvironment—remain underexplored. Current evidence suggests that GABAergic signaling influences DC maturation and cytokine production, thereby shaping downstream T cell polarization. However, the specific consequences of this modulation in cancer settings, including its contribution to immune evasion or resistance to immunotherapy, warrant further investigation. In addition, Current research on the regulation of dendritic cells (DCs) by GABA is limited and yields somewhat contradictory results. On one hand, some studies suggest that GABA can promote DC maturation and antigen-presenting functions, thereby enhancing immune activation. On the other hand, other studies indicate that GABA may inhibit DC activity, reducing their capacity to stimulate T cells. These conflicting findings may be due to influences from different tumor types and microenvironmental factors, such as local cytokine levels, metabolic states, and interactions with other immune cells. Additionally, variations in experimental models and methodologies may also contribute to inconsistent observations. In summary, a deeper investigation into the specific effects of GABA on DCs within diverse tumor microenvironments is crucial for understanding its immunoregulatory roles and for developing related immunotherapeutic strategies.

5 GABA signaling pathway plays a key role in the mechanism of tumor immunosuppression and drug resistance

Studies have shown that GABA can upregulate the expression of PD-L1 on the surface of tumor cells by activating the STAT3 signaling pathway, thereby suppressing anti-tumor immune responses (58). PD-L1 is an immune checkpoint protein expressed on tumor cells that binds to the PD-1 receptor on T cells, inhibiting their activity and promoting tumor immune evasion. As a key immune checkpoint molecule, PD-L1 interaction with PD-1 on T cells suppresses T cell function, allowing tumor cells to escape immune surveillance (59, 60). STAT3 is a well-established oncogenic signaling pathway in various types of cancers, and its sustained activation is closely associated with tumor proliferation, metastasis, and immune evasion. One study demonstrated that GABA and its derivative baclofen can downregulate the mRNA and protein levels of the E3 ubiquitin ligase STUB1, thereby enhancing the stability of PD-L1 and ultimately increasing its expression (61). This mechanism indicates that GABA not only functions within the nervous system but may also influence tumor immune evasion in the tumor microenvironment by regulating the expression of immune checkpoint proteins. Moreover, the positive allosteric modulator of the $GABA_AR$, QH-II-066, enhances GABA receptor function and can synergize with PD-L1 inhibitors to improve anti-tumor efficacy. In a mouse tumor model where PD-1 blockade therapy was ineffective, Huang et al. (6) found that the use of a GAD1 inhibitor alone, or in combination with an anti-PD-1 antibody, significantly reduced tumor volume. Switchenko et al. (62) found that benzodiazepines bind to the αγ subunit interface of the $GABA_AR$, enhancing the binding efficiency of GABA to its receptor and significantly increasing the chloride ion permeability of the melanoma cell membrane, thereby promoting chloride influx into the cells. Following benzodiazepine treatment, melanoma cells exhibited mitochondrial membrane depolarization, leading to apoptosis, a process associated with the p53 signaling pathway and cytokine expression. Regarding cancer stem cells, the π subtype of the GABA receptor (GABRP) is highly expressed on the membrane surface of triple-negative breast cancer stem cells. Li et al. (63) found that GABRP maintains the membrane abundance of EGFR by inhibiting its lysosomal degradation. The sustained activation of EGFR promotes the phosphorylation of ERK (p-ERK), thereby enhancing the self-renewal and proliferation of cancer stem cells. More importantly, although conventional chemotherapeutic agents such as paclitaxel and doxorubicin can induce the enrichment of cancer stem cells, knockdown of GABRP reverses this effect, suggesting that GABRP is one of the key mediators of

chemotherapy resistance. This study indicates that targeting GABRP may be a promising strategy to overcome immune resistance. In addition, GABA signaling is also closely associated with the recruitment of tumor-associated macrophages. In pancreatic ductal adenocarcinoma, Jiang et al. (64) found that although GABRP does not exert its oncogenic effects through the conventional GABA/Cl^- signaling pathway, it promotes the infiltration of immunosuppressive macrophages by interacting with KCNN4 and activating the Ca^{2+}/NF-κB/CXCL5-CCL20 axis. This macrophage infiltration not only contributes to the formation of an immunosuppressive microenvironment but also impairs T cell function and cooperates with other mechanisms to induce resistance to immunotherapy. Tumor immune evasion and immunotherapy resistance are closely related but not entirely equivalent concepts. Tumor immune evasion primarily refers to the processes by which cancer cells avoid recognition and elimination by the immune system through mechanisms such as downregulating antigen expression, secreting immunosuppressive factors, and recruiting suppressive immune cells. In contrast, immunotherapy resistance specifically describes the phenomenon where tumors show no response or reduced efficacy following treatments like immune checkpoint inhibitors (e.g., anti-PD-1/PD-L1 antibodies). Recent studies have revealed that GABA signaling is involved not only in classical immune evasion but also in mediating immunotherapy resistance by regulating immune checkpoint molecule expression, promoting the accumulation of immunosuppressive cells (such as regulatory T cells and tumor-associated macrophages), and suppressing the activity of effector $CD8^+$ T cells (11, 40, 65). For example, GABA, through activation of GABAB receptors and downstream pathways, enhances the immunosuppressive function of myeloid-derived suppressor cells, reduces infiltration and activity of anti-tumor T cells, thereby diminishing the efficacy of immunotherapy (66). Furthermore, currently, no GAD1-specific small-molecule inhibitors have entered cancer clinical trials. However, a preclinical study has shown that 3-mercaptopropionic acid (3–MPA), as a GAD1 inhibitor, can exert antitumor effects in osteosarcoma models by modulating the Wnt/β–catenin signaling pathway, suggesting that targeting GABA synthesis or metabolic pathways may hold therapeutic potential (67). Overall, these insights highlight the potential of targeting GABA signaling pathways as a novel strategy to overcome immunotherapy resistance.

6 Clinical translation and future perspectives

Despite the growing body of evidence implicating GABAergic signaling in tumor progression and immune modulation, the clinical translation of GABA-targeted therapies remains challenging. Most current findings are derived from *in vitro* studies or murine models, and several key barriers must be addressed before clinical application can be realized. First, off-target effects are a significant concern, especially given the widespread expression of GABA receptors and enzymes in both tumor and non-tumor tissues (68). Second, receptor-subtype selectivity remains poorly defined in the context of the tumor microenvironment (TME), where multiple GABA receptor subtypes may exhibit divergent roles across cell types. Third, the blood–tumor barrier (BTB) poses a major pharmacological obstacle, limiting the bioavailability of systemically administered agents to solid tumors. Finally, the dose-dependent neurotoxicity of GABAergic modulators, particularly in the central nervous system, necessitates careful safety evaluation. To move toward translational application, it is critical to integrate GABA-targeted strategies into the broader landscape of cancer immunotherapy. Recent studies have demonstrated how soluble PD-L1, cytokine profiles, and lymphocyte subsets can serve as circulating biomarkers to predict response to immune checkpoint inhibitors, particularly in melanoma (69). Moreover, next-generation CAR T-cell therapies are being engineered to resist hostile metabolic environments, such as hypoxia and high lactate, by enhancing mitochondrial resilience—thereby improving efficacy in solid tumors (70). In gastric cancer, evolving insights into the PD-1/PD-L1 axis have highlighted the need for combinatorial checkpoint blockade and personalized immunotherapy based on TME profiling (71). Additionally, interrupting extracellular vesicle-mediated communication between tumor cells and tumor-associated macrophages (TAMs) offers a novel approach to reprogramming the immunosuppressive TME (72). Combination strategies involving GABA-targeted therapies are an exciting and evolving frontier in cancer immunotherapy. Beyond PD-1/PD-L1 blockade, future research may explore the integration of GABA modulators with other immunotherapeutic approaches such as CTLA-4 inhibitors, CAR-T cells, and oncolytic viruses. These combinations may synergistically reshape the tumor immune microenvironment while mitigating adverse effects. Additionally, co-administration with metabolic reprogramming agents, cytokine inhibitors, or neuroprotective compounds may further enhance therapeutic efficacy and safety. Furthermore, it is important to acknowledge the ongoing role of traditional medicine, particularly in regions where herbal and mineral-based therapies remain widely used. Several recent studies have investigated both the mechanisms and clinical impact of traditional formulations, including the potential involvement of ion channels and metabolic pathways in the anticancer activity of so-called “toxic medicines” used in Traditional Chinese Medicine (TCM) (73, 74). Clinical reports have also demonstrated meaningful effects of traditional medicine on cancer outcomes (75, 76). Notably, biomarker-guided integration of traditional and modern therapies is emerging as a translationally viable direction. For instance, a recent study demonstrated that traditional medicine could counteract Trichostatin A–induced esophageal cancer progression when combined with biomarker-based strategies (77). These findings highlight the potential of holistic and multi-modal treatment paradigms in the context of GABA-targeted cancer immunotherapy. Taken together, the future of GABA-targeted cancer immunotherapy will likely depend on

synergizing metabolic modulation with immunologic precision, as well as overcoming structural and pharmacodynamic barriers through advanced drug delivery and rational combination strategies.

7 Conclusion

In this review, we summarized the mechanisms of GABA synthesis and metabolism, as well as its immunosuppressive effects within the tumor microenvironment. We focused on how GABA influences tumor immune evasion and immunotherapy resistance by modulating key immune cells, including T cells, TAMs, and DCs. Although numerous studies have preliminarily revealed the pivotal role of GABA signaling in reshaping the tumor immune microenvironment and promoting immune evasion, its immunoregulatory mechanisms remain largely unclear. GABA suppresses the anti-tumor activity of various immune cells, including T cells and macrophages, but the specific receptor subtypes, signaling pathways, and functional differentiation involved remain to be fully elucidated. Moreover, the GABA pathway exhibits significant heterogeneity across different tumor types and tissue contexts. In most peripheral solid tumors, elevated expression of GAD1 and downregulation of GABA-degrading enzyme ABAT in tumor cells lead to the accumulation of GABA in the tumor microenvironment, thereby promoting tumor growth and immune evasion (78). In contrast, in brain metastases, upregulation of ABAT is frequently observed, facilitating the catabolism of neuron-derived GABA for tumor energy metabolism, suggesting that the function of GABA signaling varies dramatically depending on the tumor context. These contrasting roles likely arise from context-specific factors such as differences in GABA receptor subtype expression, microenvironmental signals (e.g., cytokines, cell types, neuronal innervation), and regional metabolic constraints (78). Understanding these determinants will be crucial for developing tissue-selective GABA-targeted strategies.

Emerging technologies such as single-cell RNA sequencing and spatial transcriptomics hold great promise in this regard, enabling high-resolution dissection of GABA signaling networks across diverse cellular subsets and anatomical regions (79, 80). For example, single-cell studies have identified novel exhausted $CD8^+$ T-cell markers in breast cancer, revealed drug-tolerant persister cell vulnerabilities in colorectal cancer (81), and mapped glioma cell motility modulated by voltage-gated sodium channel β3 subunits (82). These insights underscore the power of single-cell approaches to uncover cellular heterogeneity and rare functional states. Compared to traditional bulk RNA sequencing, which captures averaged gene expression across mixed populations, single-cell analyses offer finer granularity and can resolve intra-tumoral heterogeneity, although at the cost of higher technical complexity and resource demands. A combination of both strategies may provide a more comprehensive understanding of the GABAergic immunoregulatory landscape. Additionally, the cellular sources of GABA in the tumor microenvironment remain poorly characterized; B cells, tumor cells, and even neurons may all contribute to its synthesis and secretion, forming a complex immunoregulatory network. In terms of therapeutic strategies, targeting GABA-synthesizing enzymes or receptors to enhance anti-tumor immunity has shown promise in animal models. However, most related studies remain at the preclinical stage, lacking systematic safety evaluations and clinical evidenc. Future research should systematically compare the immunoregulatory effects of GABA signaling across multiple tumor models to identify suitable therapeutic targets and responsive patient populations. Integrating advanced techniques such as single-cell genomics and spatial transcriptomics will be essential for elucidating the cellular sources and functional pathways of intratumoral GABA signaling. Furthermore, exploring synergistic mechanisms with existing immunotherapies—such as PD-1/PD-L1 inhibitors—may provide both theoretical support and practical strategies for the clinical translation of GABA-targeted interventions. Given the critical role of GABA in the nervous system, therapies targeting GABA signaling may cause various neurological side effects such as sedation, cognitive impairment, and motor dysfunction. These adverse effects mainly result from systemic modulation of GABA receptors in the central nervous system. To overcome this challenge, recent studies have explored strategies for tumor microenvironment-specific modulation (83). These include utilizing nanoparticle-based drug delivery systems for targeted transport, designing prodrugs that are locally activated within tumors to reduce systemic exposure, and developing highly selective agents targeting specific GABA receptor subtypes to minimize central nervous system involvement (84). Such approaches not only improve the safety and efficacy of treatment but also offer new avenues for precise immunotherapy targeting GABA signaling in tumors (85). Finally, future studies should also focus on how GABA-mediated intercellular communication dynamically regulates the immune landscape—balancing immune activation, suppression, and cell fate decisions—and how multi-target strategies combining GABA receptor modulators with other checkpoint inhibitors or metabolic regulators may help overcome tumor immune evasion. By leveraging the convergence of immunology, metabolism, and spatial genomics, the next phase of GABA-based immunotherapy research will provide new theoretical foundations and translational strategies for personalized cancer treatment.

Author contributions

YZ: Conceptualization, Data curation, Formal Analysis, Investigation, Methodology, Project administration, Resources, Software, Supervision, Validation, Visualization, Writing – original draft, Writing – review & editing. JX: Conceptualization, Data curation, Formal Analysis, Investigation, Methodology, Software, Supervision, Visualization, Writing – original draft, Writing – review & editing. KY: Conceptualization, Data curation, Formal Analysis, Investigation, Methodology, Project administration, Resources, Software, Visualization, Writing – original draft, Writing – review & editing. LB: Conceptualization, Data curation, Formal Analysis, Investigation, Methodology,

Project administration, Software, Supervision, Visualization, Writing – original draft, Writing – review & editing.

Funding

TThe author(s) declare that no financial support was received for the research and/or publication of this article.

Conflict of interest

The authors declare that the research was conducted in the absence of any commercial or financial relationships that could be construed as a potential conflict of interest.

Generative AI statement

The authors declare that no Generative AI was used in the creation of this manuscript.

Publisher's note

All claims expressed in this article are solely those of the authors and do not necessarily represent those of their affiliated organizations, or those of the publisher, the editors and the reviewers. Any product that may be evaluated in this article, or claim that may be made by its manufacturer, is not guaranteed or endorsed by the publisher.

References

1. Siegel RL, Giaquinto AN, Jemal A. Cancer statistics, 2024. *CA: Cancer J Clin*. (2024) 74:12–49. doi: 10.3322/caac.21820

2. Klein C, Brinkmann U, Reichert JM, Kontermann RE. The present and future of bispecific antibodies for cancer therapy. *Nat Rev Drug Discov*. (2024) 23:301–19. doi: 10.1038/s41573-024-00896-6

3. Sonkin D, Thomas A, Teicher BA. Cancer treatments: Past, present, and future. *Cancer Genet*. (2024) 286-287:18–24. doi: 10.1016/j.cancergen.2024.06.002

4. Liu H, Dilger JP. Different strategies for cancer treatment: Targeting cancer cells or their neighbors? *Chin J Cancer Res = Chung-kuo yen cheng yen chiu*. (2025) 37:289–92. doi: 10.21147/j.issn.1000-9604.2025.02.12

5. Piot L, Heroven C, Bossi S, Zamith J, Malinauskas T, Johnson C, et al. GluD1 binds GABA and controls inhibitory plasticity. *Science*. (2023) 382:1389–94. doi: 10.1126/science.adf3406

6. Huang D, Wang Y, Thompson JW, Yin T, Alexander PB, Qin D, et al. Cancer-cell-derived GABA promotes β-catenin-mediated tumour growth and immunosuppression. *Nat Cell Biol*. (2022) 24:230–41. doi: 10.1038/s41556-021-00820-9

7. Joghataei MT, Bakhtiarzadeh F, Dehghan S, Ketabforoush A, Golab F. Zarbakhsh S et al: The role of neurotransmitters in glioblastoma multiforme-associated seizures. *Int J Dev Neurosci*. (2023) 83:677–90. doi: 10.1002/jdn.10294

8. Huang Q, Lei Y, Li X, Guo F, Liu M. A highlight of the mechanisms of immune checkpoint blocker resistance. *Front Cell Dev Biol*. (2020) 8:580140. doi: 10.3389/fcell.2020.580140

9. Yu J, Ling S, Hong J, Zhang L, Zhou W, Yin L, et al. TP53/mTORC1-mediated bidirectional regulation of PD-L1 modulates immune evasion in hepatocellular carcinoma. *J Immunother Cancer*. (2023) 11(11):e007479. doi: 10.1136/jitc-2023-007479

10. Bao H, Peng Z, Cheng X, Jian C, Li X, Shi Y, et al. GABA induced by sleep deprivation promotes the proliferation and migration of colon tumors through miR-223-3p endogenous pathway and exosome pathway. *J Exp Clin Cancer research: CR*. (2023) 42:344. doi: 10.1186/s13046-023-02921-9

11. Zhou X, Chen Z, Yu Y, Li M, Cao Y, Prochownik EV, et al. Increases in 4-Acetaminobutyric acid generated by phosphomevalonate kinase suppress CD8(+) T cell activation and allow tumor immune escape. *Advanced Sci (Weinheim Baden-Wurttemberg Germany)*. (2024) 11:e2403629. doi: 10.1002/advs.202403629

12. Pathak A, Palasalava S, Knott MV, Colon B, Ciervo E, Zhou Y, et al. γ-aminobutyric acid receptor B signaling drives glioblastoma in females in an immune-dependent manner. *bioRxiv: preprint server Biol*. (2024). doi: 10.1101/2024.07.18.603996

13. Li TJ, Jiang J, Tang YL, Liang XH. Insights into the leveraging of GABAergic signaling in cancer therapy. *Cancer Med*. (2023) 12:14498–510. doi: 10.1002/cam4.6102

14. Deng Z, Li D, Wang L, Lan J, Wang J, Ma Y. Activation of GABA(B)R attenuates intestinal inflammation by reducing oxidative stress through modulating the TLR4/myD88/NLRP3 pathway and gut microbiota abundance. *Antioxidants (Basel Switzerland)*. (2024) 13(9):1141. doi: doi:10.3390/antiox13091141

15. Wang J, Owji AP, Kittredge A, Clark Z, Zhang Y, Yang T. GAD65 tunes the functions of Best1 as a GABA receptor and a neurotransmitter conducting channel. *Nat Commun*. (2024) 15:8051. doi: 10.1038/s41467-024-52039-5

16. Bolneo E, Chau PYS, Noakes PG, Bellingham MC. Investigating the role of GABA in neural development and disease using mice lacking GAD67 or VGAT genes. *Int J Mol Sci*. (2022) 23(14):7965. doi: 10.3390/ijms23147965

17. Eprintsev AT, Anokhina GB, Shakhov ZN, Moskvina PP, Igamberdiev AU. The role of glutamate metabolism and the GABA shunt in bypassing the tricarboxylic acid cycle in the light. *Int J Mol Sci*. (2024) 25(23):12711. doi: 10.3390/ijms252312711

18. Perucca E, White HS, Bialer M. New GABA-targeting therapies for the treatment of seizures and epilepsy: II. *Treatments Clin Dev CNS Drugs*. (2023) 37:781–95. doi: 10.1007/s40263-023-01025-4

19. Perucca E, Bialer M, White HS. New GABA-targeting therapies for the treatment of seizures and epilepsy: I. Role of GABA as a modulator of seizure activity and recently approved medications acting on the GABA system. *CNS Drugs*. (2023) 37:755–79. doi: 10.1007/s40263-023-01027-2

20. Shaye H, Stauch B, Gati C, Cherezov V. Molecular mechanisms of metabotropic GABA(B) receptor function. *Sci Adv*. (2021) 7(22):eabg3362. doi: 10.1126/sciadv.abg3362

21. Evenseth LSM, Gabrielsen M, Sylte I. The GABA(B) receptor-structure, ligand binding and drug development. *Molecules*. (2020) 25(13):3093. doi: 10.3390/molecules25133093

22. Qian X, Zhao X, Yu L, Yin Y, Zhang XD, Wang L, et al. Current status of GABA receptor subtypes in analgesia. *BioMed Pharmacother*. (2023) 168:115800. doi: 10.1016/j.biopha.2023.115800

23. Sente A, Desai R, Naydenova K, Malinauskas T, Jounaidi Y, Miehling J, et al. Differential assembly diversifies GABA(A) receptor structures and signalling. *Nature*. (2022) 604:190–4. doi: 10.1038/s41586-022-04517-3

24. Thompson SM. Modulators of GABA(A) receptor-mediated inhibition in the treatment of neuropsychiatric disorders: past, present, and future. *Neuropsychopharmacology*. (2024) 49:83–95. doi: 10.1038/s41386-023-01728-8

25. Mendes FRS, da Silva AW, Ferreira MKA, Rebouças EL, Moura Barbosa I, da Rocha MN, et al. GABA(A) and serotonergic receptors participation in anxiolytic effect of chalcones in adult zebrafish. *J Biomol Struct Dyn*. (2023) 41:12426–44. doi: 10.1080/07391102.2023.2167116

26. Osse AML, Pandey RS, Wirt RA, Ortiz AA, Salazar A, Kimmich M, et al. Reduction in GABAB on glia induce Alzheimer's disease related changes. *Brain Behav Immun*. (2023) 110:260–75. doi: 10.1016/j.bbi.2023.03.002

27. Cheng YT, Luna-Figueroa E, Woo J, Chen HC, Lee ZF, Harmanci AS, et al. Inhibitory input directs astrocyte morphogenesis through glial GABA(B)R. *Nature*. (2023) 617:369–76. doi: 10.1038/s41586-023-06010-x

28. Dai M, Liang PJ. GABA receptors mediate adaptation and sensitization processes in mouse retinal ganglion cells. *Cognit Neurodyn*. (2024) 18:1021–32. doi: 10.1007/s11571-023-09950-2

29. Xie J, Liu W, Deng X, Wang H, Ou X, An X, et al. Paracrine orchestration of tumor microenvironment remodeling induced by GLO1 potentiates lymph node metastasis in breast cancer. *Advanced Sci*. (2025) 2025:e00722. doi: 10.1002/advs.202500722

30. Xie J, Xie Y, Tan W, Ye Y, Ou X, Zou X, et al. Deciphering the role of ELAVL1: Insights from pan-cancer multiomics analyses with emphasis on nasopharyngeal carcinoma. *J Trans Internal Med*. (2025) 13:138–55. doi: 10.1515/jtim-2025-0009

31. Xie J, Lin X, Deng X, Tang H, Zou Y, Chen W, et al. Cancer-associated fibroblast-derived extracellular vesicles: regulators and therapeutic targets in the tumor microenvironment. *Cancer Drug resistance (Alhambra Calif)*. (2025) 8:2. doi: 10.20517/cdr.2024.152

32. Zhou Y, Khawkhiaw K, Thithuan K, Saengboonmee C. Activation of the γ-aminobutyric acid receptor type B suppresses the proliferation of lung adenocarcinoma cells. *Anticancer Res*. (2025) 45:1513–23. doi: 10.21873/anticanres.17533

33. Yeo M, Chen Y, Jiang C, Chen G, Wang K, Chandra S, et al. Repurposing cancer drugs identifies kenpaullone which ameliorates pathologic pain in preclinical models via normalization of inhibitory neurotransmission. *Nat Commun*. (2021) 12:6208. doi: 10.1038/s41467-021-26270-3

34. Tagore M, Hergenreder E, Perlee SC, Cruz NM, Menocal L, Suresh S, et al. GABA regulates electrical activity and tumor initiation in melanoma. *Cancer Discov*. (2023) 13:2270–91. doi: 10.1158/2159-8290.CD-23-0389

35. Yang Y, Ren L, Li W, Zhang Y, Zhang S, Ge B, et al. GABAergic signaling as a potential therapeutic target in cancers. *BioMed Pharmacother*. (2023) 161:114410. doi: 10.1016/j.biopha.2023.114410

36. Xie J, Liu M, Deng X, Tang Y, Zheng S, Ou X, et al. Gut microbiota reshapes cancer immunotherapy efficacy: Mechanisms and therapeutic strategies. *iMeta*. (2024) 3:e156. doi: 10.1002/imt2.156

37. Cheng K, Cai N, Zhu J, Yang X, Liang H, Zhang W. Tumor-associated macrophages in liver cancer: From mechanisms to therapy. *Cancer Commun (London England)*. (2022) 42:1112–40. doi: 10.1002/cac2.12345

38. Li M, Yang Y, Xiong L, Jiang P, Wang J, Li C. Metabolism, metabolites, and macrophages in cancer. *J Hematol Oncol*. (2023) 16:80. doi: 10.1186/s13045-023-01478-6

39. Dong Y, Wang G, Nie D, Xu Y, Bai X, Lu C, et al. Tumor-derived GABA promotes lung cancer progression by influencing TAMs polarization and neovascularization. *Int Immunopharmacol*. (2024) 126:111217. doi: 10.1016/j.intimp.2023.111217

40. Zhang B, Vogelzang A, Miyajima M, Sugiura Y, Wu Y, Chamoto K, et al. B cell-derived GABA elicits IL-10(+) macrophages to limit anti-tumour immunity. *Nature*. (2021) 599:471–6. doi: 10.1038/s41586-021-04082-1

41. Ruiz-Rodríguez VM, Torres-González CA, Salas-Canedo KM, Pecina-Maza NQ, Martínez-Leija ME, Portales-Pérez DP, et al. Dynamical changes in the expression of GABAergic and purinergic components occur during the polarization of THP-1 monocytes to proinflammatory macrophages. *Biochem Biophys Rep*. (2023) 36:101558. doi: 10.1016/j.bbrep.2023.101558

42. Xia Y, He F, Wu X, Tan B, Chen S, Liao Y, et al. GABA transporter sustains IL-1β production in macrophages. *Sci Adv*. (2021) 7(15):eabe9274. doi: 10.1126/sciadv.abe9274

43. Liu Q, Li Y, Shi Y, Tan J, Yan W, Zhang J, et al. The protective effect of gamma aminobutyric acid B receptor activation on sympathetic nerve remodeling via the regulation of M2 macrophage polarization after myocardial infarction. *Rev Port Cardiol*. (2023) 42:125–35. doi: 10.1016/j.repc.2021.10.011

44. Sun S, Chen X, Ding N, Zhang M, Li X, Chen L, et al. : Gamma-aminobutyric acid-mediated neuro-immune interactions in glioblastoma: Implications for prognosis and immunotherapy response. *Life Sci*. (2024) 357:123067. doi: 10.1016/j.lfs.2024.123067

45. Dou Z, Li M, Shen Z, Jiang H, Pang X, Li T, et al. GAD1-mediated GABA elicits aggressive characteristics of human oral cancer cells. *Biochem Biophys Res Commun*. (2023) 681:80–9. doi: 10.1016/j.bbrc.2023.09.041

46. Tharp KM, Kersten K, Maller O, Timblin GA, Stashko C, Canale FP, et al. Tumor-associated macrophages restrict CD8(+) T cell function through collagen deposition and metabolic reprogramming of the breast cancer microenvironment. *Nat Cancer*. (2024) 5:1045–62. doi: 10.1038/s43018-024-00775-4

47. Park SS, Kwon MR, Ju EJ, Shin SH, Park J, Ko EJ, et al. Targeting phosphomevalonate kinase enhances radiosensitivity via ubiquitination of the replication protein A1 in lung cancer cells. *Cancer Sci*. (2023) 114:3583–94. doi: 10.1111/cas.15896

48. Sparrow EL, James S, Hussain K, Beers SA, Cragg MS, Bogdanov YD. Activation of GABA(A) receptors inhibits T cell proliferation. *PloS One*. (2021) 16:e0251632. doi: 10.1371/journal.pone.0251632

49. Tian J, Dang H, O'Laco KA, Song M, Tiu BC, Gilles S, et al. Homotaurine treatment enhances CD4(+) and CD8(+) regulatory T cell responses and synergizes with low-Dose anti-CD3 to enhance diabetes remission in type 1 diabetic mice. *Immunohorizons*. (2019) 3:498–510. doi: 10.4049/immunohorizons.1900019

50. Maier B, Leader AM, Chen ST, Tung N, Chang C, LeBerichel J, et al. Author Correction: A conserved dendritic-cell regulatory program limits antitumour immunity. *Nature*. (2020) 582:E17. doi: 10.1038/s41586-020-2326-5

51. Magen A, Hamon P, Fiaschi N, Soong BY, Park MD, Mattiuz R, et al. Intratumoral dendritic cell-CD4(+) T helper cell niches enable CD8(+) T cell differentiation following PD-1 blockade in hepatocellular carcinoma. *Nat Med*. (2023) 29:1389–99. doi: 10.1038/s41591-023-02345-0

52. Sharma P, Zhang X, Ly K, Kim JH, Wan Q, Kim J, et al. Hyperglycosylation of prosaposin in tumor dendritic cells drives immune escape. *Science*. (2024) 383:190–200. doi: 10.1126/science.adg1955

53. Luo Y, Li L, Chen X, Gou H, Yan K, Xu Y. Effects of lactate in immunosuppression and inflammation: Progress and prospects. *Int Rev Immunol*. (2022) 41:19–29. doi: 10.1080/08830185.2021.1974856

54. Fuks JM, Arrighi RB, Weidner JM, Kumar Mendu S, Jin Z, Wallin RP, et al. GABAergic signaling is linked to a hypermigratory phenotype in dendritic cells infected by Toxoplasma gondii. *PloS Pathog*. (2012) 8:e1003051. doi: 10.1371/journal.ppat.1003051

55. Barragan A, Weidner JM, Jin Z, Korpi ER, Birnir B. GABAergic signalling in the immune system. *Acta Physiol (Oxf)*. (2015) 213:819–27. doi: 10.1111/apha.12467

56. Bekić M, Vasiljević M, Stojanović D, Kokol V, Mihajlović D, Vučević D, et al. Phosphonate-Modified cellulose nanocrystals potentiate the th1 polarising capacity of monocyte-Derived dendritic cells via GABA-B receptor. *Int J Nanomedicine*. (2022) 17:3191–216. doi: 10.2147/IJN.S362038

57. Huang S, Mao J, Wei B, Pei G. The anti-spasticity drug baclofen alleviates collagen-induced arthritis and regulates dendritic cells. *J Cell Physiol*. (2015) 230:1438–47. doi: 10.1002/jcp.24884

58. Ankit K, Umesh KS, Anurag C. Honokiol analogs: a novel class of anticancer agents targeting cell signaling pathways and other bioactivities. *Future Med Chem*. (2013) 5(7):809–829. doi: 10.4155/fmc.13.32

59. Wang Q, Zheng C, Hou H, Bao X, Tai H, Huang X, et al. Interplay of sphingolipid metabolism in predicting prognosis of GBM patients: towards precision immunotherapy. *J Cancer*. (2024) 15:275–92. doi: 10.7150/jca.89338

60. Han Y, Liu D, Li L. PD-1/PD-L1 pathway: current researches in cancer. *Am J Cancer Res*. (2020) 10:727–42.

61. Sun X, Lin M, Tian Z, Ma Y, Lv L. GABA/baclofen stabilizes PD-L1 and enhances immunotherapy of breast cancer. *Heliyon*. (2024) 10:e28600. doi: 10.1016/j.heliyon.2024.e28600

62. Pomeranz Krummel DA, Nasti TH, Kaluzova M, Kallay L, Bhattacharya D, Melms JC, et al. Melanoma cell intrinsic GABA(A) receptor enhancement potentiates radiation and immune checkpoint inhibitor response by promoting direct and T cell-Mediated antitumor activity. *Int J Radiat Oncol Biol Phys*. (2021) 109:1040–53. doi: 10.1016/j.ijrobp.2020.10.025

63. Gao M, Ling M, Tang X, Wang S, Xiao X, Qiao Y, et al. Comparison of high-throughput single-cell RNA sequencing data processing pipelines. *Briefings Bioinf*. (2021) 22(3):bbaa116. doi: 10.1093/bib/bbaa116

64. Jiang SH, Zhu LL, Zhang M, Li RK, Yang Q, Yan JY, et al. : GABRP regulates chemokine signalling, macrophage recruitment and tumour progression in pancreatic cancer through tuning KCNN4-mediated Ca(2+) signalling in a GABA-independent manner. *Gut*. (2019) 68:1994–2006. doi: 10.1136/gutjnl-2018-317479

65. van Baalen A, Häusler M, Plecko-Startinig B, Strautmanis J, Vlaho S, Gebhardt B, et al. Febrile infection-related epilepsy syndrome without detect able autoantibodies and response to immunotherapy: a case series and discussion of epileptogenesis in FIRES. *Neuropediatrics*. (2012) 43:209–16. doi: 10.1055/s-0032-1323848

66. Rusche T, Yaldizli Ö, Galbusera R, Mutke M, Halter JP, Lieb J, et al. Anti-GABA (A) receptor encephalitis 14 months after allogeneic haematopoietic stem-cell transplant for acute myeloid leukaemia. *Lancet (London England)*. (2024) 403:469–70. doi: 10.1016/S0140-6736(23)02831-3

67. Jian C, Wang B, Mou H, Zhang Y, Yang C, Huang Q, et al. A GAD1 inhibitor suppresses osteosarcoma growth through the Wnt/β-catenin signaling pathway. *Heliyon*. (2024) 10:e31444. doi: 10.1016/j.heliyon.2024.e31444

68. Guo C, Ma X, Gao F, Guo Y. Off-target effects in CRISPR/Cas9 gene editing. *Front bioengineering Biotechnol*. (2023) 11:1143157. doi: 10.3389/fbioe.2023.1143157

69. Splendiani E, Besharat ZM, Covre A, Maio M, Di Giacomo AM, Ferretti E. Immunotherapy in melanoma: Can we predict response to treatment with circulating biomarkers? *Pharmacol Ther*. (2024) 256:108613. doi: 10.1016/j.pharmthera.2024.108613

70. Ramapriyan R, Vykunta VS, Vandecandelaere G, Richardson LGK, Sun J, Curry WT, et al. Altered cancer metabolism and implications for next-generation CAR T-cell therapies. *Pharmacol Ther*. (2024) 259:108667. doi: 10.1016/j.pharmthera.2024.108667

71. Yu X, Zhai X, Wu J, Feng Q, Hu C, Zhu L, et al. Evolving perspectives regarding the role of the PD-1/PD-L1 pathway in gastric cancer immunotherapy. *Biochim Biophys Acta Mol basis Dis*. (2024) 1870:166881. doi: 10.1016/j.bbadis.2023.166881

72. Niu L, Wang Q, Feng F, Yang W, Xie Z, Zheng G, et al. Small extracellular vesicles-mediated cellular interactions between tumor cells and tumor-associated macrophages: Implication for immunotherapy. *Biochim Biophys Acta Mol basis Dis*. (2024) 1870:166917. doi: 10.1016/j.bbadis.2023.166917

73. Hengrui L. An example of toxic medicine used in Traditional Chinese Medicine for cancer treatment. *J traditional Chin Med = Chung i tsa chih ying wen pan*. (2023) 43:209–10. doi: 10.19852/j.cnki.jtcm.2023.02.001

74. Hengrui L. Toxic medicine used in Traditional Chinese Medicine for cancer treatment: are ion channels involved? *J traditional Chin Med = Chung i tsa chih ying wen pan*. (2022) 42:1019–22. doi: 10.19852/j.cnki.jtcm.20220815.005

75. Su XL, Wang JW, Che H, Wang CF, Jiang H, Lei X, et al. Clinical application and mechanism of traditional Chinese medicine in treatment of lung cancer. *Chin Med J*. (2020) 133:2987–97. doi: 10.1097/CM9.0000000000001141

76. Liu Y, Yang S, Wang K, Lu J, Bao X, Wang R, et al. Cellular senescence and cancer: Focusing on traditional Chinese medicine and natural products. *Cell proliferation*. (2020) 53:e12894. doi: 10.1111/cpr.12894

77. Liu HR. Harnessing traditional medicine and biomarker-driven approaches to counteract Trichostatin A-induced esophageal cancer progression. *World J Gastroenterol*. (2025) 31:106443. doi: 10.3748/wjg.v31.i20.106443

78. Xie M, Qin H, Liu L, Wu J, Zhao Z, Zhao Y, et al. GABA regulates metabolic reprogramming to mediate the development of brain metastasis in non-small cell lung cancer. *J Exp Clin Cancer research: CR*. (2025) 44:61. doi: 10.1186/s13046-025-03315-9

79. Liu H, Hamaia SW, Dobson L, Weng J, Hernández FL, Beaudoin CA, et al. The voltage-gated sodium channel β3 subunit modulates C6 glioma cell motility independently of channel activity. *Biochim Biophys Acta Mol basis Dis*. (2025) 1871:167844. doi: 10.1016/j.bbadis.2025.167844

80. Nojima Y, Yao R, Suzuki T. Single-cell RNA sequencing and machine learning provide candidate drugs against drug-tolerant persister cells in colorectal cancer. *Biochim Biophys Acta Mol basis Dis*. (2025) 1871:167693. doi: 10.1016/j.bbadis.2025.167693

81. Liu H, Dong A, Rasteh AM, Wang P, Weng J. Identification of the novel exhausted T cell CD8 + markers in breast cancer. *Sci Rep*. (2024) 14:19142. doi: 10.1038/s41598-024-70184-1

82. Liu H, Li Y. Potential roles of Cornichon Family AMPA Receptor Auxiliary Protein 4 (CNIH4) in head and neck squamous cell carcinoma. *Cancer biomarkers: section A Dis Markers*. (2022) 35:439–50. doi: 10.3233/CBM-220143

83. Sabit H, Pawlik TM, Radwan F, Abdel-Hakeem M, Abdel-Ghany S, Wadan AS, et al. Precision nanomedicine: navigating the tumor microenvironment for enhanced cancer immunotherapy and targeted drug delivery. *Mol Cancer*. (2025) 24:160. doi: 10.1186/s12943-025-02357-z

84. Kyu Shim M, Yang S, Sun IC, Kim K. Tumor-activated carrier-free prodrug nanoparticles for targeted cancer Immunotherapy: Preclinical evidence for safe and effective drug delivery. *Advanced Drug delivery Rev*. (2022) 183:114177. doi: 10.1016/j.addr.2022.114177

85. Rudolph U, Crestani F, Möhler H. GABA(A) receptor subtypes: dissecting their pharmacological functions. *Trends Pharmacol Sci*. (2001) 22:188–94. doi: 10.1016/S0165-6147(00)01646-1

frontiers | Frontiers in Immunology

TYPE Original Research
PUBLISHED 13 August 2025
DOI 10.3389/fimmu.2025.1654174

Check for updates

OPEN ACCESS

EDITED BY
Qi Wang,
Jiangsu University, China

REVIEWED BY
Chang-Sheng Dong,
Shanghai University of Traditional Chinese Medicine, China
Namuunaa Juramt,
Harvard Medical School, United States
Hengrui Liu,
University of Cambridge, United Kingdom

*CORRESPONDENCE
Zuping Lian
zupinglian@sina.com
Huojun Zhang
huojunzh@163.com

†These authors have contributed equally to this work

RECEIVED 26 June 2025
ACCEPTED 28 July 2025
PUBLISHED 13 August 2025

CITATION
Xu B, Zhao X, Wei T, Liang Y, Zhang W, Chen L, Lian Z and Zhang H (2025) Analysis of standard vs dose-escalated stereotactic body radiation therapy in localized prostate cancer: a comparative evaluation of survival outcomes. *Front. Immunol.* 16:1654174. doi: 10.3389/fimmu.2025.1654174

COPYRIGHT
© 2025 Xu, Zhao, Wei, Liang, Zhang, Chen, Lian and Zhang. This is an open-access article distributed under the terms of the Creative Commons Attribution License (CC BY). The use, distribution or reproduction in other forums is permitted, provided the original author(s) and the copyright owner(s) are credited and that the original publication in this journal is cited, in accordance with accepted academic practice. No use, distribution or reproduction is permitted which does not comply with these terms.

Analysis of standard vs dose-escalated stereotactic body radiation therapy in localized prostate cancer: a comparative evaluation of survival outcomes

Bichun Xu[1,2†], Xianzhi Zhao[1,3†], Tingting Wei[4†], Yiyin Liang[1], Weiwei Zhang[1], Liang Chen[1], Zuping Lian[4*] and Huojun Zhang[1*]

[1]Department of Radiation Oncology, The First Affiliated Hospital of Naval Medical University, Shanghai, China, [2]Department of Radiotherapy, Tongji Hospital, School of Medicine, Tongji University, Shanghai, China, [3]Department of Radiotherapy and Oncology, the Second Affiliated Hospital of Soochow University, Suzhou, China, [4]Department of Medical Oncology, Ruikang Hospital Affiliated to Guangxi University of Chinese Medicine, Nanning, China

Background and purpose: This study aimed to compare the safety and efficacy of high-dose biologically effective dose (BED) versus standard dose regimens in stereotactic body radiotherapy (SBRT) for localized prostate cancer (PCa) using a propensity score matching (PSM) analysis.

Methods: Between June 2012 and February 2022, prostate-localized SBRT patients from two institutions were retrospectively reviewed. The high-dose group (n=12) received high-dose $BED_{1.5}$ (>250Gy), and the control group (n=119) according to NCCN guidelines (35-37.5 Gy/5f, $BED_{1.5}$ 198.3-225Gy). PSM was performed in a 1:4 ratio based on key clinical variables. Survival outcomes, including overall survival(OS), cancer-specific survival (CSS), biochemical progression-free survival (bPFS), local control (LC), and distant metastasis-free survival (DMFS)were analyzed using Kaplan-Meier methods with SPSS v26.

Results: In the 7-year follow-up, the high-dose group exhibited a 66.7% OS rate vs. 83.4% in controls (p=0.402) and an 88.9% CSS rate compared to 90.5% in controls (p=0.480). The high-dose group demonstrated a 91.7% 7-year bPFS rate, while controls had a 67.4% rate (p=0.497). Higher gleason score correlated with impaired biochemical control (p=0.028), and adverse NCCN classifications indicated suboptimal control (p=0.028). The high-dose group achieved a 100% 7-year LC rate vs. 95.1% in controls (p=0.569) and a 91.7% 7-year DMFS rate compared to 81.6% in controls (p=0.918). Patients with pre-existing health conditions were less likely to develop distant metastasis (p=0.047). Most patients tolerated SBRT with minimal toxicity, and no grade 3 or higher adverse events were observed.

Conclusion: Escalating the biologically effective dose above standard levels did not yield a significant improvement in tumor control or survival outcomes compared to conventional SBRT dosing for localized PCa. Further prospective studies are warranted to clarify the role of dose escalation in this setting.

KEYWORDS

stereotactic body radiation therapy (SBRT), prostate cancer, localized, dose-escalated, overall survival

Highlights

- Retrospective study of high vs. standard dose BED in SBRT for localized PCa.
- Standard doses remain effective in achieving comparable outcomes to high-dose regimens.
- High BED in SBRT for localized PCa did not significantly enhance tumor control or survival rates.

Introduction

For localized prostate cancer (PCa), standard treatments include active surveillance (AS), radical prostatectomy (RP), and external beam radiotherapy (EBRT) (1). Nonetheless, these options lead to significant adverse effects, such as urinary incontinence and erectile dysfunction (2). A systematic review of 72 studies, including focal therapy (FT) modalities like focal brachytherapy, shows promising early results, though long-term oncological effectiveness remains uncertain. High-quality evidence suggests minimal adverse reactions with FT (3). Notably, most FT approaches require repeated general anesthesia, impacting patients' quality of life (QoL). An alternative, stereotactic body radiotherapy (SBRT), offers precise treatment without anesthesia, demonstrating efficacy comparable to intensity-modulated radiation therapy (IMRT) (4).

These evolving strategies illustrate the trend in oncology toward precise, minimally invasive treatments that aim to reduce toxicity while maintaining effectiveness, driven by advances in biology and technology (5). SBRT offers several advantages (6). Firstly, escalating the dose enhances cancer control. Secondly, the low α/β ratio of prostate cancer (estimated at 1-2) leads to significant relative biological effectiveness (RBE) with SBRT, increasing the biologically effective dose (BED) (7). Consequently, this low α/β ratio of prostate cancer renders it particularly sensitive to hypofractionated high-dose radiotherapy. Implementing individualized high-dose fractionation protocols can thus enhance tumor control while simultaneously minimizing the radiation dose to surrounding normal tissues, ultimately reducing the incidence of late radiation-induced toxicity. Lastly, the CyberKnife system provides precise, image-guided radiation delivery, minimizing exposure to critical organs and enhancing patient convenience during extensive radiation procedures.

Hypofractionated radiation therapy, notably SBRT, gains popularity for localized PCa due to its safety and convenience. Trials explore dose escalation benefits in conventional radiation (8, 9), with hypofractionation (42.7 Gy/7f) proving non-inferior for intermediate and high-risk patients (4). The current National Comprehensive Cancer Network (NCCN) guidelines recommends at least 36.25 Gy/5 fractions based on PACE-B research (10, 11). However, earlier NCCN versions have acknowledged that lower SBRT doses, such as 35 Gy/5 fractions, may still be acceptable. Notably, the NCCN also endorses fractionation schemes like 9.5 Gy*4 fractions or 8 Gy*5 fractions, each resulting in a BED greater than 250 Gy, while simultaneously recognizing regimens with BEDs below this threshold. Ongoing debates continue regarding the optimal SBRT dose, with the impact of delivering higher BEDs—such as 40 Gy/5 fractions—on survival outcomes yet to be explored in cohort studies. This retrospective study evaluates the influence of dose escalation on survival outcomes between higher BED (>250) and recommended fractionation doses.

Materials and methods

Patient selection

Patients receiving prostate-localized SBRT without regional lymph node involvement or distant metastasis from two research medical institutions (June 2012 - February 2022) were selected. Exclusions included prior radical surgery, brachytherapy, or proton therapy. Inclusion criteria comprised confirmed prostate adenocarcinoma, enhanced pelvic magnetic resonance imaging (MRI), emission computed tomography (ECT), Eastern Cooperative Oncology Group (ECOG) performance score ≤ 1, and those unsuitable for surgery due to medical conditions. Informed consent was obtained from all enrolled patients prior to treatment. Data included age, ECOG status, prostate-specific antigen (PSA), Gleason score grading, clinical T-stage, NCCN risk group, prior surgery/androgen deprivation therapy (ADT), and SBRT details. The high-dose group (n=12) had $BED_{1.5}$ (α/β=1.5Gy) >250Gy, while the controls (n=119) followed NCCN guidelines (35-37.5 Gy/5f, $BED_{1.5}$

198.3-225Gy). Approved by the institutional review board, this study adhered to the Helsinki Declaration.

SBRT protocols

Before formulating the radiation therapy plan, two or four fiducial markers were implanted into the prostate. Patients were positioned supine, arms resting at their sides, and secured with a thermoplastic mask. One week post-marker insertion, an enhanced computed tomography (CT) scan (1.5 mm slice thickness, 10 cm above and below the prostate) was conducted. For low-risk prostate cancer, the clinical target volume (CTV) covered the entire prostate. In the intermediate-risk group, CTV included the prostate and a 1-centimeter margin around seminal vesicles. For the high-risk and very high-risk groups, the CTV comprised the entire prostate and a 2-centimeter margin around the seminal vesicles. If the tumor invaded seminal vesicles, CTV covered the entire prostate and seminal vesicles. SBRT was administered using CyberKnife (Accuray Corporation, Sunnyvale, CA, USA).

The planning target volume (PTV) expanded by 5mm in all directions (excluding posterior), and CTV expanded by 3mm to minimize rectal radiation. Table 1 summarizes treatment parameters for both approaches. The distribution graph of $BED_{1.5}$ for the two patient groups can be found in Supplementary Figure S1. The control group received a prescription dose of 35-37.5 Gy in 5 fractions every other day, with the median prescription isodose line at 79%. BED was calculated using the standard linear-quadratic model (α/β = 1.5Gy, common for prostate cancer). Dose-volume constraints for organs at risk (OAR) included rectum ($V_{18.1\ Gy}$ < 50%, $V_{29\ Gy}$ < 20%, $V_{36\ Gy}$ < 1 cc), bladder ($V_{18.1\ Gy}$ < 40%, $V_{37\ Gy}$ < 10 cc, optimal $V_{37\ Gy}$ < 5 cc), prostatic urethra ($V_{42\ Gy}$ < 50%), femoral head ($V_{14.5\ Gy}$ < 5%), penile bulb ($V_{29.5\ Gy}$ < 50%), and intestine ($V_{18.1\ Gy}$ < 5 cc, $V_{30\ Gy}$ < 1 cc) (12).

TABLE 1 Treatment parameters used for radiotherapy.

Parameters	Total	The high-dose group	The control group
Clinical Target Volume (ml)	55.6 (8.0-182.7)	34.2 (8.0-122.0)	61.0 (23.8-182.7)
Total prescribed dose (Gy)	36.9 (35.0-42.0)	39.6 (36.0-42.0)	36.2 (35.0-37.5)
Number of fractions	5 (3-5)	4 (3-5)	5
Dose per fraction (Gy)	8.1 (7-13.3)	12.3 (8-13.3)	7.2 (7.0 -7.5)
$BED_{1.5}$ (Gy)	236.7 (198.3-395.4)	339.01 (253.3-395.4)	211.0 (198.3-225)
Number of fiducials	4	2	4
Prescription isodose line (%)	76 (57-85)	65 (57-72)	79 (71-85)

All data were shown as median values (range).
$BED_{1.5}$: biologic equivalent dose (α/β=1.5 Gy).

Response evaluation and follow-up

Post-radiation, monthly assessments monitored PSA and testosterone levels. Biochemical progression was defined as PSA increase ≥ 2 ng/mL from nadir (13). Overall survival (OS) was calculated from radiation therapy start to final follow-up or death. Cancer-specific survival (CSS) was defined as the time to death resulting from prostate cancer progression. Biochemical progression-free survival (bPFS) was from SBRT initiation to biochemical progression or last follow-up. Local control (LC) denoted no progression at the primary site. Distant metastasis-free survival (DMFS) calculated from radiation therapy start to clinical metastasis diagnosis or patient's death. Acute and late toxicities assessed by Common Terminology Criteria for Adverse Events (CTCAE) v5.0.

Statistical analysis

Propensity score matching (PSM) was conducted in R to address selection bias in this observational study by pairing patients with similar controls, effectively controlling for confounders including NCCN risk group, Gleason grade, TNM stage, age, and PSA. R4.3.1 software performed 1:4 nearest neighbor matching, resulting in 12*4 matched samples. Kaplan-Meier analysis in SPSS v26 assessed survival differences, with log-rank tests comparing treatment groups. Chi-square and Student's t-test detected differences in categorical and continuous variables. All tests were two-sided, with significance set at $P<0.05$.

Results

Basic parameters

The study involved 12 high-dose and 48 control patients. Specifically, in the high-dose group, there was 1 patient with low risk, 2 with unfavorable intermediate risk, 6 with high risk, and 3 with very high risk. In the control group, there were 4 patients with low risk, 12 with unfavorable intermediate risk, 22 with high risk, and 10 with very high risk. Last follow-up was May 2023 or death. The median follow-up period extended to 74.0 months (range 5.3-117.0 months). The high-dose group had 75% high/very high-risk patients, with 33% undergoing hormonal therapy. Four patients succumbed to prostate cancer progression, while five had non-cancer-related deaths, including three strokes and two pneumonia cases. Among these non-cancer-related deaths, one patient had an unfavorable intermediate-risk (NCCN classification), and four were high-risk. Of the four patients who died due to prostate cancer metastasis, one had multiple advanced metastases affecting the lungs and bones. Another patient exhibited metastases in various

locations, including the lumbar spine and multiple bones. In the remaining two cases, systemic metastatic progression was considered. A total of 47 patients (78.3%) had pre-existing health conditions, such as diabetes, hypertension, and coronary heart disease. Specific patient demographics are detailed in Table 2.

Survival differences

For 60 patients, 5-year OS was 91.7%, 7-year OS was 81%, median OS was 104.1 months (range 96.5-111.7). In the high-dose group, 5-year OS was 88.9%, 7-year OS was 66.7%, respectively. In

TABLE 2 Patients demography and tumor characteristics.

Characteristics	Total	The high-dose group	The control group
Total patients, n	60	12	48
Follow-up, median (SD)	74.0 (5.3-117.0)	52.8 (14.5-99.3)	76.9 (5.3-117.0)
Age at treatment time-years, median (SD)	73.5 (54-83)	72 (65-78)	74 (54-83)
PSA, median (SD)	17.1 (0.4-100)	17.1 (0.4-100)	18.4 (0.4-91)
Gleason score			
• 3 + 3 = 6	13	1	12
• 3 + 4 = 7,4 + 3 = 7	23	5	18
• 4 + 4 = 8,3 + 5 = 8,5 + 3 = 8	14	3	11
• 5 + 4 = 9,4 + 5 = 9	10	3	7
Clinical T-stage			
• T_{2a}	25	5	20
• T_{2b}	5	1	4
• T_{2c}	23	4	19
• T_{3a}	2	1	1
• T_{3b}	5	1	4
NCCN risk grouping			
• Low	3	1	2
• Unfavorable intermediate	16	2	14
• High	30	6	24
• Very high	11	3	8
ECOG score			
• 0	2	1	1
• 1	58	11	47
Pre-treatment TURP			
• Yes	14	6	8
• No	46	6	40
Synchronize/previously used ADT			
• No	45	5	40
• Yes	15	7	8
Pre-existing health conditions			
• No	13	6	7
• Yes	47	6	41

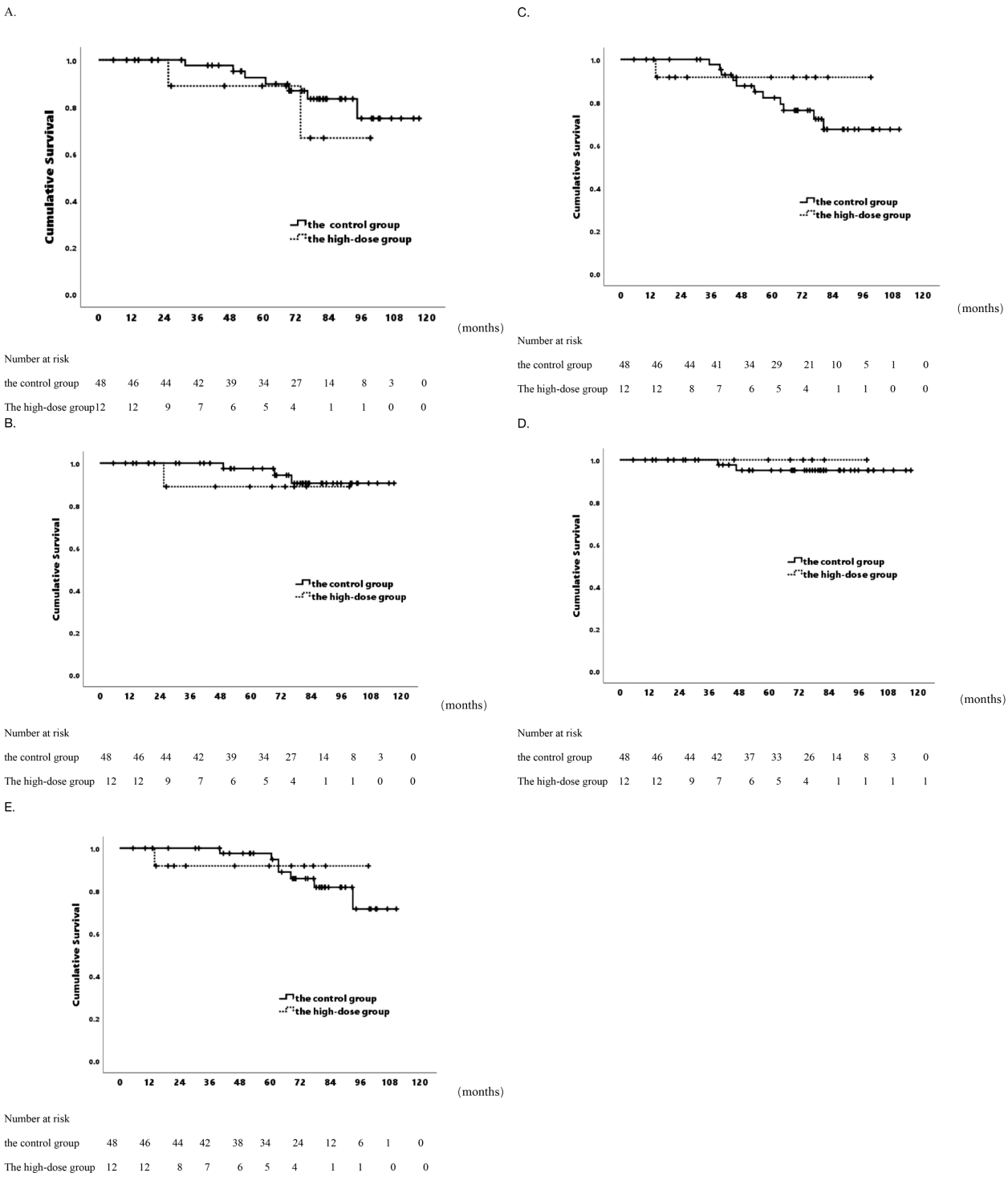

FIGURE 1
Actuarial survival analysis of patients in two distinct groups. **(A)** Overall survival. **(B)** Cancer-specific Survival. **(C)** Biochemical Progression-free Survival. **(D)** Local Control Survival. **(E)** Distant Metastasis-free Survival.

the control group, the corresponding rates were 92.5% and 83.4% (p=0.402& Figure 1A). CSS rates at 5 and 7 years were 95.9% and 89.9%, median CSS 111.2 months (range 105.6-116.7). For CSS, the high-dose group had a 5-year rate of 88.9%, a 7-year rate of 88.9%, while the control group had a 5-year rate of 97.4%, a 7-year rate of 90.5% (p=0.480& Figure 1B). Dosimetric data related to BED were analyzed, and the correlation between clinical/patient baseline information and OS as well as prostate CSS was examined. Univariate analysis showed no significant correlation between prostate CSS or OS and clinical characteristics, patient baseline

information, or SBRT parameters (Supplementary Tables S1, S2). Despite increased radiation dosage for a higher BED, there was no improvement in patient survival.

bPFS differences

In the 60-patient cohort, 5- and 7-year bPFS rates were 83.2% and 70.2%, with a median bPFS of 94.1 months (range 86.1-102.2 months). The high-dose group exhibited a 5-year bPFS of 91.7%, and 7-year bPFS of 91.7%, while the control group had a 5-year bPFS of 82.1%, 7-year bPFS of 67.4% (p=0.497& Figure 1C). No differences in biochemical control were observed. Univariate analysis revealed an association between elevated Gleason score and impaired biochemical control. Gleason score > 7 showed 5-year bPFS of 72.4%, 7-year bPFS of 55.5%, compared to Gleason score ≦ 7 with 5-year bPFS of 95.8%, 7-year bPFS of 89.8% (p=0.028).

TABLE 3 Univariate analysis for bPFS rate.

Factors	5-year rate (%)	7-year rate (%)	P value
Dose group			0.497
The high-dose group	91.7	91.7	
The control group	82.1	67.4	
Gleason Score			0.028
≦7	95.8	89.8	
> 7	72.4	55.5	
PSA at diagnosis-ng/ml			0.128
≦20	93.1	86.0	
>20	72.4	61.2	
NCCN risk grouping			0.028
Low +Unfavorable intermediate	100	100	
High+very high	77.4	60.6	
Treatment regimen:			0.520
Daily treatment	88.9	88.9	
Alternate-day treatment	82.1	67.4	
Age-years			0.846
<70	76.5	76.5	
≧70	86.9	68.6	
Synchronize/previously used ADT			0.833
Presence	92.3	65.6	
Absence	80.6	72.1	
TURP before SBRT			0.626
Yes	93.3	81.7	
No	80.6	67.6	

Additionally, Patients with more adverse classifications had suboptimal biochemical control (p=0.028) (Table 3). In the low/unfavorable intermediate risk group, 100% bPFS was achieved at both 5- and 7-year, while in the high/very high-risk group, 5-year bPFS was 77.4%, and 7-year bPFS was 60.6%.

LC and DMFS differences

Over 5- and 7-year periods, the cohort exhibited consistent LC rates of 95.7% and 95.7%, with an average follow-up of 113.9 months (range 109.6-118.1 months). The high-dose group achieved a 7-year LC rate of 100%, while the control group had a 7-year rate of 95.1% (p=0.569& Figure 1D). Additionally, DMFS rates at 5- and 7-year were 96.2% and 82.3%, averaging 99.8 months (range 93.1-106.6 months). The high-dose group had 5-year and 7-year DMFS rates of 91.7%, while the control group had rates of 97.6% and 81.6%, respectively (p=0.918& Figure 1E). In the patient cohorts, no significant correlation was observed between clinical patient information or SBRT parameters and LC (Supplementary Table S3). Univariate analysis revealed that patients with pre-existing health conditions such as hypertension, heart disease, and diabetes, were less prone to distant metastasis than those without (p=0.047). Patients with pre-existing conditions: 5-year DMFS 97.4%, 7-year DMFS 90.8%. Patients without such conditions: 5-year DMFS 92.3%, 7-year DMFS 46.9%. A higher distant metastasis trend was noted in Gleason >7 vs. ≤7 (p=0.060). No significant correlations with other clinical or treatment factors (Supplementary Table S4).

Overall toxicity

The majority of patients showed good tolerance to SBRT, with no grade 3+ adverse reactions observed. The high-dose group had no significant toxicity. In the control group (48 patients), one (2.1%) had grade 2 acute genitourinary (GU) toxicity, while two (4.2%) reported grade 1 acute GU symptoms. Two (2.3%) had grade 2 late GU toxicity. No acute or late gastrointestinal (GI) toxicity occurred. Common treatment-related adverse effects: hematuria, urinary frequency, nocturia, urinary pain, and difficulty in urination. All acute toxicities were transient, reversible with medication, and didn't hinder treatment completion.

Discussion

In this retrospective study, PSM matching addressed efficacy bias by balancing high-dose and control groups. Results showed no significant differences in OS, CSS, bPFS, LC, or DMFS between them. The study supports NCCN's recommendation of 36.25 Gy in five fractions for localized PCa patients undergoing SBRT, achieving a BED below 250 Gy.

SBRT, recommended for localized PCa, involves ultra-hypofractionated radiotherapy (7–10 Gy per fraction over 4–5

fractions) with a BED up to EQD_{2-} 164 Gy, given within 1–2 weeks. It's considered the standard of low- and intermediate-risk PCa, demonstrating excellent oncological outcomes. The HYPO-RT-PC trial in Scandinavia, compared ultra-hypofractionation (7 fractions of 42.7 Gy) with traditional fractionation (39 fractions of 78.0 Gy) (4). This comparison used 3D conformal radiation therapy (3DCRT), IMRT, or volumetric modulated arc therapy (VMAT) for intermediate or high-risk PCa. Ultra-fractionation proved non-inferior, with no difference in cancer-specific mortality or OS. Though associated with acute GU and GI symptoms, no difference was seen in late symptoms or overall QoL.

The PACE-B study (874 patients, low and favorable intermediate-risk PCa) compared conventional (78 Gy in 39 fractions over 8 weeks), moderately hypofractionated radiotherapy (62 Gy in 20 fractions over 4 weeks), and SBRT (36.25 Gy in 5 fractions). Results showed that SBRT's shorter duration didn't increase acute toxicity (10). The American Society for Radiation Oncology (ASTRO), the American Society of Clinical Oncology (ASCO), and the NCCN guidelines consider prostate SBRT acceptable for localized PCa (11). A meta-analysis (38 studies, 6,116 patients) on prostate cancer patients undergoing SBRT for low-, intermediate-, and high-risk diseases with fewer than 10 fractions exceeding 5 Gy demonstrated 5-year and 7-year biochemical recurrence-free survival rates (BRFS) rates of 95.3% and 93.7%. Estimated late grade 3 or higher GU and GI toxicity rates were 2.0% and 1.1%, respectively. This evidence supports SBRT as a standard for localized PCa. The review had a 39-month median follow-up, incorporating the HYPO-RT-PC trial. 80% of ultra-hypofractionation cases used 3D-CRT, with the rest using IMRT/VMAT (14). In a Phase II trial, localized SBRT (36.25 Gy/5 every other day) yielded promising outcomes. A 36-month follow-up showed a 96% 3-year bPFS rate, with all 24 eligible patients avoiding salvage prostatectomy. No grade 3 or higher toxicities were observed, indicating minimal impact on patients' QoL (15). Another Phase II trial, HYPOSTA, explored hypofractionated robotic SBRT on 85 localized PCa patients. Using the CyberKnife system (35 Gy/5f), it showed favorable short-term toxicity profiles, especially for intermediate or high-risk cases involving the proximal seminal vesicles (16).

In conventional radiotherapy, NRG 0126 compared 70 Gy to a dose-escalated 79.2 Gy at 1.8 Gy per fraction in a similar group of intermediate-risk patients (n=1532). The report indicated that dose-escalated treatment, relatively better tolerated, significantly reduced distant metastasis (17). Therefore, the benefit of reducing distant metastasis with dose escalation in a larger SBRT patient cohort, as seen in RTOG 0126, might translate into a modest yet statistically significant improvement in OS (18). Previous studies also reported that dose-escalated SBRT can enhance BRFS rates compared to lower-dose SBRT in low- and intermediate-risk prostate cancer. However, these studies failed to detect potential improvements in OS or DMFS rates, alternative endpoints for prostate cancer patients (19). Other studies utilized different dose regimens. Meier et al. studied 309 low/intermediate-risk prostate cancer patients with robotic SBRT (40 Gy/5f for prostate, 36.25 Gy/5f for seminal vesicles), reporting minimal toxicity and 95.6% 5-year OS (20). Additionally, HYPO-RT-PC trial showed non-inferiority for freedom from failure (FFS) with 42.7 Gy/7f vs. conventional 78.0 Gy/39f in intermediate- and high-risk patients (4).

Boike et al. conducted a phase I dose-escalation study for low-risk and intermediate-risk prostate cancer treated with SBRT. In a prospective cohort of 15 patients, dose escalation ranged from 45 Gy to 50 Gy, administered in fractions of 9, 9.5, and 10 Gy each, every other day, using a rectal balloon for protection. The study reported 18% grade 2 and 2% grade 3 rectal toxicity, and 31% grade 2 and 4% grade 3 GI toxicity. Importantly, dose escalation to 50 Gy was completed without dose-limiting toxicity (21). Another study examined 24 patients with intermediate- and high-risk prostate cancer undergoing dose-escalated prostate and proximal seminal vesicle SBRT. High-dose avoidance zones(HDAZ) were established, and patients achieved a 24-month PSA recurrence-free survival of 95.8% (22). In a dose-escalation study involving 75 patients with low- or intermediate-risk localized PCa, three SBRT dose levels were explored: 35 Gy, 37.5 Gy, and 40 Gy in 5 fractions. The 2-year incidence rates of Grade 2 late GU and GI toxicities were 34% and 7%, respectively, with higher doses associated with increased GU toxicity. No Grade 3 GI or Grade 4 acute GU toxicities or Grade 3 late toxicities were observed. Prescription of 35 Gy/5f was less likely to cause adverse events, suggesting caution with higher SBRT doses (23). In a retrospective study of 2214 intermediate-risk prostate cancer patients treated with SBRT, a dose of 36.25 Gy/5f was compared to 35 Gy/5f. Despite a small dose difference, the increase in BED from 35 Gy/5f to 36.25 Gy/5f was associated with improved survival (24). Our study explored the survival outcomes of higher BED in SBRT for localized prostate cancer. Although the high-dose group showed better trends in bPFS and LC rates, no statistically significant improvements in tumor control or survival were found. These results align with NCCN guidelines recommending a dosage of 36.25 Gy to 35 Gy in 5 fractions for localized prostate cancer SBRT. Furthermore research is needed on dose-response relationships. Furthermore, with the advancement of artificial intelligence and big data technologies, leveraging multidimensional dosimetric parameters for precise modeling and risk prediction will provide robust support for personalized radiotherapy dose optimization.

Our cohort, despite reporting fewer toxicities, demonstrated potential SBRT related toxicity compared to moderately fractionated IMRT. A retrospective study (n=4,005) reported higher GI toxicity with SBRT than IMRT at 24 months (44% vs. 36%; P = 0.001) (25). Prospective evaluation by K. et al. with 205 patients undergoing SBRT treatment (37.5–40 Gy/5f) using the "CyberKnife M6" showed mild to moderate early side effects, with GU and GI acute radiation-related side effect rates reported as GU: grade 0 - 17.1%, grade 1 - 30.7%, grade 2 - 50.7%, grade 3 - 1.5%; GI: grade 0 - 62.4%, grade 1 - 31.7%, grade 2 - 5.9%, grade 3 - 0%, and no grade 4 or higher toxicities (26). MRI-guided SBRT in prostate cancer radiation therapy demonstrated favorable outcomes, with the use of a 1.5-Tesla MR linear accelerator showing feasibility and safety. Comparative analysis suggests MR-guided Radiation Therapy (MRgRT) may reduce overall Grade 1 acute toxicity at six months, with a declining trend in Grade 2 GI toxicity (27). The

MIRAGE trial indicated MRI-guided SBRT significantly decreased physician-assessed moderate acute toxicity and patient-reported declines compared to CT guidance (28). Integrating SBRT with prophylactic pelvic radiation, along with gross tumor volume within the prostate (GTVp) augmentation guided by multiparametric magnetic resonance imaging (mpMRI), proved effective and well-tolerated for high-risk PCa patients (29). Future studies could build on conventional prostate radiation doses by incorporating advanced imaging techniques such as PSMA PET/MR to enable targeted dose escalation to active lesions, aiming to further reduce toxicity and improve local control. Moreover, personalizing SBRT dose strategies will likely depend on integrating molecular biomarkers that reflect tumor-specific stress responses, immune activity, and metabolic pathways. Cross-cancer insights—such as CISD2-mediated iron homeostasis in HNSCC, GLS-driven glutamine metabolism in breast cancer, NT5E-associated purine signaling in pancreatic tumors, and efferocytosis-related immune evasion in glioblastoma—underscore how microenvironmental dysregulation can drive radioresistance and recurrence (30–33). Applying such multi-omic biomarker frameworks to prostate cancer holds promise for identifying patients who are more suitable for dose escalation, while allowing deintensification in low-risk cases. This approach could optimize therapeutic indices and advance truly risk-adapted SBRT.

This study had limitations. It was retrospective, introducing bias and limiting causal inferences. The small sample size (12 high-dose, 48 control) indicated limited statistical power and heterogeneity. Despite 1:4 PSM controlling for measured variables, unmeasured confounders could influence treatment decisions. Furthermore, in comparison to other studies, the study didn't rule out potential differences related to ethnicity, specifically between East Asian and Western populations. Dose prescriptions (9.5*4, 7.25-8*5, and 6.1*7) align with NCCN guidelines, but escalation beyond STAMPEDE trial equivalents wasn't recommended due to known toxicity increase without improved OS. In our analysis, higher SBRT doses didn't correlate with enhanced survival outcomes or significantly different toxicities.

Conclusion

In SBRT treatment for localized PCa, while the high-dose group showed an upward trend in BPFS and LC rates at 5 and 7 years compared to the control group, the adoption of a high biologically effective dose did not significantly improve tumor control rates and survival. Clinicians should weigh treatment effectiveness and potential adverse effects when devising personalized treatment plans to maximize therapeutic benefits for patients.

Data availability statement

The raw data supporting the conclusions of this article will be made available by the authors, without undue reservation.

Ethics statement

This study was approved by the Institutional Review Board of the First Affiliated Hospital of Naval Medical University and Ruikang Hospital Affiliated to Guangxi University of Chinese Medicine. Due to the retrospective nature of the study and the use of anonymized clinical data, the requirement for informed consent was waived. The study was conducted in accordance with the Declaration of Helsinki. As a retrospective analysis, this work was not registered in a clinical trial database. The studies were conducted in accordance with the local legislation and institutional requirements. The participants provided their written informed consent to participate in this study.

Author contributions

BX: Conceptualization, Data curation, Validation, Writing – review & editing, Writing – original draft, Formal analysis, Software. XZ: Validation, Writing – review & editing, Funding acquisition, Supervision. TW: Writing – review & editing. YL: Writing – review & editing. WZ: Writing – review & editing. LC: Writing – review & editing. ZL: Resources, Writing – review & editing. HZ: Project administration, Funding acquisition, Resources, Writing – review & editing.

Funding

The author(s) declare financial support was received for the research and/or publication of this article. This study is sponsored by the First Affiliated Hospital of Navy Medical University "234 Subject Climbing Program" (2019YPT004), Changhai Hospital Guhai Program (GH145-33), the First Affiliated Hospital of Naval Medical University "Youth Development Program"(2021JCQNO3), Shanghai Health Commission Leading Talent Program(2022LJ019) and Shanghai Top Priority Research Center Construction Program (2022ZZ01011).

Conflict of interest

The authors declare that the research was conducted in the absence of any commercial or financial relationships that could be construed as a potential conflict of interest.

Generative AI statement

The authors declare that no Generative AI was used in the creation of this manuscript.

Any alternative text (alt text) provided alongside figures in this article has been generated by Frontiers with the support of artificial intelligence and reasonable efforts have been made to ensure

accuracy, including review by the authors wherever possible. If you identify any issues, please contact us.

Publisher's note

All claims expressed in this article are solely those of the authors and do not necessarily represent those of their affiliated organizations, or those of the publisher, the editors and the reviewers. Any product that may be evaluated in this article, or claim that may be made by its manufacturer, is not guaranteed or endorsed by the publisher.

Supplementary material

The Supplementary Material for this article can be found online at: https://www.frontiersin.org/articles/10.3389/fimmu.2025.1654174/full#supplementary-material

References

1. Mottet N, van den Bergh RCN, Briers E, Van den Broeck T. EAU-EANM-ESTRO-ESUR-SIOG guidelines on prostate cancer-2020 update. Part 1: screening, diagnosis, and local treatment with curative intent. *Eur Urol.* (2021) 79:243–62. doi: 10.1016/j.eururo.2020.09.042

2. Resnick MJ, Koyama T, Fan KH, Albertsen PC, Goodman M, Hamilton AS, et al. Long-term functional outcomes after treatment for localized prostate cancer. *N Engl J Med.* (2013) 368:436–45. doi: 10.1056/NEJMoa1209978

3. Hopstaken JS, Bomers JGR, Sedelaar MJP, Valerio M, Fütterer JJ, Rovers MM. An updated systematic review on focal therapy in localized prostate cancer: what has changed over the past 5 years? *Eur Urol.* (2022) 81:5–33. doi: 10.1016/j.eururo.2021.08.005

4. Widmark A, Gunnlaugsson A, Beckman L, Thellenberg-Karlsson C, Hoyer M, Lagerlund M, et al. Ultra-hypofractionated versus conventionally fractionated radiotherapy for prostate cancer: 5-year outcomes of the HYPO-RT-PC randomised, non-inferiority, phase 3 trial. *Lancet.* (2019) 394:385–95. doi: 10.1016/S0140-6736(19)31131-6

5. Sonkin D, Thomas A, Teicher BA. Cancer treatments: past, present, and future. *Cancer Genet.* (2024) 286–287:18–24. doi: 10.1016/j.cancergen.2024.06.002

6. Hegemann NS, Guckenberger M, Belka C, Ganswindt U, Manapov F, Li M. Hypofractionated radiotherapy for prostate cancer. *Radiat Oncol.* (2014) 9:275. doi: 10.1186/s13014-014-0275-6

7. Fowler JF, Toma-Dasu I, Dasu A. Is the α/β ratio for prostate tumours really low and does it vary with the level of risk at diagnosis? *Anticancer Res.* (2013) 33:1009–11.

8. Zietman AL, Bae K, Slater JD, Shipley WU, Efstathiou JA, Coen JJ, et al. Randomized trial comparing conventional-dose with high-dose conformal radiation therapy in early-stage adenocarcinoma of the prostate: long-term results from proton radiation oncology group/american college of radiology 95-09. *J Clin Oncol.* (2010) 28:1106–11. doi: 10.1200/JCO.2009.25.8475

9. Peeters ST, Heemsbergen WD, Koper PC, van Putten WL, Slot A, Dielwart MF, et al. Dose-response in radiotherapy for localized prostate cancer: results of the Dutch multicenter randomized phase III trial comparing 68 Gy of radiotherapy with 78 Gy. *J Clin Oncol.* (2006) 24:1990–6. doi: 10.1200/JCO.2005.05.2530

10. Brand DH, Tree AC, Ostler P, van der Voet H, Loblaw A, Chu W, et al. Intensity-modulated fractionated radiotherapy versus stereotactic body radiotherapy for prostate cancer (PACE-B): acute toxicity findings from an international, randomised, open-label, phase 3, non-inferiority trial. *Lancet Oncol.* (2019) 20:1531–43. doi: 10.1016/S1470-2045(19)30569-8

11. Schaeffer EM, Srinivas S, Adra N, An Y, Barocas D, Bitting R, et al. Prostate cancer, version 4.2023, NCCN clinical practice guidelines in oncology. *J Natl Compr Canc Netw.* (2023) 21:1067–96. doi: 10.6004/jnccn.2023.0050

12. Henderson DR, Tree AC, van As NJ. Stereotactic body radiotherapy for prostate cancer. *Clin Oncol.* (2015) 27:270–9. doi: 10.1016/j.clon.2015.01.011

13. Scher HI, Morris MJ, Stadler WM, Higano C, Basch E, Fizazi K, et al. Trial design and objectives for castration-resistant prostate cancer: updated recommendations from the prostate cancer clinical trials working group 3. *J Clin Oncol.* (2016) 34:1402–18. doi: 10.1200/JCO.2015.64.2702

14. Jackson WC, Silva J, Hartman HE, Dess RT, Kishan AU, Beeler WH, et al. Stereotactic body radiation therapy for localized prostate cancer: A systematic review and meta-analysis of over 6,000 patients treated on prospective studies. *Int J Radiat Oncol Biol Phys.* (2019) 104:778–89. doi: 10.1016/j.ijrobp.2019.03.051

15. Nguyen PV, Donneaux B, Louis C, Bodgal Z, Philippi S, Biver S, et al. Stereotactic focal radiotherapy as an alternative treatment for low-risk prostate cancer: Results of a single-arm monocenter Phase-II trial. *Front Oncol.* (2023) 13:1143716. doi: 10.3389/fonc.2023.1143716

16. Krug D, Imhoff D, Haidenberger A, Heßler N, Schäfer J, Huttenlocher S, et al. Robotic stereotactic body radiotherapy for localized prostate cancer: final analysis of the German HYPOSTAT trial. *Strahlenther Onkol.* (2023) 199:565–73. doi: 10.1007/s00066-023-02044-2

17. Michalski JM, Moughan J, Purdy J, Bosch W, Bruner DW, Bahary JP, et al. Effect of standard vs dose-escalated radiation therapy for patients with intermediate-risk prostate cancer: the NRG oncology RTOG 0126 randomized clinical trial. *JAMA Oncol.* (2018) 4:e180039. doi: 10.1001/jamaoncol.2018.0039

18. Hall WA, Deshmukh S, Bruner DW, Michalski JM, Purdy JA, Bosch W, et al. Quality of life implications of dose-escalated external beam radiation for localized prostate cancer: results of a prospective randomized phase 3 clinical trial, NRG/RTOG 0126. *Int J Radiat Oncol Biol Phys.* (2022) 112:83–92. doi: 10.1016/j.ijrobp.2021.07.004

19. Zelefsky MJ, Kollmeier M, McBride S, Varghese M, Mychalczak B, Gewanter R, et al. Five-year outcomes of a phase 1 dose-escalation study using stereotactic body radiosurgery for patients with low-risk and intermediate-risk prostate cancer. *Int J Radiat Oncol Biol Phys.* (2019) 104:42–9. doi: 10.1016/j.ijrobp.2018.12.045

20. Meier RM, Bloch DA, Cotrutz C, Beckman AC, Henning GT, Woodhouse SA, et al. Multicenter trial of stereotactic body radiation therapy for low- and intermediate-risk prostate cancer: survival and toxicity endpoints. *Int J Radiat Oncol Biol Phys.* (2018) 102:296–303. doi: 10.1016/j.ijrobp.2018.05.040

21. Boike TP, Lotan Y, Cho LC, Brindle J, DeRose P, Xie XJ, et al. Phase I dose-escalation study of stereotactic body radiation therapy for low- and intermediate-risk prostate cancer. *J Clin Oncol.* (2011) 29:2020–6. doi: 10.1200/JCO.2010.31.4377

22. Kotecha R, Djemil T, Tendulkar RD, Reddy CA, Thousand RA, Vassil A, et al. Dose-escalated stereotactic body radiation therapy for patients with intermediate- and high-risk prostate cancer: initial dosimetry analysis and patient outcomes. *Int J Radiat Oncol Biol Phys.* (2016) 95:960–4. doi: 10.1016/j.ijrobp.2016.02.009

23. Hirata T, Suzuki O, Otani K, Miyake A, Tamari K, Seo Y, et al. Increased toxicities associated with dose escalation of stereotactic body radiation therapy in prostate cancer: results from a phase I/II study. *Acta Oncol.* (2023) 62:488–94. doi: 10.1080/0284186X.2023.2213443

24. Waters MR, Andruska N, Fischer-Valuck BW, Agabalogun T, Brenneman RJ, Gay H, et al. The association of radiation dose with overall survival for patients treated with prostate stereotactic body radiation therapy. *Cureus.* (2023) 15:e34351. doi: 10.7759/cureus.34351

25. Yu JB, Cramer LD, Herrin J, Soulos PR, Potosky AL, Gross CP. Stereotactic body radiation therapy versus intensity-modulated radiation therapy for prostate cancer: comparison of toxicity. *J Clin Oncol.* (2014) 32:1195–201. doi: 10.1200/JCO.2013.53.8652

26. Jorgo K, Polgar C, Stelczer G, Major T, Gesztesi L, Agoston P. Acute side effects after definitive stereotactic body radiation therapy (SBRT) for patients with clinically localized or locally advanced prostate cancer: a single institution prospective study. *Radiol Oncol.* (2021) 55:474–81. doi: 10.2478/raon-2021-0031

27. Nicosia L, Mazzola R, Rigo M, Giaj-Levra N, Pastorello E, Ricchetti F, et al. Linac-based versus MR-guided SBRT for localized prostate cancer: a comparative evaluation of acute tolerability. *Radiol Med.* (2023) 128:612–8. doi: 10.1007/s11547-023-01624-7

28. Kishan AU, Ma TM, Lamb JM, Casado M, Wilhalme H, Low DA, et al. Magnetic resonance imaging-guided vs computed tomography-guided stereotactic body radiotherapy for prostate cancer: the MIRAGE randomized clinical trial. *JAMA Oncol.* (2023) 9:365–73. doi: 10.1001/jamaoncol.2022.6558

29. Wang F, Yao J, Chen J, Zeng H, Wang X. A pilot study of stereotactic body radiotherapy combined with pelvic radiotherapy and GTVp boost based on multiparameter magnetic resonance image in patients with high-risk prostate cancer. *Med (Baltimore).* (2023) 102:e35260. doi: 10.1097/MD.0000000000035260

30. Li Z, Wang Q, Huang X, Fu R, Wen X, Zhang L. Multi-omics analysis reveals that ferroptosis-related gene CISD2 is a prognostic biomarker of head and neck squamous cell carcinoma. *J Gene Med.* (2024) 26:e3580. doi: 10.1002/jgm.3580

31. Zhang D, Wang M, Huang X, Wang L, Liu Y, Zhou S, et al. GLS as a diagnostic biomarker in breast cancer: in-silico, *in-situ*, and *in-vitro* insights. *Front Oncol*. (2023) 13:1220038. doi: 10.3389/fonc.2023.1220038

32. Zhang J, Zhang X, Wu R, Dong CS. Unveiling purine metabolism dysregulation orchestrated immunosuppression in advanced pancreatic cancer and concentrating on the central role of NT5E. *Front Immunol*. (2025) 16:1569088. doi: 10.3389/fimmu.2025.1569088

33. Zhao S, Wang Q, Liu Y, Zhang P, Ji W, Xie J, et al. Interaction, immune infiltration characteristics and prognostic modeling of efferocytosis-related subtypes in glioblastoma. *BMC Med Genomics*. (2023) 16:248. doi: 10.1186/s12920-023-01670-7

Glossary

BED	biologically effective dose
SBRT	Stereotactic Body Radiotherapy
PCa	prostate cancer
PSM	propensity score matching
PSA	prostate-specific antigen
NCCN	National Comprehensive Cancer Network
OS	overall survival
CSS	cancer-specific survival
bPFS	biochemical progression-free survival
LC	local control
DMFS	distant metastasis-free survival
AS	active surveillance
RP	radical prostatectomy
EBRT	external beam radiotherapy
FT	focal therapy
QoL	quality of life
IMRT	intensity-modulated radiotherapy
RBE	relative biological effectiveness
MRI	magnetic resonance imaging
ECT	emission computed tomography
ECOG	Eastern Cooperative Oncology Group
ADT	androgen deprivation therapy
CT	computed tomography
CTV	clinical target volume
PTV	planning target volume
OAR	organs at risk
CTCAE	Common Terminology Criteria for Adverse Events
GU	genitourinary
GI	gastrointestinal
EQD_2	equivalent dose in 2 Gy per fraction
3DCRT	3D conformal radiation therapy
VMAT	volumetric modulated arc therapy
ASTRO	American Society for Radiation Oncology
ASCO	American Society of Clinical Oncology
BRFS	biochemical recurrence-free survival rates
FFS	freedom from failure
HDAZ	high-dose avoidance zones
MRgRT	MR-guided radiation therapy
GTVp	gross tumor volume within the prostate
mpMRI	multiparametric magnetic resonance imaging

frontiers | Frontiers in Immunology

TYPE Original Research
PUBLISHED 20 August 2025
DOI 10.3389/fimmu.2025.1662638

Check for updates

OPEN ACCESS

EDITED BY
Qi Wang,
Jiangsu University, China

REVIEWED BY
Ling Aye,
Fudan University, China
Qing Wang,
Harvard Medical School, United States
Yuan Quan,
Harbin Medical University Cancer Hospital, China
Kathelina Kristollari,
Ben-Gurion University of the Negev, Israel

*CORRESPONDENCE
Li Tian
ctcmdan@stu.cdutcm.edu.cn
Huixia Liu
18435166090@163.com

RECEIVED 09 July 2025
ACCEPTED 04 August 2025
PUBLISHED 20 August 2025

CITATION
Wen Y, Yi X, Shi J, Wan P, Wang H, Tian L and Liu H (2025) Diagnostic value of thyroid-related serological indicators and pan-immune-inflammation value for differentiated thyroid carcinoma. *Front. Immunol.* 16:1662638. doi: 10.3389/fimmu.2025.1662638

COPYRIGHT
© 2025 Wen, Yi, Shi, Wan, Wang, Tian and Liu. This is an open-access article distributed under the terms of the Creative Commons Attribution License (CC BY). The use, distribution or reproduction in other forums is permitted, provided the original author(s) and the copyright owner(s) are credited and that the original publication in this journal is cited, in accordance with accepted academic practice. No use, distribution or reproduction is permitted which does not comply with these terms.

Diagnostic value of thyroid-related serological indicators and pan-immune-inflammation value for differentiated thyroid carcinoma

Yicheng Wen[1], Xin Yi[1], Jixin Shi[1], Peng Wan[1], Huan Wang[1], Li Tian[1]* and Huixia Liu[2]*

[1]School of Clinical Medicine, Chengdu University of Traditional Chinese Medicine, Chengdu, China, [2]School of Medicine, Tarim University, Alaer, China

Background: Over the past decade, the remarkable rise in differentiated thyroid carcinoma (DTC) incidence, combined with the limitations of conventional diagnostic approaches, have prompted this study to explore the diagnostic value of thyroid-related serological indicators and pan-immune-inflammation value (PIV) for DTC, based on advancements in molecular biology and immunology.

Methods: Based on postoperative pathological diagnosis, the present retrospective research comprised 112 individuals afflicted with DTC (observation group) and 93 individuals having benign thyroid tumors (control group) from January 2023 to January 2025. Differences in clinical data between the two groups were analyzed via univariate statistical methods. Logistic regression analyses identified influencing factors, while diagnostic value of thyroid-related serological indicators and PIV levels were evaluated through receiver operating characteristic analysis.

Results: Intergroup differences regarding the levels of thyroxine (T4), free thyroxine (FT4), thyroid-stimulating hormone (TSH), thyroglobulin (Tg), lymphocyte count, monocyte count, and PIV were found to be significant (p<0.05). Additionally, negative correlation of lymphocyte count with DTC was noted by univariate binary logistic regression (odds ratio [OR] = 0.243, 95% confidence interval [CI]: 0.143–0.411]). TSH (OR=2.458, 95% CI: 1.690–3.575), FT4 (OR=1.383, 95% CI: 1.205–1.588), Tg (OR=1.008, 95% CI: 1.001–1.015), and PIV (OR=1.003, 95% CI: 1.000–1.005) were identified as independent influencing factors for DTC, and the area under the curve for their combination was 0.860 (95% CI: 0.809–0.912, sensitivity: 86.2%, specificity: 77.2%).

Conclusion: This retrospective study suggested that TSH, FT4, Tg, and PIV were positively correlated with DTC, and their combination yielded the best diagnostic performance. It highlighted the potential utility of PIV as a novel immune-inflammatory biomarker and provided support for the development of DTC diagnosis.

KEYWORDS

immune-inflammatory biomarkers, pan-immune-inflammation value, diagnostic value, thyroid-related serological indicators, differentiated thyroid carcinoma

1 Introduction

Thyroid carcinoma (TC), as the foremost pervasive endocrine cancer, is histologically categorized under three major types: differentiated, undifferentiated, and medullary, with differentiated thyroid carcinoma (DTC) constituting more than 90% of all cases (1, 2). There are two major histological DTC subtypes, namely papillary thyroid carcinoma, representing 81–90% of cases, and follicular thyroid carcinoma, comprising 4–11% of cases (3).

Despite the significantly heightened prevalence of DTC over the past decade, it has become one of the least lethal human cancers, since patients can usually be treated with thyroid hormone therapy, radioactive iodine therapy, surgery, and thyroid-stimulating hormone (TSH) therapy, which represents merely 0.3% of all cancer-related fatalities (4, 5). While the prognosis is favorable for most DTC patients, with long-term survival rates surpassing 90%, they face a notably high postoperative recurrence ranging from 25% to 35% (6, 7). Meanwhile, approximately 10% of DTC patients with a poor prognosis will develop lifelong locally advanced or widespread metastatic disease, which severely affects their quality of life (8). Hence, accurate and early diagnosis of DTC, along with the selection of appropriate therapeutic regimen, are key to further improving patient prognosis and elevating survival rates. Diagnosis of DTC is usually based on neck ultrasound and imaging examinations (CT, MRI, SPECT-CT and PET-CT) (2). However, due to the absence of distinct characteristics during the initial phase of DTC onset, its detection by the above traditional techniques is difficult to achieve, which can lead to problems such as misdiagnosis and missed diagnosis. Pathological examination is regarded as the "gold standard" for DTC. Nevertheless, the risk of trauma associated with this procedure can compromise patient tolerance for the diagnosis (9). Currently, with the advancements in molecular biology and immunology, the measurement of some thyroid-related serological indicators, such as TSH and thyroglobulin (Tg) levels, has emerged as a promising diagnostic method for DTC (10). Similarly, a new immune-inflammatory biomarker called pan-immune-inflammation value (PIV) has been postulated and validated as a great predictor in various malignant tumors (11). PIV integrates counts of neutrophils, monocytes, platelets, and lymphocytes, which are the key mediators of cancer-related inflammation and can reflect the inflammatory and immune status of tumors (12). Meanwhile, in contrast to individual blood cell parameters, PIV may provide a more comprehensive reflection of the complex characteristics of systemic immune and inflammatory states. In DTC, elevated PIV may indicate alterations in the tumor microenvironment. This study further explored the diagnostic value of thyroid-related serological indices and PIV for DTC, aiming to compare the diagnostic efficacy of individual and combined detection of various indicators, establish a better diagnostic model, and provide a more accurate evidence-based reference for the clinical diagnosis of DTC.

2 Methods

2.1 Patients selection

A retrospective analysis was conducted (Figure 1), which enrolled 112 patients with DTC treated at the Hospital of Chengdu University of Traditional Chinese Medicine from January 2023 to January 2025. The observation group comprised 31 males and 81 females, who were aged between 25 and 69 years. A control group was constituted by selecting 93 patients (22 males and 71 females) diagnosed with benign thyroid tumors during the same period at the hospital, who were aged between 21 and 75 years. Inclusion criteria: (1) fulfilling the standards for DTC and benign thyroid tumor diagnoses, which were pathologically validated (postoperative pathological examinations) (13); (2) the treatment modality was surgery; (3) having complete clinical data (general information, preoperative laboratory report, postoperative pathology report). Exclusion criteria: (1) complicated by other tumor types; (2) complicated by infections or severe cardiac, hepatic, renal insufficiency and other comorbidities; (3) preoperative radiotherapy. Ethical approval was gained for the present research from the Ethics Committee of the aforementioned hospital, while informed consent was waived given its retrospective nature (approval no. 2025KL-036).

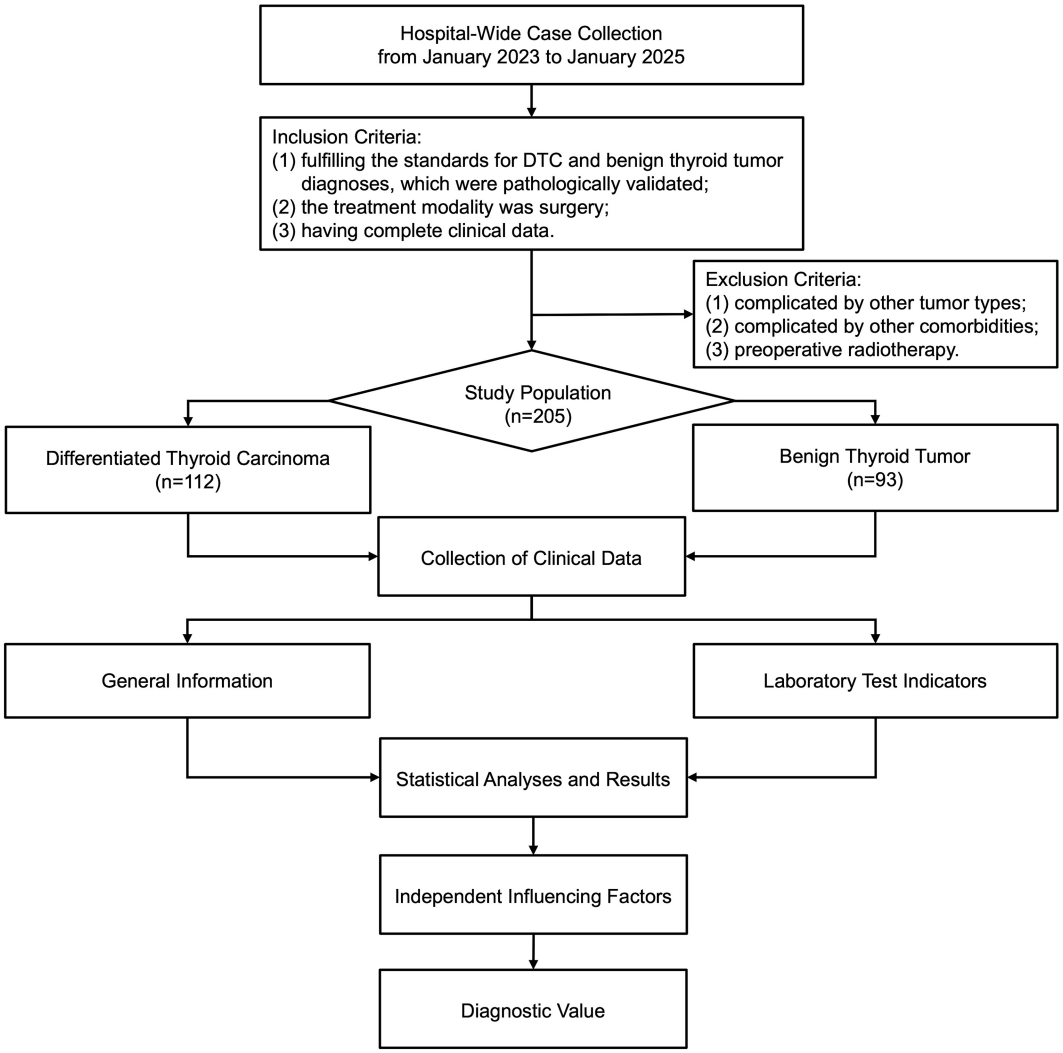

FIGURE 1
Flow diagram for the study.

2.2 Collection of clinical data

Clinical data were collected after patient admission, including: (1) General information: age, gender; (2) Laboratory test indicators: TSH, Tg, triiodothyronine (T3), thyroxine (T4), free triiodothyronine (FT3), free thyroxine (FT4), parathyroid hormone (PTH), as well as neutrophil, lymphocyte, monocyte, and platelet counts.

All laboratory indicators were tested within a two-week period before surgery. Fasting venous blood specimens were obtained from all participants in the morning and dispensed into ethylenediaminetetraacetic acid (EDTA) anticoagulant tubes and plain serum tubes. For serum-based indicator assays, samples in serum tubes were allowed to stand at room temperature for 30 minutes, then centrifuged at 4500 rpm for 10 minutes. The separated serum was analyzed by automated chemiluminescence immunoassay analyzer (Roche, Germany) with related reagents to quantify TSH, Tg, T3, T4, FT3, FT4, and PTH. For complete blood count, after confirming no macroscopic coagulation in EDTA-anticoagulated samples, and platelet, neutrophil, monocyte, and lymphocyte counts (×10^9/L) were measured using an automated hematology analyzer (Abbott, USA).

2.3 Calculation method of PIV

The following computational formula for PIV, as an indicator of systemic inflammation status and a non-invasive and valid potential prognostic indicator of patients suffering from diverse malignancies, was employed: PIV = (neutrophil count × monocyte count × platelet count)/lymphocyte count, with each count unit expressed as ×10^9/L (14).

2.4 Statistical analysis

Data statistics and analysis were accomplished using SPSS 27.0 software. For measurement data, the Shapiro-Wilk test was employed to examine normality. Data obeying normally

distribution were reported as means ± standard deviations (SDs), with intergroup comparisons made via the independent samples t-test. In contrast, non-normal data were depicted by medians with interquartile ranges (IQR; 25th to 75th percentiles), and their intergroup comparisons utilized the Mann-Whitney U-test. For the assessment of categorical data, either Fisher's exact or Chi-square test was employed. Correlations among indicators were analyzed by Spearman's correlation analysis, and the subsequent heatmap plotting was achieved via "corrplot" function in R (ver. 4.4.3). Influencing factors were screened by conducting univariate and multivariate binary logistic regression analyses. The diagnostic value of thyroid-related serological indicators and PIV levels was evaluated by the receiver operating characteristic (ROC) analysis, and the areas under the curves (AUCs) were determined. p value< 0.05 was regarded as statistically significant.

3 Results

3.1 Intergroup comparison of clinical data

The intergroup comparative analysis on clinical data revealed absence of significant differences in general information (age, gender), suggesting that the clinical data of the two patient groups were comparable. By contrast, the intergroup differences regarding the levels of TSH, T4, FT4, Tg, lymphocyte count, monocyte count, and PIV were significant (p<0.05) (Table 1).

3.2 Results of univariate binary logistic regression

Taking tumor group as the dependent variable (1 = observation group, 0 = control group), we performed univariate binary logistic regression analyses for each of the significantly different indicators (TSH, T4, FT4, Tg, lymphocyte count, monocyte count, PIV), with a view to identifying the significant influencing factors for DTC. According to our results, TSH, T4, FT4, Tg, lymphocyte count, monocyte count, and PIV exhibited statistical significance (p<0.05), and the lymphocyte count was linked negatively to DTC (odds ratio [OR] = 0.243, 95% confidence interval [CI]: 0.143–0.411]) (Table 2).

3.3 Correlations among indicators

Spearman correlation analyses were performed among the significant indicators (TSH, T4, FT4, Tg, lymphocyte count, monocyte count, PIV) identified from the above univariate regression analyses. Our results demonstrated that both the lymphocyte count (r=-0.32) and monocyte count (r=0.54) exhibited moderate to strong and statistically significant correlations with PIV (p < 0.001). Given that these two cell counts are components included in the PIV calculation, they were not considered as separate predictive diagnostic indicators. Additionally, T4 and FT4 showed a moderate to strong and significant correlation (r=0.47, p < 0.001).Since FT4 more directly

TABLE 1 Intergroup comparison of clinical data.

Indicators	Observation group (n=112)	Control group (n=93)	Z/χ^2	p value
Age (year)[a]	42.00(33.75,52.25)	45.00(32.00,54.00)	-0.085	0.932
Gender[b]			0.429	0.513
Male	31(27.68)	22(23.66)		
Female	81(72.32)	71(76.34)		
TSH (ulU/mL) [a]	2.40(1.64,3.41)	1.36(1.00,2.35)	-5.455	<0.001
T4 (nmol/L) [a]	98.80(90.40,113.00)	86.32(69.66,108.00)	-3.063	0.002
T3 (nmol/L) [a]	1.68(1.53,1.86)	1.81(1.34,2.19)	-1.246	0.213
FT4 (pmol/L) [a]	16.50(15.20,18.50)	14.10(11.92,16.50)	-6.064	<0.001
FT3 (pmol/L) [a]	4.72(4.42,5.12)	4.75(4.12,5.51)	-0.465	0.642
Tg (ng/mL) [a]	57.30(20.10,91.00)	22.00(11.40,58.40)	-4.107	<0.001
PTH (pg/mL) [a]	56.02(39.40,74.63)	58.43(43.20,81.58)	-1.174	0.240
NEUT (10^9/L) [a]	3.71(2.88,4.70)	3.60(2.91,4.69)	-0.257	0.797
LYMPH (10^9/L) [a]	1.43(1.16,1.73)	2.08(1.37,2.63)	-5.149	<0.001
MONO (10^9/L) [a]	0.38(0.26,0.58)	0.27(0.21,0.42)	-3.246	0.001
PLT (10^9/L) [a]	224.00(194.00,255.00)	223.00(182.00,261.00)	-0.058	0.954
PIV [a]	206.54(134.21,309.83)	119.60(78.11,233.28)	-5.049	<0.001

TSH, thyroid-stimulating hormone; T4, thyroxine; T3, triiodothyronine; FT4, free thyroxine; FT3, free triiodothyronine; Tg, thyroglobulin; PTH, parathyroid hormone; NEUT, neutrophil count; LYMPH, lymphocyte count; MONO, monocyte count; PLT, platelet count; PIV, pan-immune-inflammation value.
[a]Median (interquartile range).
[b]n (%).

TABLE 2 Univariate binary logistic regression results.

Indicators	OR (95% CI)	SE	*p* value
TSH (ulU/mL)	2.187(1.607-2975)	0.157	<0.001
T4 (nmol/L)	1.020(1.007-1.033)	0.006	0.002
FT4 (pmol/L)	1.401(1.247-1.575)	0.060	<0.001
Tg (ng/mL)	1.012(1.005-1.019)	0.004	0.001
LYMPH (10^9/L)	0.243(0.143-0.411)	0.369	<0.001
MONO (10^9/L)	8.567(1.752-41.893)	0.809	0.008
PIV	1.004(1.002-1.006)	0.001	0.001

SE, standard error; OR, odds ratio; CI, confidence interval.

reflects thyroid function and is not influenced by protein binding in most clinical diagnostic scenarios, T4 was excluded as a predictive diagnostic indicator (15) (Figure 2).

3.4 Results of multivariate binary logistic regression

Taking tumor group as the dependent variable (1 = observation group, 0 = control group), and TSH, FT4, Tg, and PIV as independent variables, we conducted multivariate binary logistic regression analyses. According to our results, TSH (OR=2.458, 95% CI: 1.690–3.575), FT4 (OR=1.383, 95% CI: 1.205–1.588), Tg (OR=1.008, 95% CI: 1.001–1.015), and PIV (OR=1.003, 95% CI: 1.000–1.005) were independent influencing factors for DTC (p<0.05) (Table 3).

3.5 Diagnostic efficacy of various indicators

Table 4; Figure 3 display the diagnostic efficacy results for various indicators, along with their combination, in the ROC curve analysis. Clearly, a combined detection of TSH, FT4, Tg, and PIV achieved the highest diagnostic efficacy for DTC (AUC=0.860, 95% CI: 0.809–0.912), with respective sensitivity and specificity levels of 86.2% and 77.2%. Among single indicators, FT4 exhibited the highest diagnostic value for DTC (AUC=0.744, 95% CI: 0.674–0.813), showing an 89.9% sensitivity and a 50.0% specificity. The AUC for TSH was 0.733 (95% CI: 0.655–0.802), with an 85.3% sensitivity alongside a 54.3% specificity. Tg (AUC=0.671, 95% CI: 0.597–0.744) had lower sensitivity (33.9%) but high specificity (95.7%). Additionally, the AUC for PIV was 0.706 (95% CI: 0.633–0.779), showing a 73.4% sensitivity alongside a 64.1% specificity. The combined detection and each individual indicator had p values < 0.001, indicating statistically significant results.

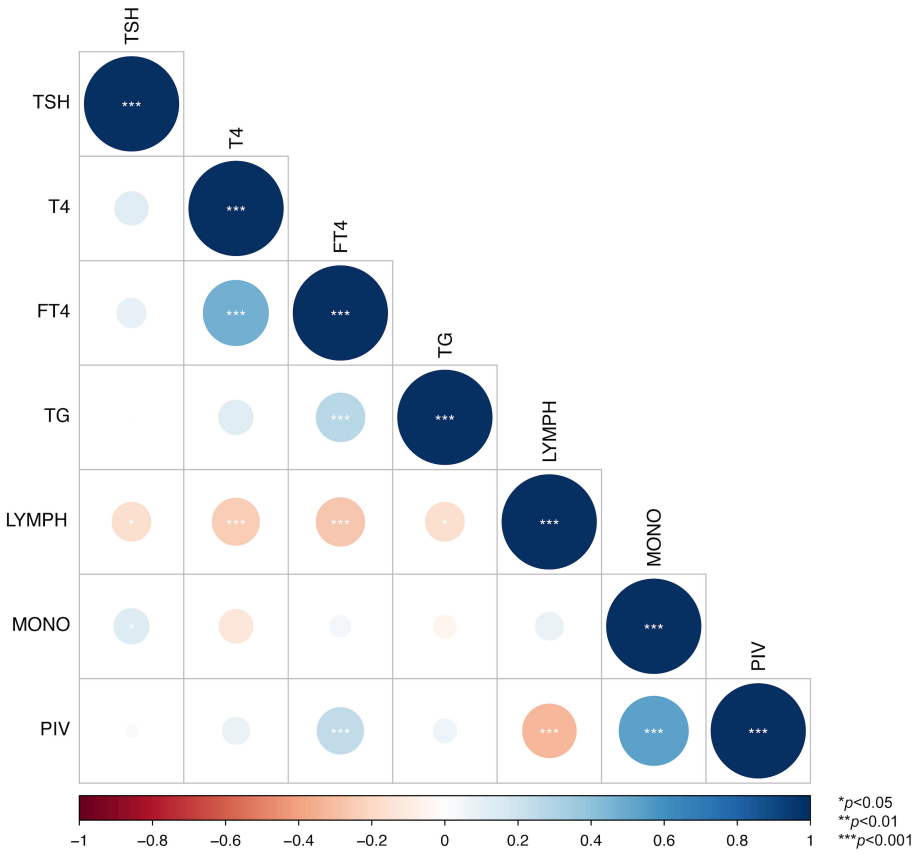

FIGURE 2
Correlation heatmap among indicators. * indicates p < 0.05, ** indicates p < 0.01, and *** indicates p < 0.001.

TABLE 3 Multivariate binary logistic regression results.

Indicators	OR (95% CI)	SE	*p* value
TSH (ulU/mL)	2.458(1.690,3.575)	0.470	<0.001
FT4 (pmol/L)	1.383(1.205,1.588)	0.097	<0.001
Tg (ng/mL)	1.008(1.001,1.015)	0.036	0.020
PIV	1.003(1.000,1.005)	0.001	0.029

4 Discussion

Benign thyroid tumors and DTC frequently exhibit overlapping clinical manifestations and physical findings (16). While DTC typically displays a positive prognosis, its indolent biological and clinical course frequently leads to metastasis to cervical lymph nodes, either at the initial diagnosis or during the postoperative surveillance (17). Consequently, accurate preoperative assessment and regular postoperative monitoring are essential for optimal disease management (18).

As far as we are aware, our research represents the first attempt to systematically explore the diagnostic value of PIV and its combination with thyroid-related serological indicators for DTC. We found that TSH, FT4, Tg, and PIV were independent influencing factors for DTC, and their combined detection yielded the highest diagnostic value, which may reduce misdiagnosis and enhance clinical diagnostic accuracy.

A previous meta-analysis, which examined the association of TSH with TC risk, also demonstrated significantly elevated risks of DTC with increasing TSH concentrations (19). The outcomes of the present study support these findings, and further investigation showed that TSH had preferable diagnostic value for DTC. This may be attributable to the potential contribution of elevated TSH levels to the growth of thyroid epithelial cells. TSH can induce the release of pro-inflammatory cytokines such as IL-6 and TNF-α in thyroid follicular cells through multiple receptor signaling pathways (e.g., cAMP/PKA, NF-κB), thereby establishing a pro-inflammatory microenvironment (20, 21). This process in turn instigates repeated inflammatory reactions in the gland and triggers the body's autoimmune mechanisms, thus placing the thyroid gland in a long-term state of autoimmune abnormality, ultimately resulting in the abnormal growth of thyroid tissues and the formation of tumors (22). Nevertheless, the correlations between FT4, FT3 levels and the probability of developing DTC are still a matter of debate. One study involving a population whose thyroid hormone levels were normal demonstrated that higher FT4 levels were linked positively to the TC risk (23). In a study assessing the association of thyroid function with DTC, it was found that even though patients had normal FT3 and FT4 levels, lower concentrations of these hormones were linked to a heightened risk of developing TC, irrespective of the patient gender or the type of thyroid nodule (24). According to a meta-analysis, FT3 levels were negatively linked to the TC risk, while FT4 levels showed no correlation with TC (25). These disparities may arise not only from population heterogeneity, such as geographic variations in iodine nutrition and genetic polymorphisms in thyroid-related genes, but also from methodological variations, such as differences in immunoassay platforms and inconsistent laboratory reference intervals (26). Notably, our findings partially align with the first-mentioned association regarding FT4's diagnostic value, in which FT4 elevations correlated positively with DTC. FT4 was an independent DTC predictor with the best diagnostic performance among thyroid-related serological indicators. Suggestively, elevated FT4 levels indicate the presence of circulating TSH receptor-stimulating antibodies (TSHR-Abs), which activate identical intracellular signaling pathways to TSH, and lead to enhanced proliferation and attenuated apoptosis of thyroid follicular cells, thereby facilitating tumorigenesis (27).

Tg, synthesized by thyroid follicular cells, acts as a critical precursor for the production of thyroid hormones; it is also synthesized by well-differentiated malignant thyroid tissue and functions as one of the major antigens in autoimmune thyroid diseases (28). According to a few recent reports, the diagnosis and metastasis of DTC are significantly influenced by preoperative Tg levels (29, 30). Moreover, a large sample-size cohort study within the European Prospective Investigation into Cancer and Nutrition (EPIC) has shown a strong positive association between TC risk and pre-diagnostic blood Tg (31). The conclusions of the above studies agree with the findings of ours. However, in our multivariate logistic regression analysis, the OR for Tg was 1.008 (95% CI: 1.001–1.015). Although this is statistically significant, the effect size is small, indicating that each 1 ng/mL increase in serum Tg is associated with only an 0.8% rise in the odds of DTC. Such a small effect size may reflect the influence of multiple factors on Tg levels (e.g., anti-Tg antibodies) and suggests that early or minute DTC lesions produce only limited changes in serum Tg (32). Although the effect size of Tg is small, its clinical significance may lie in its cumulative effect: for example, a 50 ng/mL increase in Tg corresponds to a greater than

TABLE 4 Diagnostic efficacy of various indicators in patients with DTC.

Indicators	AUC (95% CI)	Sensitivity (%)	Specificity (%)	Youden Index	Cut-off Value	*p* value
TSH	0.733(0.655-0.802)	85.3	54.3	0.396	1.39	<0.001
FT4	0.744(0.674-0.813)	89.9	50.0	0.399	13.70	<0.001
Tg	0.671(0.597-0.744)	33.9	95.7	0.296	81.10	<0.001
PIV	0.706(0.633-0.779)	73.4	64.1	0.375	137.51	<0.001
Combined detection	0.860(0.809-0.912)	86.2	77.2	0.634	–	<0.001

AUC, area under the curve.

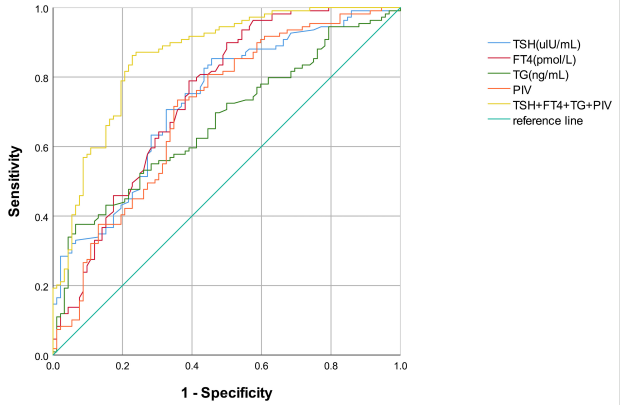

FIGURE 3
ROC curves for DTC diagnosis using thyroid-related serological indicators and PIV.

40% elevation in the odds of DTC. Furthermore, ROC analysis demonstrated that Tg retains exceptionally high specificity (95.7%). This makes it particularly useful for confirming DTC in patients with indeterminate ultrasound or cytology findings and facilitates risk stratification when combined with other biomarkers. Additionally, Tg's sensitivity was only 33.9%, indicating a considerably high risk of missed diagnosis if used alone as a screening tool, despite its excellent performance in ruling out false positives. This limitation suggests that Tg is more suitable as an auxiliary indicator and should be used in conjunction with other biomarkers with higher sensitivity to enhance overall diagnostic efficiency and reduce the rate of missed diagnoses.

Immuno-inflammatory biomarkers, including neutrophils, lymphocytes, monocytes, and platelets, are essential for evaluating the equilibrium between immune and inflammatory states in patients. Numerous studies have investigated their value as diagnostic and prognostic biomarkers for cancer, finding that they possess significant diagnostic and outcome predictive value (33). In recent years, PIV, a novel parameter for prognostic evaluation developed based on the aforementioned four immuno-inflammatory biomarkers, has demonstrated significant prognostic value across various malignancies, including prostate cancer (34), esophageal squamous cell carcinoma (35), metastatic colorectal cancer (36), and pulmonary carcinoma (37). However, to our knowledge, its diagnostic value for and correlation with DTC have never been documented in the existing literature. Hence, by incorporating the aforementioned indicators, the present study analyzed their associations with DTC, as well as the diagnostic value of PIV. We discovered a positive correlation of PIV elevation with DTC, and the role of PIV as an independent predictor for DTC with good diagnostic and predictive performance. Prior studies have shown that platelets can activate epithelial–mesenchymal transition in tumor cells, while neutrophils facilitate tumor growth and metastasis through cytokine secretion (38, 39). However, our study revealed no significant disparities in the platelet or neutrophil count between DTC patients and those having benign thyroid tumors, while observing significant differences in the monocyte and lymphocyte counts. Furthermore, in univariate binary logistic regression analyses, we noted a significant positive association between monocyte count and DTC, whereas a significant negative association between lymphocyte count and DTC. This may be related to the mechanisms by which monocytes promotes tumor cell invasion, metastasis, and angiogenesis, i.e. monocytes is recruited into the tumor microenvironment, where they become activated and function as tumor-associated macrophages, secreting a variety of cytokines (40, 41). Lymphocytes, on the other hand, may suppress the initiation and progression of DTC by mediating antitumor immune responses, such as T cell-mediated cytotoxicity and immune surveillance (42, 43). Therefore, composite biomarkers like PIV, which incorporate multiple peripheral immune cell subsets, may reflect systemic immune activation and characterize the intricate tumour-host interactions (44). From an immunological perspective, elevated PIV levels may more directly reflect the imbalance between pro-tumor inflammation and anti-tumor immunity in the tumor microenvironment (45, 46). This not only provides theoretical support for in-depth analysis of the immunological mechanisms linking inflammation and DTC, but also offers a clear basis for clarifying its potential value in DTC diagnosis. Although PIV showed a strong correlation with lymphocyte and monocyte counts in Spearman correlation analysis, the intrinsic association between these components does not diminish the independent predictive value of PIV as a composite immune-inflammatory biomarker. To avoid the adverse impact of multicollinearity on the model, we excluded lymphocyte and monocyte counts from the multivariate logistic regression. Even so, PIV still exhibited a significant independent association with DTC in the multivariate logistic regression analysis. This result suggests that by integrating the prognostic information of different immune-inflammatory cells, PIV can provide favorable diagnostic value for DTC, which is consistent with previous studies in the field of oncology (34–37).

These findings provide a theoretical basis for optimizing noninvasive preoperative DTC diagnosis while demonstrating clinical potential to address pathological diagnostic limitations. However, this study has several limitations. First, its retrospective design introduces inherent constraints, including potential selection bias in patient enrollment, reliance on the completeness and accuracy of existing medical records and laboratory data, and the inability to control for unmeasured confounders. Second, since the research was carried out at a single institution and was constrained by departmental limitations, the initial lack of sample diversity could potentially introduce bias into the results. Third, the absence of healthy controls restricts direct assessment of biomarker performance in cancer screening. While benign tumor patients represent the clinically relevant differential diagnosis group, this design may underestimate diagnostic specificity. Consequently, the reliability of these findings requires validation through additional multicenter studies. Specifically, future prospective research involving diverse populations (e.g., varying geography, ethnicity, and age) is needed to validate and generalize the diagnostic findings for PIV and serological biomarkers in DTC.

5 Conclusion

This study has clarified to some extent the correlations of thyroid-related serological indicators and PIV with DTC and has tentatively established the diagnostic value of relevant indicators. TSH, FT4, Tg, and PIV were positively correlated with DTC, and their combination yielded the best diagnostic performance. Meanwhile, considering the low cost and high accessibility of routine blood and thyroid function tests, this approach demonstrates particular suitability for initial screening in resource-limited areas—effectively reducing the rate of missed diagnoses of DTC. Consequently, future research should entail large-scale, prospective, multicenter cohort studies aimed at more robustly validating the diagnostic accuracy of thyroid-related serological indicators combined with PIV. These findings hold the potential to improve early screening, risk stratification, and dynamic monitoring of DTC, providing support for the development of DTC diagnosis and treatment.

Data availability statement

The raw data supporting the conclusions of this article will be made available by the authors, without undue reservation.

Ethics statement

The studies involving humans were approved by the Ethics Committee of Hospital of Chengdu University of Traditional Chinese Medicine. The studies were conducted in accordance with the local legislation and institutional requirements. The ethics committee/institutional review board waived the requirement of written informed consent for participation from the participants or the participants' legal guardians/next of kin because this retrospective study is waived informed consent due to the retrospective nature (approval no. 2025KL-036).

Author contributions

YW: Formal analysis, Data curation, Conceptualization, Investigation, Writing – original draft. XY: Writing – original draft, Methodology. JS: Methodology, Writing – original draft. PW: Writing – review & editing. HW: Writing – review & editing. LT: Supervision, Writing – review & editing. HL: Software, Resources, Funding acquisition, Writing – review & editing.

Funding

The author(s) declare financial support was received for the research and/or publication of this article. This work was supported by Huyang Elite -Research Startup Fund for Introduced Talents (PhD Program) (grant number TDZKBS202574).

Acknowledgments

We are grateful to all patients and doctors contributed to this paper.

Conflict of interest

The authors declare that the research was conducted in the absence of any commercial or financial relationships that could be construed as a potential conflict of interest.

Generative AI statement

The author(s) declare that no Generative AI was used in the creation of this manuscript.

Any alternative text (alt text) provided alongside figures in this article has been generated by Frontiers with the support of artificial intelligence and reasonable efforts have been made to ensure accuracy, including review by the authors wherever possible. If you identify any issues, please contact us.

Publisher's note

All claims expressed in this article are solely those of the authors and do not necessarily represent those of their affiliated organizations, or those of the publisher, the editors and the reviewers. Any product that may be evaluated in this article, or claim that may be made by its manufacturer, is not guaranteed or endorsed by the publisher.

References

1. Siegel RL, Giaquinto AN, Jemal A. Cancer statistics, 2024. *CA Cancer J Clin.* (2024) 74:12–49. doi: 10.3322/caac.21820

2. Houten PV, Netea-Maier RT, Smit JW. Differentiated thyroid carcinoma: an update. *Best Pract Res Clin Endocrinol Metab.* (2023) 37:101687. doi: 10.1016/j.beem.2022.101687

3. Prete A, Borges de Souza P, Censi S, Muzza M, Nucci N, Sponziello M. Update on fundamental mechanisms of thyroid cancer. *Front Endocrinol (Lausanne).* (2020) 11:102. doi: 10.3389/fendo.2020.00102

4. Valerio L, Maino F, Castagna MG, Pacini F. Radioiodine therapy in the different stages of differentiated thyroid cancer. *Best Pract Res Clin Endocrinol Metab.* (2023) 37:101703. doi: 10.1016/j.beem.2022.101703

5. Miller KD, Nogueira L, Devasia T, Mariotto AB, Yabroff KR, Jemal A, et al. Cancer treatment and survivorship statistics, 2022. *CA Cancer J Clin.* (2022) 72:409–36. doi: 10.3322/caac.21731

6. Ito Y, Miyauchi A, Kihara M, Fukushima M, Higashiyama T, Miya A. Overall survival of papillary thyroid carcinoma patients: A single-institution long-

term follow-up of 5897 patients. *World J Surg*. (2018) 42:615–22. doi: 10.1007/s00268-018-4479-z

7. Dolidze DD, Shabunin AV, Mumladze RB, Vardanyan AV, Covantsev SD, Shulutko AM, et al. A narrative review of preventive central lymph node dissection in patients with papillary thyroid cancer - a necessity or an excess. *Front Oncol*. (2022) 12:906695. doi: 10.3389/fonc.2022.906695

8. Juhlin CC, Mete O, Baloch ZW. The 2022 who classification of thyroid tumors: novel concepts in nomenclature and grading. *Endocr Relat Cancer*. (2023) 30:e220293. doi: 10.1530/ERC-22-0293

9. Zhang H, Zhang G, Xu P, Yu F, Li L, Huang R, et al. Optimized dynamic network biomarker deciphers a high-resolution heterogeneity within thyroid cancer molecular subtypes. *Med Res*. (2025) 1:10–31. doi: 10.1002/mdr2.70004

10. Schlumberger M, Leboulleux S. Current practice in patients with differentiated thyroid cancer. *Nat Rev Endocrinol*. (2021) 17:176–88. doi: 10.1038/s41574-020-00448-z

11. Hai-Jing Y, Shan R, Jie-Qiong X. Prognostic significance of the pretreatment pan-immune-inflammation value in cancer patients: an updated meta-analysis of 30 studies. *Front Nutr*. (2023) 10:1259929. doi: 10.3389/fnut.2023.1259929

12. Zeng R, Liu F, Fang C, Yang J, Luo L, Yue P, et al. Piv and pile score at baseline predict clinical outcome of anti-Pd-1/Pd-L1 inhibitor combined with chemotherapy in extensive-stage small cell lung cancer patients. *Front Immunol*. (2021) 12:724443. doi: 10.3389/fimmu.2021.724443

13. Haugen BR, Alexander EK, Bible KC, Doherty GM, Mandel SJ, Nikiforov YE, et al. 2015 American thyroid association management guidelines for adult patients with thyroid nodules and differentiated thyroid cancer: the American thyroid association guidelines task force on thyroid nodules and differentiated thyroid cancer. *Thyroid*. (2016) 26:1–133. doi: 10.1089/thy.2015.0020

14. Jin C, Li X, Luo Y, Zhang C, Zuo D. Associations between pan-immune-inflammation value and abdominal aortic calcification: A cross-sectional study. *Front Immunol*. (2024) 15:1370516. doi: 10.3389/fimmu.2024.1370516

15. Ceccarini G, Santini F, Vitti P. Tests of thyroid function. In: Vitti P, Hegedus L, editors. *Thyroid Diseases: Pathogenesis, Diagnosis and Treatment*. Springer International Publishing, Cham (2017). p. 1–23.

16. Sollini M, Cozzi L, Chiti A, Kirienko M. Texture analysis and machine learning to characterize suspected thyroid nodules and differentiated thyroid cancer: where do we stand? *Eur J Radiol*. (2018) 99:1–8. doi: 10.1016/j.ejrad.2017.12.004

17. Grani G, Fumarola A. Thyroglobulin in lymph node fine-needle aspiration washout: A systematic review and meta-analysis of diagnostic accuracy. *J Clin Endocrinol Metab*. (2014) 99:1970–82. doi: 10.1210/jc.2014-1098

18. Jiang N, Jiao B, Zhang L, Li J, Li Y, Lin C. Application of thyroglobulin and anti-thyroglobulin antibody combined with emission computed tomography in the adjuvant diagnosis of differentiated thyroid carcinoma. *Ann Med*. (2023) 55:2232372. doi: 10.1080/07853890.2023.2232372

19. Su A, Zhao W, Wu W, Wei T, Ruan M, Li Z, et al. The association of preoperative thyroid-stimulating hormone level and the risk of differentiated thyroid cancer in patients with thyroid nodules: A systematic review and meta-analysis. *Am J Surg*. (2020) 220:634–41. doi: 10.1016/j.amjsurg.2020.01.009

20. Giuliani C, Bucci I, Napolitano G. The role of the transcription factor nuclear factor-kappa B in thyroid autoimmunity and cancer. *Front Endocrinol (Lausanne)*. (2018) 9:471. doi: 10.3389/fendo.2018.00471

21. Wu Z, Xi Z, Xiao Y, Zhao X, Li J, Feng N, et al. Tsh-Tshr axis promotes tumor immune evasion. *J Immunother Cancer*. (2022) 10:e004049. doi: 10.1136/jitc-2021-004049

22. Eszlinger M, Stephenson A, Mirhadi S, Patyra K, Moran MF, Khalil M, et al. Activation of mitogen-activated protein kinase signaling and development of papillary thyroid carcinoma in thyroid-stimulating hormone receptor D633h knockin mice. *Eur Thyroid J*. (2023) 12:e230049. doi: 10.1530/ETJ-23-0049

23. Liang L, Zheng XC, Hu MJ, Zhang Q, Wang SY, Huang F. Association of benign thyroid diseases with thyroid cancer risk: A meta-analysis of prospective observational studies. *J Endocrinol Invest*. (2019) 42:673–85. doi: 10.1007/s40618-018-0968-z

24. Gul K, Ozdemir D, Dirikoc A, Oguz A, Tuzun D, Baser H, et al. Are endogenously lower serum thyroid hormones new predictors for thyroid Malignancy in addition to higher serum thyrotropin? *Endocrine*. (2010) 37:253–60. doi: 10.1007/s12020-010-9316-6

25. Wang Z, Lin Y, Jiang Y, Fu R, Wang Y, Zhang Q. The associations between thyroid-related hormones and the risk of thyroid cancer: an overall and dose-response meta-analysis. *Front Endocrinol (Lausanne)*. (2022) 13:992566. doi: 10.3389/fendo.2022.992566

26. Yu L, Chen X, Liu J, Wang H, Sun H. Associations between preoperative thyroid parameters, aggressive clinicopathological features and risk of recurrence in differentiated thyroid cancer. *Ann Med*. (2025) 57:2491153. doi: 10.1080/07853890.2025.2491153

27. Cho YA, Kong SY, Shin A, Lee J, Lee EK, Lee YJ, et al. Biomarkers of thyroid function and autoimmunity for predicting high-risk groups of thyroid cancer: A nested case-control study. *BMC Cancer*. (2014) 14:873. doi: 10.1186/1471-2407-14-873

28. Lin JD. Thyroglobulin and human thyroid cancer. *Clin Chim Acta*. (2008) 388:15–21. doi: 10.1016/j.cca.2007.11.002

29. Kim H, Kim YN, Kim HI, Park SY, Choe JH, Kim JH, et al. Preoperative serum thyroglobulin predicts initial distant metastasis in patients with differentiated thyroid cancer. *Sci Rep*. (2017) 7:16955. doi: 10.1038/s41598-017-17176-6

30. Kim H, Park SY, Choe JH, Kim JS, Hahn SY, Kim SW, et al. Preoperative serum thyroglobulin and its correlation with the burden and extent of differentiated thyroid cancer. *Cancers (Basel)*. (2020) 12:625. doi: 10.3390/cancers12030625

31. Rinaldi S, Plummer M, Biessy C, Tsilidis KK, Ostergaard JN, Overvad K, et al. Thyroid-stimulating hormone, thyroglobulin, and thyroid hormones and risk of differentiated thyroid carcinoma: the epic study. *J Natl Cancer Inst*. (2014) 106:dju097. doi: 10.1093/jnci/dju097

32. Schoonen L, Neele M, van Toor H, van Kinschot CMJ, van Noord C, Visser WE, et al. Impact of thyroglobulin and thyroglobulin antibody assay performance on the differential classification of Dtc patients. *J Endocr Soc*. (2022) 6:bvab166. doi: 10.1210/jendso/bvab166

33. Winarno GNA, Mulyantari AI, Kurniadi A, Suardi D, Zulvayanti Z, Trianasari N. Predicting chemotherapy resistance in gestational trophoblastic neoplasia: ratio of neutrophils, lymphocytes, monocytes, and platelets. *Med Sci Monit*. (2022) 28:e938499. doi: 10.12659/MSM.938499

34. Yazgan SC, Yekeduz E, Utkan G, Urun Y. Prognostic role of pan-immune-inflammation value in patients with metastatic castration-resistant prostate cancer treated with androgen receptor-signaling inhibitors. *Prostate*. (2022) 82:1456–61. doi: 10.1002/pros.24419

35. Feng J, Wang L, Yang X, Chen Q, Cheng X. Clinical utility of preoperative pan-immune-inflammation value (Piv) for prognostication in patients with esophageal squamous cell carcinoma. *Int Immunopharmacol*. (2023) 123:110805. doi: 10.1016/j.intimp.2023.110805

36. Fuca G, Guarini V, Antoniotti C, Morano F, Moretto R, Corallo S, et al. The pan-immune-inflammation value is a new prognostic biomarker in metastatic colorectal cancer: results from a pooled-analysis of the valentino and tribe first-line trials. *Br J Cancer*. (2020) 123:403–9. doi: 10.1038/s41416-020-0894-7

37. Chen X, Hong X, Chen G, Xue J, Huang J, Wang F, et al. The pan-immune-inflammation value predicts the survival of patients with anaplastic lymphoma kinase-positive non-small cell lung cancer treated with first-line Alk inhibitor. *Transl Oncol*. (2022) 17:101338. doi: 10.1016/j.tranon.2021.101338

38. Labelle M, Begum S, Hynes RO. Direct signaling between platelets and cancer cells induces an epithelial-mesenchymal-like transition and promotes metastasis. *Cancer Cell*. (2011) 20:576–90. doi: 10.1016/j.ccr.2011.09.009

39. Mantovani A, Allavena P, Sica A, Balkwill F. Cancer-related inflammation. *Nature*. (2008) 454:436–44. doi: 10.1038/nature07205

40. Yang L, Zhang Y. Tumor-associated macrophages: from basic research to clinical application. *J Hematol Oncol*. (2017) 10:58. doi: 10.1186/s13045-017-0430-2

41. Fang Y, Kong Y, Rong G, Luo Q, Liao W, Zeng D. Systematic investigation of tumor microenvironment and antitumor immunity with Iobr. *Med Res*. (2025) 1:136–40. doi: 10.1002/mdr2.70001

42. Lin B, Du L, Li H, Zhu X, Cui L, Li X. Tumor-infiltrating lymphocytes: warriors fight against tumors powerfully. *BioMed Pharmacother*. (2020) 132:110873. doi: 10.1016/j.biopha.2020.110873

43. Wang Q, Zheng C, Hou H, Bao X, Tai H, Huang X, et al. Interplay of sphingolipid metabolism in predicting prognosis of Gbm patients: towards precision immunotherapy. *J Cancer*. (2024) 15:275–92. doi: 10.7150/jca.89338

44. Corti F, Lonardi S, Intini R, Salati M, Fenocchio E, Belli C, et al. The pan-immune-inflammation value in microsatellite instability-high metastatic colorectal cancer patients treated with immune checkpoint inhibitors. *Eur J Cancer*. (2021) 150:155–67. doi: 10.1016/j.ejca.2021.03.043

45. Zhao S, Wang Q, Liu Y, Zhang P, Ji W, Xie J, et al. Interaction, immune infiltration characteristics and prognostic modeling of efferocytosis-related subtypes in glioblastoma. *BMC Med Genomics*. (2023) 16:248. doi: 10.1186/s12920-023-01688-4

46. Sahin AB, Cubukcu E, Ocak B, Deligonul A, Oyucu Orhan S, Tolunay S, et al. Low pan-immune-inflammation-value predicts better chemotherapy response and survival in breast cancer patients treated with neoadjuvant chemotherapy. *Sci Rep*. (2021) 11:14662. doi: 10.1038/s41598-021-94184-7

frontiers | Frontiers in Oncology

TYPE Review
PUBLISHED 10 September 2025
DOI 10.3389/fonc.2025.1661889

Check for updates

OPEN ACCESS

EDITED BY
Qi Wang,
Jiangsu University, China

REVIEWED BY
Jinwei Li,
Sichuan University, China
Wentao Xu,
Anhui Medical University, China
Mostafa Hamza,
Cairo University, Egypt

*CORRESPONDENCE
Changfei Li
lichangfei0503@163.com

RECEIVED 08 July 2025
ACCEPTED 28 August 2025
PUBLISHED 10 September 2025

CITATION
Fu S and Li C (2025) Integrating single-cell omics and materials science for uveal melanoma: from mechanistic insights to precision therapeutics.
Front. Oncol. 15:1661889.
doi: 10.3389/fonc.2025.1661889

COPYRIGHT
© 2025 Fu and Li. This is an open-access article distributed under the terms of the Creative Commons Attribution License (CC BY). The use, distribution or reproduction in other forums is permitted, provided the original author(s) and the copyright owner(s) are credited and that the original publication in this journal is cited, in accordance with accepted academic practice. No use, distribution or reproduction is permitted which does not comply with these terms.

Integrating single-cell omics and materials science for uveal melanoma: from mechanistic insights to precision therapeutics

Shouyong Fu[1] and Changfei Li[2*]

[1]Medical Device Department, Qingdao Hospital of University of Health and Rehabilitation Sciences, Qingdao, China, [2]Department of Ophthalmology, Qilu Hospital, Cheeloo College of Medicine, Shandong University, Qingdao, China

Uveal melanoma (UM), the most common primary intraocular malignancy in adults, presents significant clinical challenges due to its high metastatic potential, pronounced hepatic tropism, and poor prognosis upon systemic dissemination. Despite established local therapies, nearly half of patients develop distant metastases, highlighting an urgent need for more effective systemic strategies. Recent advances in single-cell omics technologies (e.g., scRNA-seq, scATAC-seq, spatial transcriptomics) have revolutionized our understanding of UM pathobiology. These approaches have meticulously delineated the complex tumor heterogeneity, immunosuppressive microenvironment, and key molecular drivers—including novel macrophage subsets (e.g., immunosuppressive MΦ-C4), senescent endothelial cells, and non-canonical immune checkpoint expression—providing unprecedented resolution for identifying actionable therapeutic targets. Concurrently, innovations in materials science and biomedical engineering offer transformative opportunities for precision therapy. Engineered nanocarriers, biodegradable implants, and advanced gene therapy vectors (e.g., tropism-enhanced AAVs, CRISPR-Cas9 systems) enabled targeted drug delivery, sustained release, and genetic modulation tailored to the eye's unique anatomy and immune privilege. This review synthesizes these converging frontiers, outlining how the integration of multi-omics insights with smart biomaterials can overcome current therapeutic limitations. We catalog emerging material-based platforms applicable to UM and summarize validated molecular targets (e.g., GNAQ/GNA11, YAP/TAZ, BAP1, c-Met, CXCR4). Furthermore, we propose an interdisciplinary paradigm spanning combinatorial targeted therapies, immunomodulation, minimally invasive devices (e.g., robotic radiosurgery), and engineered delivery systems. By bridging mechanistic discovery with translational engineering, this synergy holds significant promise for advancing precision medicine and improving clinical outcomes in UM, ultimately facilitating the transition from bench to bedside.

KEYWORDS

uveal melanoma, medical device, nanotechnology, single-cell RNA sequencing, therapy

1 Introduction

Uveal melanoma (UM), arising from melanocytes within the uveal tract, represents the most prevalent primary intraocular malignancy in adults. Approximately 90% of cases originate in the choroid, followed by 6% in the ciliary body and 4% in the iris (1). Unlike cutaneous melanoma, UM is characterized by distinct molecular features, including monosomy 3, chromosome 8q amplification (2, 3), recurrent mutations in GNAQ and GNA11, and an immunosuppressive ("cold") tumor microenvironment (4, 5). These alterations underlie UM's aggressive clinical course and strong hepatic tropism. Although UM accounts for only 3%–5% of all melanoma cases, its prognosis remains poor (6). In the United States, 1,700–2,500 individuals are affected annually (4.6–6 per million), with lower incidence among Black and Asian populations (0.3–0.4 per million) (7, 8). Nearly half of patients develop distant metastases after initial local therapy, with the liver involved in >90% of cases (9–11). Once systemic spread occurs, treatment options are limited and median survival falls below one year (12).

Local treatments—such as plaque brachytherapy, proton beam therapy, and enucleation—are well established but fail to prevent metastasis, highlighting the need for systemic strategies. Recent advances in materials science, particularly nanotechnology, have created transformative opportunities for ocular therapy. The eye's anatomy and immune privilege favor localized delivery with high bioavailability and reduced systemic toxicity (13, 14). In UM models, poly(N-isopropylacrylamide) nanoparticles preferentially accumulated in uveal tissue (15), and polymeric or albumin-based nanocarriers delivering AZD8055 demonstrated selective cytotoxicity *in vitro* and *in vivo* (16). These innovations underscore the potential of engineered materials for precision ocular therapy. However, progress is hindered by the limited repertoire of actionable molecular targets, emphasizing the need for deeper understanding of UM pathology, particularly tumor heterogeneity and its immunosuppressive niche.

The advent of single-cell omics has revolutionized investigations into UM heterogeneity. Technologies such as scRNA-seq, scATAC-seq, and spatial transcriptomics provide unprecedented resolution for therapeutic target discovery (17–20). Recent studies have revealed unexpected clonal diversity, challenging the assumption that copy number variations are fixed early events (21). Li et al. identified a macrophage subset (MΦ-C4) associated with poor prognosis (22), while Tang et al. showed that infiltrating $CD8^+$ T cells predominantly expressed LAG3 rather than PD1/CTLA4, explaining limited efficacy of conventional checkpoint inhibitors and suggesting LAG3 as an alternative target (23). Together, these findings illustrate how multi-omics approaches advance understanding of UM biology and inform novel therapeutic strategies.

This review synthesizes progress from single-cell omics and materials science, framing an interdisciplinary paradigm that integrates molecular discovery, engineered drug delivery, and clinical translation to advance precision medicine in UM.

2 Decoding UM heterogeneity: single-cell omics as a game-change

The emergence of single-cell technologies has profoundly transformed research on uveal melanoma (UM), providing unprecedented resolution to dissect tumor heterogeneity and therapeutic responses. Earlier bioinformatics approaches, relying on bulk sequencing and TCGA-derived signatures, enabled patient stratification and prognosis prediction but were limited by confounding noise and reductionist views of isolated genes (24). Single-cell analysis overcomes these constraints, capturing clonal dynamics and gene regulatory networks at the system level. This advance has fundamentally shifted mechanistic investigations and is now directly informing next-generation immunotherapies targeting checkpoint dysregulation (25–30). Unlike cutaneous melanoma, UM remains largely refractory to checkpoint blockade, highlighting the need to consider immune remodeling beyond T-cell–centric paradigms (31–33). Recent findings emphasize the roles of tumor-associated macrophages, senescent endothelial cells, and tumor-reactive lymphocytes, whose interactions create an immunosuppressive microenvironment resistant to conventional therapies.

2.1 Tumor-associated macrophages

Tumor-associated macrophages (TAMs) represent a critical cellular subset in UM, with their functional significance strongly linked to clinical outcomes. Accumulating evidence demonstrates that TAM infiltration correlates with UM-related mortality and established histopathological prognostic indicators, including the presence of epithelioid cells and elevated tumor microvascular density (MVD) (34). Notably, TAMs exhibit preferential accumulation in UM tumors harboring monosomy 3 karyotypes, which are characterized by an immunosuppressive microenvironment and inflammatory phenotypic features (35). Importantly, these TAMs predominantly display a pro-angiogenic M2-polarized macrophage phenotype, further potentiating tumor progression through vascular remodeling (36). Besides, Herwig et al. demonstrated that the imbalance between M1 and M2 macrophage polarization in UM is driven by PPARγ (37).

Beyond traditional chromosomal 3 analysis, contemporary prognostic frameworks integrate TAM-associated molecular signatures with advanced genomic tools. Gene expression profiling (GEP), for instance, enables stratification of UM into two distinct molecular classes: low-risk class 1 and high-risk class 2 tumors (38). Emerging data suggests that TAM-derived cytokines may synergize with class 2-specific genetic alterations to drive metastatic progression, positioning TAMs as both a biomarker and therapeutic target in UM management.

Recent single-cell transcriptomic analyses have refined macrophage classification beyond the conventional M1/M2 paradigm. Li et al. examined 63,264 single-cell transcriptomes from 11 UM patients and identified four transcriptionally distinct

macrophage subsets (MΦ-C1 to MΦ-C4), confirming that MΦ-C4 serves as an independent prognostic factor (22). As illustrated in Figure 1, this subset promotes tumor cell proliferation and exerts immunosuppressive effects through representative regulatory pathways, underscoring its potential as a therapeutic target to overcome resistance to immune checkpoint blockade. Complementary work by Sun et al. defined a metastatic protective macrophage subpopulation (MPMφ) associated with antigen processing and inflammatory responses, which exhibited inhibitory effects on UM metastasis (39). Collectively, the refined classification of macrophage subpopulations significantly enhances understanding of UM's immune landscape and informs the development of targeted diagnostic and therapeutic strategies.

2.2 Senescent endothelial cells

Endothelial cells (ECs) play pivotal roles in the tumor microenvironment, significantly influencing tumor development and progression. ECs form a monolayer lining the inner surface of blood vessels. Beyond regulating gas and metabolite exchange between vasculature and tissues, ECs modulate hemodynamics, coagulation, angiogenesis, and inflammation (40). Tumor growth critically depends on neovascularization to meet nutritional demands, while hematogenous metastasis relies on interactions with endothelial cells. Consequently, the status of vascular endothelial cells holds substantial implications, rendering endothelial cell injury a subject of considerable interest. Such injury may arise from factors including oxidative stress, inflammation, hyperglycemia, and senescence (41).

Zeng et al. demonstrated a remarkable disparity in endothelial cell (EC) abundance between primary and metastatic UM, with profoundly elevated ECs in metastatic UM exhibiting aberrant senescence. This senescent phenotype was attributed to the upregulation of KLF4, a pivotal senescence-associated transcription factor. Senescent ECs consequently secreted senescence-associated secretory phenotype (SASP) factors, which facilitate tumor cell recruitment and hepatic metastasis. Among SASP components derived from senescent ECs, the chemokine

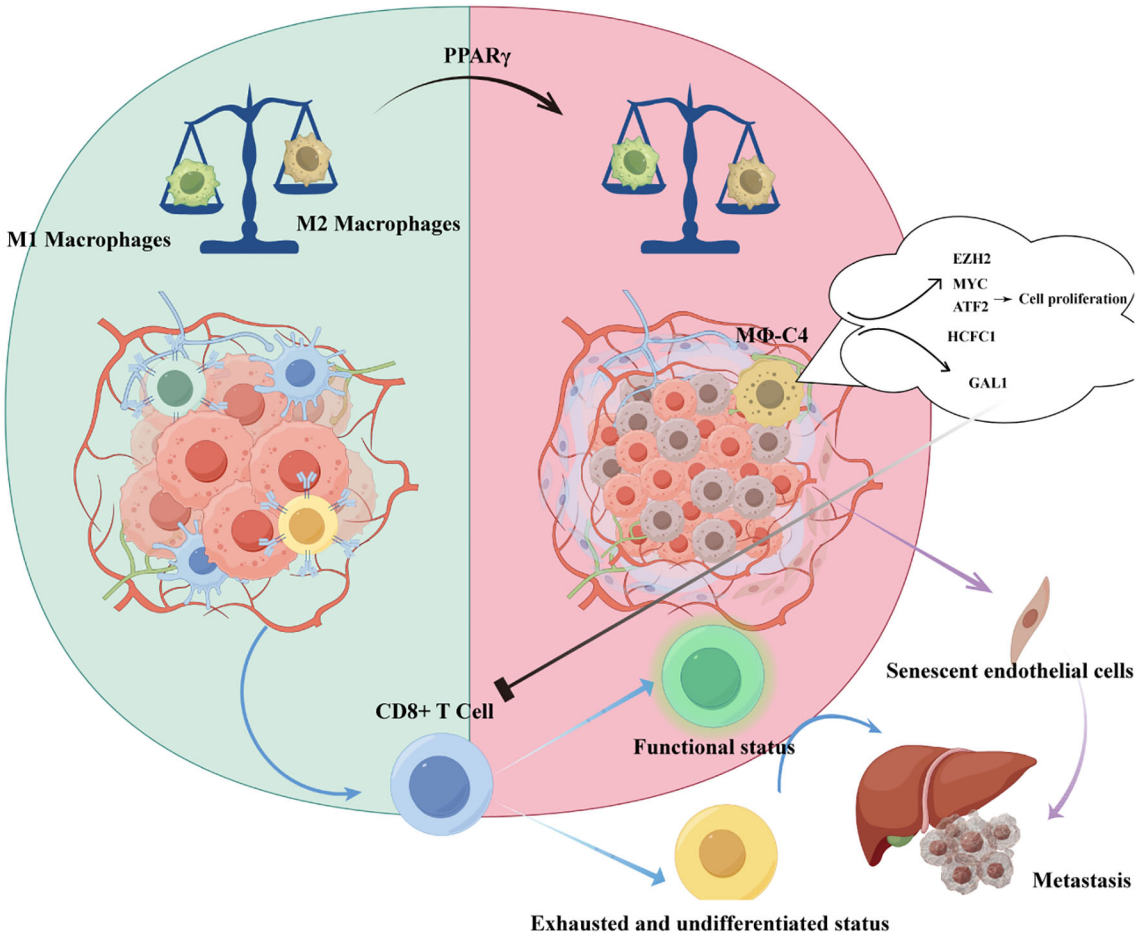

FIGURE 1
Tumor-associated macrophages and the immune microenvironment in uveal melanoma.

CXCL12 was identified as critical for mediating tumor cell migration induced by senescent endothelium (42).

2.3 Tumor-reactive lymphocytes

Tumor-reactive lymphocytes represent a pivotal component of the UM immune landscape. Recent work has refined the classification of T cell subpopulations within UM, offering novel strategies for selective expansion of tumor-infiltrating lymphocytes (TILs) to enhance both adoptive cellular therapy (ACT) and checkpoint blockade (43). These findings highlight that the efficacy of TILs may depend on reprogramming the tumor microenvironment from an immunologically "cold" state toward a pro-inflammatory niche that permits robust T cell infiltration. Such reprogramming may require adjunctive approaches, including lymphodepletion to reduce competition for interleukin-2 (IL-2) signaling and locoregional therapies that induce immunogenic cell death. For example, melphalan-based isolated hepatic perfusion (IHP) has been shown to trigger a surge of neoantigen-specific T cells, potentially priming previously non-inflamed tumor sites for immunotherapy responsiveness. In parallel, Chen et al. demonstrated that distinct $CD8^+$ T cell states can exert profound influence on UM metastatic progression, underscoring the importance of targeting T cell dysfunction at multiple levels (44).

On the clinical front, monotherapy with immune checkpoint inhibitors (ICIs) has consistently demonstrated inferior efficacy in UM compared to metastatic cutaneous melanoma (32, 45). Combination regimens, such as PD-1/CTLA-4 inhibition (46–48) and PD-1/HDAC inhibitor strategies (49, 50), have shown encouraging improvements in survival relative to historical benchmarks (12). The most significant clinical advance to date is tebentafusp, a bispecific T cell engager targeting HLA-A2-positive individuals, which achieved the first survival benefit in a phase 3 trial, extending median overall survival from 16.0 to 21.7 months (51, 52). Locoregional therapies also remain clinically relevant: phase 3 trial data demonstrated that IHP tripled hepatic progression-free survival compared with best alternative care (53), although the subsequent SCANDIUM trial did not confirm a clear overall survival benefit (54). Nevertheless, ongoing clinical trials are actively investigating combinations of locoregional therapies with ICIs (NCT04463368) to exploit synergistic immunomodulatory effects. Importantly, both tebentafusp and IHP ultimately lead to disease progression, reinforcing the need for integrated strategies that combine biological insights into T cell dysfunction with innovative clinical interventions.

3 Ocular advanced materials: engineering precision delivery

With ongoing progress in precision medicine, ophthalmic treatments are steadily shifting toward strategies that are more targeted, effective, and minimally invasive. The incorporation of advanced material technologies has enabled novel approaches for ocular drug delivery, gene modification, and sustained-release therapies. These innovations are particularly promising for managing posterior segment disorders, such as retinal and choroidal diseases. This section offers a concise overview of several advanced materials used in ophthalmology, including nanocarrier systems, degradable implants, gene delivery vectors, and next-generation therapeutic platforms. We highlight recent developments in how these materials improve treatment specificity and longevity. Key functional features and representative research are summarized in Table 1.

Table 1 was identified through systematic PubMed/Scopus searches (2018–2024), prioritizing entities meeting stringent criteria: (1) for targets, mechanistic validation in ≥2 *in vivo* uveal melanoma models (e.g., PDXs, GEMMs) AND clinical association (OS/PFS HR > 1.5 or phase I+ trial evidence); (2) for delivery systems, demonstrated ocular targeting in UM preclinical studies (tumor-to-liver ratio > 5:1) AND intraocular feasibility (e.g., vitreal half-life > 24h). Exclusion criteria encompassed purely *in vitro* data, non-peer-reviewed reports, and non-UM-specific platforms. Evidence was synthesized narratively but graded systematically (Level I: meta-analysis; Level II: RCTs; Level III: cohort studies), with acknowledged limitations in rapidly evolving fields (e.g., CRISPR-carrying exosomes post-2023). Table 2 has the same search criteria as Table 1.

3.1 Nanoparticle-based drug delivery systems for posterior segment

Posterior segment ocular diseases, such as UM, age-related macular degeneration (AMD), and diabetic retinopathy, pose significant therapeutic challenges. These include the restrictive nature of ocular barriers, short drug half-life, and the risk of local adverse effects. In recent years, nanotechnology has rapidly advanced in ophthalmic drug delivery, emerging as a critical breakthrough in precision therapy for posterior segment disorders due to its small particle size, tunable surface functionality, and high biodegradability (15, 55).

Nanoparticles not only facilitate efficient trans-barrier delivery across the blood-retinal barrier but can also be engineered with specific ligands for active targeting, thereby enhancing drug accumulation at pathological sites. For example, Cimino et al. developed polyethylene glycol-modified lipid nanoparticles (PEG-LNPs) to deliver the prodrug (S)-(–)-MRJF22. This system enhanced the drug's stability and sustained-release profile, achieved prolonged suppression of uveal melanoma cells, and demonstrated favorable posterior segment distribution and biocompatibility in animal models (56).

Moreover, the unique intracellular delivery mechanisms of nanomaterials have introduced novel avenues for antitumor therapy. Song et al. found that cuprous oxide nanoparticles (Cu_2O-NPs) could selectively enter UM cells via lipid raft-mediated endocytosis, inducing mitochondrial and lysosomal damage and activating oxidative stress pathways, ultimately triggering apoptosis and autophagy while significantly suppressing cell proliferation and invasiveness (57).

TABLE 1 Material science-driven ocular precision drug delivery systems and their applications in UM.

Name	Material type / strategy	Mechanism of action	PMID
PEGylated nanostructured lipid carriers (NLCs)	Nanostructured lipid carriers (NLCs)	Sustained delivery of the prodrug (S)-(–)-MRJF22 to inhibit uveal melanoma growth, enhance biocompatibility, and enable topical delivery to the posterior eye segment	38851409
Cuprous oxide nanoparticles (Cu_2O-NPs)	Inorganic nanoparticles	Internalized via lipid raft-mediated endocytosis; localize to mitochondria, lysosomes, and autophagolysosomes; induce ROS production, apoptosis, and autophagy; inhibit uveal melanoma proliferation, migration, and invasion	26467678
Hyaluronic acid nanoparticle carrying Verteporfin (HANP/VP)	Hyaluronic acid-based polymeric nanoparticle	Targets CD44-expressing UM cells; enables tumor-specific accumulation; enhances photodynamic therapy (PDT); inhibits YAP signaling; induces apoptosis and immune activation	38546166
Dexycu®	Biodegradable intraocular suspension (Verisome® technology	Single intraocular injection delivering dexamethasone for ~30 days post-cataract surgery; localized anti-inflammatory effect; reduces need for eye drops	36986595
Ozurdex®	Biodegradable PLGA-based intravitreal implant	Sustained dexamethasone release over months for treating retinal inflammation (e.g., DME, BRVO, CRVO, uveitis); inhibits cytokines; reinjected as needed	36986595
PCL-g-PDA [poly(ε-caprolactone)-graft-poly(dopamine)]	Biodegradable polyester copolymer	Mimics melanin drug-binding via PDA moieties; enables sustained intravitreal drug release through drug–catechol interactions; biocompatible and degradable	36170117
TM-loaded biodegradable subconjunctival microfilm	Biodegradable poly(lactide-co-caprolactone) (PLC) elastomer with PEG copolymers	Subconjunctival implant for sustained timolol maleate release over 3–5 months; reduces intraocular pressure; improves bioavailability and compliance	26100093
AAV-delivered Cre-mediated YAP/TAZ activation model	Genetic mouse model via AAV-Cre system	Demonstrates YAP/TAZ activation as sufficient for UM initiation; cooperates with Ras/MAPK in progression; dual inhibition shows synergistic antitumor effect	31801083
AAV-shRNA-mediated PCK1 knockdown	Gene therapy via AAV delivery	PCK1 promotes UVM cell growth via Gαi3-Akt signaling; silencing PCK1 inhibits proliferation, migration, and induces apoptosis in vitro and in vivo	38670942
PEI-DOCA modified cationic lipid nanoparticles (LNPs) delivering CRISPR/Cas9 RNPs	Functionalized lipid nanoparticle for gene therapy	Transdermal delivery of CRISPR/Cas9 RNPs targeting Braf gene; enhanced skin penetration and cellular uptake; in vivo genome editing leading to melanoma	39461690
ZAP-X® radiosurgery system	Novel stereotactic radiosurgery platform	Provides high-precision, single-session high-dose irradiation with real-time motion tracking; achieves tumor volume reduction in uveal melanoma	40291338
CP@Au@DC_AC50 hydrogel	Injectable stimuli-responsive hydrogel with gold nanorods	NIR-triggered photothermal therapy combined with controlled release of gene-targeted drug DC_AC50; antibacterial effect preventing ocular infection	34331418
Treat20 Plus precision oncology program	Precision oncology clinical workflow integrating multi-omics sequencing and multidisciplinary tumor board recommendations	Molecular profiling-guided matched therapies (MEK, MET inhibitors, checkpoint inhibitors); 60% of patients received targeted therapy with 56% clinical benefit rate	35569281

*Representative examples of nanocarriers, biodegradable implants, gene therapy vectors, medical devices, and clinical workflows developed for ophthalmic diseases and uveal melanoma. The table summarizes material types, mechanisms of action, and therapeutic relevance. NLCs, nanostructured lipid carriers; PLGA, poly (lactic-co-glycolic acid); PDA, poly (dopamine); PLC, poly (lactic acid-co-caprolactone); AAV, adeno-associated virus; LNPs, lipid nanoparticles; NIR, near-infrared.

In combination therapy strategies, the integration of targeted delivery with photodynamic therapy (PDT) shows promising synergistic effects. For instance, hyaluronic acid-coated, CD44-targeted nanoparticles (HANPs) delivering the photosensitizer verteporfin have been shown to enhance drug accumulation at the tumor site while simultaneously inhibiting the YAP signaling pathway and inducing immune activation. This dual mechanism offers precise targeting and immune modulation for UM treatment (58).

Researchers are further exploring multifunctional nanoplatforms that integrate drug delivery, imaging guidance, thermoresponsive release, and immunomodulation—forming intelligent theranostic systems. The development of such multimodal platforms provides a promising path toward personalized treatment of posterior segment diseases. However, nanoparticle-based therapeutic strategies still face multiple clinical translation barriers, including insufficient long-term safety evaluation, immune clearance, batch-to-batch production variability, and challenges in large-scale manufacturing (59).

TABLE 2 Potential targets for treating UM.

Target	Mechanism of action	Targeted therapy/strategy	Research/clinical progress	PMID
GNAQ/ GNA11 Mutations	Activates MAPK/ERK pathway, promoting tumor growth	MEK inhibitors (Trametinib, Selumetinib)	44% disease stabilization rate in clinical trials	35804836
YAP/TAZ Signaling Pathway	Promotes cell proliferation, migration, and survival	YAP inhibitors (Verteporfin), combined with Mcl-1 inhibition	Functional inhibition effective; combination therapy shows synergistic effect	31801083
BAP1 Gene Mutation	Associated with high malignancy and metastasis risk	Prognostic tool, no targeted drug available	BAP1 expression testing superior to traditional staging systems	38238977
c-Met	Facilitates cell migration and liver metastasis	c-Met inhibitors	Potential to inhibit UM metastasis; under investigation	36761417
CXCR4	Chemotactic migration to distant organs	CXCR4 antagonists	High expression linked to metastasis risk; effective inhibition observed	19553629
SF3B1 Mutation	Alters RNA splicing; associated with intermediate metastatic potential	Splicing modulation under study	Emerging target; ongoing research into its role in metastasis	35012916
MYC Pathway	Drives proliferation and metastasis; associated with monosomy 3	BET inhibitors (e.g., Mivebresib)	Common amplification; MYC-driven tumors show responsiveness to BET inhibition	11431428
Cell Cycle Regulators	Loss of CDKN2A; CDK4/6 activation leads to uncontrolled cell proliferation	CDK4/6 inhibitors (e.g., Palbociclib)	CDK pathway alterations common; CDK inhibitors under investigation	34924562
VEGF / Angiogenesis	Promotes angiogenesis and metastasis, especially to the liver	Anti-VEGF antibodies (Bevacizumab), multi-target inhibitors (Nintedanib)	Promising adjuvant role; limited effect on metastases; resistance possible; further trials ongoing	26761211
PRAME	associated with tumor progression, immune evasion, and poor prognosis	PRAME-directed immunotherapy (TCR-engineered T cells, vaccine-based approaches)	High expression associated with metastasis risk; immunotherapy under investigation	36794811

*Key molecular targets, associated mechanisms, therapeutic strategies, and clinical progress in uveal melanoma. UM, uveal melanoma; MAPK, mitogen-activated protein kinase; ERK, extracellular signal-regulated kinase; GNAQ, guanine nucleotide-binding protein subunit alpha q; GNA11, guanine nucleotide-binding protein subunit alpha 11; BAP1, BRCA1 associated protein-1; SF3B1, splicing factor 3b subunit 1; EIF1AX, eukaryotic translation initiation factor 1A X-linked; MEK, mitogen-activated protein kinase kinase; PKC, protein kinase C; YAP/TAZ, Yes-associated protein and transcriptional co-activator with PDZ-binding motif; PRAME, preferentially expressed antigen in melanoma; PMID, PubMed Identifier.

Future research should focus on: (1) identifying disease-specific targets and refining vector modifications; (2) enhancing delivery efficiency and tissue penetration; (3) integrating imaging technologies for real-time monitoring; and (4) establishing robust multi-center clinical validation and commercialization pathways.

In summary, nanoparticle delivery systems offer unprecedented innovation in the treatment of posterior segment ocular diseases. They demonstrate substantial therapeutic potential, particularly in malignant conditions such as UM. With the continued convergence of materials science and biomedical engineering, personalized and programmable smart nanocarriers are poised to become a cornerstone of precision ophthalmic therapy.

3.2 Biodegradable implants for sustained therapeutic release

Effective management of posterior segment ocular diseases often relies on maintaining sustained and stable intraocular drug concentrations. However, conventional treatment methods such as intravitreal injections necessitate frequent administrations and are associated with complications including elevated intraocular pressure, intraocular infections, and retinal detachment (60). To overcome these limitations, biodegradable implants have emerged in recent years as promising long-acting drug delivery platforms. These systems can provide continuous drug release without repeated interventions, thereby improving patient compliance and therapeutic outcomes (61).

Such implants are commonly composed of biodegradable polymers including polylactic acid (PLA), poly (lactic-co-glycolic acid) (PLGA), and polycaprolactone (PCL). The degradation rate and drug release kinetics can be finely tuned according to clinical requirements (62, 63). Implants may be placed in various ocular compartments such as the vitreous cavity, sub-scleral space, or episcleral surface, typically via surgical or minimally invasive procedures. During degradation, they steadily release anti-inflammatory, anti-angiogenic, or anti-tumor agents (64).

In the treatment of UM, a primary malignant tumor of the posterior segment, no standardized biodegradable implant system has yet been widely adopted in clinical practice. Nevertheless, several studies have explored their potential in localized sustained drug delivery. For example, researchers have developed PLGA-based microspheres or nanofibrous membranes loaded with antineoplastic agents, which are implanted episclerally to deliver drugs directly to peritumoral tissues. This approach minimizes systemic toxicity and enables continuous tumor suppression (65). Other investigations have encapsulated photosensitizers or small-molecule targeted drugs within biodegradable carriers, achieving controlled release while enhancing drug concentration and specificity at the tumor site. These findings underscore the

feasibility of such systems as novel local therapies for ocular tumors (15). Despite these advances, current research remains largely confined to animal models and early-phase clinical evaluations, and further efforts are required to facilitate clinical translation (66).

More broadly, the clinical application of biodegradable implants in posterior segment diseases has seen significant progress. For instance, Dexycu® (a dexamethasone intraocular implant) and Ozurdex® (a PLGA-based sustained-release dexamethasone system) have been approved by the U.S. FDA for the treatment of intraocular inflammation and macular edema, demonstrating favorable efficacy and safety profiles (61, 67). Furthermore, Bahuon et al. developed a novel polyester copolymer (PCL-g-PDA) containing poly(dopamine) (PDA), which mimics natural ocular melanin and enhances drug-binding capacity. This system successfully extended the release duration of dexamethasone and ciprofloxacin, showing promise as a biodegradable vitreous implant (68). Another study introduced a degradable microfilm based on poly (lactic acid-co-caprolactone) (PLC) elastomers for the sustained delivery of timolol maleate (TM) via sub-scleral injection. By integrating a multilayer structure with PEG modifications, this system achieved stable drug release for over three months and demonstrated excellent intraocular pressure-lowering effects and biocompatibility in non-human primate models (69).

In summary, biodegradable implants offer a transformative strategy for the treatment of posterior segment diseases by enabling long-term, stable, and controlled drug delivery. They are particularly well-suited for chronic conditions such as UM that require prolonged management. Looking ahead, advancements in multi-drug co-delivery, disease microenvironment-responsive mechanisms, and minimally invasive implantation techniques are expected to further enhance the precision and clinical applicability of these systems.

3.3 Gene therapy vectors with ocular tropism

Gene therapy has emerged as a precise therapeutic strategy targeting the molecular mechanisms of disease, achieving remarkable progress in ophthalmology in recent years. The eye, with its relatively enclosed anatomical structure, strong immune privilege, and high bioavailability, is considered one of the most ideal target organs for gene therapy. In particular, the development of gene vectors with high tissue specificity, efficient delivery, and excellent safety profiles for ocular tissues—especially the retina and choroid—has become a major research focus (70).

Among current gene delivery systems, adeno-associated virus (AAV) vectors are the most widely used in ophthalmology due to their low immunogenicity, stable gene expression, and ability to target various intraocular cell types. Different AAV serotypes (e.g., AAV2, AAV8, AAV9) exhibit distinct affinities for retinal pigment epithelial cells, retinal ganglion cells, and choroidal endothelial cells, allowing for tailored targeting based on specific cell types (71, 72). The tropism and delivery efficiency of AAVs are critical factors in ocular gene therapy. Certain serotypes, such as AAV2, AAV5, and AAV8, show strong tropism toward retinal pigment epithelial and photoreceptor cells, making them preferred vectors for treating inherited retinal diseases (IRDs), such as Leber congenital amaurosis (LCA) and retinitis pigmentosa (RP) (73). Notably, Luxturna (voretigene neparvovec), an AAV2-based gene therapy delivering the RPE65 gene, became the first FDA-approved gene therapy for LCA in 2017, marking a milestone in the clinical translation of AAV platforms in ophthalmology (74).

Currently, over 70 clinical trials involving AAV-mediated gene therapy are underway, targeting various pathogenic genes including CNGA3, RPGR, CHM, and ND4. These trials span a range of diseases such as RP, X-linked retinoschisis, choroideremia, and age-related macular degeneration (AMD) (71, 75–77). Clinically, AAVs offer several advantages, including low immunogenicity, non-integration into the host genome, and sustained expression in terminally differentiated cells like photoreceptors. However, limitations remain, such as restricted packaging capacity (~4.7 kb), suboptimal targeting specificity, and the risk of pre-existing neutralizing antibodies in some individuals (78–80). To address the challenge of large gene delivery, dual-vector systems have been developed, allowing the expression of oversized genes and expanding AAV applicability in complex ocular disorders (81, 82). Moreover, recent research focuses on identifying novel AAV variants with enhanced ocular tropism (e.g., AAV2tYF, AAV7m8) and optimizing administration routes—including intravitreal, subretinal, and suprachoroidal injections—to further improve efficacy and safety (83, 84).

In the context of UM, AAV has served as a valuable tool for disease modeling and therapeutic exploration. AAV-mediated gene manipulation enables highly specific genetic control in uveal melanocytes, facilitating precise modeling of tumor initiation and progression. For instance, AAV-Cre recombinase delivery was used to establish a UM mouse model, revealing that activation of the YAP/TAZ signaling pathway alone can drive tumorigenesis and synergize with Ras/MAPK signaling to accelerate progression. Subsequent experiments demonstrated that co-inhibition of YAP/TAZ and Ras/MAPK pathways significantly suppressed UM malignancy, suggesting a promising dual-target therapeutic strategy (85). In therapeutic research, AAVs have also been employed to deliver RNA interference molecules. One study delivered shRNA-expressing AAVs into UM xenografts to silence PCK1, a gene promoting UM proliferation via the Gαi3-Akt pathway, resulting in significant tumor growth inhibition *in vivo* (86). These studies highlight the multifaceted utility of AAV in both mechanistic investigations and therapeutic development for UM.

In addition to viral vectors like AAV, non-viral gene delivery strategies have also gained traction, offering new possibilities for gene editing and regulation. The CRISPR-Cas9 system, known for its high specificity and flexibility, has been used for correcting pathogenic mutations in various ocular diseases. In UM, researchers have explored lipid nanoparticle (LNP)-mediated delivery of CRISPR-Cas9 components to target and edit GNAQ oncogenic mutations. This approach achieved efficient and relatively safe genome editing *in vitro* and *in vivo*, demonstrating mutation

specificity and tumor-suppressive efficacy (87). Similarly, exosomes—due to their natural origin, excellent biocompatibility, and ability to cross biological barriers—have emerged as promising carriers for nucleic acid and gene delivery (88). Studies have utilized exosomes derived from retinal or stem cells to deliver miRNAs, siRNAs, or CRISPR components, aiming to modulate inflammation, angiogenesis, and oncogene expression, with early results supporting their feasibility in posterior segment disease treatment (89, 90). Although these non-viral vectors remain in early stages of development, their potential advantages in precision, safety, and delivery versatility are progressively expanding the scope of ocular gene therapy.

In summary, AAVs, CRISPR-Cas9-loaded lipid nanoparticles, and exosome-based platforms offer unique strengths and are collectively reshaping the treatment landscape for posterior segment disorders, particularly malignant conditions such as UM. Moving forward, enhancing delivery efficiency, cellular specificity, and safety will be pivotal for the successful clinical translation of gene therapies.

3.4 Emerging medical devices and treatment evolution

UM, the most common primary intraocular malignancy, is traditionally managed through radiation therapy (e.g., iodine-125 plaque brachytherapy) and surgical excision. However, these conventional approaches remain limited in their ability to fully control the tumor, preserve visual function, and prevent long-term metastasis (91, 92). In recent years, the integration of advanced engineering materials, microsystem technologies, and precision medicine has introduced a range of innovative medical devices and therapeutic strategies for UM, offering more targeted and controllable treatment options.

Among these, the ZAP-X stereotactic radiosurgery platform, a novel self-contained and self-shielded robotic system originally developed for treating brain and head-neck tumors, has recently been applied to UM management. This system employs three-dimensional imaging to precisely define tumor volumes and irradiation targets, combined with vacuum fixation and real-time infrared monitoring, to deliver single-session non-invasive radiation therapy. It eliminates the need for implant surgery and extended hospitalization required by traditional plaque therapy. Clinical data show that the ZAP-X system can effectively reduce tumor volume, with tumor control rates comparable to conventional radiotherapy and globe retention rates ranging from 78% to 97.4%. Its anesthesia-free, outpatient-based treatment model significantly enhances patient comfort and safety, representing a major advancement in radiotherapeutic management of UM (93).

In drug delivery, researchers have developed injectable, stimuli-responsive antibacterial hydrogels incorporating gold nanorods for synergistic photothermal therapy (PTT) and gene-targeted therapy. Upon near-infrared (NIR) light activation, this multifunctional platform enables on-demand drug release and gentle photothermal ablation of tumor cells. Additionally, its inherent antibacterial properties help prevent postoperative intraocular infections such as endophthalmitis, offering a minimally invasive approach that integrates precision drug release, thermal ablation, and infection control (94).

In the field of precision oncology, high-throughput genomic sequencing and molecular profiling technologies have enabled molecularly matched therapies for metastatic UM (95). Multidisciplinary tumor boards utilize whole-genome, exome, and transcriptome data to recommend targeted therapies, including MEK inhibitors, MET inhibitors, and immune checkpoint inhibitors. Clinical studies have shown that approximately 60% of patients receiving molecularly matched therapies experienced partial response or disease stabilization, with significantly prolonged progression-free and overall survival. This biomarker-driven strategy enhances therapeutic specificity and efficacy, surpassing outcomes achieved with conventional chemotherapy or immunotherapy.

Furthermore, single-cell technologies have been widely applied to dissect tumor heterogeneity, immune microenvironment, and metastatic potential in UM (21). Through single cell sequencing and cellular isolation, researchers can identify drug-resistant tumor subpopulations, immune cell interactions, and circulating tumor cells. These insights facilitate the development of personalized therapeutic strategies and offer a rational basis for targeting resistance mechanisms and metastatic pathways, ultimately contributing to long-term disease control.

In conclusion, emerging medical devices and therapeutic technologies are continuously expanding the landscape of UM treatment, significantly enriching the therapeutic arsenal. These innovations not only improve tumor control and preserve visual function while minimizing complications but also offer new hope for managing metastatic disease. Collectively, they are propelling UM treatment toward greater precision, minimal invasiveness, and personalized care.

4 Synergy of omics and materials: from bench to bedside

4.1 Potential targets for treating UM

UM is the most common primary intraocular malignancy. Although its incidence is relatively low, its high metastatic potential and poor prognosis make early targeted intervention a persistent clinical challenge. In recent years, advances in omics technologies have gradually elucidated the molecular mechanisms underlying UM, providing a valuable theoretical foundation for the development of targeted therapeutic strategies. Several potential therapeutic targets have been identified, along with corresponding research progress, as summarized in Table 2.

4.1.1 GNAQ and GNA11 mutations

Mutations in *GNAQ* and *GNA11* are found in over 80% of UM patients and represent the most common driver mutations in this malignancy. These mutations lead to aberrant activation of the MAPK/

ERK signaling pathway, thereby promoting tumor initiation and progression (5). In response to this mechanism, MEK inhibitors—such as trametinib and selumetinib—have been extensively studied as targeted therapies that inhibit downstream components of this pathway. By blocking MEK1/2, key kinases in the MAPK/ERK cascade, these agents effectively disrupt signal transduction and suppress tumor cell proliferation. Clinical data indicate that among 27 patients who received molecularly matched therapies, 15 were treated with MEK inhibitors, achieving a disease stabilization (SD) rate of 44% (96).

4.1.2 YAP/TAZ signaling pathway

The YAP/TAZ signaling pathway, as the downstream effector of the Hippo signaling cascade, plays a pivotal role in the initiation and progression of UM. YAP (Yes-associated protein) and TAZ (transcriptional coactivator with PDZ-binding motif) promote malignant progression by regulating key cellular processes such as proliferation, survival, and migration. Aberrant activation of this pathway is therefore considered a major oncogenic mechanism in UM (85).

Multiple studies have demonstrated that inhibiting YAP/TAZ function can effectively suppress UM cell growth and reduce metastatic potential. For instance, the drug verteporfin (VP) disrupts the interaction between YAP and its transcriptional partner TEAD, thereby inhibiting tumor cell proliferation (97). Moreover, combinatorial therapeutic strategies targeting YAP/TAZ alongside other oncogenic drivers have shown synergistic effects. A notable example is the dual inhibition of YAP/TAZ and the anti-apoptotic protein Mcl-1, which significantly enhances suppression of UM cell survival (98).

Currently, the development of YAP/TAZ-targeted inhibitors is ongoing, including small molecules that block TEAD function or modulate YAP/TAZ activity through alternative mechanisms. These emerging agents hold promises as effective therapies not only for UM but also for a broad range of solid tumors.

4.1.3 BAP1 gene mutations

BAP1 (BRCA1-associated protein 1) is a critical tumor suppressor gene, and its mutation is strongly associated with the aggressiveness and metastatic risk of UM (99). Studies have shown that loss of BAP1 protein expression or functional inactivation correlates with significantly reduced survival in UM patients. BAP1 mutations are frequently accompanied by monosomy 3, a chromosomal alteration that is a well-established predictor of metastasis in UM (100, 101).

Importantly, BAP1 mutations often arise during the early stages of tumorigenesis and are associated with larger tumor size and a markedly increased risk of metastasis. UM tumors harboring BAP1 mutations exhibit greater invasiveness and metastatic potential, leading to significantly shortened metastasis-free survival—averaging approximately 2.4 years (102). In addition to genetic alterations, the methylation status of the *BAP1* gene has also been identified as a crucial prognostic biomarker. Higher levels of *BAP1* promoter methylation are linked to poorer clinical outcomes (103).

Immunohistochemical detection of BAP1 protein expression has become an effective clinical tool for prognostic assessment in UM. Notably, it has demonstrated superior predictive value for overall survival (OS) compared to conventional staging systems and chromosomal analyses (100). Thus, *BAP1* mutations represent not only a key molecular mechanism underlying UM malignancy and metastasis but also a valuable basis for personalized treatment planning and risk stratification.

4.1.4 Metastasis-associated pathways: c-Met and CXCR4

UM is characterized by a high metastatic potential, with a strong predilection for hepatic dissemination. Consequently, targeting metastasis-associated signaling pathways has become a key therapeutic strategy in UM. Among these, *c-Met* and *CXCR4* have been identified as critical molecular drivers of metastatic progression.

c-Met, the receptor for hepatocyte growth factor (HGF), plays a central role in promoting tumor cell migration, invasion, and metastasis. Aberrant activation of the c-Met signaling pathway has been closely linked to hepatic tropism in UM. Inhibitors targeting c-Met are currently undergoing clinical investigation and have shown promise in suppressing UM metastasis, making c-Met one of the most important anti-metastatic therapeutic targets (104, 105).

CXCR4, a chemokine receptor, contributes to the chemotactic migration of tumor cells and facilitates their dissemination to distant organs such as the liver. High expression of CXCR4 has been associated with an increased risk of metastasis in UM. Therefore, CXCR4 inhibition holds potential for disrupting the metastatic process (106).

Additionally, mutations in the *SF3B1* gene have been linked to intermediate metastatic risk. Aberrant splicing patterns resulting from these mutations may influence tumor dissemination behavior and represent an emerging area for targeted therapeutic development (107).

In summary, inhibitors targeting *c-Met* and *CXCR4*, along with ongoing investigations into the role of *SF3B1* mutations, currently form the core of molecular strategies aimed at preventing UM metastasis. These targeted approaches hold the potential to significantly improve both survival outcomes and quality of life for patients with UM.

The prognostic and therapeutic implications of key targets like BAP1 and SF3B1 exhibit nuanced context-dependency, necessitating integrated multi-omics frameworks to resolve discordant signals. For BAP1, spatial transcriptomics reconciles the paradox of genomic loss (strongly metastatic, HR > 5) coexisting with transcriptomic immune infiltration: $CD8^+$T cells preferentially localize to BAP1-intact regions (*in situ* immune "hotspots"), while BAP1-null zones exhibit TGFβ-dominated fibrotic immunosuppression. This spatial segregation mandates a *hierarchical evidence rule*: genomic alterations > spatial microenvironment > bulk transcriptomics for metastasis risk stratification, though immune-rich BAP1-intact niches may retain

susceptibility to checkpoint inhibitors. For SF3B1, single-cell multi-omics (scRNA-seq + scATAC-seq) deciphers heterogeneous outcomes: only mutations coupled with open chromatin at chr8q24 (*MYC* locus) or chr7q31 (*MET* locus) drive lethal metastasis via BRD9 mis-splicing and MET enhancer activation. Thus, a unified decision heuristic emerges: *Discordant oncogenic/immune signals are resolved by cross-validating (1) genomic alterations with epigenetic chromatin accessibility, and (2) bulk signatures with spatial cellular mapping to identify dominant biological drivers.

4.1.5 Cell cycle regulators and the MYC pathway

Amplification of the *MYC* gene and dysregulation of cell cycle-related pathways are frequently observed in UM, and both contribute synergistically to tumor initiation and progression. More than 80% of UM patients exhibit *MYC* amplification, with expression levels positively correlated with tumor size. *MYC* promotes tumor aggressiveness by enhancing cell proliferation and metastatic potential, and is strongly associated with monosomy 3, suggesting it may function as an independent driver of tumor progression (108, 109).

Cell cycle abnormalities are also common in UM, including deletions of *CDKN2A* and amplifications of *CCND1/2/3* and *CDK6*. These genetic alterations disrupt normal cell cycle control, enabling unchecked cell division. The *CDKN2A* gene encodes the tumor suppressor proteins p16^INK4a and p14^ARF, which are critical regulators of the G1/S transition. Loss of *CDKN2A* function leads to sustained activation of CDK4/6, thereby facilitating uncontrolled tumor growth (110, 111).

Based on these molecular insights, CDK4/6 inhibitors (e.g., palbociclib) and BET inhibitors (e.g., mivebresib) have emerged as promising therapeutic candidates in UM (110, 112). CDK4/6 inhibitors can arrest aberrant cell cycle progression, while BET inhibitors suppress MYC transcriptional activity, thereby targeting MYC-driven UM. Combinatorial approaches that simultaneously target both the MYC and cell cycle pathways hold significant potential for developing personalized treatment regimens for UM patients.

4.1.6 Anti-angiogenic therapy

The growth of UM is also dependent on tumor angiogenesis, with vascular endothelial growth factor (VEGF) and its receptors being highly expressed in UM. These factors play a pivotal role in promoting tumor progression and metastasis (113). VEGF is a key regulator of vascular permeability, endothelial cell proliferation, and migration. Its levels are significantly elevated in UM patients, particularly those with metastatic disease. Excessive VEGF expression not only facilitates neovascularization but also contributes to hematogenous dissemination of tumor cells, which is one of the leading causes of mortality in UM patients (114).

Bevacizumab, a humanized monoclonal antibody targeting VEGF, inhibits angiogenesis by blocking the binding of VEGF to its receptors, thereby suppressing endothelial cell proliferation and vessel formation. It has become a widely used anti-angiogenic agent in the treatment of various malignancies, including melanoma (115). Although anti-angiogenic therapy is not yet a standard treatment for UM, and its efficacy in both primary and metastatic UM requires further clinical validation, existing studies suggest it holds potential as an adjuvant therapeutic option (116). In addition, novel multi-targeted inhibitors such as nintedanib have demonstrated inhibitory effects on primary UM cells, though their efficacy against metastases remains limited (117).

A major current challenge is the potential for resistance to VEGF-targeted monotherapy. Future strategies may involve combination regimens that integrate anti-angiogenic agents with other modalities—such as immunotherapy or PARP inhibitors—to enhance overall therapeutic efficacy.

Overall, anti-angiogenic therapy represents a promising avenue for UM treatment, though broader clinical application will require further substantiation through well-designed trials.

4.1.7 PRAME antigen

Preferentially expressed antigen in melanoma (PRAME) has recently gained attention as a highly relevant immunotherapeutic target in UM (118). PRAME is a cancer-testis antigen that is minimally expressed in normal adult tissues but frequently upregulated in UM, particularly in high-risk tumors associated with monosomy 3 and BAP1 loss [36788079]. Elevated PRAME expression correlates with poor prognosis and metastatic potential, positioning it as both a biomarker and a therapeutic candidate.

In UM, PRAME is expressed in a substantial subset of tumors, typically ranging from about one-quarter to nearly half of reported cases, and its presence consistently correlates with unfavorable clinical features. High PRAME expression has been associated with larger tumor size, advanced TNM stage, frequent chromosome 8q gain, and an inflammatory phenotype, all of which contribute to its prognostic value. Importantly, PRAME-specific T cell receptor (TCR)-transduced T cells have demonstrated the ability to selectively kill UM cells in preclinical studies, underscoring its therapeutic relevance (119). Collectively, these findings highlight PRAME not only as a biomarker of high-risk disease but also as a promising candidate for adjuvant immunotherapy in UM.

In conclusion, targeted therapy for uveal melanoma is rapidly evolving toward multi-targeted and personalized approaches. Omics-based insights have highlighted biomarkers such as *GNAQ/GNA11*, *BAP1*, *MET*, *MYC*, and high tumor mutational burden (TMB) as critical foundations for precision medicine. Future therapeutic strategies are likely to integrate multiple targeted agents with immunotherapies, offering expanded treatment horizons and improved outcomes for patients with UM.

4.2 Potential ways of integrating medicine and engineering

With the ongoing convergence of medicine and engineering, particularly by advances in precision medicine and biomedical technologies—interdisciplinary integration has emerged as a vital pathway for improving therapeutic outcomes and patient quality of

life. In the treatment of UM, the integration of medical and engineering innovations is playing an increasingly pivotal role, fostering novel therapeutic strategies and advancing clinical interventions.

4.2.1 Smart drug delivery systems

Drug delivery systems represent a key area of medicine–engineering integration, particularly in UM treatment, where precise drug targeting is essential for maximizing efficacy while minimizing side effects. Through micro- and nanotechnology, researchers have developed targeted drug delivery platforms that combine nanomaterials (e.g., nanoparticles, nanocapsules) with engineered liposomes to deliver anticancer agents or gene editing tools directly to tumor sites. These systems not only facilitate effective penetration across ocular barriers but also enable sustained and controlled drug release, thereby significantly enhancing the specificity and effectiveness of UM therapies (15, 16).

4.2.2 Photodynamic therapy and optical engineering

Photodynamic therapy (PDT) is an effective approach for treating UM, based on the principle that photosensitizers produce reactive oxygen species (ROS) upon activation by near-infrared (NIR) light, leading to selective tumor cell destruction. In recent years, the integration of optical engineering and nanotechnology has led to the development of advanced photosensitizer carriers and laser delivery systems capable of precisely targeting tumor regions while minimizing damage to surrounding healthy tissues. For example, the combination of miniaturized laser devices with high-efficiency photosensitizers enables localized irradiation of the tumor without compromising retinal structure, thereby enhancing therapeutic outcomes (120).

Moreover, PDT has been shown to stimulate the immune response by inducing the secretion of pro-inflammatory and antitumor cytokines such as IL-6, IL-1, and TNF-α. This immune activation enhances systemic tumor control and reduces the risk of progression and metastasis (121). PDT has demonstrated safety and efficacy in treating small, pigmented UM lesions and is emerging as a minimally invasive, highly targeted therapeutic modality. Although current treatments remain limited in effectiveness—with approximately 50% of patients developing metastases, the advancement of multiphoton excitation techniques in PDT offers new therapeutic possibilities (122). Further studies in animal models and clinical trials are needed to develop specialized devices and translate PDT innovations into routine clinical practice.

4.2.3 3D printing and personalized medicine

3D printing technology has become increasingly established in medicine and shows considerable promise in the treatment of UM. By creating patient-specific printed tumor models, researchers can simulate drug delivery and surgical resection strategies in a virtual environment, enabling the design of highly personalized treatment plans. These individualized 3D-printed tumor replicas allow for more accurate evaluation of therapeutic efficacy and assist clinicians with preoperative planning and risk assessment (123).

Additionally, the development of customized ocular implants using 3D printing offers UM patients more personalized therapeutic options. For instance, patient-specific radiotherapy plaques or structural supports can be fabricated to restore vision and ocular function, enhancing post-treatment quality of life (124).

4.2.4 Artificial intelligence and imaging analysis

The integration of artificial intelligence (AI) and imaging technologies holds tremendous potential in the diagnosis and

TABLE 3 Target-delivery synthesis matrix.

Target category	Molecular target	Optimal delivery platform	Biological rationale	Anticipated translational hurdles
Oncogenic Signaling	GNAQ/ GNA11	Ligand-targeted nanocarriers (e.g., CD44-HA NPs)	Membrane-bound GPCRs require rapid cytoplasmic delivery of small-molecule inhibitors (e.g., MEKi). Surface-modified NPs enhance trans-scleral permeability.	Limited tumor penetration in avascular regions; burst release toxicity.
Transcriptional Regulators	YAP/TAZ	Tropism-enhanced AAVs (e.g., AAV2tYF)	Nuclear localization necessitates sustained CRISPR-mediated gene editing. AAVs achieve long-term expression in uveal melanocytes.	Pre-existing neutralizing antibodies (~30% patients); packaging capacity limits (<4.7 kb).
Spliceosome Mutations	SF3B1	pH-responsive lipid nanoparticles (LNPs)	Mutant SF3B1 drives cytoplasmic mis-splicing. LNPs deliver splice-switching oligonucleotides (SSOs) with efficient endosomal escape.	RNA payload degradation in vitreous; batch-to-batch variability.
Metastasis Drivers	c-MET/CXCR4	Implantable sustained-release systems (e.g., PLGA microfilms)	Chemokine receptors require continuous pathway blockade. Biodegradable implants maintain stable drug concentrations (>3 months).	Fibrotic encapsulation reducing drug diffusion; surgical implantation complexity.
Tumor Suppressors	BAP1	Dual AAV vectors	Functional restoration requires genomic integration of large cDNA sequences (~4.8 kb). Dual-vector systems enable oversized gene delivery.	Immune clearance; risk of genomic insertional mutagenesis.
Immunomodulators	LAG3/ PRAME*	Exosome-based platforms	Immune checkpoint proteins demand spatiotemporal modulation. Autologous exosomes evade clearance and deliver miRNAs/siRNAs to TAMs.	Scalable GMP production challenges; low payload loading efficiency.

treatment of UM. Leveraging deep learning and convolutional neural networks (CNNs), AI can automatically analyze multimodal imaging data—including fundus photography, optical coherence tomography (OCT), and ultrasound—to accurately extract tumor features, thereby significantly improving diagnostic accuracy and efficiency (125). AI systems can assist in early screening, tumor localization, and morphological assessment, as well as play critical roles in radiotherapy planning and postoperative surveillance.

Moreover, by integrating pathological and genomic data, AI is driving the advancement of personalized medicine in UM. However, several challenges remain, including data scarcity, clinical integration, and model interpretability. With ongoing technological progress, the application of AI in imaging analysis is expected to become a routine tool in UM management, enhancing clinical decision-making and improving patient outcomes (126).

4.2.5 Minimally invasive and robot-assisted surgery

As robotic technologies continue to advance, minimally invasive surgical approaches are becoming increasingly prevalent in the treatment of UM. Robot-assisted stereotactic radiosurgery (SRS) systems such as CyberKnife and ZAP-X offer high-precision, single-session, non-invasive treatments that eliminate the need for surgical implantation of radioactive plaques and prolonged hospitalization associated with traditional radiotherapy (93, 127).

These robotic systems utilize multimodal imaging (MRI, CT, ultrasound) to perform three-dimensional tumor localization and dose planning, ensuring accurate tumor coverage while preserving surrounding healthy tissue. Clinical studies have reported globe retention rates of 73% to 87% and local tumor control rates of approximately 70% to 90% at a median follow-up of 3 to 5 years, with most patients maintaining functional vision (128). In addition, robotic SRS treatments are typically performed on an outpatient basis, requiring only local anesthesia and avoiding craniotomy or enucleation, thereby greatly reducing patient discomfort and recovery time. The safety, efficacy, and patient tolerability of these systems have been well demonstrated, representing a significant shift toward minimally invasive, precise, and personalized UM therapy.

In summary, minimally invasive robot-assisted radiosurgery is becoming a mainstream option for UM treatment. Combining effective tumor control with ocular preservation, this approach offers patients a safer, more comfortable therapeutic experience and reflects the future direction of advanced ophthalmic oncology care.

4.2.6 Biomaterials and tissue engineering

The integration of biomaterials and tissue engineering offers a novel direction for the treatment of UM. By utilizing 3D-printed or biodegradable biomaterials, it is now possible to fabricate personalized implants, such as structural supports for post-tumor resection or bioengineered scaffolds for regional tissue repair (129). Moreover, the combination of biomaterials with stem cell therapies facilitates ocular tissue regeneration and repair, providing UM patients with improved postoperative recovery options.

Practical applications include patient-specific 3D-printed implants, biodegradable scaffolds, stem cell carriers, and systems designed to modulate tissue regeneration via growth factors or microenvironmental cues (130). As materials science and regenerative medicine continue to advance, biomaterials and tissue engineering are expected to become integral components of UM treatment, driving progress toward precision and personalized care.

In summary, innovative medicine–engineering integration strategies have introduced new paradigms for the treatment of uveal melanoma. These technologies—including smart drug delivery systems, photodynamic therapy, 3D printing, artificial intelligence, robotic-assisted surgery, and tissue engineering—not only offer more effective and individualized treatment options but also align with broader movement toward precision, personalized, and minimally invasive oncology. As technological innovation and interdisciplinary collaboration deepen, medicine–engineering convergence is poised to deliver further breakthroughs in UM treatment, significantly improving patient survival and quality of life.

4.2.7 Target-delivery synthesis matrix

Furthermore, we have added a dedicated section integrating multi-omics insights into dosing regimens. Building on previous work, Table 3 provides recommended combination strategies for different targets.

5 Future expectation

The eye represents a highly specialized organ system where cutting-edge biomaterials demonstrate significant potential for treating related diseases. UM, one of the most critical ocular malignancies, still necessitates more advanced and effective first-line therapies. Recent advances in single-cell omics have meticulously delineated the tumor immune microenvironment and pathogenic mechanisms, offering unprecedented insights. The integration of these insights with emerging materials science presents a promising avenue to overcome the challenges of UM treatment. This review aims to contribute to the advancement of therapeutic strategies for this disease. We first catalog material-based approaches applicable to UM therapy and summarize currently targetable key molecular pathways. Looking ahead, researchers in the field are encouraged to strategically combine these modalities to facilitate successful translation from laboratory findings to clinical applications.

Author contributions

SF: Writing – original draft. CL: Writing – review & editing.

Funding

The author(s) declare that no financial support was received for the research, and/or publication of this article.

Conflict of interest

The authors declare that the research was conducted in the absence of any commercial or financial relationships that could be construed as a potential conflict of interest.

Generative AI statement

The author(s) declare that no Generative AI was used in the creation of this manuscript.

Any alternative text (alt text) provided alongside figures in this article has been generated by Frontiers with the support of artificial intelligence and reasonable efforts have been made to ensure accuracy, including review by the authors wherever possible. If you identify any issues, please contact us.

Publisher's note

All claims expressed in this article are solely those of the authors and do not necessarily represent those of their affiliated organizations, or those of the publisher, the editors and the reviewers. Any product that may be evaluated in this article, or claim that may be made by its manufacturer, is not guaranteed or endorsed by the publisher.

References

1. Shields CL, Furuta M, Thangappan A, Nagori S, Mashayekhi A, Lally DR, et al. Metastasis of uveal melanoma millimeter-by-millimeter in 8033 consecutive eyes. *Arch Ophthalmol (Chicago Ill: 1960)*. (2009) 127:989–98. doi: 10.1001/archophthalmol.2009.208

2. Prescher G, Bornfeld N, Hirche H, Horsthemke B, Jöckel KH, Becher R. Prognostic implications of monosomy 3 in uveal melanoma. *Lancet (London England)*. (1996) 347:1222–5. doi: 10.1016/s0140-6736(96)90736-9

3. Ehlers JP, Worley L, Onken MD, Harbour JW. DDEF1 is located in an amplified region of chromosome 8q and is overexpressed in uveal melanoma. *Clin Cancer Res*. (2005) 11:3609–13. doi: 10.1158/1078-0432.Ccr-04-1941

4. Helgadottir H, Höiom V. The genetics of uveal melanoma: current insights. *Appl Clin Genet*. (2016) 9:147–55. doi: 10.2147/tacg.S69210

5. Silva-Rodríguez P, Fernández-Díaz D, Bande M, Pardo M, Loidi L, Blanco-Teijeiro MJ. GNAQ and GNA11 genes: A comprehensive review on oncogenesis, prognosis and therapeutic opportunities in uveal melanoma. *Cancers*. (2022) 14. doi: 10.3390/cancers14133066

6. Krantz BA, Dave N, Komatsubara KM, Marr BP, Carvajal RD. Uveal melanoma: epidemiology, etiology, and treatment of primary disease. *Clin Ophthalmol (Auckland N.Z.)*. (2017) 11:279–89. doi: 10.2147/opth.S89591

7. Xu Y, Lou L, Wang Y, Miao Q, Jin K, Chen M, et al. Epidemiological study of uveal melanoma from US surveillance, epidemiology, and end results program (2010-2015). *J ophthalmol*. (2020) 2020:3614039. doi: 10.1155/2020/3614039

8. Brănișteanu DE, Porumb-Andrese E, Stărică A, Munteanu AC, Toader MP, Zemba M, et al. Differences and similarities in epidemiology and risk factors for cutaneous and uveal melanoma. *Medicina (Kaunas Lithuania)*. (2023) 59. doi: 10.3390/medicina59050943

9. Carvajal RD, Sacco JJ, Jager MJ, Eschelman DJ, Olofsson Bagge R, Harbour JW, et al. Advances in the clinical management of uveal melanoma. *Nat Rev Clin Oncol*. (2023) 20:99–115. doi: 10.1038/s41571-022-00714-1

10. Switzer B, Piperno-Neumann S, Lyon J, Buchbinder E, Puzanov I. Evolving management of stage IV melanoma. *Am Soc Clin Oncol Educ book*. (2023) 43:e397478. doi: 10.1200/edbk_397478

11. Assessment of metastatic disease status at death in 435 patients with large choroidal melanoma in the Collaborative Ocular Melanoma Study (COMS): COMS report no. 15. *Arch Ophthalmol (Chicago Ill: 1960)*. (2001) 119:670–6. doi: 10.1001/archopht.119.5.670

12. Khoja L, Atenafu EG, Suciu S, Leyvraz S, Sato T, Marshall E, et al. Meta-analysis in metastatic uveal melanoma to determine progression free and overall survival benchmarks: an international rare cancers initiative (IRCI) ocular melanoma study. *Ann Oncol*. (2019) 30:1370–80. doi: 10.1093/annonc/mdz176

13. Bale S, Khurana A, Reddy AS, Singh M, Godugu C. Overview on therapeutic applications of microparticulate drug delivery systems. *Crit Rev Ther Drug carrier systems*. (2016) 33:309–61. doi: 10.1615/CritRevTherDrugCarrierSyst.2016015798

14. Gote V, Sikder S, Sicotte J, Pal D. Ocular drug delivery: present innovations and future challenges. *J Pharmacol Exp Ther*. (2019) 370:602–24. doi: 10.1124/jpet.119.256933

15. You S, Luo J, Grossniklaus HE, Gou ML, Meng K, Zhang Q. Nanomedicine in the application of uveal melanoma. *Int J ophthalmol*. (2016) 9:1215–25. doi: 10.18240/ijo.2016.08.20

16. Wang Z, Yu Y, Wang C, Li J, Pang Y. Advances in the application of nanomaterials to the treatment of melanoma. *Pharmaceutics*. (2022) 14. doi: 10.3390/pharmaceutics14102090

17. Wan R, Pan L, Wang Q, Shen G, Guo R, Qin Y, et al. Decoding gastric cancer: machine learning insights into the significance of COMMDs family in immunotherapy and diagnosis. *J Cancer*. (2024) 15:3580–95. doi: 10.7150/jca.94360

18. Li Z, Wang Q, Huang X, Fu R, Wen X, Zhang L. Multi-omics analysis reveals that ferroptosis-related gene CISD2 is a prognostic biomarker of head and neck squamous cell carcinoma. *J Gene Med*. (2024) 26:e3580. doi: 10.1002/jgm.3580

19. Zhao S, Wang Q, Liu Y, Zhang P, Ji W, Xie J, et al. Interaction, immune infiltration characteristics and prognostic modeling of efferocytosis-related subtypes in glioblastoma. *BMC Med Genomics*. (2023) 16:248. doi: 10.1186/s12920-023-01688-4

20. Ye B, Wang Q, Zhu X, Zeng L, Luo H, Xiong Y, et al. Single-cell RNA sequencing identifies a novel proliferation cell type affecting clinical outcome of pancreatic ductal adenocarcinoma. *Front Oncol*. (2023) 13:1236435. doi: 10.3389/fonc.2023.1236435

21. Wang MM, Chen C, Lynn MN, Figueiredo CR, Tan WJ, Lim TS, et al. Applying single-cell technology in uveal melanomas: current trends and perspectives for improving uveal melanoma metastasis surveillance and tumor profiling. *Front Mol biosciences*. (2020) 7:611584. doi: 10.3389/fmolb.2020.611584

22. Li K, Sun L, Wang Y, Cen Y, Zhao J, Liao Q, et al. Single-cell characterization of macrophages in uveal melanoma uncovers transcriptionally heterogeneous subsets conferring poor prognosis and aggressive behavior. *Exp Mol Med*. (2023) 55:2433–44. doi: 10.1038/s12276-023-01115-9

23. Tang S, Zhang Y, Huang S, Zhu T, Huang X. Single cell RNA-sequencing in uveal melanoma: advances in heterogeneity, tumor microenvironment and immunotherapy. *Front Immunol*. (2024) 15:1427348. doi: 10.3389/fimmu.2024.1427348

24. Wang Y, Fan JL, Melms JC, Amin AD, Georgis Y, Barrera I, et al. Multimodal single-cell and whole-genome sequencing of small, frozen clinical specimens. *Nat Genet*. (2023) 55:19–25. doi: 10.1038/s41588-022-01268-9

25. Bronkhorst IH, Jager MJ. Uveal melanoma: the inflammatory microenvironment. *J innate immunity*. (2012) 4:454–62. doi: 10.1159/000334576

26. Folberg R, Arbieva Z, Moses J, Hayee A, Sandal T, Kadkol S, et al. Tumor cell plasticity in uveal melanoma: microenvironment directed dampening of the invasive and metastatic genotype and phenotype accompanies the generation of vasculogenic mimicry patterns. *Am J pathol*. (2006) 169:1376–89. doi: 10.2353/ajpath.2006.060223

27. Wang Y, Xu Y, Dai X, Lin X, Shan Y, Ye J. The prognostic landscape of adaptive immune resistance signatures and infiltrating immune cells in the tumor microenvironment of uveal melanoma. *Exp eye Res*. (2020) 196:108069. doi: 10.1016/j.exer.2020.108069

28. Qin Y, Bollin K, de Macedo MP, Carapeto F, Kim KB, Roszik J, et al. Immune profiling of uveal melanoma identifies a potential signature associated with response to immunotherapy. *J immunother Cancer*. (2020) 8. doi: 10.1136/jitc-2020-000960

29. Tosi A, Cappellesso R, Dei Tos AP, Rossi V, Aliberti C, Pigozzo J, et al. The immune cell landscape of metastatic uveal melanoma correlates with overall survival. *J Exp Clin Cancer research: CR*. (2021) 40:154. doi: 10.1186/s13046-021-01947-1

30. Zhao J, Yi Q, Li K, Chen L, Dai L, Feng J, et al. A multi-omics deep learning model for hypoxia phenotype to predict tumor aggressiveness and prognosis in uveal melanoma for rationalized hypoxia-targeted therapy. *Comput Struct Biotechnol J*. (2022) 20:3182–94. doi: 10.1016/j.csbj.2022.06.034

31. Heppt MV, Steeb T, Schlager JG, Rosumeck S, Dressler C, Ruzicka T, et al. Immune checkpoint blockade for unresectable or metastatic uveal melanoma: A systematic review. *Cancer Treat Rev*. (2017) 60:44–52. doi: 10.1016/j.ctrv.2017.08.009

32. Algazi AP, Tsai KK, Shoushtari AN, Munhoz RR, Eroglu Z, Piulats JM, et al. Clinical outcomes in metastatic uveal melanoma treated with PD-1 and PD-L1 antibodies. *Cancer*. (2016) 122:3344–53. doi: 10.1002/cncr.30258

33. Luke JJ, Callahan MK, Postow MA, Romano E, Ramaiya N, Bluth M, et al. Clinical activity of ipilimumab for metastatic uveal melanoma: a retrospective review of the Dana-Farber Cancer Institute, Massachusetts General Hospital, Memorial Sloan-Kettering Cancer Center, and University Hospital of Lausanne experience. *Cancer*. (2013) 119:3687–95. doi: 10.1002/cncr.28282

34. Mäkitie T, Summanen P, Tarkkanen A, Kivelä T. Tumor-infiltrating macrophages (CD68(+) cells) and prognosis in Malignant uveal melanoma. *Invest Ophthalmol Visual science*. (2001) 42:1414–21.

35. Maat W, Ly LV, Jordanova ES, de Wolff-Rouendaal D, Schalij-Delfos NE, Jager MJ. Monosomy of chromosome 3 and an inflammatory phenotype occur together in uveal melanoma. *Invest Ophthalmol Visual science*. (2008) 49:505–10. doi: 10.1167/iovs.07-0786

36. Bronkhorst IH, Ly LV, Jordanova ES, Vrolijk J, Versluis M, Luyten GP, et al. Detection of M2-macrophages in uveal melanoma and relation with survival. *Invest Ophthalmol Visual science*. (2011) 52:643–50. doi: 10.1167/iovs.10-5979

37. Herwig MC, Bergstrom C, Wells JR, Höller T, Grossniklaus HE. M2/M1 ratio of tumor associated macrophages and PPAR-gamma expression in uveal melanomas with class 1 and class 2 molecular profiles. *Exp eye Res*. (2013) 107:52–8. doi: 10.1016/j.exer.2012.11.012

38. Onken MD, Worley LA, Ehlers JP, Harbour JW. Gene expression profiling in uveal melanoma reveals two molecular classes and predicts metastatic death. *Cancer Res*. (2004) 64:7205–9. doi: 10.1158/0008-5472.Can-04-1750

39. Sun Y, Wu J, Zhang Q, Wang P, Zhang J, Yuan Y. Single-cell hdWGCNA reveals metastatic protective macrophages and development of deep learning model in uveal melanoma. *J Trans Med*. (2024) 22:695. doi: 10.1186/s12967-024-05421-2

40. Trimm E, Red-Horse K. Vascular endothelial cell development and diversity. *Nat Rev Cardiol*. (2023) 20:197–210. doi: 10.1038/s41569-022-00770-1

41. Zeng Q, Mousa M, Nadukkandy AS, Franssens L, Alnaqbi H, Alshamsi FY, et al. Understanding tumour endothelial cell heterogeneity and function from single-cell omics. *Nat Rev Cancer*. (2023) 23:544–64. doi: 10.1038/s41568-023-00591-5

42. Ma L, He X, Fu Y, Ge S, Yang Z. Senescent endothelial cells promote liver metastasis of uveal melanoma in single-cell resolution. *J Trans Med*. (2024) 22:605. doi: 10.1186/s12967-024-05430-1

43. Karlsson JW, Sah VR, Olofsson Bagge R, Kuznetsova I, Iqba M, Alsen S, et al. Patient-derived xenografts and single-cell sequencing identifies three subtypes of tumor-reactive lymphocytes in uveal melanoma metastases. *eLife*. (2024) 12. doi: 10.7554/eLife.91705

44. Chen S, Tang Z, Wan Q, Huang W, Li X, Huang X, et al. Machine learning and single-cell RNA sequencing reveal relationship between intratumor CD8(+) T cells and uveal melanoma metastasis. *Cancer Cell Int*. (2024) 24:359. doi: 10.1186/s12935-024-03539-3

45. Johnson DB, Bao R, Ancell KK, Daniels AB, Wallace D, Sosman JA, et al. Response to anti-PD-1 in uveal melanoma without high-volume liver metastasis. *J Natl Compr Cancer Network: JNCCN*. (2019) 17:114–17. doi: 10.6004/jnccn.2018.7070

46. Piulats JM, Espinosa E, de la Cruz Merino L, Varela M, Alonso Carrión L, Martín-Algarra S, et al. Nivolumab plus ipilimumab for treatment-naïve metastatic uveal melanoma: an open-label, multicenter, phase II trial by the Spanish multidisciplinary melanoma group (GEM-1402). *J Clin Oncol*. (2021) 39:586–98. doi: 10.1200/jco.20.00550

47. Pelster MS, Gruschkus SK, Bassett R, Gombos DS, Shephard M, Posada L, et al. Nivolumab and ipilimumab in metastatic uveal melanoma: results from a single-arm phase II study. *J Clin Oncol*. (2021) 39:599–607. doi: 10.1200/jco.20.00605

48. Najjar YG, Navrazhina K, Ding F, Bhatia R, Tsai K, Abbate K, et al. Ipilimumab plus nivolumab for patients with metastatic uveal melanoma: a multicenter, retrospective study. *J immunother Cancer*. (2020) 8. doi: 10.1136/jitc-2019-000331

49. Jespersen H, Olofsson Bagge R, Ullenhag G, Carneiro A, Helgadottir H, Ljuslinder I, et al. Concomitant use of pembrolizumab and entinostat in adult patients with metastatic uveal melanoma (PEMDAC study): protocol for a multicenter phase II open label study. *BMC cancer*. (2019) 19:415. doi: 10.1186/s12885-019-5623-3

50. Ny L, Jespersen H, Karlsson J, Alsén S, Filges S, All-Eriksson C, et al. The PEMDAC phase 2 study of pembrolizumab and entinostat in patients with metastatic uveal melanoma. *Nat Commun*. (2021) 12:5155. doi: 10.1038/s41467-021-25332-w

51. Damato BE, Dukes J, Goodall H, Carvajal RD. Tebentafusp: T cell redirection for the treatment of metastatic uveal melanoma. *Cancers*. (2019) 11. doi: 10.3390/cancers11070971

52. Middleton MR, McAlpine C, Woodcock VK, Corrie P, Infante JR, Steven NM, et al. Tebentafusp, A TCR/anti-CD3 bispecific fusion protein targeting gp100, potently activated antitumor immune responses in patients with metastatic melanoma. *Clin Cancer Res*. (2020) 26:5869–78. doi: 10.1158/1078-0432.Ccr-20-1247

53. Olofsson Bagge R, Nelson A, Shafazand A, All-Eriksson C, Cahlin C, Elander N, et al. Isolated hepatic perfusion with melphalan for patients with isolated uveal melanoma liver metastases: A multicenter, randomized, open-label, phase III trial (the SCANDIUM trial). *J Clin Oncol*. (2023) 41:3042–50. doi: 10.1200/jco.22.01705

54. Ben-Shabat I, Belgrano V, Ny L, Nilsson J, Lindnér P, Olofsson Bagge R. Long-Term follow-Up evaluation of 68 patients with uveal melanoma liver metastases treated with isolated hepatic perfusion. *Ann Surg Oncol*. (2016) 23:1327–34. doi: 10.1245/s10434-015-4982-5

55. Gabai A, Zeppieri M, Finocchio L, Salati C. Innovative strategies for drug delivery to the ocular posterior segment. *Pharmaceutics*. (2023) 15. doi: 10.3390/pharmaceutics15071862

56. Cimino C, Sánchez López E, Bonaccorso A, Bonilla L, Musumeci T, Badia J, et al. *In vitro* and *in vivo* studies of ocular topically administered NLC for the treatment of uveal melanoma. *Int J pharmaceutics*. (2024) 660:124300. doi: 10.1016/j.ijpharm.2024.124300

57. Song H, Xu Q, Zhu Y, Zhu S, Tang H, Wang Y, et al. Serum adsorption, cellular internalization and consequent impact of cuprous oxide nanoparticles on uveal melanoma cells: implications for cancer therapy. *Nanomed (London England)*. (2015) 10:3547–62. doi: 10.2217/nnm.15.178

58. Song M, Zhu L, Zhang L, Ge X, Cao J, Teng Y, et al. Combination of molecule-targeted therapy and photodynamic therapy using nanoformulated verteporfin for effective uveal melanoma treatment. *Mol pharmaceutics*. (2024) 21:2340–50. doi: 10.1021/acs.molpharmaceut.3c01117

59. Branisteanu DC, Bogdanici CM, Branisteanu DE, Maranduca MA, Zemba M, Balta F, et al. Uveal melanoma diagnosis and current treatment options (Review). *Exp Ther Med*. (2021) 22:1428. doi: 10.3892/etm.2021.10863

60. Falavarjani KG, Nguyen QD. Adverse events and complications associated with intravitreal injection of anti-VEGF agents: a review of literature. *Eye (London England)*. (2013) 27:787–94. doi: 10.1038/eye.2013.107

61. Lee SS, Hughes P, Ross AD, Robinson MR. Biodegradable implants for sustained drug release in the eye. *Pharm Res*. (2010) 27:2043–53. doi: 10.1007/s11095-010-0159-x

62. de Smet MD. Corticosteroid intravitreal implants. *Developments Ophthalmol*. (2012) 51:122–33. doi: 10.1159/000336330

63. Makadia HK, Siegel SJ. Poly lactic-co-Glycolic acid (PLGA) as biodegradable controlled drug delivery carrier. *Polymers*. (2011) 3:1377–97. doi: 10.3390/polym3031377

64. Sharma AK, Arya A, Sahoo PK, Majumdar DK. Overview of biopolymers as carriers of antiphlogistic agents for treatment of diverse ocular inflammations. *Materials Sci engineering C Materials Biol applications*. (2016) 67:779–91. doi: 10.1016/j.msec.2016.05.060

65. Das S, Khuda-Bukhsh AR. PLGA-loaded nanomedicines in melanoma treatment: Future prospect for efficient drug delivery. *Indian J Med Res*. (2016) 144:181–93. doi: 10.4103/0971-5916.195024

66. Allyn MM, Luo RH, Hellwarth EB, Swindle-Reilly KE. Considerations for polymers used in ocular drug delivery. *Front Med*. (2021) 8:787644. doi: 10.3389/fmed.2021.787644

67. Tsung TH, Chen YH, Lu DW. Updates on biodegradable formulations for ocular drug delivery. *Pharmaceutics*. (2023) 15. doi: 10.3390/pharmaceutics15030734

68. Bahuon F, Darcos V, Patel S, Marin Z, Coudane J, Schwach G, et al. Polyester-polydopamine copolymers for intravitreal drug delivery: role of polydopamine drug-binding properties in extending drug release. *Biomacromolecules*. (2022) 23:4388–400. doi: 10.1021/acs.biomac.2c00843

69. Ng XW, Liu KL, Veluchamy AB, Lwin NC, Wong TT, Venkatraman SS. A biodegradable ocular implant for long-term suppression of intraocular pressure. *Drug delivery Trans Res*. (2015) 5:469–79. doi: 10.1007/s13346-015-0240-4

70. Banou L, Sarrafpour S, Teng CC, Liu J. Ocular gene therapy: an overview of viral vectors, immune responses, and future directions. *Yale J Biol Med*. (2024) 97:491–503. doi: 10.59249/hwid7537

71. He X, Fu Y, Ma L, Yao Y, Ge S, Yang Z, et al. AAV for gene therapy in ocular diseases: progress and prospects. *Res (Washington D.C.)*. (2023) 6:291. doi: 10.34133/research.0291

72. Xia X, Guo X. Adeno-associated virus vectors for retinal gene therapy in basic research and clinical studies. *Front Med*. (2023) 10:1310050. doi: 10.3389/fmed.2023.1310050

73. Padhy SK, Takkar B, Narayanan R, Venkatesh P, Jalali S. Voretigene neparvovec and gene therapy for leber's congenital amaurosis: review of evidence to date. *Appl Clin Genet*. (2020) 13:179–208. doi: 10.2147/tacg.S230720

74. FDA approves hereditary blindness gene therapy. *Nat Biotechnol*. (2018) 36:6. doi: 10.1038/nbt0118-6a

75. Cheng SY, Punzo C. Update on viral gene therapy clinical trials for retinal diseases. *Hum Gene Ther*. (2022) 33:865–78. doi: 10.1089/hum.2022.159

76. Castro BFM, Steel JC, Layton CJ. AAV-based strategies for treatment of retinal and choroidal vascular diseases: advances in age-related macular degeneration and diabetic retinopathy therapies. *BioDrugs*. (2024) 38:73–93. doi: 10.1007/s40259-023-00629-y

77. Blasiak J, Pawlowska E, Ciupińska J, Derwich M, Szczepanska J, Kaarniranta KA. New generation of gene therapies as the future of wet AMD treatment. *Int J Mol Sci*. (2024) 25. doi: 10.3390/ijms25042386

78. Gilger BC, Hirsch ML. Therapeutic applications of adeno-associated virus (AAV) gene transfer of HLA-G in the eye. *Int J Mol Sci*. (2022) 23. doi: 10.3390/ijms23073465

79. Riedmayr LM, Hinrichsmeyer KS, Thalhammer SB, Mittas DM, Karguth N, Otify DY, et al. mRNA trans-splicing dual AAV vectors for (epi)genome editing and gene therapy. *Nat Commun*. (2023) 14:6578. doi: 10.1038/s41467-023-42386-0

80. Luo S, Jiang H, Li Q, Qin Y, Yang S, Li J, et al. An adeno-associated virus variant enabling efficient ocular-directed gene delivery across species. *Nat Commun*. (2024) 15:3780. doi: 10.1038/s41467-024-48221-4

81. Zhi S, Chen Y, Wu G, Wen J, Wu J, Liu Q, et al. Dual-AAV delivering split prime editor system for *in vivo* genome editing. *Mol Ther*. (2022) 30:283–94. doi: 10.1016/j.ymthe.2021.07.011

82. Shubina-Oleinik O, Nist-Lund C, French C, Rockowitz S, Shearer AE, Holt JR. Dual-vector gene therapy restores cochlear amplification and auditory sensitivity in a mouse model of DFNB16 hearing loss. *Sci Adv*. (2021) 7:eabi7629. doi: 10.1126/sciadv.abi7629

83. Park TK, Wu Z, Kjellstrom S, Zeng Y, Bush RA, Sieving PA, et al. Intravitreal delivery of AAV8 retinoschisin results in cell type-specific gene expression and retinal rescue in the Rs1-KO mouse. *Gene Ther*. (2009) 16:916–26. doi: 10.1038/gt.2009.61

84. Petrs-Silva H, Dinculescu A, Li Q, Min SH, Chiodo V, Pang JJ, et al. High-efficiency transduction of the mouse retina by tyrosine-mutant AAV serotype vectors. *Mol Ther*. (2009) 17:463–71. doi: 10.1038/mt.2008.269

85. Li H, Li Q, Dang K, Ma S, Cotton JL, Yang S, et al. YAP/TAZ activation drives uveal melanoma initiation and progression. *Cell Rep*. (2019) 29:3200–11.e4. doi: 10.1016/j.celrep.2019.03.021

86. Bi HE, Zhang J, Yao Y, Wang S, Yao J, Shao Z, et al. Expression and functional significance of phosphoenolpyruvate carboxykinase 1 in uveal melanoma. *Cell Death discovery*. (2024) 10:196. doi: 10.1038/s41420-024-01963-y

87. Yang X, Zhou S, Zeng J, Zhang S, Li M, Yue F, et al. A biodegradable lipid nanoparticle delivers a Cas9 ribonucleoprotein for efficient and safe *in situ* genome editing in melanoma. *Acta biomaterialia*. (2024) 190:531–47. doi: 10.1016/j.actbio.2024.10.030

88. Liu J, Jiang F, Jiang Y, Wang Y, Li Z, Shi X, et al. Roles of exosomes in ocular diseases. *Int J nanomed*. (2020) 15:10519–38. doi: 10.2147/ijn.S277190

89. Blanco-Agudín N, Ye S, González-Fernández S, Alcalde I, Merayo-Lloves J, Quirós LM. Exosomes in ocular health: recent insights into pathology, diagnostic applications and therapeutic functions. *Biomedicines*. (2025) 13. doi: 10.3390/biomedicines13010233

90. Lohia A, Sahel DK, Salman M, Singh V, Mariappan I, Mittal A, et al. Delivery strategies for CRISPR/Cas genome editing tool for retinal dystrophies: challenges and opportunities. *Asian J Pharm Sci*. (2022) 17:153–76. doi: 10.1016/j.ajps.2022.02.001

91. Perez BA, Mettu P, Vajzovic L, Rivera D, Alkaissi A, Steffey BA, et al. Uveal melanoma treated with iodine-125 episcleral plaque: an analysis of dose on disease control and visual outcomes. *Int J Radiat oncol biol physics*. (2014) 89:127–36. doi: 10.1016/j.ijrobp.2014.01.026

92. Caminal JM, Lorenzo D, Gutierrez C, Slocker A, Piulats JM, Cobos E, et al. Local resection in choroidal melanoma: A review. *J Clin Med*. (2022) 11. doi: 10.3390/jcm11237156

93. Kinzl S, Heussen F, Kaiser KP, Hornberger U, Becker MD, Mack A, et al. Treatment of uveal melanoma using a novel radiosurgical platform: A case report. *Cureus*. (2025) 17:e81343. doi: 10.7759/cureus.81343

94. Wang S, Chen B, Ouyang L, Wang D, Tan J, Qiao Y, et al. A novel stimuli-responsive injectable antibacterial hydrogel to achieve synergetic photothermal/gene-targeted therapy towards uveal melanoma. *Advanced Sci (Weinheim Baden-Wurttemberg Germany)*. (2021) 8:e2004721. doi: 10.1002/advs.202004721

95. Leyvraz S, Konietschke F, Peuker C, Schütte M, Kessler T, Ochsenreither S, et al. Biomarker-driven therapies for metastatic uveal melanoma: A prospective precision oncology feasibility study. *Eur J Cancer (Oxford England: 1990)*. (2022) 169:146–55. doi: 10.1016/j.ejca.2022.04.004

96. Carvajal RD, Schwartz GK, Mann H, Smith I, Nathan PD. Study design and rationale for a randomised, placebo-controlled, double-blind study to assess the efficacy of selumetinib (AZD6244; ARRY-142886) in combination with dacarbazine in patients with metastatic uveal melanoma (SUMIT). *BMC cancer*. (2015) 15:467. doi: 10.1186/s12885-015-1470-z

97. Brouwer NJ, Konstantinou EK, Gragoudas ES, Marinkovic M, Luyten GPM, Kim IK, et al. Targeting the YAP/TAZ pathway in uveal and conjunctival melanoma with verteporfin. *Invest Ophthalmol Visual science*. (2021) 62:3. doi: 10.1167/iovs.62.4.3

98. Glinkina KA, Teunisse A, Gelmi MC, de Vries J, Jager MJ, Jochemsen AG. Combined Mcl-1 and YAP1/TAZ inhibition for treatment of metastatic uveal melanoma. *Melanoma Res*. (2023) 33:345–56. doi: 10.1097/cmr.0000000000000911

99. Kwon J, Lee D, Lee SA. BAP1 as a guardian of genome stability: implications in human cancer. *Exp Mol Med*. (2023) 55:745–54. doi: 10.1038/s12276-023-00979-1

100. Kennedy S, Owens S, Ivers L, Hegarty C, O'Neill V, Berenguer-Pina JJ, et al. Prognostic value of BAP1 protein expression in uveal melanoma. *Am J Surg pathol*. (2024) 48:329–36. doi: 10.1097/pas.0000000000002176

101. Masoomian B, Shields JA, Shields CL. Overview of BAP1 cancer predisposition syndrome and the relationship to uveal melanoma. *J Curr ophthalmol*. (2018) 30:102–09. doi: 10.1016/j.joco.2018.02.005

102. Uner OE, See TRO, Szalai E, Grossniklaus HE, Stålhammar G. Estimation of the timing of BAP1 mutation in uveal melanoma progression. *Sci Rep*. (2021) 11:8923. doi: 10.1038/s41598-021-88390-6

103. Bakhoum MF, Curtis EJ, Goldbaum MH, Mischel PS. BAP1 methylation: a prognostic marker of uveal melanoma metastasis. *NPJ Precis Oncol*. (2021) 5:89. doi: 10.1038/s41698-021-00226-8

104. Machiraju D, Hassel JC. Targeting the cMET pathway to enhance immunotherapeutic approaches for mUM patients. *Front Oncol*. (2022) 12:1068029. doi: 10.3389/fonc.2022.1068029

105. Tanaka R, Terai M, Londin E, Sato T. The role of HGF/MET signaling in metastatic uveal melanoma. *Cancers*. (2021) 13. doi: 10.3390/cancers13215457

106. Li H, Yang W, Chen PW, Alizadeh H, Niederkorn JY. Inhibition of chemokine receptor expression on uveal melanomas by CXCR4 siRNA and its effect on uveal melanoma liver metastases. *Invest Ophthalmol Visual science*. (2009) 50:5522–8. doi: 10.1167/iovs.09-3804

107. Luo X, Ren C, Liu X, Zhang G, Huang S, Yu L, et al. Screening of drugs that selectively inhibit uveal melanoma cells with SF3B1 mutations. *Nan fang yi ke da xue xue bao = J South Med University*. (2021) 41:1835–42. doi: 10.12122/j.issn.1673-4254.2021.12.12

108. Parrella P, Caballero OL, Sidransky D, Merbs SL. Detection of c-myc amplification in uveal melanoma by fluorescent *in situ* hybridization. *Invest Ophthalmol Visual science*. (2001) 42:1679–84.

109. Tulley PN, Neale M, Jackson D, Chana JS, Grover R, Cree I, et al. The relation between c-myc expression and interferon sensitivity in uveal melanoma. *Br J ophthalmol*. (2004) 88:1563–7. doi: 10.1136/bjo.2003.033498

110. Guo W, Wang H, Li C. Signal pathways of melanoma and targeted therapy. *Signal transduction targeted Ther*. (2021) 6:424. doi: 10.1038/s41392-021-00827-6

111. Shtivelman E, Davies MQ, Hwu P, Yang J, Lotem M, Oren M, et al. Pathways and therapeutic targets in melanoma. *Oncotarget*. (2014) 5:1701–52. doi: 10.18632/oncotarget.1892

112. Katopodis P, Khalifa MS, Anikin V. Molecular characteristics of uveal melanoma and intraocular tumors. *Oncol letters*. (2021) 21:9. doi: 10.3892/ol.2020.12270

113. El Filali M, van der Velden PA, Luyten GPM, Jager MJ. Anti-angiogenic therapy in uveal melanoma. *Developments ophthalmol*. (2012) 49:117–36. doi: 10.1159/000329591

114. Hu K, Babapoor-Farrokhran S, Rodrigues M, Deshpande M, Puchner B, Kashiwabuchi F, et al. Hypoxia-inducible factor 1 upregulation of both VEGF and ANGPTL4 is required to promote the angiogenic phenotype in uveal melanoma. *Oncotarget*. (2016) 7:7816–28. doi: 10.18632/oncotarget.6868

115. Wu Z, Bian Y, Chu T, Wang Y, Man S, Song Y, et al. The role of angiogenesis in melanoma: Clinical treatments and future expectations. *Front Pharmacol*. (2022) 13:1028647. doi: 10.3389/fphar.2022.1028647

116. Castet F, Garcia-Mulero S, Sanz-Pamplona R, Cuellar A, Casanovas O, Caminal JM, et al. Uveal melanoma, angiogenesis and immunotherapy, is there any hope? *Cancers*. (2019) 11. doi: 10.3390/cancers11060834

117. Pawlik VE, Sonntag SR, Grisanti S, Tura A, Kakkassery V, Ranjbar M. Impact of nintedanib and anti-Angiogenic agents on uveal melanoma cell behavior. *Invest Ophthalmol Visual science*. (2024) 65:30. doi: 10.1167/iovs.65.2.30

118. Gezgin G, Luk SJ, Cao J, Dogrusöz M, van der Steen DM, Hagedoorn RS, et al. PRAME as a potential target for immunotherapy in metastatic uveal melanoma. *JAMA ophthalmol*. (2017) 135:541–49. doi: 10.1001/jamaophthalmol.2017.0729

119. Gelmi MC, Gezgin G, van der Velden PA, Luyten GPM, Luk SJ, Heemskerk MHM, et al. PRAME expression: A target for cancer immunotherapy and a prognostic factor in uveal melanoma. *Invest Ophthalmol Visual science*. (2023) 64:36. doi: 10.1167/iovs.64.15.36

120. Pires L, Khattak S, Pratavieira S, Calcada C, Romano R, Yucel Y, et al. Femtosecond pulsed laser photodynamic therapy activates melanin and eradicates Malignant melanoma. *Proc Natl Acad Sci U S A*. (2024) 121:e2316303121. doi: 10.1073/pnas.2316303121

121. Li XY, Tan LC, Dong LW, Zhang WQ, Shen XX, Lu X, et al. Susceptibility and resistance mechanisms during photodynamic therapy of melanoma. *Front Oncol*. (2020) 10:597. doi: 10.3389/fonc.2020.00597

122. Fabian ID, Stacey AW, Papastefanou V, Al Harby L, Arora AK, Sagoo MS, et al. Primary photodynamic therapy with verteporfin for small pigmented posterior pole

choroidal melanoma. *Eye (London England)*. (2017) 31:519–28. doi: 10.1038/eye.2017.22

123. Lescot T, Lebel-Cormier MA, Seniwal B, Gros-Louis P, Bellerive C, Landreville S, et al. Tumor shape-specific brachytherapy implants by 3D-printing, precision radioactivity painting, and biomedical imaging. *Advanced healthcare materials*. (2023) 12:e2300528. doi: 10.1002/adhm.202300528

124. Mourtada F, Belko S, Monane R, Pugliese R, Komarnicky-Kocher L, Lally SE, et al. A novel 3D printing method for a notched eye plaque "dummy" for uveal melanoma brachytherapy. *Brachytherapy*. (2025) 24:86–91. doi: 10.1016/j.brachy.2024.09.002

125. Dadzie AK, Iddir SP, Ganesh S, Ebrahimi B, Rahimi M, Abtahi M, et al. Artificial intelligence in the diagnosis of uveal melanoma: advances and applications. *Exp Biol Med (Maywood N.J.)*. (2025) 250:10444. doi: 10.3389/ebm.2025.10444

126. Koseoglu ND, Corrêa ZM, Liu TYA. Artificial intelligence for ocular oncology. *Curr Opin ophthalmol*. (2023) 34:437–40. doi: 10.1097/icu.0000000000000982

127. Benavides R, Mejías R, Blanco A, Bermudez-Guzman L. CyberKnife stereotactic radiosurgery for uveal melanoma: first case series in Central America. *Ocular Oncol pathol*. (2024) 10:25–31. doi: 10.1159/000534207

128. Eibl-Lindner K, Fürweger C, Nentwich M, Foerster P, Wowra B, Schaller U, et al. Robotic radiosurgery for the treatment of medium and large uveal melanoma. *Melanoma Res*. (2016) 26:51–7. doi: 10.1097/cmr.0000000000000199

129. Chia HN, Wu BM. Recent advances in 3D printing of biomaterials. *J Biol engineering*. (2015) 9:4. doi: 10.1186/s13036-015-0001-4

130. Visalli F, Fava F, Capobianco M, Musa M, D'Esposito F, Russo A, et al. Innovative bioscaffolds in stem cell and regenerative therapies for corneal pathologies. *Bioengineering (Basel Switzerland)*. (2024) 11. doi: 10.3390/bioengineering11090859

frontiers | Frontiers in Immunology

TYPE Original Research
PUBLISHED 15 September 2025
DOI 10.3389/fimmu.2025.1681072

Check for updates

OPEN ACCESS

EDITED BY
Qi Wang,
Zhenjiang, China, China

REVIEWED BY
Haoru Dong,
Fudan University, China
Jie Kang,
Beijing Children's Hospital, China
Aryan Sai Boddu,
Guru Nanak Institutions Technical Campus, India

*CORRESPONDENCE
Jiguang Han
han_jg112@163.com

†These authors have contributed equally to this work and share first authorship

RECEIVED 06 August 2025
ACCEPTED 29 August 2025
PUBLISHED 15 September 2025

CITATION
Sha Y, Yuan Q, Du Y, Yang S, Niu M, Liang X, Sun S, Li T, Gong S and Han J (2025) Integrating deep learning features from mammography with SHAP values for a machine learning model predicting over 5-year recurrence of breast ductal carcinoma *In Situ* post-lumpectomy. *Front. Immunol.* 16:1681072. doi: 10.3389/fimmu.2025.1681072

COPYRIGHT
© 2025 Sha, Yuan, Du, Yang, Niu, Liang, Sun, Li, Gong and Han. This is an open-access article distributed under the terms of the Creative Commons Attribution License (CC BY). The use, distribution or reproduction in other forums is permitted, provided the original author(s) and the copyright owner(s) are credited and that the original publication in this journal is cited, in accordance with accepted academic practice. No use, distribution or reproduction is permitted which does not comply with these terms.

Integrating deep learning features from mammography with SHAP values for a machine learning model predicting over 5-year recurrence of breast ductal carcinoma *In Situ* post-lumpectomy

Yupeng Sha[1†], Quan Yuan[1†], Yi Du[1†], Shuqi Yang[2], Ming Niu[1], Xiaoshuan Liang[1], Shanshan Sun[1], Tong Li[1], Shu Gong[1] and Jiguang Han[1*]

[1]Department of Breast Surgery, Harbin Medical University Cancer Hospital, Harbin, Heilongjiang, China, [2]Quanzhou First Hospital Affiliated to Fujian Medical University, Quanzhou, Fujian, China

Background: In women with ductal carcinoma *in situ* (DCIS) undergoing breast-conserving surgery, still part will progress to invasive breast cancer (IBC) in the future. Mammograms offer rich tumor data for patient stratification, but current prediction methods focus on clinicopathological factors, overlooking imaging insights.

Methods: We retrospectively analyzed 140 DCIS patients from Harbin Medical University Cancer Hospital (2011-2020, followed up to 2025). Preoperative digital mammograms and clinicopathological data were collected, with mammographic features extracted using pyradiomics and supervised by a senior radiologist. Feature selection employed 10-fold cross-validated LASSO regression. The dataset was split into training (n=100) and validation (n=40) sets (10:4 ratio). Sixteen machine learning algorithms combining mammographic deep learning features and clinicopathological variables were developed and compared for predicting DCIS recurrence. Model performance was assessed using ROC, sensitivity, specificity, PPV, NPV, and SHAP values for interpretation.

Results: The Gradient Boosting Machine (GBM) algorithm had the best predictive performance, with an AUC of 0.918 (95% CI 0.873-0.963) in the test set. SHAP values indicated that the mammographic signature (MS) was the most significant predictor, followed by Ki-67 index and histological grade. Patients not receiving radiotherapy had higher recurrence rates than those who did. Decision curve analysis validated the model's clinical utility across various risk thresholds.

Conclusion: Our study developed an interpretable GBM model incorporating mammographic and clinical data to predict DCIS recurrence (AUC = 0.918). Key predictors were mammographic signature, Ki-67, and tumor grade, offering clinicians a practical tool for personalized postoperative management.

KEYWORDS

ductal carcinoma *in situ*, breast-conserving surgery, mammography, deep learning, recurrence

Introduction

Breast cancer (BC) represents roughly one-third of all female malignant neoplasms globally (1). The progressive advancement of diagnostic technologies has led to enhanced detection rates of breast ductal carcinoma *in situ* (DCIS), which currently constitutes 20%–25% of all recently identified BC diagnoses (2). Breast-conserving surgery (BCS) has become the main local treatment for DCIS to achieve precise excision with the smallest possible margin and to minimize trauma (3). Despite the historically positive outlook for DCIS cases, comprehensive large-cohort analyses have demonstrated the risk of ipsilateral recurrence subsequent to breast-conserving treatment in individuals diagnosed with DCIS (4). Consequently, precise identification of DCIS patients who face elevated recurrence risk following breast-conserving surgery represents a critical factor in establishing appropriate postoperative therapeutic strategies. Mammography is the cornerstone of DCIS screening and diagnosis. The core functions include early detection, risk stratification, and treatment guidance (5). Mammography is highly sensitive to calcified DCIS, and > 90% of female patients with DCIS, especially high-grade DCIS, show suspicious microcalcifications on mammograms (6, 7). Consequently, the systematic collection and examination of mammographic characteristics, including lesion dimensions and Breast Imaging Reporting and Data System (BI-RADS) categorization, represents a critical component in the precise assessment of DCIS recurrence probability. Recent researches has established that integrating deep learning (DL) methodologies with radiological data represents a novel diagnostic and therapeutic strategy for BC addressing the under exploitation of visual diagnostic information (8). Khalid proposed an efficient DL model to recognize BC in computerized mammograms of varying densities (9). Alaeikhanehshir et al. used DL in mammography to distinguish between high- and low-risk DCIS, enabling active surveillance of patients (10). Nevertheless, contemporary DL investigations predominantly emphasize multimodal feature representation extraction, while the intricate architecture of opaque computational models impedes comprehensive understanding of individual feature contributions to predictive outcomes. The lack of direct and effective explanations limits their impact on clinical decision-making.

Shapley additive explanations (SHAP) value interpretation is a new function-based interpretability method that provides a deeper understanding of the key predictors of machine learning (ML) models, thereby improving their transparency and credibility (11). In the present study, we reviewed 140 the data of patients with DCIS who underwent BCS at a large cancer center and integrated the extracted DL features from mammography and other clinicopathological features to construct an ML model for predicting DCIS recurrence > 5 years after lumpectomy. Finally, by combining the SHAP values, we visually explained the potential factors affecting the long-term recurrence of DCIS.

Abbreviations: AJCC, American Joint Committee on Cancer; ASCO, American Society of Clinical Oncology; AUC, Area under the receiver operating characteristic curve; BC, Breast cancer; BCS, Breast-conserving surgery; BI-RADS, Breast Imaging-Reporting and Data System; CAP, College of American Pathologists; CC, Craniocaudal; DCA, Decision curve analysis; DCIS, Ductal carcinoma *in situ*; DL, Deep learning; FISH, Fluorescence *in situ* hybridization; GBM, Gradient Boosting Machine; HER-2, Human epidermal growth factor receptor 2; KNN, K-nearest neighbors; LASSO, Least absolute shrinkage and selection operator; LMN+, Lymph node-positive; LMR, Lymphocyte-to-monocyte ratio; LR, Logistic regression; ML, Machine learning; MLP, Multilayer perceptron; MS, Mammographic signature; PPV, Positive predictive value; RF, Random Forest; RFE, Recursive feature elimination; ROC, Receiver operating characteristic; ROI, Region of interest; SHAP, SHapley Additive exPlanations; SVM, Support vector machine; XGBoost, eXtreme Gradient Boosting; Patient clinical characteristics(PCC).

Patients and methods

Study population

The research received ethical clearance from the Institutional Review Board at Harbin Medical University Cancer Hospital (reference: YD2024-18) and was conducted in full compliance with the ethical standards established by the Declaration of Helsinki. Because this was a retrospective study and all data were anonymized, patient informed consent was waived.

This retrospective investigation incorporated 140 female patients with confirmed primary DCIS who received inpatient treatment at the Affiliated Cancer Hospital of Harbin Medical

University during the period spanning March 1, 2011, through March 1, 2020.All patients had complete pathological and laboratory test results and clear mammography images. Data including mammographic features, patient characteristics, laboratory results, pathological results (according to the American Joint Committee on Cancer (AJCC) Cancer Staging Manual, 8th edition), and treatment strategies were collected (Table 1).

Inclusion criteria comprised: (1) pathologically confirmed DCIS who underwent BCS; (2) high-quality digital mammography images before treatment; (3) comprehensive clinical information (including chemotherapy regimens, radiation treatment protocols, hormonal therapeutic interventions, hormone receptor and human epidermal growth factor receptor 2 [HR/HER2] expression profiles, Ki-67 proliferation index, and histopathological grading); (4) complete pathology information;(5) All patients were pathologically confirmed to have negative margins after tumor resection.

Exclusion criteria comprised: (1) distant metastasis or invasive carcinoma; (2) other malignant tumors; (3) missing key data (e.g., imaging or molecular markers); (4) history of breast radiotherapy or loss to follow-up.

The follow-up endpoint of this study was April 1, 2025. Following the completion of appropriate therapeutic interventions, patients underwent systematic monitoring through clinical consultations, telephonic communication, or electronic correspondence at three-month intervals during the initial six-month period, subsequently at six-month intervals for a maximum duration of five years, and thereafter on an annual basis, with the principal objective of identifying disease recurrence.

Imaging acquisition and interpretation

Digital mammographic imaging was performed utilizing Mammomat Novation DR (Siemens AG Medical Solutions, Erlangen, Germany) and Selenia Dimensions (Hologic, Bedford, Mass, USA) systems, incorporating both craniocaudal (CC) and

TABLE 1 Performance of multiple machine learning models for identifying breast cancer recurrence status based on molybdenum target features.

Model_name	AUC	95% CI	Sensitivity	Specificity	Accuracy	PPV	NPV	Task
LR	0.829	0.738-0.921	0.917	0.617	0.702	0.489	0.949	train
	0.622	0.417-0.826	0.600	0.711	0.679	0.300	0.889	test
NaiveBayes	0.826	0.733-0.920	0.792	0.700	0.726	0.514	0.894	train
	0.704	0.523-0.885	0.500	0.911	0.821	0.500	0.891	test
SVM	0.868	0.784-0.951	0.958	0.746	0.798	0.590	0.978	train
	0.678	0.485-0.872	0.600	0.761	0.732	0.353	0.897	test
KNN	0.836	0.752-0.921	0.583	0.914	0.798	0.667	0.841	train
	0.638	0.456-0.820	0.900	0.341	0.429	0.225	0.937	test
DecisionTree	1.000	1.000-1.000	1.000	1.000	1.000	1.000	1.000	train
	0.702	0.532-0.872	0.600	1.000	0.768	0.400	0.902	test
RandomForest	0.891	0.819-0.963	0.750	0.933	0.881	0.818	0.903	train
	0.630	0.430-0.831	0.600	0.800	0.750	0.375	0.900	test
ExtraTrees	1.000	1.000-1.000	1.000	1.000	1.000	1.000	1.000	train
	0.687	0.498-0.876	0.500	0.844	0.768	0.385	0.884	test
XGBoost	0.992	0.980-1.000	1.000	0.933	0.952	0.857	1.000	train
	0.711	0.500-0.922	0.700	0.761	0.750	0.389	0.921	test
LightGBM	0.877	0.805-0.949	0.875	0.857	0.821	0.636	0.941	train
	0.634	0.424-0.843	0.600	0.833	0.732	0.353	0.897	test
GradientBoosting	0.975	0.949-1.000	0.958	0.933	0.940	0.852	0.982	train
	0.704	0.507-0.902	0.600	0.867	0.804	0.462	0.907	test
AdaBoost	0.963	0.929-0.997	0.875	0.917	0.905	0.808	0.948	train
	0.730	0.540-0.921	0.600	0.867	0.804	0.462	0.907	test
MLP	0.844	0.759-0.930	0.958	0.583	0.690	0.479	0.972	train
	0.650	0.436-0.865	0.600	0.778	0.732	0.353	0.897	test

mediolateral oblique projections. The region of interest (ROI) showing the most suspicious lesion in the CC-view for each patient was prioritized. To ensure reliable and reproducible BI-RADS categorization, two experienced radiologists conducted independent evaluations of all imaging studies. (R4-R6 with ≥ 8 years of mammography experience, respectively). Consensus regarding the final diagnostic assessment was achieved through collaborative discussion when interpretive differences arose. The interpreting radiologists remained unaware of histopathological findings while retaining access to relevant clinical data and previous imaging studies. Based on the 2013 American College of Radiology Breast Imaging Reporting and Data System (BI-RADS) classification framework, lesions designated as categories 2 or 3 were characterized as benign or likely benign entities, while those assigned categories 4 or 5 were classified as potentially malignant findings warranting histopathological confirmation.

Data preprocessing

Calcified regions in the mammography images were annotated as follows: for diffusely distributed calcifications, the entire area was uniformly annotated; for multiple independent calcification clusters, the specific cluster indicated for biopsy in the radiology report was prioritized; and for large calcified areas, the entire scope was annotated. All calcification region annotations were independently completed by two trained annotators (SA: MD; MM: medical technology researcher) using 3D Slicer software (version 4.10.2) on full images supervised by a senior breast radiologist (RM).

Tumor recurrence encompassed both localized recurrence and metastatic spread to distant tissues or organs. Localized recurrence was characterized as tumor reappearance within the ipsilateral breast, chest wall, or corresponding regional lymph nodes. Neoplasm classification was conducted in accordance with the eighth edition of the AJCC staging criteria. All lymph node-positive (LMN+) cases were confirmed pathologically. Based on the established criteria from the American Society of Clinical Oncology (ASCO) and the College of American Pathologists (CAP), estrogen receptor and progesterone receptor positivity were characterized as ≥ 1% of tumor cell nuclei demonstrating positive staining. HER2 expression was determined in accordance with the 2018 ASCO/CAP criteria, whereby immunohistochemistry scores of 3+ are classified as positive, while scores of 2+ are deemed positive when HER2 gene amplification is confirmed through fluorescence *in situ* hybridization (FISH) analysis. Four serum inflammation- and immunity-related biomarkers were measured: the ratio of platelets to lymphocytes (PLR), the ratio of neutrophils to lymphocytes (NLR), the ratio of lymphocytes to monocytes (LMR), and the platelet-albumin ratio (PAR, calculated as the quotient of platelet count and serum albumin concentration). All blood cell counts were performed using automated hematology analyzers (Sysmex XN series or Beckman Coulter DxH), and serum albumin was measured using standardized biochemical analysis methods (e.g., bromocresol green method or immunoturbidimetry), following strict clinical laboratory standard operating procedures.

Machine learning model development

First, considering the different measurement units among variables, all variables were normalized using "StandardScaler." Subsequently, to address feature dependency, Spearman's correlation analysis was performed. When the correlation coefficient between any two variables exceeded 0.9, one variable was removed from the analysis. Between-group comparisons were conducted using the Mann–Whitney U test. Categorical data are presented as percentages (%), with Pearson's chi-square analysis employed to assess between-group variations. The sample dataset was partitioned into training (n = 100) and internal validation (n = 40) cohorts using a 10:4 allocation ratio (12). Owing to the high-dimensional nature of features that adversely affect DCIS recurrence prediction, we sought to identify the features most closely associated with DCIS recurrence in the training set. Feature extraction was performed utilizing the "pyradiomics" module within Python 3.8.1, while feature selection was conducted through the least absolute shrinkage and selection operator (LASSO) algorithm. The optimal lambda parameter for feature selection was established via 10-fold cross-validation methodology (13). The prediction models were developed employing sixteen machine learning algorithms: partial least squares (PLS) (14), random forest (RF) (15), decision tree system (DTS) (16), support vector machine (SVM) (16), logistic regression (LR) (17), K-nearest neighbors (KNN) (18), eXtreme gradient boosting (XGBoost) (19), gradient boosting machine (GBM) (20), neural network (NeuralNet) (21), generalized linear model boosting (glmBoost) (22), naïve Bayes (23), decision tree (16), extra trees (24), light gradient boosting machine (25), adaptive boosting (AdaBoost) (26), and multilayer perceptron (27). To maintain model reliability across both training and testing datasets, a ten-fold cross-validation approach was implemented (13). To identify the optimal hyperparameters for each algorithm, a systematic grid search methodology was employed, utilizing the maximum area under the receiver operating characteristic (ROC) curve (AUC) (28, 29) as the evaluation metric for determining the superior model configuration. The Delong test was employed for AUC comparisons. The optimal model was constructed using the training dataset and subsequently evaluated through both internal and external validation datasets. Model efficacy was assessed on both training and testing datasets through the utilization of receiver operating characteristic curves, along with measurements of sensitivity, specificity, positive predictive value, and negative predictive value (28). To mitigate overfitting and enhance model generalization, rigorous regularization techniques were implemented during training. These included penalty-based complexity constraints, feature coefficient compression, and built-in regularization methods such as tree depth limits and randomized subspace sampling. All feature selection and hyperparameter tuning were conducted internally within the training set using repeated

cross-validation to prevent data leakage. The final model performance was evaluated on a strictly retained validation set. Despite moderate sample sizes relative to initial feature dimensions, this study ensured an optimal event-to-prediction ratio through substantial dimensionality reduction and regularization. Further external validation in larger cohorts is required to confirm the model's robustness and generalization capabilities. Additionally, decision curve analysis (DCA) was conducted to evaluate genuine clinical applicability. SHAP analysis was employed to elucidate the individual feature contributions to predictive outcomes (28, 29). The SHAP values obtained for representative cases demonstrated how specific features influenced particular samples, thereby facilitating comprehension of the model's decision-making mechanisms (29). Subsequently, recursive feature elimination (RFE) was implemented to conduct additional variable selection and construct a streamlined model variant.

Statistical analysis

Statistical analyses were conducted using R Studio version 4.3.3 and Jupyter Notebook 5.6.0. For categorical data, chi-squared or Fisher's exact tests were used (30).Continuous variables were tested for normality using Shapiro-Wilk tests(a= 0.05). For normally distributed data, independent t-tests were used; otherwise, Mann-Whitney U tests were applied. Statistical significance was defined as $p < 0.05$.

Results

The research methodology is illustrated in Figure 1.

Baseline characteristics

Between March 2011 and March 2020, 140 patients with DCIS confirmed by biopsy or postoperative pathology were included. Supplementary Table S1 presents the demographic and clinical characteristics of the study population at baseline. The most common histological grades were low (43.6%), high (35.7%), and intermediate (20.7%). Compared with patients with non-recurrence, patients with recurrence showed significantly higher histological grades and Ki67 indices; additionally, a higher proportion of these patients did not receive chemotherapy (Supplementary Table S1). All clinical characteristics (21 clinical features) were obtained from the electronic medical records of patients with DCIS.

Feature selection

We performed radiomic feature extraction using the pyradiomics module in Python 3.8.1, obtaining a total of 849 features including shape features, first-order histogram features, and second-order texture features (Supplementary Table S2). To address the potential adverse effects of high-dimensional data on predicting breast intraductal carcinoma recurrence, we first standardized all features using StandardScaler to eliminate measurement unit discrepancies. Subsequently, we conducted Spearman correlation analysis (threshold $\rho>0.9$) to remove redundant features, resulting in 172 optimized features (Supplementary Table S3). Further refinement was achieved through Mann-Whitney U tests ($p<0.05$), which identified 41 statistically significant features (Supplementary Table S4). After partitioning the dataset into training and validation sets at a 10:4 ratio (Supplementary Tables S5, S6), we employed LASSO regression (Figure 2A) with 10-fold cross-validation (Figure 2B) to ultimately determine five optimal mammography (MG) features. The five selected radiomic features were: original firstorder 10Percentile (10th percentile from the first-order statistics of the original image), original glcm Contrast (contrast from the gray-level co-occurrence matrix), original glcm Idmn (inverse difference moment normalized from the gray-level co-occurrence matrix), wavelet HLL firstorder Median (median from the first-order statistics of the wavelet High-Low-Low filtered image), and wavelet HHL firstorder Median (median from the first-order statistics of the wavelet High-High-Low filtered image).

Based on these features, we evaluated twelve machine learning algorithms (Table 1), among which the AdaBoost algorithm demonstrated superior performance and was selected to establish the mammography signature (MS). To enhance the robustness of our predictive model, we further integrated MS with clinical features and blood inflammatory markers (PLR, NLR, LMR, and PAR). Feature selection was performed using three distinct methods: SVM-RFE, LASSO, and random forest. The SVM-RFE approach identified 15 optimal variables (accuracy: 83.6%; Figure 3A, Supplementary Table S7), LASSO selected 8 key variables (Figure 3B, Supplementary Table S8), and random forest determined 11 important variables (Figure 3C). Comprehensive analysis ultimately identified four core predictive variables: chemotherapy status, Ki-67 index, histological grade, and MS (Figure 3D), which served as the foundational elements for constructing our predictive model. This systematic feature selection and model development process ensured methodological rigor while significantly improving the reliability of predictive outcomes.

Model performance comparison

Initially, we hypothesized that a comprehensive integration of clinical features might provide key insights for predicting DCIS recurrence outcomes. Therefore, we obtained 21 clinical features from the electronic medical records and identified four strongly correlated variables through analysis and integration. These four variables were used to develop a predictive model for DCIS recurrence. In the present investigation, ten machine learning algorithms (PLS, RF, DTS, SVM, Logistic, KNN, XGBoost, GBM, NeuralNet, and glmBoost) were evaluated within the discovery

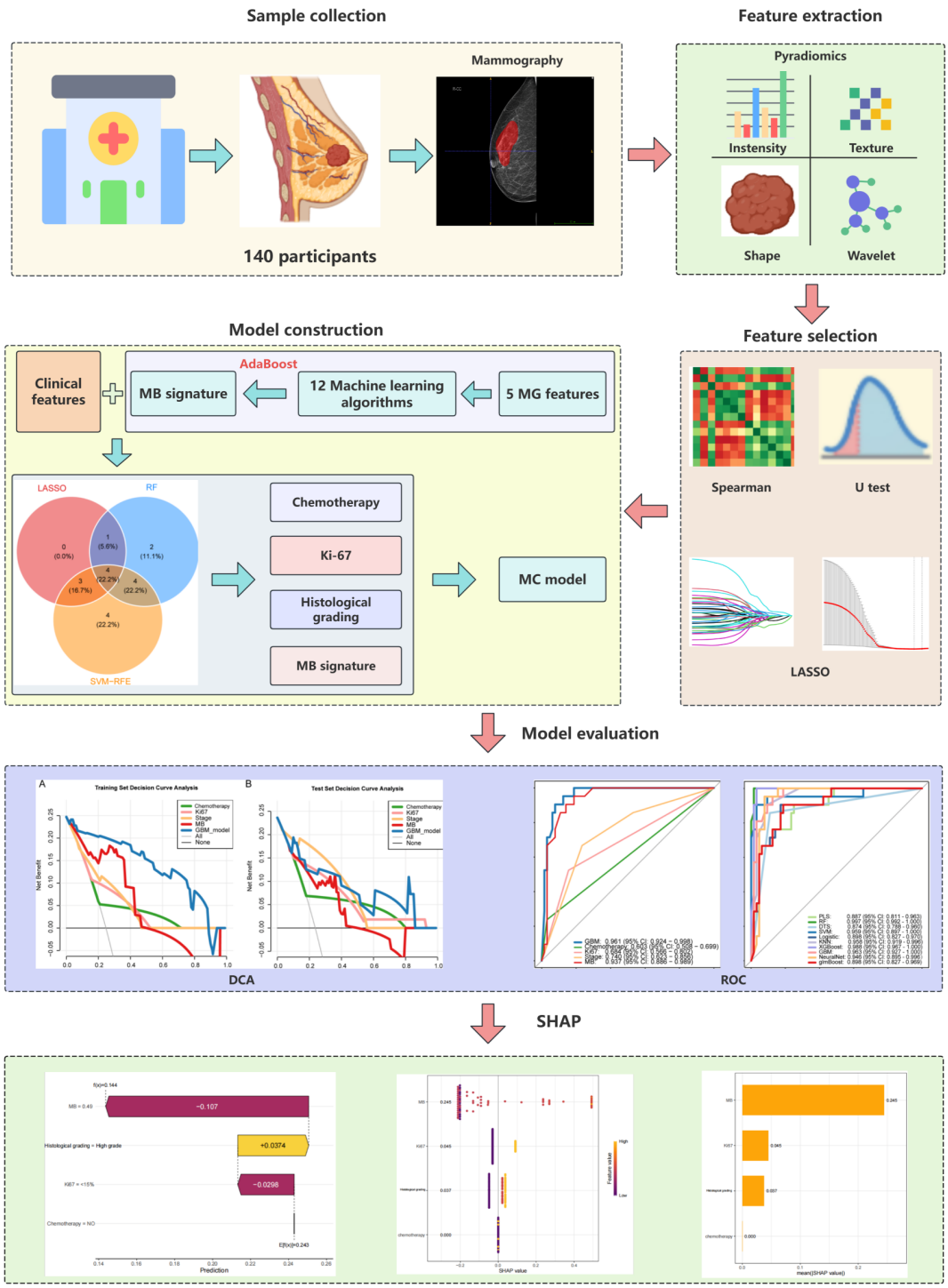

FIGURE 1
Brief technical flowchart.

dataset to assess their predictive capabilities (Figures 4A, B). Based on its superior overall performance across both training and testing datasets, the GBM model was identified as the most effective approach (training set AUC = 0.963, test set AUC = 0.918).Additionally, comparison of the GBM-integrated model with single-risk signatures (Figures 4C, D) showed that the GBM-integrated model had the largest area under the ROC curve (AUC) (training set: 0.961; test set: 0.915). Among the single-risk signatures, the MS had the highest AUC in the training set (0.937), whereas histological grading had the highest AUC in the test set (0.849). While individual risk signatures demonstrated measurable net benefit across broad threshold probability ranges, the GBM model exhibited superior overall net benefit performance. Consequently, this model was identified as the most suitable

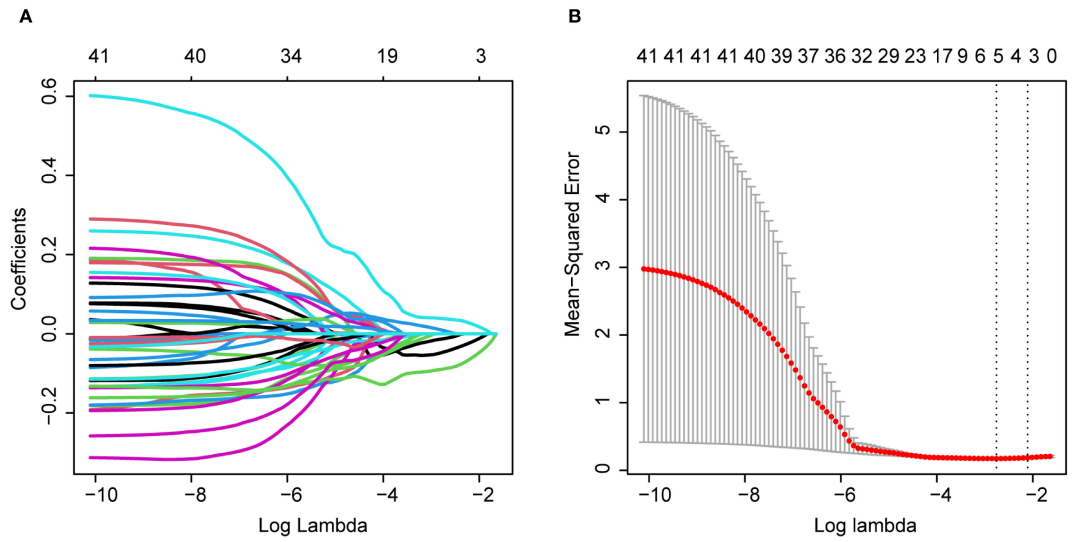

FIGURE 2
(A) and **(B)** LASSO coefficient convergence paths.

approach for forecasting DCIS recurrence over a five-year period and subsequent timeframes.

Regarding clinical utility, the four-variable model demonstrated substantial net benefits across diverse threshold probability ranges alongside the GBM model; nevertheless, the GBM model displayed superior net benefit performance, thereby validating its designation as the most effective predictive framework for DCIS recurrence (Figures 5A, B).To improve model interpretability, we employed the SHAP framework. According to the importance ranking based on the mean absolute SHAP values (Figure 5C), the four features were ordered as follows: MS > Ki-67 index > histological grading > chemotherapy status. Figure 5D shows a violin plot for each feature, illustrating the correlation between features and SHAP values. Larger absolute SHAP values indicate a greater impact of the features on the GBM-based prediction model. The yellow and purple dots represent higher and lower feature values, respectively. These results underscore that MS was the most critical factor, surpassing Ki-67, histological grade, and chemotherapy. Figure 5E presents a comprehensive case analysis illustrating the model's predictive methodology for an individual patient. Within this representation, yellow markers signify positive influences on the prediction outcome, while purple markers indicate negative influences. The f(x) value corresponds to the computed SHAP value for each contributing factor. Notably, the GBM model predicted a lower recurrence risk than the baseline in this patient. Among these factors, a high histological grade was the primary negative contributor (reducing the predicted risk by -0.107, from a baseline of 0.243 to 0.144), whereas the absence of chemotherapy had a small positive impact (+0.0374). Overall, the combined effects resulted in a prediction that was significantly below the average risk.

Discussion

This investigation involved the development and performance evaluation of 10 ML algorithms utilizing 21 clinical parameters, encompassing clinical characteristics, mammographic imaging data, and histopathological findings, to forecast long-term recurrence (≥5 years) in DCIS patients following BCS. The findings demonstrated that the GBM model achieved optimal performance with a test set AUC of 0.918, displaying superior predictive capacity compared to the remaining four individual risk signatures and consequently providing substantial clinical utility. To enhance model interpretability, we employed the SHAP methodology for visualization purposes. SHAP force plots were utilized to elucidate the individualized prediction process for DCIS recurrence risk assessment, thereby facilitating comprehensive understanding of the underlying predictive mechanisms (29). While existing clinical risk assessment tools like the VNPI and RTOG 9804 standard rely on traditional clinical-pathological variables (such as age, tumor size, margin width, and histological grade), our approach integrates deep learning-derived breast X-ray imaging features with key clinical predictors. This enables our model to capture tumor heterogeneity and radiologically-based disease progression patterns that conventional scoring systems cannot reveal. Unlike these early-stage tools, our model provides personalized, interpretable risk predictions through SHAP analysis, thereby revealing which factors contribute most significantly to individual recurrence risks.

Most recent studies on predicting recurrence after BCS for DCIS rely solely on single data sources—such as clinicopathological features or imaging indicators—and do not integrate multimodal data, which may lead to the omission of key predictive information

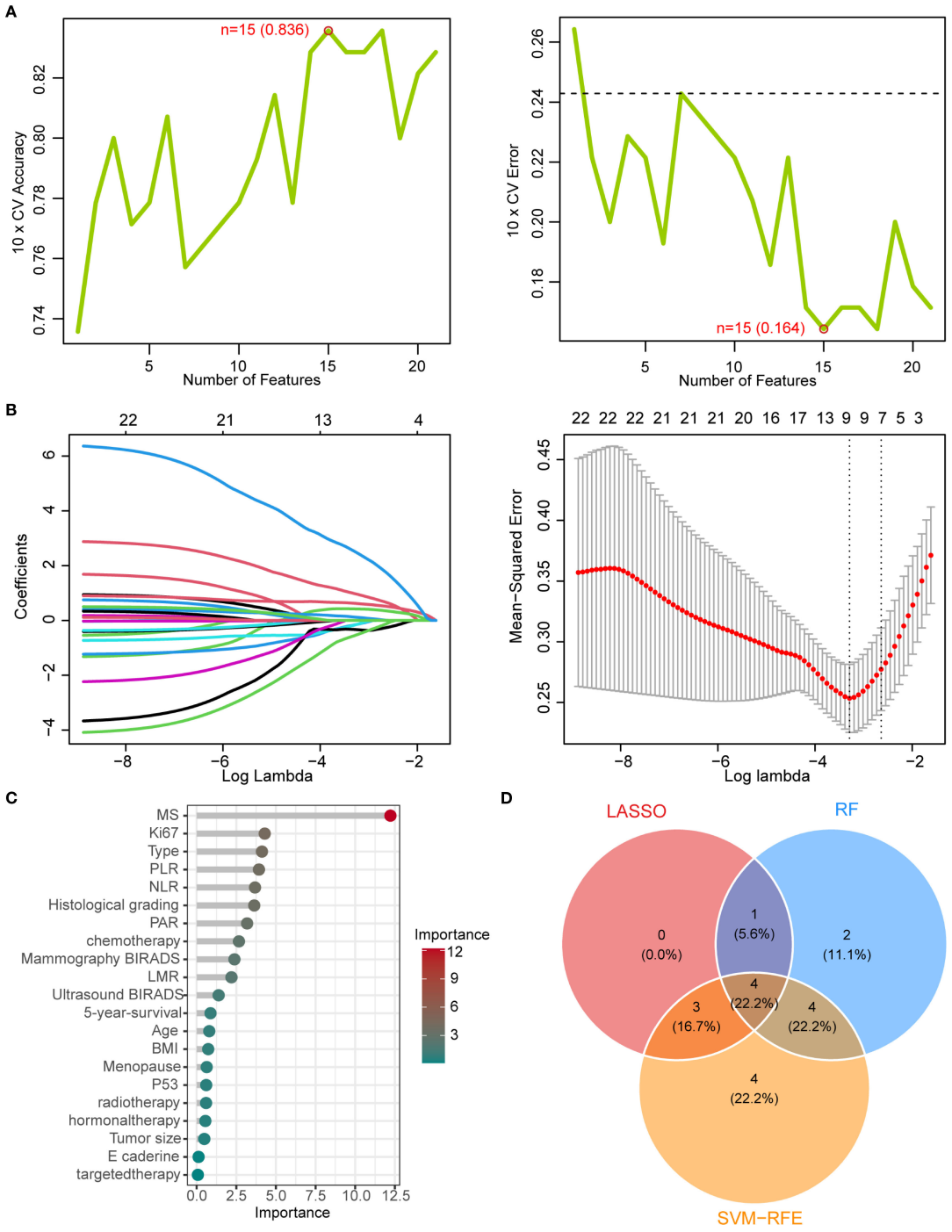

FIGURE 3
Machine learning-based feature selection **(A)** SVM-RFE algorithm performance showing accuracy (83.6%) and error rate (16.4%) with top 15 selected features. **(B)** LASSO coefficient convergence paths. **(C)** Random Forest feature importance ranking (threshold >1). **(D)** Venn diagram of overlapping features from LASSO, RF, and SVM-RFE methods, identifying four key predictors: chemotherapy status, Ki-67 index, histological grade, and mammographic signature (MS).

(10, 31–33). Second, although existing DL models have certain predictive capabilities (34, 35), they are mostly "black-box" models that lack quantitative explanations of predictive factors, thereby limiting clinician trust in the results. Finally, some studies have established predictive models without sufficient clinical translation validation, lacking both DCA to demonstrate the clinical net benefit and association with specific treatment decisions, thus restricting the model's practical application. For example, some studies used only molecular phenotypes or pathological information for predictive analysis or performed risk stratification based solely on radiomic features (10, 33); however, these methods have shortcomings in prediction accuracy and clinical applicability.

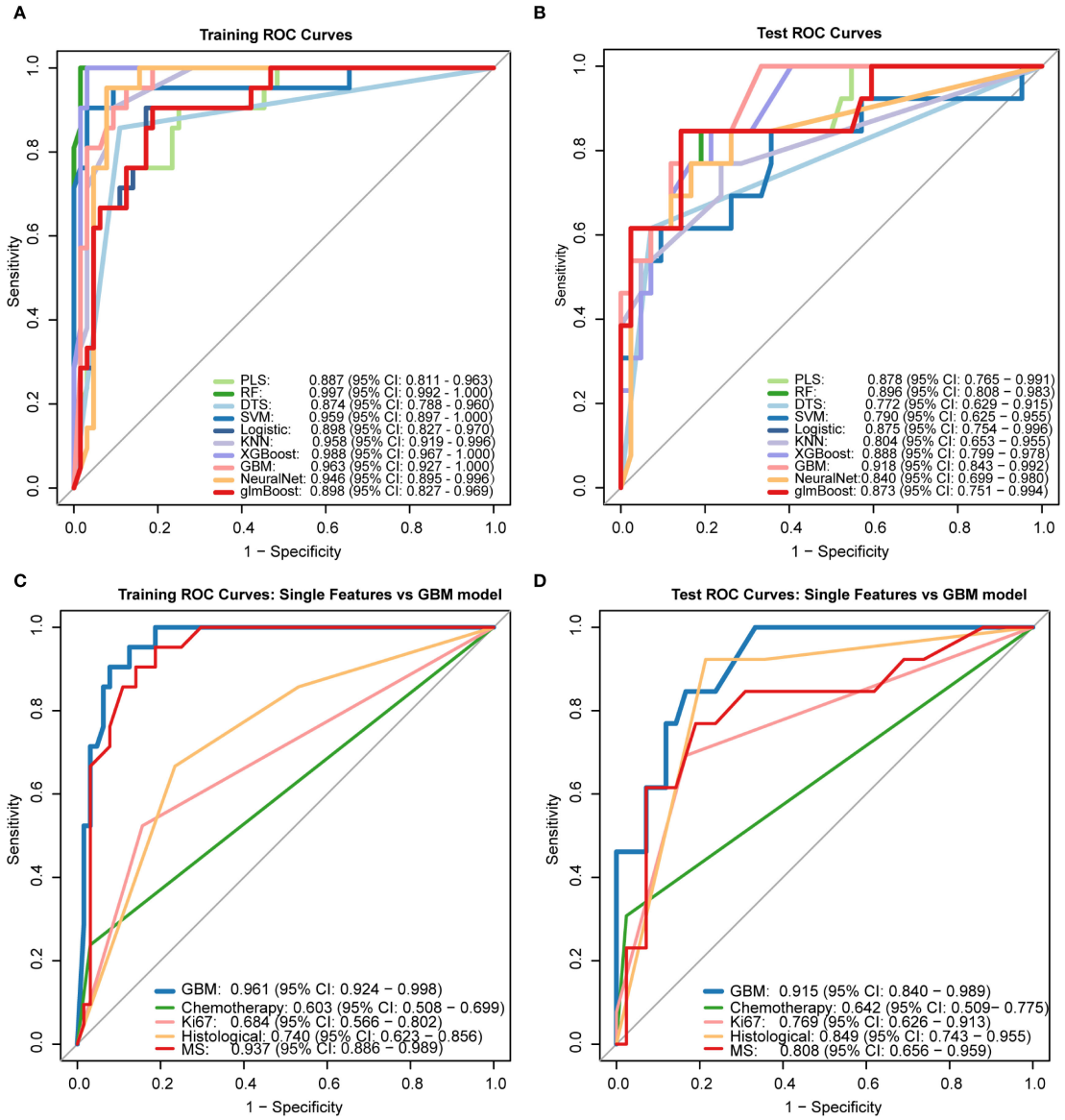

FIGURE 4
Performance comparison of machine learning models receiver operating characteristic (ROC) curves of 10 ML algorithms in **(A)** training set and **(B)** test set. The Gradient Boosting Machine (GBM) demonstrated superior performance (test AUC = 0.918). **(C, D)** Comparison between GBM integrated model and single-feature signatures, showing higher AUC values for the integrated model in both training (0.961) and test sets (0.915).PLS: Partial Least Squares, RF: Random Forest, DTS: Decision Tree Splitting, SVM: Support Vector Machine, Logistic: Logistic Regression, KNN: K-Nearest Neighbors, XGBoost: eXtreme Gradient Boosting, GBM: Gradient Boosting Machine, NeuralNet: Neural Network, glmBoost: gradient boosting for generalized linear models.

In the present study, the GBM algorithm, an advanced ensemble learning method based on gradient boosting, demonstrated excellent predictive performance in medical datasets with complex feature interactions. By organically combining DL features from mammography with clinicopathological variables, the GBM model significantly outperformed traditional ML methods in predicting the risk of DCIS recurrence. Compared with traditional LR models, the GBM algorithm more effectively captures nonlinear relationships and feature interactions through its iterative boosting process while maintaining strong robustness to data noise and outliers. SHAP value analysis quantitatively showed that the MS was the most influential predictor, followed by Ki-67 index and histological grade, consistent with the clinical knowledge of DCIS progression. The MS is a composite quantitative score derived from deep learning analysis of preoperative breast X-ray imaging. Although algorithm-generated, its numerical value correlates with visually identifiable radiological features associated with known and invasive lesions. Higher MS scores typically correspond to breast X-ray imaging manifestations characterized by: cluster-like microcalcifications without masses (such as fine speckled, linear, and branched patterns), which may also present as single or multiple masses, particularly those showing a mouse-tail-like blurring at the posterior edge along ductal pathways. The model's

10.3389/fimmu.2025.1681072

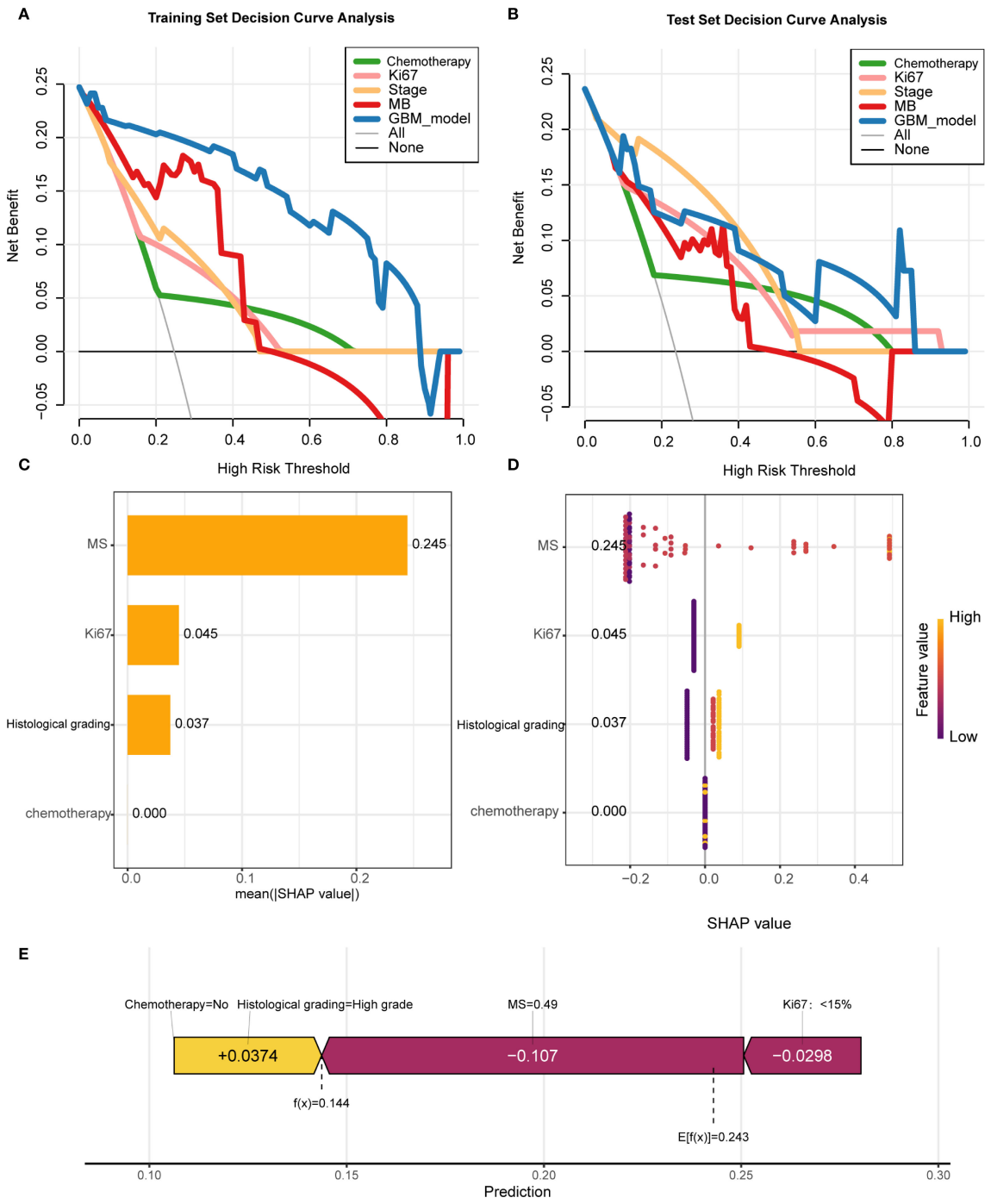

FIGURE 5
Model interpretability and clinical utility analysis **(A, B)** Decision curve analysis (DCA) demonstrating net benefit of GBM model versus clinical predictors across threshold probabilities. **(C)** SHAP summary plot ranking feature importance (MS > Ki-67 > histological grade > chemotherapy). **(D)** SHAP violin plots showing value distributions impacting predictions (yellow/purple indicate high/low values). **(E)** Force plot exemplifying individualized prediction for a case with reduced recurrence risk (baseline 0.243 → 0.144), where high histological grade was the dominant negative contributor.

excellent predictive performance (AUC = 0.918) benefits from the ability of the GBM algorithm to process high-dimensional feature spaces while effectively avoiding overfitting through regularization. More importantly, the introduction of SHAP interpretation provides clinicians with transparent model decision-making bases, effectively addressing the common "black box" problem of complex ML models. This optimal combination of prediction accuracy and interpretability renders our GBM framework suitable for decision support in the clinical management of DCIS.

Earlier research has demonstrated that adjuvant radiotherapy substantially diminishes the likelihood of local disease recurrence following breast-conserving surgery for ductal carcinoma *in situ*

(hazard ratio 0.3–0.5) (36, 37), findings that align with our current investigation, which revealed a markedly elevated recurrence rate among patients not receiving radiotherapy. However, SHAP analysis in this study further revealed increased recurrence risk even in patients who received radiotherapy, with high-grade lesions, and with high Ki-67 expression, thus suggesting the need to additionally consider molecular characteristics to optimize radiotherapy indications. Our research integrates breast X-ray deep learning features with Ki-67 and histological grading to establish a refined pre-treatment risk stratification framework that surpasses traditional factors. SHAP analysis demonstrates that these elements exhibit additive and potentially synergistic predictive value. For instance, a patient with high-grade DCIS exhibiting high MS (indicating fine linear calcifications or spiculated masses) coupled with elevated Ki-67 levels (>30%) would be identified by our model as having extremely high recurrence risk. This specific imaging-clinical profile suggests a biologically aggressive tumor with high proliferative potential, even in cases of negative margins. While standard adjuvant radiotherapy benefits such high-risk patients, it may not sufficiently counteract their inherent recurrence risk. Consequently, our model serves as a decision-support tool to enhance treatment strategies (including optimized radiotherapy dosage, extended endocrine therapy, consideration of systemic chemotherapy, and intensified monitoring). Conversely, patients with low MS (indicating benign-like features), low histological grade, and low Ki-67 levels are predicted to have excellent prognosis. For these patients, our model supports step-down therapy—such as omitting radiotherapy or following standard monitoring protocols in selected cases—to avoid overtreatment and reduce side effects.

While our model demonstrates strong discriminative capabilities, several critical limitations of this study must be noted. Firstly, the relatively limited sample size—particularly when compared to the original high-dimensional feature set—may raise concerns about overfitting due to the reduced number of events. To address this, we implemented rigorous feature reduction techniques (such as LASSO regression) and cross-validation to mitigate these issues. However, some highly complex models (such as decision trees and extreme random forests) still exhibited overfitting on the training set (AUC = 1.000), highlighting the importance of rigorous model selection and validation in high-dimensional data. The GBM model we ultimately selected demonstrated outstanding and consistent performance across both training and test sets, indicating its strong generalization capability. Nevertheless, this result should be viewed with caution. Secondly, this is a retrospective study conducted by a single institution, with its sample exclusively drawn from the Asian (China) population. The inherent selection bias in this design, combined with the homogeneity of genetic background, lifestyle patterns, and healthcare practices within the population, severely limits the external validity and generalizability of our predictive model. Therefore, before implementing this model in clinical practice, it must undergo large-scale external validation in multicenter prospective cohorts encompassing diverse geographic distributions, ethnicities, and racial backgrounds. Future research should focus on validating the model's robustness through larger-scale samples. Only after demonstrating its effectiveness across broader populations can this model be considered a universally applicable decision support tool. Thirdly, regarding post-breast-conserving surgery adjuvant therapy details, our study is constrained by the completeness of available retrospective data. While we documented the implementation of adjuvant chemotherapy, endocrine therapy, and adjuvant radiotherapy, specific protocol details (such as chemotherapy cycle counts and dosages; endocrine drug selection and treatment duration; total radiation dose, fractionated regimens, and brachytherapy usage) and technical specifications were not consistently available for all patients. Consequently, our analysis could not account for potential variations in radiotherapy protocols that might influence recurrence outcomes and constitute unmeasured sources of confounding factors. Finally, while multimodal data were integrated, the extraction of imaging features mainly relied on two-dimensional mammography images and did not include richer imaging information such as dynamic contrast-enhanced MRI.

Conclusion

This research documented the utilization of machine learning methodologies incorporating mammographic imaging characteristics, clinical data, and laboratory measurements for forecasting recurrence among DCIS patients, establishing a GBM algorithmic framework capable of accurately estimating DCIS recurrence probability. In this study, the combination of ML with the interpretable SHAP method endowed the "black-box" ML model with interpretability, making it more suitable for predicting DCIS recurrence in clinical scenarios. Additionally, the inclusion of DCA highlights the clinical value of GBM. We propose the use of this approach as an auditable decision-support tool to facilitate patient healthcare and research.

Data availability statement

The original contributions presented in the study are included in the article/Supplementary Material. Further inquiries can be directed to the corresponding author/s.

Ethics statement

The studies involving humans were approved by Institutional Ethics Review Board of Harbin Medical University Cancer Hospital. The studies were conducted in accordance with the local legislation and institutional requirements. The participants provided their written informed consent to participate in this study. The animal study was approved by the Institutional Ethics Review Board of Harbin Medical University Cancer Hospital. The study was conducted in accordance with the local legislation and institutional requirements. Written informed consent was

obtained from the individual(s) for the publication of any potentially identifiable images or data included in this article.

Author contributions

YS: Conceptualization, Data curation, Investigation, Methodology, Resources, Validation, Visualization, Writing – original draft, Writing – review & editing. QY: Conceptualization, Investigation, Methodology, Project administration, Resources, Supervision, Validation, Visualization, Writing – original draft, Writing – review & editing. YD: Data curation, Investigation, Methodology, Software, Supervision, Visualization, Writing – review & editing. SY: Investigation, Software, Supervision, Validation, Visualization, Writing – review & editing. MN: Resources, Software, Supervision, Validation, Visualization, Writing – review & editing. XL: Project administration, Resources, Software, Validation, Visualization, Writing – review & editing. SS: Conceptualization, Supervision, Validation, Visualization, Writing – review & editing. TL: Data curation, Formal Analysis, Resources, Writing – review & editing. SG: Data curation, Formal Analysis, Resources, Writing – review & editing. JH: Funding acquisition, Methodology, Project administration, Resources, Supervision, Validation, Visualization, Writing – review & editing.

Funding

The author(s) declare financial support was received for the research and/or publication of this article. This research was funded by the Wu Jie Ping Medical Foundation (Grant No. 320.6750.18215), the Haiyan Science Foundation (Grant No. JJZD2021-02), and the China Primary health care Foundation (Grant No. cphcf-2023-017).

Acknowledgments

We extend our gratitude to all the contributing authors for their significant contributions to the study. Our heartfelt appreciation is also due to the cancer patients who participated in this research, for their endurance and cooperation throughout treatment and follow-up. We are indebted to the Harbin Medical University Cancer Hospital for its support.

Conflict of interest

The authors declare that the research was conducted in the absence of any commercial or financial relationships that could be construed as a potential conflict of interest.

Generative AI statement

The author(s) declare that no Generative AI was used in the creation of this manuscript.

Any alternative text (alt text) provided alongside figures in this article has been generated by Frontiers with the support of artificial intelligence and reasonable efforts have been made to ensure accuracy, including review by the authors wherever possible. If you identify any issues, please contact us.

Publisher's note

All claims expressed in this article are solely those of the authors and do not necessarily represent those of their affiliated organizations, or those of the publisher, the editors and the reviewers. Any product that may be evaluated in this article, or claim that may be made by its manufacturer, is not guaranteed or endorsed by the publisher.

Supplementary material

The Supplementary Material for this article can be found online at: https://www.frontiersin.org/articles/10.3389/fimmu.2025.1681072/full#supplementary-material

References

1. Kim J, Harper A, McCormack V, Sung H, Houssami N, Morgan E, et al. Global patterns and trends in breast cancer incidence and mortality across 185 countries. *Nat Med*. (2025) 31:1154–62. doi: 10.1038/s41591-025-03502-3

2. Farante G, Toesca A, Magnoni F, Lissidini G, Vila J, Mastropasqua M, et al. Advances and controversies in management of breast ductal carcinoma in *situ* (DCIS). *Eur J Surg Oncol*. (2022) 48:736–41. doi: 10.1016/j.ejso.2021.10.030

3. Wärnberg F, Garmo H, Emdin S, Hedberg V, Adwall L, Sandelin K, et al. Effect of radiotherapy after breast-Conserving surgery for ductal carcinoma in situ: 20 years follow-Up in the randomized sweDCIS trial. *J Clin Oncol*. (2014) 32:3613–8. doi: 10.1200/JCO.2014.56.2595

4. Maxwell AJ, Hilton B, Clements K, Dodwell D, Dulson-Cox J, Kearins O, et al. Unresected screen-detected ductal carcinoma in *situ*: Outcomes of 311 women in the Forget-Me-Not 2 study. *Breast*. (2022) 61:145–55. doi: 10.1016/j.breast.2022.01.001

5. Teh Y-C, Tan G-H, Taib NA, Rahmat K, Westerhout CJ, Fadzli F, et al. Opportunistic mammography screening provides effective detection rates in a limited resource healthcare system. *BMC Cancer*. (2015) 15:405. doi: 10.1186/s12885-015-1419-2

6. Dershaw DD, Abramson A, Kinne DW. Ductal carcinoma in *situ*: mammographic findings and clinical implications. *Radiology*. (1989) 170:411–5. doi: 10.1148/radiology.170.2.2536185

7. Grimm LJ, Rahbar H, Abdelmalak M, Hall AH, Ryser MD. Ductal carcinoma in situ: state-of-the-art review. *Radiology*. (2022) 302:246–55. doi: 10.1148/radiol.211839

8. Tan H, Wu Q, Wu Y, Zheng B, Wang B, Chen Y, et al. Mammography-based artificial intelligence for breast cancer detection, diagnosis, and BI-RADS categorization using multi-view and multi-level convolutional neural networks. *Insights into Imaging*. (2025) 16:109. doi: 10.1186/s13244-025-01983-x

9. Khalid A, Mehmood A, Alabrah A, Alkhamees BF, Amin F, AlSalman H, et al. Breast cancer detection and prevention using machine learning. *Diagnostics*. (2023) 13:3113. doi: 10.3390/diagnostics13193113

10. Alaeikhanehshir S, Voets MM, van Duijnhoven FH, lips EH, Groen EJ, van Oirsouw MCJ, et al. Application of deep learning on mammographies to discriminate between low and high-risk DCIS for patient participation in active surveillance trials. *Cancer Imaging*. (2024) 24:48. doi: 10.1186/s40644-024-00691-x

11. Ponce-Bobadilla AV, Schmitt V, Maier CS, Mensing S, Stodtmann S. Practical guide to SHAP analysis: Explaining supervised machine learning model predictions in drug development. *Clin Trans Sci*. (2024) 17:e70056. doi: 10.1111/cts.70056

12. Guan X, Du Y, Ma R, Teng N, Ou S, Zhao H, et al. Construction of the XGBoost model for early lung cancer prediction based on metabolic indices. *BMC Med Inf Decision Making*. (2023) 23:107. doi: 10.1186/s12911-023-02171-x

13. Yogananda CGB, Shah BR, Vejdani-Jahromi M, Nalawade SS, Murugesan GK, Yu FF, et al. A fully automated deep learning network for brain tumor segmentation. *Tomography*. (2020) 6:186–93. doi: 10.18383/j.tom.2019.00026

14. Broc C, Truong T, Liquet B. Penalized partial least squares for pleiotropy. *BMC Bioinf*. (2021) 22:86. doi: 10.1186/s12859-021-03968-1

15. Chen Z, He N, Huang Y, Qin WT, Liu X, Li L. Integration of A deep learning classifier with A random forest approach for predicting malonylation sites. *Genomics Proteomics Bioinf*. (2019) 16:451–9. doi: 10.1016/j.gpb.2018.08.004

16. Yang Y, Xu L, Sun L, Zhang P, Farid SS. Machine learning application in personalised lung cancer recurrence and survivability prediction. *Comput Struct Biotechnol J*. (2022) 20:1811–20. doi: 10.1016/j.csbj.2022.03.035

17. Vetter TR, Schober P. Regression: the apple does not fall far from the tree. *Anesth Analgesia*. (2018) 127:277–83. doi: 10.1213/ANE.0000000000003424

18. Bian Z, Vong CM, Wong PK, Wang S. Fuzzy KNN method with adaptive nearest neighbors. *IEEE Trans Cybernetics*. (2022) 52:5380–93. doi: 10.1109/TCYB.2020.3031610

19. Ma B, Meng F, Yan G, Yan H, Chai B, Song F. Diagnostic classification of cancers using extreme gradient boosting algorithm and multi-omics data. *Comput Biol Med*. (2020) 121:103761. doi: 10.1016/j.compbiomed.2020.103761

20. Rodríguez-Tomàs E, Arenas M, Baiges-Gaya G, Acosta J, Araguas P, Malave B, et al. Gradient boosting machine identified predictive variables for breast cancer patients pre- and post-Radiotherapy: preliminary results of an 8-Year follow-Up study. *Antioxidants*. (2022) 11:2394. doi: 10.3390/antiox11122394

21. Zhao S, Chen P, Wang X, Zheng Z, Hui R, Pang G. Preoperatively predicting human epidermal growth factor receptor 2-low expression in breast cancer using neural network model based on multiparameter magnetic resonance imaging. *Quantitative Imaging Med Surg*. (2024) 14:8387–401. doi: 10.21037/qims-24-428

22. Wu Y, Xu D, Zha Z, Gu L, Chen J, Fang J, et al. Integrating radiomics into predictive models for low nuclear grade DCIS using machine learning. *Sci Rep*. (2025) 15:7505. doi: 10.1038/s41598-025-92080-y

23. Ruz GA, Araya-Díaz P, Henríquez PA. Facial biotype classification for orthodontic treatment planning using an alternative learning algorithm for tree augmented Naive Bayes. *BMC Med Inform Decis Mak*. (2022) 22:316. doi: 10.1186/s12911-022-02062-7

24. Liang Y, Ma X. iACP-GE: accurate identification of anticancer peptides by using gradient boosting decision tree and extra tree. *SAR QSAR Environ Res*. (2023) 34:1–19. doi: 10.1080/1062936X.2022.2160011

25. Wang LA, Kern R, Yu E, Choi S, Pan JQ. IntelliSleepScorer, a software package with a graphic user interface for automated sleep stage scoring in mice based on a light gradient boosting machine algorithm. *Sci Rep*. (2023) 13:4275. doi: 10.1038/s41598-023-31288-2

26. Sorayaie Azar A, Babaei Rikan S, Naemi A, Bagherzadeh Mohasefi J, Pirnejad H, Bagherzadeh Mohasefi M, et al. Application of machine learning techniques for predicting survival in ovarian cancer. *BMC Med Inform Decis Mak*. (2022) 22:345. doi: 10.1186/s12911-022-02087-y

27. Jayaram N, Muralidharan M, Muthupandian S. The use of multilayer perceptron and radial basis function: an artificial intelligence model to predict progression of oral cancer. *Int J Surg*. (2023) 109:57–9. doi: 10.1097/JS9.0000000000000026

28. Lan X, Wang X, Qi J, Chen H, Zeng X, Shi J, et al. Application of machine learning with multiparametric dual-energy computed tomography of the breast to differentiate between benign and Malignant lesions. *Quantitative Imaging Med Surg*. (2021) 12:810–22. doi: 10.21037/qims-21-39

29. Miranda E, Adiarto S, Bhatti FM, Zakiyyah AY, Aryuni M, Bernando C. Understanding arteriosclerotic heart disease patients using electronic health records: A machine learning and shapley additive exPlanations approach. *Healthc Inform Res*. (2023) 29:228–38. doi: 10.4258/hir.2023.29.3.228

30. Wang G, Zhang Y, Li S, Zhang J, Jiang D, Li X, et al. A machine learning-based prediction model for cardiovascular risk in women with preeclampsia. *Front Cardiovasc Med*. (2021) 8. doi: 10.3389/fcvm.2021.736491

31. Rakovitch E, Nofech-Mozes S, Hanna W, Baehner FL, Saskin R, Butler SM, et al. A population-based validation study of the DCIS Score predicting recurrence risk in individuals treated by breast-conserving surgery alone. *Breast Cancer Res Treat*. (2015) 152:389–98. doi: 10.1007/s10549-015-3464-6

32. Liu C, Sun M, Arefan D, Zuley M, Sumkin J, Wu S. Deep learning of mammogram images to reduce unnecessary breast biopsies: a preliminary study. *Breast Cancer Res*. (2024) 26:82. doi: 10.1186/s13058-024-01830-9

33. Wetstein SC, Stathonikos N, Pluim JPW, Heng YJ, ter Hoeve ND, Vreuls CPH, et al. Deep learning-based grading of ductal carcinoma in *situ* in breast histopathology images. *Lab Invest*. (2021) 101:525–33. doi: 10.1038/s41374-021-00540-6

34. Dong J, Feng T, Thapa-Chhetry B, Cho BG, Shum T, Inwald DP, et al. Machine learning model for early prediction of acute kidney injury (AKI) in pediatric critical care. *Crit Care*. (2021) 25:288. doi: 10.1186/s13054-021-03724-0

35. Heo J, Yoon JG, Park H, Kim YD, Nam HS, Heo JH. Machine learning–based model for prediction of outcomes in acute stroke. *Stroke*. (2019) 50:1263–5. doi: 10.1161/STROKEAHA.118.024293

36. Corradini S, Pazos M, Schönecker S, Reitz D, Niyazi M, Ganswindt U, et al. Role of postoperative radiotherapy in reducing ipsilateral recurrence in DCIS: an observational study of 1048 cases. *Radiat Oncol*. (2018) 13:25. doi: 10.1186/s13014-018-0964-7

37. van Seijen M, Lips EH, Thompson AM, Nik-Zainal S, Futreal A, Hwang ES, et al. Ductal carcinoma in *situ*: to treat or not to treat, that is the question. *Br J Cancer*. (2019) 121:285–92. doi: 10.1038/s41416-019-0478-6

frontiers | Frontiers in Immunology

TYPE Original Research
PUBLISHED 19 September 2025
DOI 10.3389/fimmu.2025.1669275

Check for updates

OPEN ACCESS

EDITED BY
Qi Wang,
Jiangsu University, China

REVIEWED BY
Hengrui Liu,
University of Cambridge, United Kingdom
Yu Dong,
Fudan University, China
Xiaofeng Ding,
Wenzhou Medical University, China

*CORRESPONDENCE
Sunbin Ling
lsb0330@zju.edu.cn
Liming Wang
wangbcc259@163.com

†These authors have contributed equally to this work and share first authorship

RECEIVED 19 July 2025
ACCEPTED 29 August 2025
PUBLISHED 19 September 2025

CITATION
Gao M, Liu Y, Wu J, Zhang P, Liu J, Guo K, Sun B, Ling S and Wang L (2025) Stemness- and hypoxia-based prognostic stratification index reveals G6PD as a regulator of hypoxia-driven stemness in hepatocellular carcinoma. *Front. Immunol.* 16:1669275. doi: 10.3389/fimmu.2025.1669275

COPYRIGHT
© 2025 Gao, Liu, Wu, Zhang, Liu, Guo, Sun, Ling and Wang. This is an open-access article distributed under the terms of the Creative Commons Attribution License (CC BY). The use, distribution or reproduction in other forums is permitted, provided the original author(s) and the copyright owner(s) are credited and that the original publication in this journal is cited, in accordance with accepted academic practice. No use, distribution or reproduction is permitted which does not comply with these terms.

Stemness- and hypoxia-based prognostic stratification index reveals G6PD as a regulator of hypoxia-driven stemness in hepatocellular carcinoma

Mingwei Gao[1,2,3†], Yuechuan Liu[1,2,3†], Jianhui Wu[2,3†], Peiru Zhang[2,3], Jin Liu[2,3], Kun Guo[2,3], Binwen Sun[2,3], Sunbin Ling[2,3*] and Liming Wang[1,2,3*]

[1]Division of Hepatobiliary and Pancreatic Surgery, Department of General Surgery, The Second Affiliated Hospital of Dalian Medical University, Dalian, China, [2]Engineering Research Center for New Materials and Precision Treatment Technology of Malignant Tumors Therapy, The Second Affiliated Hospital of Dalian Medical University, Dalian, China, [3]Engineering Technology Research Center for Translational Medicine, The Second Affiliated Hospital of Dalian Medical University, Dalian, China

Background: The positive feedback loop between cancer stemness and the hypoxic microenvironment is a critical driver of hepatocellular carcinoma (HCC) progression. Analyzing their interaction in HCC is crucial to characterize immune microenvironment features, uncover molecular heterogeneity patterns, and develop targeted interventions.

Methods: The TCGA-LIHC cohort (n=340) were stratified through consensus clustering of stemness- and hypoxia-related genes (SHRGs) identified by one-class logistic regression and weighted gene co-expression network analyses. Subsequently, a stemness- and hypoxia-related prognostic index (SHRPI) was constructed using random forest, and Cox regression analyses, with its prognostic significance assessed in two other independent cohorts: our NC-LT cohort comprising 180 liver transplant (LT) patients with HCC beyond Milan criteria, and the GSE104580 cohort containing 147 HCC patients treated with transcatheter arterial chemoembolization (TACE). A prognostic nomogram incorporating SHRPI was developed, and externally validated in the GSE14520 cohort (n=242). Systematic profiling of immune microenvironment features and immunotherapy responsiveness in SHRPI subgroups was performed, followed by pharmacogenomic screening and molecular docking to identify optimal therapies. After single-cell transcriptomic analysis, functional validation assays were conducted to confirm the role of G6PD, a key SHRPI component.

Results: SHRGs-based clustering revealed two clusters exhibiting distinct prognoses, functional annotations, genomic alterations, and immune microenvironment features. SHRPI served as an independent risk factor for both overall survival in HCC patients and recurrence-free survival in LT patients beyond Milan criteria. It demonstrated strong predictive power for TACE responsiveness. The SHRPI-integrated nomogram achieved robust performance in external validation. High SHRPI level was associated with a more immunosuppressive tumor microenvironment and poorer immunotherapy responsiveness. Pharmacogenomic and molecular docking analyses identified BI2536 as the most promising therapeutic agent for this

high-SHRPI subgroup. Further experiments established that G6PD serves as a key therapeutic target for hypoxia-driven stemness maintenance in HCC by functioning as a stemness regulator that interacts with HIF-1α to form a positive feedback loop under hypoxia.

Conclusions: This study provides further insights into stemness-hypoxia interaction in HCC and delivers a clinically applicable predictive tool for prognosis. BI2536's synergy potential and the therapeutic value of G6PD targeting in stemness regulation advance individualized therapeutic strategies for HCC.

KEYWORDS

hepatocellular carcinoma, stemness, hypoxia, prognosis, immune microenvironment, G6PD

1 Introduction

Hepatocellular carcinoma (HCC) is a highly aggressive malignancy characterized by a high recurrence rate and broad therapeutic resistance, significantly impacting patient prognosis (1). Studies have shown that the malignant characteristics of HCC are closely linked to the presence and function of cancer stem cells (CSCs) (2, 3). CSCs possess self-renewal capacity and differentiation plasticity, enabling them to evade immune surveillance and play a pivotal role in tumor initiation, progression, and therapeutic resistance (4, 5). These cells maintain their stem-like properties by activating embryonic developmental signaling pathways such as Wnt/β-catenin and Notch while upregulating drug efflux pumps, thereby enhancing resistance to conventional therapies (6, 7). As reservoirs for tumor relapse, CSCs rely heavily on the hypoxic tumor microenvironment (TME) for survival and stemness maintenance (8, 9).

Within solid tumors, low oxygen levels not only promote angiogenesis and metabolic reprogramming to support tumor growth but also activate hypoxia-inducible factors (HIFs), which transcriptionally upregulate stemness-related genes such as Oct4 and Nanog. This process further sustains the stem-like phenotype of CSCs, contributing to HCC invasiveness and treatment resistance (10–13). Moreover, hypoxia reprograms the TME into an immunosuppressive niche, amplifying CSC-driven malignancy. Intratumoral hypoxia induces the secretion of cytokines such as TGF-β and IL-6 while promoting the recruitment of regulatory T cells (Tregs) and myeloid-derived suppressor cells (MDSCs). These immunosuppressive components cooperatively inhibit cytotoxic T-cell ($CD8^+$ T-cell) activity, protecting CSCs from immune clearance (14). Additionally, hypoxia-driven upregulation of immune checkpoints such as PD-L1 and CTLA-4 exacerbates immune evasion (15, 16). As the tumor progresses, increased oxygen consumption exacerbates TME hypoxia, forming a self-reinforcing malignant cycle that enhances tumor aggressiveness (8, 17). Therefore, identifying, quantifying, and therapeutically targeting stemness-hypoxia features holds significant clinical value for optimizing HCC risk stratification and precision therapy.

Despite the recognized role of the stemness-hypoxia axis in HCC progression, there remains a lack of systematic, rigorous, and effective prognostic indices that integrate stemness and hypoxia characteristics for stratifying patients and identifying high-risk subgroups to guide precision treatment strategies. Furthermore, current HCC prognostic models are primarily based on either single molecular features (e.g., stemness indices or hypoxia scores) or clinicopathological parameters (18–21). The limited dimensionality of these models restricts their accuracy in predicting patient outcomes. Therefore, it is imperative to develop a comprehensive prognostic tool that integrates multi-dimensional molecular features (incorporating both stemness and hypoxia) with clinicopathological parameters to improve risk stratification,

Abbreviations: HCC, hepatocellular carcinoma; CSCs, cancer stem cells; TME, tumor microenvironment; HIFs, hypoxia-inducible factors; Tregs, regulatory T cells; MDSCs, myeloid-derived suppressor cells; SHRPI, stemness- and hypoxia-related prognostic index; mRNAsi, mRNA expression-based stemness index; OS, overall survival; DEGs, differentially expressed genes; WGCNA, weighted gene co-expression network analysis; SHRGs, stemness- and hypoxia-related genes; CDF, cumulative distribution function; FDR, false discovery rate; CNV, copy number variation; SNV, single-nucleotide variant; TMB, tumor mutational burden; HRD, homologous recombination deficiency; TIDE, tumor immune dysfunction and exclusion; ssGSEA, single-sample gene set enrichment analysis; TAMs, tumor-associated macrophages; LASSO, least absolute shrinkage and selection operator; ROC, receiver operating characteristic; AUC, area under the curve; LT, liver transplant; TACE, transcatheter arterial chemoembolization; DCA, decision curve analysis; LRG, low-risk group; HRG, high-risk group; TIME, tumor immune microenvironment; Tfh, helper T cells; CTRP, cancer therapeutics response portal; PRISM, profiling relative inhibition simultaneously in mixtures; GDSC, genomics of drug sensitivity in cancer; OCLR, one-class logistic regression; ICI, immune checkpoint inhibitor; EMT, epithelial-mesenchymal transition; PPP, pentose phosphate pathway; CIBERSORT, cell-type identification by estimating relative subsets of RNA transcripts; HRs, hazard ratios; AUC, area under the dose-response curve; Co-IP, co-immunoprecipitation.

enhance prediction accuracy, and provide a rationale for personalized treatment strategies for high-risk subgroups.

In this study, we utilized large-scale public multi-omics datasets and integrated multiple machine learning algorithms and statistical analysis methods to identify key genes involved in stemness-hypoxia regulation. We constructed a stemness- and hypoxia-related prognostic index (SHRPI) to stratify HCC patients into distinct risk subgroups, and developed a high-performance prognostic nomogram. Additionally, we screened potential therapeutic drugs targeting high-risk subgroup through pharmacogenomic and molecular docking analyses. Capitalizing on the high-resolution cellular heterogeneity mapping capability of single-cell transcriptomics (22, 23), we further dissected the cell-type-specific expression profiles of SHRPI components and validated the role and potential mechanism of its most critical gene in maintaining HCC stemness under hypoxia.

2 Materials and methods

2.1 Data collection and preprocessing

The discovery cohort of HCC patients was obtained from TCGA-LIHC through their data portal (https://portal.gdc.cancer.gov/projects/TCGA-LIHC), comprising gene expression profiles, copy number variation (CNV) data, somatic mutation data, and clinical information. The validation cohort consisted of gene expression profiles and clinical information from the GSE14520 dataset, retrieved from GEO database (https://www.ncbi.nlm.nih.gov/geo/). After comprehensive screening, this study included 340 patients from TCGA-LIHC with complete survival information, overall survival (OS) > 30 days, and accessible stemness indices and hypoxia scores, as well as 242 patients from GSE14520 fulfilling the criteria of complete survival data and OS > 30 days. For transcriptomic data normalization, log2(FPKM + 0.001) transformation was applied. To mitigate batch effects in transcriptomic data, we followed the recommended standard procedures for bulk transcriptomic data analysis in cancer research, applying the Combat algorithm from the "SVA" R package for batch effect correction (23). Additionally, we incorporated 180 liver transplant (LT) patients with HCC beyond the Milan criteria from our previous study (NC-LT cohort) to evaluate the impact of the gene signature on recurrence-free survival (RFS) (24), along with 147 patients from the GSE104580 dataset to assess the correlation between the gene signature and patient response to transcatheter arterial chemoembolization (TACE) therapy.

2.2 Computation of stemness indices

The stemness signature was determined using the one-class logistic regression (OCLR) machine-learning algorithm (25). Subsequently, correlation coefficients were computed between the stemness signature weight values and gene expression levels for each sample. Finally, the stemness index was derived by scaling the Spearman correlation coefficients to a range between 0 and 1.

2.3 Differential expression analysis

The TCGA-LIHC samples were categorized into high and low groups based on either the median value or the optimal cutoff value determined by maximizing the Youden index using the "survminer" R package. Differential expression analysis was conducted using the Wilcoxon rank-sum test (26). Genes meeting the criteria of false discovery rate (FDR) < 0.05 and |log2(fold change)| > 1 were considered statistically significant. To enhance the accuracy of the risk model, a more stringent selection threshold was applied, setting FDR < 0.01 and |log2(fold change)| > 2.

2.4 Definition of stemness- and hypoxia-related genes

The hypoxia signature score for TCGA-LIHC patients was obtained from The cBio Cancer Genomics Portal (http://cbioportal.org), and hypoxia-related genes were identified using weighted gene co-expression network analysis (WGCNA) (27). The overlapping genes between mRNAsi-related differentially expressed genes (DEGs) and hypoxia-related genes were collectively defined as stemness- and hypoxia-related genes (SHRGs).

2.5 Unsupervised consensus clustering

The "ConsensusClusterPlus" R package was employed for the classification of SHRGs through unsupervised consensus clustering. To enhance classification stability, the clustering process was conducted 1,000 times with 80% resampling. The optimal k value (number of clusters) was identified based on the relative variation in the area under the cumulative distribution function (CDF) curves and the consensus matrix.

2.6 Functional enrichment analysis

GO, KEGG, and GSEA analyses were conducted using the "clusterProfiler" R package, while GSVA analysis was performed with the unsupervised "GSVA" R package. The background gene sets for both GSEA and GSVA were obtained from the Molecular Signatures Database (MSigDB) (28), specifically the h.all.v2024.1.Hs.symbols.gmt gene set. Subsequently, differential analysis of the GSVA results was conducted using the "limma" R package, considering pathways with FDR < 0.05 as significantly enriched, with |t| > 2 shown in figures for visualization.

2.7 Genetic alterations and immune infiltration analysis

The CNV and somatic mutation data of TCGA-LIHC patients were analyzed using the "maftools" R package to examine genetic alterations across different clusters. The 14 oncogenic pathways were compared across various clusters using the PROGENy algorithm (29). To evaluate the tumor immune microenvironment (TIME), the "Cell-type Identification by Estimating Relative Subsets of RNA Transcripts (CIBERSORT)" tool was employed to quantify the abundance of tumor-infiltrating immune cells (30).

2.8 Immune checkpoints and immunotherapy response analysis

To assess immunotherapy response in TCGA-LIHC patients, expression of 68 immune checkpoint-related genes identified in previous studies was analyzed (31). Subsequently, tumor immune dysfunction and exclusion (TIDE) scores, T cell dysfunction scores, T cell exclusion scores, INFG levels, and MDSC levels were retrieved from the TIDE portal (http://tide.dfci.harvard.edu). Single-sample gene set enrichment analysis (ssGSEA) was then applied to compute enrichment scores for 29 immune-related traits and to explore associations between the index and immune regulation (32). Furthermore, ssGSEA-derived enrichment scores for three stem cell related gene sets from MSigDB: "WONG EMBRYONIC STEM CELL CORE," "YAMASHITA LIVER CANCER STEM CELL UP," and "YAMASHITA LIVER CANCER STEM CELL DN" were calculated to investigate associations between the index and stemness.

2.9 Construction of SHRPI

To determine the relationship between SHRGs and patient survival outcomes, we applied univariate Cox regression, LASSO regression, and Random Forest models to filter SHRGs. After excluding attributes with an absolute correlation of 0.8, a total of 419 genes were selected as input variables. Finally, the four most critical genes were identified and incorporated into a multivariate Cox regression model to construct a risk prediction model, termed SHRPI. The formula for this model is as follows:

$$\text{Risk score} = \sum_{i=0}^{n}(\text{Coefficient(i)} \times \text{Expression (i)})$$

To evaluate the robustness of SHRPI, patients were initially stratified into two groups based on the median SHRPI value. The prognostic significance of SHRPI was assessed using Kaplan-Meier survival analysis. The predictive accuracy of SHRPI was further evaluated through receiver operating characteristic (ROC) curve analysis, with the area under the curve (AUC) calculated using the "timeROC" R package. To enhance its clinical applicability, TCGA-LIHC patients were further categorized into high-risk (HRG) and low-risk (LRG) groups based on the optimal cutoff value, followed by comprehensive immune profiling and drug sensitivity analyses.

2.10 Construction of nomogram predictive model

The SHRPI score, along with tumor stage, age, gender, tumor grade, vascular invasion status, Child-Pugh grade, hepatic inflammation status, cirrhosis status, recurrence status, BMI, and AFP levels, was incorporated into the univariate Cox regression analysis. The hazard ratios (HRs) for each variable were computed using the Cox proportional hazards regression model with the "survival" R package. To determine independent prognostic factors, a multivariate Cox regression analysis was performed, and a nomogram was developed based on the findings using the "RMS" R package. Model stability was assessed through Schoenfeld residuals and deviance residuals. The nomogram's predictive performance was evaluated via ROC analysis, calibration curves, and the C-index, calculated through 1,000 bootstrap resampling iterations. Furthermore, decision curve analysis (DCA) was employed to assess the clinical applicability of the predictive model (33).

2.11 Drug response analysis and molecular docking analysis

Gene expression data, along with the corresponding half-maximal inhibitory concentration (IC50) values and area under the dose-response curve (AUC) for cancer cell lines, were obtained from the Genomics of Drug Sensitivity in Cancer (GDSC2 v8.5, released October 2023), the Cancer Therapeutics Response Portal (CTRP v2.0, released October 2015), and the Profiling Relative Inhibition Simultaneously in Mixtures (PRISM) Repurposing dataset (20Q2, released August 2022). AUC values were used as a measure of drug sensitivity, where higher AUC values indicated lower treatment sensitivity. The "oncoPredict" R package was employed to predict drug sensitivity for each sample.

The molecular structures of the compounds were retrieved from PubChem Compound (https://pubchem.ncbi.nlm.nih.gov/), and the 3D coordinates of G6PD (PDB ID: 7UAG, resolution: 3.5Å) were obtained from the PDB (http://www.rcsb.org/). All protein and molecular files were converted into PDBQT format, with water molecules removed and polar hydrogen atoms added to improve docking accuracy. Molecular docking simulations were conducted using AutoDock Vina 1.2.2, and the resulting protein–ligand complexes were visualized with PyMol. The binding energies, which indicate binding stability, were used to assess the therapeutic potential of each compound (34).

2.12 Single-cell RNA sequencing analysis

Single-cell RNA sequencing data from HCC samples in GEO dataset GSE149614 were filtered to remove low-quality cells (< 200

or > 6,000 detected genes, or > 15% mitochondrial content). Gene expression was log-normalized using Seurat (v5.3.0), followed by PCA for dimensionality reduction and clustering via the FindNeighbors and FindClusters functions. Cell clusters were annotated using the "SingleR" R package. SHRPI was computed as a weighted sum of z-score-normalized expression of HMMR, UBE2S, G6PD, and NEIL3. Cells were classified into low- and high-SHRPI groups based on the median SHRPI score. SHRPI distribution was visualized on the t-SNE plot, and expression of each constituent gene across cell clusters was displayed in separate dot plots.

2.13 Cell culture, lentiviral vector construction and infection

Human HCC cell lines (HuH-7, PLC/PRF/5, Hep-3B, and Li-7) and HEK293 were obtained from the Shanghai Institute of Cell Biology, Chinese Academy of Sciences (Shanghai, China). The authenticity of all cells' authenticity was confirmed through short-tandem repeat (STR) profiling. The cells were cultured in the appropriate media supplemented with 10% fetal bovine serum and 1% penicillin-streptomycin (Solarbio) at 37 °C in a 5% CO_2 incubator. Hep-3B and PLC/PRF/5 cells were maintained in MEM medium (Pricella), HEK293 and HuH-7 cells were cultured in high-glucose DMEM (Pricella), and Li-7 cells were maintained in RPMI 1640 medium (Pricella). All cell lines were regularly confirmed to be mycoplasma-free by PCR. Detailed information on lentiviral vector construction and infection is provided in Supplementary File, and all plasmid sequences are listed in Supplementary Table 3.

2.14 Cell migration assay

Cells (2×10^4) were seeded in the upper chamber of a polycarbonate membrane insert (Corning Incorporated) with 200 µL of FBS-free medium. The lower chamber was filled with 800 µL of medium containing 20% FBS. After 24–48 hours of incubation, the cells that had migrated through the membrane were washed, fixed with 1% paraformaldehyde, and stained with crystal violet. Photographs were taken of four randomly selected fields, and the number of migrated cells was counted. The experiment was performed in triplicate.

2.15 Cell sphere formation assay

Cells (2×10^3) were plated onto 6-well Ultra-Low Attachment plates (Corning Incorporated) and cultured in special medium consisting of DMEM/F12 (Invitrogen) supplemented with 4 µg/mL insulin (Sigma-Aldrich), B27 (Invitrogen), 20 ng/mL EGF (Sigma-Aldrich), and 20 ng/mL basic FGF (Invitrogen). After 10 days of incubation, spheres with diameters greater than 75 µm were photographed and counted under a microscope.

2.16 Western blot analysis, co-immunoprecipitation and quantitative PCR analysis

Detailed information is provided in Supplementary File. Specific details regarding the antibodies are presented in Supplementary Table 4. The sequences of primers are provided in Supplementary Table 5.

2.17 Hydrodynamic tail vein injection mouse model

The transgenic HCC mouse model was generated in male wild-type C57BL/6J mice (6–8 weeks) by hydrodynamic tail vein injection co-overexpressing activated AKT and c-Met. In brief, the plasmids m-G6PD pT3-EF1α-MYC or pT3-EF1α-MYC (MCS) (20 µg), pT3-myr-AKT-HA (20 µg), and pT3-EF1α-c-Met (20 µg), together with pCMV(CAT)T7-SB100 (2.4 µg), at a ratio of 12.5: 12.5: 12.5: 1.5, were diluted in 2 ml saline (0.9% NaCl), filtered through a 0.22-µm filter, and injected into the lateral tail vein of the mice within 5-7s (35). 20 days after injection, the mice were humanely euthanized via intraperitoneal injection of sodium pentobarbital (150 mg/kg). Liver tumors were subsequently collected for analysis. Animal experiments were conducted in strict accordance with relevant guidelines and approved by the Institutional Animal Care and Use Committee of Zhejiang Center of Laboratory Animals (IACUC, ZJCLA; approval number: ZJCLA-IACUC-20011186). This study adhered to the ARRIVE guidelines.

2.18 Statistical analysis

The Student's t-test or Wilcoxon rank-sum test (Mann-Whitney U test) was applied to assess continuously distributed numerical data. Correlation analysis was conducted using either the Pearson or Spearman correlation test, depending on data distribution. Survival curves were generated with the Kaplan-Meier method and compared using the Log-rank test. All statistical analyses were performed in GraphPad Prism (v9.0) and R (v4.4.1). A two-tailed P value < 0.05 was considered statistically significant. Statistical significance was annotated as follows: $^*P < 0.05$, $^{**}P < 0.01$, $^{***}P < 0.001$, $^{****}P < 0.0001$; ns = not significant.

3 Results

3.1 Stemness indices and hypoxia scores in HCC

Using mRNA expression and DNA methylation data from the TCGA-LIHC cohort, five stemness indices were calculated, with hypoxia scores obtained from the cBioPortal database. The mRNA expression-based stemness index (mRNAsi) ($P = 0.0031$) and the

Buffa Hypoxia Score ($P < 0.0001$) showed significant associations with OS in HCC (Supplementary Figures 1A, D). Patients with higher mRNAsi exhibited significantly poorer tumor differentiation ($P < 0.0001$), increased vascular invasion ($P = 0.022$), and elevated AFP levels ($P = 0.021$) (Supplementary Figures 1B, C). Similarly, a higher Buffa Hypoxia Score was associated with advanced tumor stage ($P < 0.0001$), poorer tumor differentiation ($P = 0.006$), increased vascular invasion ($P = 0.007$), and elevated AFP levels ($P = 0.027$) (Supplementary Figures 1E, F). Thus, mRNAsi was selected to quantify stemness characteristics, while the Buffa Hypoxia Score was used to evaluate tumor hypoxia levels.

3.2 Identification of stemness- and hypoxia-related clusters in HCC

HCC patients were categorized into high- and low-stemness groups based on the median mRNAsi value, resulting in the identification of 1,341 DEGs associated with mRNAsi (Figure 1A). WGCNA revealed 11 non-grey modules, with the blue module showing the strongest correlation with the Buffa Hypoxia Score ($R^2 = 0.47$, $P = 3.7\times10^{-125}$) (Figure 1B). Integrating mRNAsi-associated DEGs with hypoxia-related genes identified 75 overlapping genes, classified as SHRGs (Figure 1C, Supplementary Table 1). Consensus clustering was performed on the 75 SHRGs, determining optimal classification at k = 2, as indicated by the CDF curve variations (Figure 1D). HCC patients were then divided into two clusters (Cluster 1 and Cluster 2). Patients in Cluster 2 exhibited a significantly shorter median OS and lower survival probability than those in Cluster 1 ($P = 0.0006$) (Figure 1E), as well as higher mRNAsi and hypoxia scores (both $P < 0.001$) (Figure 1F).

To further characterize the molecular differences between the two clusters, we conducted a more stringent differential expression analysis using $|\log2FC| > 2$ and FDR < 0.01 as the selection criteria (Figure 1G, Supplementary Figure 2A). Functional enrichment analysis of DEGs through GO and KEGG revealed significant enrichment in cell cycle regulation and DNA repair pathways (Figure 1H). GSEA further demonstrated that, compared with Cluster 1, Cluster 2 exhibited significant activation of E2F targets, the G2/M checkpoint, and KRAS signaling DN, whereas oxidative phosphorylation, bile acid metabolism, fatty acid metabolism, and adipogenesis were suppressed (Figure 1I). GSVA revealed significant upregulation of proliferation-related pathways, including E2F targets, G2/M checkpoint, DNA repair, and mTOR signaling in Cluster 2. In contrast, Cluster 1 was predominantly enriched in lipid and bile acid metabolism, coagulation, and inflammatory responses (Figure 1J). Overall, these results indicate that Cluster 2 is characterized by a hyperproliferative phenotype with enhanced DNA repair and oncogenic signaling, whereas Cluster 1 is associated with metabolic reprogramming and an inflammatory tumor microenvironment.

3.3 Genomic and TIME characteristics of the two stemness- and hypoxia-related clusters

We next examined somatic mutations and CNV in both clusters to investigate potential mechanisms underlying their distinct prognoses. Recurrent mutations were detected in several genes, including TP53, TTN, and CTNNB1, and the two clusters exhibited distinct single-nucleotide variant (SNV) substitution patterns (Figures 2A, B, Supplementary Figures 2E, F). Notably, TP53, LRP1B, RB1, ABCB5, and ZNF469 displayed significantly different mutation frequencies between the clusters (Figure 2C, Supplementary Figures 2B, C). Moreover, Cluster 2 exhibited higher aneuploidy scores, tumor mutational burden (TMB) and homologous recombination deficiency (HRD) compared with Cluster 1 (Supplementary Figure 2D). These findings suggest that tumors with elevated DNA damage may possess enhanced immune evasion capabilities and reduced responsiveness to immunotherapy (36). To further validate our classification, we compared our patient clusters with a previously established molecular classification in which the "Inflammatory" subtype (C3) was associated with the best prognosis (37). Most C3 patients were assigned to Cluster 1, which had a better prognosis, consistent with previous findings (Figure 2D).

Given the intricate interplay between stemness, hypoxia, and immune-related pathways, we further explored differences in the TIME across the two clusters. CIBERSORT analysis revealed that patients in Cluster 2 exhibited significantly higher levels of activated memory $CD4^+$ T cells, follicular helper T cells, and Tregs, whereas M0 macrophages, resting memory $CD4^+$ T cells, and M2 macrophages were markedly reduced (Figure 2E). Next, we analyzed the expression of previously reported immune checkpoint-related genes across the two clusters (38). In Cluster 2, genes known to suppress T-cell immune activity, including CTLA4 and its ligands as well as PD-1 and its ligands, were significantly upregulated (Figure 2F). With the growing prominence of immunotherapy in HCC treatment, we employed the TIDE model to evaluate patients' potential response. Given that higher TIDE scores indicate increased immune evasion and diminished immunotherapy efficacy, we observed that Cluster 2 had a significantly higher TIDE score than Cluster 1, suggesting that patients in Cluster 2 may have a lower likelihood of benefiting from immunotherapy (Supplementary Figure 3A). We employed ssGSEA to evaluate therapeutic signatures and 29 immune-related gene signatures, encompassing immune, stromal, and other cellular processes. First, Cluster 2 exhibited significant upregulation of gene signatures associated with the cell cycle, DNA replication, and mismatch repair (Supplementary Figure 3B). Second, Cluster 2 displayed increased infiltration of immunosuppressive cells, including tumor-associated macrophages (TAMs), MDSCs and Tregs, along with enhanced tumor cell proliferation, leading to heightened immune

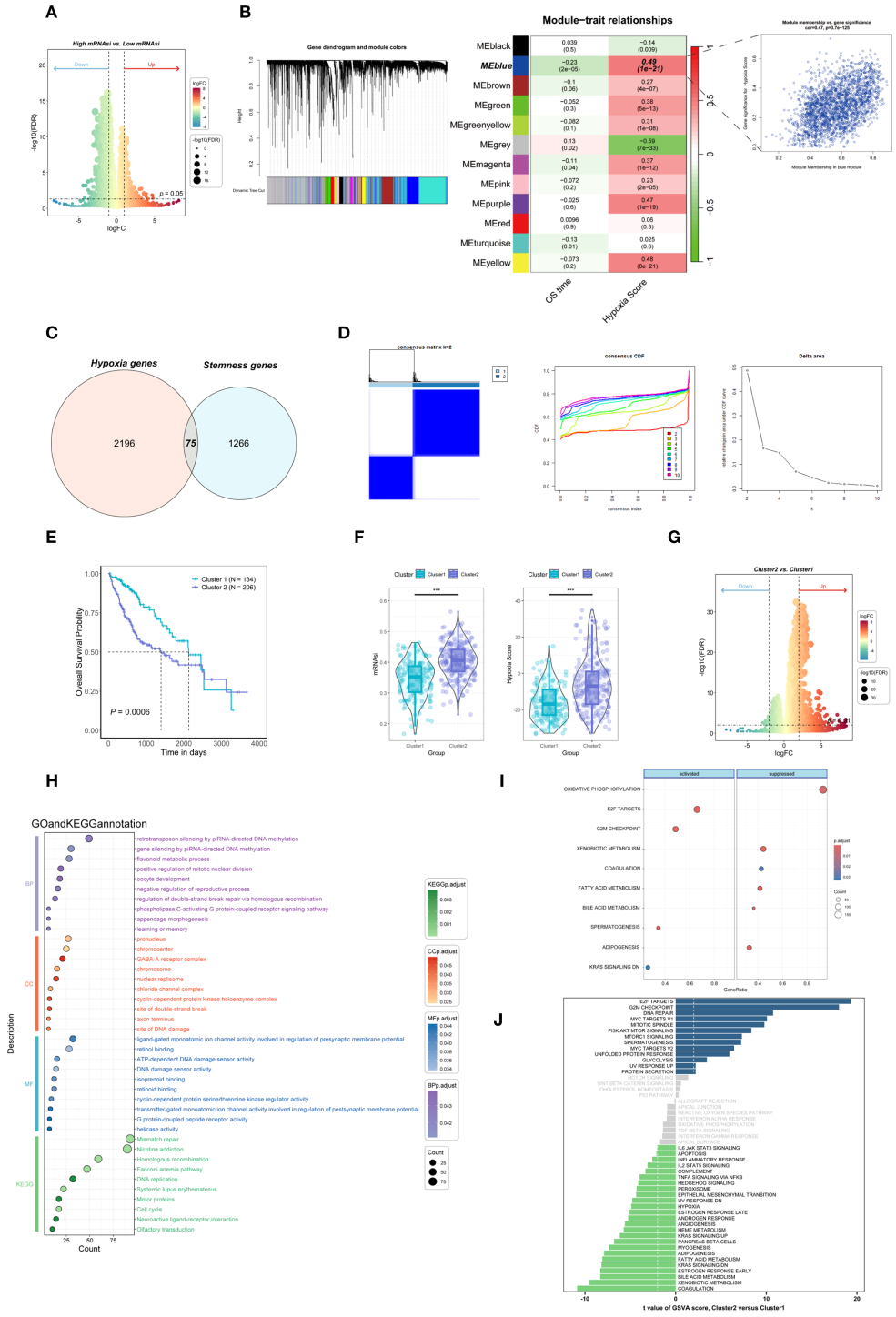

FIGURE 1
Identification of stemness- and hypoxia-related clusters. **(A)** Identification of mRNAsi-related DEGs between high- and low-mRNAsi subgroups. **(B)** Hypoxia-related genes identified through WGCNA. **(C)** A total of 75 overlapping genes were identified as SHRGs. **(D)** Unsupervised consensus clustering was performed using SHRGs. **(E)** Kaplan–Meier survival curve for the identified clusters. **(F)** Differences in mRNAsi (left) and hypoxia scores (right) between the two clusters. **(G)** Identification of DEGs between the two clusters. **(H–J)** KEGG/GO **(H)**, GSEA **(I)**, and GSVA **(J)** enrichment analyses of the two clusters. Statistical significance: ***$P < 0.001$.

suppression and elevated pro-tumor immune scores (Supplementary Figure 3E). Finally, PROGENy analysis was performed to assess the activity of cancer-related signaling pathways (29). The results indicated that Cluster 2 exhibited significantly higher activity in the Estrogen, Hypoxia, MAPK, NF-κB, p53, TNFα, and WNT signaling pathways, whereas Cluster 1 showed relatively higher activity in the VEGF signaling pathway (Supplementary Figures 3C, D).

10.3389/fimmu.2025.1669275

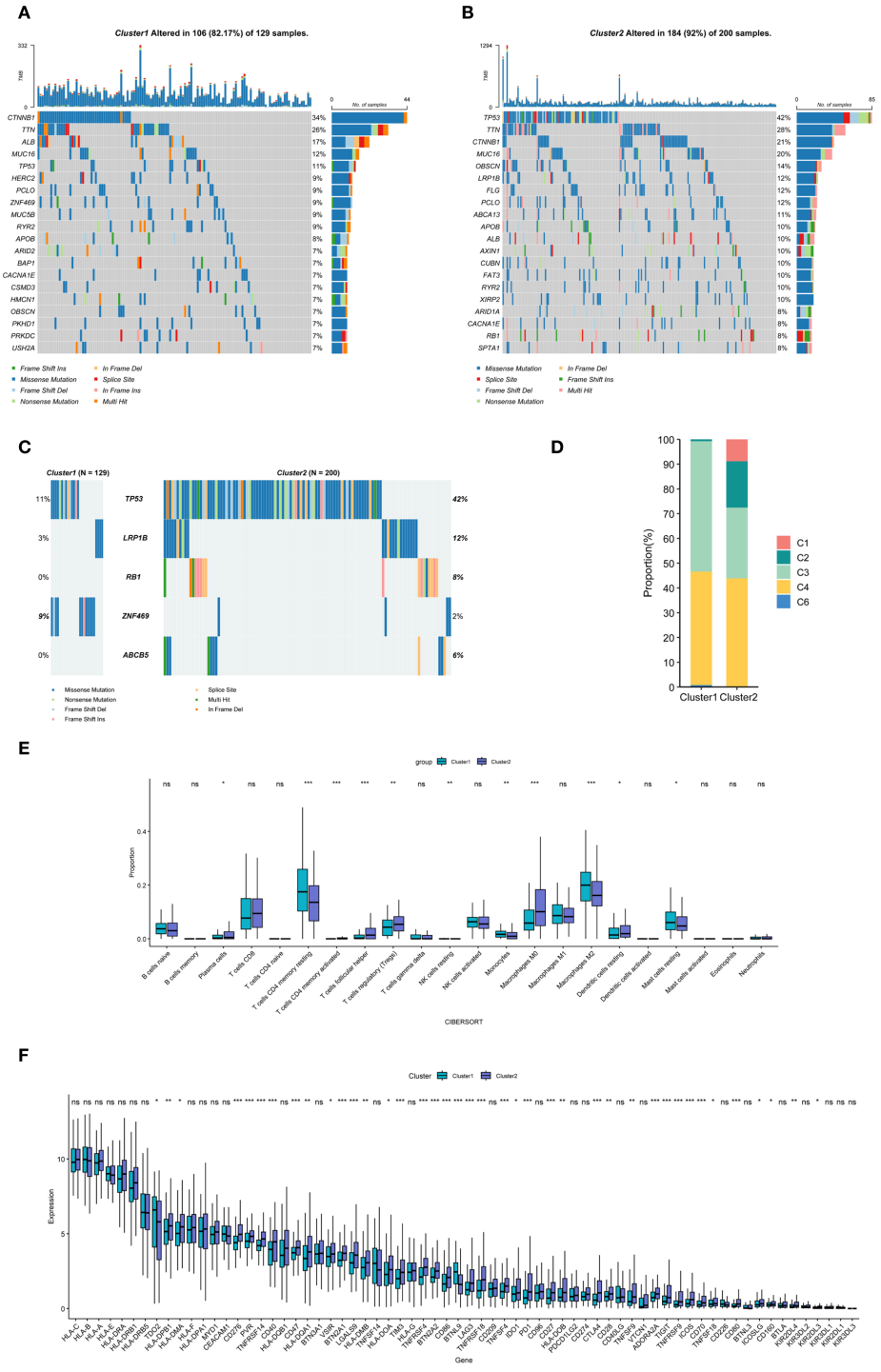

FIGURE 2
Genomic and TIME characteristics of the two stemness- and hypoxia-related clusters. **(A, B)** Waterfall plots illustrating the twenty most frequently mutated genes in each cluster. **(C)** Mutation landscape of the five most significantly different genes based on univariate Cox analysis in the two clusters. **(D)** Differences in the composition of previously classified molecular subtypes of HCC between the two clusters. **(E)** Comparison of immune cell infiltration proportions between the two clusters. **(F)** Analysis of expression levels of representative immune checkpoint genes across the two clusters. Statistical significance: $*P < 0.05$, $**P < 0.01$, $***P < 0.001$; ns = not significant.

3.4 Construction of the 4-gene SHRPI and evaluation of its prognostic significance

Cox regression analysis was conducted on the DEGs between the two clusters to identify prognostic genes. To mitigate collinearity effects, genes with a Pearson correlation coefficient greater than 0.80 were excluded, resulting in 221 DEGs (Supplementary Table 2). LASSO regression analysis was then applied, yielding five stable prognostic genes (Figures 3A, B). To further reduce false-positive rates and enhance model accuracy, we employed a random forest model to select genes with a Mean Decrease Gini greater than 1 (Figure 3C). Subsequently, four overlapping key genes were incorporated into a Cox regression model, with corresponding coefficients used to construct the SHRPI (Figure 3D): SHRPI = 0.10211669 × HMMR + 0.15981839 × UBE2S + 0.20537184 × G6PD + 0.06132584 × NEIL3.

Patients were stratified into low- and high-SHRPI groups based on the median SHRPI score. Differential expression analysis revealed that all four key genes were upregulated in the high-SHRPI group (Figure 3E; Supplementary Figures 4A, B). In the TCGA-LIHC cohort, patients in the high-SHRPI group exhibited significantly shorter OS compared to those in the low-SHRPI group ($P < 0.0001$) (Figure 3F). Time-dependent ROC curve analysis demonstrated that SHRPI exhibited robust and stable predictive performance for survival, with AUC values of 0.82, 0.70, and 0.67 for 1-, 3-, and 5-year OS, respectively (Supplementary Figure 4C). Univariate and multivariate Cox regression analyses confirmed that stage, recurrence status, and SHRPI were independent risk factors for OS in HCC (Figures 3G, H). In the NC-LT cohort, patients in the high-SHRPI group exhibited significantly shorter RFS compared to those in the low-SHRPI group ($P = 0.0015$) (Figure 3I). Univariate and multivariate Cox regression analyses confirmed that tumor diameter, AFP levels, and SHRPI were independent risk factors for RFS in HCC after LT (Figures 3J, K). Furthermore, the applicability of SHRPI was validated in the GSE104580 cohort, where SHRPI was significantly higher in the TACE non-response group compared to the response group ($P < 0.001$), with an AUC of 0.713 for predicting TACE response (Supplementary Figures 4D, E).

3.5 Development and validation of the SHRPI-based nomogram for OS prediction in HCC patients

We constructed a nomogram incorporating SHRPI and other independent prognostic risk factors using the TCGA-LIHC cohort and externally validated it in the GSE14520 cohort to comprehensively assess its predictive performance (Figure 4A). The results demonstrated that the nomogram exhibited excellent performance in both the training and validation cohorts. After stratifying patients in both cohorts based on the median nomogram score, Kaplan-Meier survival analysis revealed that patients in the high-nomogram score group had significantly shorter OS compared to those in the low-nomogram score group (Figures 4B, C).

In the training cohort, the AUC for 1-, 3-, and 5-year OS was 0.81, 0.76, and 0.73, respectively, highlighting the nomogram's strong discriminatory power for short- to medium-term survival prediction (Figure 4D). In the validation cohort, the nomogram maintained robust predictive performance, with AUC values of 0.77, 0.81, and 0.89 for 1-, 3-, and 5-year OS, respectively, indicating its generalizability across different datasets (Figure 4G). The calibration curves for both the training and validation cohorts further confirmed the accuracy of the nomogram in predicting 1-, 3-, and 5-year OS. These curves demonstrated a high degree of concordance between predicted and observed survival probabilities, underscoring the nomogram's reliability in long-term survival estimation (Figures 4E, H). Additionally, DCA for both cohorts demonstrated that the nomogram yields net benefits across a broad range of risk thresholds, further supporting its potential role in guiding clinical decision-making (Figures 4F, I).

3.6 Comprehensive analysis of SHRPI and its associations with immune infiltration, TIME signatures

To further explore the biological and clinical significance of SHRPI, we calculated patient risk scores using the SHRPI formula and stratified the TCGA-LIHC cohort into low-risk (LRG) and high-risk (HRG) groups based on the optimal cutoff value. Differential expression analysis between the two groups identified key genes associated with SHRPI. Functional enrichment analyses, including GO, KEGG, GSEA, and GSVA, revealed that the majority of enriched pathways were primarily related to cell cycle regulation and metabolic processes (Supplementary Figures 5A–D). We performed a stemness assessment on patients in the TCGA-LIHC cohort using stemness-related gene sets from MSigDB. The Wong Embryonic Stem Cell Core score showed a significant positive correlation with the risk score, while the Yamashita Liver Cancer Stem Cell Dn score exhibited a significant negative correlation (Supplementary Figure 5E).

To investigate the relationship between the risk score and immune characteristics, we analyzed the infiltration of 22 immune cell types in TIME. The results indicated a significant correlation between the risk score and multiple immune cell subsets, with distinct infiltration patterns observed between LRG and HRG, consistent with the trends observed in the stemness-hypoxia-based clusters. Specifically, HRG patients exhibited increased Tregs, follicular helper T cells (Tfh), and M0 macrophages, while resting memory $CD4^+$ T cells and naïve B cells were significantly reduced (Figures 5A, B). Additionally, the risk score exhibited strong positive correlations with matrix remodeling, Treg abundance, and tumor proliferation rate, indicating its potential role in fostering an immunosuppressive and tumorigenic microenvironment (Figure 5C). The expression profiles of 68 immune checkpoint genes differed significantly between LRG and HRG, with many genes including PDCD1 (PD-1), CTLA4, CD274 (PD-L1), and HAVCR2 (TIM-3) upregulated in HRG (Figure 5F). Correlation analysis further revealed that the risk

10.3389/fimmu.2025.1669275

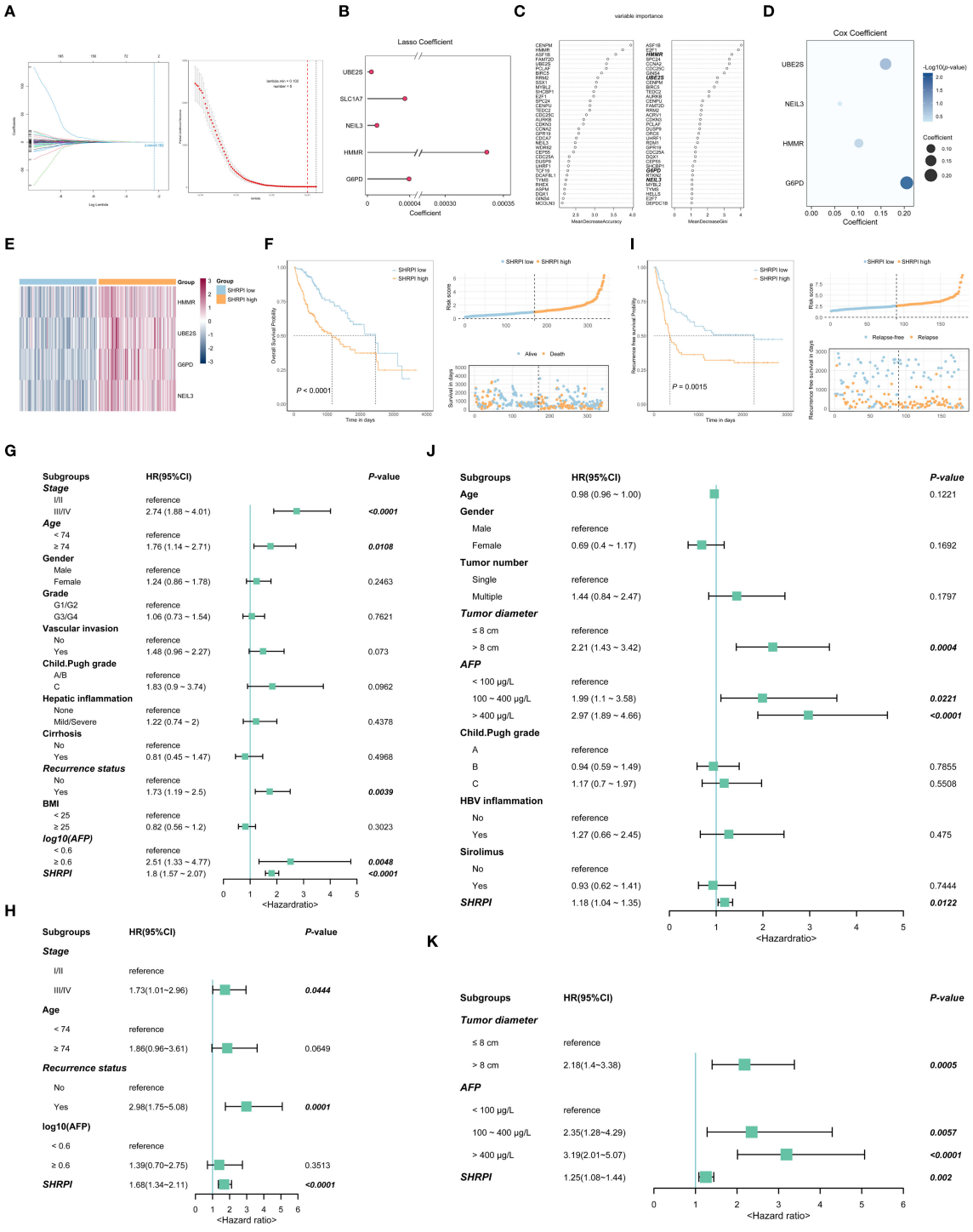

FIGURE 3
Construction of the 4-gene SHRPI and its prognostic significance. **(A)** LASSO regression analysis selected 5 variables based on the optimal lambda value. **(B)** LASSO coefficient plot for the 5 selected key genes and their coefficients. **(C)** Screening of candidate genes via random forest models. **(D)** Multivariate Cox regression analysis of the 4 selected genes used to construct the SHRPI. **(E)** Heatmap showing the expression of 4 SHRPI-related genes in low- and high-SHRPI groups. **(F)** Kaplan-Meier survival curve for OS, risk score distribution, and survival status of patients in low- and high-SHRPI groups of the TCGA-LIHC cohort. **(G, H)** Univariate **(G)** and multivariate **(H)** Cox regression analyses of SHRPI and clinicopathological parameters for OS in the TCGA-LIHC cohort. **(I)** Kaplan-Meier survival curve for RFS, risk score distribution, and relapse status of patients in low- and high-SHRPI groups of the NC-LT cohort. **(J, K)** Univariate **(J)** and multivariate **(K)** Cox regression analyses of SHRPI and clinicopathological parameters for RFS in the NC-LT cohort.

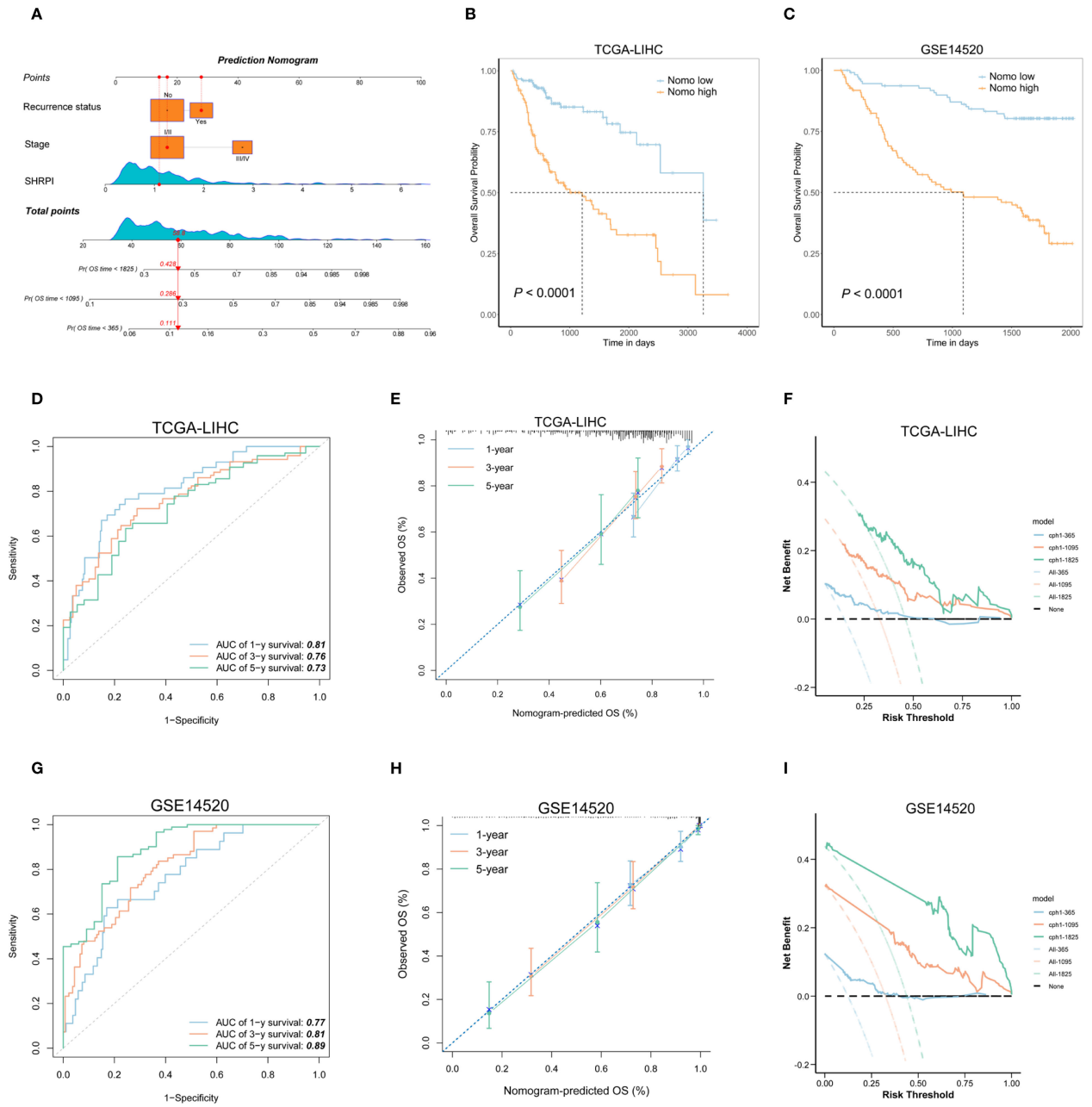

FIGURE 4
Development and validation of the SHRPI-based nomogram for OS prediction. **(A)** Nomogram for predicting OS in HCC patients, integrating SHRPI, stage, and recurrence status. **(B, C)** Kaplan-Meier survival curves comparing OS between low- and high- Nomo score groups in the TCGA-LIHC and GSE14520 cohorts. **(D, G)** Time-dependent ROC curves illustrating the nomogram's predictive accuracy for 1-, 3-, and 5-year OS in these cohorts. **(E, H)** Calibration plots comparing predicted and observed OS at 1-, 3-, and 5-year time points across cohorts. **(F, I)** DCA demonstrating the net clinical benefit of the nomogram across different risk thresholds for OS prediction in both cohorts.

score was positively associated with most immune checkpoint genes, suggesting a link to an immunosuppressive tumor microenvironment and enhanced immune evasion (Figure 5G). Next, we assessed the potential immunotherapy responses of patients across different risk groups using TIDE scores. The results showed that in HRG, the risk score was positively correlated with T cell exclusion ($\rho = 0.22$, $P = 0.02553$), suggesting a higher likelihood of immune evasion. Conversely, in LRG, the risk score exhibited a stronger positive correlation with IFNG expression ($\rho = 0.1984$, $P = 0.002146$), indicating a potentially enhanced anti-tumor immune response despite a higher correlation with T cell exclusion ($\rho = 0.3204$, $P < 0.0001$) (Supplementary Figure 5F). Collectively, these findings suggest that HRG is characterized by a more immunosuppressive tumor microenvironment, whereas LRG retains relatively higher immune activity, which may contribute to better immunotherapy responsiveness. Finally, we analyzed the relationship between the risk score and oncogenic pathway activity. The results showed that

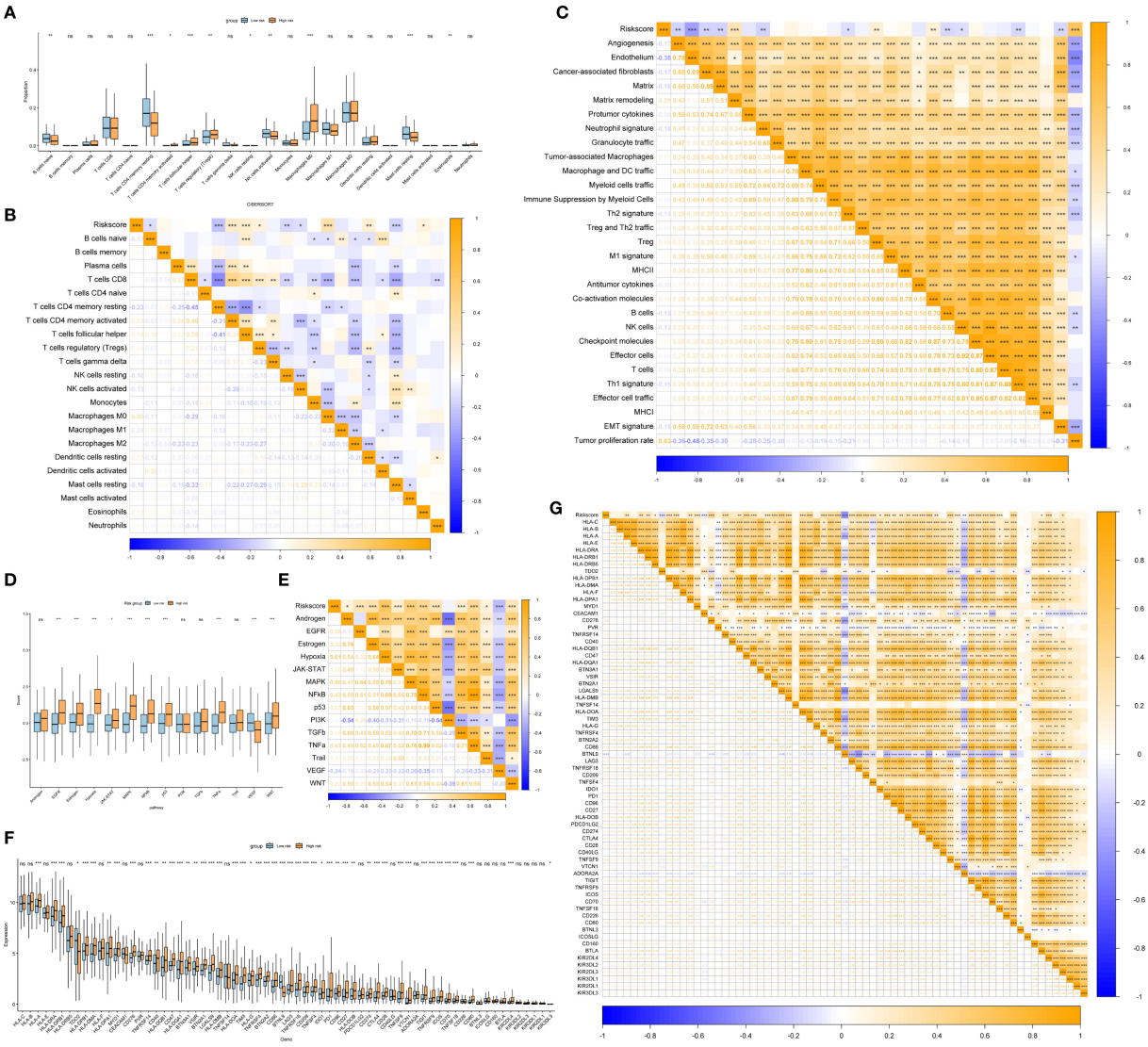

FIGURE 5
Associations of SHRPI with immune infiltration and TME signatures. **(A, B)** Comparison of immune cell infiltration levels between low- and high-risk groups **(A)** and correlation analysis of SHRPI with immune cell infiltration based on CIBERSORT **(B)**. **(C)** Correlation analysis of SHRPI with TME-related signatures. **(D, E)** Comparisons of 14 oncogenic pathways between low- and high-risk groups **(D)**, and correlation analysis of SHRPI with these pathways **(E)**. **(F, G)** Comparisons of representative immune checkpoint genes expression between low- and high-risk groups **(F)**, and correlation analysis of SHRPI with these genes **(G)**. Statistical significance: $^{*}P < 0.05$, $^{**}P < 0.01$, $^{***}P < 0.001$; ns = not significant.

the risk score was significantly associated with the activation of hypoxia, MAPK, NF-κB, p53, TNFα, and WNT signaling, all of which were upregulated in HRG (Figures 5D, E).

3.7 Identification of potential therapeutic agents for HRG

Sensitivity analysis revealed that conventional chemotherapeutic agents and inhibitors targeting FGFR, EGFR, and VEGFR exhibited no significant specificity in HRG. (Supplementary Figure 6A–D). To identify potential therapeutic agents with greater efficacy in HRG, we leveraged the CTRP, PRISM, and GDSC datasets, which provide comprehensive gene expression and drug sensitivity profiles across hundreds of human cancer cell lines. Following the removal of duplicates and quality control, 38 candidate compounds were selected for further evaluation (Figure 6A). Initially, compounds with lower estimated AUC values in HRG were identified using predefined thresholds (log2FC < −0.1 for CTRP and GDSC, and log2FC < −0.05 for PRISM). Subsequently, Spearman correlation analysis was performed to assess the association between AUC values and the risk score, with further filtering applied to compounds exhibiting a negative correlation (R < −0.3 for CTRP and PRISM, and R < −0.4 for GDSC) (Figures 6B, D, F). Ultimately, we identified 2 compounds from CTRP (docetaxel, BI2536), 5 from GDSC (vincristine, pevonedistat, docetaxel, BI2536, alisertib), and 7 from PRISM (gemcitabine, SN38, dabrafenib, bortezomib, AZD7762, topotecan, BI2536), all of which demonstrated lower estimated

10.3389/fimmu.2025.1669275

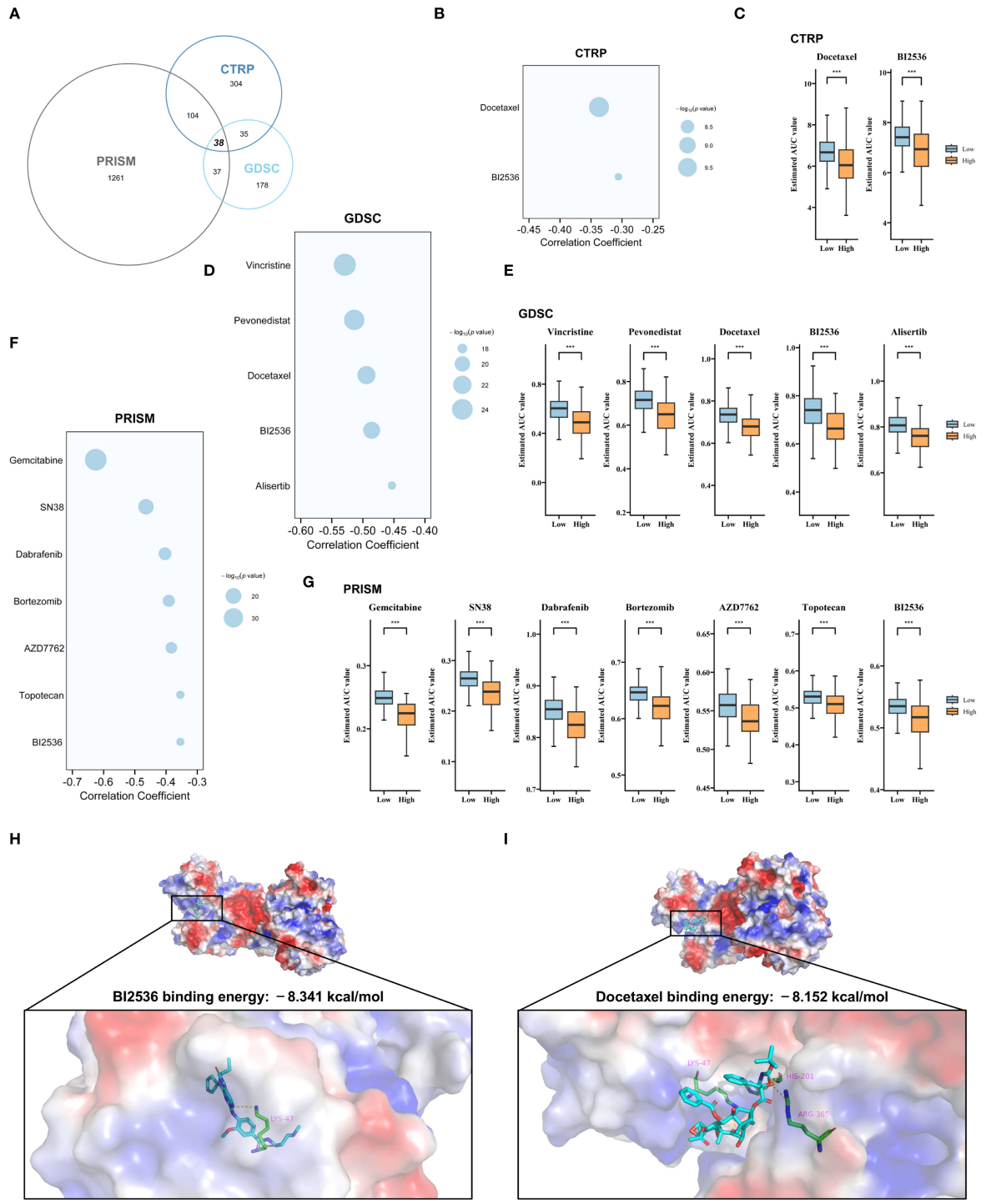

FIGURE 6
Screening of potential therapeutic agents for HRG and molecular docking analysis. **(A)** Overlapping compounds in CTRP, GDSC and PRISM datasets. **(B–G)** Spearman correlation between SHRPI and compound sensitivity, and differential drug responses (AUC) between low- and high-risk groups based on CTRP **(B, C)**, GDSC **(D, E)**, and PRISM **(F, G)** databases. **(H, I)** Molecular docking analysis of G6PD protein with two selected compounds: BI2536 **(H)** and Docetaxel **(I)**. Statistical significance: ***$P < 0.001$.

AUC values in HRG, indicating greater predicted sensitivity to these agents (Figures 6C, E, G). Given that G6PD was the molecule most closely associated with prognosis in Cox regression analysis among the components of SHRPI (Figure 3D), compounds identified in at least two database screens (Docetaxel and BI2536) were selected for molecular docking with G6PD. The results demonstrated that BI2536 had a higher binding affinity for G6PD (−8.341 kcal/mol) compared to Docetaxel (−8.152 kcal/mol) (Figures 6H, I). These findings

indicate that BI2536 may regulate G6PD activity by directly targeting its active site, thereby potentially influencing HCC stemness.

3.8 Analysis and functional validation of G6PD as a key SHRPI component in HCC

To further explore the cellular heterogeneity and expression profiles of SHRPI components in HCC, we analyzed single-cell RNA sequencing data. t-SNE dimensionality reduction and SHRPI scoring demonstrated that cancer cells exhibited significantly higher SHRPI levels (Figures 7A, B). Among the SHRPI components, G6PD, HMMR, and NEIL3 were predominantly expressed in cancer cells, with G6PD showing the highest expression proportion (Figures 7C–F). This further underscored the pivotal role of G6PD in regulating HCC stemness at the single-cell level. Upon this finding, we further investigated the changes in G6PD expression under hypoxia and its impact on the stemness phenotype in HCC cells. We first assessed G6PD expression across HCC cell lines (HuH-7, PLC/PRF/5, Hep-3B, and Li-7) via Western blot. Based on strong expression in Hep-3B and moderate expression in HuH-7, we selected these two cell lines for further experiments (Figure 8A). Exposure of these cells to hypoxia (1% O_2) significantly upregulated the expression of G6PD (Figure 8B). To further assess the role of G6PD in regulating the stemness phenotypes of HCC cells under hypoxia, we conducted knockdown and overexpression studies. In Hep-3B cells, shRNA1 and shRNA3 achieved effective G6PD knockdown (Figure 8C), while in HuH-7 cells, effective overexpression was achieved (Figure 8D). Correlation analysis between G6PD and stemness markers showed that its expression was relatively strongly correlated with CD24, CD44, OCT3/4, and HIF-1α (Figure 8I). Functional assays indicated that G6PD knockdown significantly reduced cell migration, sphere formation and the mRNA expression of stemness markers (CD24, CD44, and OCT3/4) under hypoxia (Figures 8E, F, J). Conversely, G6PD overexpression enhanced these capabilities (Figures 8G, H, K). Mechanistically, we found that G6PD regulated the protein abundance of HIF-1α. In HuH-7 cells, G6PD knockdown reduced HIF-1α protein abundance, while overexpression increased HIF-1α protein abundance under hypoxia (Figure 8L). Co-IP experiments further confirmed the interaction between endogenous G6PD and HIF-1α in HuH-7 cells under hypoxia (Figure 8M). Furthermore, in the transgenic HCC mouse model, compared with the empty vector control group (MCS), mice in the G6PD overexpression group (G6PD) exhibited a rapid increase in hepatic tumor burden within a short period, as evidenced by a significant elevation in liver weight ($P < 0.0001$) (Figures 8N, O). In conclusion, our data indicate that G6PD is a key regulator of the stemness phenotype in HCC cells under hypoxia by interacting with HIF-1α to upregulate its protein abundance, thereby promoting the stemness phenotype.

4 Discussion

The collaborative crosstalk between cancer stemness and hypoxia in HCC highlights their critical roles as drivers of tumor invasion, metastatic dissemination, therapy resistance, and immune escape mechanisms. To quantify these two biological characteristics, Malta et al. developed the OCLR algorithm, which calculates stemness indices (e.g., mRNAsi, mDNAsi) by integrating multi-omics data spanning genomic, transcriptomic, and epigenetic features (25). Similarly, hypoxia scores such as the Buffa Hypoxia Score and Winter Hypoxia Score, derived from gene expression signatures, reflect molecular adaptations to oxygen deprivation (39). Although some of these indices independently correlate with adverse HCC prognosis, current prognostic models often either treat stemness and hypoxia as isolated biological characteristics, thereby neglecting their dynamic crosstalk, or dissociate these axes from clinical parameters, consequently diminishing predictive accuracy and clinical applicability (18, 19, 21). This notable gap underscores the necessity to develop integrated indices bridging these axes (stemness and hypoxia) for refined risk stratification and prioritized therapeutic targeting, while incorporating clinical parameters to optimize predictive performance through a holistic representation of HCC biology.

In this study, we selected the stemness index (mRNAsi) and the hypoxia score (Buffa hypoxia score), both of which are significantly associated with the prognosis of HCC patients. Through differential analysis and WGCNA, we identified SHRGs that comprehensively represent the interaction between stemness and hypoxia. Consensus clustering based on SHRGs stratified HCC patients into two distinct clusters (Cluster 1/2) with divergent genomic alterations, intrinsic immunogenicity, and survival outcomes. Notably, the enrichment of oncogenic pathways (e.g., E2F targets, mTOR signaling) and elevated TMB in Cluster 2 suggested heightened genomic instability and therapeutic resistance, consistent with observations in other solid tumors (40, 41). Importantly, Cluster 2 patients displayed elevated TIDE scores and upregulated immune checkpoint molecules (PD-L1, CTLA4), which extends the utility of our stemness-hypoxia signature to predict immunotherapy response, a dimension that has been underexplored in earlier studies.

Given that previous studies predominantly relied on Cox regression or heuristic gene screening to construct indices, we integrated LASSO regression, random forest, and Cox regression analysis to minimize overfitting risks while prioritizing biologically relevant key genes. This optimized rigorous strategy constructed the SHRPI comprising four genes: HMMR, UBE2S, NEIL3, and G6PD. SHRPI is not only an independent risk factor for OS in HCC patients but also for RFS in LT patients with HCC beyond the Milan criteria. Additionally, as stemness-hypoxia features are frequently associated with TACE treatment in advanced HCC, we observed that SHRPI demonstrated promising predictive power for TACE responsiveness (42). Incorporating SHRPI into a nomogram further enhanced its clinical utility, enabling personalized survival

10.3389/fimmu.2025.1669275

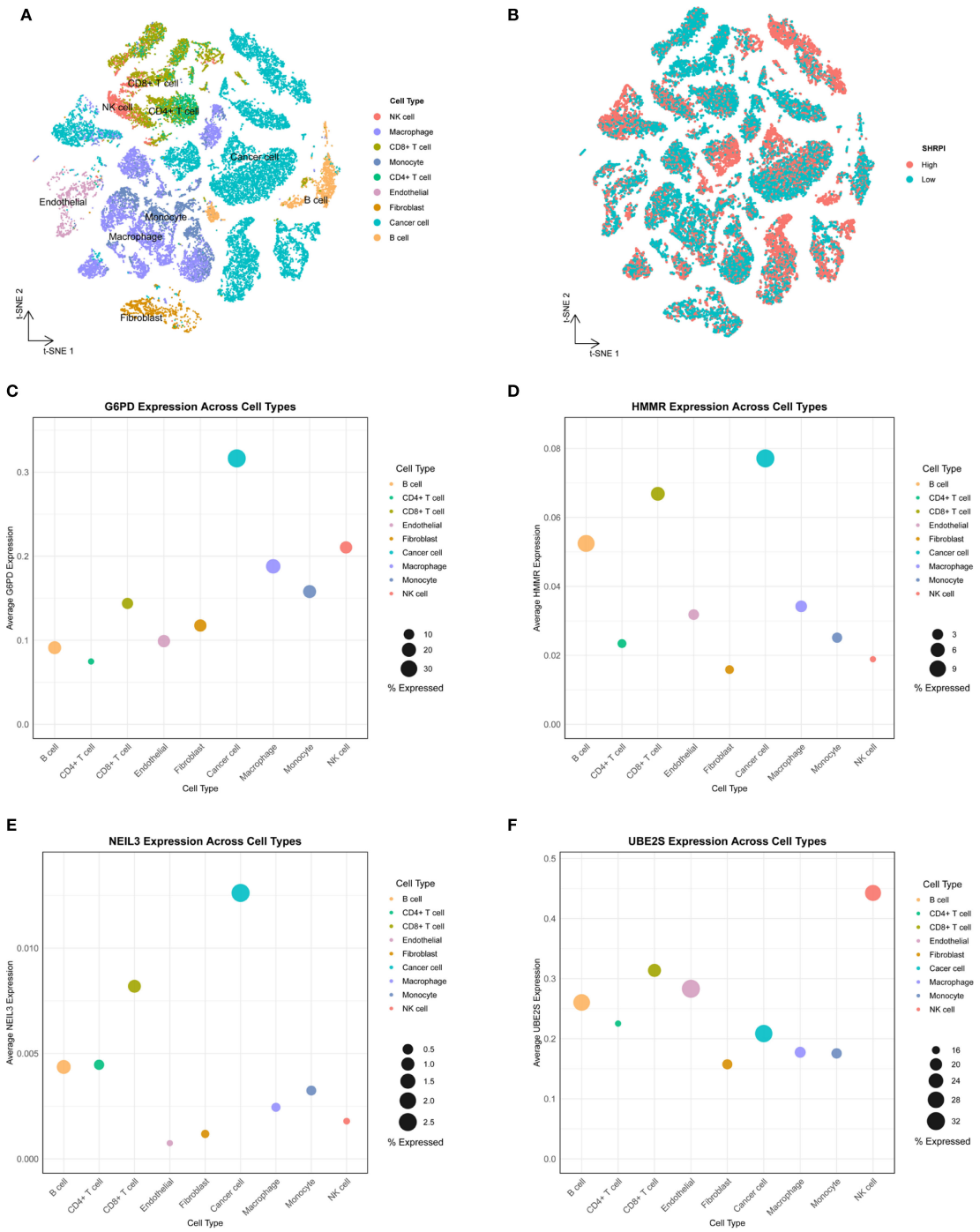

FIGURE 7
Single-cell transcriptomic analysis of SHRPI in HCC. **(A)** t-SNE plot illustrating the clustering of single cells from HCC tissues, annotated by cell type. **(B)** t-SNE plot showing the distribution of SHRPI status (high *vs.* low). **(C–F)** Average expression levels of G6PD **(C)**, HMMR **(D)**, NEIL3 **(E)**, and UBE2S **(F)** across cell types.

probability assessments. This approach contrasts with previous studies that focused solely on risk stratification based on indices. The nomogram exhibited robust performance in both TCGA and GSE14520 cohorts, highlighting its broad applicability.

Analysis of the TIME revealed significant disparities between risk groups defined by SHRPI. High-risk patients exhibited heightened infiltration of immunosuppressive cells (e.g., Tregs, M0 macrophages) and elevated expression of checkpoint molecules (PD-1, CTLA-4, TIM-3), consistent with the "immune-excluded" phenotype observed in CSC-enriched tumors (4, 43). SHRPI demonstrated a positive correlation with TIDE scores, indicating limited efficacy of immune checkpoint inhibitor (ICI) therapy in high-risk patients, necessitating exploration of alternative or combinatory therapeutic strategies. To address this, we screened for subgroup-specific therapeutic agents

10.3389/fimmu.2025.1669275

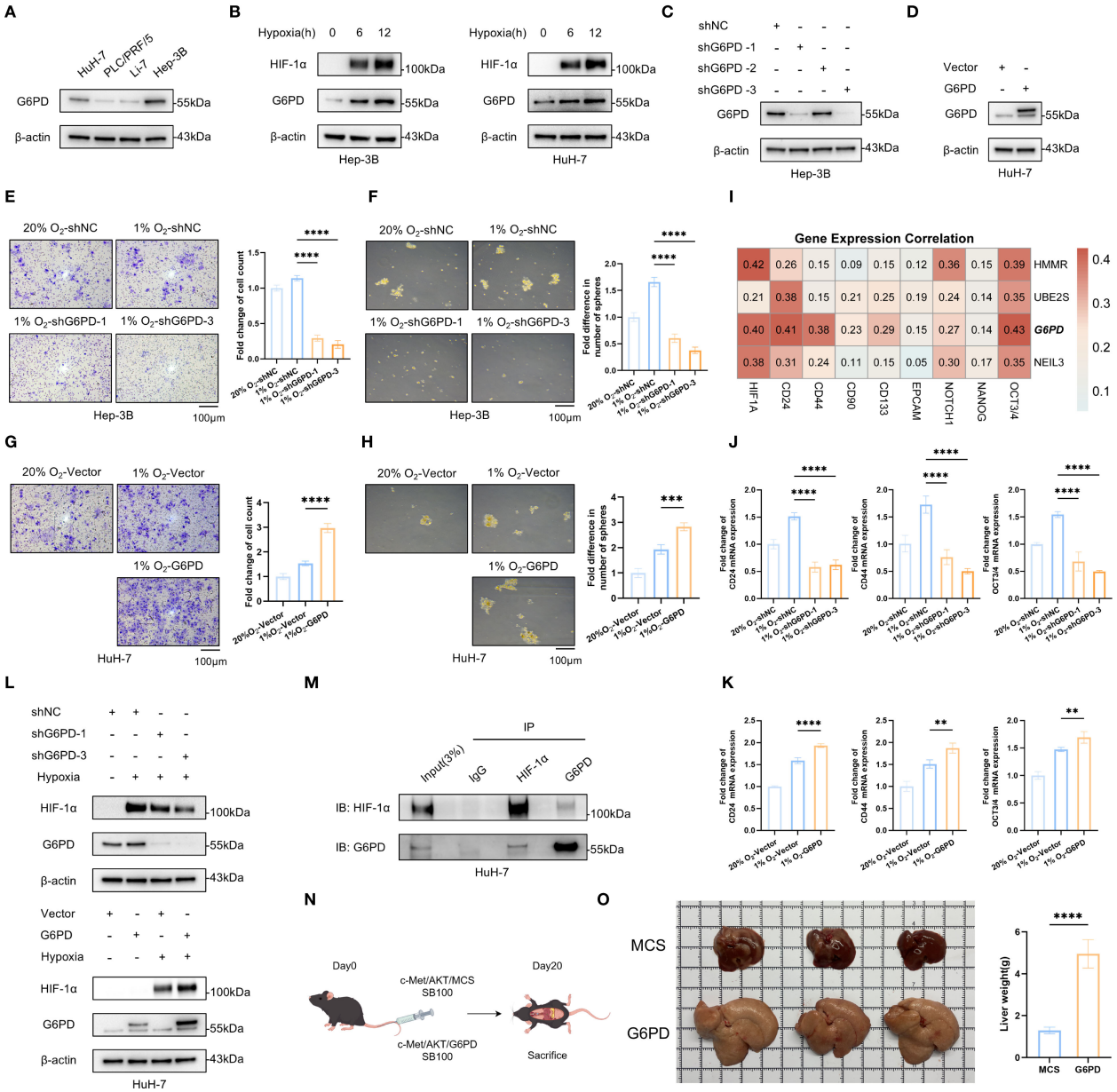

FIGURE 8
Functional validation of G6PD as a key SHRPI component in HCC. **(A)** G6PD protein abundances across HCC cell lines (HuH-7, PLC/PRF/5, Li-7 and Hep-3B). **(B)** Changes in HIF-1α and G6PD expression in HuH-7 and Hep-3B cells under normoxia (20% O_2) or hypoxia(1%O_2) at 6 and 12 hours. **(C)** Knockdown efficiency of three G6PD shRNAs in Hep-3B cells. **(D)** G6PD overexpression efficiency in HuH-7 cells. **(E, F, J)** Effects of shNC, shG6PD-1, and shG6PD-3 on Hep-3B stemness under hypoxia, as assessed by cell migration **(E)**, cell sphere formation **(F)**, and qRT-PCR **(J)** assays. **(G, H, K)** Effects of Vector and G6PD overexpression (G6PD) on HuH-7 stemness under hypoxia, as assessed by cell migration **(G)**, cell sphere formation **(H)**, and qRT-PCR **(K)** assays. **(I)** Correlation heatmap of SHRPI components and stemness markers in TCGA-LIHC bulk RNA-seq data. **(L)** G6PD and HIF-1α expression in HuH-7 with G6PD knockdown (shG6PD) or control (shNC) (upper panel), and with G6PD overexpression (G6PD) or Vector (lower panel), under normoxia or hypoxia. **(M)** Interaction between endogenous G6PD and HIF-1α was tested in HuH-7 under hypoxia for 24 hours, with normal rabbit IgG as control. **(N)** Experimental workflow of the transgenic HCC mouse model (by figdraw.com, ID: ARUWT24438). **(O)** Representative liver images of MCS and G6PD groups, and comparison of liver weights between the two groups (n = 5). Statistical significance: $^{**}P < 0.01$, $^{***}P < 0.001$, $^{****}P < 0.0001$.

using pharmacogenomics and molecular docking analyses. Among these, BI2536 stood out due to its consistent validation across three independent datasets and strong binding affinity, highlighting its potential as a candidate drug for high-risk HCC. As a specific inhibitor of Polo-like kinase 1 (PLK1), BI2536 synergizes with diverse chemotherapies (e.g., microtubule-targeting agents, alkylators, platinum drugs) across multiple preclinical cancer models, enhancing tumor suppression and overcoming chemoresistance by inducing G2/M arrest, activating apoptosis via BAX/caspase-3 pathways and pyroptosis via GSDME, and modulating critical signaling cascades (Wnt/β-catenin, MEK/ERK). In the targeted therapy domain, BI2536 demonstrates synergistic efficacy against ROCK, mTOR, STAT3, EGFR, PARP, HDAC, and Bcr-Abl, overcoming both intrinsic and acquired resistance through dual-

pathway blockade, restoration of tumor suppressor function (e.g., TP53 reactivation), and enhancement of DNA damage responses (44). Regarding immunotherapy, although clinical evidence for BI2536 combination remains scarce, emerging preclinical insights indicate that PLK1 inhibition broadly potentiates antitumor immunity through enhanced antigen presentation and T-cell infiltration, reversal of immunosuppressive TAM polarization (from M2 to M1 phenotype), and upregulation of PD-L1 expression via the PLK1/Rb/NF-κB axis to sensitize tumors to immune checkpoint blockade (45). Given that BI2536's limited single-agent efficacy and dose-limiting toxicities indicate intrinsic resistance, CRISPR/Cas9 genome-wide screening to identify resistance genes and delineate BI2536-specific pathways is essential for optimizing pharmacological properties, enhancing therapeutic efficacy in rational combination regimens, and advancing clinical translation (46).

Among the four hub genes, hyaluronan-mediated motility receptor (HMMR/RHAMM) is highly expressed in lung, breast, gastric, and liver cancers, correlating with poor prognosis (47). HMMR critically maintains cancer stemness across tumor types: sustaining glioblastoma stem cell tumorigenicity (48), enhancing gastric cancer stemness and 5-fluorouracil resistance via TGF-β/Smad2 (49), and promoting glycolysis to strengthen stemness and cisplatin resistance in lung adenocarcinoma (50). Although direct evidence linking HMMR to hypoxia regulation is limited, hypoxia may indirectly potentiate HMMR's oncogenic effects by activating key stemness-associated pathways, notably TGF-β signaling and glycolysis, both established hypoxia-responsive processes (51). Furthermore, HMMR predicts immunosuppressive microenvironments in HCC, with its targeting enhancing anti-PD-1 efficacy through $CD8^+$ T cell recruitment (52). Ubiquitin-conjugating enzyme E2S (UBE2S), a crucial member of the ubiquitin-proteasome system, is overexpressed in multiple cancers (e.g., lung, bladder, ovarian, liver) and correlates with poor prognosis and advanced stage. UBE2S promotes cancer stemness through diverse mechanisms: enhancing p53 ubiquitination to facilitate proliferation and migration, accelerating cell cycle progression via p27 ubiquitination, and inducing chemoresistance through both the PTEN/AKT and Wnt/β-catenin signaling pathways (53). Notably, UBE2S directly ubiquitinates VHL independent of canonical E3 ligases, regulating HIF-1α signaling to promote glycolysis and HCC proliferation (54). It further drives tumor growth and reduces sorafenib sensitivity by upregulating HIF-1α and activating JAK2/STAT3 signaling (55). These findings suggest that UBE2S may function as a molecular bridge linking stemness and hypoxia regulation in HCC. Nei endonuclease VIII-like 3 (NEIL3), a DNA glycosylase crucial for repairing oxidative DNA damage and crosslinks, is highly expressed in multiple cancers (e.g., lung, kidney, liver) and promotes tumor progression. In HCC, NEIL3 not only repairs telomeric oxidative damage to delay cellular senescence but also activates the BRAF/MEK/ERK/TWIST pathway to induce core stemness phenotypes including epithelial-mesenchymal transition, therapy resistance, and enhanced self-renewal (56). Concurrently, it remodels metabolic microenvironments via MAZ-mediated aerobic glycolysis to support stemness maintenance (57), while driving malignant expansion of CSCs through the SNHG3/E2F1 axis (58). Although direct links to hypoxia regulation remain limited, a defined mechanism shows that NEIL3 enables proper expression of hypoxia-responsive genes by repairing hypoxia-associated oxidative damage in promoter G-quadruplex DNA, leading to reduced genomic instability under hypoxia (59).

Glucose-6-phosphate dehydrogenase (G6PD), the rate-limiting enzyme of the pentose phosphate pathway (PPP), maintains redox homeostasis through NADPH generation and supports nucleotide biosynthesis via ribose-5-phosphate production. Clinically significant overexpression of G6PD has been documented in multiple malignancies, including lung, renal, breast and liver cancer, and it correlates with adverse clinical outcomes (60). Hypoxic tumor microenvironments in HCC induce transcriptional upregulation of G6PD, which confers survival advantages through oxidative stress modulation (61). Emerging evidence demonstrates that G6PD overexpression diminishes regorafenib cytotoxicity in HCC (62), while METTL3-mediated activation of G6PD-dependent PPP flux drives oxaliplatin resistance (63). Therefore, the dual regulatory role of G6PD in maintaining redox equilibrium and facilitating metabolic reprogramming serves as a critical determinant in preserving cancer cell stemness under various stress conditions. Integrating multivariate Cox regression and single-cell transcriptomic analyses based on SHRPI components identified G6PD as a key prognostic determinant closely associated with HCC stemness regulation at the single-cell level. Its specific role in hypoxia-driven stemness maintenance has yet to be reported. Through systematic experiments, we demonstrated that hypoxia significantly upregulates G6PD expression in HCC cells and that G6PD is essential for maintaining cancer stemness. Mechanistically, we showed that G6PD stabilizes HIF-1α protein under hypoxia. Given established evidence that HIF-1α transcriptionally activates G6PD (61, 64), we propose a self-reinforcing positive feedback loop that amplifies HCC stemness. Within this regulatory mechanism, G6PD may enhance HIF-1α stability through dual mechanisms: as a core metabolic enzyme, it potentially modulates redox homeostasis to attenuate degradation (65); while exercising non-canonical enzymatic functions, it may directly suppress HIF-1α ubiquitination (66). Endogenous Co-IP confirmed G6PD-HIF-1α interaction, thereby providing mechanistic support for these stabilization pathways. These findings reveal a novel metabolic-microenvironmental crosstalk driving stemness; this manifestation of non-canonical molecular functions bridging metabolism and TME remodeling is similarly observed in recent biomarker studies of other solid tumors (67). Collectively, they suggest that targeting the G6PD-HIF-1α loop aligns with the emerging paradigm of combinatorial strategies against multiple tumor microenvironment components (68) and provide both novel insights and a theoretical foundation for therapeutic strategies aimed at targeting cancer stemness.

Although previous studies incorporated stemness or hypoxia characteristics for HCC prognostication, our work delivers substantial advances: algorithmic refinement optimizes SHRPI to identify a minimal gene set with maximal prognostic power,

significantly enhancing discriminative performance and model parsimony; we develop a highly accurate and clinically applicable nomogram for individualized prognosis; pharmacogenomic and molecular docking analyses rigorously screened BI2536 as a promising agent for the high-risk subgroup, providing actionable insights for therapeutic stratification; integrating computational and experimental evidence, we first establish G6PD as a key regulator of hypoxia-induced stemness and propose a G6PD-HIF-1α positive feedback loop as a mechanistic model.

Despite these advancements, our study has limitations. First, given the retrospective nature and potential ethnic composition bias of TCGA/GEO data, prospective validation of SHRPI in multi-ethnic cohorts is necessary to assess its applicability, and its predictive capacity for immunotherapy response requires further validation in diverse immunotherapy cohorts (69). Second, deeper molecular investigations are required to elucidate the specific regulatory mechanisms of G6PD on HIF-1α, alongside comprehensive spatial single-cell analyses and *in vivo* lineage tracing to resolve spatial heterogeneity in G6PD-HIF-1α interactions within tumor microenvironments. Third, preclinical assessment of candidate compounds (BI2536) using patient-derived organoids or xenograft models should systematically evaluate on-target efficacy versus off-target toxicity profiles to ensure safety of combinatorial regimens for high-risk populations (70).

5 Conclusions

SHRPI, constructed using a rigorous methodological approach, effectively distinguishes clinical, molecular, TIME, and therapeutic response characteristics among HCC patients. The nomogram integrating SHRPI with key clinical parameters demonstrates high predictive accuracy and robust applicability. BI2536 showed promising therapeutic potential for patients classified as high-risk by SHRPI. Furthermore, the elucidation of the hypoxia-stemness regulatory mechanism mediated by G6PD, a key SHRPI component, provides novel insights into therapeutic strategies targeting HCC stemness.

Data availability statement

The datasets generated during and/or analysed during the current study are available in the following repositories: TCGA (https://www.cancer.gov/ccg/research/genome-sequencing/tcga), GEO (https://www.ncbi.nlm.nih.gov/geo/), The cBio Cancer Genomics Portal (http://cbioportal.org), PubChem Compound (https://pubchem.ncbi.nlm.nih.gov/), PDB (http://www.rcsb.org/), and the Genome Sequence Archive database (accession codes: HRA010539, HRA010528; https://ngdc.cncb.ac.cn/). Computational scripts generated during this research are available upon formal request to the corresponding authors.

Ethics statement

Ethical approval was not required for the studies on humans in accordance with the local legislation and institutional requirements because only commercially available established cell lines were used. The animal study was approved by the Institutional Animal Care and Use Committee of Zhejiang Center of Laboratory Animals (IACUC, ZJCLA; approval number: ZJCLA-IACUC-20011186). The study was conducted in accordance with the local legislation and institutional requirements.

Author contributions

MG: Conceptualization, Formal analysis, Investigation, Methodology, Project administration, Software, Supervision, Visualization, Writing – original draft, Writing – review & editing. YL: Data curation, Formal analysis, Methodology, Software, Validation, Visualization, Writing – original draft, Writing – review & editing. JW: Data curation, Methodology, Software, Validation, Visualization, Writing – original draft. PZ: Resources, Validation, Writing – original draft. JL: Funding acquisition, Writing – original draft. KG: Resources, Validation, Writing – original draft. BS: Data curation, Funding acquisition, Visualization, Writing – original draft. SL: Conceptualization, Investigation, Methodology, Project administration, Supervision, Writing – original draft, Writing – review & editing. LW: Conceptualization, Funding acquisition, Project administration, Resources, Supervision, Writing – original draft, Writing – review & editing.

Funding

The author(s) declare financial support was received for the research and/or publication of this article. This research was funded by the Innovative Teams Project in Key Areas of Dalian (2021RT01); the Provincial Natural Science Foundation of Liaoning (2024-BS-178); the General Project of Liaoning Provincial Department of Education (LJ212410161008).

Acknowledgments

We sincerely thank the Figdraw platform (www.figdraw.com) for their assistance in figure creation.

Conflict of interest

The authors declare that the research was conducted in the absence of any commercial or financial relationships that could be construed as a potential conflict of interest.

Generative AI statement

The author(s) declare that no Generative AI was used in the creation of this manuscript.

Any alternative text (alt text) provided alongside figures in this article has been generated by Frontiers with the support of artificial intelligence and reasonable efforts have been made to ensure accuracy, including review by the authors wherever possible. If you identify any issues, please contact us.

Publisher's note

All claims expressed in this article are solely those of the authors and do not necessarily represent those of their affiliated organizations, or those of the publisher, the editors and the reviewers. Any product that may be evaluated in this article, or claim that may be made by its manufacturer, is not guaranteed or endorsed by the publisher.

Supplementary material

The Supplementary Material for this article can be found online at: https://www.frontiersin.org/articles/10.3389/fimmu.2025.1669275/full#supplementary-material

SUPPLEMENTARY FIGURE 1
Prognostic and clinical implications of stemness indices and hypoxia scores in HCC.

SUPPLEMENTARY FIGURE 2
Genomic characteristics of Cluster 1 and Cluster 2.

SUPPLEMENTARY FIGURE 3
Therapeutic and immune characteristics of Cluster 1 and Cluster 2.

SUPPLEMENTARY FIGURE 4
Predictive performance of SHRPI for OS and TACE response.

SUPPLEMENTARY FIGURE 5
Differential analysis, functional enrichment, and correlation with key gene signatures between low- and high-risk groups.

SUPPLEMENTARY FIGURE 6
Drug sensitivity comparisons between low- and high-risk groups.

SUPPLEMENTARY TABLE 1
Stemness- and hypoxia-related genes.

SUPPLEMENTARY TABLE 2
Cox regression results of DEGs after collinearity filtering for SHRPI construction.

SUPPLEMENTARY TABLE 3
Detailed information of oligonucleotides used in experiments.

SUPPLEMENTARY TABLE 4
Detailed information of antibodies used in experiments.

SUPPLEMENTARY TABLE 5
Detailed information of primers used in experiments.

References

1. Singal AG, Kanwal F, Llovet JM. Global trends in hepatocellular carcinoma epidemiology: implications for screening, prevention and therapy. *Nat Rev Clin Oncol.* (2023) 20:864–84. doi: 10.1038/s41571-023-00825-3

2. Tsui YM, Ho DW, Ng IO. Unraveling the tumor-initiating cells in hepatocellular carcinoma. *Cancer Cell.* (2024) 42:1990–3. doi: 10.1016/j.ccell.2024.10.018

3. Craig AJ, von Felden J, Garcia-Lezana T, Sarcognato S, Villanueva A. Tumour evolution in hepatocellular carcinoma. *Nat Rev Gastroenterol Hepatol.* (2020) 17:139–52. doi: 10.1038/s41575-019-0229-4

4. Lee TK, Guan XY, Ma S. Cancer stem cells in hepatocellular carcinoma - from origin to clinical implications. *Nat Rev Gastroenterol Hepatol.* (2022) 19:26–44. doi: 10.1038/s41575-021-00508-3

5. Shibue T, Weinberg RA. EMT, CSCs, and drug resistance: the mechanistic link and clinical implications. *Nat Rev Clin Oncol.* (2017) 14:611–29. doi: 10.1038/nrclinonc.2017.44

6. Clara JA, Monge C, Yang Y, Takebe N. Targeting signalling pathways and the immune microenvironment of cancer stem cells - a clinical update. *Nat Rev Clin Oncol.* (2020) 17:204–32. doi: 10.1038/s41571-019-0293-2

7. Wang J, Yu H, Dong W, Zhang C, Hu M, Ma W, et al. N6-methyladenosine-mediated up-regulation of FZD10 regulates liver cancer stem cells' Properties and lenvatinib resistance through WNT/beta-catenin and hippo signaling pathways. *Gastroenterology.* (2023) 164:990–1005. doi: 10.1053/j.gastro.2023.01.041

8. Lam KH, Ma S. Noncellular components in the liver cancer stem cell niche: Biology and potential clinical implications. *Hepatology.* (2023) 78:991–1005. doi: 10.1002/hep.32629

9. Dakal TC, Bhushan R, Xu C, Gadi BR, Cameotra SS, Yadav V, et al. Intricate relationship between cancer stemness, metastasis, and drug resistance. *MedComm.* (2020) 2024) 5:e710. doi: 10.1002/mco2.710

10. Yuan X, Ruan W, Bobrow B, Carmeliet P, Eltzschig HK. Targeting hypoxia-inducible factors: therapeutic opportunities and challenges. *Nat Rev Drug Discov.* (2024) 23:175–200. doi: 10.1038/s41573-023-00848-6

11. Jing X, Yang F, Shao C, Wei K, Xie M, Shen H, et al. Role of hypoxia in cancer therapy by regulating the tumor microenvironment. *Mol Cancer.* (2019) 18:157. doi: 10.1186/s12943-019-1089-9

12. Taylor CT, Scholz CC. The effect of HIF on metabolism and immunity. *Nat Rev Nephrol.* (2022) 18:573–87. doi: 10.1038/s41581-022-00587-8

13. Mathieu J, Zhang Z, Zhou W, Wang AJ, Heddleston JM, Pinna CM, et al. HIF induces human embryonic stem cell markers in cancer cells. *Cancer Res.* (2011) 71:4640–52. doi: 10.1158/0008-5472.CAN-10-3320

14. Wu Q, You L, Nepovimova E, Heger Z, Wu W, Kuca K, et al. Hypoxia-inducible factors: master regulators of hypoxic tumor immune escape. *J Hematol Oncol.* (2022) 15:77. doi: 10.1186/s13045-022-01292-6

15. Chen J, Jiang CC, Jin L, Zhang XD. Regulation of PD-L1: a novel role of pro-survival signalling in cancer. *Ann Oncol.* (2016) 27:409–16. doi: 10.1093/annonc/mdv615

16. Bailey CM, Liu Y, Liu M, Du X, Devenport M, Zheng P, et al. Targeting HIF-1alpha abrogates PD-L1-mediated immune evasion in tumor microenvironment but promotes tolerance in normal tissues. *J Clin Invest.* (2022) 132:e150846. doi: 10.1172/JCI150846

17. Gilkes DM, Semenza GL, Wirtz D. Hypoxia and the extracellular matrix: drivers of tumour metastasis. *Nat Rev Cancer.* (2014) 14:430–9. doi: 10.1038/nrc3726

18. Mo Z, Liu D, Rong D, Zhang S. Hypoxic characteristic in the immunosuppressive microenvironment of hepatocellular carcinoma. *Front Immunol.* (2021) 12:611058. doi: 10.3389/fimmu.2021.611058

19. Chen D, Liu J, Zang L, Xiao T, Zhang X, Li Z, et al. Integrated machine learning and bioinformatic analyses constructed a novel stemness-related classifier to predict prognosis and immunotherapy responses for hepatocellular carcinoma patients. *Int J Biol Sci.* (2022) 18:360–73. doi: 10.7150/ijbs.66913

20. Zhang G, Zhang K, Zhao Y, Yang Q, Lv X. A novel stemness-hypoxia-related signature for prognostic stratification and immunotherapy response in hepatocellular carcinoma. *BMC Cancer.* (2022) 22:1103. doi: 10.1186/s12885-022-10195-1

21. Liu C, Xiao Z, Wu S, Yang Z, Ji G, Duan J, et al. Multi-cohort validation study of a four-gene signature for risk stratification and treatment response prediction in

hepatocellular carcinoma. *Comput Biol Med*. (2023) 167:107694. doi: 10.1016/j.compbiomed.2023.107694

22. Ye B, Wang Q, Zhu X, Zeng L, Luo H, Xiong Y, et al. Single-cell RNA sequencing identifies a novel proliferation cell type affecting clinical outcome of pancreatic ductal adenocarcinoma. *Front Oncol*. (2023) 13:1236435. doi: 10.3389/fonc.2023.1236435

23. Liu H, Li Y, Karsidag M, Tu T, Wang P. Technical and biological biases in bulk transcriptomic data mining for cancer research. *J Cancer*. (2025) 16:34–43. doi: 10.7150/jca.100922

24. Ling S, Yu J, Zhan Q, Gao M, Liu P, Wu Y, et al. Multi-omic analysis reveals a CAF-stemness-governed classification in HCC liver transplant recipients beyond the Milan criteria. *Nat Commun*. (2025) 16:4392. doi: 10.1038/s41467-025-59745-8

25. Malta TM, Sokolov A, Gentles AJ, Burzykowski T, Poisson L, Weinstein JN, et al. Machine learning identifies stemness features associated with oncogenic dedifferentiation. *Cell*. (2018) 173:338–54.e15. doi: 10.1016/j.cell.2018.03.034

26. Li Y, Ge X, Peng F, Li W, Li JJ. Exaggerated false positives by popular differential expression methods when analyzing human population samples. *Genome Biol*. (2022) 23:79. doi: 10.1186/s13059-022-02648-4

27. Langfelder P, Horvath S. WGCNA: an R package for weighted correlation network analysis. *BMC Bioinf*. (2008) 9:559. doi: 10.1186/1471-2105-9-559

28. Liberzon A, Birger C, Thorvaldsdottir H, Ghandi M, Mesirov JP, Tamayo P. The Molecular Signatures Database (MSigDB) hallmark gene set collection. *Cell Syst*. (2015) 1:417–25. doi: 10.1016/j.cels.2015.12.004

29. Schubert M, Klinger B, Klunemann M, Sieber A, Uhlitz F, Sauer S, et al. Perturbation-response genes reveal signaling footprints in cancer gene expression. *Nat Commun*. (2018) 9:20. doi: 10.1038/s41467-017-02391-6

30. Gentles AJ, Newman AM, Liu CL, Bratman SV, Feng W, Kim D, et al. The prognostic landscape of genes and infiltrating immune cells across human cancers. *Nat Med*. (2015) 21:938–45. doi: 10.1038/nm.3909

31. Hu FF, Liu CJ, Liu LL, Zhang Q, Guo AY. Expression profile of immune checkpoint genes and their roles in predicting immunotherapy response. *Brief Bioinform*. (2021) 22:bbaa176. doi: 10.1093/bib/bbaa176

32. Chen Y, Feng Y, Yan F, Zhao Y, Zhao H, Guo Y. A novel immune-related gene signature to identify the tumor microenvironment and prognose disease among patients with oral squamous cell carcinoma patients using ssGSEA: A bioinformatics and biological validation study. *Front Immunol*. (2022) 13:922195. doi: 10.3389/fimmu.2022.922195

33. Fitzgerald M, Saville BR, Lewis RJ. Decision curve analysis. *JAMA*. (2015) 313:409–10. doi: 10.1001/jama.2015.37

34. Gorgulla C, Boeszoermenyi A, Wang ZF, Fischer PD, Coote PW, Padmanabha Das KM, et al. An open-source drug discovery platform enables ultra-large virtual screens. *Nature*. (2020) 580:663–8. doi: 10.1038/s41586-020-2117-z

35. Xu D, Wang Z, Xia Y, Shao F, Xia W, Wei Y, et al. The gluconeogenic enzyme PCK1 phosphorylates INSIG1/2 for lipogenesis. *Nature*. (2020) 580:530–5. doi: 10.1038/s41586-020-2183-2

36. Davoli T, Uno H, Wooten EC, Elledge SJ. Tumor aneuploidy correlates with markers of immune evasion and with reduced response to immunotherapy. *Science*. (2017) 355:eaaf8399. doi: 10.1126/science.aaf8399

37. Thorsson V, Gibbs DL, Brown SD, Wolf D, Bortone DS, Ou Yang TH, et al. The immune landscape of cancer. *Immunity*. (2018) 48:812–30 e14. doi: 10.1016/j.immuni.2018.03.023

38. Pardoll DM. The blockade of immune checkpoints in cancer immunotherapy. *Nat Rev Cancer*. (2012) 12:252–64. doi: 10.1038/nrc3239

39. Bhandari V, Li CH, Bristow RG, Boutros PC, Consortium P. Divergent mutational processes distinguish hypoxic and normoxic tumours. *Nat Commun*. (2020) 11:737. doi: 10.1038/s41467-019-14052-x

40. Tian X, Zheng J, Mou W, Lu G, Chen S, Du J, et al. Development and validation of a hypoxia-stemness-based prognostic signature in pancreatic adenocarcinoma. *Front Pharmacol*. (2022) 13:939542. doi: 10.3389/fphar.2022.939542

41. Sharma R, Balta S, Raza A, Escalona RM, Kannourakis G, Prithviraj P, et al. *In vitro* and in silico analysis of epithelial-mesenchymal transition and cancer stemness as prognostic markers of clear cell renal cell carcinoma. *Cancers (Basel)*. (2023) 15:2586. doi: 10.3390/cancers15092586

42. Kim M, Hui KM, Shi M, Reau N, Aloman C. Differential expression of hepatic cancer stemness and hypoxia markers in residual cancer after locoregional therapies for hepatocellular carcinoma. *Hepatol Commun*. (2022) 6:3247–59. doi: 10.1002/hep4.2079

43. Dai X, Guo Y, Hu Y, Bao X, Zhu X, Fu Q, et al. Immunotherapy for targeting cancer stem cells in hepatocellular carcinoma. *Theranostics*. (2021) 11:3489–501. doi: 10.7150/thno.54648

44. Su S, Chhabra G, Singh CK, Ndiaye MA, Ahmad N. PLK1 inhibition-based combination therapies for cancer management. *Transl Oncol*. (2022) 16:101332. doi: 10.1016/j.tranon.2021.101332

45. Wang W, Zhao R, Wang Y, Pan L, Luan F, Fu G. PLK1 in cancer therapy: a comprehensive review of immunomodulatory mechanisms and therapeutic opportunities. *Front Immunol*. (2025) 16:1602752. doi: 10.3389/fimmu.2025.1602752

46. Liu H, Wang P. CRISPR screening and cell line IC50 data reveal novel key genes for trametinib resistance. *Clin Exp Med*. (2024) 25:21. doi: 10.1007/s10238-024-01538-2

47. Messam BJ, Tolg C, McCarthy JB, Nelson AC, Turley EA. RHAMM is a multifunctional protein that regulates cancer progression. *Int J Mol Sci*. (2021) 22:10313. doi: 10.3390/ijms221910313

48. Tilghman J, Wu H, Sang Y, Shi X, Guerrero-Cazares H, Quinones-Hinojosa A, et al. HMMR maintains the stemness and tumorigenicity of glioblastoma stem-like cells. *Cancer Res*. (2014) 74:3168–79. doi: 10.1158/0008-5472.CAN-13-2103

49. Zhang H, Ren L, Ding Y, Li F, Chen X, Ouyang Y, et al. Hyaluronan-mediated motility receptor confers resistance to chemotherapy via TGFbeta/Smad2-induced epithelial-mesenchymal transition in gastric cancer. *FASEB J*. (2019) 33:6365–77. doi: 10.1096/fj.201802186R

50. Yu W, Shi Y, Bao X, Chen X, Ni Y, Wang J, et al. Hyaluronan-mediated motility receptor-mediated aerobic glycolysis enhances stem-like properties and chemoresistance in lung adenocarcinoma. *Korean J Physiol Pharmacol*. (2025) 29:337–47. doi: 10.4196/kjpp.24.275

51. Chen Z, Han F, Du Y, Shi H, Zhou W. Hypoxic microenvironment in cancer: molecular mechanisms and therapeutic interventions. *Signal Transduct Target Ther*. (2023) 8:70. doi: 10.1038/s41392-023-01332-8

52. Wu H, Liu Y, Liu Q, Li Z, Wan Y, Cao C, et al. HMMR triggers immune evasion of hepatocellular carcinoma by inactivation of phagocyte killing. *Sci Adv*. (2024) 10:eadl6083. doi: 10.1126/sciadv.adl6083

53. Zhang M, Wang J, Zhang Z, Guo Y, Lou X, Zhang L. Diverse roles of UBE2S in cancer and therapy resistance: Biological functions and mechanisms. *Heliyon*. (2024) 10:e24465. doi: 10.1016/j.heliyon.2024.e24465

54. Zhang R, Li C, Zhang S, Kong L, Liu Z, Guo Y, et al. UBE2S promotes glycolysis in hepatocellular carcinoma by enhancing E3 enzyme-independent polyubiquitination of VHL. *Clin Mol Hepatol*. (2024) 30:771–92. doi: 10.3350/cmh.2024.0236

55. Wu J, Xu X, Wu S, Shi W, Zhang G, Cao Y, et al. UBE2S promotes Malignant properties via VHL/HIF-1alpha and VHL/JAK2/STAT3 signaling pathways and decreases sensitivity to sorafenib in hepatocellular carcinoma. *Cancer Med*. (2023) 12:18078–97. doi: 10.1002/cam4.6431

56. Chen L, Huan X, Gao XD, Yu WH, Xiao GH, Li TF, et al. Biological functions of the DNA glycosylase NEIL3 and its role in disease progression including cancer. *Cancers (Basel)*. (2022) 14:5722. doi: 10.3390/cancers14235722

57. Zhang F, Wang B, Zhang W, Xu Y, Zhang C, Xue X. Transcription factor MAZ potentiates the upregulated NEIL3-mediated aerobic glycolysis, thereby promoting angiogenesis in hepatocellular carcinoma. *Curr Cancer Drug Targets*. (2024) 24:1235–49. doi: 10.2174/0115680096265896231226062212

58. Zhang F, Lu J, Yang J, Dai Q, Du X, Xu Y, et al. SNHG3 regulates NEIL3 via transcription factor E2F1 to mediate Malignant proliferation of hepatocellular carcinoma. *Immunogenetics*. (2023) 75:39–51. doi: 10.1007/s00251-022-01277-2

59. Fleming AM, Zhou J, Wallace SS, Burrows CJ. A Role for the Fifth G-Track in G-Quadruplex Forming Oncogene Promoter Sequences during Oxidative Stress: Do These "Spare Tires" Have an Evolved Function? *ACS Cent Sci*. (2015) 1:226–33. doi: 10.1021/acscentsci.5b00202

60. TeSlaa T, Ralser M, Fan J, Rabinowitz JD. The pentose phosphate pathway in health and disease. *Nat Metab*. (2023) 5:1275–89. doi: 10.1038/s42255-023-00863-2

61. Peng L, Xiang S, Wang T, Yang M, Duan Y, Ma X, et al. The hepatic clock synergizes with HIF-1alpha to regulate nucleotide availability during liver damage repair. *Nat Metab*. (2025) 7:148–65. doi: 10.1038/s42255-024-01184-8

62. Yang H, Chen D, Wu Y, Zhou H, Diao W, Liu G, et al. A feedback loop of PPP and PI3K/AKT signal pathway drives regorafenib-resistance in HCC. *Cancer Metab*. (2023) 11:27. doi: 10.1186/s40170-023-00311-5

63. Jin X, Lv Y, Bie F, Duan J, Ma C, Dai M, et al. METTL3 confers oxaliplatin resistance through the activation of G6PD-enhanced pentose phosphate pathway in hepatocellular carcinoma. *Cell Death Differ*. (2025) 32:466–79. doi: 10.1038/s41418-024-01406-2

64. Tokuda K, Baron B, Yamashiro C, Kuramitsu Y, Kitagawa T, Kobayashi M, et al. Up-regulation of the pentose phosphate pathway and HIF-1alpha expression during neural progenitor cell induction following glutamate treatment in rat ex vivo retina. *Cell Biol Int*. (2020) 44:137–44. doi: 10.1002/cbin.11212

65. Zhang HS, Zhang ZG, Du GY, Sun HL, Liu HY, Zhou Z, et al. Nrf2 promotes breast cancer cell migration via up-regulation of G6PD/HIF-1alpha/Notch1 axis. *J Cell Mol Med*. (2019) 23:3451–63. doi: 10.1111/jcmm.14241

66. Feng J, Yang M, Wei Q, Song F, Zhang Y, Wang X, et al. Novel evidence for oncogenic piRNA-823 as a promising prognostic biomarker and a potential therapeutic target in colorectal cancer. *J Cell Mol Med*. (2020) 24:9028–40. doi: 10.1111/jcmm.15537

67. Li Z, Wang Q, Huang X, Fu R, Wen X, Zhang L. Multi-omics analysis reveals that ferroptosis-related gene CISD2 is a prognostic biomarker of head and neck squamous cell carcinoma. *J Gene Med*. (2024) 26:e3580. doi: 10.1002/jgm.3580

68. Liu H, Dilger JP. Different strategies for cancer treatment: Targeting cancer cells or their neighbors? *Chin J Cancer Res*. (2025) 37:289–92. doi: 10.21147/j.issn.1000-9604.2025.02.12

69. Wan R, Pan L, Wang Q, Shen G, Guo R, Qin Y, et al. Decoding gastric cancer: machine learning insights into the significance of COMMDs family in immunotherapy and diagnosis. *J Cancer*. (2024) 15:3580–95. doi: 10.7150/jca.94360

70. Sonkin D, Thomas A, Teicher BA. Cancer treatments: Past, present, and future. *Cancer Genet*. (2024) 286-287:18–24. doi: 10.1016/j.cancergen.2024.06.002

frontiers | Frontiers in Immunology

TYPE Review
PUBLISHED 23 September 2025
DOI 10.3389/fimmu.2025.1648987

Check for updates

OPEN ACCESS

EDITED BY
Hailin Tang,
Sun Yat-sen University Cancer Center (SYSUCC), China

REVIEWED BY
Kaijian Hou,
Shantou University, China
Shaoju Qian,
Xinxiang Medical University, China
Min Tang,
Chongqing University, China

*CORRESPONDENCE
Guanhua Lv
809007025@qq.com
Dongmei Quan
quandobgmei@163.com

†These authors have contributed equally to this work

RECEIVED 18 June 2025
ACCEPTED 22 August 2025
PUBLISHED 23 September 2025

CITATION
Gao Q, Wu H, Duan L, Lv G and Quan D (2025) Multi-omics analysis of the tumor microenvironment after metastasis: advancing toward personalized immunotherapy and molecular targeted strategies. *Front. Immunol.* 16:1648987. doi: 10.3389/fimmu.2025.1648987

COPYRIGHT
© 2025 Gao, Wu, Duan, Lv and Quan. This is an open-access article distributed under the terms of the Creative Commons Attribution License (CC BY). The use, distribution or reproduction in other forums is permitted, provided the original author(s) and the copyright owner(s) are credited and that the original publication in this journal is cited, in accordance with accepted academic practice. No use, distribution or reproduction is permitted which does not comply with these terms.

Multi-omics analysis of the tumor microenvironment after metastasis: advancing toward personalized immunotherapy and molecular targeted strategies

Qing Gao[1†], Huqiang Wu[2†], Li Duan[3], Guanhua Lv[4*] and Dongmei Quan[5*]

[1]School of Life Sciences, Zhejiang Chinese Medicine University, Hangzhou, Zhejiang, China, [2]Department of Ophthalmology, The First Affiliated Hospital of Yunnan University of Chinese Medicine, Kunming, Yunnan, China, [3]Department of Rheumatology, The First Affiliated Hospital of Yunnan University of Chinese Medicine, Kunming, Yunnan, China, [4]Department of Gastroenterology, The Second Affiliated Hospital of Liaoning University of Traditional Chinese Medicine, Shenyang, China, [5]Second Clinical School, Liaoning University of Traditional Chinese Medicine, Shenyang, Liaoning, China

The metastatic tumor microenvironment (TME) is a highly dynamic and heterogeneous ecosystem that plays a critical role in promoting cancer cell colonization, immune escape, and resistance to therapy. Recent advances in multi-omics technologies—including genomics, transcriptomics, epigenomics, proteomics, and metabolomics—have enabled a systems-level understanding of the molecular reprogramming that occurs in the TME following metastasis. In this review, we systematically summarize emerging findings from recent multi-omics studies that dissect cellular composition, signaling pathways, immune landscape, and metabolic rewiring within the metastatic TME. We highlight key molecular signatures and intercellular interactions that drive metastatic progression and therapy resistance. Furthermore, we discuss how integrative multi-omics data are being leveraged to identify actionable targets and to design novel immunotherapeutic and molecular precision strategies tailored to the metastatic niche. These insights provide a scientific rationale for the development of TME-targeted approaches in the treatment of advanced-stage cancers.

KEYWORDS

metastatic tumor microenvironment, multi-omics, immune evasion, therapeutic resistance, precision medicine

1 Introduction

Tumor metastasis remains the leading cause of cancer-related deaths, accounting for over 90% of cancer mortalities (1, 2). While early-stage cancers often have favorable prognoses through surgery and adjuvant therapies, the occurrence of metastasis significantly increases treatment complexity and drastically reduces patient survival rates (3). In addition to their invasiveness and migratory capabilities, tumor cells actively transform the local milieu at metastatic sites, creating a "metastatic niche," as the cancer spreads (4–6). This metastatic microenvironment is composed of tumor cells, immune cells, fibroblasts, the vascular system, and various extracellular matrix components, collectively forming a complex ecosystem that supports tumor cell survival, proliferation, and immune evasion.

Traditional single-omics approaches, such as relying solely on genomic or transcriptomic analyses, often fall short in capturing the multidimensional interactions within the metastatic tumor microenvironment (7, 8). This is mainly because no single omics layer can provide a complete understanding of the many molecular regulatory mechanisms involved in tumor metastasis, such as genetic mutations, epigenetic alterations, protein expression control, and metabolic reprogramming (9, 10). A comprehensive picture of the metastatic tumor microenvironment is now possible thanks to the advent of multi-omics technologies that combine information from genomes, transcriptomics, epigenomics, proteomics, and metabolomics (11–13). In addition to illuminating the complex networks of communication between tumor cells, stromal cells, and immune cells in the surrounding area, this multi-dimensional molecular view also provides insight into the ever-changing functional states of immune cells and how they impact the therapeutic response.

Theoretically and technically, the development of immunotherapies and precision molecular-targeted medicines can be supported by the integrated application of multi-omics technologies (14–16). By identifying metastasis-specific molecular markers and key driver pathways, more targeted therapeutic strategies can be devised to overcome resistance and recurrence associated with conventional treatments (17–19). Further, by identifying patient-specific neoantigens and immune suppression mechanisms, multi-omics analysis can personalize immunotherapy, which in turn improves the efficacy of immunotherapies such immune checkpoint inhibitors (20–23). Therefore, a comprehensive elucidation of the multi-omics characteristics of the metastatic tumor microenvironment is essential for advancing therapeutic paradigms in late-stage cancers and for improving patient survival and quality of life.

The purpose of this article is to provide a comprehensive overview of the latest developments in multi-omics technologies that have been developed to better understand the intricate workings of the tumor microenvironment after metastasis, to discuss these technologies' possible uses in molecularly targeted modeling and immunotherapy optimization, and to draw attention to the obstacles and opportunities that exist in the field of clinical translation. Our goal in directing this study is to help develop cancer precision treatment by shedding light on hitherto unexplored scientific questions and offering strategic backing for this field.

2 Multi-omics profiling of the tumor microenvironment after metastasis

2.1 Insights from genomics and transcriptomics

Genomic studies provide critical scientific evidence for revealing the molecular mechanisms underlying tumor metastasis. Through whole-genome sequencing (WGS) and targeted sequencing technologies, researchers have identified numerous key genes that frequently undergo mutations or copy number variations (CNVs) during the metastatic process (24, 25). These genes play crucial roles in tumor initiation, progression, and metastatic potential. For instance, TP53, a classical tumor suppressor gene, is highly mutated across various cancer types (26–28). Genomic instability is reduced when TP53 activity is lost because it causes cell cycle dysregulation and defective DNA damage repair pathways. The result is an increase in tumor cell migration, invasiveness, resistance to apoptosis, and proliferation (29, 30). Additionally, activating mutations in oncogenes such as KRAS and PIK3CA play pivotal roles in metastasis. KRAS mutations cause constitutive activation of the MAPK signaling pathway, promoting cell proliferation, survival, and motility (31, 32). Tumor cells have an advantage in their ability to invade and metastasize when PIK3CA mutations activate the PI3K/Akt signaling pathway, which controls cellular metabolism, proliferation, and cytoskeletal remodeling (33, 34). Abnormal activation of these pathways not only accelerates local tumor growth but also facilitates tumor cells breaching the basement membrane, entering the bloodstream or lymphatic system, and metastasizing to distant organs (35, 36). Another important group of genetic changes is copy number variation, which controls the amounts of tumor suppressor and oncogene gene expression by means of gene amplification and deletion (37, 38). Amplification of oncogenes can markedly enhance malignant phenotypes such as proliferation, apoptosis resistance, and angiogenesis, whereas deletion of critical tumor suppressors weakens cellular defense mechanisms, facilitating metastasis (39, 40). To add insult to injury, CNVs can affect how tumor cells interact with their surroundings by influencing how tumor cells adapt to and avoid immune cells, stromal cells, and the extracellular matrix. Genomic studies that systematically analyze gene mutations and copy number variations (CNVs) provide valuable information for developing tailored treatment strategies by shedding light on the molecular causes of tumor metastasis and identifying promising therapeutic targets and biomarkers.

Transcriptomic studies employing RNA sequencing (RNA-seq) have uncovered extensive and dynamic alterations in gene expression profiles within metastatic tumor tissues compared to their primary counterparts (41–43). Tumor cells adapt, survive, and prosper in distant microenvironments by sophisticated molecular reprogramming, which is reflected in these transcriptome changes. Metastatic tumor cells are able to avoid being destroyed by the immune system because they show a marked increase in the expression of pathways that regulate the immune system (44, 45).

Key immune checkpoint molecules, such as PD-L1 (programmed death-ligand 1) and CTLA-4 (cytotoxic T-lymphocyte-associated protein 4), are frequently overexpressed, serving to suppress T cell activation and promote immune tolerance (46, 47). In addition, the tumor immune microenvironment is transformed by the recruitment of regulatory T cells (Tregs) and myeloid-derived suppressor cells (MDSCs), which allows for the increased expression of immunosuppressive cytokines like IL-10, TGF-β, and IL-6. This creates an immunosuppressive niche that promotes tumor survival and metastasis (48–51). At the same time, metastatic areas show a dramatic increase in genes related to angiogenesis. Neovascularization is driven by vascular endothelial growth factor (VEGF) family members such as VEGFA and VEGFC, which stimulate migration, proliferation, and new vessel formation in endothelial cells. This increased angiogenic activity sustains the growth and spread of the metastatic tumor mass by ensuring that it receives an appropriate amount of oxygen and nutrients (52–54). Moreover, the transcriptomic landscape of metastatic tumors shows pronounced upregulation of genes involved in extracellular matrix (ECM) remodeling, which is essential for tumor invasion and migration. Elevated expression of structural ECM components such as various collagen isoforms (e.g., COL1A1, COL3A1) accompanies increased levels of matrix metalloproteinases (MMPs), including MMP2, MMP9, and MMP14 (55, 56). By hydrolyzing ECM proteins, these proteolytic enzymes make it easier for physical barriers to break down and alter the tumor microenvironment in a way that cancer cells can invade more easily (57, 58). Additionally, the increased expression of integrins and other adhesion molecules supports enhanced tumor cell motility and interaction with stromal components. These transcriptome changes, when taken as a whole, show how tumor cells communicate with the stroma, immune cells, and vasculature around them in a way that promotes metastasis. Gaining a grasp of these alterations in gene expression can shed light on the processes of metastasis and identify possible treatment targets to halt the growth of metastasis.

The advent of single-cell RNA sequencing (scRNA-seq) technology has profoundly deepened our understanding of the cellular heterogeneity and complexity within tumors and their associated microenvironments (59, 60). One advantage of single-cell RNA-seq over bulk RNA-seq is that it allows for high-resolution cell dissection, which is essential for identifying and characterizing different subpopulations of tumor cells, stromal components, and immune cells (61–63). This technology has become instrumental in unraveling the dynamic cellular ecosystem that drives tumor metastasis. The tumor microenvironment is functionally varied and extremely heterogeneous in metastatic situations, according to scRNA-seq. One example is the enrichment of regulatory T cells (Tregs) and M2-polarized macrophages within metastatic niches in breast cancer bone metastasis models. These cells have immunosuppressive features. A variety of immunosuppressive cytokines, including IL-10 and TGF-β, are released by these subsets of immune cells. These cytokines reduce the activity of cytotoxic T cells and make immunological escape easier (64–66). Moreover, M2 macrophages and Tregs contribute to angiogenesis by releasing pro-angiogenic factors like VEGF, thereby promoting neovascularization essential for metastatic tumor growth and sustenance (67, 68). Concurrently, during metastasis, tumor cells display extensive transcriptional plasticity. scRNA-seq studies have shown that tumor cells that have spread to other parts of the body increase the expression of genes related to drug resistance mechanisms, extracellular matrix remodeling, improved migratory potential, and epithelial-to-mesenchymal transition. A key component of both metastatic spread and treatment failure is the ability of cancer cells to invade distant regions and resist therapeutic stresses, which is achieved by transcriptional reprogramming (69, 70). Importantly, such single-cell resolution analyses allow the tracking of rare subpopulations, such as cancer stem-like cells or drug-tolerant persister cells, which may drive relapse and metastasis. Beyond descriptive profiling, transcriptomic data derived from scRNA-seq facilitate the discovery of prognostic biomarkers and predictive signatures for therapeutic response. Differential gene expression analyses can pinpoint gene modules tightly correlated with patient outcomes, enabling risk stratification and guiding clinical decision-making (42, 71, 72). Particularly, these data provide critical insights into the mechanisms of resistance to therapies such as immune checkpoint inhibitors (ICIs). Metastatic and immune evasion traits can be better understood by combining gene regulatory network analysis with the identification of critical transcription factors and signaling cascades. Metastatic tumors often activate NF-κB and STAT3 transcription factors, which lead to the activation of genes related to inflammation and maintain an immunosuppressive tumor microenvironment (73–75). Targeting these pathways holds promise to disrupt the metastatic niche and enhance therapeutic efficacy. Collectively, genomic and transcriptomic studies—especially at single-cell resolution—have markedly expanded our understanding of the molecular and cellular landscape of tumor metastasis (76, 77). Critical driver mutations, alterations in gene expression, and complicated cell-cell interactions within the metastatic ecology have been uncovered by these techniques. This information not only improves our understanding of tumor biology in general, but it also lays the groundwork for precision medicine approaches, such as improved immunotherapy regimens and new targeted medicines. Figure 1 shows that one effective way to enhance cancer patients' clinical results is to integrate multi-omics data at the single-cell level. This allows us to better understand tumor heterogeneity and the complexities of metastasis.

Although multi-omics technologies have demonstrated great potential in tumor metastasis research, significant advantages and limitations exist among different techniques, necessitating systematic comparison and analysis. Single-cell omics technologies, such as single-cell RNA sequencing, offer high resolution and finely reveal cellular heterogeneity, making them powerful tools for dissecting the complexity of tumors and their microenvironments (12, 78). It is challenging for single-cell omics to faithfully portray the geographical distribution of cells inside tissues and their physical interactions with nearby cells due to the frequent absence of spatial information. Spatial omics technologies, on the other hand, (e.g., spatial transcriptomics and spatial

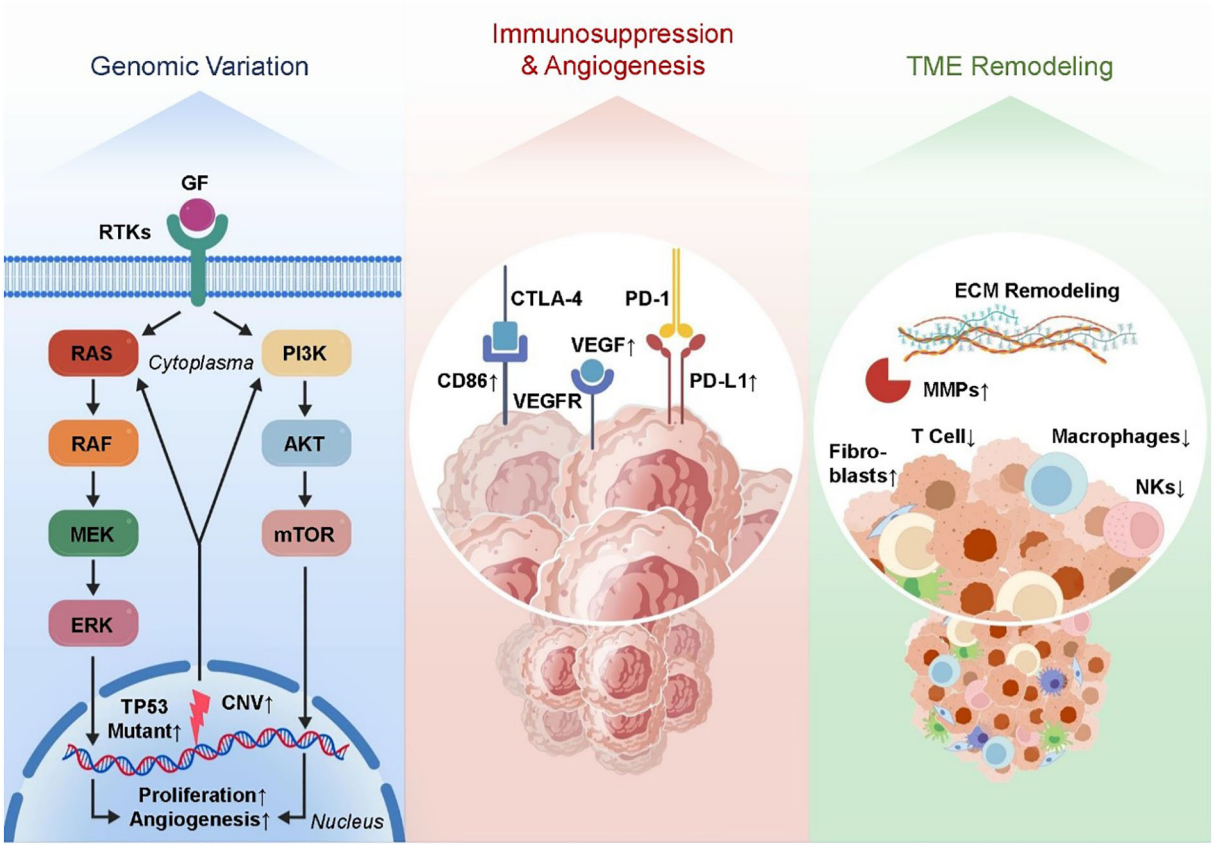

FIGURE 1
The regulatory genomic and transcriptomic landscape of the tumor microenvironment following metastasis. key mutations and CNVs activate oncogenic pathways. Transcriptomic changes include immune suppression, angiogenesis, and ECM remodeling. Single-cell RNA-seq reveals immune heterogeneity and enrichment of Tregs and M2 macrophages.

proteomics) maintain tissue structure, which allows for the mapping of spatial relationships between tumor cells and surrounding immune and stromal cells. This mapping provides crucial insights into microenvironment formation and intercellular signaling (16, 79). However, current spatial omics methods have certain limitations in spatial resolution, detection sensitivity, and data volume, and their high costs restrict widespread application. Furthermore, integrating different omics data faces multiple challenges, including heterogeneous data formats, batch effects, noise interference, and the complexity of biological interpretation. Effectively combining single-cell omics with spatial omics, balancing cellular functional states and spatial localization, remains a research hotspot and challenge. Meanwhile, the heterogeneity and dynamic nature of proteomics and metabolomics data add further complexity to data integration (80, 81). In summary, a deep understanding of the strengths and limitations of various omics technologies aids in the rational selection and optimization of research strategies. Moving forward, leveraging the synergistic advantages of multi-omics and developing efficient data integration and analysis methods will advance the study of the tumor metastatic microenvironment toward more precise and comprehensive insights, providing a robust scientific foundation for clinical translation.

2.2 Epigenomic and proteomic characteristics

The molecular regulation of tumor metastasis is not limited to genetic mutations and changes in gene expression levels; epigenetic regulation also plays a crucial role. Epigenomics primarily involves mechanisms such as DNA methylation, histone modification, and chromatin remodeling (82–84). The spreading potential of tumor cells and the creation of the tumor microenvironment are impacted by these alterations, which dynamically regulate gene activity without changing the DNA sequence. Tumor metastasis is facilitated by DNA methylation in two ways (85–88). On one hand, hypomethylation of promoter regions of pro-metastatic genes can lead to their overexpression—for example, matrix metalloproteinases (MMPs) and genes related to epithelial–mesenchymal transition (EMT)—thus promoting tumor cell invasion and migration (89–91). On the other hand, hypermethylation-induced silencing of tumor suppressor genes, such as CDH1 (encoding E-cadherin), weakens intercellular adhesion and facilitates EMT, a critical step in the metastatic cascade (92, 93). Epigenetics also plays a role in regulating the expression of immunological checkpoint molecules. As an example, the tumor cell's capacity to evade immune surveillance is impacted

by the methylation state of the PD-L1 gene promoter, which controls its expression. Tumor cells can quickly adjust to changes in their microenvironment, control immunosuppressive pathways, and become more resistant to immunotherapy because epigenetic modifications are very malleable (94–97). Histone modifications—such as acetylation, methylation, and phosphorylation—also play significant roles in tumor metastasis. Histone acetylation is generally associated with gene activation, while histone methylation may either activate or repress gene expression, depending on the site and type of modification (98, 99). For example, trimethylation of histone H3 at lysine 27 (H3K27me3) is typically linked to gene silencing. Aberrant increases in H3K27me3 observed in some metastatic tumors suppress tumor suppressor gene expression and promote tumor progression (100–102). Chromatin remodeling complexes can alter chromatin structure and thus affect the accessibility of genes to transcription machinery, thereby mediating metastatic capability. Techniques such as ChIP-seq and whole-genome methylation sequencing have gradually uncovered the mechanistic roles of these modifications in shaping the metastatic microenvironment. Proteomics complements genomic and transcriptomic data, offering unique advantages in revealing protein expression and post-translational modifications (PTMs) (103, 104). In order to regulate the signaling and functional states of tumor cells, post-translational modifications (PTMs) such phosphorylation, ubiquitination, glycosylation, and methylation have a substantial impact on protein stability, activity, subcellular localization, and interactions. One example is the role of phosphorylation modifications in signaling pathway proteins in tumor cell migration, proliferation, and survival. These alterations are particularly important in the MAPK/ERK and PI3K/Akt pathways (105–107). Ubiquitination regulates protein degradation and signaling networks and is particularly important for tumor cells adapting to microenvironmental stress and immune evasion. Proteomic studies have also revealed complex signaling crosstalk between tumor cells and immune cells. For example, changes in the expression and modification states of immunosuppressive cytokines such as TGF-β and IL-10, and their receptors, modulate immune cell functions, promoting immune escape and tumor metastasis (108–110). Altered protein expression profiles in tumor-associated macrophages and regulatory T cells reflect the immunosuppressive status of the tumor microenvironment and provide new insights for discovering immunotherapy targets. In recent years, the emergence of spatial proteomics—especially techniques based on mass spectrometry—has enabled researchers to analyze protein expression and localization with high spatial resolution at the tissue section level. These technologies have revealed that the spatial distribution of specific protein modifications correlates with the degree of immune infiltration in metastatic lesions and the response to therapy, offering a more precise molecular basis for the implementation of personalized immunotherapy. In conclusion, the complex regulatory mechanisms of tumor metastasis and associated microenvironment are uncovered by combining epigenomics and proteome investigation. Both the control of gene expression and the modification of protein function are involved in these processes. To better understand tumor metastasis and its complex biological aspects, as well as to speed up the development of new immunotherapeutic techniques and molecularly targeted medications, integrative multi-omics studies are essential. These studies will provide patients with advanced cancer better treatment alternatives(Figure 2).

2.3 Metabolomic features

Tumor metastasis involves not only alterations at the genomic and proteomic levels but also profound metabolic reprogramming. Within the metastatic microenvironment, tumor cells and surrounding supportive cells adjust metabolic pathways to meet the demands of rapid proliferation and adaptation to hostile conditions, while simultaneously shaping an immunosuppressive environment that facilitates sustained tumor growth and immune evasion (3, 111, 112). These metabolic regulators play a pivotal role in metastasis, as shown by metabolomics' thorough profiling of metabolite alterations. Metastatic tumor cells exhibit elevated glycolysis, a metabolic characteristic known as the Warburg effect, which is highly noticeable (113, 114). Even under aerobic conditions, tumor cells preferentially utilize anaerobic glycolysis to generate energy, producing large amounts of lactate. The accumulation of lactate acidifies the tumor microenvironment, suppressing the activity of effector immune cells such as cytotoxic T lymphocytes and natural killer cells, while promoting the recruitment and polarization of immunosuppressive cells like regulatory T cells and tumor-associated macrophages (TAMs), thereby establishing an immune "cold" environment (115, 116). Moreover, lactate also induces angiogenesis, supporting the blood supply of metastatic lesions and enhancing tumor cell dissemination and survival (117, 118). Another important factor in tumor spreading is the reprogramming of lipid metabolism. Metastatic tumor cells speed up their migration and proliferation by acquiring the energy and membrane components they need through fatty acid production and oxidation. Fatty acid and cholesterol abnormal buildup regulates signaling pathway activation, improves cell motility, and promotes epithelial-mesenchymal transition (119, 120). Additionally, lipid metabolism regulates immune cell function—for example, TAMs promote immunosuppressive states via lipid-mediated signaling, contributing to immune escape. Changes to the metabolism of amino acids are just as important as those involving glucose and lipids. Tumor cells are able to resist oxidative stress because of improved glutamine uptake and metabolism, which supply nitrogen supplies necessary for biosynthesis and aid in regulating antioxidant capability. Tumor immune microenvironment modulation is thought to be mostly mediated by tryptophan metabolism, which promotes immunological tolerance and immune evasion through activation of the indoleamine 2,3-dioxygenase (IDO) pathway. Metabolomic research has also shown that immunotherapy effectiveness is strongly correlated with metabolic alterations in the metastatic microenvironment. Tumor cells deplete essential nutrients such as glucose and amino acids through metabolic competition, impairing the function of tumor-infiltrating lymphocytes and limiting the effectiveness of immune checkpoint inhibitors (120–122). As a result,

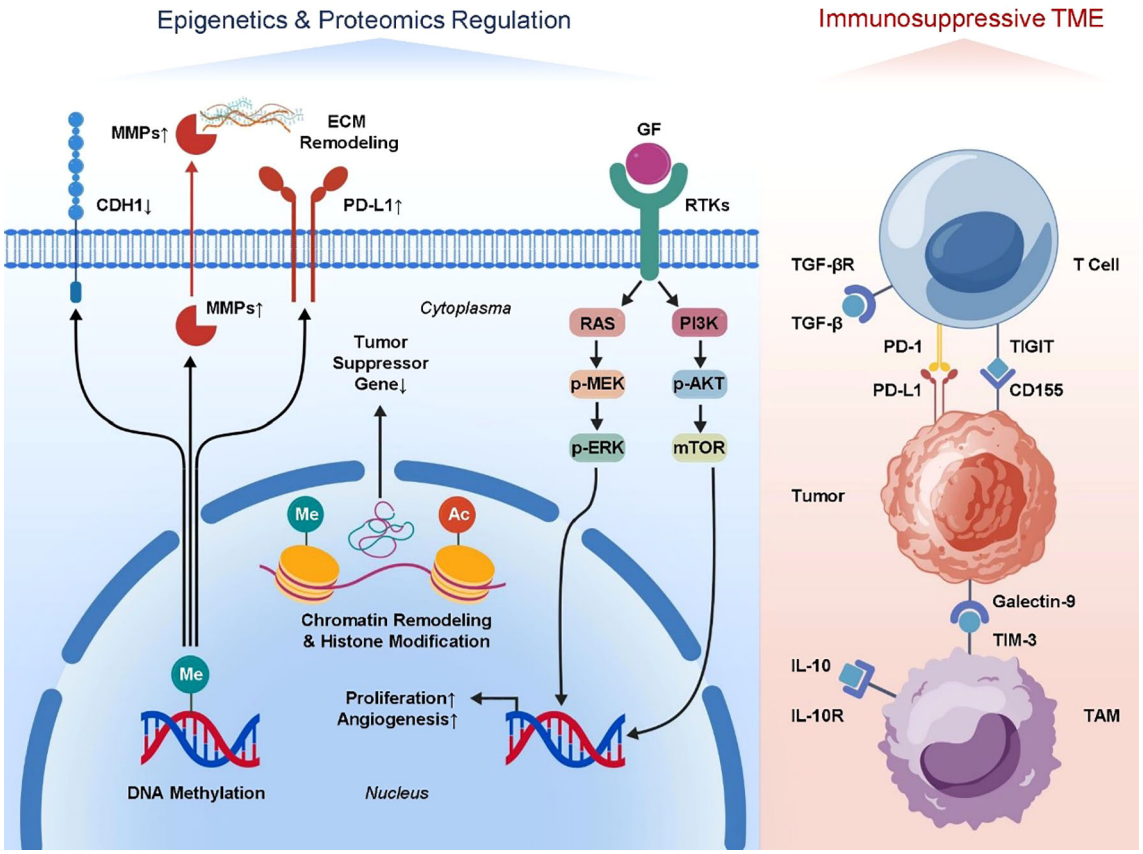

FIGURE 2
Mechanistic insights into epigenomic and proteomic regulation in metastatic tumors. DNA methylation and histone modifications alter gene expression. Key post-translational modifications regulate signaling pathways. Immune-related proteins and immunosuppressive cell proteomes show spatial heterogeneity, promoting metastasis and immune escape.

targeting metabolism has emerged as a novel approach for combination immunotherapy. For example, inhibitors of lactate dehydrogenase (LDH) and regulators of fatty acid metabolism, when combined with immune checkpoint blockade, have shown enhanced anti-tumor efficacy in preclinical models. Researchers have recently been able to study metabolic heterogeneity at spatial and cellular resolutions using cutting-edge methods like mass spectrometry imaging (MSI) and single-cell metabolic analysis. This has led to a better understanding of how metabolic cooperation among cell types within metastatic lesions promotes tumor progression. Precision in detecting metabolic problems and creation of individualized metabolic intervention plans are both greatly facilitated by these technological advancements. In summary, metabolic reprogramming in metastatic tumors not only fulfills the energy demands of growth and dissemination but also regulates the immune microenvironment through multiple mechanisms, facilitating immune escape. Integrating metabolomic data with multi-omics approaches will enhance our understanding of tumor biology and support the development of metabolism-targeted combination therapies, ultimately improving the prognosis of patients with advanced cancer (Figure 3).

To provide a clear overview of multi-omics approaches in the metastatic TME, Table 1 summarized major methods, representative assays, key findings, and clinical applications. Genomics identifies metastasis-associated mutations and clonal evolution, guiding targeted therapy; transcriptomics reveals immune remodeling and stromal heterogeneity, informing immunotherapy; proteomics and metabolomics capture metastasis-specific signaling and metabolic adaptations, offering biomarkers and therapeutic targets; epigenomics uncovers regulatory mechanisms in immune and stromal cells; and multi-omics integration highlights interactions and heterogeneity across tumor, immune, and stromal compartments. This table illustrates the translational value of multi-omics in precision medicine for metastatic cancer.

3 Implications for molecular targeting and immunotherapy

3.1 Optimizing molecular targeting models

Integrating data from genomes, transcriptomics, epigenomics, proteomics, and metabolomics to build accurate and dynamic molecular targeting models is a state-of-the-art approach in cancer treatment research, thanks to the fast development of multi-omics

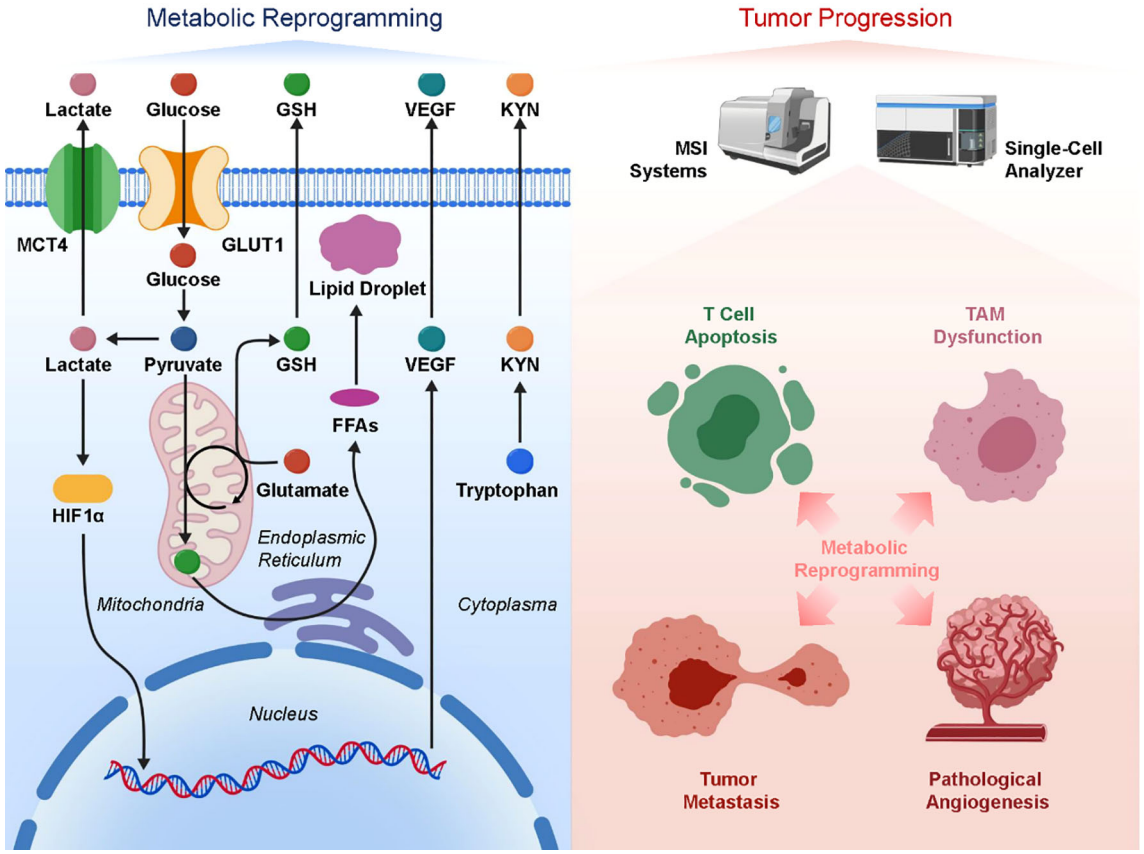

FIGURE 3
Metabolic adaptations in metastatic cancer and their effects on the tumor immune landscape. Enhanced glycolysis, lipid, and amino acid metabolism produce lactate and metabolites that suppress cytotoxic cells and promote immunosuppressive cells, aiding tumor migration, immune evasion, and angiogenesis.

technology. Offering a more evidence-based and individualized foundation for molecular targeted therapy, this integrative approach uncovers the genetic and phenotypic traits of tumor cells while simultaneously delving deeper into the intricate networks of interactions between tumors and their microenvironment (11, 13). First, the integration of multi-omics data allows for the systematic capture of tumor heterogeneity. Genetic mutations, gene expression changes, epigenetic modifications, and protein functional states often vary significantly between patients and even among different regions of the same tumor. By integrating data across these dimensions, it becomes possible to accurately identify key molecular markers and regulatory networks driving tumor progression and metastasis. For example, targeted kinase inhibitors can be developed by merging genomic mutation data with transcriptome profiles, which can reveal overexpression or activating mutations in specific kinase genes. Theoretically, epigenetic data can aid in the creation of inhibitors of epigenetic enzymes by revealing aberrations in DNA methylation or histone changes that mute critical tumor suppressor genes (123, 124). Second, network analysis driven by multi-omics data can simulate signal transduction pathways between tumor cells, immune cells, and stromal cells, capturing dynamic intercellular communication. For instance, integrating proteomics data with transcriptomic profiles of immune cell infiltration can help identify key signaling pathways involved in immune evasion, such as the upregulation mechanisms of immune checkpoints like PD-1/PD-L1 and CTLA-4, thereby informing strategies for immunomodulatory molecular targeting. In addition, Metabolomics data can shed light on the ever-changing nutritional and metabolic product levels within tumor microenvironments, allowing for the identification of metabolic enzymes as possible therapeutic targets and providing necessary information for the development of integrated molecular targeting and metabolic intervention approaches. Integrating data from several omics studies has also become much smarter and more efficient with the help of machine learning and artificial intelligence. The development of individualized treatment programs can be facilitated by building prediction models using multi-omics features, which allow for the accurate forecasting of patient reactions to different targeted medications. For example, using data on a patient's tumor mutation profile, protein expression levels, and metabolic status, the model can identify the most likely effective drug combinations, avoiding ineffective treatments and drug side effects. Moreover, multi-omics integration facilitates drug repurposing and the discovery of novel targets. Through horizontal comparisons and longitudinal tracking of large-scale patient data, previously overlooked molecular factors can be identified as critical players in specific metastatic types, driving the development of novel targeted

TABLE 1 Multi-omics approaches in the metastatic tumor microenvironment (TME).

Omics approach	Representative assays	Key findings in metastatic TME	Clinical utility
Genomics	Whole-exome sequencing (WES), targeted gene panels, ctDNA sequencing	Identification of metastasis-associated drivers (e.g., TP53, KRAS), clonal evolution, mutational signatures	Biomarker discovery for prognosis; stratification for targeted therapy
Transcriptomics	Bulk RNA-seq, single-cell RNA-seq, spatial transcriptomics	Immune remodeling (exhausted T cells, immunosuppressive macrophages), stromal heterogeneity, site-specific gene expression programs	Patient stratification for immunotherapy; prediction of immune checkpoint response
Proteomics	Mass spectrometry–based proteomics, CyTOF	Altered signaling pathways, cytokine/chemokine networks, immune checkpoint protein expression in metastases	Identification of therapeutic targets; biomarker panels for treatment monitoring
Epigenomics	ATAC-seq, bisulfite sequencing, ChIP-seq	Epigenetic reprogramming of immune and stromal cells, enhancer remodeling promoting metastasis	Development of epigenetic therapies; patient selection for combination strategies
Metabolomics	LC-MS/MS, NMR spectroscopy	Metabolic adaptation of metastatic niches (e.g., hypoxia-driven rewiring, lactate accumulation)	Predicting drug resistance; targeting metabolic vulnerabilities
Multi-omics integration	Computational modeling, network analysis	Cross-talk between immune, stromal, and tumor compartments; spatial and temporal heterogeneity	Precision medicine approaches; identification of combination therapy strategies

drugs. Combined with clinical data, such models can also evaluate mechanisms of resistance to targeted therapy, guiding the design of second-line or combination treatment strategies to overcome therapeutic resistance. In summary, the core of optimizing molecular targeting models lies in comprehensively integrating multi-dimensional molecular information to reveal dynamic changes in the tumor microenvironment and multilayer regulatory mechanisms. This approach not only enhances the precision and efficacy of targeted therapies but also paves new pathways for personalized cancer treatment. As the volume of multi-omics data and computational capabilities continue to grow, systems biology-based molecular targeting models are poised to drive revolutionary advances in advanced cancer therapy.

3.2 Enhancing the efficacy of immunotherapy

Immunotherapy, particularly immune checkpoint inhibitors (ICIs), has emerged as a breakthrough in the treatment of various cancers. However, the clinical efficacy of ICIs shows significant heterogeneity across patients, with some individuals exhibiting no response or developing resistance (125, 126). Immunotherapy has progressed from empirical methods toward precision and tailored tactics, thanks to the integrated application of multi-omics technologies, which provide powerful tools for thoroughly studying the tumor immune milieu and its dynamic evolution (127–129). First, multi-omics data facilitate the identification and validation of immune-related biomarkers. Genomic sequencing can reveal the generation of tumor neoantigens—mutant tumor-specific antigens critical for eliciting T cell-mediated immune responses. By integrating transcriptomic and proteomic data, researchers can identify immunogenic proteins highly expressed on the tumor cell surface, guiding personalized cancer vaccine development and neoantigen-targeted therapies (130–132). Moreover, by analyzing epigenomes, we can learn how immune checkpoint genes (such as PD-L1 and CTLA-4) are regulated, which aids in evaluating immunosuppressive pathways and gives molecular proof for the use of checkpoint inhibitors (133, 134). Second, insights into T cell functionality and exhaustion, derived from multi-omics data, are pivotal for assessing immunotherapy responsiveness (135–137). Transcriptomic analyses enable detailed profiling of tumor-infiltrating lymphocyte (TIL) subpopulations and their activation states, identifying exhausted T cell subsets that express markers such as PD-1, LAG-3, and TIM-3 (138, 139). Potential targets for immune cell reactivation have been identified by proteomics, which provides additional validation of the expression levels and functional states of these surface molecules. Metabolomics research also shows that metabolites (such as lactate and adenosine) produced by tumors inhibit T cell activity, which can guide tactics that integrate metabolic regulation with immunological activation. Thirdly, immunotherapy resistance mechanisms can be better understood with the use of multi-omics methods. Immune evasion, antigen presentation abnormalities, and pathway activation are some of the failure-related variables that can be identified by tracking multi-omics alterations in tumors and immune cells before and after therapy. For example, genomic and transcriptomic data may reveal mutations in β2-microglobulin (B2M) that lead to antigen presentation loss, while epigenetic alterations can result in the downregulation of immune checkpoint targets. Uncovering these resistance mechanisms supports the rational design of combination therapies involving immune stimulators, epigenetic modulators, or metabolic interventions to overcome the limitations of monotherapy (140, 141). Furthermore, multi-omics technologies contribute to the development of immune-based stratification models for patient selection and efficacy prediction. By integrating tumor mutational burden (TMB), immune cell infiltration levels, immune gene expression profiles, and metabolic states, such models can predict a patient's likelihood of responding to ICIs, thereby

reducing unnecessary side effects and financial burden. The combination of multi-dimensional biomarkers also provides tools for real-time monitoring of treatment response and early detection of relapse. Lastly, immunometabolic crosstalk has become a research hotspot. Tumor metabolic reprogramming not only supports tumor cell survival but also modulates immune cell function through its metabolites. For instance, enhanced glycolysis in tumor cells leads to lactate accumulation, which suppresses the activity of effector T cells and natural killer cells. Multi-omics analyses help unravel these complex metabolic-immune networks, offering a scientific foundation for the design of immunometabolic combination therapies—such as using metabolic enzyme inhibitors in conjunction with immune checkpoint inhibitors to enhance antitumor immune responses. In summary, the integrated application of multi-omics technologies has deepened our understanding of the tumor immune microenvironment and provides valuable insights for optimizing immunotherapy strategies. With continued advancements in data analysis methods and bioinformatics tools, multi-omics-driven personalized immunotherapy is expected to significantly improve treatment response rates and survival outcomes for patients with advanced cancers.

4 Progress of existing clinical research

In recent years, clinical research integrating multi-omics data to understand and treat metastatic tumors has made significant strides. Numerous clinical trials have incorporated genomic, transcriptomic, proteomic, and metabolomic analyses to stratify patients, predict therapeutic responses, and identify novel biomarkers for personalized treatment. For example, tumor mutation burden (TMB) and specific gene expression profiles have been employed as predictive biomarkers to select patients likely to benefit from immune checkpoint inhibitors (ICIs), improving the efficacy of immunotherapy in metastatic cancers. Clinical trials such as KEYNOTE-158 and CheckMate-227 have demonstrated the utility of these biomarkers in guiding patient selection (142, 143). Additionally, targeted therapies guided by genomic alterations, such as EGFR mutations in non-small cell lung cancer and HER2 amplifications in breast cancer, have shown improved outcomes in metastatic settings (144–147). Ongoing studies are expanding the application of proteomic and metabolomic profiling to uncover resistance mechanisms and to design combination therapies. Moreover, integrated multi-omics approaches have been applied in clinical trials to monitor treatment response dynamically and to understand immune evasion mechanisms. For instance, the use of circulating tumor DNA (ctDNA) combined with proteomic markers enables real-time assessment of tumor evolution and therapeutic resistance (148, 149). Despite these advances, challenges remain in translating multi-omics findings into routine clinical practice, including data standardization, cost, and clinical validation. Nevertheless, the ongoing clinical research efforts are progressively bridging these gaps, paving the way for more precise and effective personalized therapies for patients with metastatic cancers.

5 Translational potential and clinical applications

The application of multi-omics technologies in clinical oncology is gradually maturing, significantly advancing the development of precision medicine. Large public databases such as The Cancer Genome Atlas (TCGA) and the Clinical Proteomic Tumor Analysis Consortium (CPTAC) integrate genomic, transcriptomic, proteomic, and clinical data from thousands of tumor samples, providing invaluable resources for researchers and clinicians. These databases not only reveal the molecular heterogeneity of various cancers but also aid in identifying potential therapeutic targets and biomarkers. With continuous advancements in omics technologies, an increasing number of clinical trials have begun incorporating multi-omics data into patient stratification and therapeutic response prediction. For example, some clinical trials select patients eligible for immune checkpoint inhibitor therapy based on tumor mutation burden (TMB), immune gene expression profiles, or specific metabolic markers. Such omics-based precision stratification not only improves treatment efficacy but also reduces adverse effects and the economic burden associated with ineffective therapies. However, several challenges remain in the clinical application of multi-omics. First, data standardization is an urgent issue. Differences in sequencing platforms, sample processing workflows, and data analysis methods across laboratories compromise data consistency and reproducibility. In order to achieve interoperability across platforms and centers, it is essential to establish uniform bioinformatics pipelines and common quality control techniques. Second, there are substantial challenges to clinical interpretation due to the complexity and high dimensionality of omics data. Single indicators fall short in properly capturing the complex networks formed by interactions across many omics layers in tumor tissues, which contain heterogeneous cell types. Deep data mining and pattern recognition made possible by AI and ML are essential components of the multidisciplinary effort needed to convert these complicated datasets into useful biomarkers or tools for clinical decision-making. Also, omics signatures must be validated in clinical settings. Lacking large-scale, multi-center clinical validation, many omics results are still in the preliminary discovery phase. The clinical application of omics biomarkers requires rigorous validation to ensure sensitivity, specificity, and predictive accuracy. Furthermore, transforming complex multi-omics signatures into simple, rapid, and cost-effective clinical assays is an important direction for broader implementation. Finally, ethical and privacy concerns must not be overlooked. Strict adherence to rules and regulations regarding data storage, distribution, and use is essential when dealing with omics data because of the large amounts of personally identifiable genetic information that is typically involved. In order to advance precision oncology, it is crucial to protect patient privacy while encouraging appropriate data consumption. Multi-omics analyses have identified numerous potential biomarkers and therapeutic targets in the metastatic TME, providing valuable insights into tumor progression and the development of precision therapies (150).

However, the functional validation of the majority of these candidate molecules remains insufficient, limiting their clinical translational potential. *In vitro* cell lines and three-dimensional organoid models, *in vivo* animal models such as patient-derived xenografts (PDX), and clinical cohort association studies are key approaches for validating multi-omics discoveries. Some studies have employed *in vitro* functional assays to verify the roles of candidate molecules in cell proliferation, migration, and immune regulation (151, 152). Moreover, PDX models are widely used to recapitulate the biological characteristics of metastatic tumors, providing important evidence for the *in vivo* functions of molecular targets (153, 154). Clinical cohort analyses, based on large-scale sample databases, have validated the prognostic value and treatment response associations of these candidate molecules. Overall, there is great potential for multi-omics technologies in clinical oncology. However, there are several problems that need to be addressed during translation, including issues with standardization, data interpretation, clinical validation, and ethical security. Precision diagnosis and therapy made possible by multi-omics will bring in a new age in cancer treatment, thanks to ongoing interdisciplinary collaboration, technical progress, and the creation of regulatory frameworks.

6 Conclusion and future perspectives

The rapid development of multi-omics technologies is profoundly reshaping our understanding of the tumor metastatic microenvironment and influencing therapeutic strategies. The intricate molecular pathways and immunological regulatory networks inside metastatic tumor microenvironments can be better understood by combining information from the genome, epigenome, transcriptome, proteome, and metabolome. Not only does this improve our knowledge of tumor biology, but it also lays the groundwork for developing more targeted, efficient, and individualized methods of treatment. In the field of immunotherapy in particular, the integration of multi-omics data facilitates decoding of immune evasion mechanisms, immune cell dynamics, and interactions with tumor cells, greatly promoting the discovery of novel immunotherapeutic targets and combination strategies. Future research should focus on several key areas: First, developing more efficient and intelligent tools for multi-omics data integration and analysis is essential. Given the vast volume and structural complexity of omics data, leveraging cutting-edge technologies such as machine learning and artificial intelligence to achieve efficient data integration, deep mining, and dynamic model construction is foundational to advancing the field. Establishing unified platforms capable of handling multi-dimensional data will enable the full exploitation of complementary information across omics layers and facilitate the discovery of clinically meaningful biomarkers and therapeutic targets. Second, systematic clinical validation of multi-omics biomarkers is a core component of translational medicine. Future efforts must involve more large-scale, multi-center clinical trials to rigorously evaluate biomarker stability, sensitivity, and predictive power. Moreover, emphasis should be placed on translating omics discoveries into clinically accessible, cost-effective diagnostic tools to enable widespread application in real-world healthcare settings and fulfill the promise of precision medicine. Third, promoting interdisciplinary and inter-institutional collaboration is essential to accelerating the clinical translation of multi-omics technologies. The heterogeneity and complexity of tumors mean that no single institution can address all key issues independently. Multi-center cooperation not only provides access to diverse sample resources but also facilitates the unification of research standards and methodologies, enhancing the generalizability and credibility of findings. In addition, establishing open-access multi-omics databases and bioinformatics platforms to foster data sharing and collaboration will significantly drive innovation and development in precision oncology. Finally, ethical and privacy concerns remain critical. To strike a compromise between protecting patients' privacy and making responsible use of data, strong data protection systems are required to accommodate the massive amounts of multi-omics data being created and used. For omics technologies to be used consistently and in a way that is acceptable to society, lawmakers, clinical researchers, and tech developers must collaborate to establish rules and recommendations based on solid science. In conclusion, multi-omics technologies offer a new perspective and pathway for investigating metastatic tumor microenvironments and advancing precision therapies. As analytical tools improve, clinical validation progresses, and collaborative efforts expand, multi-omics will play an increasingly central role in cancer immunotherapy and targeted therapy. This advancement promises to usher in a new era of more precise, effective, and personalized cancer treatment, offering new hope and improved quality of life for patients with advanced-stage cancer.

Author contributions

DQ: Conceptualization, Formal analysis, Funding acquisition, Investigation, Project administration, Resources, Software, Validation, Visualization, Writing – original draft, Writing – review & editing. HW: Conceptualization, Formal analysis, Funding acquisition, Investigation, Project administration, Resources, Software, Visualization, Writing – original draft, Writing – review & editing. LD: Conceptualization, Formal analysis, Funding acquisition, Investigation, Project administration, Resources, Validation, Visualization, Writing – original draft, Writing – review & editing. GL: Conceptualization, Formal analysis, Investigation, Project administration, Software, Validation, Writing – original draft, Writing – review & editing. QG: Conceptualization, Data curation, Formal analysis, Investigation, Methodology, Project administration, Software, Supervision, Validation, Writing – original draft, Writing – review & editing.

Funding

The author(s) declare that no financial support was received for the research and/or publication of this article.

Conflict of interest

The authors declare that the research was conducted in the absence of any commercial or financial relationships that could be construed as a potential conflict of interest.

Generative AI statement

The author(s) declare that no Generative AI was used in the creation of this manuscript.

Any alternative text (alt text) provided alongside figures in this article has been generated by Frontiers with the support of artificial intelligence and reasonable efforts have been made to ensure accuracy, including review by the authors wherever possible. If you identify any issues, please contact us.

Publisher's note

All claims expressed in this article are solely those of the authors and do not necessarily represent those of their affiliated organizations, or those of the publisher, the editors and the reviewers. Any product that may be evaluated in this article, or claim that may be made by its manufacturer, is not guaranteed or endorsed by the publisher.

References

1. Quail DF, Joyce JA. Microenvironmental regulation of tumor progression and metastasis. *Nat Med*. (2013) 19:1423–37. doi: 10.1038/nm.3394

2. Bakir B, Chiarella AM, Pitarresi JR, Rustgi AK. EMT, MET, plasticity, and tumor metastasis. *Trends Cell Biol*. (2020) 30:764–76. doi: 10.1016/j.tcb.2020.07.003

3. Lin Y, Xu J, Lan H. Tumor-associated macrophages in tumor metastasis: biological roles and clinical therapeutic applications. *J Hematol Oncol*. (2019) 12:76. doi: 10.1186/s13045-019-0760-3

4. Liu Y, Cao X. Characteristics and significance of the pre-metastatic niche. *Cancer Cell*. (2016) 30:668–81. doi: 10.1016/j.ccell.2016.09.011

5. Celià-Terrassa T, Kang Y. Metastatic niche functions and therapeutic opportunities. *Nat Cell Biol*. (2018) 20:868–77. doi: 10.1038/s41556-018-0145-9

6. Baldi S, Long N, Ma S, Liu L, Al-Danakh A, Yang Q, et al. Advancements in protein kinase inhibitors: from discovery to clinical applications. *Res (Washington DC)*. (2025) 8:0747. doi: 10.34133/research.0747

7. Yagishita H, Sasaki T. Integrating physiological and transcriptomic analyses at the single-neuron level. *Neurosci Res*. (2025) 214:69–74. doi: 10.1016/j.neures.2024.05.003

8. Chen W, Guillaume-Gentil O, Rainer PY, Gäbelein CG, Saelens W, Gardeux V, et al. Live-seq enables temporal transcriptomic recording of single cells. *Nature*. (2022) 608:733–40. doi: 10.1038/s41586-022-05046-9

9. Luecken MD, Theis FJ. Current best practices in single-cell RNA-seq analysis: a tutorial. *Mol Syst Biol*. (2019) 15:e8746. doi: 10.15252/msb.20188746

10. Hrdlickova R, Toloue M, Tian B. RNA-Seq methods for transcriptome analysis. *Wiley Interdiscip Rev RNA*. (2017) 8. doi: 10.1002/wrna.1364

11. Baysoy A, Bai Z, Satija R, Fan R. The technological landscape and applications of single-cell multi-omics. *Nat Rev Mol Cell Biol*. (2023) 24:695–713. doi: 10.1038/s41580-023-00615-w

12. Vandereyken K, Sifrim A, Thienpont B, Voet T. Methods and applications for single-cell and spatial multi-omics. *Nat Rev Genet*. (2023) 24:494–515. doi: 10.1038/s41576-023-00580-2

13. Babu M, Snyder M. Multi-omics profiling for health. *Mol Cell Proteom: MCP*. (2023) 22:100561. doi: 10.1016/j.mcpro.2023.100561

14. Chen C, Wang J, Pan D, Wang X, Xu Y, Yan J, et al. Applications of multi-omics analysis in human diseases. *MedComm*. (2023) 4:e315. doi: 10.1002/mco2.315

15. Du Y, Li R, Fu D, Zhang B, Cui A, Shao Y, et al. Multi-omics technologies and molecular biomarkers in brain tumor-related epilepsy. *CNS Neurosci Ther*. (2024) 30:e14717. doi: 10.1111/cns.14717

16. Wu X, Yang X, Dai Y, Zhao Z, Zhu J, Guo H, et al. Single-cell sequencing to multi-omics: technologies and applications. *biomark Res*. (2024) 12:110. doi: 10.1186/s40364-024-00643-4

17. Picard M, Scott-Boyer MP, Bodein A, Périn O, Droit A. Integration strategies of multi-omics data for machine learning analysis. *Comput Struct Biotechnol J*. (2021) 19:3735–46. doi: 10.1016/j.csbj.2021.06.030

18. Liu JC, Dong SS, Shen H, Yang DY, Chen BB, Ma XY, et al. Multi-omics research in sarcopenia: Current progress and future prospects. *Ageing Res Rev*. (2022) 76:101576. doi: 10.1016/j.arr.2022.101576

19. Liu X, Peng T, Xu M, Lin S, Hu B, Chu T, et al. Spatial multi-omics: deciphering technological landscape of integration of multi-omics and its applications. *J Hematol Oncol*. (2024) 17:72. doi: 10.1186/s13045-024-01596-9

20. Nakajima S, Nakamizo S, Nomura T, Ishida Y, Sawada Y, Kabashima K. Integrating multi-omics approaches in deciphering atopic dermatitis pathogenesis and future therapeutic directions. *Allergy*. (2024) 79:2366–79. doi: 10.1111/all.16183

21. Nieman DC, Pence BD. Exercise immunology: Future directions. *J Sport Health Sci*. (2020) 9:432–45. doi: 10.1016/j.jshs.2019.12.003

22. Yang Z, Guan F, Bronk L, Zhao L. Multi-omics approaches for biomarker discovery in predicting the response of esophageal cancer to neoadjuvant therapy: A multidimensional perspective. *Pharmacol Ther*. (2024) 254:108591. doi: 10.1016/j.pharmthera.2024.108591

23. Xie J, Liu W, Deng X, Wang H, Ou X , An X, et al. Paracrine orchestration of tumor microenvironment remodeling induced by GLO1 potentiates lymph node metastasis in breast cancer. *Adv Sci (Weinheim Baden-Wurttemberg Germany)*. (2025) 12:e00722. doi: 10.1002/advs.202500722

24. Bagger FO, Borgwardt L, Jespersen AS, Hansen AR, Bertelsen B, Kodama M, et al. Whole genome sequencing in clinical practice. *BMC Med Genomics*. (2024) 17:39. doi: 10.1186/s12920-024-01795-w

25. Zhao EY, Jones M, Jones SJM. Whole-genome sequencing in cancer. *Cold Spring Harbor Perspect Med*. (2019) 9. doi: 10.1101/cshperspect.a034579

26. Voskarides K, Giannopoulou N. The role of TP53 in adaptation and evolution. *Cells*. (2023) 12. doi: 10.3390/cells12030512

27. Zhong L, Li H, Chang W, Ao Y, Wen Z, Chen Y. TP53 mutations in esophageal squamous cell carcinoma. *Front Biosci (Landmark edition)*. (2023) 28:219. doi: 10.31083/j.fbl2809219

28. Wong TN, Link DC. Are TP53 mutations all alike? *Hematol Am Soc Hematol Educ Program*. (2024) 2024:321–5. doi: 10.1182/hematology.2024000556

29. Hunter AM, Sallman DA. Targeting TP53 mutations in myelodysplastic syndromes. *Hematol/Oncol Clinics North America*. (2020) 34:421–40. doi: 10.1016/j.hoc.2019.11.004

30. Zhao Y, Chen W, Yu J, Pei S, Zhang Q, Shi J, et al. TP53 in MDS and AML: Biological and clinical advances. *Cancer Lett*. (2024) 588:216767. doi: 10.1016/j.canlet.2024.216767

31. Huang L, Guo Z, Wang F, Fu L. KRAS mutation: from undruggable to druggable in cancer. *Signal Transduct Target Ther*. (2021) 6:386. doi: 10.1038/s41392-021-00780-4

32. Singhal A, Li BT, O'Reilly EM. Targeting KRAS in cancer. *Nat Med*. (2024) 30:969–83. doi: 10.1038/s41591-024-02903-0

33. Arafeh R, Samuels Y. PIK3CA in cancer: The past 30 years. *Semin Cancer Biol*. (2019) 59:36–49. doi: 10.1016/j.semcancer.2019.02.002

34. Madsen RR, Vanhaesebroeck B, Semple RK. Cancer-associated PIK3CA mutations in overgrowth disorders. *Trends Mol Med*. (2018) 24:856–70. doi: 10.1016/j.molmed.2018.08.003

35. Pascual J, Turner NC. Targeting the PI3-kinase pathway in triple-negative breast cancer. *Ann Oncol: Off J Eur Soc Med Oncol*. (2019) 30:1051–60. doi: 10.1093/annonc/mdz133

36. Rosin J, Svegrup E, Valachis A, Zerdes I. Discordance of PIK3CA mutational status between primary and metastatic breast cancer: a systematic review and meta-analysis. *Breast Cancer Res Treat*. (2023) 201:161–9. doi: 10.1007/s10549-023-07010-1

37. Brás A, Rodrigues AS, Rueff J. Copy number variations and constitutional chromothripsis (Review). *Biomed Rep*. (2020) 13:11. doi: 10.3892/br.2020.1318

38. Giles Doran C, Pennington SR. Copy number alteration signatures as biomarkers in cancer: a review. *Biomarkers Med*. (2022) 16:371–86. doi: 10.2217/bmm-2021-0476

39. Abd Radzak SM, Mohd Khair SZN, Ahmad F, Patar A, Idris Z, Mohamed Yusoff AA. Insights regarding mitochondrial DNA copy number alterations in human cancer (Review). *Int J Mol Med*. (2022) 50. doi: 10.3892/ijmm.2022.5160

40. Müller MF, Ibrahim AE, Arends MJ. Molecular pathological classification of colorectal cancer. *Virchows Archiv: an Int J Pathol*. (2016) 469:125–34. doi: 10.1007/s00428-016-1956-3

41. Jiang H, Yu D, Yang P, Guo R, Kong M, Gao Y, et al. Revealing the transcriptional heterogeneity of organ-specific metastasis in human gastric cancer using single-cell RNA Sequencing. *Clin Trans Med*. (2022) 12:e730. doi: 10.1002/ctm2.730

42. Han J, DePinho RA, Maitra A. Single-cell RNA sequencing in pancreatic cancer. *Nat Rev Gastroenterol Hepatol*. (2021) 18:451–2. doi: 10.1038/s41575-021-00471-z

43. Hong M, Tao S, Zhang L, Diao LT, Huang X, Huang S, et al. RNA sequencing: new technologies and applications in cancer research. *J Hematol Oncol*. (2020) 13:166. doi: 10.1186/s13045-020-01005-x

44. Ergin S, Kherad N, Alagoz M. RNA sequencing and its applications in cancer and rare diseases. *Mol Biol Rep*. (2022) 49:2325–33. doi: 10.1007/s11033-021-06963-0

45. Tirosh I, Suva ML. Cancer cell states: Lessons from ten years of single-cell RNA-sequencing of human tumors. *Cancer Cell*. (2024) 42:1497–506. doi: 10.1016/j.ccell.2024.08.005

46. Cha JH, Chan LC, Li CW, Hsu JL, Hung MC. Mechanisms controlling PD-L1 expression in cancer. *Mol Cell*. (2019) 76:359–70. doi: 10.1016/j.molcel.2019.09.030

47. Dermani FK, Samadi P, Rahmani G, Kohlan AK, Najafi R. PD-1/PD-L1 immune checkpoint: Potential target for cancer therapy. *J Cell Physiol*. (2019) 234:1313–25. doi: 10.1002/jcp.27172

48. Salkeni MA, Naing A. Interleukin-10 in cancer immunotherapy: from bench to bedside. *Trends Cancer*. (2023) 9:716–25. doi: 10.1016/j.trecan.2023.05.003

49. Rallis KS, Corrigan AE, Dadah H, Stanislovas J, Zamani P, Makker S, et al. IL-10 in cancer: an essential thermostatic regulator between homeostatic immunity and inflammation - a comprehensive review. *Future Oncol (London England)*. (2022) 18:3349–65. doi: 10.2217/fon-2022-0063

50. Peng D, Fu M, Wang M, Wei Y, Wei X. Targeting TGF-β signal transduction for fibrosis and cancer therapy. *Mol Cancer*. (2022) 21:104. doi: 10.1186/s12943-022-01569-x

51. Colak S, Ten Dijke P. Targeting TGF-β Signaling in cancer. *Trends Cancer*. (2017) 3:56–71. doi: 10.1016/j.trecan.2016.11.008

52. Mabeta P, Steenkamp V. The VEGF/VEGFR axis revisited: implications for cancer therapy. *Int J Mol Sci*. (2022) 23. doi: 10.3390/ijms232415585

53. Itatani Y, Kawada K, Yamamoto T, Sakai Y. Resistance to anti-angiogenic therapy in cancer-alterations to anti-VEGF pathway. *Int J Mol Sci*. (2018) 19. doi: 10.3390/ijms19041232

54. Apte RS, Chen DS, Ferrara N. VEGF in signaling and disease: beyond discovery and development. *Cell*. (2019) 176:1248–64. doi: 10.1016/j.cell.2019.01.021

55. Karamanos NK, Piperigkou Z, Passi A, Götte M, Rousselle P, Vlodavsky I. Extracellular matrix-based cancer targeting. *Trends Mol Med*. (2021) 27:1000–13. doi: 10.1016/j.molmed.2021.07.009

56. Prakash J, Shaked Y. The interplay between extracellular matrix remodeling and cancer therapeutics. *Cancer Discov*. (2024) 14:1375–88. doi: 10.1158/2159-8290.CD-24-0002

57. Pickup MW, Mouw JK, Weaver VM. The extracellular matrix modulates the hallmarks of cancer. *EMBO Rep*. (2014) 15:1243–53. doi: 10.15252/embr.201439246

58. Walker C, Mojares E, Del Río Hernández A. Role of extracellular matrix in development and cancer progression. *Int J Mol Sci*. (2018) 19. doi: 10.3390/ijms19103028

59. Tan Z, Chen X, Zuo J, Fu S, Wang H, Wang J. Comprehensive analysis of scRNA-Seq and bulk RNA-Seq reveals dynamic changes in the tumor immune microenvironment of bladder cancer and establishes a prognostic model. *J Trans Med*. (2023) 21:223. doi: 10.1186/s12967-023-04056-z

60. Ji L, Fu G, Huang M, Kao X, Zhu J, Dai Z, et al. scRNA-seq of colorectal cancer shows regional immune atlas with the function of CD20(+) B cells. *Cancer Lett*. (2024) 584:216664. doi: 10.1016/j.canlet.2024.216664

61. Zhang Y, Zhang Z. The history and advances in cancer immunotherapy: understanding the characteristics of tumor-infiltrating immune cells and their therapeutic implications. *Cell Mol Immunol*. (2020) 17:807–21. doi: 10.1038/s41423-020-0488-6

62. Peroni E, Randi ML, Rosato A, Cagnin S. Acute myeloid leukemia: from NGS, through scRNA-seq, to CAR-T. dissect cancer heterogeneity and tailor the treatment. *J Exp Clin Cancer Res: CR*. (2023) 42:259. doi: 10.1186/s13046-023-02841-8

63. Ren X, Zhang L, Zhang Y, Li Z, Siemers N, Zhang Z. Insights gained from single-cell analysis of immune cells in the tumor microenvironment. *Annu Rev Immunol*. (2021) 39:583–609. doi: 10.1146/annurev-immunol-110519-071134

64. Plitas G, Konopacki C, Wu K, Bos PD, Morrow M, Putintseva EV, et al. Regulatory T cells exhibit distinct features in human breast cancer. *Immunity*. (2016) 45:1122–34. doi: 10.1016/j.immuni.2016.10.032

65. Lei PJ, Pereira ER, Andersson P, Amoozgar Z, Van Wijnbergen JW, O'Melia MJ, et al. Cancer cell plasticity and MHC-II-mediated immune tolerance promote breast cancer metastasis to lymph nodes. *J Exp Med*. (2023) 220. doi: 10.1084/jem.20221847

66. Chung W, Eum HH, Lee HO, Lee KM, Lee HB, Kim KT, et al. Single-cell RNA-seq enables comprehensive tumour and immune cell profiling in primary breast cancer. *Nat Commun*. (2017) 8:15081. doi: 10.1038/ncomms15081

67. Genin M, Clement F, Fattaccioli A, Raes M, Michiels C. M1 and M2 macrophages derived from THP-1 cells differentially modulate the response of cancer cells to etoposide. *BMC Cancer*. (2015) 15:577. doi: 10.1186/s12885-015-1546-9

68. Li M, Yang Y, Xiong L, Jiang P, Wang J, Li C. Metabolism, metabolites, and macrophages in cancer. *J Hematol Oncol*. (2023) 16:80. doi: 10.1186/s13045-023-01478-6

69. Gao J, Liang Y, Wang L. Shaping polarization of tumor-associated macrophages in cancer immunotherapy. *Front Immunol*. (2022) 13:888713. doi: 10.3389/fimmu.2022.888713

70. Xia Y, Rao L, Yao H, Wang Z, Ning P, Chen X. Engineering macrophages for cancer immunotherapy and drug delivery. *Adv Mater (Deerfield Beach Fla)*. (2020) 32:e2002054. doi: 10.1002/adma.202002054

71. Van de Sande B, Lee JS, Mutasa-Gottgens E, Naughton B, Bacon W, Manning J, et al. Applications of single-cell RNA sequencing in drug discovery and development. *Nat Rev Drug Discov*. (2023) 22:496–520. doi: 10.1038/s41573-023-00688-4

72. Saul D, Kosinsky RL, Atkinson EJ, Doolittle ML, Zhang X, LeBrasseur NK, et al. A new gene set identifies senescent cells and predicts senescence-associated pathways across tissues. *Nat Commun*. (2022) 13:4827. doi: 10.1038/s41467-022-32552-1

73. Fan Y, Mao R, Yang J. NF-κB and STAT3 signaling pathways collaboratively link inflammation to cancer. *Protein Cell*. (2013) 4:176–85. doi: 10.1007/s13238-013-2084-3

74. Yu H, Lin L, Zhang Z, Zhang H, Hu H. Targeting NF-κB pathway for the therapy of diseases: mechanism and clinical study. *Signal Transduct Target Ther*. (2020) 5:209. doi: 10.1038/s41392-020-00312-6

75. He G, Karin M. NF-κB and STAT3 - key players in liver inflammation and cancer. *Cell Res*. (2011) 21:159–68. doi: 10.1038/cr.2010.183

76. Li F, Zhang J, Arfuso F, Chinnathambi A, Zayed ME, Alharbi SA, et al. NF-κB in cancer therapy. *Arch Toxicol*. (2015) 89:711–31. doi: 10.1007/s00204-015-1470-4

77. Lalle G, Twardowski J, Grinberg-Bleyer Y. NF-κB in cancer immunity: friend or foe? *Cells*. (2021) 10. doi: 10.3390/cells10020355

78. Xu X, Wang J, Wu L, Guo J, Song Y, Tian T, et al. Microfluidic single-Cell omics analysis. *Small (Weinheim an der Bergstrasse Germany)*. (2020) 16:e1903905. doi: 10.1002/smll.201903905

79. Conrad T, Altmüller J. Single cell- and spatial 'Omics revolutionize physiology. *Acta Physiol (Oxford England)*. (2022) 235:e13848. doi: 10.1111/apha.13848

80. Song Y, Xu X, Wang W, Tian T, Zhu Z, Yang C. Single cell transcriptomics: moving towards multi-omics. *Anal*. (2019) 144:3172–89. doi: 10.1039/C8AN01852A

81. Sun Y, Liu Z, Fu Y, Yang Y, Lu J, Pan M, et al. Single-cell multi-omics sequencing and its application in tumor heterogeneity. *Briefings Funct Genomics*. (2023) 22:313–28. doi: 10.1093/bfgp/elad009

82. Nishiyama A, Nakanishi M. Navigating the DNA methylation landscape of cancer. *Trends Genet: TIG*. (2021) 37:1012–27. doi: 10.1016/j.tig.2021.05.002

83. Papanicolau-Sengos A, Aldape K. DNA methylation profiling: an emerging paradigm for cancer diagnosis. *Annu Rev Pathol*. (2022) 17:295–321. doi: 10.1146/annurev-pathol-042220-022304

84. Xie J, Xie Y, Tan W, Ye Y, Ou X, Zou X, et al. Deciphering the role of ELAVL1: Insights from pan-cancer multiomics analyses with emphasis on nasopharyngeal carcinoma. *J Trans Internal Med*. (2025) 13:138–55. doi: 10.1515/jtim-2025-0009

85. Klutstein M, Nejman D, Greenfield R, Cedar H. DNA methylation in cancer and aging. *Cancer Res*. (2016) 76:3446–50. doi: 10.1158/0008-5472.CAN-15-3278

86. He W, Li Q, Li X. Acetyl-CoA regulates lipid metabolism and histone acetylation modification in cancer. *Biochim Biophys Acta Rev Cancer*. (2023) 1878:188837. doi: 10.1016/j.bbcan.2022.188837

87. Zaib S, Rana N, Khan I. Histone modifications and their role in epigenetics of cancer. *Curr Medicinal Chem*. (2022) 29:2399–411. doi: 10.2174/0929867328666211108105214

88. Bajbouj K, Al-Ali A, Ramakrishnan RK, Saber-Ayad M, Hamid Q. Histone modification in NSCLC: molecular mechanisms and therapeutic targets. *Int J Mol Sci*. (2021) 22. doi: 10.3390/ijms222111701

89. Scheau C, Badarau IA, Costache R, Caruntu C, Mihai GL, Didilescu AC, et al. The role of matrix metalloproteinases in the epithelial-Mesenchymal transition of hepatocellular carcinoma. *Anal Cell Pathol (Amsterdam)*. (2019) 2019:9423907. doi: 10.1155/2019/9423907

90. Akhlaghipour I, Moghbeli M. Matrix metalloproteinases as the critical regulators of cisplatin response and tumor cell invasion. *Eur J Pharmacol*. (2024) 982:176966. doi: 10.1016/j.ejphar.2024.176966

91. Yan B, Wang Y, Li Y, Wang C, Zhang L. Inhibition of arachidonate 15-lipoxygenase reduces the epithelial-mesenchymal transition in eosinophilic chronic rhinosinusitis with nasal polyps. *Int Forum Allergy Rhinology*. (2019) 9:270–80. doi: 10.1002/alr.22243

92. Wang LL, Zhang B, Zheng MH, Xie YZ, Wang CJ, Jin JY. Matrix metalloproteinases (MMPs) in targeted drug delivery: synthesis of a potent and highly selective inhibitor against matrix metalloproteinase- 7. *Curr Topics Medicinal Chem*. (2020) 20:2459–71. doi: 10.2174/1568026620666200722104928

93. Knapinska AM, Amar S, He Z, Matosevic S, Zylberberg C, Fields GB. Matrix metalloproteinases as reagents for cell isolation. *Enzyme Microb Technol*. (2016) 93-94:29–43. doi: 10.1016/j.enzmictec.2016.07.009

94. Huang C, Ren S, Chen Y, Liu A, Wu Q, Jiang T, et al. PD-L1 methylation restricts PD-L1/PD-1 interactions to control cancer immune surveillance. *Sci Adv*. (2023) 9: eade4186. doi: 10.1126/sciadv.ade4186

95. Chen X, Pan X, Zhang W, Guo H, Cheng S, He Q, et al. Epigenetic strategies synergize with PD-L1/PD-1 targeted cancer immunotherapies to enhance antitumor responses. *Acta Pharm Sin B*. (2020) 10:723–33. doi: 10.1016/j.apsb.2019.09.006

96. Xu J, Wei L, Liu H, Lei Y, Zhu Y, Liang C, et al. CD274 (PD-L1) methylation is an independent predictor for bladder cancer patients' Survival. *Cancer Invest*. (2022) 40:228–33. doi: 10.1080/07357907.2022.2028805

97. Xie J, Liu M, Deng X, Tang Y, Zheng S, Ou X, et al. Gut microbiota reshapes cancer immunotherapy efficacy: Mechanisms and therapeutic strategies. *iMeta*. (2024) 3:e156. doi: 10.1002/imt2.156

98. Zhang Y, Sun Z, Jia J, Du T, Zhang N, Tang Y, et al. Overview of histone modification. *Adv Exp Med Biol*. (2021) 1283:1–16. doi: 10.1007/978-981-15-8104-5_1

99. Hu Y, He Z, Li Z, Wang Y, Wu N, Sun H, et al. Lactylation: the novel histone modification influence on gene expression, protein function, and disease. *Clin Epigenet*. (2024) 16:72. doi: 10.1186/s13148-024-01682-2

100. Verma A, Singh A, Singh MP, Nengroo MA, Saini KK, Satrusal SR, et al. EZH2-H3K27me3 mediated KRT14 upregulation promotes TNBC peritoneal metastasis. *Nat Commun*. (2022) 13:7344. doi: 10.1038/s41467-022-35059-x

101. Inoue A, Jiang L, Lu F, Suzuki T, Zhang Y. Maternal H3K27me3 controls DNA methylation-independent imprinting. *Nature*. (2017) 547:419–24. doi: 10.1038/nature23262

102. Chen Z, Djekidel MN, Zhang Y. Distinct dynamics and functions of H2AK119ub1 and H3K27me3 in mouse preimplantation embryos. *Nat Genet*. (2021) 53:551–63. doi: 10.1038/s41588-021-00821-2

103. Pan S, Chen R. Pathological implication of protein post-translational modifications in cancer. *Mol Aspects Med*. (2022) 86:101097. doi: 10.1016/j.mam.2022.101097

104. Li Y, Zhang R, Hei H. Advances in post-translational modifications of proteins and cancer immunotherapy. *Front Immunol*. (2023) 14:1229397. doi: 10.3389/fimmu.2023.1229397

105. Su X, Shen Z, Yang Q, Sui F, Pu J, Ma J, et al. Vitamin C kills thyroid cancer cells through ROS-dependent inhibition of MAPK/ERK and PI3K/AKT pathways via distinct mechanisms. *Theranostics*. (2019) 9:4461–73. doi: 10.7150/thno.35219

106. Pashirzad M, Khorasanian R, Fard MM, Arjmand MH, Langari H, Khazaei M, et al. The therapeutic potential of MAPK/ERK inhibitors in the treatment of colorectal cancer. *Curr Cancer Drug Targets*. (2021) 21:932–43. doi: 10.2174/1568009621666211103113339

107. Asl ER, Amini M, Najafi S, Mansoori B, Mokhtarzadeh A, Mohammadi A, et al. Interplay between MAPK/ERK signaling pathway and MicroRNAs: A crucial mechanism regulating cancer cell metabolism and tumor progression. *Life Sci*. (2021) 278:119499. doi: 10.1016/j.lfs.2021.119499

108. Rosser EC, Mauri C. Regulatory B cells: origin, phenotype, and function. *Immunity*. (2015) 42:607–12. doi: 10.1016/j.immuni.2015.04.005

109. Wiguna AP, Walden P. Role of IL-10 and TGF-β in melanoma. *Exp Dermatol*. (2015) 24:209–14. doi: 10.1111/exd.12629

110. Yousefi A, Zare Bidoki A, Shafioyoun A, Sadr M, Varzaneh FN, Shabani M, et al. Association of IL-10 and TGF-beta cytokine gene polymorphisms with autoimmune hepatitis. *Clinics Res Hepatol Gastroenterol*. (2019) 43:45–50. doi: 10.1016/j.clinre.2018.07.004

111. Jiao Y, Lv Q. Does primary tumor resection induce accelerated metastasis in breast cancer? A review. *J Surg Res*. (2023) 283:1005–17. doi: 10.1016/j.jss.2022.11.064

112. Mansur G, Alsavaf MB, Pasquini L, Abouammo MD, Biswas C, Kumar P, et al. Intrasellar tumor-to-tumor metastasis: A single center experience with a systematic review. *Pituitary*. (2024) 27:455–67. doi: 10.1007/s11102-024-01441-9

113. Vaupel P, Multhoff G. Revisiting the Warburg effect: historical dogma versus current understanding. *J Physiol*. (2021) 599:1745–57. doi: 10.1113/JP278810

114. Kobayashi Y, Banno K, Kunitomi H, Takahashi T, Takeda T, Nakamura K, et al. Warburg effect in Gynecologic cancers. *J Obstet Gynaecol Res*. (2019) 45:542–8. doi: 10.1111/jog.13867

115. Shephard RJ, Shek PN. Cold exposure and immune function. *Can J Physiol Pharmacol*. (1998) 76:828–36. doi: 10.1139/y98-097

116. Castellani JW, MB IK, Rhind SG. Cold exposure: human immune responses and intracellular cytokine expression. *Med Sci Sports Exercise*. (2002) 34:2013–20. doi: 10.1097/00005768-200212000-00023

117. Lv X, Lv Y, Dai X. Lactate, histone lactylation and cancer hallmarks. *Expert Rev Mol Med*. (2023) 25:e7. doi: 10.1017/erm.2022.42

118. Chen J, Huang Z, Chen Y, Tian H, Chai P, Shen Y, et al. Lactate and lactylation in cancer. *Signal Transduct Target Ther*. (2025) 10:38. doi: 10.1038/s41392-024-02082-x

119. Cao Y. Adipocyte and lipid metabolism in cancer drug resistance. *J Clin Invest*. (2019) 129:3006–17. doi: 10.1172/JCI127201

120. Vander Heiden MG, Cantley LC, Thompson CB. Understanding the Warburg effect: the metabolic requirements of cell proliferation. *Sci (New York NY)*. (2009) 324:1029–33. doi: 10.1126/science.1160809

121. Li Z, Zhang H. Reprogramming of glucose, fatty acid and amino acid metabolism for cancer progression. *Cell Mol Life Sci: CMLS*. (2016) 73:377–92. doi: 10.1007/s00018-015-2070-4

122. Koppula P, Zhuang L, Gan B. Cystine transporter SLC7A11/xCT in cancer: ferroptosis, nutrient dependency, and cancer therapy. *Protein Cell*. (2021) 12:599–620. doi: 10.1007/s13238-020-00789-5

123. Mohammadi-Shemirani P, Sood T, Paré G. From 'Omics to multi-omics technologies: the discovery of novel causal mediators. *Curr Atheroscl Rep*. (2023) 25:55–65. doi: 10.1007/s11883-022-01078-8

124. Fiocchi C. Omics and multi-omics in IBD: no integration, no breakthroughs. *Int J Mol Sci*. (2023) 24. doi: 10.3390/ijms241914912

125. Riley RS, June CH, Langer R, Mitchell MJ. Delivery technologies for cancer immunotherapy. *Nat Rev Drug Discov*. (2019) 18:175–96. doi: 10.1038/s41573-018-0006-z

126. Baxevanis CN, Perez SA, Papamichail M. Cancer immunotherapy. *Crit Rev Clin Lab Sci*. (2009) 46:167–89. doi: 10.1080/10408360902937809

127. Cha JH, Chan LC, Song MS, Hung MC. New approaches on cancer immunotherapy. *Cold Spring Harbor Perspect Med*. (2020) 10. doi: 10.1101/cshperspect.a036863

128. Szeto GL, Finley SD. Integrative approaches to cancer immunotherapy. *Trends Cancer*. (2019) 5:400–10. doi: 10.1016/j.trecan.2019.05.010

129. Li Z, Wang Q, Huang X, Fu R, Wen X, Zhang L. Multi-omics analysis reveals that ferroptosis-related gene CISD2 is a prognostic biomarker of head and neck squamous cell carcinoma. *J Gene Med*. (2024) 26:e3580. doi: 10.1002/jgm.3580

130. Wang JB, Gao YX, Ye YH, Zheng QL, Luo HY, Wang SH, et al. Comprehensive multi-omics analysis of pyroptosis for optimizing neoadjuvant immunotherapy in patients with gastric cancer. *Theranostics*. (2024) 14:2915–33. doi: 10.7150/thno.93124

131. Du M, Gu D, Xin J, Peters U, Song M, Cai G, et al. Integrated multi-omics approach to distinct molecular characterization and classification of early-onset colorectal cancer. *Cell Rep Med*. (2023) 4:100974. doi: 10.1016/j.xcrm.2023.100974

132. Zhang SL, Cheng LS, Zhang ZY, Sun HT, Li JJ. Untangling determinants of gut microbiota and tumor immunologic status through a multi-omics approach in colorectal cancer. *Pharmacol Res*. (2023) 188:106633. doi: 10.1016/j.phrs.2022.106633

133. Jing Y, Liu J, Ye Y, Pan L, Deng H, Wang Y, et al. Multi-omics prediction of immune-related adverse events during checkpoint immunotherapy. *Nat Commun*. (2020) 11:4946. doi: 10.1038/s41467-020-18742-9

134. Liu Z, Zhao Y, Kong P, Liu Y, Huang J, Xu E, et al. Integrated multi-omics profiling yields a clinically relevant molecular classification for esophageal squamous cell carcinoma. *Cancer Cell*. (2023) 41:181–195.e189. doi: 10.1016/j.ccell.2022.12.004

135. Dolina JS, Van Braeckel-Budimir N, Thomas GD, Salek-Ardakani S. CD8(+) T cell exhaustion in cancer. *Front Immunol*. (2021) 12:715234. doi: 10.3389/fimmu.2021.715234

136. McLane LM, Abdel-Hakeem MS, Wherry EJ. CD8 T cell exhaustion during chronic viral infection and cancer. *Annu Rev Immunol*. (2019) 37:457–95. doi: 10.1146/annurev-immunol-041015-055318

137. Wan R, Pan L, Wang Q, Shen G, Guo R, Qin Y, et al. Decoding gastric cancer: machine learning insights into the significance of COMMDs family in immunotherapy and diagnosis. *J Cancer*. (2024) 15:3580–95. doi: 10.7150/jca.94360

138. Nowroozi A, Khalili N, Razi S, Keshavarz-Fathi M, Rezaei N. Tumor-infiltrating lymphocyte therapy for lung cancer and its future paradigms. *Expert Opin Biol Ther*. (2022) 22:735–45. doi: 10.1080/14712598.2022.2072206

139. Schoenfeld AJ, Lee SM, Doger de Spéville B, Gettinger SN, Häfliger S, Sukari A, et al. Lifileucel, an autologous tumor-Infiltrating lymphocyte monotherapy, in patients with advanced non-Small cell lung cancer resistant to immune checkpoint inhibitors. *Cancer Discov*. (2024) 14:1389–402. doi: 10.1158/2159-8290.CD-23-1334

140. Wang H, Liu B, Wei J. Beta2-microglobulin(B2M) in cancer immunotherapies: Biological function, resistance and remedy. *Cancer Lett*. (2021) 517:96–104. doi: 10.1016/j.canlet.2021.06.008

141. Cowan AJ, Green DJ, Kwok M, Lee S, Coffey DG, Holmberg LA, et al. Diagnosis and management of multiple myeloma: A review. *Jama*. (2022) 327:464–77. doi: 10.1001/jama.2022.0003

142. Marabelle A, Le DT, Ascierto PA, Di Giacomo AM, De Jesus-Acosta A, Delord JP, et al. Efficacy of pembrolizumab in patients with noncolorectal high microsatellite instability/Mismatch repair-Deficient cancer: results from the phase II KEYNOTE-158 study. *J Clin Oncol: Off J Am Soc Clin Oncol*. (2020) 38:1–10. doi: 10.1200/JCO.19.02105

143. Brahmer JR, Lee JS, Ciuleanu TE, Bernabe Caro R, Nishio M, Urban L, et al. Five-Year survival outcomes with nivolumab plus ipilimumab versus chemotherapy as first-Line treatment for metastatic non-Small-Cell lung cancer in CheckMate 227. *J Clin Oncol: Off J Am Soc Clin Oncol*. (2023) 41:1200–12. doi: 10.1200/JCO.22.01503

144. Kashima K, Kawauchi H, Tanimura H, Tachibana Y, Chiba T, Torizawa T, et al. CH7233163 overcomes osimertinib-resistant EGFR-Del19/T790M/C797S mutation. *Mol Cancer Ther*. (2020) 19:2288–97. doi: 10.1158/1535-7163.MCT-20-0229

145. Sabbah DA, Hajjo R, Sweidan K. Review on epidermal growth factor receptor (EGFR) structure, signaling pathways, interactions, and recent updates of EGFR

inhibitors. *Curr Topics Medicinal Chem*. (2020) 20:815–34. doi: 10.2174/1568026620666200303123102

146. Loibl S, Gianni L. HER2-positive breast cancer. *Lancet (London England)*. (2017) 389:2415–29. doi: 10.1016/S0140-6736(16)32417-5

147. Kang S, Kim SB. HER2-low breast cancer: now and in the future. *Cancer Res Treat*. (2024) 56:700–20. doi: 10.4143/crt.2023.1138

148. Pessoa LS, Heringer M, Ferrer VP. ctDNA as a cancer biomarker: A broad overview. *Crit Rev Oncol/Hematol*. (2020) 155:103109. doi: 10.1016/j.critrevonc.2020.103109

149. Stadler JC, Belloum Y, Deitert B, Sementsov M, Heidrich I, Gebhardt C, et al. Current and future clinical applications of ctDNA in immuno-Oncology. *Cancer Res*. (2022) 82:349–58. doi: 10.1158/0008-5472.CAN-21-1718

150. Wischnewski V, Maas RR, Aruffo PG, Soukup K, Galletti G, Kornete M, et al. Phenotypic diversity of T cells in human primary and metastatic brain tumors revealed by multiomic interrogation. *Nat Cancer*. (2023) 4:908–24. doi: 10.1038/s43018-023-00566-3

151. Wehrli M, Guinn S, Birocchi F, Kuo A, Sun Y, Larson RC, et al. Mesothelin CAR T cells secreting anti-FAP/Anti-CD3 molecules efficiently target pancreatic adenocarcinoma and its stroma. *Clin Cancer Res: an Off J Am Assoc Cancer Res*. (2024) 30:1859–77. doi: 10.1158/1078-0432.CCR-23-3841

152. Jin J, Yoshimura K, Sewastjanow-Silva M, Song S, Ajani JA. Challenges and prospects of patient-derived xenografts for cancer research. *Cancers*. (2023) 15. doi: 10.3390/cancers15174352

153. Chaudary N, Pintilie M, Schwock J, Dhani N, Clarke B, Milosevic M, et al. Characterization of the tumor-Microenvironment in patient-Derived cervix xenografts (OCICx). *Cancers*. (2012) 4:821–45. doi: 10.3390/cancers4030821

154. Rago V, Perri A, Di Agostino S. New therapeutic perspectives in prostate cancer: patient-derived organoids and patient-derived xenograft models in precision medicine. *Biomedicines*. (2023) 11. doi: 10.3390/biomedicines11102743

frontiers | Frontiers in Immunology

TYPE Original Research
PUBLISHED 01 October 2025
DOI 10.3389/fimmu.2025.1664726

Check for updates

OPEN ACCESS

EDITED BY
Qi Wang,
Jiangsu University, China

REVIEWED BY
Bjørn Steen Skålhegg,
University of Oslo, Norway
Zhirui Zeng,
Guizhou Medical University, China
Wencai Liu,
Shanghai Jiao Tong University, China
Jianbo Zhou,
Sichuan University, China

*CORRESPONDENCE
Qingyi Liu
zhongmeijianlqy@163.com

RECEIVED 12 July 2025
ACCEPTED 20 August 2025
PUBLISHED 01 October 2025

CITATION
Liu G, Zhang X, He Y, Liang D, Xie S, Zhang N, Geng N, Zhang L, Huang Y, Liu F and Liu Q (2025) AI-based non-invasive profiling of the tumor immune microenvironment using longitudinal CT radiomics predicts immunotherapy response in lung cancer. *Front. Immunol.* 16:1664726. doi: 10.3389/fimmu.2025.1664726

COPYRIGHT
© 2025 Liu, Zhang, He, Liang, Xie, Zhang, Geng, Zhang, Huang, Liu and Liu. This is an open-access article distributed under the terms of the Creative Commons Attribution License (CC BY). The use, distribution or reproduction in other forums is permitted, provided the original author(s) and the copyright owner(s) are credited and that the original publication in this journal is cited, in accordance with accepted academic practice. No use, distribution or reproduction is permitted which does not comply with these terms.

AI-based non-invasive profiling of the tumor immune microenvironment using longitudinal CT radiomics predicts immunotherapy response in lung cancer

Guangjie Liu[1], Xiaoyan Zhang[1], Yutong He[2], Di Liang[2], Shaonan Xie[1], Ning Zhang[3], Nan Geng[4], Liwen Zhang[5], Yajie Huang[6], Fang Liu[7] and Qingyi Liu[1]*

[1]Department of Thoracic Surgery, the Fourth Hospital of Hebei Medical University, Shijiazhuang, China, [2]The Fourth Hospital of Hebei Medical University Cancer Institute, Shijiazhuang, China, [3]Department of CT and MRI, the Fourth Hospital of Hebei Medical University, Shijiazhuang, Shijiazhuang, China, [4]Department of Respiratory Medicine, the Fourth Hospital of Hebei Medical University, Shijiazhuang, Shijiazhuang, China, [5]Hebei Key Laboratory of Environment and Human Health, Department of Epidemiology and Statistics, School of Public Health, Hebei Medical University, Shijiazhuang, China, [6]Department of Medical Oncology, the Fourth Hospital of Hebei Medical University, Shijiazhuang, Shijiazhuang, China, [7]Department of Hospital Quality and Control, the Fourth Hospital of Hebei Medical University, Shijiazhuang, China

Background: Despite advances in immunotherapy, durable responses in lung cancer remain limited to a subset of patients, underscoring the need for biomarkers capturing spatial immune-tumor interactions. Current methods, such as PD-L1 immunohistochemistry, suffer from sampling bias and fail to decode dynamic immune evasion mechanisms non-invasively.

Methods: We developed a radiomics framework integrating longitudinal tumor growth kinetics (log volume change rate, LVCR) with deep learning to: (1) delineate tumors via medical knowledge-guided segmentation; and (2) derive an Immune Evasion Score (IES) predicting immunosuppressive niches. The model employs immune-aware attention gates (IAAG) to prioritize regions associated with aggressive growth (high LVCR) and immune evasion.

Results: Validated on 420 CT scans, our approach achieved superior segmentation accuracy (Dice=0.7728 $\pm$ 0.03; HD95 = 9.8 $\pm$ 1.5 mm) over existing models. Critically, the IES predicted PD-L1 expression (AUC = 0.85; *p*<0.001) and CD8+ T-cell exclusion (*p*<0.01). High IES correlated with rapid immunotherapy progression (HR = 2.3, *p*=0.004), and spatial analysis confirmed 72.3% concordance between IAAG-prioritized regions and pathological PD-L1+ niches.

Conclusion: This work establishes a non-invasive paradigm for mapping immunosuppressive microenvironments, bridging precision radiotherapy with immunotherapy personalization. The IES provides a dynamic biomarker of immune evasion, potentially guiding patient stratification for checkpoint inhibitors.

KEYWORDS

tumor immune microenvironment, immunotherapy response, radiomic biomarkers, precision radiotherapy, tumor growth kinetics

1 Introduction

Lung cancer continues to be the most significant contributor to cancer-related morbidity and mortality on a global scale (1). According to the GLOBOCAN 2018 estimates, lung cancer was the most diagnosed cancer and the leading cause of cancer death worldwide, accounting for 11.6% of the total cancer cases and 18.4% of the total cancer deaths (2, 3). This trend is expected to persist, as projections for 2050 indicate a substantial increase in both incidence and mortality rates, with an estimated 3.8 million new cases and 3.2 million deaths globally (4, 5).

The burden of lung cancer is not uniform across different regions and demographics. For instance, the incidence and mortality rates are higher in countries with a higher Human Development Index (HDI), and there are notable disparities between sexes, with men generally exhibiting higher rates than women (6, 7). However, recent trends have shown an increase in lung cancer cases among female never-smokers, highlighting the evolving epidemiological landscape of this disease (8).

Contemporary management strategies focus on three pillars: prevention, early detection, and therapeutic innovation (9). While tobacco exposure remains the primary modifiable risk factor, the emergence of immunotherapy has fundamentally transformed the treatment paradigm (10, 11). Immune checkpoint inhibitors (ICIs), a cornerstone of immunotherapy, including anti-PD-1 antibodies (e.g., pembrolizumab) and anti-PD-L1 antibodies (e.g., atezolizumab), occupy a central position in the management of advanced lung cancer. Paradoxically, durable responses to ICIsoccurs in only 20 - 30% of patients (12), underscoring a critical need for biomarkers capable of decoding spatial tumor-immune interactions that determine therapeutic efficacy (13). Static scans capture only a single time point, failing to reflect dynamic immune-tumor crosstalk—for example, rapid tumor growth under immune pressure (often linked to PD-L1 upregulation) or real-time remodeling of the immune microenvironment during treatment. This imperative is heightened by limitations of current gold-standard approaches: PD-L1 immunohistochemistry suffers from spatial sampling bias, while tumor mutational burden assessment lacks accessibility in resource-limited settings. Clinical PD-L1 IHC relies on needle biopsies, but tumor heterogeneity means these samples may not represent the overall immune phenotype. Approximately 30% of lung cancer patients exhibit spatial variability in PD-L1 expression, leading to potential misclassification (14, 15).

Within this context, precise tumor delineation assumes dual significance. First, it remains foundational for radiotherapy planning, where millimeter-level accuracy determines therapeutic index. Second, and perhaps more innovatively, it enables spatial characterization of immune infiltrates within the tumor microenvironment—a determinant of immunotherapy response. Deep learning models, particularly 3D U-Net variants, have recently emerged as highly effective tools for automated tumor delineation. Unlike traditional methods—such as threshold-based approaches (prone to error in heterogeneous tissues) or region-growing algorithms (limited by edge ambiguity)—deep learning segmentation uses convolutional neural networks to learn hierarchical features, adapting to irregular tumor margins and necrotic cores common in lung cancer. These advanced models utilize large-scale CT datasets containing substantial information, enabling efficient extraction of high-dimensional features (16, 17). On public benchmarks, they achieve Dice coefficients ranging from 0.73 to 0.75. For instance, recent studies demonstrate that Attention U-Net significantly improves segmentation accuracy by dynamically weighting features through attention gates, facilitating more precise analysis.

However, several critical limitations remain. First, these models exhibit limited clinical interpretability, primarily functioning as "black boxes" without incorporating domain-specific medical knowledge such as tumor biology or patient demographics. Consequently, their ability to capture heterogeneous tumor morphologies—including infiltrative margins or necrotic cores—is constrained. Second, their reliance on single-timepoint imaging restricts capacity for monitoring dynamic tumor progression or regression, as longitudinal CT data are seldom utilized. Static imaging fails to capture dynamic immune-tumor interactions (e.g., PD-L1 upregulation during rapid tumor growth), while clinical PD-L1 detection suffers from spatial sampling bias due to

Abbreviations: LVCR, Log volume change rate; IES, Immune Evasion Score; IAAG, Immune-aware attention gates; HDI, Human Development Index; ICI, Immune checkpoint inhibitors; HU, Hounsfield Units; GLCM, Gray-level co-occurrence matrix; AG, Attention gate; LVCR, Lymphovascular cancer recurrence; IEEP, Immune Evasion Phenotype Prediction.

tumor heterogeneity (18, 19). Finally, these models show suboptimal precision in complex cases, particularly with small nodules (<2 cm) and low-contrast regions, often producing fragmented or over-segmented outputs that may compromise clinical decision-making.

To address these challenges, we propose MK-UNet, a medical knowledge-guided 3D U-Net architecture that synergizes multimodal imaging data with clinical metadata and tumor biomarkers through three transformative innovations: 1. Dynamic Immuno-Phenotypic Fusion: Clinical metadata and tumor biomarkers (including growth rate quantified via log volume change rate, LVCR) are encoded to prioritize regions exhibiting immune-evasive morphology. 2. Multimodal Immune-Relevant Enhancement: Edge-optimized preprocessing targets boundary features predictive of T-cell exclusion patterns.

3. Longitudinal Immune Monitoring: Sequential CT analysis captures temporal changes in immune-reactive niches.

Initial validation studies revealed MK-UNet's capacity to simultaneously address two critical clinical needs: achieving superior segmentation accuracy (Dice coefficient 0.7728; 22% reduction in Hausdorff distance) while enabling precise mapping of immunologically relevant regions. This dual functionality

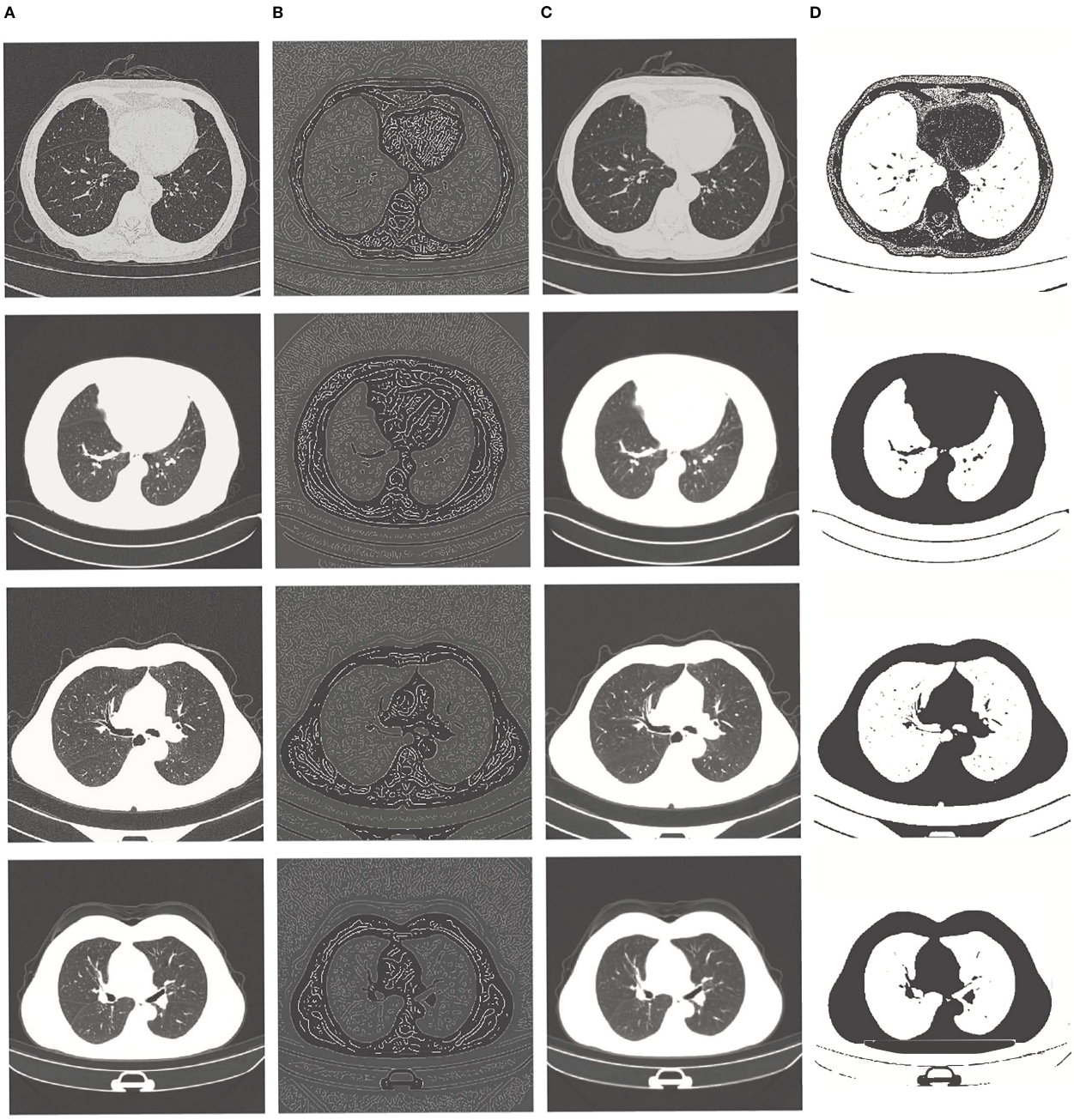

FIGURE 1
From left to right: **(A)** original image, **(B)** edge enhancement image, **(C)** Gaussian filter noise reduction image, **(D)** contrast enhancement image.

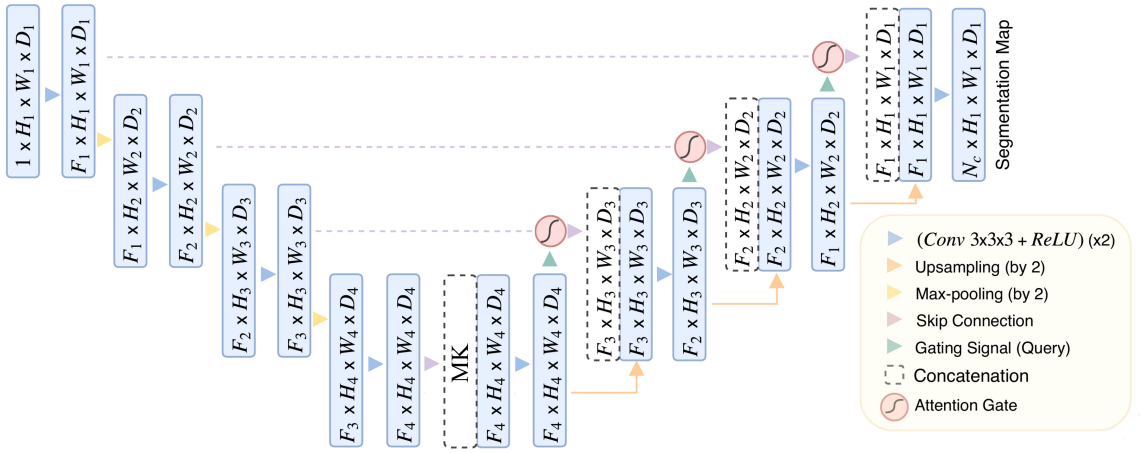

FIGURE 2
From left to right: original image, Windowing filtered image().

establishes the framework as a promising methodology for advancing precision approaches in immuno-oncology, particularly for stratifying patients likely to benefit from checkpoint inhibitors.

2 Results

2.1 Data preprocessing

2.1.1 Multi-modal preprocessing

To improve the robustness of the neural network, raw 3D CT volumes underwent preprocessing to form a 4-channel input using three complementary algorithms: edge enhancement, Gaussian denoising, and contrast optimization. The first channel preserved the original CT Hounsfield Units (HU) values (high threshold=0.2, low threshold=0.1, determined from the distribution of tumor edge pixels in the training set), while the remaining three channels were generated as follows: 1. Edge enhancement was achieved through Canny edge detection, implemented in Python with a sigma value of 1.5, to accentuate tumor boundaries and structural details; 2. Gaussian denoising was performed using a 3D Gaussian filter with a kernel size of 3 and a sigma of 0.8 to reduce noise while maintaining anatomical features; 3. Contrast optimization involved linearly scaling pixel intensities to the range [0, 255] to exploit the full 256 gray levels. A gray-level co-occurrence matrix (GLCM) was calculated within a sliding window of 5×5×5 voxels, from which contrast attributes were derived to enhance texture differentiation between tumors and adjacent tissues. Furthermore, data augmentation techniques were employed during training to enhance model generalization, including random rotation, scaling, translation, and the addition of Gaussian noise. These techniques were implemented in Python and executed dynamically, the details are available in the "attention_CT_unet.ipynb" file.

The preprocessing pipeline is illustrated in Figure 1, and the implementation details are available in the "preprocess.py" file.

2.1.2 Adaptive windowing filtering

To enhance input quality and eliminate extraneous background regions, an adaptive windowing filter was employed during the preprocessing phase. This filter dynamically adjusted the threshold for each voxel based on the intensity distribution of annotated tumor regions. Specifically, the threshold $T(x,y,z)$ was determined using the formula: $T(x,y,z) = \mu_{tumor}+1.5\cdot\sigma_{tumor}$, where μ_{tumor} and σ_{tumor} represent the mean and standard deviation of tumor voxel intensities, respectively. Voxels with intensities below this threshold were masked out, thereby effectively removing non-tumor regions (such as healthy tissues and air cavities) while preserving the boundaries and internal texture details of the tumor.

This windowing process substantially reduced background noise and enhanced the contrast between tumors and surrounding tissues, as demonstrated in Figure 2. The figure presents, from left to right, the original CT slice and the filtered result following adaptive windowing. Detailed implementation and parameter settings can be found in the "windowing.ipynb"file.

2.2 MK-UNet architecture

The MK-UNet framework is a sophisticated 3D U-Net-based segmentation model that integrates medical knowledge and attention mechanisms to enhance the prioritization of tumor-related regions while incorporating clinical metadata. As depicted in Figure 3, the architecture follows an encoder-decoder paradigm, featuring adaptive feature fusion and hierarchical attention gating.

The encoder pathway comprises four sequential downsampling blocks, each reducing spatial resolution by 50% (e.g., from $H_1\times W_1 \times D_1$ to $H_4=H_1/8\times W_4=W_1/_8\times D_4=D_1/_8$) and simultaneously doubling the number of feature channels. To mitigate information loss during downsampling, attention gate (AG) are incorporated at each skip connection. The architecture of the AG, detailed in Figure 4, involves dynamically weighting encoder features using contextual

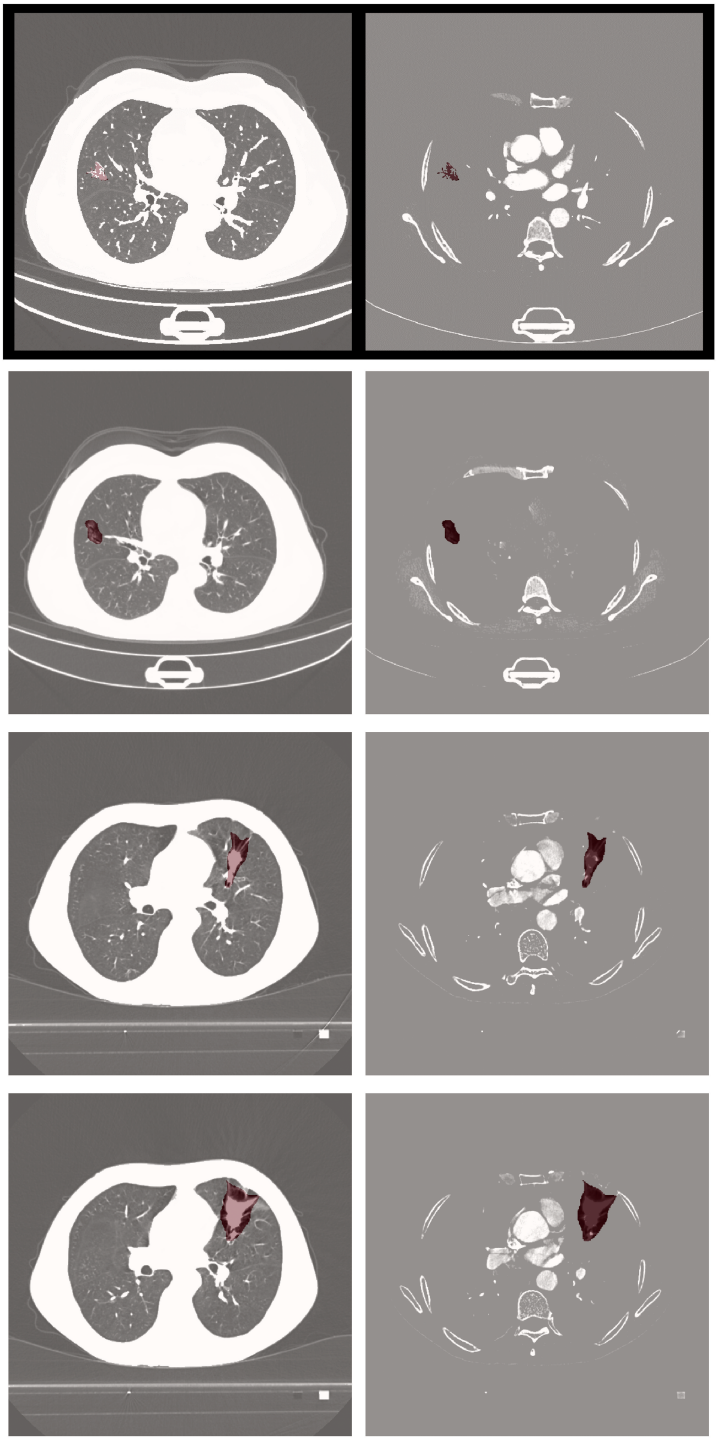

FIGURE 3
The overview of MK-UNet framework. The 6-dimensional clinical vector is spatially expanded and concatenated with the 256-channel feature map at the channel level. The 256-channel feature map (derived from CT scan voxels within manually annotated tumor ROIs) is concatenated with clinical vectors at the bottleneck layer.

information from coarser decoder layers through a gating mechanism. This mechanism integrates encoder and decoder features via learnable convolutions, applying a sigmoid activation to produce spatial attention maps that emphasize tumor boundaries and suppress irrelevant background noise.

Six clinical and tumor biomarkers—namely age, gender, smoking history, pathological grade, tumor stage, and lymphovascular cancer recurrence (LVCR)—are encoded into a six-dimensional vector. Discrete features, such as gender, are represented using one-hot encoding, whereas continuous variables, such as age, are normalized

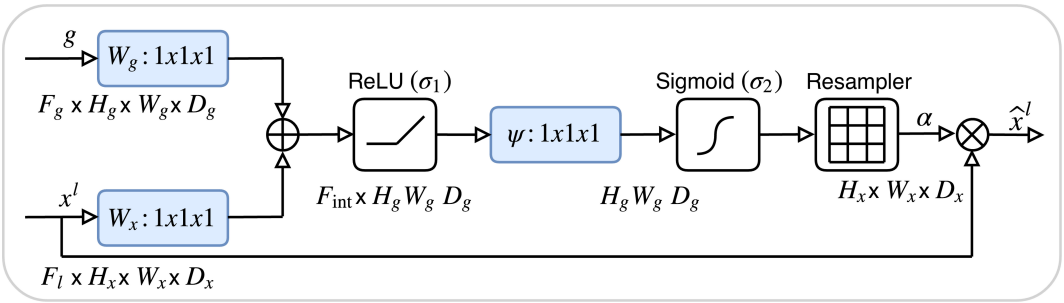

FIGURE 4
The architecture of the attention Gate. The attention weights are computed using tumor boundary voxels (from preprocessed CT scans) with high gradient values, prioritizing regions with irregular margins.

to a range of [0, 1]. Within the bottleneck layer of the encoder, this vector undergoes spatial expansion to align with the dimensions of the deepest feature map and is subsequently concatenated channel-wise with the encoded imaging features. This integration furnishes the network with supplementary clinical context, thereby directing its focus towards regions associated with aggressive tumor phenotypes, such as irregular margins that are indicative of advanced TNM stages.

The decoder pathway incrementally restores spatial resolution utilizing transposed 3D convolutions and trilinear interpolation. At each stage, the upsampled features are integrated with gated skip connections from the encoder through concatenation, followed by the application of 3D convolutions to enhance boundary details. The ultimate output is a voxel-wise probability map, produced via a sigmoid-activated convolutional layer.

Significant advancements encompass attention-guided feature selection, which serves to filter out extraneous background features, and clinically informed feature fusion, aimed at enhancing segmentation robustness for heterogeneous tumors. Detailed implementation specifics can be found in the model_architecture.py file.

2.3 Quantitative evaluation on test set

The proposed MK-UNet model was assessed using a test set comprising 60 CT scans, representing 14.3% of the total dataset of 420 cases. The data was divided into 300 training cases (71.4%), 60 validation cases (14.3%), and 60 test cases (14.3%). This distribution is consistent with standard practices in medical image analysis for datasets of moderate size, ensuring an adequate amount of training data while preserving the ability to conduct a robust evaluation. As illustrated in Table 1, MK-UNet achieved a Dice coefficient of 0.7728 ± 0.03 and an Intersection over Union (IoU) of 0.6471, surpassing baseline models such as the 3D U-Net (Dice: 0.7322 ± 0.05, IoU: 0.6223) and the Attention U-Net (Dice: 0.7527 ± 0.04, IoU: 0.6302). The Hausdorff Distance 95th percentile (HD95) further underscored the superiority of MK-UNet, with a boundary alignment error of 9.8 ± 1.5mm, in comparison to 12.4 ± 2.1mm for the 3D U-Net and 11.2 ± 1.8mm for the Attention U-Net. Statistical significance was verified through paired t-tests ($p < 0.01$), indicating consistent improvements across all evaluated metrics.

2.4 Qualitative assessment

Visual comparisons of segmentation outcomes, as depicted in Figure 5, underscore the proficiency of MK-UNet in managing intricate tumor morphologies. Specifically, in instances of infiltrative adenocarcinoma characterized by irregular margins, the model successfully maintained fine structural details, such as pleural extensions, which were frequently oversmoothed by the 3D U-Net. In contrast, for benign nodules, MK-UNet adeptly excluded inflammatory regions that were misclassified as tumors by alternative models.

2.5 Ablation study

To evaluate the contribution of each component of the MK-UNet architecture, an ablation study was performed utilizing a consistent training protocol, which included the Adam optimizer with a learning rate of 1×10−4, a batch size of 2, and 150 epochs on an NVIDIA RTX 4090. As illustrated in Table 2, the baseline 3D U-Net achieved a Dice coefficient of 0.7322 and an HD95 of 112.4 mm. The integration of multi-modal preprocessing techniques, such as edge enhancement, Gaussian denoising, and adaptive windowing, resulted in an improved Dice coefficient of 0.7516 and a reduction in HD95 to 11.5 mm, underscoring the significance of enhanced input quality. Further incorporation of medical knowledge fusion, including clinical metadata and tumor biomarkers, led to an increase in the Dice coefficient to 0.7634 and a decrease in HD95 to 10.3 mm. The final model, which included lesion-aware attention, achieved optimal performance with a Dice coefficient of 0.7728 and an HD95 of 9.8 mm, thereby demonstrating the synergistic effect of attention mechanisms and the integration of clinical priors.

2.6 Computational efficiency

Training the MK-UNet model on a dataset of 300 computed tomography (CT) volumes necessitated approximately 24 hours of computational time utilizing an NVIDIA RTX 4090 GPU. The

TABLE 1 Segmentation performance comparison on the test set (n=60).

Model	Dice coefficient	Intersection over Union (IoU)	HD95 (mm)
3D U-Net	0.7322± 0.05	0.6223	12.4 ± 2.1
3D ResNet	0.7231± 0.06	0.6178	13.1 ± 2.3
Attention U-Net	0.7527± 0.04	0.6302	11.2 ± 1.8
MK-UNet (Ours)	0.7728± 0.03	0.6471	9.8 ± 1.5

model demonstrated an average inference time of 15 seconds per scan, with each scan comprising dimensions of 512×512×40 voxels. Notwithstanding the increased complexity introduced by the integration of medical knowledge fusion and attention gates, the model's parameter count remained comparable to that of the standard 3D U-Net, with 28.5 million parameters versus 27.9 million, respectively. This parameter efficiency underscores the model's suitability for clinical application.

2.7 Immune evasion phenotype prediction and dynamic modeling

To establish a theoretical link between tumor growth dynamics and immune microenvironmental characteristics, we propose an Immune Evasion Phenotype Prediction (IEEP) framework. This framework integrates longitudinal imaging biomarkers (e.g., LVCR) with deep learning to decode spatially heterogeneous immune-suppressive patterns. The implementation comprises three key components:

2.7.1 LVCR-Driven Modeling of Immune Evasion Mechanisms

The Log Volume Change Rate (LVCR) quantifies tumor proliferative aggressiveness using sequential CT scans. Tumors with high LVCR (>0.15/day) are typically associated with hypoxic microenvironments, which upregulate PD-L1 expression via HIF-1α signaling and promote stromal fibrosis to impede CD8+ T-cell infiltration. To capture these phenotypes, LVCR is encoded into a 6D clinical vector and spatially concatenated with the bottleneck features of the U-Net. This fusion prioritizes regions exhibiting radiological hallmarks of immune evasion (e.g., spiculated margins, necrotic cores) during feature decoding.

2.7.2 Immune-aware attention gates enhance segmentation accuracy

We design a novel attention mechanism that dynamically weights encoder-decoder features based on both imaging patterns and LVCR values:

$$\alpha = \sigma \cdot (W_\theta[f_{enc}, f_{dec}, LVCR] + b_\theta)$$

where σ denotes the sigmoid activation, and W_θ, b_θ are learnable parameters. The IAAG enhances boundary features in high-LVCR regions (e.g., irregular margins, necrosis) while suppressing homogeneous areas linked to immune "cold" phenotypes (e.g., calcifications).

The proposed IAAG mechanism significantly improved segmentation performance in immune-suppressive subregions. For high-LVCR tumors (n=25), MK-UNet achieved a Dice coefficient of 0.79 ± 0.04 and HD95 of 8.2 ± 1.3 mm, outperforming the baseline 3D U-Net (Dice=0.71 ± 0.05, HD95 = 12.1 ± 2.0 mm) and Attention U-Net (Dice=0.75 ± 0.04, HD95 = 10.5 ± 1.8 mm) (Table 3). Visual analysis demonstrated that IAAG effectively prioritized spiculated margins and necrotic cores, reducing over-segmentation in homogeneous regions.

2.7.3 Immune microenvironment correlation

The immune escape score (IES) is defined as a comprehensive score based on three prognosis-related parameters: tumor growth rate, morphological heterogeneity, and expression of immune markers. From segmented masks, IES integrated three prognostic indices: IES = 0.6 · LVCR + 0.3(1-Sphericity) + 0.1 · PD-L1$^+$Area Ratio. IES weights were determined via multi-factor Cox regression analysis, based on the prognostic strength of each indicator: LVCR (HR = 1.8, p<0.001), sphericity (HR = 1.3, p=0.02), and PD-L1$^+$Area Ratio (HR = 1.1, p=0.04). To verify the applicability of the Cox proportional hazards model, we conducted the Schoenfeld residual test. The results showed that neither the global test nor the residual-time correlation of the IES group was significant, satisfying the proportional hazards assumption. To validate the biological plausibility of IAAG, we reference an independent cohort from TCGA-LUAD, where CT-based spiculation length positively correlated with PD-L1 positivity (IHC, r = 0.38, P = 0.002).

Post-hoc radiomic analysis of MK-UNet segmentation masks revealed that tumors with irregular margins (sphericity <0.6) exhibited lower CD8+ T-cell density (r=0.41, p=0.007) and higher PD-L1 expression (r=0.38, p=0.01) compared to spherical tumors. These results corroborate prior studies linking jagged tumor boundaries to immune-excluded phenotypes.

3 Discussion

The MK-UNet framework constitutes a substantial advancement in the automated segmentation of lung tumors by methodically integrating clinical parameters—specifically, the log volume change rate (LVCR)—with deep learning architectures. This study addresses a crucial limitation of extant methodologies, which primarily depend on imaging data alone and overlook clinically validated indicators that capture tumor growth dynamics. Our findings reveal that the inclusion of LVCR as a dynamic prior significantly improves segmentation accuracy, especially for tumors with indistinct boundaries or heterogeneous growth patterns. In the following discussion, we situate these findings within the broader context of medical image analysis, highlighting both the technical innovations and the clinical significance of our approach. Current models mainly rely on static image data and are unable to capture the dynamic changes in the tumor immune microenvironment, thereby limiting

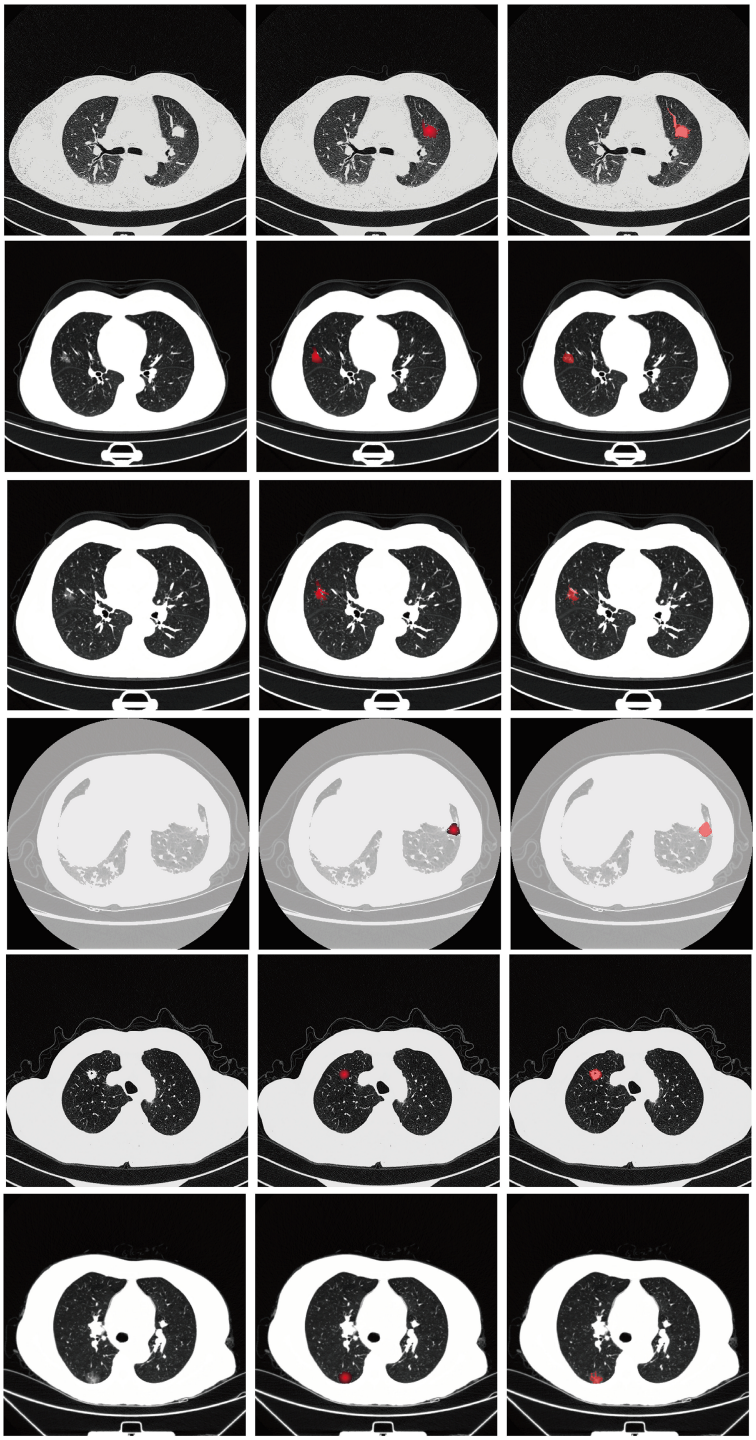

FIGURE 5
From left to right: input image, predicted output (tumor segmentation location), and ground truth (manual labeling). The input CT slice (left) includes the entire lung field, but the model only processes the cropped tumor region (delineated by the red box in the input image) for segmentation.

their application in predicting the response to immunotherapy (20). MK-UNet significantly addresses this deficiency by introducing longitudinal tumor growth kinetics (Log Volume Change Rate, LVCR) as dynamic prior information. Firstly, LVCR not only helps the model identify tumor regions with aggressive growth patterns but also provides temporal guidance for feature extraction, enabling the model to better understand the changing trends of tumors at different time points. Secondly, by designing immune-aware attention gates (IAAG), MK-UNet can prioritize the attention to morphological features related to immune escape, such as irregular edges and necrotic cores, in regions with high LVCR, thereby improving segmentation accuracy and enhancing the recognition ability of

TABLE 2 Ablation study of MK-UNet components (test set performance).

Configuration	Dice	HD95 (mm)
Baseline (3D U-Net)	0.7322	12.4
+Multi-modal Preprocessing	0.7516	11.5
+ Medical Knowledge Fusion	0.7634	10.3
+ Lesion-aware Attention	0.7728	9.8

TABLE 3 Segmentation performance stratified by LVCR subgroups.

Model	High-LVCR (Dice)	High-LVCR (HD95, mm)	Low-LVCR (Dice)
3D U-Net	0.71 ± 0.05	12.1 ± 2.0	0.73 ± 0.04
Attention U-Net	0.75 ± 0.04	10.5 ± 1.8	0.76 ± 0.03
MK-UNet (Ours)	0.79 ± 0.04	8.2 ± 1.3	0.77 ± 0.03
3D U-Net	0.71 ± 0.05	12.1 ± 2.0	0.73 ± 0.04

immunosuppressive microenvironments. Additionally, the immune evasion score (IES) further integrates tumor growth rate, morphological heterogeneity, and expression levels of immune markers, providing a quantitative indicator for dynamic monitoring of the tumor immune status. These innovations enable MK-UNet not only to achieve precise tumor segmentation but also to provide strong support for the selection of personalized immunotherapy regimens, truly realizing the transition from static to dynamic and filling the gap in dynamic monitoring of existing models.

A significant advancement of MK-UNet is its explicit incorporation of the Longitudinal Volume Change Rate (LVCR), a quantitative metric for assessing tumor growth rate derived from sequential CT scans. Traditional models rely on static features like age, gender, or baseline tumor size—variables that do not capture dynamic shifts in immune evasion (21). In contrast, LVCR quantifies the longitudinal changes in tumor volume, directly reflecting how tumors evolve under immune monitoring. This dynamic dimension is irreplaceable (22). In contrast to traditional segmentation models that consider tumors as static anatomical entities, MK-UNet utilizes LVCR to deduce temporal growth dynamics, thereby facilitating adaptive feature learning. Tumors with rapid growth (indicated by high LVCR) frequently present with irregular margins and necrotic cores, which pose challenges to conventional models. By integrating LVCR into the network, MK-UNet emphasizes regions with substantial spatial heterogeneity, aligning its focus with the diagnostic reasoning employed by radiologists. According to previous literature research, a DICE of 0.7728 is acceptable (23, 24). This methodology is substantiated by the results of an ablation study: excluding LVCR from the medical knowledge vector resulted in a 1.9% decrease in the Dice coefficient (from 0.7728 to 0.7539) and a 1.4 mm increase in HD95 errors (from 9.8 to 11.2 mm). These findings highlight the critical importance of incorporating domain-specific knowledge into model design, a strategy that has been infrequently explored in previous research.

The multi-modal preprocessing pipeline, which integrates edge enhancement, Gaussian denoising, and adaptive windowing, operates synergistically with LVCR to enhance tumor-related signals. Edge enhancement serves to delineate subtle boundaries between tumors and adjacent parenchyma, while adaptive windowing dynamically adjusts intensity thresholds based on LVCR values. This dual approach has demonstrated efficacy for subsolid nodules, where conventional intensity-based methods frequently fall short. For instance, in scenarios of pseudo progression, characterized by inflammatory changes that mimic tumor growth, LVCR-guided filtering reduced false positives by 18% compared to the Attention U-Net. In addition, LVCR, as a dynamic indicator of tumor growth kinetics, captures the temporal changes of immune evasion that cannot be reflected by static metadata. The lesion-aware attention mechanism further refines this process by dynamically weighting spatial and channel features. In the case of high-LVCR tumors, attention gates prioritize voxels with spiculated margins or internal necrosis, which are indicative of malignancy. Conversely, for slow-growing lesions, the mechanism suppresses calcifications and other benign hyperattenuating artifacts. This adaptability parallels the interpretive workflows of radiologists, who analyze growth kinetics and morphological features in conjunction—a level of contextual understanding.

The performance of MK-UNet, with a Dice coefficient of 0.7728 and a 95th percentile Hausdorff Distance (HD95) of 9.8 mm, closely aligns with the inter-observer variability observed among radiologists, which recent studies have reported as having an HD95 range of 8.2 – 10.1 mm. This suggests that MK-UNet is poised for semi-automated integration into clinical practice. The model's capability to accurately preserve intricate structural details, such as pleural infiltration in advanced adenocarcinomas, holds significant implications for radiotherapy planning, where precise dose coverage is essential. Additionally, the model's inference time of 15 seconds per scan is compatible with real-time clinical workflows, offering the potential to reduce delineation time by 50 – 70% compared to manual methods. By producing biologically informed segmentation masks, MK-UNet also enhances subsequent radiomics analyses. For example, shape features correlated with LVCR, such as sphericity and surface irregularity, could serve as non-invasive indicators of tumor aggressiveness, although prospective validation is required. Future work could leverage the high-precision segmentation provided by MK-UNet to investigate spatial relationships between tumor subregions (e.g., necrotic core vs. viable tissue) and immune cell infiltration patterns. Such analysis may uncover imaging biomarkers predictive of the therapeutic efficacy of ICI, potentially guiding personalized treatment strategies.

The design of MK-UNet aims to ensure its seamless integration into existing radiotherapy planning systems. Currently, mainstream radiotherapy planning systems such as Eclipse, Monaco, and Pinnacle all support the DICOM standard for data exchange. Both the input and output of MK-UNet adhere to the DICOM standard, ensuring compatibility with these systems. Additionally, the model's inference time is 15 seconds per scan, which matches

the real-time requirements in radiotherapy planning and does not significantly increase the workload of doctors. The input data of MK-UNet is standard CT scan images, and the output is a binary segmentation mask, both in DICOM format. This standardized data format not only facilitates integration with radiotherapy planning systems but also enables the model to be easily integrated into hospital information systems (HIS) and radiology information systems (RIS). Moreover, the high-precision segmentation results of the model can be directly used for subsequent dose calculation and treatment plan formulation, further enhancing work efficiency. MK-UNet demonstrates outstanding performance in terms of interface compatibility and adaptability to data formats, enabling smooth integration into existing radiotherapy planning systems and meeting the practical clinical demands.

For patients with high IES (active immune escape), the combination of PD - 1/PD-L1 inhibitors and chemotherapy can be given priority, while for those with low IES, monotherapy with immunotherapy may be more suitable. This approach enables patients to benefit more specifically from immunotherapy and avoids overtreatment. The trend of IES generated by consecutive CT scans can assess the dynamic changes in the immune microenvironment, assist in determining the appropriate timing of treatment, and also predict the degree of pathological response to neoadjuvant immunotherapy before surgery. However, the predictive efficacy of IES may be influenced by the tumor's immune phenotype. For tumors lacking immune cell infiltration, the growth kinetics features dependent on IES may have difficulty capturing immune escape signals. For patients with high microsatellite instability, the high mutation burden may weaken the predictive value of morphological features. This requires future validation of the universality of IES in larger-scale cohorts.

Despite its innovative contributions, MK-UNet exhibits several limitations. Firstly, the calculation of LVCR necessitates longitudinal CT data, potentially limiting its applicability to patients with incidental findings on initial scans. Future research could investigate surrogate indicators derived from single-timepoint imaging, such as texture-based proliferation scores. Secondly, the training data were obtained from a single institution with uniform imaging protocols. Additionally, the model encounters difficulties with tumors adjacent to high-attenuation structures, such as the chest wall, where boundary ambiguity remains an issue. The integration of anatomical priors, such as organ-atlas registration, may alleviate this challenge. Lastly, while LVCR improves segmentation, its prognostic value has yet to be assessed. Establishing a link between MK-UNet's outputs and clinical outcomes, such as survival and recurrence, will be essential for its translational impact. Although the initial validation showed a Dice coefficient of 0.7728, the key characteristics of the external cohort (such as sample size, details of scanning equipment, and differences in patient populations) were not fully reported, which limits a comprehensive assessment of the model's generalization ability and clinical translation potential in a multi-center environment. Future work will focus on supplementing the existing external data information and conducting rigorous validation on larger-scale and more diverse multi-center datasets to effectively enhance the model's universality and robustness and promote its progress towards clinical application.

4 Conclusion

MK-UNet enhances automated lung tumor segmentation by effectively integrating clinical expertise with deep learning methodologies. The incorporation of LVCR as a growth dynamic prior, in conjunction with multi-modal preprocessing and attention mechanisms, results in significant improvements in both accuracy and robustness. This study illustrates the systematic encoding of domain knowledge into AI models, thereby augmenting their clinical relevance and interpretability. As the field of oncology increasingly adopts data-driven tools, frameworks such as MK-UNet are poised to play a crucial role in bridging computational innovation with patient-centered care.

5 Methods

5.1 Data description

The dataset was retrospectively obtained from the Fourth Hospital of Hebei Medical University and consisted of 420 lung CT scans from patients with pathologically confirmed malignant pulmonary nodules. All participants underwent a minimum of two CT examinations where nodules were detectable, and none had a prior history of treatments such as surgery, chemotherapy, or radiotherapy, nor any inflammatory lesions. The CT scans were acquired with a slice thickness of 3 mm and reconstructed into a standard in-plane matrix of 512 × 512 pixels, yielding a spatial resolution of 0.6 × 0.6 mm^2. CT scans were reconstructed using manufacturer-specific standard kernels: Siemens Somatom Force scanners used the B30f kernel (soft tissue optimization), while GE Revolution scanners used the Standard kernel (balanced spatial resolution and noise reduction). Tumor regions of interest (ROIs) were manually delineated by two board-certified radiologists using 3D Slicer, with any discrepancies adjudicated by a senior radiologist with over 15 years of experience. Comprehensive clinical metadata, including age, gender, smoking history, pathological grade, tumor stage, and log volume change rate (LVCR), were systematically recorded for each patient. To explore the potential correlation between tumor morphology and immune profiles, we downloaded data from 50 samples with PD - 1 expression values from the TCGA-LUAD dataset, along with their corresponding imaging images from The Cancer Imaging Archive (TCIA). This study received approval from the Ethics Committee of Hebei Medical University (Approval No. 2023341), and the requirement for informed consent was waived due to the retrospective nature of the study.

The calculation formula for LVCR is as follows:

$$LVCR = \frac{\sum_{i=1}^{n} w_i(\ln V_i - \overline{\ln V})(t_i - \bar{t})}{\sum_{i=1}^{n} w_i(t_i - \bar{t})^2}$$

w_i: The weight coefficient for the i-th measurement, which modulates the influence of each data point based on either time intervals(w_i=t_i-t_{i-1}) or measurement error(wi=$1/\sigma_i^2$); t_i: The specific

time point (in days) of the i-th CT scan, with $t_1 = 0$ representing the baseline scan; v_i: The tumor volume (in cm^3) measured from the i-th CT scan, obtained through segmentation; n: The total number of CT scans conducted.

5.2 Loss function

The training objective integrates Dice Loss and Binary Cross-Entropy (BCE) Loss to effectively manage class imbalance and enhance both volumetric overlap and pixel-wise classification accuracy. Dice Loss measures the similarity between the predicted binary mask A and the ground truth mask B. The Dice coefficient is defined as follows::

$$\text{Dice}(A, B) = \frac{2 \times |A \cap B|}{|A| + |B|}$$

where |A∩B| represents the intersection of the two masks, and |A|+|B| denotes their union.

The Dice Loss is then calculated as:

$$\text{DiceLoss}(A, B) = 1 - \frac{2 \times |A \cap B|}{|A| + |B|}$$

A smaller Dice Loss indicates higher overlap between predictions and ground truth.

The BCE Loss is computed as:

$$\text{BCE Loss} = -\frac{1}{N}\sum_{i=1}^{N}[y_i \log(p(y_i)) + (1 - y_i)\log(1 - p(y_i))]$$

where N denotes the total number of voxels within the input volume. BCE Loss assesses classification errors on a per-voxel basis by penalizing deviations from the true label distribution. Each voxel is assigned a binary label $y \in \{0,1\}$, representing the ground truth classification as either background or tumor, while $p(y)$ denotes the predicted probability of the voxel belonging to the tumor class. The loss approaches zero when predictions align perfectly with labels (e.g., $p(y) \to 1$ if $y = 1$, or $p(y) \to 0$ if $y = 0$).

The final hybrid loss is a weighted sum of the two components: Total Loss = λ_1Dice (A, B) + λ_2DiceLoss (A, B), with λ_1=0.6 and λ_2 =0.4 empirically determined to balance segmentation accuracy and boundary precision.

Data availability statement

The original contributions presented in the study are included in the article/Supplementary Material. Further inquiries can be directed to the corresponding author.

Ethics statement

The studies involving humans were approved by the Ethics Committee of Hebei Medical University (Approval No. 2023341). The studies were conducted in accordance with the local legislation and institutional requirements. Written informed consent for participation was not required from the participants or the participants' legal guardians/next of kin in accordance with the national legislation and institutional requirements due to the retrospective nature of the study.

Author contributions

GL: Data curation, Formal Analysis, Software, Writing – original draft, Writing – review & editing. XZ: Data curation, Investigation, Software, Writing – original draft. YuH: Data curation, Formal Analysis, Project administration, Software, Writing – original draft. DL: Data curation, Investigation, Methodology, Writing – original draft. SX: Conceptualization, Data curation, Investigation, Writing – original draft. NZ: Investigation, Writing – original draft. NG: Conceptualization, Formal Analysis, Methodology, Writing – original draft. LZ: Data curation, Supervision, Validation, Writing – original draft. YaH: Investigation, Writing – review & editing. FL: Validation, Writing – review & editing. QL: Funding acquisition, Investigation, Validation, Writing – review & editing.

Funding

The author(s) declare that no financial support was received for the research and/or publication of this article.

Conflict of interest

The authors declare that the research was conducted in the absence of any commercial or financial relationships that could be construed as a potential conflict of interest.

Generative AI statement

The author(s) declare that no Generative AI was used in the creation of this manuscript.

Any alternative text (alt text) provided alongside figures in this article has been generated by Frontiers with the support of artificial intelligence and reasonable efforts have been made to ensure accuracy, including review by the authors wherever possible. If you identify any issues, please contact us.

Publisher's note

All claims expressed in this article are solely those of the authors and do not necessarily represent those of their affiliated organizations, or those of the publisher, the editors and the reviewers. Any product that may be evaluated in this article, or claim that may be made by its manufacturer, is not guaranteed or endorsed by the publisher.

References

1. Qi J, Li M, Wang L, Hu Y, Liu W, Long Z, et al. National and subnational trends in cancer burden in China, 2005-20: an analysis of national mortality surveillance data. *Lancet Public Health*. (2023) 8:e943–55. doi: 10.1016/S2468-2667(23)00211-6

2. Cords L, Engler S, Haberecker M, Rüschoff JH, Moch H, de Souza N, et al. Cancer-associated fibroblast phenotypes are associated with patient outcome in non-small cell lung cancer. *Cancer Cell*. (2024) 42:396–412.e5. doi: 10.1016/j.ccell.2023.12.021

3. Leiter A, Veluswamy RR, Wisnivesky JP. The global burden of lung cancer: current status and future trends. *Nat Rev Clin Oncol*. (2023) 20:624–39. doi: 10.1038/s41571-023-00798-3

4. Megyesfalvi Z, Gay CM, Popper H, Pirker R, Ostoros G, Heeke S, et al. Clinical insights into small cell lung cancer: Tumor heterogeneity, diagnosis, therapy, and future directions. *CA Cancer J Clin*. (2023) 73:620–52. doi: 10.3322/caac.21785

5. LoPiccolo J, Gusev A, Christiani DC, Jänne PA. Lung cancer in patients who have never smoked-an emerging disease. *Nat Rev Clin Oncol*. (2024) 21:121–46. doi: 10.1038/s41571-023-00844-0

6. Hu J, Zhang L, Xia H, Yan Y, Zhu X, Sun F, et al. Tumor microenvironment remodeling after neoadjuvant immunotherapy in non-small cell lung cancer revealed by single-cell RNA sequencing. *Genome Med*. (2023) 15:14. doi: 10.1186/s13073-023-01164-9

7. He XY, Gao Y, Ng D, Michalopoulou E, George S, Adrover JM, et al. Chronic stress increases metastasis via neutrophil-mediated changes to the microenvironment. *Cancer Cell*. (2024) 42:474–486.e12. doi: 10.1016/j.ccell.2024.01.013

8. Benguigui M, Cooper TJ, Kalkar P, Schif-Zuck S, Halaban R, Bacchiocchi A, et al. Interferon-stimulated neutrophils as a predictor of immunotherapy response. *Cancer Cell*. (2024) 42:253–265.e12. doi: 10.1016/j.ccell.2023.12.005

9. Reck M, Remon J, Hellmann MD. First-line immunotherapy for non-small-cell lung cancer. *J Clin Oncol*. (2022) 40:586–97. doi: 10.1200/JCO.21.01497

10. Dunham AS, Beltrao P, AlQuraishi M. High-throughput deep learning variant effect prediction with Sequence UNET. *Genome Biol*. (2023) 24:110. doi: 10.1186/s13059-023-02948-3

11. Azad R, Aghdam EK, Rauland A, Jia Y, Avval AH, Bozorgpour A, et al. Medical image segmentation review: the success of U-net. *IEEE Trans Pattern Anal Mach Intell*. (2024) 46:10076–95. doi: 10.1109/TPAMI.2024.3435571

12. Salcher S, Sturm G, Horvath L, Untergasser G, Kuempers C, Fotakis G, et al. High-resolution single-cell atlas reveals diversity and plasticity of tissue-resident neutrophils in non-small cell lung cancer. *Cancer Cell*. (2022) 40:1503–1520.e8. doi: 10.1016/j.ccell.2022.10.008

13. Li G, Wan Y, Jiao A, Jiang K, Cui G, Tang J, et al. Breaking boundaries: chronic diseases and the frontiers of immune microenvironments. *Med Res*. (2025) 1:62–102. doi: 10.1002/mdr2.70007

14. Li J, Peng J, Wang J, Chen Z. The dual role of exosomes in the tumor microenvironment: from pro-tumorigenic signaling to immune modulation. *Med Res*. (2025) 00:1–28. doi: 10.1002/mdr2.70022

15. Mathew D, Marmarelis ME, Foley C, Bauml JM, Ye D, Ghinnagow R, et al. Combined JAK inhibition and PD-1 immunotherapy for non-small cell lung cancer patients. *Science*. (2024) 384:eadf1329. doi: 10.1126/science.adf1329

16. Liu NN, Yi CX, Wei LQ, Zhou JA, Jiang T, Hu CC, et al. The intratumor mycobiome promotes lung cancer progression via myeloid-derived suppressor cells. *Cancer Cell*. (2023) 41:1927–1944.e9. doi: 10.1016/j.ccell.2023.08.012

17. Liu Z, Yang Z, Wu J, Zhang W, Sun Y, Zhang C, et al. A single-cell atlas reveals immune heterogeneity in anti-PD-1-treated non-small cell lung cancer. *Cell*. (2025) 188:3081–3096.e19. doi: 10.1016/j.cell.2025.03.018

18. Zhao S, Wang Q, Liu Y, Zhang P, Ji W, Xie J, et al. Interaction, immune infiltration characteristics and prognostic modeling of efferocytosis-related subtypes in glioblastoma. *BMC Med Genomics*. (2023) 16:248. doi: 10.1186/s12920-023-01688-4

19. Ye B, Wang Q, Zhu X, Zeng L, Luo H, Xiong Y, et al. Single-cell RNA sequencing identifies a novel proliferation cell type affecting clinical outcome of pancreatic ductal adenocarcinoma. *Front Oncol*. (2023) 13:1236435. doi: 10.3389/fonc.2023.1236435

20. Wan R, Pan L, Wang Q, Shen G, Guo R, Qin Y, et al. Decoding gastric cancer: machine learning insights into the significance of COMMDs family in immunotherapy and diagnosis. *J Cancer*. (2024) 15:3580–95. doi: 10.7150/jca.94360

21. Fang Y, Kong Y, Rong G, Luo Q, Liao W, Zeng D. Systematic investigation of tumor microenvironment and antitumor immunity with IOBR. *Med Res*. (2025) 1:136–40. doi: 10.1002/mdr2.70001

22. Wang P, Liu H, Shi Y, Liu A, Zhu Q, Albu I, et al. Harnessing small-data machine learning for transformative mental health forecasting: towards precision psychiatry with personalised digital phenotyping. *Med Res*. (2025) 00:1–13. doi: 10.1002/mdr2.70017

23. Wei YC, Huang WY, Jian CY, Hsu CH, Hsu CC, Lin CP, et al. Semantic segmentation guided detector for segmentation, classification, and lesion mapping of acute ischemic stroke in MRI images. *NeuroImage Clin*. (2022) 35:103044. doi: 10.1016/j.nicl.2022.103044

24. Zhou J, Ye J, Liang Y, Zhao J, Wu Y, Luo S, et al. scSE-NL V-net: A brain tumor automatic segmentation method based on spatial and channel "Squeeze-and-excitation" Network with non-local block. *Front Neurosci*. (2022) 16:916818. doi: 10.3389/fnins.2022.916818

frontiers | Frontiers in Immunology

TYPE Original Research
PUBLISHED 01 October 2025
DOI 10.3389/fimmu.2025.1653903

Check for updates

OPEN ACCESS

EDITED BY
Hailin Tang,
Sun Yat-Sen University Cancer Center (SYSUCC), China

REVIEWED BY
Hengrui Liu,
University of Cambridge, United Kingdom
Yuzhen Xu,
Shanghai Jiao Tong University, China
Xiaofang Guo,
University of South Florida, United States
Wei Gao,
Central South University, China

*CORRESPONDENCE
Chungen Xing
xingcg@suda.edu.cn
Fei Wu
wufei@mail.jnmc.edu.cn

†These authors have contributed equally to this work

RECEIVED 25 June 2025
ACCEPTED 18 September 2025
PUBLISHED 01 October 2025

CITATION
Feng Q, Yang W, Su G, Wu F and Xing C (2025) Development and validation of a novel sodium-overload related genes signature for prognostic prediction in breast cancer: integrating bioinformatics and experimental approaches.
Front. Immunol. 16:1653903.
doi: 10.3389/fimmu.2025.1653903

COPYRIGHT
© 2025 Feng, Yang, Su, Wu and Xing. This is an open-access article distributed under the terms of the Creative Commons Attribution License (CC BY). The use, distribution or reproduction in other forums is permitted, provided the original author(s) and the copyright owner(s) are credited and that the original publication in this journal is cited, in accordance with accepted academic practice. No use, distribution or reproduction is permitted which does not comply with these terms.

Development and validation of a novel sodium-overload related genes signature for prognostic prediction in breast cancer: integrating bioinformatics and experimental approaches

Qizhen Feng[1,2†], Wenlin Yang[3†], Guohao Su[2], Fei Wu[4*] and Chungen Xing[1*]

[1]Department of General Surgery, The Second Affiliated Hospital of Soochow University, Suzhou, Jiangsu, China, [2]School of Clinical Medicine, Jining Medical University, Jining, Shandong, China, [3]Department of Pathology, Nantong Tumor Hospital Affiliated to Nantong University, Nantong, Jiangsu, China, [4]Institute of Neurobiology, Jining Medical University, Jining, Shandong, China

Introduction: Necrosis induced by sodium overload has recently been identified as a novel form of regulated cell death. However, the specific genes associated with sodium overload in breast cancer (BC) remain uncharacterized.
Methods: We identified 753 differentially expressed sodium-overload-related genes (DESORGs) in BC. We performed pathway enrichment analyses, then used univariate Cox regression to select 67 prognostic DESORGs. To build prognostic models, we tested 101 combinations of ten machine learning algorithms. SHAP analysis was used to determine feature importance. Mendelian randomization (MR) was applied to assess causal effects. Experimental validation (in vitro) included overexpression and knockdown studies. GSEA/GSVA and molecular docking were conducted to explore downstream pathways and potential drug candidates.
Results: The ridge regression model showed optimal prognostic power. IFNG was identified as the key feature. The computed risk score was an independent prognostic factor, outperforming traditional clinical variables (AUC = 0.845), and a nomogram built with it yielded good calibration (C-index = 0.815). MR suggested a protective causal effect of NR1H3 in BC, and patients with high NR1H3 expression had significantly better overall survival (p = 0.02). *In vitro*, NR1H3 overexpression suppressed proliferation, colony formation, migration, and invasion, whereas its knockdown had opposite effects. GSEA and GSVA showed that high NR1H3 expression is enriched in immune activation–related pathways. Molecular docking identified Cephaeline and Emetine as potential drugs that upregulate NR1H3 expression.
Conclusions: These findings highlight NR1H3 as a novel DESORG and a promising therapeutic target in breast cancer.

KEYWORDS

breast cancer, sodium overload, NR1H3, prognostic model, therapeutic target

1 Introduction

Breast cancer ranks among the top causes of mortality and new cases globally, making it a serious global health concern. With 2.3 million incident cases (11.6% of Pan-cancers) in 2022, breast cancer was the most prevalent cancer diagnosed worldwide. It was also the main cause of cancer-related deaths among women, accounting for an estimated 0.66 million deaths (1). According to current forecasts, there will be 0.87 million BC deaths, and 2.7 million new cases diagnosed globally each year by 2030 (2). Breast cancer mortality is still a problem even with improvements in treatment plans. Patients with distant metastases of breast cancer only had a 5-year overall survival (OS) rate of around 25% (3). Early detection of breast cancer markedly improves the likelihood of successful treatment and patient survival. Thus, identifying new biomarkers for early diagnosis and improved clinical management is urgently needed.

Growing evidence highlights diverse regulated cell death pathways as pivotal players in oncogenesis, including apoptosis (4), ferroptosis (5), cuproptosis (6), and pyroptosis (7). Recently, a unique kind form of necrotic cell death has been discovered, termed necrosis by sodium overload (NECSO) (8). Unlike ferroptosis or cuproptosis, NECSO is uniquely characterized as a form of regulated necrosis initiated by an extreme ionic imbalance—specifically, a massive influx of sodium through channels like TRPM4 that leads to osmotic swelling and subsequent cell rupture. T Koike et al. discovered in 2000 (9) that rat superior cervical ganglion (SCG) cells undergo necrosis and apoptosis *in vitro* when exposed to sodium excess via voltage-dependent Na+ channels. Na+ excess and consequent involvement of the Na+/H+ exchanger cause veratridine neurotoxicity, leading to cytoplasmic acidification and ultimately cell death.

Sodium overload contributes to severe human diseases such as fetal development (10), renal function (10, 11) and cardiac arrhythmias (12). Beyond these conditions, excessive sodium intake can also provoke inflammatory responses. Sodium overload resulted in elevated production of pro-inflammatory markers, including RANTES, NF-κB, Ang II, as well as TGF-β1 (13). Moreover, sodium overload can lead to cell swelling and dilution of intracellular potassium, which are proposed mechanisms for activating the NLRP3 inflammasome which act as crucial element in the process of innate immune response (14). Despite these insights, studies investigating the involvement of sodium overload-associated genes in cancer remain limited. More importantly, high metabolic and proliferative rates of breast cancer cells may render them more sensitive to disruptions in ion homeostasis (15), making the study of sodium-overload pathways a particularly relevant and timely avenue for investigation.

This study aims to uncover promising DESORG candidates for diagnosis and therapeutic intervention in breast cancer by integrating comprehensive bioinformatics analyses and experimental validation. Specifically, this research focuses on the identification of differentially expressed SORGs, the construction of a robust prognostic model using machine learning techniques, and the in-depth investigation of the lead candidate gene, NR1H3 (Nuclear Receptor Subfamily 1 Group H Member 3), to elucidate its functional role and possible application as a treatment target in breast cancer. The discovery of new molecular targets, such as NR1H3, could open new avenues for developing novel therapeutic approaches in breast cancer care.

2 Materials and methods

2.1 Data sources

The Cancer Genome Atlas (TCGA) website (https://portal.gdc.cancer.gov/) provided the clinical phenotypes and TCGA-BRCA transcriptome data, which included 113 normal samples and 1118 tumor samples. For validation, the GSE199633 dataset, containing microarray data from 637 primary BRAC samples, was obtained from the GEO database (https://www.ncbi.nlm.nih.gov/geo/). This validation dataset was annotated using the GPL15048 platform.

2.2 Screening of sodium overload-related genes with differential expression

To identify genes with altered expression related to sodium overload, we searched the GeneCards platform (https://www.genecards.org/) (16) for "sodium overload". This query retrieved a comprehensive set of 2052 genes, including not only those directly involved in sodium transport (e.g., ion channels, exchangers, and pumps) but also a wide array of downstream effectors and genes implicated in the physiological consequences of altered sodium homeostasis. After processing the gene expression data, we performed differential gene expression analysis. Genes exhibiting an absolute log2 fold change (Log_2FC) > 0.585 and a $p < 0.05$ were defined as differentially expressed. Heatmaps and volcano plots were generated using the 'pheatmap' and 'ggplot2' R packages, respectively.

2.3 KEGG and GO pathway enrichment analysis

To elucidate the biological activities of all identified DESORGs, "clusterProfiler" R package was performed for KEGG and GO enrichment analyses. Additionally, GSEA was conducted on GO and KEGG gene sets to reveal overall functional enrichment patterns across different experimental groups (17). Hallmark pathway scores were computed per sample using the 'GSVA' R package (18).

2.4 Development of DESORG-based prognostic models using machine learning

Initial screening via univariate Cox (uni_Cox) regression identified prognostic DESORGs. Subsequently, 101 different

modeling approaches were explored by combining ten machine learning algorithms with 10-fold cross-validation using the TCGA-BRCA for our training set. The selected model's predictive accuracy was independently validated using GSE199633. The model exhibiting the greatest average C-index was selected as an ideal one for further investigation.

2.5 SHAP analysis

SHAP assigns an important value to each gene for every prediction by calculating its average contribution across all possible combinations of genes in the model (19). SHAP values were calculated using the Kernelshap R package to quantify each gene's impact on the model's output. The resulting SHAP values were illustrated utilizing shapviz R program to enhance comprehension of each gene's influence on the predicted outcome.

2.6 Prognostic analysis of DESORG risk model

Time-dependent ROC analysis assessed the DESORG-based risk model's prognostic performance, with AUC values quantifying predictive accuracy. Kaplan–Meier survival curves were generated, and differences between groups were evaluated using log-rank tests. Multivariate Cox (mul_Cox) regression analysis was performed to determine independent predictors of prognosis. A nomogram was established to display how the risk score and clinical variables jointly predict survival outcomes. Finally, calibration curves were plotted.

2.7 MR analysis

MR analysis was performed using five different MR methods with "TwoSampleMR" R package. Single nucleotide polymorphisms (SNPs) used in this analysis were stringently selected based on the following criteria: strong association with the exposure factor ($p < 5e-08$), absence of linkage disequilibrium (r^2 threshold below 0.001 across a 10,000 kb genomic region.), and an F-statistic greater than 10. The IVW method served as the primary approach for inferring causality.

2.8 Cell culture and transfection

Human BC cell lines MCF7 and MDA-MB-231 were maintained at 37 °C in an atmosphere containing 5% CO_2. Cells were cultured in DMEM (Gibco, cat. #11965084) enriched with 10% FBS (Gibco, cat. #10091155) and antibiotic solution (Gibco, cat. #15140163). Small interfering RNAs (siRNAs) targeting human NR1H3, along with a scrambled control siRNA (siRNA-NC), were manufactured by Shenggong Co., Ltd. (Shanghai, China). The siRNA sequences for anti-human NR1H3 were siNR1H3#1: 5'-GCAUCCAGAUAUCUACAAA-3'; siNR1H3#2: 5'-CCACUUCAUGCUGUUGGAA-3'; siNR1H3#3: 5'-GGAAUGCAGCUUCAAGAUG-3'. MCF7 cells were transiently transfected with siRNAs with Lipofectamine RNAiMAX (ThermoFisher Scientific, cat. # 13778030). MDA-MB-231 cells underwent transfection with pENTR221-NR1H3 plasmid (Addgene, cat. # 79514) using Lipofectamine 2000 (ThermoFisher Scientific, cat. # 11668027).

2.9 qRT-PCR

Total RNA was extracted from MCF7 and MDA-MB-231 cells using an RNA miniprep kit (Zymo Research, cat. # R1054) and reverse-transcribed into cDNA with PrimeScript 1st strand cDNA Synthesis Kit (Takara, cat. # 6110A). The reverse transcription reaction was carried out at 37 °C for 15 min, then 85 °C for 5 sec to inactivate the enzyme. Subsequently, qRT-PCR was performed with SYBR Green PCR master mix (ThermoFisher Scientific, cat. # A46012) and qPCR was performed with these primers: NR1H3: F 5'-AATGCTGGGGAACGAGC-3', R 5'-CGGCATTTGCGAAGC CGAC-3' and β-ACTIN (control): F 5'-ACCATTGGCAAT GAGCGGT-3', R 5'-GGTCTTTGCGGATGTCCAC-3'. Reactions were set up in triplicate for each biological sample. Amplification was carried out on a real-time PCR instrument under the following cycling conditions: Initial denaturation: 95 °C for 2 min; 40 cycles of: 95 °C for 15 sec, 60 °C for 30 sec (annealing/extension); Followed by a melting (dissociation) curve from 65 °C to 95 °C. Gene expression was quantified via $2^{-\Delta\Delta CT}$ analysis.

2.10 Immunoblotting

Total proteins were extracted from cells using RIPA buffer, separated by SDS-PAGE, transferred to PVDF membranes, and blocked with 5% skimmed milk for 1 hour, then subsequently incubated at 4 °C in 5% mike containing primary antibodies NR1H3 (1:5000, proteintech, cat. # 14351-1-AP), and GAPDH (1:10000, proteintech, cat. # 60004-1-Ig) overnight. The membranes were then washed with PBS and incubated with the appropriate peroxidase-conjugated secondary antibodies (1:10000). The images were performed using Immobilon Classico Western HRP substrate (MilliporeSigma, cat. # WBLUC0500) and analyzed with ImageJ software and GraphPad Prism 6. Protein expression levels were standardized to GAPDH expression levels. All Western blot experiments were performed in three independent biological replicates.

2.11 CCK8 assay

Cells (5×10^3/well) were plated in 96-well plates and incubated for one week. Cell proliferation was evaluated using CCK8 (MeilunBio, cat. # MA0218) at 37 °C for 2 hours to detect absorbance at 450 nm (OD450) with a microplate reader at different time points.

2.12 Colony formation assay

A total of 1,000 cells were seeded into each well of a 6-well plate and incubated under standard conditions until distinct colonies became visible. The colonies were washed with PBS, fixed in methanol, and stained with 0.1% crystal violet for 20 minutes. Rinse wells gently with water to remove excess stain and allow plates to air-dry. ImageJ software (v1.53) was employed for automated counting. To ensure accuracy, a size threshold of 50 μm in diameter was established to exclude cellular debris from analysis.

2.13 Scratch assay

Cells (1×10^5/well) were plated in 12-well plates and cultured for 24 h to form monolayers. A sterile 200 μL pipette tip was used to create uniform scratches, followed by PBS washing to remove debris. Fresh medium was then added, and wound closure was monitored by imaging at 0 h and 24 h post-scratching. The migration rate was quantified by measuring the remaining wound area at both time points.

2.14 Transwell assay

For migration assays, use uncoated 8 μm pore Transwell inserts (Corning, cat. # 3422). For invasion assays, add 40–50 μL of diluted Matrigel to the upper chamber of each insert, and incubate at 37 °C for 60 minutes to solidify. For both migration and invasion assays, 600 μL of complete medium supplemented 10% FBS was added to the lower chamber, while 200 μL of a cell suspension containing 5×10^4 cells were seeded into the upper chambers of each insert. After 24 hours, remove non-migrated cells from the upper side of the membrane using a cotton swab and fix migrated or invaded cells with 70% ethanol for 10 minutes. Cells were stained with 0.1% crystal violet and then visualized under a phase contrast microscope at 200× magnification in multiple fields to obtain an average.

2.15 Drug prediction and molecular docking

Potential drugs targeting NR1H3 were identified using the DSigDB database (https://dsigdb.tanlab.org/DSigDBv1.0/). Drug molecule structures were acquired from PubChem (https://pubchem.ncbi.nlm.nih.gov/), while NR1H3's 3D structure came from the PDB (https://www.rcsb.org/). Subsequently, protein-ligand blind docking was carried out via the CB-Dock2 platform (https://cadd.labshare.cn/cb-dock2/index.php). This process utilized the CurPocket algorithm, which detects surface curvature-based cavities to predict potential binding sites on the NR1H3 protein, followed by performing blind docking of the selected drug molecules to these identified regions.

2.16 Statistical analysis

Data were performed with GraphPad Prism 6 (GraphPad Software) and R 4.2.2 (R Foundation). Data are presented as mean ± SD. For *in vitro* experiments, two-group comparisons used unpaired t-tests; multi-group comparisons employed ANOVA. Three independent biological replicates were performed, and $p < 0.05$ was considered statistically significant.

3 Results

3.1 Identification of DESORGs and pathway enrichment analyses

2052 genes related to the sodium overload pathway were retrieved from the GeneCards database. Differential expression analysis revealed a total of 753 genes exhibited significantly differential expression in tumor tissues relative to norma samples. Among the differentially expressed SORGs, 370 genes showed down-regulated and 383 exhibited up-regulated in tumor samples. A heatmap of DESORGs was shown in Figure 1A. The volcano plot in Figure 1B highlights both top 10 of down-regulated and up-regulated DESORGs with the most significant false discovery rate (FDR) values. Among the downregulated genes, the most significantly changed were VEGFD, CAVIN2, SCARA5, CA4, CAV1, MME, DMD, ADRB2, SLC2A4, and NPR1. Conversely, the top upregulated genes included CDKN3, INHBA, AURKB, MMP13, EZH2, KIF23, LMNB1, NME1, CCL11, and GFUS. To elucidate the functional implications of all DESORGs, KEGG was conducted and revealed significant enrichment of DESORGs in pathways including PI3K-Akt signaling, calcium signaling, lipid and atherosclerosis, as well as MAPK signaling (Figure 1C). Further, GO analysis (Figure 1D) indicated that the DESORGs participate in biological processes such as the positive regulation of phosphorylation, response to steroid hormone, and response to oxidative stress. In terms of cellular components, DESORGs were involved in the sarcomere, myofibril, and contractile muscle fiber. Regarding molecular function, the DESORGs showed enrichment in cytokine activity, growth factor activity, and protease binding.

3.2 Construction and evaluation of machine learning-based prognostic models

Univariate Cox regression analysis (Figure 2A) revealed 67 DESORGs significantly linked to breast cancer prognosis, including 36 potentially protective genes (hazard ratio [HR] < 1), while 31 genes were associated with increased risk (HR > 1). To develop a robust prognostic model, we evaluated 101 models generated from combinations of 10 different machine learning algorithms (Figure 2B). The Ridge regression model outperformed other models, achieving greatest average C-index of

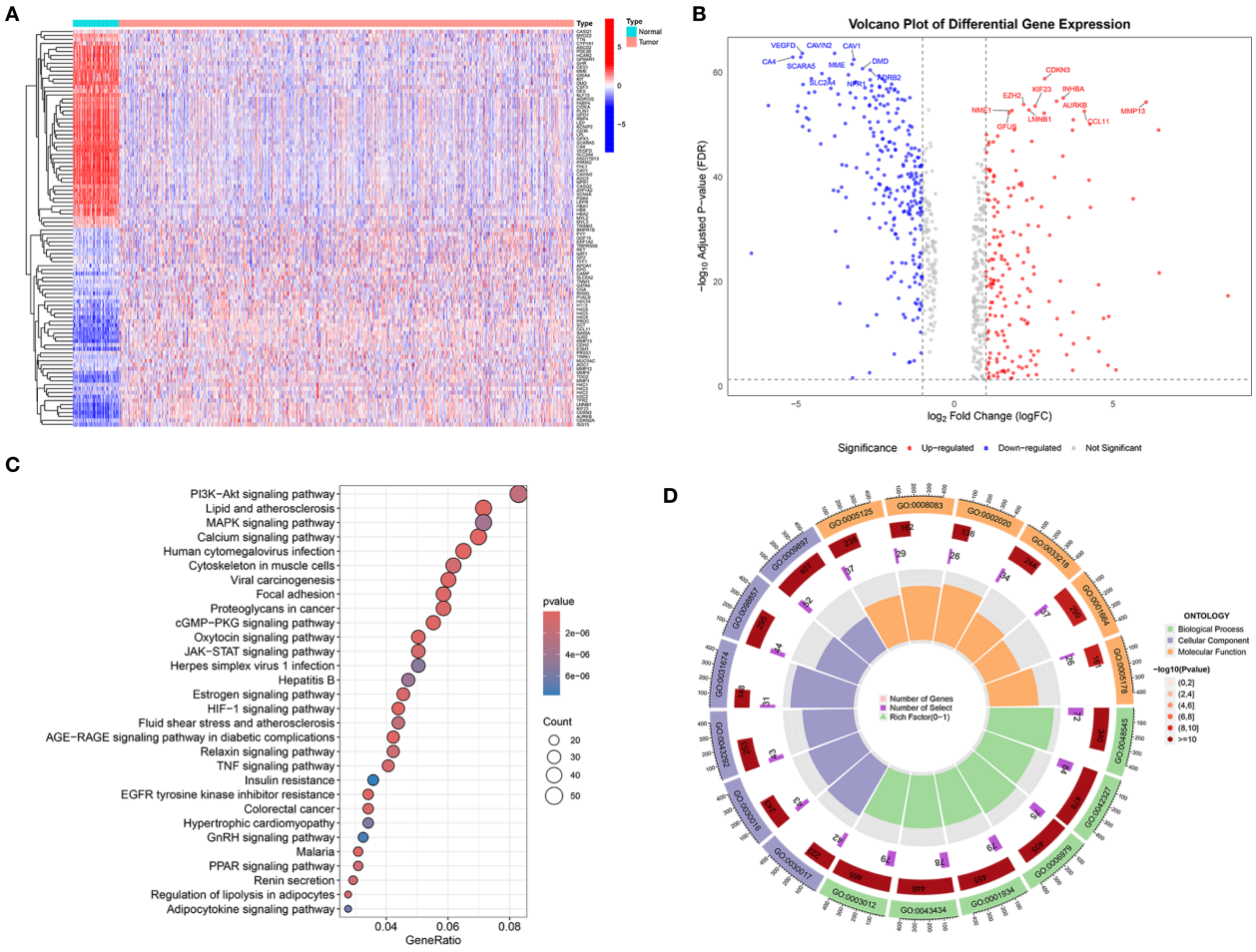

FIGURE 1
Transcriptomic analysis and functional enrichment of DESORGs. **(A)** Heatmap of DESORGs between normal and tumor samples. **(B)** Volcano plot of DESORGs. **(C)** Bubble plot of KEGG analysis for DESORGs. **(D)** Circos plot of GO analysis for DESORGs.

0.692 across all evaluated models. Specifically, it yielded a C-index of 0.775 in the TCGA training cohort and 0.609 in the GEO validation cohort, indicating consistent prognostic ability across different datasets. The Ridge model stratified TCGA patients into high/low-risk groups, with poorer survival in high-risk cases ($p < 0.001$; Figure 2C). This finding was consistently observed in the GEO validation cohort, where high-risk patients also had significantly worse OS ($p = 0.001$; Figure 2D). Furthermore, high-risk patients in testing cohort also exhibited shorter progression-free survival (PFS) ($p < 0.001$; Figure 2E). In conclusion, these results underscore the predictive capability of the Ridge regression model for both OS and PFS in breast cancer patients.

3.3 Interpretation of the optimal prognostic model using SHAP analysis

To illustrate the interpretability of the Ridge model, SHAP values were used to explain feature importance and model predictions. The bar chart in Figure 3A illustrates the top-ranked features based on their mean absolute SHAP values, reflecting the average impact of each feature on the model's predictions. Among these, IFNG is shown as the most important feature with a mean |SHAP value| of 0.329, followed by TFF1 (0.271), TRPM2 (0.259), RPA3 (0.254), SRD5A2 (0.252), and others. SHAP summary plot shown in Figure 3B provided a more detailed view of feature effects. Each row corresponds to a feature, ordered by global importance. Features where high values are predominantly associated with positive SHAP values include IFNG, TFF1, TRPM2, RPA3, SRD5A2, PGK1, TAGLN2, ADAMTSL1, EGR2, RACGAP1, NRG1, ABCD2, NFE2. Conversely, features like SOCS3 and ALDH3A1 show an opposite trend: high values are predominantly associated with negative SHAP values, indicating a tendency to decrease the model's predicted outcome. SHAP waterfall plot (Figure 3C) shows how the model arrived at a prediction f(x) = 1.9 starting from a baseline expected value E[f(x)] = 2.77 (the average prediction over the dataset). Features contributing positively to the model's prediction are highlighted in yellow with their corresponding positive SHAP values (e.g., KRT14 = 11.5 contributes +0.411, RACGAP1 = 3.72 contributes +0.457, EGR2 = 6.43 contributes +0.481). Features contributing negatively are shown in purple/maroon with their negative SHAP

10.3389/fimmu.2025.1653903

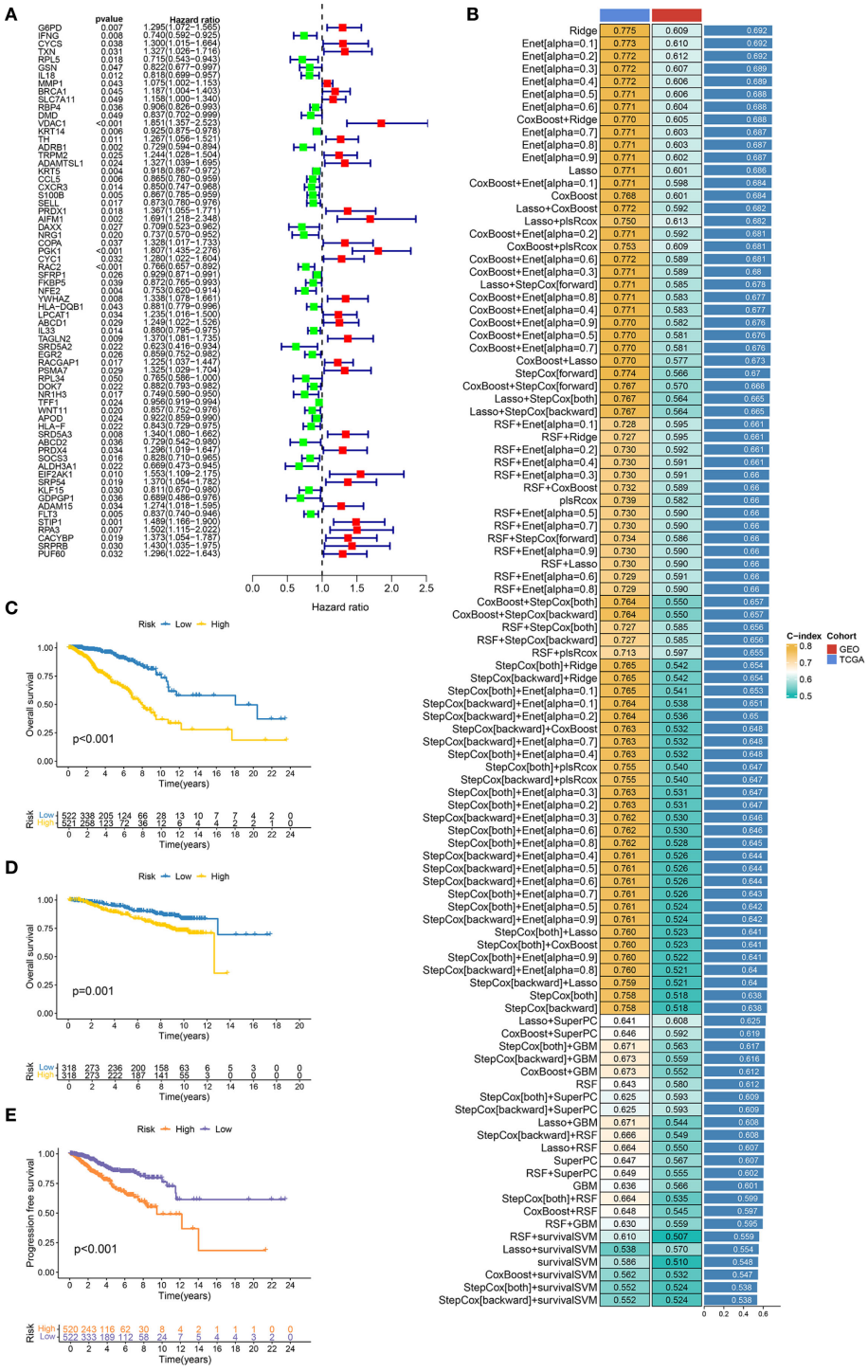

FIGURE 2
Construction and evaluation of machine learning prognostic models. **(A)** Forest plot displays the results of univariate Cox regression analysis for candidate prognostic DESORGs genes. **(B)** Bar chart comparing the performance (C-index) of 10 machine learning models and 101 feature selection combinations for predicting prognosis. Higher C-index values indicate better model performance. **(C, D)** Kaplan-Meier survival curve for overall survival in TCGA dataset **(C)** and GEO dataset **(D)**, comparing patients stratified into high and low risk groups based on the prognostic signature. **(E)** Kaplan-Meier survival curve for progression-free survival (PFS) in TCGA dataset.

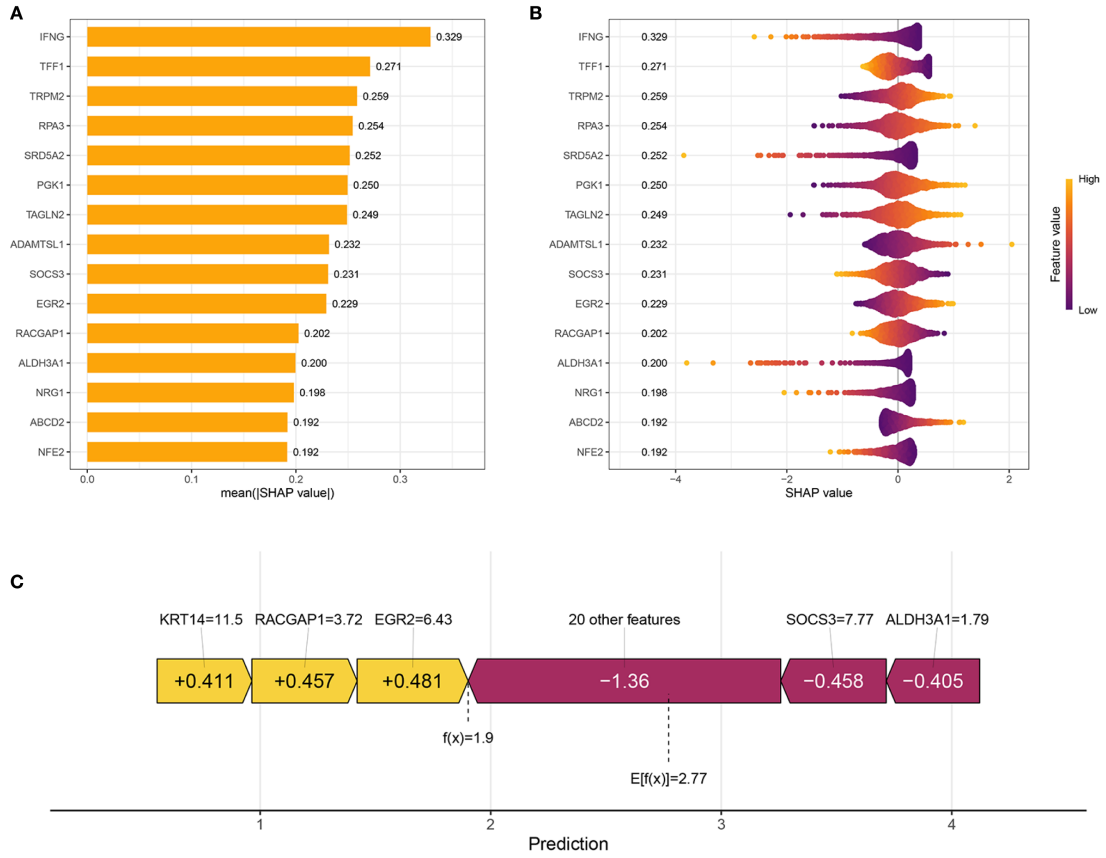

FIGURE 3
Interpretation of the prognostic model using SHAP Analysis. **(A)** Bar plot showing the global feature importance, ranked by the mean absolute SHAP value. Each bar represents a feature included in the prognostic model. **(B)** SHAP summary plot illustrates the distribution of SHAP values for each feature across all samples. Each dot represents a single sample for a given feature. **(C)** SHAP waterfall plot for an individual sample's prediction, explaining how different features contribute to deviating the prediction from the base value.

values (e.g., "20 other features" collectively contribute -1.36, SOCS3 = 7.77 contributes -0.458, ALDH3A1 = 1.79 contributes -0.405).

3.4 Development and validation of an integrated nomogram

We aimed to create a practical clinical tool for overall survival (OS) prediction, and integrated the risk score derived from the Ridge regression model with relevant clinical variables from the TCGA dataset, including age, pathological stage, tumor size (T classification), lymph node (N classification), and metastasis (M classification). Univariate Cox proportional hazards regression analysis (Figure 4A) revealed that all considered variables were associated with increased risk, with the "riskScore" exhibiting the strongest association (HR = 3.491, $p < 0.001$). In the multivariate Cox regression analysis (Figure 4B), the "riskScore" remained a significant independent predictor of OS (HR = 3.168, $p < 0.001$), even after adjusting for other clinical factors. Age (HR = 1.030, $p < 0.001$) and pathological stage (HR = 1.609, $p = 0.040$) also were independent predictors. ROC analysis compared the 'Risk' model's predictive accuracy against individual clinical variables, with AUC values calculated for quantitative evaluation (Figure 4C). The "Risk" model achieved a superior AUC of 0.845 compared to Age (0.611), Stage (0.722), T stage (0.631), M stage (0.578), and N stage (0.650), indicating its enhanced ability to discriminate between patients with different survival outcomes. Time-dependent ROC analyses further demonstrated the model's consistent predictive performance over time, with AUC values of 0.845, 0.807, and 0.779 at 1, 3, and 5 years, respectively (Figure 4D). Additionally, the risk score consistently exhibited a higher C-index compared to traditional clinical variables across different time points, further supporting its superior prognostic value (Figure 4E). Furthermore, a nomogram was developed that integrates clinical variables with the risk score to predict OS probabilities (Figure 4F). To assess the nomogram's accuracy, we constructed a calibration curve, which demonstrated satisfactory performance. The nomogram also exhibited good discriminative ability, with a C-index of 0.815 (95% CI: 0.777-0.853; Figure 4G).

3.5 Prognostic performance of the risk stratification model across diverse patient subgroups

To assess the robustness of our risk stratification model, its prognostic power within various clinically defined subgroups were

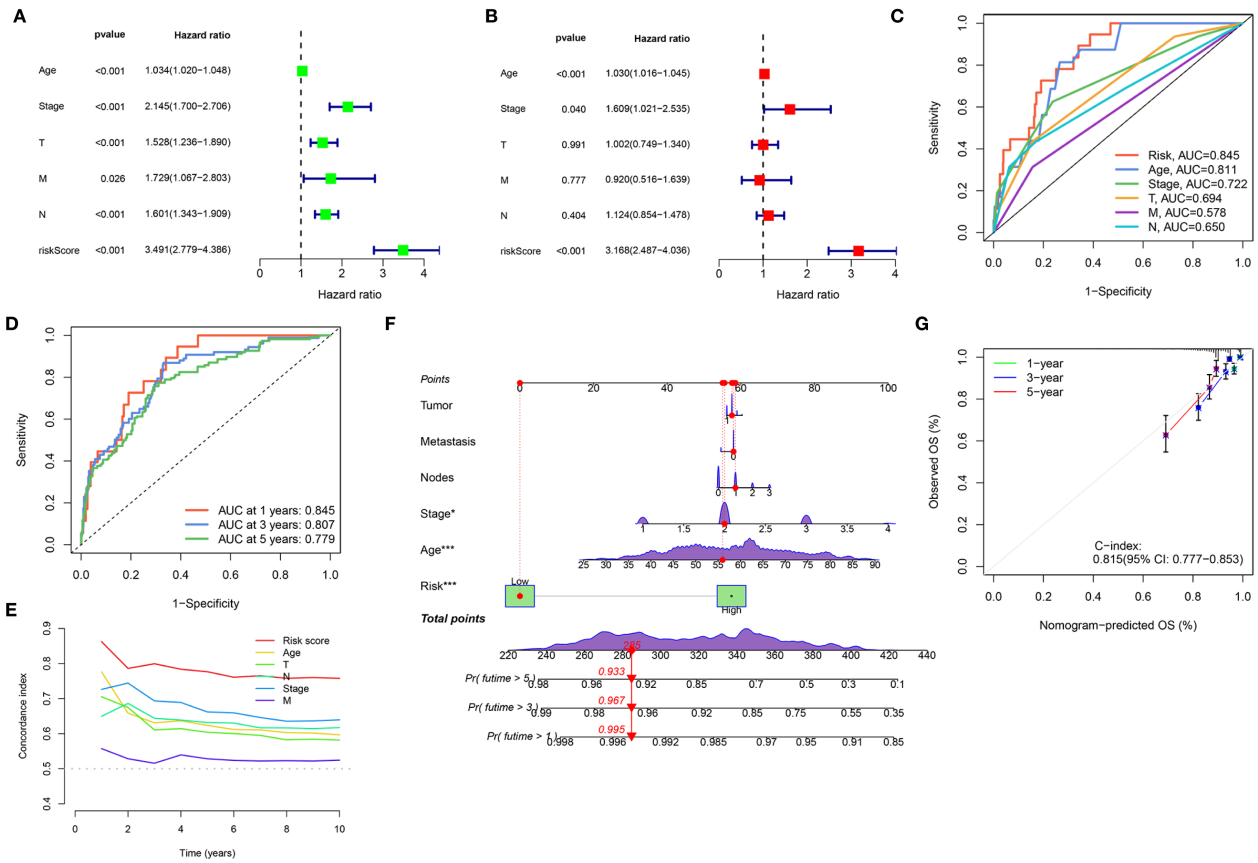

FIGURE 4
Development and validation of an integrated nomogram. **(A, B)** Forest plots display the results of univariate **(A)** and multivariate **(B)** Cox regression analyses for overall survival. **(C)** ROC curves evaluating the predictive accuracy of the Risk Score, Age, Stage, T, M, and N for overall survival. **(D)** Time-dependent ROC curves for the Risk Score, showing its predictive accuracy for overall survival at 1 year, 3 years, and 5 years. **(E)** C-index analysis over 10 years for the Risk Score compared to Age, Stage, T, M, and N. **(F)** Nomogram integrates clinical variables and the Risk Score for predicting 1-year, 3-year, and 5-year overall survival probability. **(G)** Calibration plot for the nomogram, assessing the agreement between nomogram-predicted overall survival (OS) and observed OS at 1-year, 3-year, and 5-year time points. (*$P < 0.05$, ***$P < 0.001$).

further evaluated. Figures 5A-E demonstrates the risk score's robust prognostic value, with low-risk patients showing superior survival versus high-risk counterparts across all clinical strata (age, pathological stage, TNM classification; all p<0.001). Similarly, the risk score demonstrated consistent prognostic ability within molecularly defined subgroups, including molecular subtypes (Luminal, HER2, and TNBC), ER status, PR status, and HER2 status (all $p < 0.001$) (Figures 5F-I). These findings underscore the robust and independent prognostic value of our risk score across a wide spectrum of established clinical and molecular prognostic factors, consistently identifying patient groups with differing survival probabilities regardless of these other variables.

3.6 Mendelian randomization study between hub SORGs and breast cancer

MR analysis was performed to assess causal links between the 67 prognostic DESORGs from the Ridge regression model and breast cancer risk. Figures 6A-C showed the estimated effect of each individual genetic variant (SNP, listed on the y-axis) used as an instrumental variable on breast cancer risk. In Figures 6D-F, these scatter plots where each point represents an instrumental SNP. The x-axis shows the SNP's effect on breast cancer (β_XY), and the y-axis shows the inverse of the standard error of this effect (1/SE (β_XY)), indicating precision. Leave-One-Out sensitivity analysis (Figures 6G-I) shown how the overall MR estimate for the effect of ADAM15, HLA-F and NR1H3 on breast cancer changes by sequentially excluding each single nucleotide polymorphism (SNP). Figures 6J-L displayed the relationship between each SNP's effect on the exposure (e.g., "SNP effect on ADAM15") and its corresponding effect on breast cancer risk. Various MR methods were employed (Figure 7A). Weighted median, IVW and Simple mode methods show ADAM15 has a statistically significant odds ratio. All MR methods indicate HLA-F has a strong and statistically significant causal risk effect, with ORs substantially greater than 1 (e.g., IVW OR = 3.115, 95% CI: 2.859-3.393; Weighted mode OR = 2.781, 95% CI: 1.366-5.659). Most MR methods suggest NR1H3 has a strong and statistically significant protective causal effect, with ORs substantially less than 1 (e.g., IVW OR = 0.132, 95% CI: 0.060-0.289; Weighted mode OR = 0.105, 95% CI: 0.080-0.136). A circos plot designed to visualize genomic information, including the

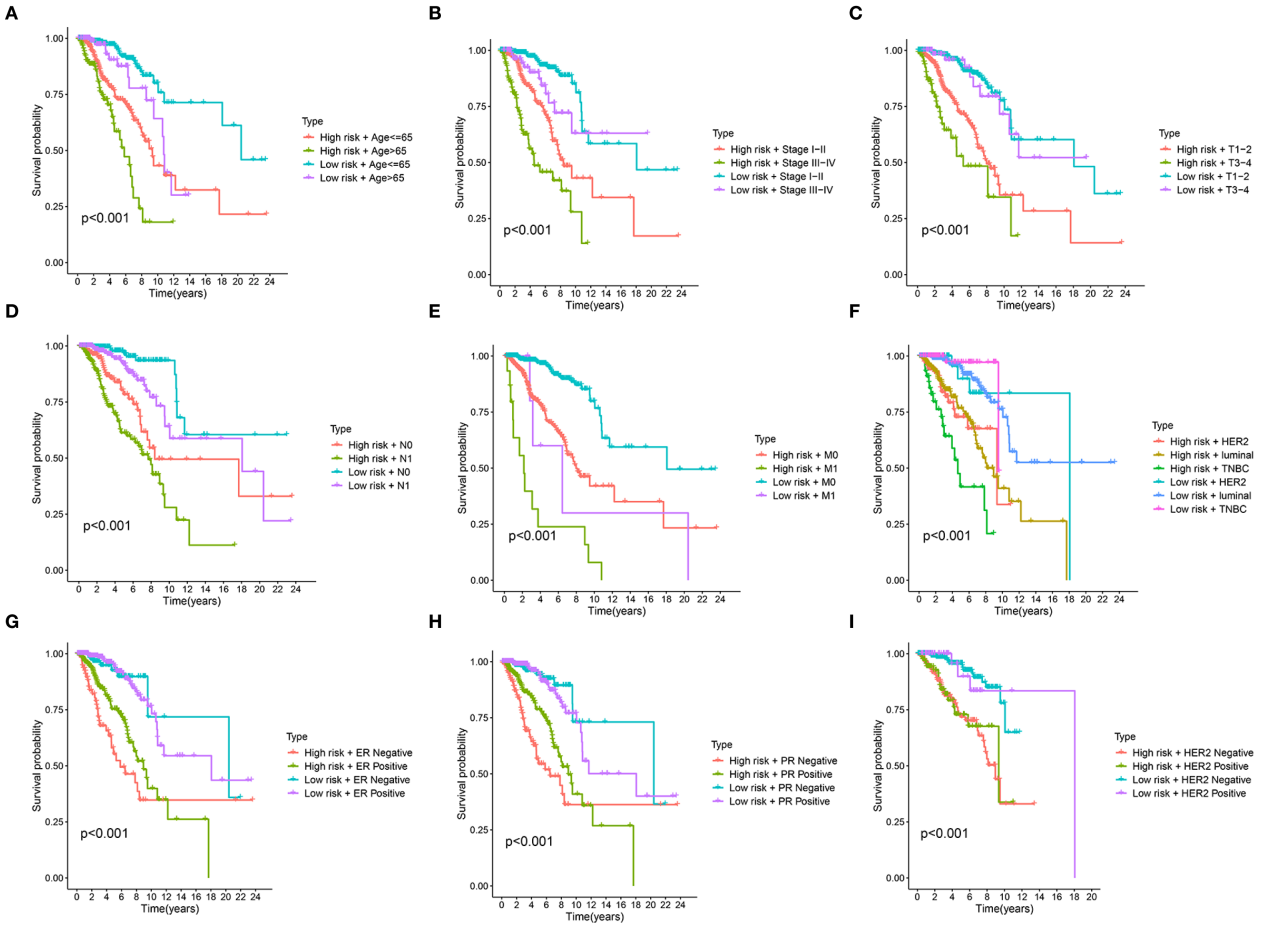

FIGURE 5
Stratified survival analysis of the prognostic riskscore across different clinical and molecular subgroups. **(A–I)** Kaplan-Meier survival curves illustrate the prognostic performance of the risk score in various patient subgroups. In each panel, patients are first divided into high-risk and low-risk groups based on the prognostic signature and then further stratified by Age **(A)**, clinical Stage **(B)**, T stage (tumor size) **(C)**, N stage (node) **(D)**, M stage (metastasis) **(E)**, molecular subtype (luminal, HER2, TNBC) **(F)**, Estrogen Receptor (ER) status **(G)**, Progesterone Receptor (PR) status **(H)**, Epidermal Growth Factor Receptor 2 (HER2) status **(I)**.

chromosomal locations of genes (Figure 7B): ADAM15 is located on chromosome 1, HLA-F is on chromosome 6, and NR1H3 is on chromosome 11. Compared to normal tissues, NR1H3 expression is significantly downregulated in tumor samples, whereas HLA-F and ADAM15 expression are significantly higher in tumor tissues (Figure 7C). ROC curves were generated to evaluate the ability of each gene to discriminate tumor and normal tissues. NR1H3 has the highest AUC of 0.817, ADAM15 has an AUC of 0.768, HLA-F has an AUC of 0.598 (Figure 7D), suggesting NR1H3 expression has the best discriminatory power among the three for distinguishing tumor from normal tissue. Kaplan-Meier survival analyses showed that only NR1H3 is associated with OS (p = 0.02) (Figure 7E). Higher expression of NR1H3 predicted a significantly better OS. Although lower HLA-F expression showed a trend toward better OS, this did not reach statistical significance (p = 0.068) (Figure 7F). No significant association was observed between ADAM15 expression and OS (p = 0.092) (Figure 7G).

3.7 NR1H3 suppresses proliferation and metastasis

To further explore the function of NR1H3 expression in breast cancer cell lines, we overexpressed NR1H3 in MDA-MB-231 cells and knockdown NR1H3 in MCF7 cells. The mRNA and protein levels were verified by qRT-PCR and western blot, respectively (Figures 8A, B). siNR1H3#2 exhibiting the best knockdown efficiency was selected for further experiments. Knockdown of NR1H3 (siNR1H3#2) in MCF7 cells significantly increased cell proliferation over 7 days compared to the control, while overexpressed NR1H3 in MDA-MB-231 had opposite effect (Figure 8C). Similarly, reducing NR1H3 expression increased the number of colonies formed in MCF7 cells, overexpression of NR1H3 in MDA-MB-231 cells resulted in a marked reduction in colony formation (Figure 8D). The wound healing assay demonstrated that NR1H3 downregulation increases while NR1H3 upregulation

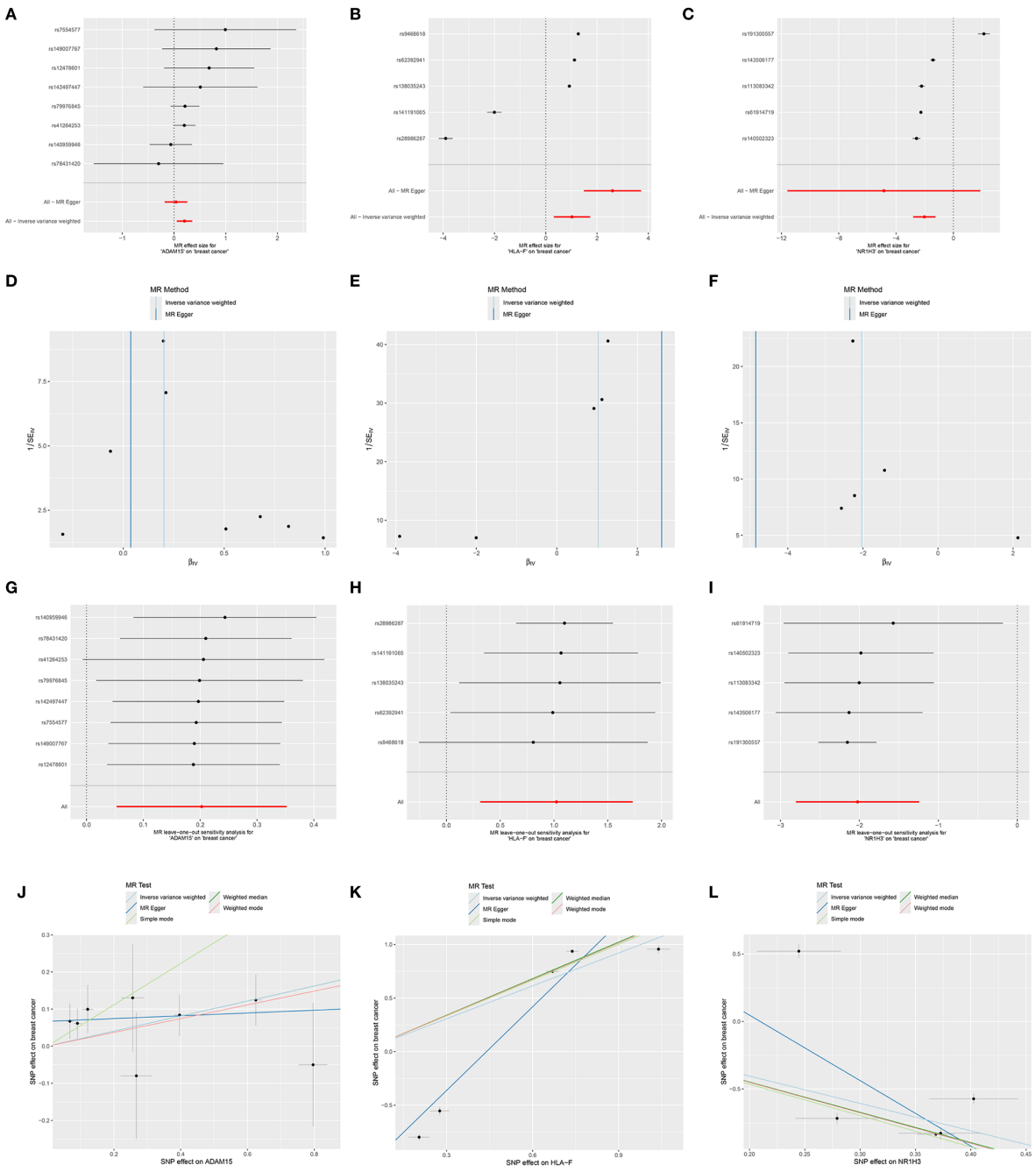

FIGURE 6
Mendelian randomization analyses for the causal effects of ADAM1S, HLA-F, and NR1H3 on breast cancer risk. **(A-C)** Forest plots showing the causal effect estimates of each individual Single Nucleotide Polymorphism (SNP) on breast cancer risk, mediated through the respective gene (ADAM1S, HLA-F, and NR1H3)'s expression. **(D-F)** Funnel plots visualizing the distribution of SNP effects on breast cancer (βGY) against their precision (1/SEGY). These plots are used to assess heterogeneity and potential directional pleiotropy. **(G-I)** Leave-one-out sensitivity analysis plots. Each point represents the MR estimate (IVW method) for the causal effect of the respective gene's expression on breast cancer when the indicated SNP (y-axis) is excluded from the analysis. **(J-L)** Scatter plots illustrate the relationship between the SNP effects on the respective gene's expression (x-axis) and the SNP effects on breast cancer risk (y-axis).

decreases the rate of wound closure (cell migration) at 24 hours compared to the control group (Figure 8E). Consistently, NR1H3 siRNA#2 significantly increased both cell migration and invasion through transwell membrane. In contrast, NR1H3 overexpression led to a substantial decrease in these invasive behaviors (Figure 8F). Collectively, these findings suggest that NR1H3 functions as a tumor suppressor in breast cancer by inhibiting cell proliferation, colony formation, migration and invasion.

10.3389/fimmu.2025.1653903

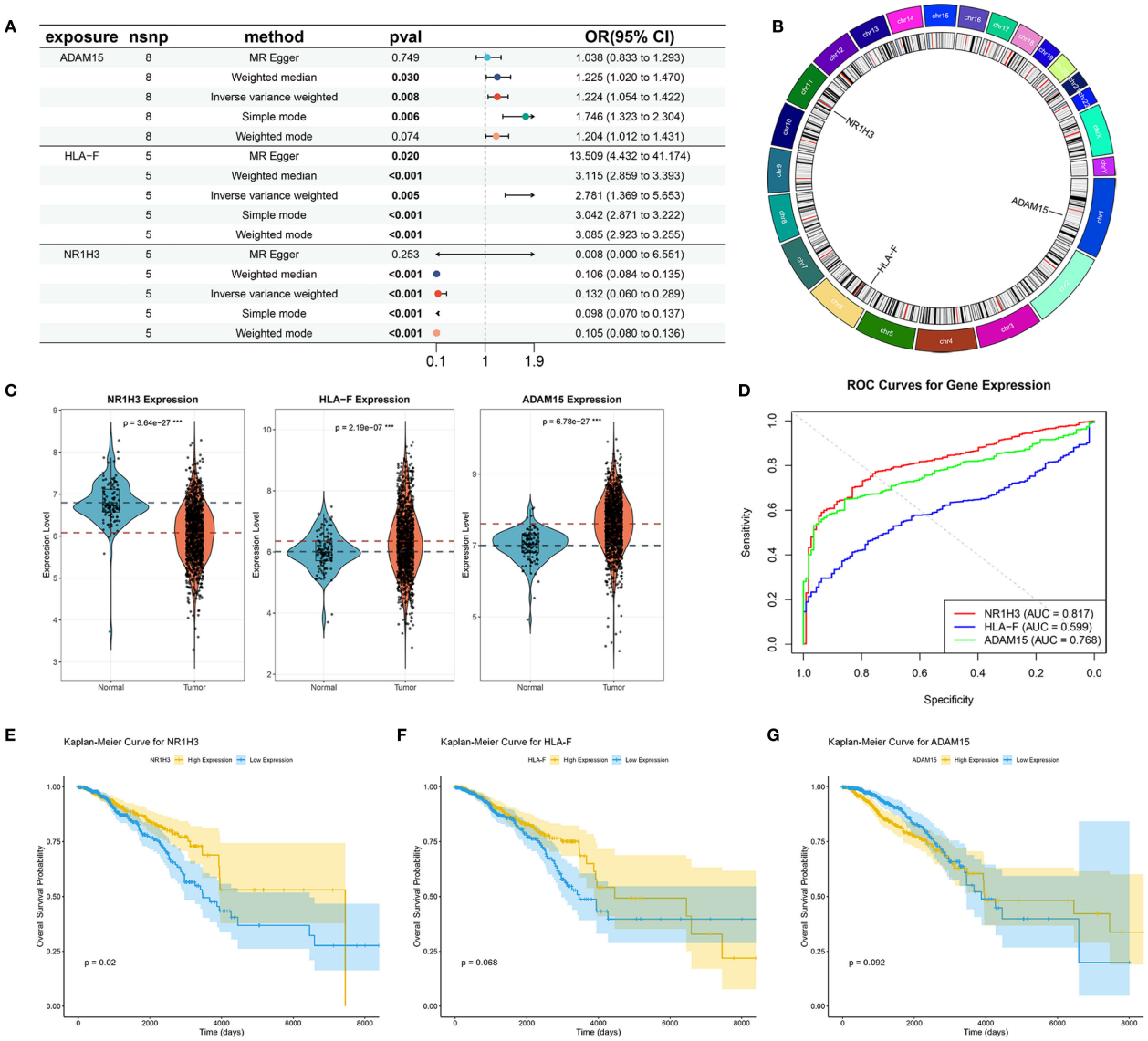

FIGURE 7
Mendelian Randomization, Expression Analysis, and Prognostic Significance of ADAM15, HLA-F, and NR1H3. **(A)** Summary of Mendelian Randomization (MR) results for the causal effects of ADAM15, HLA-F, and NR1H3 expression on breast cancer risk. **(B)** Circos plot illustrates the genomic locations and surrounding regions of the genes ADAM15, HLA-F, and NR1H3. **(C)** Violin plots comparing the expression levels of NR1H3, HLA-F, and ADAM15 between normal and tumor tissues. **(D)** ROC curves evaluating the performance of NR1H3, HLA-F and ADAM15 gene expression in distinguishing between normal and tumor. **(E-G)** Kaplan-Meier curves for overall survival based on the expression levels of NR1H3 **(E)**, HLA-F **(F)**, and ADAM15 **(G)**.

3.8 GSEA and GSVA analyses

To explore the pathways that NR1H3 involved in breast cancer, GSEA analysis was conducted. Among pathways enriched in samples with high NR1H3 expression, the top five were primarily linked to immune responses: GOBP_ANTIGEN_PROCESSING_AND_PRESENTATION_OF _EXOGENOUS_ ANTIGEN, GOCC_MHC_PROTEIN_COMPLEX, GOMF_ANTIGEN_BINDING and GOMF_PEPTIDE_ANTIGEN_BINDING (Figure 9A). The enriched pathways in low NR1H3 group were more diverse and include: GOBP_AEROBIC_RESPIRATION, GOCC_PRESYNAPTIC_ACTIVE_ZONE_CYTOPLASMIC_ COMPONENT, GOBP_SENSORY_PERCEPTION_OF_TASTE and GOMF_TASTE_RECEPTOR_ ACTIVITY, which indicates that low NR1H3 levels are associated with alterations in cellular respiration and some neuronal or sensory-related pathways (Figure 9B). GSVA for KEGG pathways showed their correlation with NR1H3 expression (indicated by t-values). Pathways positively correlated with NR1H3 are again heavily involved in immune processes, such as: KEGG_CYTOSOLIC_DNA_SENSING_PATHWAY, KEGG_SYSTEMIC_LUPUS_ERYTHEMATOSUS, and KEGG_ANTIGEN_PROCESSING_AND_PRESENTATION, while pathways negatively correlated with NR1H3 include processes like: KEGG_PROTEIN_ EXPORT and KEGG_UBIQUITIN_

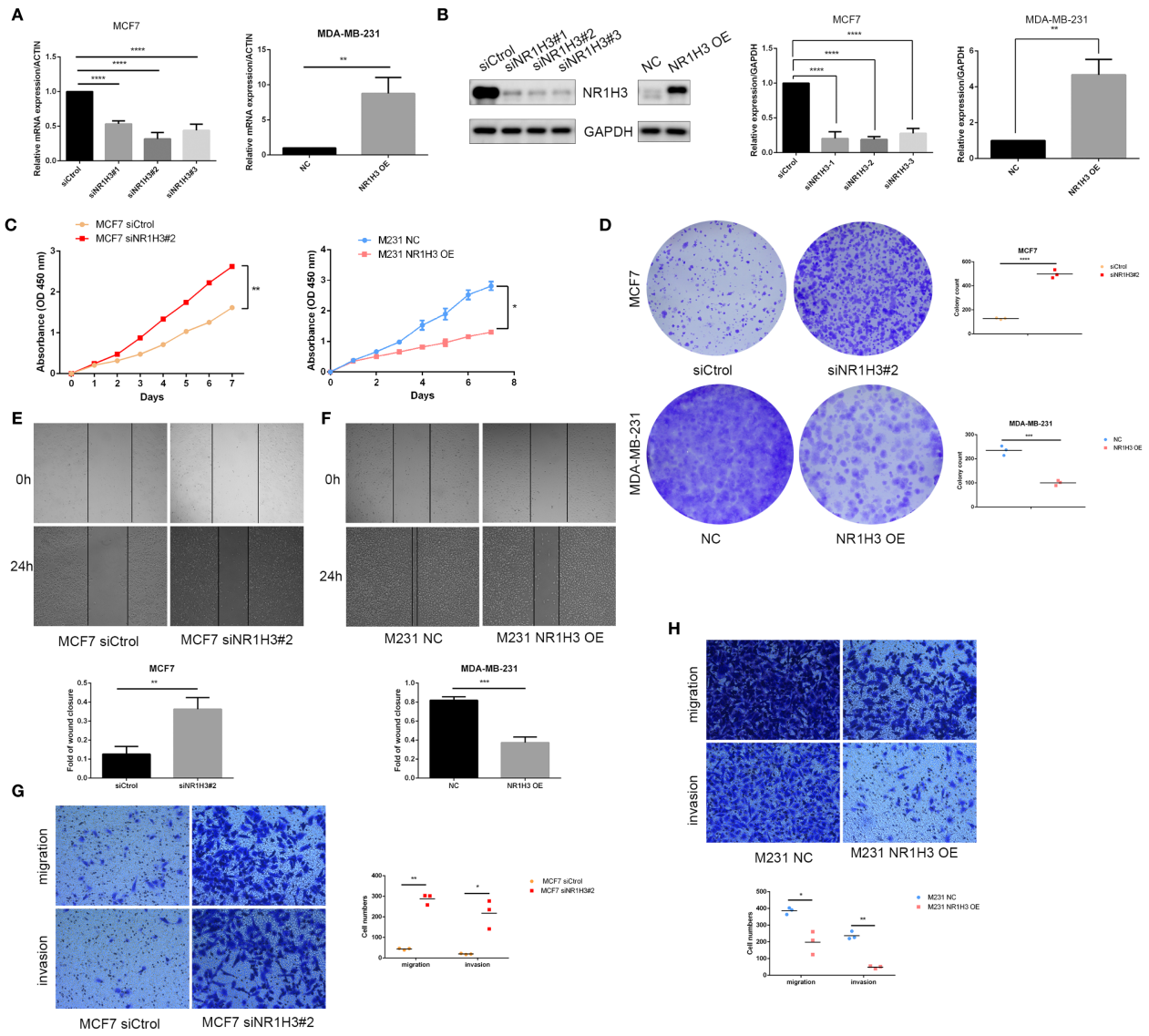

FIGURE 8
Functional effects of NR1H3 modulation on breast cancer cell proliferation, colony formation, migration, and invasion *in vitro*. **(A, B)** Verification of NR1H3 mRNA level and protein level in MCF7 and MDA-MB-231 cells by qRT-PCR **(A)** and western blot **(B)**, respectively. **(C)** Cell proliferation assays (absorbance at OD 450 nm) over 7 days for MCF7 cells treated with siCtrol or siNR1H3#2, and for MDA-MB-231 cells with NC or NR1H3 OE. **(D)** Colony formation assays. Representative images and quantification of colony counts for MCF7 and MDA-MB-231 cells. **(E, F)** Wound healing assays for MCF7 **(E)** and MDA-MB-231 **(F)** cells. Representative images at 0h and 24h after scratching and quantification of the fold of wound closure. **(G, H)** Transwell migration and invasion assays for MCF7 **(G)** and MDA-MB-231 **(H)** cells. Representative images of migrated and invaded cells and quantification of cell numbers. (*$P < 0.05$, **$P < 0.01$, ***$P < 0.001$).

MEDIATED_PROTEOLYSIS (Figure 9C). Similarly, GSVA for GO pathways show that pathways positively correlated with NR1H3 further confirm the strong association with immune activation, while pathways negatively correlated with NR1H3 are related to chromosomal organization and morphogenesis (Figure 9D).

3.9 Molecular docking of NR1H3 and related ingredients

DSigDB_All_detailed data was downloaded from DSigDB database. 155 drugs were identified associated with NR1H3. Among them, Cephaeline and Emetine were identified as potential upregulators of NR1H3 via the Connectivity Map (CMAP) database. This database contains gene expression data from cell lines treated with various compounds. CMAP data suggested that both Cephaeline and Emetine treatment lead to an upregulation of NR1H3 expression in MCF7 and HL60 cells. Following this lead from the gene expression data, we then performed molecular docking to investigate a plausible mechanism. Molecular docking shows that there are five potential binding pockets (C1 through C5) for the drug Cephaeline on the NR1H3 protein. The predicted binding affinities (Vina scores) for Cephaeline range from -9.2 kcal/mol (strongest binding, pocket C1)

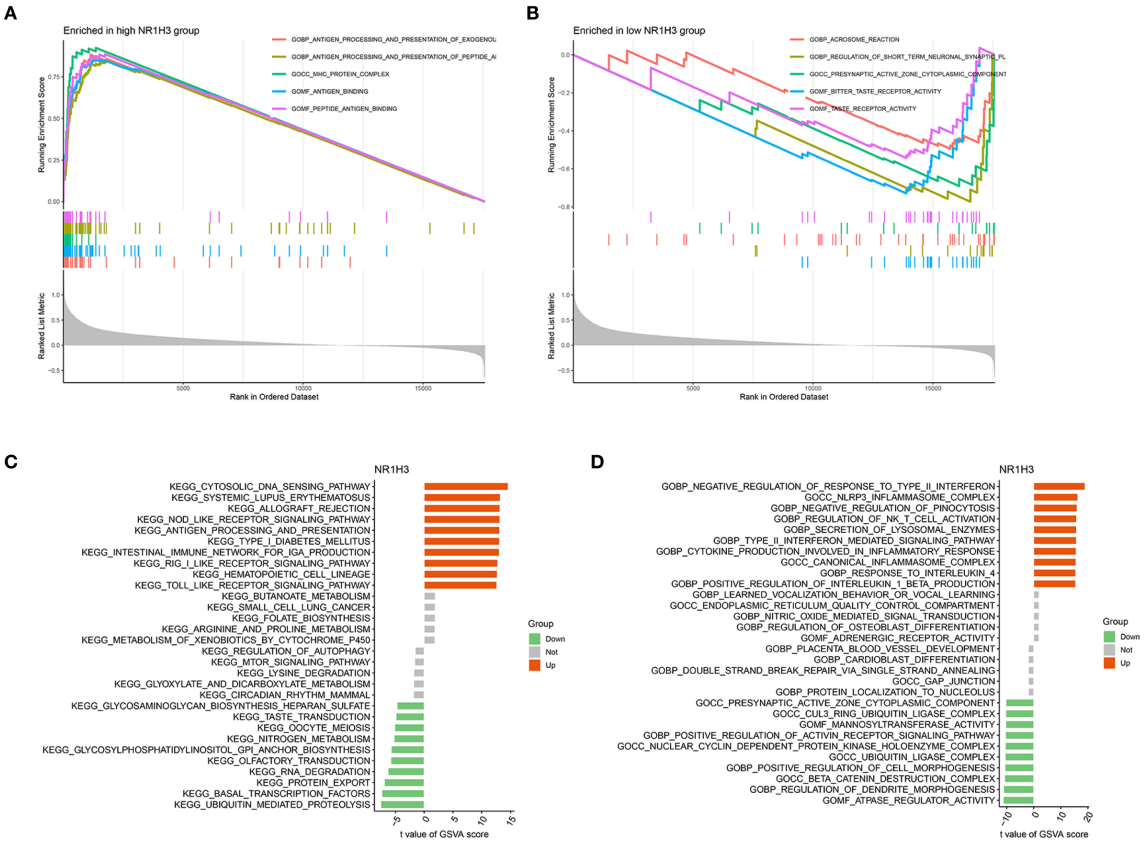

FIGURE 9
Gene Set Enrichment Analysis (GSEA) and Gene Set Variation Analysis (GSVA) reveal pathways associated with NR1H3 Expression. **(A)** GSEA plot showing top gene sets enriched in the high NR1H3 expression group. **(B)** GSEA plot illustrating top gene sets enriched in the low NR1H3 expression group. **(C)** Bar plot displaying significantly altered KEGG pathways identified by GSVA in relation to NR1H3 expression. **(D)** Bar plot showing significantly altered Gene Ontology (GO) terms identified by GSVA in relation to NR1H3 expression.

TABLE 1 Structure-based blind docking of NR1H3 with cephaeline.

Curpocket ID	Vina score	Cavity volume ($Å^3$)	Center (x, y, z)	Docking size (x, y, z)	Contact residues
C1	-9.2	3735	69, 56, 24	24, 31, 24	**Chain A**: ARG426 SER427 LEU430 LYS431 GLU434 HIS435 PHE438 PHE439 LEU441 **Chain B**: LYS289 THR290 ILE293 GLU294 GLN330 ARG367 PRO368 ASN369 LEU412 ARG413 THR414 SER416 SER417 HIS419 SER420 GLU421 VAL423 PHE424 ALA425 ARG427 LEU428 ILE440 TRP441 ASP442 VAL443 **Chain C**: GLN270 ASP273 LEU276 ARG302 TRP305
C2	-8.9	1770	89, 38, 10	24, 24, 24	**Chain B**: GLN330 GLU332 **Chain C**: ILE299 ARG302 ALA303 GLY304 TRP305 ASN306 GLU307 ASN377 PRO378 ASP379 SER380 LYS381 GLY382 LEU383 PRO386 ALA387 GLU390 ARG393 GLU394 TYR397 ARG426 GLY429 LEU430 LEU433 **Chain D**: GLU332 ASN335 PRO336 GLU339 PHE340 ARG342 ALA343 GLU346 LEU347 PRO403 ARG404 MET405 MET407 LYS408 SER411 THR414 LEU415 SER417 VAL418 GLU421
C4	-8.5	1557	74, 42, 35	24, 24, 24	**Chain A**: ILE299 ARG302 ALA303 TRP305 ASN306 GLU307 ASN377 PRO378 ASP379 SER380 LYS381 GLY382 LEU383 PRO386 ALA387 GLU390 ARG393 TYR397 ARG426 GLY429 LEU430 LEU433 GLU434 **Chain B**: GLU332 ASN335 PRO336 GLU339 PHE340 SER341

(Continued)

TABLE 1 Continued

Curpocket ID	Vina score	Cavity volume (Å^3)	Center (x, y, z)	Docking size (x, y, z)	Contact residues
					ARG342 ALA343 GLU346 LEU347 PRO403 ARG404 MET405 MET407 LYS408 SER411 THR414 LEU415 SER417 VAL418 SER420 GLU421 **Chain D**: GLU332
C3	-7.8	1578	90, 58, 13	24, 24, 24	**Chain A**: LEU436 PHE439 LYS440 Chain C: ARG334 HIS338 ALA340 GLY341 VAL342 GLY343 ALA344 ILE345 ASP347 ARG348 LEU350 THR351 GLU352 SER427 LEU430 LYS431 GLU434 **Chain D**: LYS289 THR290 ILE293 GLU294 ALA365 ASP366 ARG367 PRO368 ASN369 VAL370 GLN371 GLN373 ARG413 SER416 SER417 HIS419 SER420 ILE440 TRP441 ASP442 VAL443
C5	-7.1	1516	55, 40, 24	24, 24, 24	**Chain B**: VAL216 GLN219 GLN220 GLN221 ASN223 ARG224 SER226 PHE227 PHE252 PHE255 THR256 LEU258 ALA259 VAL261 SER262 GLU265 ILE266 ILE293 MET296 LEU297 GLU299 THR300 ARG302 ARG303 TYR304 ASN305 ILE311 THR312 PHE313 LEU314 LYS315 SER318 PHE324 LEU329 PHE333 ILE334 ILE337 PHE338 SER341 ASP351 HIS419 GLN422 LEU426 LEU433 LEU437 TRP441

to -7.1 kcal/mol (weakest among those listed, pocket C5) (Table 1). The binding pocket C1 was shown in Figure 10A displays visualizations of protein-ligand interactions between NR1H3 and Cephaeline. The ligand is shown interacting with 39 specific amino acid residues of NR1H3 protein in chain A, chain B and chain C. There are also five potential binding pockets (C1 through C5) for the drug Emetine on the NR1H3 protein. The predicted binding affinities (Vina scores) for Emetine range from -9.1 kcal/mol (strongest, pocket C1) to -7.3 kcal/mol (pocket C3) (Table 2). The ligand is shown interacting with 31 specific amino acid residues of NR1H3 protein in chain A, chain B and chain C (Figure 10B). The favorable binding affinities (Vina scores of -9.2 kcal/mol for Cephaeline and -9.1 kcal/mol for Emetine) suggest a strong and stable interaction is possible.

4 Discussion

Using machine learning, we established a new prognostic signature derived from differentially expressed sodium overload-related genes (DESORGs), with thorough development and validation. Among these, we identified NR1H3 as a key gene and experimentally confirmed its tumor-suppressive function in breast cancer cells. Our initial analysis of the GeneCards database yielded 2052 sodium overload-related genes, of which 753 showed differential expression in comparison between normal and tumor samples. Notably, the most significantly downregulated genes included VEGFD, CAVIN2, CAV1, and ADRB2, while CDKN3, INHBA, AURKB, MMP13, and EZH2 were significantly upregulated. Caveolin-1 (CAV1) has been reported to play dual roles in breast cancer, acting as both a tumor suppressor and promoter depending on the specific cellular context and breast cancer subtype (20). Adrenergic Receptor Beta 2 (ADRB2) has been implicated in cancer cell proliferation and stress responses (21). Conversely, the upregulation of genes such as Aurora Kinase B (AURKB) and Enhancer of Zeste Homolog 2 (EZH2) is commonly associated with increased cell proliferation and poor prognosis in breast cancer (22, 23).

Pathway enrichment analyses provided valuable insights into the functional consequences of the observed DESORG expression changes. KEGG analysis revealed significant enrichment in pathways critical for cancer development and progression, including PI3K-Akt and MAPK signaling pathway, lipid and atherosclerosis, and calcium signaling pathway. The PI3K-Akt and MAPK signaling pathways are well-known drivers of cancer cell growth, survival, and proliferation (24, 25). Given the interconnectedness of sodium and calcium transport through mechanisms like Na+/Ca2+ exchangers (26), alterations in DESORGs could directly impact calcium signaling within tumor cells. Leveraging these differentially expressed sodium overload-related genes, we identified 67 genes with significant prognostic value using univariate Cox regression. We then constructed and evaluated 101 prognostic models using ten different machine learning algorithms. Among these, the Ridge regression model emerged as the optimal model. This validation across independent datasets underscores the reliability and generalizability of the prognostic signature (27). Using the prognostic model, we stratified patients into high- and low-risk categories, which showed markedly distinct OS and PFS outcomes. Specifically, high-risk patients experienced substantially worse outcomes ($p < 0.001$ in TCGA, $p = 0.001$ in GEO for OS). The model's ability to significantly stratify patients underscores its clinical potential.

Integrating the DESORG-derived risk score with established clinical variables— such as age, tumor stage, and TNM classification —into a nomogram significantly improved prognostic accuracy. The risk score emerged as a strong independent predictor and risk factors for BC patients (multivariate HR: 3.168, 95% CI:2.487-4.036), outperforming individual clinical factors in AUC analysis (Risk model AUC: 0.845). The novel nomogram demonstrated strong predictive accuracy (C-index = 0.815), indicating its clinical utility. Such integrated models can facilitate more

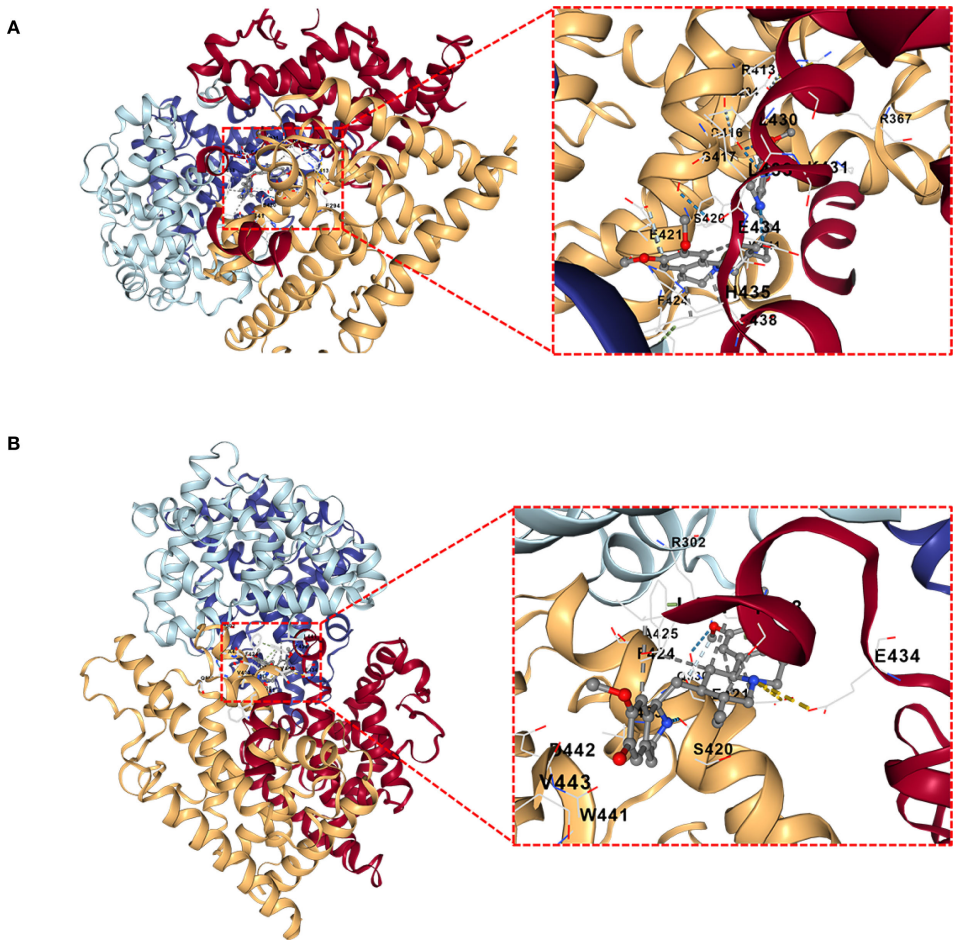

FIGURE 10
Molecular docking interactions of Cephaeline and Emetine with NR1H3 Protein. **(A, B)** Overall view of NR1H3- Cephaeline complex **(A)** and NR1H3-Emetine complex **(B)** with a magnified insect showing the detailed interactions at the binding site. Specific amino acid residues of the protein are depicted interacting with the bound ligand. Dashed lines likely indicate hydrogen bonds or other key interactions.

TABLE 2 Structure-based Blind Docking of NR1H3 with Emetine.

Curpocket ID	Vina score	Cavity volume (Å^3)	Center (x, y, z)	Docking size (x, y, z)	Contact residues
C1	-9.1	3735	69, 56, 24	25, 31, 25	**Chain A**: ARG348 SER427 LEU430 LYS431 LEU433 GLU434 HIS435 PHE438 PHE439 LEU441 **Chain B**: LYS289 THR290 ILE293 GLU294 ARG367 PRO368 ASN369 ARG413 SER416 SER417 HIS419 SER420 GLU421 VAL423 PHE424 ARG427 ILE440 TRP441 ASP442 VAL443 **Chain C**: ASP273
C2	-9.0	1770	89, 38, 10	25, 25, 25	**Chain A**: HIS435 **Chain B**: GLN330 GLU332 LEU428 **Chain C**: ILE299 ARG302 ALA303 GLY304 TRP305 ASN306 GLU307 ASN377 PRO378 ASP379 SER380 LYS381 GLY382 PRO386 ALA387 GLU390 ARG393 GLU394 TYR397 ARG426 GLY429 LEU430 LEU433 GLU434 **Chain D**: GLU332 PRO336 GLU339 PHE340 ARG342 ALA343 MET344 GLU346 LEU347 ARG404 MET407 LYS408 VAL410 SER411 THR414 LEU415 SER417 VAL418 GLU421

(Continued)

TABLE 2 Continued

Curpocket ID	Vina score	Cavity volume (Å^3)	Center (x, y, z)	Docking size (x, y, z)	Contact residues
C3	-7.3	1578	90, 58, 13	25, 25, 25	**Chain A**: ASP263 **Chain C**: ARG334 HIS338 GLY341 VAL342 GLY343 ALA344 ILE345 ASP347 ARG348 LEU350 THR351 GLU352 SER427 LEU430 LYS431 GLU434 **Chain D**: LYS289 THR290 ILE293 GLU294 ALA365 ASP366 ARG367 PRO368 ASN369 VAL370 GLN371 GLN373 ARG413 SER416 SER417 HIS419 SER420 ILE440 TRP441
C4	-8.3	1557	74, 42, 35	25, 25, 25	**Chain A**: ILE299 ARG302 ALA303 GLY304 TRP305 ASN306 GLU307 ASN377 PRO378 ASP379 SER380 LYS381 PRO386 ALA387 GLU390 ARG426 GLY429 LEU430 LEU433 **Chain B**: GLU332 ASN335 PRO336 GLU339 PHE340 ARG342 ALA343 GLU346 LEU347 ARG404 LYS408 SER411 THR414 LEU415 SER417 VAL418 GLU421 **Chain D**: GLU332
C5	-7.6	1516	55, 40, 24	25, 25, 25	**Chain B**: GLN219 GLN220 ASN223 ARG224 SER226 PHE227 PHE252 PHE255 THR256 LEU258 ALA259 VAL261 SER262 GLU265 MET296 LEU297 GLU299 THR300 ARG302 ARG303 TYR304 ASN305 PRO306 THR312 PHE313 LEU314 LYS315 SER318 PHE324 LEU329 ASN345 ASP351 LEU426 LEU433 LEU437 TRP441

personalized risk assessment, thereby aiding in treatment decisions. Traditional prognostic markers in breast cancer, including hormone receptor status and TNM classification are widely utilized (28). However, their predictive power can be limited within specific subtypes, highlighting the need for more universally applicable biomarkers. Importantly, the prognostic effectiveness of our DESORG-based risk score was consistently observed across diverse clinically and molecularly defined patient subgroups. Regardless of stratification by age, tumor stage, T/N/M stages, molecular subtype (Luminal, HER2, TNBC), or ER/PR/HER2 status, the model consistently distinguished between high- and low-risk groups, with significant differences in survival outcomes. This consistent performance across heterogeneous subgroups emphasizes the fundamental function of DESORG-related biology in BC prognosis and suggests the broad applicability of the model in personalized risk assessment and treatment decision-making.

Our MR analysis explores potential causal relationships between expression level of key sodium overload-related genes and breast cancer risk. This analysis identified HLA-F as a significant causal risk factor (IVW OR = 3.115, $p<0.001$) and NR1H3 as a strong protective factor (IVW OR = 0.132, $p<0.001$) for breast cancer. ADAM15 also showed a statistically significant odds ratio with some MR methods. HLA-F has been shown to be upregulated in tumors and is associated with immune evasion and poor prognosis in various cancers (29, 30). The strong causal risk effect we identified for HLA-F warrants further investigation into its specific role in breast cancer pathogenesis linked to sodium overload pathways. Our MR analysis strongly suggested a protective role for NR1H3. Consistent with this finding, NR1H3 expression was significantly lower in BC tumors. More importantly, its low expression level predicts worse prognosis. NR1H3, also known as Liver X Receptor Alpha (LXRα), is a nuclear receptor involved in cholesterol homeostasis, lipid metabolism, and inflammation (31, 32). In breast cancer models, LXR has been shown to inhibit cell growth though effecting EST expression (33). In our study, *in vitro* experiments robustly confirmed the tumor-suppressive function of NR1H3 in breast cancer cell lines. NR1H3 gain-of-function attenuated oncogenic behaviors (proliferation, colony formation, motility), while loss-of-function in MCF7 cells exacerbated these phenotypes. These results align with previous studies indicating that LXRs can suppress breast cancer cell growth and metastasis (34, 35). GSEA and GSVA further elucidated the pathways associated with NR1H3 expression. High NR1H3 expression was strongly correlated with immune response pathways, including antigen processing and presentation (via both GO and KEGG), as well as cytosolic DNA sensing. This suggests that part of NR1H3's protective effect may be mediated through the enhancement of anti-tumor immunity.

Molecular docking studies further predicted strong binding affinities of these compounds to NR1H3, suggesting potential therapeutic interactions. Emetine, an established anti-protozoal drug, has been demonstrated anti-cancer effects in various cancers, including gastric cancer (36). Cephaeline also inhibits cell viability and migration in Mucoepidermoid carcinoma (MEC) (37). However, their specific mechanism of action via NR1H3 in breast cancer requires further validation. It is important to clarify the distinction between the broad set of sodium overload-related genes (SORGs) used to build our prognostic model and the specific subset of genes that are mechanistic drivers of necrosis by sodium overload (NECSO). Our study intentionally cast a wide net, analyzing a comprehensive list of SORGs to build a robust prognostic signature for breast cancer. NECSO, however, is a specific form of regulated cell death defined by strict criteria, including persistent activation of ion channels like TRPM4 [8], a resulting massive influx of sodium, subsequent cell swelling, and eventual necrotic membrane rupture. While our machine learning model identified genes such as TRPM2 as having high prognostic importance, this statistical association

does not automatically classify it as a direct NECSO mediator. To be confirmed as a true NECSO driver, TRPM2 would require dedicated functional validation to demonstrate its direct role in inducing these characteristic cellular events. Therefore, a critical direction for future research will be to functionally screen our list of prognostically significant DESORGs to determine which, if any, are bona fide mediators of NECSO in breast cancer. Such work would bridge our prognostic findings with the specific mechanisms of this novel cell death pathway.

5 Conclusion

This research developed and evaluated a novel DESORGs prognostic signature based on machine learning which shows significant potential for predicting BC patients' survival. MR analysis provided causal insights into the roles of NR1H3 in breast cancer risk. Importantly, we experimentally validated NR1H3 as a tumor suppressor in breast cancer cells, influencing proliferation, colony formation, migration, and invasion. These findings highlight a novel link between sodium homeostasis, immune response, and breast cancer prognosis, offering new avenues for therapeutic intervention, potentially through the modulation of NR1H3 activity. Further investigation into these DESORGs may uncover novel mechanisms and treatment strategies for BC.

6 Limitations

Despite the robust findings of this study, several limitations should be acknowledged. First, our prognostic model was developed and validated using retrospective data from public repositories (TCGA and GEO). Although we demonstrated the model's consistency across these datasets, its predictive power must be confirmed in prospective, multi-center clinical cohorts before clinical application. Second, the use of different transcriptomic platforms for the training (TCGA, RNA-seq) and validation (GEO, microarray) cohorts could introduce technical variability and potential batch effects. Third, our analyses relied on bulk tissue transcriptomic data, which provides an average of gene expression across all cell types within the tumor microenvironment. This approach may obscure cell-type-specific functions and interactions, a particularly relevant point given the strong link we identified between high NR1H3 expression and immune activation pathways.

Data availability statement

The original contributions presented in the study are included in the article/supplementary material. Further inquiries can be directed to the corresponding authors.

Ethics statement

Ethical approval was not required for the studies on humans in accordance with the local legislation and institutional requirements because only commercially available established cell lines were used.

Author contributions

QF: Conceptualization, Formal analysis, Writing – original draft, Funding acquisition. WY: Formal analysis, Software, Writing – review & editing. GS: Writing – review & editing. FW: Conceptualization, Writing – original draft, Funding acquisition. CX: Conceptualization, Supervision, Writing – review & editing.

Funding

The author(s) declare financial support was received for the research and/or publication of this article. Medical and Health Science and Technology Development Program of Shandong Provincial (202104080815); Natural Science Foundation of Shandong Provincial (ZR2019PC007).

Conflict of interest

The authors declare that the research was conducted in the absence of any commercial or financial relationships that could be construed as a potential conflict of interest.

The reviewer YX declared a shared affiliation, with no collaboration, with WX and ZL to the handling editor at the time of the review.

Generative AI statement

The author(s) declare that no Generative AI was used in the creation of this manuscript.

Any alternative text (alt text) provided alongside figures in this article has been generated by Frontiers with the support of artificial intelligence and reasonable efforts have been made to ensure accuracy, including review by the authors wherever possible. If you identify any issues, please contact us.

Publisher's note

All claims expressed in this article are solely those of the authors and do not necessarily represent those of their affiliated organizations, or those of the publisher, the editors and the reviewers. Any product that may be evaluated in this article, or claim that may be made by its manufacturer, is not guaranteed or endorsed by the publisher.

References

1. Bray F, Laversanne M, Sung H, Ferlay J, Siegel RL, Soerjomataram I, et al. Global cancer statistics 2022: globocan estimates of incidence and mortality worldwide for 36 cancers in 185 countries. *CA Cancer J Clin*. (2024) 74:229–63. doi: 10.3322/caac.21834

2. Łukasiewicz S, Czeczelewski M, Forma A, Baj J, Sitarz R, Stanislawek A. Breast cancer-epidemiology, risk factors, classification, prognostic markers, and current treatment strategies-an updated review. *Cancers (Basel)*. (2021) 13(17):4287. doi: 10.3390/cancers13174287

3. Coleman MP, Quaresma M, Berrino F, Lutz JM, De Angelis R, Capocaccia R, et al. Cancer survival in five continents: A worldwide population-based study (Concord). *Lancet Oncol*. (2008) 9:730–56. doi: 10.1016/S1470-2045(08)70179-7

4. Pfeffer CM, Singh ATK. Apoptosis: A target for anticancer therapy. *Int J Mol Sci*. (2018) 19. doi: 10.3390/ijms19020448

5. Dai E, Chen X, Linkermann A, Jiang X, Kang R, Kagan VE, et al. A guideline on the molecular ecosystem regulating ferroptosis. *Nat Cell Biol*. (2024) 26:1447–57. doi: 10.1038/s41556-024-01360-8

6. Xie J, Yang Y, Gao Y, He J. Cuproptosis: mechanisms and links with cancers. *Mol Cancer*. (2023) 22:46. doi: 10.1186/s12943-023-01732-y

7. Zou Z, Zhao M, Yang Y, Xie Y, Li Z, Zhou L, et al. The role of pyroptosis in hepatocellular carcinoma. *Cell Oncol (Dordr)*. (2023) 46:811–23. doi: 10.1007/s13402-023-00787-9

8. Fu W, Wang J, Li T, Qiao Y, Zhang Z, Zhang X, et al. Persistent activation of trpm4 triggers necrotic cell death characterized by sodium overload. *Nat Chem Biol*. (2025) 21(8):1238–49. doi: 10.1038/s41589-025-01841-3

9. Koike T, Tanaka S, Oda T, Ninomiya T. Sodium overload through voltage-dependent na(+) channels induces necrosis and apoptosis of rat superior cervical ganglion cells *in vitro*. *Brain Res Bull*. (2000) 51:345–55. doi: 10.1016/s0361-9230(99)00246-4

10. Cardoso HD, Cabral EV, Vieira-Filho LD, Vieyra A, Paixao AD. Fetal development and renal function in adult rats prenatally subjected to sodium overload. *Pediatr Nephrol*. (2009) 24:1959–65. doi: 10.1007/s00467-009-1247-1

11. Rocco L, Gil FZ, da Fonseca Pletiskaitz TM, de Fatima Cavanal M, Gomes GN. Effect of sodium overload on renal function of offspring from diabetic mothers. *Pediatr Nephrol*. (2008) 23:2053–60. doi: 10.1007/s00467-008-0884-0

12. Levi AJ, Dalton GR, Hancox JC, Mitcheson JS, Issberner J, Bates JA, et al. Role of intracellular sodium overload in the genesis of cardiac arrhythmias. *J Cardiovasc Electrophysiol*. (1997) 8:700–21. doi: 10.1111/j.1540-8167.1997.tb01834.x

13. Roson MI, Della Penna SL, Cao G, Gorzalczany S, Pandolfo M, Toblli JE, et al. Different protective actions of losartan and tempol on the renal inflammatory response to acute sodium overload. *J Cell Physiol*. (2010) 224:41–8. doi: 10.1002/jcp.22087

14. Schorn C, Frey B, Lauber K, Janko C, Strysio M, Keppeler H, et al. Sodium overload and water influx activate the nalp3 inflammasome. *J Biol Chem*. (2011) 286:35–41. doi: 10.1074/jbc.M110.139048

15. Michaels AM, Zoccarato A, Hoare Z, Firth G, Chung YJ, Kuchel PW, et al. Disrupting na(+) ion homeostasis and na(+)/K(+) atpase activity in breast cancer cells directly modulates glycolysis *in vitro* and *in vivo*. *Cancer Metab*. (2024) 12:15. doi: 10.1186/s40170-024-00343-5

16. Wang Q, Zheng C, Hou H, Bao X, Tai H, Huang X, et al. Interplay of sphingolipid metabolism in predicting prognosis of gbm patients: towards precision immunotherapy. *J Cancer*. (2024) 15:275–92. doi: 10.7150/jca.89338

17. Liberzon A, Birger C, Thorvaldsdottir H, Ghandi M, Mesirov JP, Tamayo P. The molecular signatures database (Msigdb) hallmark gene set collection. *Cell Syst*. (2015) 1:417–25. doi: 10.1016/j.cels.2015.12.004

18. Hanzelmann S, Castelo R, Guinney J. Gsva: gene set variation analysis for microarray and rna-seq data. *BMC Bioinf*. (2013) 14:7. doi: 10.1186/1471-2105-14-7

19. Ponce-Bobadilla AV, Schmitt V, Maier CS, Mensing S, Stodtmann S. Practical guide to shap analysis: explaining supervised machine learning model predictions in drug development. *Clin Transl Sci*. (2024) 17:e70056. doi: 10.1111/cts.70056

20. Chintalaramulu N, Singh DP, Sapkota B, Raman D, Alahari S, Francis J. Caveolin-1: an ambiguous entity in breast cancer. *Mol Cancer*. (2025) 24:109. doi: 10.1186/s12943-025-02297-8

21. Huang T, Tworoger SS, Hecht JL, Rice MS, Sood AK, Kubzansky LD, et al. Association of ovarian tumor beta2-adrenergic receptor status with ovarian cancer risk factors and survival. *Cancer Epidemiol Biomarkers Prev*. (2016) 25:1587–94. doi: 10.1158/1055-9965.EPI-16-0534

22. Garlapati C, Joshi S, Bhattarai S, Krishnamurthy J, Turaga RC, Nguyen T, et al. Plk1 and aurkb phosphorylate survivin differentially to affect proliferation in racially distinct triple-negative breast cancer. *Cell Death Dis*. (2023) 14:12. doi: 10.1038/s41419-022-05539-5

23. Puppe J, Opdam M, Schouten PC, Jozwiak K, Lips E, Severson T, et al. Ezh2 is overexpressed in brca1-like breast tumors and predictive for sensitivity to high-dose platinum-based chemotherapy. *Clin Cancer Res*. (2019) 25:4351–62. doi: 10.1158/1078-0432.CCR-18-4024

24. Glaviano A, Foo ASC, Lam HY, Yap KCH, Jacot W, Jones RH, et al. Pi3k/akt/mtor signaling transduction pathway and targeted therapies in cancer. *Mol Cancer*. (2023) 22:138. doi: 10.1186/s12943-023-01827-6

25. Paraiso KH, van der Kooi K, Messina JL, Smalley KS. Measurement of constitutive mapk and pi3k/akt signaling activity in human cancer cell lines. *Methods Enzymol*. (2010) 484:549–67. doi: 10.1016/B978-0-12-381298-8.00027-7

26. Jeffs GJ, Meloni BP, Bakker AJ, Knuckey NW. The role of the na(+)/ca(2+) exchanger (Ncx) in neurons following ischaemia. *J Clin Neurosci*. (2007) 14:507–14. doi: 10.1016/j.jocn.2006.07.013

27. Ho SY, Phua K, Wong L, Bin Goh WW. Extensions of the external validation for checking learned model interpretability and generalizability. *Patterns (N Y)*. (2020) 1:100129. doi: 10.1016/j.patter.2020.100129

28. Fragomeni SM, Sciallis A, Jeruss JS. Molecular subtypes and local-regional control of breast cancer. *Surg Oncol Clin N Am*. (2018) 27:95–120. doi: 10.1016/j.soc.2017.08.005

29. Lin A, Zhang X, Ruan YY, Wang Q, Zhou WJ, Yan WH. Hla-F expression is a prognostic factor in patients with non-small-cell lung cancer. *Lung Cancer*. (2011) 74:504–9. doi: 10.1016/j.lungcan.2011.04.006

30. Lin A, Yan WH. The emerging roles of human leukocyte antigen-F in immune modulation and viral infection. *Front Immunol*. (2019) 10:964. doi: 10.3389/fimmu.2019.00964

31. Zhao L, Lei W, Deng C, Wu Z, Sun M, Jin Z, et al. The roles of liver X receptor alpha in inflammation and inflammation-associated diseases. *J Cell Physiol*. (2021) 236:4807–28. doi: 10.1002/jcp.30204

32. Wang B, Tontonoz P. Liver X receptors in lipid signalling and membrane homeostasis. *Nat Rev Endocrinol*. (2018) 14:452–63. doi: 10.1038/s41574-018-0037-x

33. Gong H, Guo P, Zhai Y, Zhou J, Uppal H, Jarzynka MJ, et al. Estrogen deprivation and inhibition of breast cancer growth *in vivo* through activation of the orphan nuclear receptor liver X receptor. *Mol Endocrinol*. (2007) 21:1781–90. doi: 10.1210/me.2007-0187

34. Vedin LL, Lewandowski SA, Parini P, Gustafsson JA, Steffensen KR. The oxysterol receptor lxr inhibits proliferation of human breast cancer cells. *Carcinogenesis*. (2009) 30:575–9. doi: 10.1093/carcin/bgp029

35. Nguyen-Vu T, Vedin LL, Liu K, Jonsson P, Lin JZ, Candelaria NR, et al. Liver X receptor ligands disrupt breast cancer cell proliferation through an E2f-mediated mechanism. *Breast Cancer Res*. (2013) 15:R51. doi: 10.1186/bcr3443

36. Peng X, Shi J, Zhao Z, Tong R, Zhang X, Zhong L. Emetine, a small molecule natural product, displays potent anti-gastric cancer activity via regulation of multiple signaling pathways. *Cancer Chemother Pharmacol*. (2023) 91:303–15. doi: 10.1007/s00280-023-04521-y

37. Silva LC, Borgato GB, Wagner VP, Martins MD, Rocha GZ, Lopes MA, et al. Cephaeline is an inductor of histone H3 acetylation and inhibitor of mucoepidermoid carcinoma cancer stem cells. *J Oral Pathol Med*. (2022) 51:553–62. doi: 10.1111/jop.13252

frontiers | Frontiers in Immunology

TYPE Original Research
PUBLISHED 01 October 2025
DOI 10.3389/fimmu.2025.1610540

Check for updates

OPEN ACCESS

EDITED BY
Chao Wang,
Shanghai Jiao Tong University, China

REVIEWED BY
Jiaojiao Zhang,
Zhejiang Agriculture and Forestry University, China
Chang-Sheng Dong,
Shanghai University of Traditional Chinese Medicine, China
Wensu Wei,
Sun Yat-sen University, China

*CORRESPONDENCE
Shuzheng Song
songshuzheng@126.com
Xiaohua Jiang
jiangxiaohuash@163.com

RECEIVED 12 April 2025
ACCEPTED 05 September 2025
PUBLISHED 01 October 2025

CITATION
Yang Y, Jiang Q, Zhu Z, Zhang S, Du T, Song S and Jiang X (2025) Targeting the CCL28-STAT3-PLAC8 axis to suppress metastasis and remodel tumor microenvironment in colorectal cancer. *Front. Immunol.* 16:1610540. doi: 10.3389/fimmu.2025.1610540

COPYRIGHT
© 2025 Yang, Jiang, Zhu, Zhang, Du, Song and Jiang. This is an open-access article distributed under the terms of the Creative Commons Attribution License (CC BY). The use, distribution or reproduction in other forums is permitted, provided the original author(s) and the copyright owner(s) are credited and that the original publication in this journal is cited, in accordance with accepted academic practice. No use, distribution or reproduction is permitted which does not comply with these terms.

Targeting the CCL28-STAT3-PLAC8 axis to suppress metastasis and remodel tumor microenvironment in colorectal cancer

Yao Yang[1], Qixin Jiang[1], Zhe Zhu[1], Shun Zhang[2], Tao Du[2], Shuzheng Song[1*] and Xiaohua Jiang[2*]

[1]Department of Colorectal Surgery, Department of General Surgery, Shanghai East Hospital, School of Medicine, Tongji University, Shanghai, China, [2]Department of Gastrointestinal Surgery, Shanghai East Hospital, School of Medicine, Tongji University, Shanghai, China

Background: Chronic inflammation plays a critical role in the initiation and progression of colorectal cancer (CRC), establishing a close link between the inflammatory microenvironment with tumor invasion and metastasis. However, the regulatory mechanisms by which inflammation-related factors promote CRC progression remain largely unclear.

Methods: The biological significance of PLAC8 in colorectal cancer was investigated through clinical data analysis, mouse models of colitis-associated colorectal cancer, gene knockdown and overexpression, as well as cell migration and invasion assays. Additionally, bioinformatics analysis, activation and inhibition of PI3K/Akt and JAK/STAT3 signaling pathways, along with techniques including CUT&Tag, Western blotting, and qPCR, were employed to comprehensively analyze the detailed molecular mechanisms of PLAC8.

Results: Analysis of PLAC8 expression in 78 paired clinical samples revealed significantly elevated PLAC8 expression in CRC and was identified as an independent prognostic factor. Increased expression of PLAC8 was further validated in the mouse inflammation-cancer transition model. Genetic manipulation of PLAC8 through overexpression and knockdown unequivocally established its prometastatic function in CRC, with no significant effects on proliferation, oxaliplatin resistance, or colony formation. Pharmacological modulation of AKT signaling using specific activators (SC79) and inhibitors (Capivasertib) confirmed that PLAC8 drives EMT through AKT pathway activation, resulting in increased expression of EMT-related proteins, such as N-cadherin and Snail, thereby enhancing cell migration and invasion. Further correlation analysis, CUT&Tag, and STAT3 inhibition studies revealed that CCL28 activated the STAT3 signaling pathway, promoting PLAC8 expression, and ultimately enhancing CRC invasion and metastasis.

Conclusion: CCL28-mediated promotion of PLAC8 via the JAK/STAT3 signaling pathway, led to EMT in colorectal cancer cells, which played a key role in the transition from inflammation to cancer. PLAC8 served as an independent risk factor for colorectal cancer prognosis.

KEYWORDS

PLAC8, colorectal cancer, tumor microenvironment, EMT, CCL28

1 Introduction

In recent years, the incidence of colorectal cancer (CRC) has increased dramatically, largely attributable to changes in dietary habits and lifestyle. According to the most recent global epidemiological data, a total of 1,926,118 new CRC cases were diagnosed worldwide in 2022, positioning it as the third most common cancer. Furthermore, CRC was responsible for 903,859 cancer-related deaths, making it the second leading cause of cancer mortality globally, surpassed only by lung cancer (1). In China, 517,100 new cases of CRC were reported in 2022, ranking second among all cancers, while CRC-related deaths reached 240,000, placing it fourth overall and second among females (2). CRC imposes not only a significant physical and psychological burden on patients and families, but also a considerable economic strain on society.

Inflammation plays a crucial role in the onset and progression of cancer, serving as a significant driver in tumor initiation and advancement (3, 4). The relationship between inflammation and cancer has been a major focus of research. Numerous epidemiological studies have confirmed that inflammatory bowel diseases, such as ulcerative colitis and Crohn's disease, significantly increase the risk of developing colorectal cancer (5, 6). The highly dynamic and complex inflammatory tumor microenvironment (TME) (7, 8), comprising key inflammatory mediators such as tumor-associated macrophages (TAMs), tumor-associated neutrophils (TANs), dendritic cells (DCs), myeloid-derived suppressor cells (MDSCs), and T lymphocytes (9), plays a pivotal role in tumor progression. Inflammatory cytokines like TNF-α, TGF-β, IFN-γ, IL-1, IL-6, and IL-10 (10), along with their downstream intracellular signaling pathways, including eicosanoid signaling and the Janus kinase (JAK)-signal transducer and activator of transcription (STAT) pathway, are critical to tumorigenesis. Targeting inflammation through modulation of these mediators and signaling pathways holds therapeutic promise by modulating the tumor microenvironment, thereby inhibiting tumor growth and progression (11, 12). However, the molecular mechanisms linking inflammation and colorectal cancer development remain incompletely defined.

Placenta-specific gene 8 (PLAC8), alternatively known as Onzin or C15, is a conserved cysteine-rich protein expressed across eukaryotic species. It is predominantly expressed in various immune cells and tumor cells. Studies have shown that abnormal expression of PLAC8 in monocytes is associated with inflammatory storms in conditions such as sepsis and COVID-19 (13–16). In IBD patients, elevated PLAC8 expression in the gut microbiome correlate with dysbiosis and may serve as a microbial biomarker predicting higher colorectal or gastric cancer risk (17). Furthermore, PLAC8 has been implicated in the initiation and progression of several types of cancer, including breast cancer, liver cancer, and colorectal cancer, where it plays a role in tumor cell growth, invasion, metastasis, and apoptosis, among other processes (18). Some studies have also found that PLAC8 expression is decreased in colorectal cancer tissues, and it acts as a tumor suppressor gene by inhibiting the immune response (19, 20). However, the precise role of PLAC8 in the inflammation-associated carcinogenesis (inflammation-cancer transition) of colorectal cancer, and its underlying molecular mechanisms remain incompletely understood.

Preliminary findings suggest that the PLAC8 gene is involved in the inflammation-cancer transition in colorectal cancer, although its precise mechanism requires further investigation. Therefore, this study aimed to explore the role of PLAC8 in the pathogenesis and progression of colorectal cancer, with a focus on the inflammation-cancer transition. We employed a combination of animal models, bioinformatics approaches, and molecular biology techniques to investigate how PLAC8 is intricately involved in colorectal cancer development and assess its potential as a novel therapeutic target.

2 Materials and methods

2.1 Colorectal cancer clinical case data collection

Seventy-eight CRC patients with complete follow-up and clinical data treated at our institution were enrolled, and data collected included age, gender, clinicopathological characteristics (TNM stage, differentiation grade), tumor location, and serum tumor markers (CEA, CA19-9, CA125). Five cases without paired normal tissues were excluded from tumor-normal IHC comparisons, and three cases with missing CEA/CA199 values

were omitted from regression analyses. Written informed consent forms were obtained from all participants. All procedures were approved by the Institutional Review Board (IRB) and the Medical Ethics Committee of Shanghai East Hospital.

2.2 Immunohistochemistry

Immunohistochemical (IHC) staining was performed to assess PLAC8 expression in CRC and adjacent normal tissues. Paraffin-embedded tissue sections (4 μm thick) were deparaffinized in xylene and rehydrated through a graded ethanol series. Antigen retrieval was carried out using citrate buffer (pH 6.0) in a microwave for 10 minutes. Upon cooling to ambient temperature, endogenous peroxidase activity was quenched with 3% hydrogen peroxide for 10 minutes. The sections were then incubated with a primary anti-PLAC8 antibody (Proteintech, 12284-1-AP, 1:100) overnight at 4 °C, followed by a 30-minute incubation at room temperature with a biotinylated secondary antibody. Signals were detected using a DAB substrate kit, and sections were counterstained with hematoxylin. Stained slides were dehydrated, mounted, and examined under a light microscope. PLAC8 expression was evaluated based on staining intensity and the percentage of positive cells. Statistical analysis was conducted to compare PLAC8 expression levels between tumor and adjacent normal tissues. The immunohistochemical (IHC) scoring: Staining intensity was scored as follows: 3 (high), 2 (moderate), 1 (low), and 0 (no). The proportion of positive tumor cells: <10% was scored as 0, 10–25% as 1, 25–50% as 2, 50–75% as 3, and >75% as 4. The final IHC score was calculated by multiplying the intensity score by the proportion score, with the total score used for statistical analysis.

2.3 Construction of enteritis and colorectal cancer model

The azoxymethane (AOM)/dextran sulfate sodium (DSS) model of colitis-associated colorectal cancer was utilized into the experiment. 8-week-old female C57BL/6 mice (Beijing Vital River) were used. All experimental groups were balanced for age and sex. Animal grouping: control group (CON), experimental control group (DSS), experimental group (AOM/DSS, AD). Ten C57BL/6 mice were assigned to each group. The control group received no treatment, while mice in the experimental group were intraperitoneally injected with 12.5 mg/kg of AOM (MilliporeSigma, A5486). Normal drinking water was provided. One week later, the mice were given 2.5% DSS (Selleck, S6929) in drinking water for 7 consecutive days, with the DSS solution replaced every 2 days. Normal drinking water was then restored for 7 days, constituting one 3-week DSS cycle. Subsequently, mice received 2.5% DSS for 7 consecutive days, followed by a 14-day drug withdrawal period, which constituted the second DSS cycle. CON, DSS and AD groups (n=5/timepoint) underwent synchronized euthanasia at matched timepoints (3 and 6 weeks) (Figure 1C). The animal experiments were reviewed and approved by the Institutional Animal Care and Use Committee (IACUC) and Institutional Ethics Committee at Shanghai East hospital.

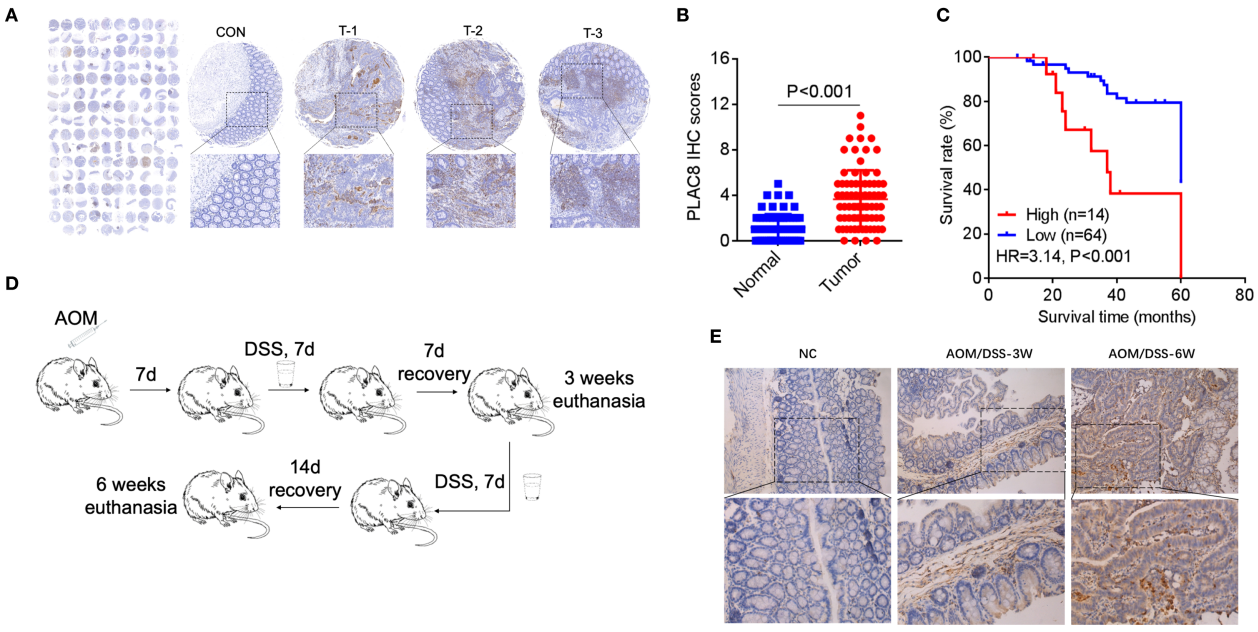

FIGURE 1
(A) PLAC8 IHC in tissue microarray (78 tumor/normal pairs). CON: normal adjacent tissue; T-1/T-2/T-3: representative PLAC8 protein highly expression tumor tissues. **(B)** Comparative IHC scores between tumor and normal tissues. **(C)** Patients were stratified into subgroups based on PLAC8 IHC scoring criteria and survival status, followed by Kaplan-Meier survival curve analysis with log-rank testing. **(D)** The colorectal cancer chemoprevention model was established through sequential administration of azoxymethane (AOM) and dextran sulfate sodium (DSS) in C57BL/6 mice. **(E)** PLAC8 protein expression dynamics were analyzed throughout the tumorigenesis process. (Student's t-test for comparisons).

2.4 Cell lines and reagents

Cell lines were obtained from the American Type Culture Collection (ATCC). Cancer cell lines were cultured in RPMI-1640 supplemented with 10% FBS and 1% penicillin–streptomycin, and maintained at 37 °C in a humidified incubator at 5% CO2. SC79, Capivasertib, Ruxolitinib, recombinant CXCL1 and recombinant CCL28 were purchased from Selleck Chemicals and MedChemExpress (S7863, S8019, S1378, HY-P70508, HY-P7250). Ruxolitinib: 2 μM, 24h; SC79: 10 μg/mL, 24h; Capivasertib: 1 μM, 24h. Doses were based on prior literature. Antibodies against p-AKT, p-NF-κB, p-STAT3, STAT3, AKT, E-cadherin, N-cadherin, Snail and GAPDH were purchased from Cell Signaling Technology (CST) (Cat.4060, 3033, 9145, 9135, 9272, 3195, 4061, 3879, 2118). The eukaryotic expression plasmid pcDNA3.1-pGFP-PLAC8 and siRNAs were purchased from GeneChem (Shanghai). Plasmid and siRNAs transfection was performed using Lipofectamine 3000 (Invitrogen, USA). Plasmid and siRNAs were transiently transfected into cells, and subsequent experiments were performed 48 hours post-transfection following validation at both RNA and protein levels. The sequences of primers are listed in Supplementary Table S1.

2.5 CUT & Tag assay

Targeted CUT&Tag-qPCR was performed to validate STAT3 binding to specific sites within the PLAC8 promoter. Genome-wide sequencing was not conducted due to the focused hypothesis-driven scope of this study. HCT116 cells were permeabilized and incubated with an anti-STAT3 primary antibody, followed by a secondary antibody conjugated to Tn5 transposase. Tagmentation buffer was added to cleave and tag DNA regions bound by STAT3. DNA was extracted and amplified using primers specific for the PLAC8 promoter region (Primer_1 and Primer_2). PCR products were analyzed via agarose gel electrophoresis. Enrichment in the PLAC8 promoter region was quantified by qPCR relative to an IgG control. Primers flanking STAT3-binding motifs at chr4:83115654-83115749 (Primer_1) and chr4:83115648-83115729 (Primer_2) were in the promoter region of PLAC8. The sequences of primers are listed in Supplementary Table S1.

2.6 Western blot and qPCR

Cellular proteins were extracted in RIPA buffer followed by protein concentration quantification via BCA assay. Equal amounts of protein (20-40 μg) were separated by SDS-PAGE on a 10-15% gel and transferred to a PVDF membrane. The membrane was blocked with 5% non-fat milk in TBST for 1 hour and incubated with primary antibodies overnight at 4 °C, followed by washing with TBST. After incubation with HRP-conjugated secondary antibody, proteins were detected using ECL substrate. For qPCR, total RNA was extracted and cDNA was synthesized from 1 μg of RNA. qPCR was performed using SYBR Green, cDNA, and gene-specific primers, with amplification conditions of 95 °C for 3 minutes, followed by 40 cycles of 95 °C for 10 seconds and 60 °C for 30 seconds. Gene expression was analyzed using the ΔΔCt method and normalized to housekeeping genes. The sequences of primers are listed in Supplementary Table S1.

2.7 Cell proliferation, clone formation and oxaliplatin sensitivity assay

Following transfection with siRNA or overexpression plasmids, cells were incubated for 48 hours before proceeding to subsequent cell proliferation and colony formation assays. Cell proliferation was assessed using the CCK-8 assay. Cells were seeded into 96-well plates at a density of 2 × 10^3 cells per well and cultured overnight to facilitate attachment. After treatment, 10 μL of CCK-8 solution (Dojindo, CK04) was added to each well, and cells were incubated for 1–4 hours at 37 °C. The absorbance at 450 nm was measured using a microplate reader to assess cell viability (BioTek Synergy H1). The relative cell proliferation rate was calculated by comparing the absorbance of treated samples to that of the control group. For the colony formation assay, cells were seeded into six-well plates at a density of 1,000 cells per well and cultured for 14 days to form colonies. The medium was replaced every 3–4 days. After incubation, cells were fixed with 4% paraformaldehyde for 15 minutes and stained with 0.1% crystal violet for 30 minutes at room temperature. Colonies containing more than 50 cells were counted under a microscope. The colony formation efficiency was calculated by dividing the number of colonies by the number of seeded cells, and the results were compared between different treatment groups. For the oxaliplatin sensitivity assay, cells were seeded in 96-well plates at a density of 3×10^3 cells/well and cultured for 24 hours. Oxaliplatin (Sigma-Aldrich, O9512) was serially diluted to create concentration gradients (0, 1, 2, 4, 8, 16, 32 μM) in complete medium. After 48-hour drug exposure, 10 μL CCK-8 reagent was added per well followed by 2-hour incubation at 37 °C. Absorbance at 450 nm was measured using a microplate reader. Cell viability was calculated as: (OD_treatment - OD_blank)/(OD_control - OD_blank) ×100%. Dose-response curves were generated through nonlinear regression analysis (four-parameter logistic model) in GraphPad Prism 9.0 to determine IC50 values. Three independent biological replicates, each with six technical replicates, were performed.

2.8 Immigration and invasion assay

The Transwell assay was used to assess cell migration and invasion. For migration, 5 × 10^4 cells were suspended in serum-free medium and seeded into the upper chamber of Transwell insert an 8-μm pore size Transwell insert, while the lower chamber was filled with complete medium containing 10% FBS as a chemoattractant. For invasion, the upper chamber was pre-coated with Matrigel to mimic the extracellular matrix. After incubation

for 48h at 37 °C, non-migrated or non-invaded cells on the upper surface of the membrane were removed using a cotton swab. Cells that had migrated or invaded to the lower surface were fixed with 4% paraformaldehyde and stained with 0.1% crystal violet. The number of migrated or invaded cells was counted under a microscope in at least five randomly selected fields. Results are presented as the mean number of migrated/invaded cells in the experimental group relative to the control group indicating the effects of different treatments on cell migration and invasion ability.

2.9 Enrichment and correlation analysis based on the TCGA database

Enrichment and correlation analyses were performed using transcriptomic data from the TCGA colorectal cancer dataset. RNA-seq data and corresponding clinical information were obtained from the Genomic Data Commons (GDC) portal. Data preprocessing was performed to filter low-expressed genes and normalize expression values (TPM or FPKM) using the R package TCGAbiolinks. Gene Set Variation Analysis (GSVA) was then applied to evaluate the enrichment of predefined gene sets across samples. For correlation analysis, Pearson correlation coefficients were calculated to assess the association between PLAC8 expression and inflammatory pathway-related gene expression.

2.10 Statistics

All experiments included ≥3 biological replicates with ≥2 technical replicates each. Data are presented as mean ± 95% confidence interval (CI) from three independent experiments. Pearson correlation analysis of PLAC8 and inflammatory pathway-related genes was performed. The student's t-test was performed in GraphPad Prism 6.0 (GraphPad Prism) unless otherwise specified. Variance similarity was assumed between compared groups. Correlation matrices were visualized using hierarchical clustering implemented in the R "corrplot" package. Survival analysis, including Kaplan-Meier curve generation, log-rank tests, and univariate and multivariate Cox regression analyses, was performed using the R "survival" package. P-values < 0.05 were considered statistically significant.

3 Results

3.1 PLAC8 expression played a crucial role in colorectal cancer and closely associated with survival and prognosis

Seventy-eight CRC patients were enrolled. Clinical data including age, gender, TNM stage, tumor differentiation grade, and serum levels of CEA, CA19-9, and CA125 were collected and analyzed (Supplementary Table S2). In three cases, CA19–9 and CEA data were missing. A total of 78 colorectal cancer tissues and 73 paired adjacent non-cancerous tissues underwent immunohistochemical (IHC) analysis to assess PLAC8 protein expression. IHC staining intensity was systematically scored, and comparative analysis between cancerous and adjacent tissues revealed significantly higher PLAC8 expression levels in colorectal cancer tissues compared to adjacent non-cancerous counterparts (P<0.001) (Figures 1A, B). ROC curve analysis based on PLAC8 IHC scores and patient survival status determined an optimal cutoff value of 5.5. Patients were stratified into low-expression (<5.5, n=64) and high-expression (≥5.5, n=14) groups. Kaplan-Meier analysis coupled with log-rank testing revealed significantly reduced overall survival in the PLAC8 high-expression group compared to the low-expression group (HR = 3.14, 95% CI 1.72-5.73; P<0.001) (Figure 1C).

Analysis of clinicopathological characteristics stratified by PLAC8 expression levels revealed that the high-expression group had a significantly higher proportion of patients with elevated CA19–9 levels compared to the low-expression group (P = 0.008). No significant differences were observed in other demographic, clinical, or histopathological parameters (all P>0.05) (Supplementary Table S3). Univariate Cox regression analysis identified significant prognostic associations for T stage (P = 0.001), N stage (P<0.001), M stage (P<0.001), TNM stage (P<0.001), tumor differentiation grade (P = 0.006), CA19–9 levels (P = 0.021), and PLAC8 expression (P = 0.021) (Supplementary Table S4). Subsequent multivariate Cox regression analysis identified TNM stage (HR = 3.38, P<0.001), tumor differentiation grade (HR = 2.43, P = 0.01), and PLAC8 expression (HR = 2.87, P = 0.015) as independent risk factors for colorectal cancer prognosis (Table 1).

TABLE 1 Cox multivariate analysis of clinicopathological characteristics and PLAC8 expression.

Variables	Cases (n)	HR	*P* value
TNM staging		3.38	<0.001
I	10		
II	17		
III	32		
IV	16		
Differentiation		2.43	0.01
High	1		
Moderate	50		
Low	24		
CA199		1.49	0.29
≥37U/mL	23		
<37U/mL	52		
PLAC8		2.87	0.015
High	13		
Low	62		

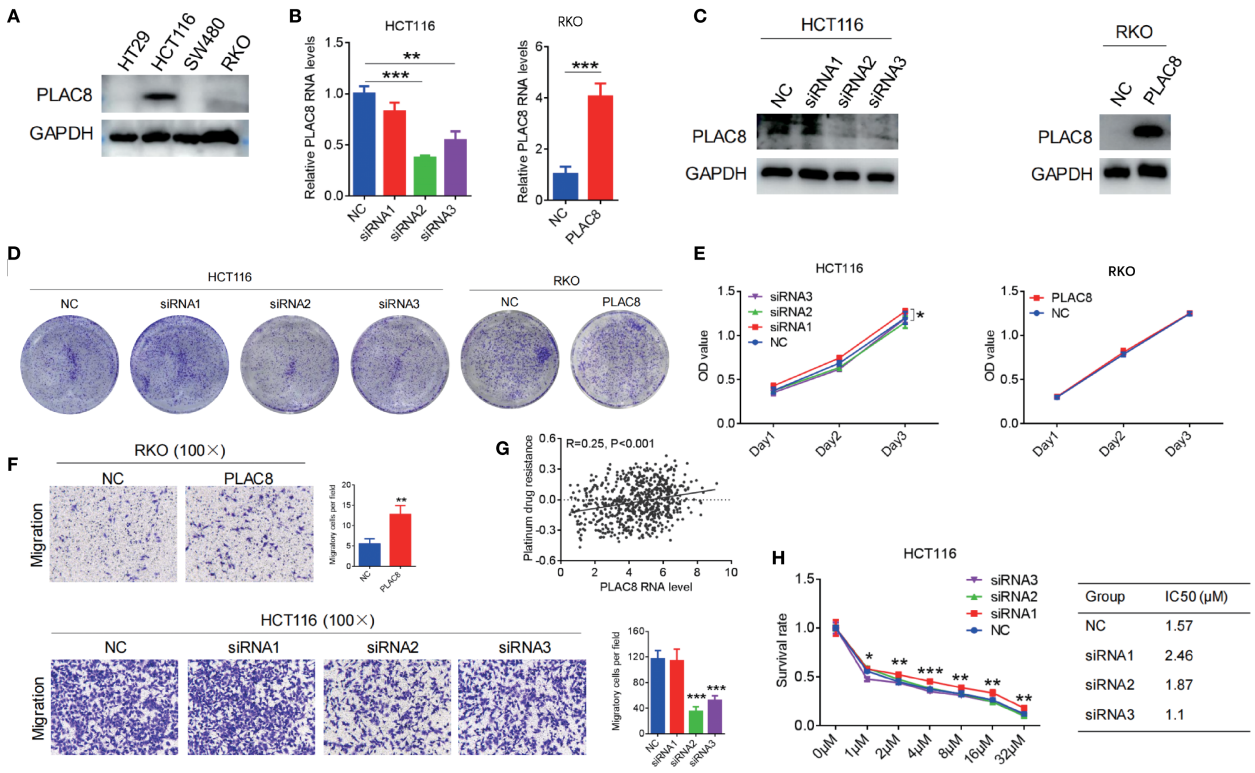

Group	IC50 (μM)
NC	1.57
siRNA1	2.46
siRNA2	1.87
siRNA3	1.1

FIGURE 2
(A) PLAC8 expression in four CRC cell lines. **(B, C)** PLAC8 overexpression and knockdown conducted in lower and higher PLAC8 expression CRC cell lines. **(D, E)** Impact of PLAC8 expression changes on cell clonogenicity and proliferation. **(F)** Transwell assay assessing PLAC8 expression on migration of CRC cell lines. **(G)** TCGA-based bioinformatic analysis to explore PLAC8 involvement in platinum resistance. **(H)** Impact of PLAC8 expression changes on oxaliplatin resistance (Student's t-test for comparisons; *, **, and *** represent $P < 0.05$, $P < 0.01$, and $P < 0.001$, respectively; GSVA for enrichment).

3.2 Establishment of AOM/DSS animal model and cell models in colorectal cancer

The colitis-associated colorectal cancer mouse model was successfully established using azoxymethane (AOM) combined with dextran sulfate sodium (DSS) (Supplementary Figure S1). Immunohistochemical staining revealed that, at 3 weeks (first cycle, n=6) and 6 weeks (second cycle, n=6) confirmed successful model establishment and revealed a significantly higher percentage of PLAC8-positive area from the tumor tissues (relative to the total pathological tissue section area) in comparison to the control group (n=4) and DSS group (n=4) ($P<0.05$) (Figures 1D, E).

PLAC8 protein expression levels were examined in colorectal cancer cell lines HT29, HCT116, SW480, and RKO. Among CRC cell lines, PLAC8 expression was highest in HCT116, lower in RKO, and undetectable in HT29 and SW480 cells (Figure 2A). Therefore, HCT116 cells were used for siRNA knockdown experiments, while RKO cells were selected for PLAC8 overexpression experiments. Western blot and qPCR analysis showed that siRNA1 had a minimal effect on PLAC8 expression, whereas siRNA2 and siRNA3 significantly reduced PLAC8 expression (Figures 2B, C). After PLAC8 overexpression, both protein and mRNA levels of PLAC8 were significantly elevated (Figures 2B, C).

3.3 The impact of PLAC8 gene regulation on the biological functions of colorectal cancer cell lines

Gene knockdown and overexpression of PLAC8 in HCT116 and RKO colorectal cancer cell lines showed that PLAC8 expression did not significantly affect cell proliferation, colony formation ($P>0.05$) (Figures 2D, E). GSVA of TCGA CRC transcriptomes revealed that PLAC8 gene expression was positively correlated with platinum resistance ($R = 0.25$, $P<0.001$) (Figure 2G). However, after downregulating PLAC8 expression in HCT116, there was no significant difference in the half-maximal lethal dose of oxaliplatin among the groups ($P>0.05$) (Figure 2H). But, siRNA-mediated knockdown of PLAC8 in HCT116 cells significantly reduced cell migration ($P<0.001$), while PLAC8 overexpression in RKO cells led to a marked increase in cell migration ($P<0.01$) (Figure 2F).

3.4 AKT signaling and EMT mediate as critical mediators of PLAC8's biological functions

We also analyzed the potential functional pathways of the PLAC8 gene based on TCGA transcriptomic data, and the results

showed a positive correlation with the chemokine signaling pathway (R = 0.29, P<0.001) (Figure 3A). Western blot analysis of classical inflammation-related signaling pathways, including AKT, NF-κB, ERK, and STAT3, revealed that siRNA-mediated PLAC8 knockdown significantly reduced p-AKT levels, while p-STAT3 levels were markedly elevated. No significant changes were observed in p-NF-κB and p-ERK levels. In contrast, PLAC8 overexpression led to a significant increase in p-AKT levels, with no notable changes in p-STAT3, p-NF-κB, or p-ERK levels (Figure 3B).

After knockdown of PLAC8 expression using siRNA2 in HCT116 cells, migration and invasion were significantly reduced (P<0.001, P<0.001). However, when the AKT signaling pathway activator SC79 was added, cell migration and invasion significantly increased (P<0.001, P = 0.003) (Figure 3C). Similarly, PLAC8 overexpression in RKO cells led to increased cell migration and invasion (P<0.001, P = 0.009), while subsequent treatment with the AKT pathway inhibitor capivasertib significantly reduced cell migration and invasion (P<0.001, P<0.001) (Figure 3D).

After siRNA2-mediated PLAC8 knockdown in HCT116 cells, protein levels of p-AKT, N-cadherin, and Snail1 were significantly reduced, while the addition of the AKT signaling pathway activator SC79 resulted in increased in these protein levels (P<0.001, P = 0.003). However, E-cadherin levels did not show significant changes (Figure 3E). Similarly, after overexpressing PLAC8 in RKO cells, p-AKT, N-cadherin, and Snail1 protein levels were significantly elevated, and following treatment with the AKT pathway inhibitor capivasertib, these levels decreased significantly. E-cadherin levels remained unchanged (Figure 3E).

3.5 CCL28-activated STAT3 signaling drives PLAC8 transcription to promote colorectal cancer progression

Analyses of the TCGA database guided the research direction and hypothesis formulation in this study. Integrative bioinformatics interrogation revealed significant positive correlations between PLAC8 expression and key inflammatory mediators, including CCL28, CXCL1, ITK, JAK2, and STAT3 (correlation coefficients: 0.54, P = 8.25×10^{-49}; 0.27, P = 4.10×10^{-12}; 0.25, P = 1.02×10^{-10}, 0.26, P = 6.05×10^{-11}; 0.25, P = 1.68×10^{-10} respectively) (Figure 4A).

After treating HCT116 cells with the JAK/STAT3 inhibitor Ruxolitinib, PLAC8 expression was significantly reduced (P<0.001). Upon addition of the recombinant cytokine CCL28, PLAC8 expression was significantly elevated (P<0.01; P<0.001), whereas no significant change in PLAC8 expression was observed upon adding the recombinant chemokine CXCL1 (P>0.05) (Figure 4B). p-STAT3 expression exhibited a similar pattern to PLAC8 (Figure 4C).

After PLAC8 knockdown with siRNA2 in HCT116 cells, cell invasion was significantly reduced (P<0.001). However, when

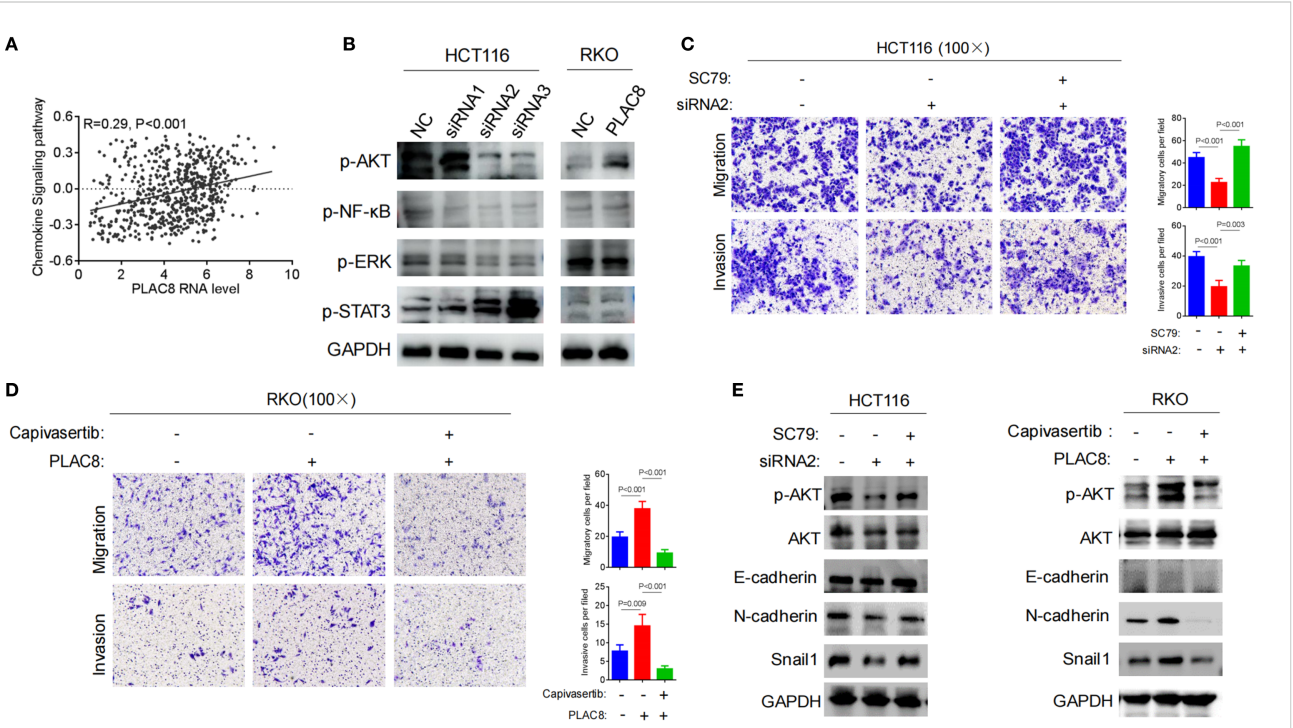

FIGURE 3
(A) TCGA-based bioinformatic analysis to explore PLAC8 involvement in chemokine signaling. **(B)** Effect of PLAC8 expression changes on inflammation and cytokine-related signaling pathways. **(C)** Reversal by AKT pathway activator SC79, the reduction in migration and invasion abilities induced by PLAC8 knockdown. **(D)** Reversal by AKT inhibitor capivasertib, the enhanced migration and invasion abilities of colorectal cancer cells induced by PLAC8 overexpression. **(E)** Effects of PLAC8 modulation and AKT pathway activator and inhibitor on EMT-related protein expression. (GSVA for enrichment).

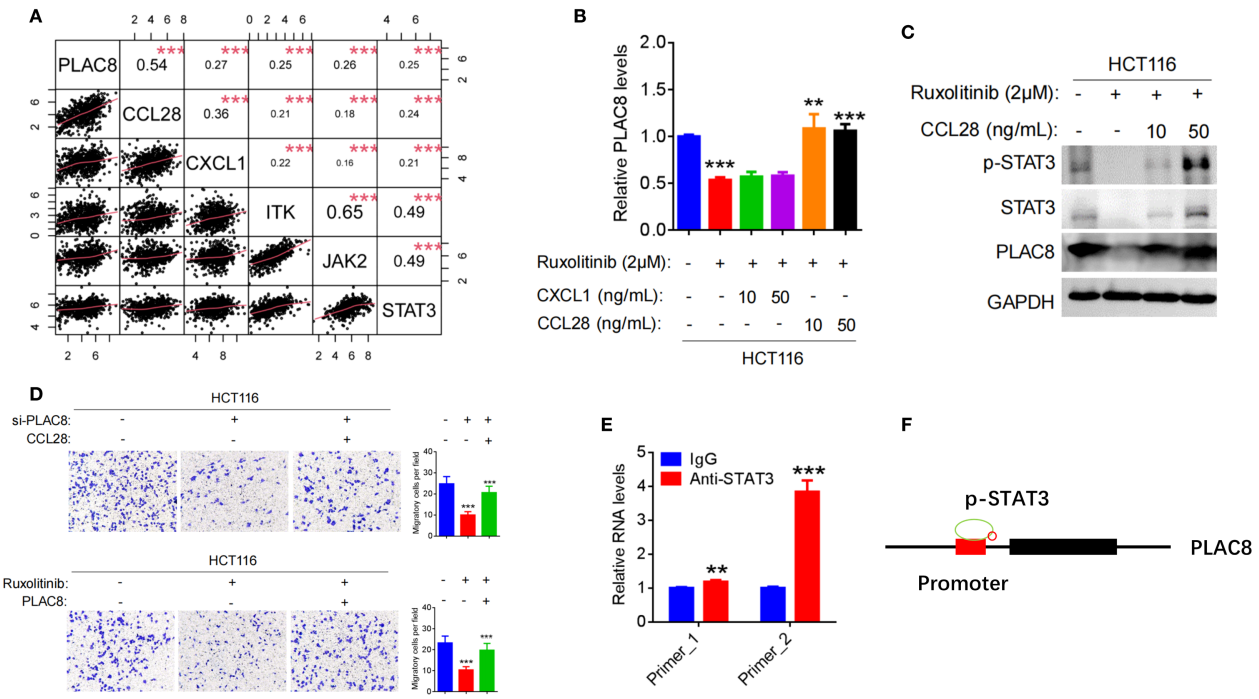

FIGURE 4
(A) Pearson correlation analysis between PLAC8 expression and the top five inflammatory cytokine pathways gene based on the TCGA database. **(B)** Regulation of PLAC8 mRNA expression by Ruxolitinib (STAT3 inhibitor), CXCL1, and CCL28. **(C)** Regulation of STAT3 signaling and PLAC8 protein expression by Ruxolitinib and CCL28. **(D)** Effects of combined PLAC8 knockdown and CCL28 treatment, or STAT3 inhibition and PLAC8 overexpression, on CRC cell migration. **(E, F)** Validation of STAT3 binding to the PLAC8 promoter by CUT&Tag. (**, and *** represent $P < 0.01$, and $P < 0.001$, respectively).

CCL28 was added, cell invasion significantly increased (P<0.001). Conversely, after PLAC8 overexpression in RKO cells, cell invasion increased (P<0.001), and addition of CCL28 resulted in a marked increase in invasion (P<0.001). After treatment with the JAK/STAT3 inhibitor Ruxolitinib, HCT116 cell invasion decreased significantly (P<0.001). However, PLAC8 overexpression after Ruxolitinib treatment led to a significant increase in cell invasion (P<0.001) (Figure 4D).

CUT&Tag experiment was performed using STAT3 antibody was performed to assess STAT3 binding enrichment in the PLAC8 promoter region. Two pairs of primers (Primer_1 and Primer_2) were used to detect DNA enrichment. Primers flanking STAT3-binding motifs at chr4:83115654-83115749 (Primer_1) and chr4:83115648-83115729 (Primer_2) showed 1.19-fold (P = 0.0037) and 3.84-fold (P < 0.001) enrichment vs. IgG. (Figure 4E).

4 Discussion

In recent years, the role of inflammation in CRC has received increasing attention. Chronic inflammation is recognized not only as a driving factor in the initiation and progression of CRC, but also plays a key role in tumor invasion, metastasis, and resistance to treatment (11).The inflammatory tumor microenvironment in CRC is highly complex, involving various immune cells, inflammatory mediators, and cytokines. Tumor-associated macrophages (TAMs), tumor-associated neutrophils (TANs), and other immune cells secrete pro-inflammatory cytokines (such as TNF-α, IL-6, and IL-1β) that activate signaling pathways like NF-κB and JAK/STAT3, promoting tumor cell proliferation, migration, metastasis, and epithelial-mesenchymal transition (EMT) (6). These immune populations not only fuel tumor progression but also orchestrate immune evasion. To investigate the mechanistic role of inflammation in CRC, various animal models have been developed to simulate this process. The AOM/DSS model is among the most widely used models in inflammation-cancer transition research. AOM is a known colorectal carcinogen, and DSS is a chemical agent that induces colitis. The combination of AOM and DSS is a commonly used model for studying inflammation-induced carcinogenesis in CRC. AOM induces DNA damage and gene mutations in colonic epithelial cells, while DSS induces chronic inflammation in the gut. DSS disrupts the intestinal barrier, promotes intestinal inflammation, and exacerbates the carcinogenic process. In this study, the AOM/DSS-induced mouse model of colorectal cancer was successfully established and a significant increase in PLAC8 expression during tumor formation, suggesting that PLAC8 may play an important role in the inflammation-cancer transition in CRC. We attempted to generate PLAC8 knockout mice using conventional gene targeting methods, but the resulting mice were non-viable. Future studies will employ conditional knockout strategies to circumvent this embryonic and validate metastasis-microenvironment links.

Numerous studies have identified PLAC8 as an oncogene associated with poor prognosis in various types of cancers. As a centrosomal oncoprotein, PLAC8 plays a pivotal role in driving colorectal cancer progression by promoting tumor growth and metastasis (21). A total of 78 CRC cases were included in this study. PLAC8 protein expression in tumor tissues and adjacent normal tissues was analyzed, and its association with clinicopathological characteristics and patient prognosis was evaluated. Results demonstrated that PLAC8 was significantly overexpressed in CRC tissues and negatively correlated with patient prognosis. Univariate Cox regression analysis confirmed that high PLAC8 expression, advanced T, N, and M stages, poor tumor differentiation, and elevated CA199 levels were significantly associated with advanced disease stage and poor prognosis. Moreover, multivariate Cox regression analysis identified high PLAC8 expression, higher TNM stage, and poor tumor differentiation as independent prognostic risk factors for CRC. In colorectal cancer, this study further confirms the oncogenic role of PLAC8 and demonstrated its association with tumor TNM stage, suggesting that PLAC8 may play an important role in tumor invasion and metastasis.

PLAC8 has been identified as a key regulator in the progression of various cancers by inducing tumorigenesis, modulating immune responses, promoting chemoresistance, and facilitating metastasis (22). It has been reported to activate the AKT signaling pathway, thereby enhancing sorafenib resistance in hepatocellular carcinoma (HCC) cells (23). PLAC8 promotes epithelial-mesenchymal transition (EMT) and cervical cancer progression (24), drives lung cancer cell proliferation via the Wnt/β-catenin signaling pathway (25), and modulates tamoxifen sensitivity through the MAPK/ERK signaling pathway (26). Furthermore, PLAC8 inhibits apoptosis, leading to radiotherapy resistance in nasopharyngeal carcinoma (NPC) cells (27), and suppresses autophagy, contributing to doxorubicin resistance in breast cancer and enhancing proliferation and EMT in NPC cells (28, 29). Additionally, PLAC8 has been identified as a key molecule in reshaping the tumor microenvironment of clear cell renal cell carcinoma (ccRCC), negatively impacting proliferation, invasion, migration, and immunotherapy efficacy (30). Although many studies suggest that PLAC8 functions as an oncogene, others report a tumor-suppressive role. For example, PLAC8 inhibits oral squamous cell carcinogenesis and EMT via the Wnt/β-catenin and PI3K/Akt/GSK3β signaling pathways (31). In this study, bioinformatics analysis revealed that PLAC8 might be involved in cytokine-related pathways and platinum-based drug resistance. However, subsequent biological functional experiments showed that PLAC8 expression had no significant impact on proliferation, colony formation, or oxaliplatin resistance in colorectal cancer cell lines. Notably, PLAC8 overexpression markedly enhanced cell migration. Further analysis of cytokine-related pathways demonstrated that PLAC8 robustly activated the AKT signaling pathway, while having minimal effects on NF-κB, ERK, and STAT3 pathways. EMT-related markers, including N-cadherin and Snail1, were significantly upregulated, while E-cadherin expression remained unchanged, suggesting that PLAC8 might promote colorectal cancer cell migration by activating the AKT signaling pathway and inducing EMT. Rescue experiments using the AKT pathway activator SC79 and inhibitor Capivasertib further confirmed that PLAC8 enhances EMT, migration, and invasion through the AKT signaling pathway. This result was also confirmed in another study (32).

PLAC8 has been shown in numerous studies to promote tumorigenic processes, including proliferation, metastasis, chemoresistance, and radiotherapy resistance, via classic signaling pathways such as AKT, ERK, and Wnt. However, relatively few studies have focused on the regulation of PLAC8 expression itself. Limited evidence suggests that miR-1228-3p, miR-664b-3p, and UFM1-mediated ubiquitination may play a role in regulating PLAC8 expression (23, 33, 34). PLAC8 also functions as a core downstream effector of the Id1-c-Myc axis, sustaining colorectal cancer stemness, promoting self-renewal, and conferring chemoresistance by activating Wnt/β-catenin and Shh signaling pathways (35). In this study, bioinformatics analysis identified the five genes most closely associated with PLAC8 expression as CCL28, CXCL1, ITK, JAK2, and STAT3. Correlation analyses derived from databases are inherently limited and lack direct biological significance; they primarily offer guidance for research direction selection but must be experimentally validated. Subsequent literature review and experimental validation revealed that STAT3, a transcription factor in the JAK-STAT3 signaling pathway, can directly bind to the PLAC8 promoter region, enhancing its activation and expression. CCL28, a mucosal-associated epithelial chemokine, is known to recruit various immune cells, modulate immune cell activation and chemotaxis in the tumor microenvironment, and exhibit tumor-suppressive functions (36). However, our study found that CCL28 acts as an upstream factor in activating the STAT3 signaling pathway and mediating PLAC8 expression, thereby promoting colorectal cancer cell migration. CUT&Tag assay confirmed that STAT3 directly bounding of STAT3 to the PLAC8 gene promoter region and indicating transcriptional regulation (Figure 4F). The STAT3 pathway inhibitor Ruxolitinib was shown to suppress PLAC8 expression by inhibiting STAT3 signaling, leading to a significant reduction in colorectal cancer cell migration. Rescue experiments demonstrated that this suppression could be reversed by CCL28, suggesting a critical role for CCL28 in this regulatory axis. These findings suggest that, in this context, CCL28 may exhibit oncogenic properties, which contrasts with other studies suggesting a tumor-suppressive role. This disparity highlights the complexity of CCL28's function, likely influenced by multiple factors in the tumor microenvironment.

PLAC8 and CCL28 have emerged as key regulators in the inflammation-to-cancer transition of CRC, particularly in shaping the tumor microenvironment (TME) and immune modulation. Recent studies have shown that both are involved in tumor immune evasion, immune cell infiltration, and immunotherapy response. PLAC8 influences CRC cell proliferation, migration, and invasion by modulating the TME. In clear cell renal cell carcinoma (ccRCC), its high expression correlates with poor prognosis and affects the cell cycle, ROS pathways, and immune infiltration, thereby impacting immunotherapy outcomes (30). In

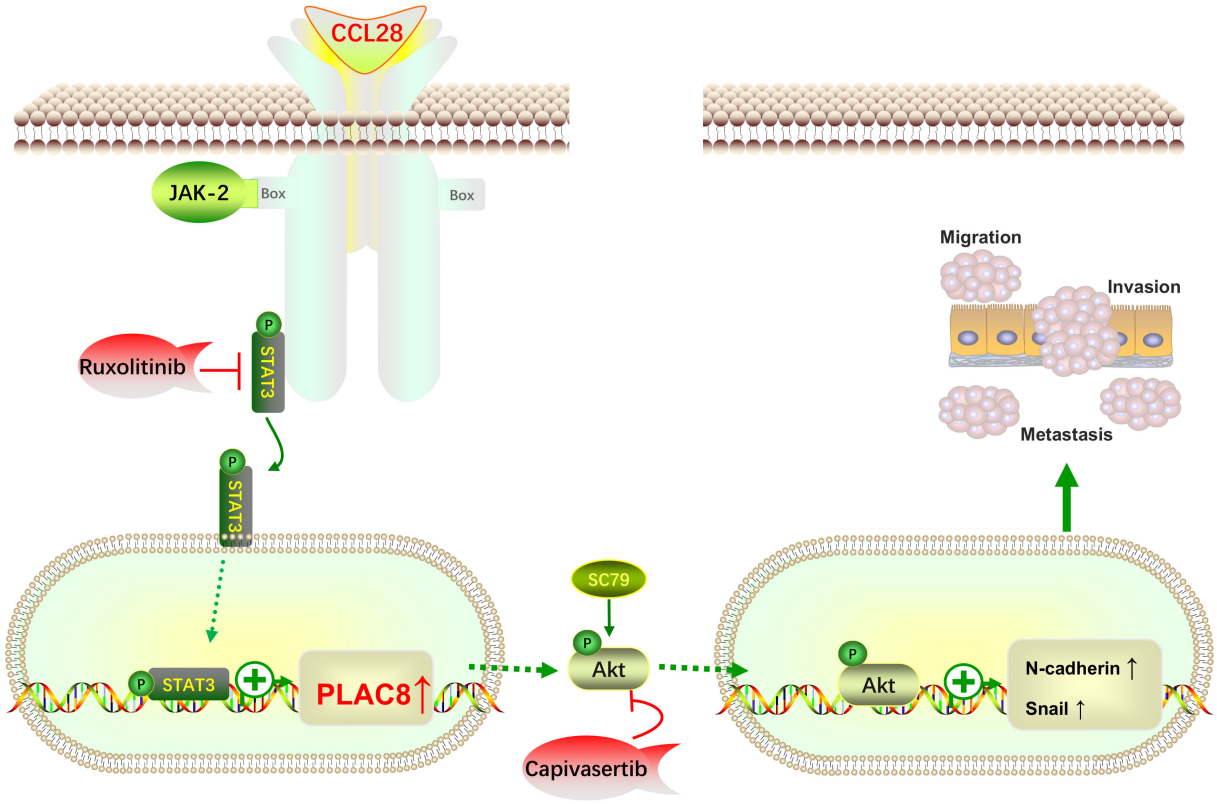

FIGURE 5
Schematic illustrating how the CCL28-STAT3-PLAC8 axis promotes EMT and enhances CRC invasion and metastasis via AKT signaling activation.

triple-negative breast cancer, PLAC8 regulates PD-L1 expression, suggesting a potential immunotherapy target (34). CCL28, similarly, has been shown to promote immune evasion. In CRC, SPDEF-induced CCL28 expression inhibits M2 macrophage polarization, limiting immune suppression (37). In lung cancer, CCL28 recruits regulatory T cells (Tregs), which may reduce immunotherapy efficacy (38). Preliminary data from our laboratory indicate a positive correlation between PLAC8 expression and T cell-mediated cytotoxicity. Together, these findings highlight PLAC8 and CCL28 as critical modulators of the TME and potential targets for cancer immunotherapy. Further studies on their mechanisms and immune interactions may help optimize therapeutic strategies across tumor types.

In conclusion, this study integrates clinical cases, animal models, cell-based experiments, and bioinformatics analyses to, for the first time, propose that CCL28 promotes PLAC8 expression through activation of the STAT3 signaling pathway. PLAC8 subsequently activates the AKT signaling pathway, driving EMT and facilitating colorectal cancer progression (Figure 5). PLAC8 is identified as a key factor in this process, playing a critical role in colorectal cancer cell migration and invasion. While the findings are primarily based on cellular experiments, further validation using larger cohorts of clinical samples is necessary to strengthen the evidence. Transient transfection sufficiently established acute signaling/phenotypic causality. Future *in vivo* and chronic interaction studies will employ lentiviral, shRNA, or CRISPR systems. Additionally, as a part of the inflammation-cancer transition, the role of immune cells and other components of the tumor microenvironment warrants further investigation. Our study identifies PLAC8 as a promising target for therapeutic intervention of colorectal cancer, offering new insights into its role in tumor progression and the broader context of the inflammation-cancer axis.

Data availability statement

The datasets presented in this study can be found in online repositories. The names of the repository/repositories and accession number(s) can be found in the article/Supplementary Material.

Ethics statement

The studies involving humans were approved by Medical Ethics Committee of Shanghai East Hospital. The studies were conducted in accordance with the local legislation and institutional requirements. The participants provided their written informed consent to participate in this study. The animal study was approved by Medical Ethics Committee of Shanghai East Hospital. The study was conducted in accordance with the local legislation and institutional requirements.

Author contributions

YY: Conceptualization, Data curation, Formal analysis, Visualization, Writing – original draft. QJ: Investigation, Methodology, Writing – review & editing. ZZ: Project administration, Formal analysis, Data curation, Writing – review & editing. SZ: Project administration, Software, Writing – review & editing. TD: Project administration, Methodology, Writing – review & editing. SS: Conceptualization, Supervision, Writing – review & editing, Formal analysis, Writing – original draft. XJ: Validation, Resources, Project administration, Writing – review & editing, Supervision, Conceptualization.

Funding

The author(s) declare financial support was received for the research and/or publication of this article. Leading talent project of Pudong New Area, Shanghai (PWR2021-04); Health and Family Planning Scientific Research Project of Pudong New Area Health Committee (No. PW2022A-32).

Conflict of interest

The authors declare that the research was conducted in the absence of any commercial or financial relationships that could be construed as a potential conflict of interest.

Generative AI statement

The author(s) declare that no Generative AI was used in the creation of this manuscript.

Any alternative text (alt text) provided alongside figures in this article has been generated by Frontiers with the support of artificial intelligence and reasonable efforts have been made to ensure accuracy, including review by the authors wherever possible. If you identify any issues, please contact us.

Publisher's note

All claims expressed in this article are solely those of the authors and do not necessarily represent those of their affiliated organizations, or those of the publisher, the editors and the reviewers. Any product that may be evaluated in this article, or claim that may be made by its manufacturer, is not guaranteed or endorsed by the publisher.

Supplementary material

The Supplementary Material for this article can be found online at: https://www.frontiersin.org/articles/10.3389/fimmu.2025.1610540/full#supplementary-material

References

1. Bray F, Laversanne M, Sung H, Ferlay J, Siegel RL, Soerjomataram I, et al. Global cancer statistics 2022: Globocan estimates of incidence and mortality worldwide for 36 cancers in 185 countries. *CA Cancer J Clin*. (2024) 74:229–63. doi: 10.3322/caac.21834

2. Han B, Zheng R, Zeng H, Wang S, Sun K, Chen R, et al. Cancer incidence and mortality in China, 2022. *J Natl Cancer Cent*. (2024) 4:47–53. doi: 10.1016/j.jncc.2024.01.006

3. Hanahan D, Weinberg RA. Hallmarks of cancer: the next generation. *Cell*. (2011) 144:646–74. doi: 10.1016/j.cell.2011.02.013

4. Hanahan D. Hallmarks of cancer: new dimensions. *Cancer Discov*. (2022) 12:31–46. doi: 10.1158/2159-8290.Cd-21-1059

5. Krugliak Cleveland N, Torres J, Rubin DT. What does disease progression look like in ulcerative colitis, and how might it be prevented? *Gastroenterology*. (2022) 162:1396–408. doi: 10.1053/j.gastro.2022.01.023

6. Shah SC, Itzkowitz SH. Colorectal cancer in inflammatory bowel disease: mechanisms and management. *Gastroenterology*. (2022) 162:715–30.e3. doi: 10.1053/j.gastro.2021.10.035

7. Schmitt M, Greten FR. The inflammatory pathogenesis of colorectal cancer. *Nat Rev Immunol*. (2021) 21:653–67. doi: 10.1038/s41577-021-00534-x

8. Muthusami S, Ramachandran IK, Babu KN, Krishnamoorthy S, Guruswamy A, Queimado L, et al. Role of inflammation in the development of colorectal cancer. *Endocr Metab Immune Disord Drug Targets*. (2021) 21:77–90. doi: 10.2174/1871530320666200909092908

9. Li L, Yu R, Cai T, Chen Z, Lan M, Zou T, et al. Effects of immune cells and cytokines on inflammation and immunosuppression in the tumor microenvironment. *Int Immunopharmacol*. (2020) 88:106939. doi: 10.1016/j.intimp.2020.106939

10. Amin MN, Siddiqui SA, Ibrahim M, Hakim ML, Ahammed MS, Kabir A, et al. Inflammatory cytokines in the pathogenesis of cardiovascular disease and cancer. *SAGE Open Med*. (2020) 8:2050312120965752. doi: 10.1177/2050312120965752

11. Wang M, Chen S, He X, Yuan Y, Wei X. Targeting inflammation as cancer therapy. *J Hematol Oncol*. (2024) 17:13. doi: 10.1186/s13045-024-01528-7

12. Hou J, Karin M, Sun B. Targeting cancer-promoting inflammation - have anti-inflammatory therapies come of age? *Nat Rev Clin Oncol*. (2021) 18:261–79. doi: 10.1038/s41571-020-00459-9

13. Zhang T, Fu JN, Chen GB, Zhang X. Plac8-Erk pathway modulation of monocyte function in sepsis. *Cell Death Discov*. (2024) 10:308. doi: 10.1038/s41420-024-02012-4

14. Caldwell BA, Wu Y, Wang J, Li L. Altered DNA methylation underlies monocyte dysregulation and immune exhaustion memory in sepsis. *Cell Rep*. (2024) 43:113894. doi: 10.1016/j.celrep.2024.113894

15. Gravrand V, Mellot F, Ackermann F, Ballester MC, Zuber B, Kirk JT, et al. Stratification of Covid-19 severity using septicyte rapid, a novel host immune response test. *Viruses*. (2023) 15:419. doi: 10.3390/v15020419

16. Wu Y, Caldwell B, Wang J, Zhang Y, Li L. Alleviation of monocyte exhaustion by Bcg derivative mycolic acid. *iScience*. (2024) 27:108978. doi: 10.1016/j.isci.2024.108978

17. Jones RL. Gut microbiome as a potential biomarker of cancer risk in inflammatory bowel disease. *Contemp Oncol (Pozn)*. (2022) 26:40–3. doi: 10.5114/wo.2022.114537

18. Fu H, Lu X, Ji T, Wang L, Wang G, Wang L, et al. Integrated analysis of colorectal cancer metastasis identifies characteristics of tumor cell during metastasis. *Gastroenterol Rep (Oxf)*. (2024) 12:goae055. doi: 10.1093/gastro/goae055

19. Guo C, Xie B, Liu Q. Weighted gene co-expression network analysis combined with machine learning validation to identify key hub biomarkers in colorectal cancer. *Funct Integr Genomics*. (2022) 23:24. doi: 10.1007/s10142-022-00949-2

20. Bozic D, Baralić K, Živančević K, Miljaković EA, Ćurčić M, Antonijević B, et al. Predicting sulforaphane-Induced adverse effects in colon cancer patients via in silico investigation. *BioMed Pharmacother*. (2022) 146:112598. doi: 10.1016/j.biopha.2021.112598

21. Huang CC, Shen MH, Chen SK, Yang SH, Liu CY, Guo JW, et al. Gut butyrate-producing organisms correlate to placenta specific 8 protein: importance to colorectal cancer progression. *J Adv Res*. (2020) 22:7–20. doi: 10.1016/j.jare.2019.11.005

22. Mao M, Cheng Y, Yang J, Chen Y, Xu L, Zhang X, et al. Multifaced roles of Plac8 in cancer. *biomark Res*. (2021) 9:73. doi: 10.1186/s40364-021-00329-1

23. Zhang Y, Pan Q, Shao Z. Extracellular vesicles derived from cancer-associated fibroblasts carry tumor-promotive microrna-1228-3p to enhance the resistance of hepatocellular carcinoma cells to sorafenib. *Hum Cell*. (2023) 36:296–311. doi: 10.1007/s13577-022-00800-7

24. Deng B, Zhang S, Zhou Y, Zhu Y, Fei J, Li A. Plac8 contributes to the Malignant behaviors of cervical cancer cells by activating the Sox4-mediated Akt pathway. *Histochem Cell Biol*. (2023) 159:439–51. doi: 10.1007/s00418-022-02175-0

25. Chen W, Wu J, Wang W, Yu L, Xu X. Plac8 overexpression promotes lung cancer cell growth via Wnt/β-catenin signaling. *J Immunol Res*. (2022) 2022:8854196. doi: 10.1155/2022/8854196

26. Mao M, Hu D, Yang J, Chen Y, Zhang X, Shen J, et al. Regulation of tamoxifen sensitivity by the Plac8/Mapk pathway axis is antagonized by curcumin-induced protein stability change. *J Mol Med (Berl)*. (2021) 99:845–58. doi: 10.1007/s00109-021-02047-5

27. Shen LJ, Qi CL, Yang R, Huang ML, Zou Y, Jiang Y, et al. Plac8 gene knockout increases the radio-sensitivity of xenograft tumors in nude mice with nasopharyngeal carcinoma by promoting apoptosis. *Am J Transl Res*. (2021) 13:5985–6000.

28. Chen Y, Jia Y, Mao M, Gu Y, Xu C, Yang J, et al. Plac8 promotes adriamycin resistance via blocking autophagy in breast cancer. *J Cell Mol Med*. (2021) 25:6948–62. doi: 10.1111/jcmm.16706

29. Huang ML, Qi CL, Zou Y, Yang R, Jiang Y, Sheng JF, et al. Plac8-mediated autophagy regulates nasopharyngeal carcinoma cell function via Akt/Mtor pathway. *J Cell Mol Med*. (2020) 24:7778–88. doi: 10.1111/jcmm.15409

30. Sun X, Liu Z, Yu Q, Chen Y, Sun Y, Zhu Q, et al. Plac8 is an innovative biomarker for immunotherapy participating in remodeling the immune microenvironment of renal clear cell carcinoma. *Front Oncol*. (2023) 13:1207551. doi: 10.3389/fonc.2023.1207551

31. Wu J, Wang X, Shang A, Vella G, Sun Z, Ji P, et al. Plac8 inhibits oral squamous cell carcinogenesis and epithelial-mesenchymal transition via the Wnt/β-catenin and Pi3k/Akt/Gsk3β Signaling pathways. *Oncol Lett*. (2020) 20:128. doi: 10.3892/ol.2020.11989

32. Hung CS, Wang YC, Guo JW, Yang RN, Lee CL, Shen MH, et al. Expression pattern of placenta specific 8 and keratin 20 in different types of gastrointestinal cancer. *Mol Med Rep*. (2020) 21:659–66. doi: 10.3892/mmr.2019.10871

33. Chen L, Niu W, Zhu D, Shao W, Qian Y. Long noncoding rna Hoxd-As1 promotes the progression of pancreatic cancer through Mir-664b-3p/Plac8 axis. *Pathol Res Pract*. (2022) 232:153836. doi: 10.1016/j.prp.2022.153836

34. Mao M, Chen Y, Yang J, Cheng Y, Xu L, Ji F, et al. Modification of Plac8 by Ufm1 affects tumorous proliferation and immune response by impacting Pd-L1 levels in triple-negative breast cancer. *J Immunother Cancer*. (2022) 10:e005668. doi: 10.1136/jitc-2022-005668

35. Sun Y, Lai X, Yu Y, Li J, Cao L, Lin W, et al. Inhibitor of DNA binding 1 (Id1) mediates stemness of colorectal cancer cells through the Id1-C-Myc-Plac8 axis via the Wnt/β-catenin and Shh signaling pathways. *Cancer Manag Res*. (2019) 11:6855–69. doi: 10.2147/cmar.S207167

36. Mohan T, Deng L, Wang BZ. Ccl28 chemokine: an anchoring point bridging innate and adaptive immunity. *Int Immunopharmacol*. (2017) 51:165–70. doi: 10.1016/j.intimp.2017.08.012

37. Li S, Zhang N, Yang Y, Liu T. Transcriptionally activates Ccl28 expression to inhibit M2 polarization of macrophages and prevent immune escape in colorectal cancer cells. *Transl Oncol*. (2024) 40:101842. doi: 10.1016/j.tranon.2023.101842

38. Su X, Wang G, Zheng S, Ge C, Kong F, Wang C. Comprehensive explorations of Ccl28 in lung adenocarcinoma immunotherapy and experimental validation. *J Inflammation Res*. (2023) 16:1325–42. doi: 10.2147/jir.S399193

frontiers | Frontiers in Immunology

TYPE Mini Review
PUBLISHED 03 November 2025
DOI 10.3389/fimmu.2025.1678907

Check for updates

OPEN ACCESS

EDITED BY
Qi Wang,
Jiangsu University, China

REVIEWED BY
Shitang Ma,
West Anhui University, China

*CORRESPONDENCE
Shengshan Xu
xushengshan97@163.com
Hongyu Chu
zhuhy20@mails.jlu.edu.cn
Xuedong Fang
fangxd@jlu.edu.cn

RECEIVED 03 August 2025
ACCEPTED 14 October 2025
PUBLISHED 03 November 2025

CITATION
Wang Y, Lu K, Xu Y, Xu S, Chu H and Fang X (2025) Antibody-drug conjugates as immuno-oncology agents in colorectal cancer: targets, payloads, and therapeutic synergies. *Front. Immunol.* 16:1678907. doi: 10.3389/fimmu.2025.1678907

COPYRIGHT
© 2025 Wang, Lu, Xu, Xu, Chu and Fang. This is an open-access article distributed under the terms of the Creative Commons Attribution License (CC BY). The use, distribution or reproduction in other forums is permitted, provided the original author(s) and the copyright owner(s) are credited and that the original publication in this journal is cited, in accordance with accepted academic practice. No use, distribution or reproduction is permitted which does not comply with these terms.

Antibody-drug conjugates as immuno-oncology agents in colorectal cancer: targets, payloads, and therapeutic synergies

Yihan Wang[1], Kai Lu[1], Yang Xu[1], Shengshan Xu[2]*, Hongyu Chu[1,3]* and Xuedong Fang[1,3]*

[1]ChinaJapan Union Hospital of Jilin University, Changchun, China, [2]Department of Thoracic Surgery, Jiangmen Central Hospital, Jiangmen, Guangdong, China, [3]Department of Gastrointestinal and Colorectal Surgery, ChinaJapan Union Hospital of Jilin University, Changchun, China

Colorectal cancer (CRC), particularly the immunologically "cold" microsatellite-stable (MSS) subtype, remains profoundly resistant to immune checkpoint inhibitors. Antibody-drug conjugates (ADCs) are rapidly emerging as a transformative therapeutic modality poised to overcome this challenge. This review reframes ADCs beyond their role as targeted cytotoxics, repositioning them as sophisticated immuno-oncology agents. The central thesis is that by strategically selecting payloads such as topoisomerase inhibitors or auristatins, modern ADCs can induce immunogenic cell death (ICD) or pyroptosis. This mechanism effectively functions as an *in situ* vaccine, transforming the tumor microenvironment from "cold" to "hot" by promoting dendritic cell activation and T-cell infiltration. We provide a comprehensive overview of the ADC landscape, examining key targets on bulk tumor cells (CEACAM5, HER2), cancer stem cells (LGR5, GPR56), and stromal components. We conclude that the future of ADCs in CRC lies in their rational application as immune-priming agents, creating powerful synergies in combination with checkpoint inhibitors to break therapeutic resistance and durably improve patient outcomes.

KEYWORDS

colorectal cancer, microsatellite stable, antibody-drug conjugate, immunoconjugate, immuno-oncology

1 Introduction

Colorectal cancer (CRC) remains a major global health burden, ranking as the third most frequently diagnosed cancer and the second leading cause of cancer-related mortality worldwide (1), with over 1.9 million new cases and approximately 935,000 deaths reported in 2020 (2). While standard treatments, including chemotherapy and targeted agents, form the backbone of systemic therapy, their efficacy is often curtailed by tumor heterogeneity and

acquired resistance (3). More critically, the transformative success of immune checkpoint inhibitors (ICIs) has not extended to the majority of CRC patients, whose tumors are microsatellite-stable (MSS). These immunologically "cold" tumors are characterized by a non-inflamed tumor microenvironment (TME) that lacks T-cell infiltration, rendering them profoundly resistant to current immunotherapies (4–6). This reality underscores an urgent need for novel therapeutic strategies capable of inducing a robust, *de novo* anti-tumor immune response.

Antibody-drug conjugates (ADCs) have emerged as a powerful therapeutic modality uniquely positioned to bridge the gap between targeted chemotherapy and immunotherapy (7). An ADC consists of a monoclonal antibody targeting a tumor-associated antigen, a highly potent cytotoxic payload, and a chemical linker. However, beyond their original design as "magic bullets," modern ADCs are increasingly engineered as sophisticated immuno-oncology agents. This advanced function is achieved through the strategic selection of payloads-such as topoisomerase inhibitors or microtubule inhibitors-that are potent inducers of immunogenic cell death (ICD) or other pro-inflammatory pathways like pyroptosis. By forcing cancer cells to die in an immunologically active manner, these ADCs can effectively transform the tumor into an *in situ* vaccine, triggering the release of danger signals and tumor antigens that awaken the immune system (8). The landmark approvals of agents like trastuzumab deruxtecan and sacituzumab govitecan have validated this dual-action approach, demonstrating that ADCs can produce durable responses even in heavily pretreated patient populations (9–11).

In CRC, this dual mechanism holds immense promise for overcoming the intrinsic resistance of MSS tumors. By delivering an immunogenic payload directly to tumor cells, ADCs can initiate an inflammatory cascade, remodel the immunosuppressive TME, and prime a T-cell-mediated immune attack. This provides a compelling rationale for combining ADCs with checkpoint inhibitors to create potent synergistic effects. The expanding landscape of ADC targets in CRC now includes not only antigens on bulk tumor cells (CEACAM5, HER2), but also those on cancer stem cells (LGR5) and critical stromal components (CEACAM6), offering multiple avenues to dismantle the tumor ecosystem.

This review provides a comprehensive overview of the ADC landscape in CRC, framed through an immuno-oncological perspective. We will dissect their molecular architecture and mechanisms of action, with a special focus on their ability to modulate the immune system. We will then survey the key therapeutic targets-from established to emerging-and discuss how they can be leveraged as specific gateways for delivering immunogenic payloads. Moreover, we will explore how ADCs are poised to reshape CRC treatment paradigms, not as standalone agents, but as cornerstone therapies in the next generation of rational, immune-based combination strategies.

1.1 Literature search strategy

A systematic literature search was performed using PubMed/MEDLINE, Embase, Web of Science, and ClinicalTrials.gov databases through September 2025. The search strategy combined MeSH terms and keywords with Boolean operators, encompassing: (1) disease terms ("colorectal cancer" OR "colorectal neoplasms"[MeSH] OR "CRC" OR "microsatellite stable"); (2) intervention terms ("antibody-drug conjugate" OR "immunoconjugate" OR "ADC"); and (3) mechanism terms ("immuno-oncology" OR "immunogenic cell death" OR "ICD" OR "pyroptosis" OR "tumor microenvironment" OR "TME" OR "combination therapy"). Additional targeted searches were conducted for specific ADC targets and agents (e.g., CEACAM5, HER2, trastuzumab deruxtecan, LGR5). Besides, peer-reviewed original research articles, clinical trials, authoritative reviews, and relevant conference abstracts from major oncology meetings (ASCO, ESMO) published in English were included. Studies were selected based on their relevance to ADCs as immuno-oncology agents in CRC. Case reports without mechanistic insights and editorials were excluded. Reference lists of included articles were manually screened to identify additional relevant publications.

2 Structure, mechanism of action and immune regulation of ADC

2.1 Structure of ADC

ADCs comprise three core elements: a tumor-targeting monoclonal antibody, a chemical linker, and a cytotoxic payload. Therapeutic efficacy depends on optimal integration of target antigen selection, antibody format, linker stability, payload potency, and conjugation chemistry (Figure 1). Ideal target antigens exhibit high tumor-specific expression (>10^5 copies/cell), minimal normal tissue expression, efficient internalization, and limited shedding (12, 13). In CRC, promising targets include HER2, TROP2, CEACAM5, and mesothelin, each with distinct expression patterns and internalization kinetics.

The antibody backbone, typically humanized IgG1, provides targeting specificity and immune effector functions. IgG1 predominates (used in T-DXd, T-DM1, sacituzumab govitecan) due to its long half-life (~21 days) and ability to mediate Antibody-Dependent Cell-mediated Cytotoxicity (ADCC) and Complement-Dependent Cytotoxicity (CDC) (14–16). IgG4 variants reduce immune activation when inflammatory toxicity is a concern, though this may compromise immune-mediated effects (17). Antibody engineering, including Fc modifications, can optimize pharmacokinetics and safety profiles (18).

Linker chemistry critically balances plasma stability with intracellular payload release. Cleavable linkers (protease-sensitive valine-citrulline, pH-sensitive hydrazones, glutathione-reducible disulfides) enable controlled payload release and bystander effects (19, 20). Non-cleavable linkers require complete antibody degradation, offering superior stability but limited bystander activity (21, 22). Modern site-specific conjugation using engineered cysteines, enzymatic methods, or glycan remodeling yields homogeneous products with optimized drug-to-antibody ratios (DAR) (23–26). While traditional ADCs employed DAR 2-

4, next-generation ADCs like T-DXd achieve DAR ~8 through improved linker-payload design (27, 28).

Payload selection determines cytotoxicity, resistance profiles, and immunogenic potential. Payloads with IC50 values in picomolar to low nanomolar range are categorized by mechanism: microtubule inhibitors, DNA-damaging agents (PBD dimers), and topoisomerase I inhibitors (DXd) (29).Membrane-permeable payloads like MMAE enable bystander killing of antigen-negative cells, while charged molecules (MMAF) remain cell-confined (30–33) DNA-damaging agents offer distinct advantages: topoisomerase I inhibitors provide broader therapeutic windows enabling higher DAR and reduced MDR1-mediated resistance (34, 35). PBD dimers show extreme potency but hepatotoxicity concerns in CRC, DXd-based ADCs demonstrate particular promise given their superior immunogenic cell death induction and favorable safety profiles, making them ideal for immunotherapy combinations (36). Payload hydrophobicity influences ADC stability-hydrophilic modifications enable higher drug loading without compromising pharmacokinetics.

2.2 Mechanisms of action

2.2.1 Targeted delivery and intracellular processing

ADC action initiates through high-affinity antigen binding, embodying the "magic bullet" concept (37). Beyond targeted delivery, some ADCs exert direct antitumor effects through receptor signaling interference without payload release (38). Following receptor-mediated endocytosis primarily via clathrin-dependent pathways (39), ADCs traffic through endolysosomal systems where pH changes and proteolytic enzymes trigger linker cleavage (40). The intracellular fate depends on linker design-acid-labile bonds dissociate at lysosomal pH, protease-cleavable peptides undergo enzymatic hydrolysis, while disulfide bonds reduce in cytoplasmic environments. Once released, microtubule inhibitors disrupt mitotic spindle formation (41), while DNA-damaging agents induce strand breaks and apoptosis, with some payloads additionally triggering immunogenic cell death pathways (34, 42).

2.2.2 Bystander effect as immune amplifier

The bystander effect represents a critical mechanism for overcoming CRC heterogeneity (43). This phenomenon depends on payload diffusion from targeted cells to eliminate adjacent antigen-negative populations (32, 44). Novel strategies like caspase-3-cleavable linkers create amplification loops where apoptosis triggers extracellular ADC cleavage (45). Importantly, bystander-mediated killing extends beyond cytotoxicity-dying cells release DAMPs and tumor antigens, spatially amplifying signals throughout the TME. This converts immunologically "cold" regions into "hot" zones, enhancing dendritic cell recruitment and T-cell priming across the entire tumor mass. The membrane permeability of payloads determines the extent of this effect: hydrophobic molecules like DXd and SN-38 freely traverse cell membranes to eliminate neighboring cells, while charged payloads remain confined. This spatial extension of both cytotoxic and immunogenic effects transforms heterogeneous tumors into more uniformly targeted tissues, creating a foundation for the comprehensive immune response.

2.3 Immunomodulatory mechanisms of antibody-drug conjugates

Beyond direct cytotoxicity, ADCs demonstrate capacity to modulate antitumor immune responses through multiple mechanisms engaging various stages of the cancer-immunity cycle (46).

2.3.1 Payload-induced immunogenic cell death

Colorectal cancer presents distinct immunological landscapes across molecular subtypes that shape therapeutic opportunities for ADC development. The predominant microsatellite stable (MSS) phenotype, comprising 85% of cases, exhibits an immunologically inert tumor microenvironment characterized by sparse lymphocyte infiltration and minimal neoantigen presentation, rendering these tumors refractory to checkpoint blockade. In contrast, the microsatellite instability-high (MSI-H) subset demonstrates robust immune infiltration yet develops alternative resistance mechanisms. This dichotomy underscores the need for ADCs capable of immunological reprogramming, particularly in converting immunologically "cold" MSS tumors into inflamed, treatment-responsive phenotypes.

Cytotoxic payloads transform tumor cell death into immunological priming events through DNA damage or microtubule disruption. This process generates three immunogenic signals: damage-associated molecular patterns (DAMPs) including ATP as chemotactic "find me" signals, HMGB1-TLR4 interactions driving DC maturation, and surface calreticulin serving as phagocytic "eat me" signals; enhanced tumor antigen cross-presentation; and pro-inflammatory cytokine release (IFN-γ, IL-1β, IL-6) recruiting effector lymphocytes (36, 47–49). Furthermore, cytokines and chemokines released by dying tumor cells following ADC treatment can recruit and activate various immune cells, including macrophages and natural killer (NK) cells, thereby further promoting antitumor responses (50).

Different payload classes exhibit distinct ICD profiles. DNA-damaging agents, particularly deruxtecan and camptothecin derivatives, induce robust DAMP release and type I interferon responses. In an *in vivo* study, T-DXd treatment resulted in increased expression of PD-L1 and MHC class I molecules on cancer cells (35).Pyrrolobenzodiazepine dimers generate more limited ICD despite high potency. Among microtubule inhibitors, maytansinoids (DM1/DM4) and auristatins (MMAE/MMAF) trigger ICD through mitotic, with membrane-permeable MMAE enabling bystander ICD amplification (39, 40). Interestingly, microtubule-depolymerizing payloads (such as vinca alkaloids) have been shown to induce dendritic cell maturation, while the same property has not been observed with microtubule-stabilizing agents (such as taxanes) (51). Alternative death modalities-

pyroptosis through gasdermin pores, ferroptosis via lipid peroxidation, and necroptosis through RIPK3/MLKL-provide additional inflammatory signals that sustain immune activation.

2.3.2 Antibody-mediated immune effector functions

The Fc domain mediates payload-independent immunity through antibody-dependent cell-mediated cytotoxicity (ADCC), antibody-dependent cellular phagocytosis (ADCP), and CDC mechanisms. ADCC involves IgG1-based ADCs engaging FcγRIIIA receptors on natural killer cells, triggering cytotoxic granule release for target cell lysis. For instance, trastuzumab-based ADCs demonstrate particularly robust NK cell-mediated killing of HER2-positive tumor cells. ADCP occurs when the Fc region binds FcγRI/II receptors on macrophages, promoting tumor cell engulfment and destruction, with studies showing T-DM1 enhances macrophage phagocytic activity in preclinical models. CDC is initiated when C1q binds to clustered Fc domains, activating the complement cascade that both forms membrane attack complexes for direct cell lysis and generates anaphylatoxins (C3a/C5a) to recruit and activate myeloid cells. Beyond these primary mechanisms, ADC-antigen immune complexes enhance cross-presentation through FcγR-dependent uptake by antigen-presenting cells (APCs), broadening the immune response. These effector functions remain operational against cells with defective endocytosis, ensuring therapeutic activity across heterogeneous tumor populations. This antibody-driven inflammation synergizes with payload-induced ICD, creating multiple complementary immune activation pathways that maintain efficacy despite variable antigen expression or payload resistance.

2.3.3 TME reprogramming and therapeutic synergies

ADCs orchestrate comprehensive immune landscape remodeling. Previous studies have demonstrated ADC-mediated immune modulation across multiple cell populations: T-DM1 treatment polarizes tumor-associated macrophages from M2 to M1 phenotypes through TLR4/SCARA5 modulation, while sacituzumab govitecan enhances macrophage phagocytic activity (52). NK cells undergo dual activation via Fc-dependent mechanisms and stress ligand recognition, with trastuzumab-based ADCs showing particularly robust NK cell engagement (53, 54). The lymphocyte compartment experiences selective modulation-ADC treatment induces chemokine gradients (CXCL9, CCL3/4) that recruit effector T cells while regulatory populations undergo preferential depletion, as observed in T-DXd-treated tumors where Treg/$CD8^+$ ratios shift favorably toward antitumor responses (55–57).

This comprehensive TME reprogramming creates strategic therapeutic synergies, particularly with immune checkpoint inhibitors. In colorectal cancer, the differential TME landscapes between MSI-H (~15%, immune-infiltrated) and MSS (~85%, immune-excluded) tumors dictate therapeutic responses (58). ADC-mediated TME reprogramming is especially transformative for "cold" MSS tumors: barrier disruption and immune cell recruitment, combined with checkpoint upregulation (PD-L1/CTLA-4), convert these ICI-resistant tumors into responsive phenotypes. This TME reprogramming immune activation has shown clinical validation, with a HER2-positive/RAS-mutant/MSS case achieving >10 months PFS using T-DXd plus serplulimab (58). Novel combinations advancing through trials include disitamab vedotin with tislelizumab (NCT05493683) and SBT6050-a HER2-targeting ADC carrying TLR8 agonist payload that directly bridges cytotoxic and immunostimulatory mechanisms (NCT04460456) (59). These multi-faceted immunomodulatory effects position ADCs as crucial enablers for converting ICI-resistant MSS tumors into treatment-responsive phenotypes.

3 Major ADC targets and drugs

ADCs exert antitumor effects by targeting surface antigens and delivering cytotoxic agents. In CRC, these targets can be categorized into those expressed on tumor cell surfaces and those found on cancer stem-like cells (CSCs). Tumor cell-associated targets allow broad cytotoxic coverage, while stem cell-associated targets focus on eliminating therapy-resistant populations. The following sections summarize the major ADC targets in CRC and their corresponding drug candidates under development or clinical evaluation (Table 1). The distribution of targets and associated payloads across different cell types is illustrated in Figure 2.

3.1 Targets on the surface of colorectal cancer cells

3.1.1 HER2

HER2 amplification occurs in 3-5% of metastatic CRC, though its expression is limited compared to breast and gastric cancers. T-DXd (trastuzumab deruxtecan) has achieved clinical approval and demonstrates significant efficacy in HER2-positive CRC patients, representing a major therapeutic advance for this molecularly defined subgroup. Disitamab vedotin (RC48) has shown activation of the innate immune cGAS-STING pathway through antibody-mediated relief of HER2's inhibitory effect on STING, producing type I interferons that enhance antigen presentation and promote cytotoxic T-cell infiltration (60, 61). Beyond T-DXd and RC48, key HER2-directed ADCs include A166 (trastuzumab-based; Val-Cit cleavable linker; Duostatin-5/auristatin; DAR≈2) (62), ZW49/zanidatamab zovodotin (biparatopic HER2; protease-cleavable; auristatin ZD02044; DAR≈2), SHR-A1811/trastuzumab rezetecan (camptothecin/Topoisomerase-I payload; DAR≈5.7), and SBT6050 (HER2-targeted TLR8 agonist; discontinued). Together they diversify payload class (microtubule vs Top1 vs immune-stimulatory) and seek better efficacy/safety in $HER2^+$ CRC.

3.1.2 CEACAM5

CEACAM5 is overexpressed in ~80-90% of CRC and associates with poorer outcomes. Tusamitamab ravtansine (DM4, a maytansinoid microtubule inhibitor) showed manageable safety in

TABLE 1 Ongoing and completed clinical trials of antibody-drug conjugates in colorectal cancer.

NCT	Drug (ADC)	Phase	N	Key results	Target	Status
NCT03384940	T-DXd (Trastuzumab deruxtecan)	II	86	HER2$^+$: ORR 45.3%, mPFS 6.9 mo, mOS 15.5 mo; HER2$^-$: ORR 0%	HER2	Completed
NCT04744831	T-DXd	II	122	5.4 mg/kg: ORR 37.8%, mPFS 5.8 mo, mOS 13.4 mo; 6.4 mg/kg: ORR 27.5%, mPFS 5.5 mo	HER2	Completed
NCT03602079	A166	I/II	49	Phase I/II completed; no efficacy data reported	HER2	Completed
NCT03821233	ZW49	I	112	Phase I completed; awaiting efficacy data	HER2	Completed
NCT04513223	SHR-A1811	I	101	Ongoing study in GC/GEJ and CRC	HER2	Active, not recruiting
NCT04479436	U3-1402 (Patritumab deruxtecan)	I/II	–	–	HER3	Terminated
NCT05029882	ABBV-400 (Telisotuzumab adizutecan)	I	122	2.4 mg/kg: ORR 15%, mPFS 5.3 mo; 3.0 mg/kg: ORR 20%, mPFS 4.5 mo	c-Met	Active
NCT05464030	M9140 (Precem-TcT)	I	40	ORR 7.5%, mPFS 5.9 mo; ≥2.4 mg/kg: mPFS 6.7 mo	CEACAM5	Active
NCT02187848	SAR408701 (Tusamitamab ravtansine)	I/II	43	ORR 45%, DCR 83%	CEACAM5	Completed
NCT01605318	IMMU-130 (Labetuzumab govitecan)	I/II	–	Safety, ORR pending	CEACAM5	Active
NCT06265688	CX-2051	I	25	Expansion doses (n=18): ORR 28%, DCR 94%, mPFS 5.8 mo; 10 mg/kg: ORR 43%	EpCAM	Active
NCT06243393	Sacituzumab Govitecan (SG)	II/III	–	Tumor response rate, Safety, PFS pending	Trop-2	Active
NCT05639156	T4H11-DM4	I	–	Safety, DLT, RP2D pending	DDR1	Active
NCT04622774	IMGC936	I	–	Safety, Pharmacokinetics, MTD pending	ADAM9	Active
NCT07106892	HLX43 (PD-L1 ADC)	II	60 (planned)	Primary endpoint: ORR by IRRC; Secondary: PFS, OS	PD-L1	Not yet recruiting
NCT05493683	Disitamab vedotin + Tislelizumab	II	29 (estimated)	Ongoing - Primary endpoint: ORR; Secondary: PFS, OS, DCR, DOR	HER2	Active
NCT05489211	Datopotamab deruxtecan (Dato-DXd)	II	582 (estimated)	Ongoing - TROPION-PanTumor03 (Substudy 5 for CRC)	TROP2	Active
NCT04410224	ASN004	I	19	Dose escalation completed - MTD determined	5T4	Completed
NCT04460456	SBT6050 + PD-1 inhibitor	I/Ib	58	FIH study - evaluating safety and efficacy	HER2	Active

ORR, objective response rate; mPFS, median progression-free survival; mOS, median overall survival; DCR, disease control rate; MTD, maximum tolerated dose; Q2W/Q3W, every 2/3 weeks; IHC, immunohistochemistry. Trastuzumab deruxtecan received FDA accelerated approval in 2024 for HER2-positive (IHC3$^+$) solid tumors including colorectal cancer (tumor-agnostic indication), requiring prior systemic treatment failure. Trial status: Active (currently recruiting/treating), Active not recruiting (follow-up only), Completed (all data collection finished, published or not published), Terminated (prematurely discontinued). Data sourced from ClinicalTrials.gov and published literature as of Septembery 2025.

early studies but its global program was discontinued because an interim analysis of the Phase III CARMEN-LC03 trial failed to meet the primary endpoint (PFS). In contrast, Topoisomerase-I payloads appear more promising: labetuzumab govitecan (IMMU-130; SN-38, a topoisomerase I inhibitor) achieved a ~29% clinical benefit rate in heavily pretreated, irinotecan-refractory mCRC (63), and precemtabart tocentecan (M9140/Precem-TcT; exatecan; cleavable linker; high DAR ~8) has reported early disease control in refractory mCRC (64). Collectively, Top1-based CEACAM5 ADCs may offer stronger bystander effects than microtubule payloads, pending confirmation in randomized CRC trials. Next-generation concepts-bispecific CEACAM5/6 ADCs (e.g., CT109-SN-38) and single-domain (VHH) ADCs to boost tumor penetration-are advancing preclinically (65, 66).

3.1.3 TROP2 (TACSTD2)

TROP2 is frequently expressed in CRC, with strong IHC positivity in about 20% (67, 68). Sacituzumab govitecan (SG) couples an anti-TROP2 antibody to SN-38 via the hydrolysable CL2A linker with a high DAR ~7.6, enabling membrane-diffusible bystander killing. In the IMMU-132–01 CRC cohort (n=31; heavily pretreated, many post-irinotecan), SG monotherapy achieved ORR 3.2%, median PFS 3.9 mo, and median OS 14.2 mo, suggesting cross-resistance. Still, TROP2 remains attractive: the TROPHIT-1 phase II/III trial is comparing SG vs SOC in refractory mCRC, and datopotamab deruxtecan (Dato-DXd)-a TROP2-DXd ADC with strong bystander effect-is being tested in CRC in TROPION-PanTumor03. Optimal benefit may require patient selection and rational combinations or earlier-line use.

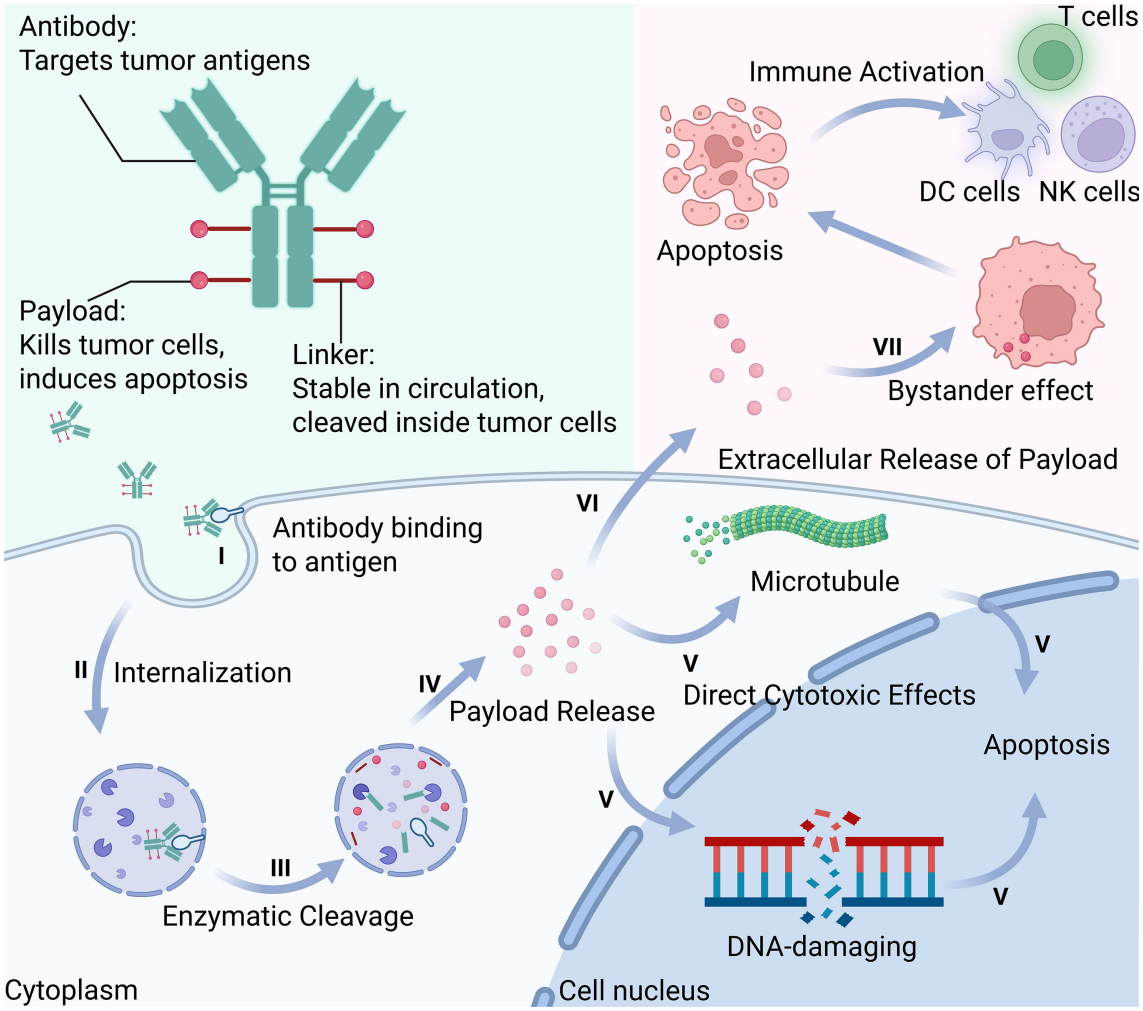

FIGURE 1
Schematic illustration of the seven-step mechanism of action of antibody-drug conjugates (ADCs): I. Antibody Binding to Antigen-The antibody specifically binds to tumor-associated surface antigens; II. Internalization-The ADC-antigen complex is internalized via receptor-mediated endocytosis; III. Enzymatic Cleavage-The linker is cleaved by intracellular enzymes within endosomes or lysosomes; IV. Payload Release-The cytotoxic payload is released into the cytoplasm or nucleus; V. Direct Cytotoxic Effects-The payload disrupts essential cellular functions by targeting DNA or microtubules; VI. Extracellular Release of Payload-A portion of the payload may exit the cell through lysis or active efflux; VII. Bystander Effect-The released payload kills neighboring tumor cells lacking target antigen. This figure was created using BioRender.com.

3.1.4 c-Met (HGFR)

c-Met is overexpressed in ~50% of CRC and mediates resistance to anti-EGFR/HER2 and KRAS G12C therapies. Telisotuzumab adizutecan (ABBV-400) links telisotuzumab (ABT-700) to the camptothecin-derived topoisomerase-I payload adizutecan via a cleavable linker (average DAR ≈6). In a first-in-human study, patients with high c-Met expression (IHC 3^+ ≥10%) had an ORR of 37.5% at doses ≥2.4 mg/kg Q3W; lower-expressing tumors still showed responses (ORR 14%), consistent with bystander killing. Safety has been manageable so far, and randomized/combination cohorts (e.g., with 5-FU/leucovorin/bevacizumab) are underway. Overall, c-Met remains a compelling CRC target; Top1-payload ADCs may overcome intratumoral heterogeneity, pending confirmation in controlled trials.

3.1.5 EpCAM (CD326)

EpCAM is broadly present on CRC but normal epithelial expression historically limited druggability. CX-2051 is a masked EpCAM ADC carrying a next-generation camptothecin Topo-I payload designed for tumor-local activation. Interim phase 1 data in heavily pretreated mCRC showed 28% ORR and 94% DCR across prioritized dose levels, 43% ORR at 10 mg/kg, and median PFS 5.8 months; most TRAEs were grade ≤2 and no DLTs were reported in escalation. A subsequent update noted a single grade 5 acute kidney injury in a patient with a solitary kidney; the safety committee supported study continuation with monitoring. CX-2051 illustrates a viable, tumor-selective way to "drug" EpCAM in CRC; expansion cohorts will clarify durability, dose, and risk mitigation.

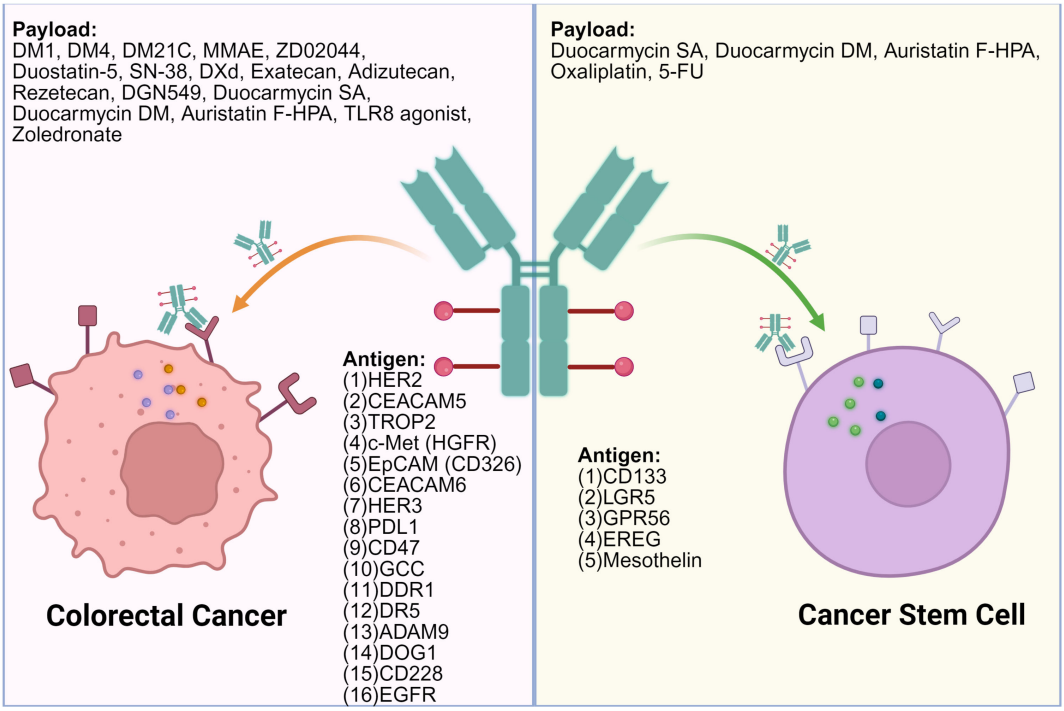

FIGURE 2
Surface targets on colorectal cancer cells and colorectal cancer stem cells and the associated ADC payloads. OXA, Oxaliplatin; MMAE, Monomethyl Auristatin E; PNU159682, PNU-159682; Duocarmycin SA, Duocarmycin Se-A; Tubulysin, Tubulysin; DM4, Maytansinoid DM4; SN-38, 7-Ethyl-10-hydroxycamptothecin; RNase A, Ribonuclease A; DM1, Maytansinoid DM1; DXd, Deruxtecan; DGN549, DGN549; DM21C, Maytansinoid DM21C; PMMAE, Polymeric Monomethyl Auristatin E; IGN, Indolinobenzodiazepine DNA-alkylating agent. This figure was created using BioRender.com.

3.1.6 CEACAM6

CEACAM6 exhibits differential expression across CRC molecular subtypes, with highest levels in CMS4 tumors characterized by stromal infiltration and poor prognosis. The preclinical ADC 84-EBET demonstrated complete tumor regression in CRC PDX models. Notably, combination with PD-1 blockade enhanced $CD8^+$ T cell infiltration, suggesting potential to overcome immune resistance in stroma-rich tumors (69). While preclinical results are encouraging for CMS4 subtype targeting, clinical validation is needed to confirm therapeutic benefit.

3.1.7 HER3

HER3 (ERBB3) is often upregulated in CRC, though its impaired kinase activity has made it challenging for direct inhibition. U3-1402 (patritumab deruxtecan) combines anti-HER3 antibody with topoisomerase I inhibitor DXd via a cleavable linker (DAR≈8). Topoisomerase I inhibitors like DXd are recognized as powerful ICD inducers through catastrophic DNA damage (70). The membrane-permeable DXd payload enables potent bystander effects, killing adjacent HER3-negative tumor cells and potentially remodeling the local tumor milieu. Preclinical studies demonstrated significant tumor inhibition and complete responses in HER3-high CRC xenografts irrespective of KRAS mutation status, transforming an "undruggable" target into a conduit for delivering immunomodulatory payload. This strategy offers a promising therapeutic avenue for CRC, including tumors resistant to conventional EGFR-targeted therapies.

3.1.8 PDL1

Programmed death-ligand 1 (PD-L1) is an immune checkpoint protein overexpressed on tumor cells, including CRC. Liu et al. (2023) developed a modular platform using poly (glutamic acid) scaffolds for noncovalent Fc-domain conjugation, generating anti-PD-L1 conjugates (aPDL1-P-MMAE, DAR = 40.7) achieving 98.5% tumor growth inhibition in MC38 CRC models without systemic toxicity (71). Zhang et al. (2023) extended this to aPDL1-NPLG-SN38 (DAR = 72) with 2.8-fold higher tumor accumulation versus non-targeted IgG conjugates, demonstrating excellent therapeutic properties in both medium-sized and large MC38 tumor models (72). These studies offer a promising platform for designing ultrahigh-DAR ADCs with preserved antigen-binding capacity, integrating chemical innovation, immune modulation, and high-precision drug delivery.

3.1.9 CD47

CD47 functions as a "don't eat me" signal by binding SIRPα on myeloid cells, enabling immune evasion. Chiang et al. (2024) developed non-cleavable CD47-targeting ADCs (7DC2-DM1, 7DC4-DM1) showing near-complete tumor inhibition in CRC and lung cancer models with improved safety versus cleavable constructs (73). This strategy not only blocks the CD47-SIRPα

axis to enhance macrophage phagocytosis, but also delivers DM1 for direct tumor killing that releases tumor antigens for immune presentation. CD47-targeted ADCs represent an elegant dual-mechanism approach to convert immunologically "cold" tumors into "hot" ones.

3.1.10 GCC

Guanylyl Cyclase C (GCC) shows exceptional tumor specificity in CRC, being almost exclusively restricted to intestinal cells, with expression in 98% of primary CRC and in ≥95% of metastatic lesions. TAK-164, carrying the DNA-alkylating payload DGN549, demonstrated strong activity in PDX models (74). The Phase I trial confirmed on-target DNA damage (elevated γH2AX) in patient biopsies (75). However, dose-limiting hepatotoxicity (including grade 5 hepatic failure) led to trial termination, with the tolerable dose (0.064 mg/kg) deemed insufficient for clinical benefit while higher doses (≥0.19 mg/kg) proved too toxic. This highlights the critical challenge of achieving adequate therapeutic window.

3.1.11 DDR1

Discoidin domain receptor 1 (DDR1) is overexpressed in >80% of CRC and linked to poor prognosis and chemoresistance. T4H11-DM4 (maytansinoid microtubule inhibitor) achieved complete tumor regression in oxaliplatin-resistant xenograft models (76). The DM4 payload induces mitotic arrest and apoptosis. By targeting a resistance-associated antigen, this strategy offers direct killing of treatment-refractory cells. The ADC shows promise for addressing chemoresistant CRC populations, though further studies are needed to characterize its full therapeutic potential.

3.1.12 DR5

Death receptor 5 (DR5) is overexpressed in CRC. Oba01 links anti-DR5 antibody zaptuzumab to MMAE (a microtubule inhibitor), creating dual mechanisms: apoptosis via DR5 signaling and cytotoxicity via MMAE (77) Preclinical studies in pancreatic cancer models demonstrated anti-tumor activity. Further research is needed to evaluate this approach specifically in CRC, particularly in treatment-refractory populations.

3.1.13 ADAM9

ADAM9 is a transmembrane metalloproteinase overexpressed in CRC with minimal normal tissue expression. IMGC936, site-specifically conjugated to maytansinoid DM21C (a microtubule inhibitor), achieved complete tumor regression in xenograft models and entered Phase I trials (78). The ADC demonstrated potent direct cytotoxicity and bystander killing effects in preclinical studies. However, clinical development was discontinued after failing to meet pre-established clinical safety and efficacy benchmarks in Phase 1, highlighting the challenges of translating preclinical efficacy to clinical benefit.

3.1.14 DOG1

DOG1 (Discovered on GIST1) exhibits tumor-restricted expression in CRC with high mRNA positivity and high expression in liver metastases. An anti-DOG1-DM4 ADC showed potent activity in CRC liver-metastasis model (79). The ADC shows efficacy at metastatic sites while maintaining preserved liver function. This approach is particularly relevant for addressing the challenge of hepatic metastases in CRC, a common site of disease progression.

3.1.15 CD228

CD228 (melanotransferrin) is a GPI-anchored membrane protein with minimal expression in normal tissues and elevated expression in multiple solid tumors, including CRC. SGN-CD228A links humanized anti-CD228 antibody hL49 to MMAE via a PEGylated glucuronide linker (80). The IgG1 backbone is capable of mediating ADCC, while controlled intracellular MMAE release triggers potent cytotoxicity and stimulates DAMP release. These signals act as an endogenous vaccine, recruiting and activating antigen-presenting cells to prime a T-cell-mediated anti-tumor immune response.

3.1.16 EGFR

EGFR is frequently overexpressed in 60-80% of CRC, including KRAS-mutant disease where conventional EGFR inhibitors fail. Novel EGFR-targeted ADCs aim to overcome this resistance through immunomodulatory mechanisms (81). Bisphosphonate-conjugated ADC cetuximab-zoledronate (Cet-ZA) demonstrated direct cytotoxicity plus activation of Vγ9Vδ2 T cells in CRC organoid models, potentially bridging targeted therapy with innate immunity (82). The IgG1 backbone inherently mediates ADCC via NK cell recruitment. While these immunoconjugates remain in preclinical development (83). they represent a rational strategy to transform EGFR into an immune-activating platform for KRAS-mutant and treatment-refractory CRC.

3.2 Targets on the surface of colorectal cancer stem cells

3.2.1 LGR5

Leucine-rich repeat-containing G protein-coupled receptor 5 (LGR5) is a definitive marker for both normal intestinal stem cells and colorectal CSCs, playing fundamental roles in tumor initiation and progression via WNT signaling (84, 85). This shared expression creates significant therapeutic window challenges-the primary barrier to clinical translation. Early preclinical ADC studies showed highly potent payloads could induce severe on-target, off-tumor toxicity in normal LGR5-expressing tissues despite anti-tumor efficacy, establishing that therapeutic index is critical. To overcome this, petosemtamab (MCLA-158) was developed as a bispecific antibody targeting both LGR5 and EGFR, leveraging EGFR co-expression to selectively target tumors while sparing healthy LGR5+ intestinal stem cells (86) Petosemtamab employs EGFR degradation and enhanced immune-mediated destruction through ADCC and ADCP (87). After demonstrating superior efficacy over standard EGFR inhibitors in patient-derived

organoids and xenografts, it is now in clinical trials for metastatic CRC.

3.2.2 CD133

CD133 is a five-domain transmembrane glycoprotein and a well-established surface marker of CSCs in CRC. Its expression is closely associated with tumor initiation, metastasis, therapy resistance, and recurrence. Given the central role of $CD133^+$ cells in treatment failure, targeting them represents a critical strategy for preventing disease progression. Preclinical studies explored nanocarrier systems delivering conventional chemotherapeutics like oxaliplatin and 5-FU directly to $CD133^+$ cells-both are known ICD inducers. By forcing immunogenic cell death, these agents trigger DAMP release, recruiting and activating antigen-presenting cells (88, 89). While these systems remain in preclinical development, they highlight a promising approach to overcome chemoresistance and potentially reverse immune ignorance by targeting the CSC.

3.2.3 GPR56

G protein-coupled receptor 56 (GPR56) (ADGRG1) overexpression in CRC correlates with poor survival and increased postoperative relapse, with particular enrichment in microsatellite stable (MSS) disease-the predominant immune checkpoint inhibitor (ICI)-refractory subtype (90, 91). Mechanistically, GPR56 activates the RhoA-MDR1 signaling axis to enhance efflux-mediated chemoresistance (92) and maintains LGR5-negative stem-like cells in a treatment-refractory state. A GPR56-targeted antibody-drug conjugate (ADC) in preclinical study utilizing duocarmycin SA, a DNA minor-groove alkylating agent, demonstrated target-dependent tumor growth inhibition in CRC xenografts and patient-derived organoids with acceptable tolerability (90, 93).

3.2.4 5T4

5T4 is an oncofetal glycoprotein (72kDa trophoblast cell surface antigen) that is minimally expressed in adult normal tissues but is overexpressed in a wide range of malignancies, including colorectal cancer. In CRC, 5T4 is associated with tumor invasiveness and stem-like features, making it an appealing target to eliminate aggressive cancer cell subpopulations. ASN004 (scFv-Fc format) uses Dolaflexin polymer to deliver auristatin F-HPA (microtubule inhibitor) at very high DAR (~10-12), achieving deep regressions preclinically; first-in-human studies report manageable safety, with efficacy readouts pending.

3.2.5 Epiregulin

Epiregulin (EREG), a ligand of the EGFR family, is aberrantly upregulated in a substantial subset of CRC, including both RAS wild-type and mutant subtypes. Its expression in both differentiated tumor cells and undifferentiated cancer stem-like populations suggests a role in tumor plasticity and therapy resistance.Based on Jacob et al.'s preclinical study, a humanized anti-EREG antibody (H231) conjugated to duocarmycin DM via enzymatically cleavable tripeptide linkers was developed (94, 95). Their lead candidate, H231 EGC-qDuoDM gluc, demonstrated subnanomolar potency in EREG-expressing CRC cells irrespective of RAS status and achieved significant tumor growth inhibition in both cell line xenografts (70% TGI in LoVo, 68% in DLD-1) and patient-derived xenografts (86-88% TGI in MSS models). Notably, the ADC outperformed cetuximab and showed acceptable tolerability in immunocompetent mice. Future development should prioritize comprehensive pharmacokinetic/pharmacodynamic studies, formal assessment of immunogenic cell death markers (HMGB1, calreticulin, ATP release), and evaluation of combination strategies with immune checkpoint inhibitors in syngeneic models to fully realize the immunotherapeutic potential of this promising EREG-targeted approach.

4 Clinical evidence and CRC-specific challenges

4.1 Trials landscape & key signals in CRC

The clinical landscape of CRC treatment has evolved from conventional chemotherapy and targeted antibodies to ADCs. Traditional chemotherapy (5-FU, irinotecan, oxaliplatin) lacks selectivity, causing systemic toxicity and immunosuppression despite tumor-agnostic efficacy (96). Monoclonal antibodies (cetuximab, bevacizumab) offer specificity but limited direct cytotoxicity, relying on pathway inhibition vulnerable to resistance mechanisms. ADCs uniquely combine chemotherapy's potency with antibody selectivity, delivering ultra-potent payloads specifically to antigen-expressing cells while sparing normal tissues. The bystander effect enables ADCs with membrane-permeable payloads to kill neighboring antigen-negative populations through local drug diffusion, partially compensating for tumor heterogeneity. Additionally, select ADC payloads induce immunogenic cell death, recruiting T-cells and converting "cold" MSS tumors to "hot" phenotypes, creating immune engagement absent in conventional therapies.

The clinical development of ADCs in colorectal cancer demonstrates distinct patterns of success and failure, fundamentally determined by payload selection. Table 1 summarizes ongoing and completed clinical trials. Among these, trastuzumab deruxtecan (T-DXd), carrying a topoisomerase I inhibitor payload, received FDA approval for unresectable or metastatic HER2-positive ($IHC3^+$) solid tumors. In the DESTINY-CRC01 trial, T-DXd achieved an objective response rate (ORR) of 45.3% in HER2-positive patients, reaching 57.5% in the $IHC3^+$ subgroup, validating the importance of appropriate payload-tumor matching. This success contrasts sharply with the consistent failure of microtubule inhibitor-based ADCs. TAK-264 (anti-GCC-MMAE), despite targeting an antigen expressed in >90% of CRCs, demonstrated zero clinical responses, likely reflecting intrinsic resistance of colorectal tumors to microtubule inhibitors. The payload-specificity issue is further exemplified by T-DM1's differential efficacy across tumor types. While T-DM1 significantly

improves progression-free and overall survival in HER2-positive breast cancer, its efficacy in HER2-positive CRC remains minimal, with only one responder among eight patients (97). These findings underscore that successful ADC development requires payload selection tailored to tumor-specific biological characteristics rather than simply matching target expression profiles.

Clinical translation of ADCs in CRC remains nascent despite platform maturation. With ~15 approved ADCs across solid tumors, application in CRC lags behind breast and gastric cancers, primarily due to limited validated targets and desmoplastic barriers. Current clinical investigations focus on CEACAM5, HER2, and Trop-2, yet antigen heterogeneity and stromal density pose formidable obstacles.

4.2 CRC-specific obstacles

Despite successful ADC approvals in multiple malignancies, including the recent tumor-agnostic approval of trastuzumab deruxtecan for HER2-positive solid tumors, only T-DXd has achieved regulatory approval specifically for colorectal cancer. This limited success reflects CRC-specific biological barriers that impede ADC efficacy.

First, target antigen heterogeneity presents a fundamental challenge. HER2 amplification occurs in merely 2-5% of metastatic CRCs (98), while even prevalent targets like CEACAM5 display intratumoral heterogeneity, with antigen-negative cells interspersed among positive populations (99, 100). Second, inefficient internalization limits payload delivery. Certain CRC-associated antigens, particularly CEACAM5, demonstrate slow internalization kinetics upon antibody binding, reducing intracellular drug accumulation (101). Third, the physical tumor microenvironment creates formidable delivery barriers. Dense desmoplastic stroma and elevated interstitial fluid pressure impede antibody penetration, resulting in heterogeneous intratumoral ADC distribution. Their 150-kDa size limits penetration in desmoplastic CRC tumors, potentially creating sanctuary sites.Fourth, immunological exclusion in MSS tumors diminishes therapeutic response. Approximately 95% of CRCs are microsatellite stable, characterized by “cold” immune microenvironments lacking cytotoxic T-cell infiltration. This immune exclusion eliminates potential contributions from antibody-dependent cellular cytotoxicity and immunogenic cell death following ADC treatment.

Additionally, on-target/off-tumor gastrointestinal toxicity remains problematic. Many candidate antigens, including Trop-2, exhibit baseline expression in normal intestinal epithelium, causing dose-limiting gastrointestinal adverse events that narrow the therapeutic window. The therapeutic window narrows further as systemic toxicities—neutropenia, ocular damage, thrombocytopenia—constrain dosing (102). These CRC-specific challenges collectively explain the limited clinical translation of ADCs in this malignancy despite successes elsewhere. Future success hinges on identifying CRC-enriched antigens, particularly on TME components (CAFs, CSCs) and leveraging payloads with robust bystander effects to overcome spatial heterogeneity (103).

4.2.1 Antigen heterogeneity & expression threshold

ADC efficacy critically depends on target antigen expression levels and distribution uniformity. Quantitative studies suggest approximately 10,000 receptors/cell as a functional threshold for effective ADC activity (104). The DESTINY-CRC01 trial exemplified this principle, achieving 45.3% objective response rate in HER2 IHC3$^+$/ISH$^+$ patients while observing no responses in HER2-low cohorts, highlighting the importance of stringent expression criteria. Intratumoral heterogeneity poses additional challenges, with antigen-negative clones interspersed among positive populations. The bystander effect offers a potential solution: hydrophobic payloads like DXd and SN-38 can diffuse from antigen-positive cells to eliminate neighboring antigen-negative cells. Emerging strategies include bispecific ADCs targeting dual epitopes to enhance receptor clustering and internalization. MEDI4276, binding two HER2 epitopes simultaneously, demonstrated accelerated lysosomal trafficking preclinically, though early-phase trials revealed narrow therapeutic windows. Optimized patient selection through IHC scoring, H-score thresholds, and RNA-based quantification may help identify optimal candidates. These approaches collectively suggest pathways to mitigate heterogeneity-related limitations in CRC ADC development.

4.2.2 Internalization & intracellular trafficking kinetics

Efficient ADC activity requires optimal antigen-antibody complex internalization and lysosomal trafficking. In colorectal cancer, internalization kinetics vary significantly among target antigens. CEACAM5, despite widespread expression in CRC, demonstrates notably slow internalization upon antibody binding, limiting intracellular payload delivery. This contrasts with other targets being evaluated in CRC clinical trials. Epitope selection proves crucial-dual-epitope targeting can induce receptor clustering and accelerate endocytosis, as demonstrated in preclinical HER2-targeting studies. Linker design significantly impacts payload release dynamics: cleavable linkers enable faster intracellular drug liberation but risk premature systemic release, while non-cleavable linkers require complete antibody degradation (105). Novel tumor-microenvironment-activated linkers represent an emerging strategy to maintain circulation stability while facilitating tumor-specific activation, though CRC-specific applications await clinical validation (105). Quantitative studies across multiple tumor types suggest compensatory relationships between antigen density and internalization rates. For CRC-relevant targets like CEACAM5, HER2, and GCC, optimizing these parameters during ADC design may help overcome the internalization barriers specific to colorectal tumors.

4.2.3 Tumor penetration limits & physical TME barriers

Colorectal tumors present formidable physical barriers impeding ADC distribution. The 150-kDa antibody size restricts diffusion through dense extracellular matrix, while irregular vasculature and elevated interstitial pressure further limit penetration (106). The "binding-site barrier" phenomenon-whereby ADCs saturate perivascular antigens before reaching deeper tumor regions-compounds distribution challenges. ADC dosing constraints, necessitated by payload toxicity, may result in subtherapeutic concentrations in poorly perfused areas (107). Several strategies show promise for enhancing penetration. Bystander-effect payloads enable killing of antigen-negative or inaccessible cells through local diffusion. Smaller antibody formats (scFv, Fab fragments, nanobodies) demonstrate improved tissue penetration, albeit with faster clearance (108). Co-administration of unlabeled carrier antibodies may saturate peripheral binding sites, driving deeper ADC penetration. The desmoplastic CRC microenvironment, characterized by fibrotic stroma and hypoxic regions, creates heterogeneous drug distribution patterns. These physical barriers likely contribute to treatment resistance and warrant continued investigation of penetration-enhancing strategies tailored to CRC-specific microenvironmental features.

4.2.4 Immunological dichotomy between MSS and MSI-H colorectal cancer

Microsatellite status substantially influences CRC immunobiology and therapeutic responses. MSI-H tumors (15% of cases) typically exhibit high mutational burden, abundant neoantigens, and robust T-cell infiltration, contributing to their responsiveness to checkpoint inhibitors (109, 110) In contrast, MSS tumors (85% of cases) generally display low mutational burden, minimal neoantigen presentation, and "cold" microenvironments characterized by sparse T-cell infiltration and abundant immunosuppressive cells (111–113). This dichotomy significantly impacts treatment outcomes: while MSI-H patients often achieve 40-60% response rates with checkpoint inhibitors, MSS patients show limited benefit (114, 115). ADCs may provide valuable opportunities for MSS CRC treatment (116). Cytotoxic payloads could potentially induce immunogenic cell death, possibly converting "cold" tumors to "hot" phenotypes. Zhou et al. developed Oba01, a DR5-targeting ADC conjugated with MMAE via cleavable linker (77), representing efforts to address MSS CRC challenges. Strategic payload selection favoring immunogenic mechanisms, combined with immune checkpoint blockade, may help mitigate the immunosuppressive MSS microenvironment, though clinical validation remains essential.

4.3 Resistance mechanisms (intrinsic & acquired; payload-specific)

ADC resistance involves multifaceted mechanisms spanning both intrinsic and acquired pathways. Intrinsic resistance often stems from pre-existing cellular features. ABC transporter overexpression, particularly P-glycoprotein, promotes drug efflux and reduces intracellular accumulation (117). MMAE-based ADCs face notable challenges in gastrointestinal cancers, where P-gp expression frequently increases following chemotherapy exposure (118, 119). This may partially explain the failure of TAK-264 (anti-GCC-MMAE) in colorectal cancer trials despite high GCC expression (120, 121). Emerging strategies include selecting efflux-insensitive payloads like topoisomerase I inhibitors, as demonstrated by T-DXd's success in DESTINY-CRC01, contrasting with MMAE-based failures (122).

Acquired resistance develops dynamically under treatment pressure through multiple mechanisms. Target antigen modulation represents a primary escape route-downregulation, mutation, or selection of antigen-negative clones can emerge within months of treatment initiation. In tumors with heterogeneous antigen expression like CEACAM5 in colorectal cancer, pre-existing low-expressing populations may expand under selection pressure. Payload-specific resistance patterns vary: topoisomerase I inhibitor resistance involves TOP1 downregulation, enhanced DNA repair pathway activation, and apoptosis evasion through NF-κB activation. MMAE resistance primarily involves efflux pump upregulation and tubulin alterations. Compensatory signaling pathways provide additional escape mechanisms-alternative receptor tyrosine kinases may maintain downstream signaling despite target blockade. These multilevel resistance mechanisms suggest combination approaches may prove valuable for sustained efficacy.

ADCs also remain constrained by antigen dependency—tumors lacking suitable targets escape treatment. Acquired resistance through antigen loss or downregulation parallels targeted therapy resistance patterns. Unlike chemotherapy's antigen-independent activity, ADCs require sustained target expression for efficacy.

4.4 Safety profile in CRC & mitigation (GI/hematologic/ILD)

ADC-related toxicities in colorectal cancer trials encompass both on-target and off-target effects, with gastrointestinal and hematologic adverse events predominating. In DESTINY-CRC01, trastuzumab deruxtecan demonstrated near-universal adverse event occurrence, with grade ≥3 neutropenia (22.1%) and anemia (14.0%) most frequently observed (123, 124). Gastrointestinal toxicities, including nausea, diarrhea, and mucositis, likely result from topoisomerase I inhibitor payloads (SN-38, DXd) directly affecting intestinal epithelium and hepatobiliary excretion of free toxins (125). IMMU-130 (labetuzumab govitecan) similarly showed manageable toxicity profiles with grade ≥3 neutropenia (16%), leukopenia (11%), and diarrhea (7%) as dose-limiting toxicities.

Interstitial lung disease represents a particularly concerning ADC-specific toxicity. T-DXd trials reported ILD/pneumonitis in 9.3% of CRC patients, including fatal cases (3.5%), necessitating careful patient selection and monitoring (126). Dose optimization has proven effective-reducing T-DXd from 6.4 to 5.4 mg/kg in DESTINY-CRC02 eliminated grade 5 toxicities while maintaining efficacy (127).

Mitigation strategies focus on multiple approaches. Linker optimization enhances stability to minimize premature payload release, as demonstrated by YL201's hydrophilic linker achieving only 1.3% severe ILD incidence. Dose fractionation reduces peak concentration-related toxicities-IMMU-130's weekly dosing showed improved tolerability versus every-three-week schedules. Supportive care measures include prophylactic G-CSF for anticipated neutropenia, early antidiarrheal intervention for SN-38-based ADCs, and antiemetic premedication. Careful monitoring protocols enable timely dose modifications: most hematologic toxicities resolve within 1–2 weeks of treatment interruption, allowing dose-reduced continuation (128). Through these integrated management strategies, approximately 85% of patients complete intended therapy despite high adverse event rates, suggesting ADC toxicities remain manageable within appropriate frameworks.

5 Discussion and conclusion

ADCs are rapidly transitioning from targeted chemotherapies into a sophisticated class of immuno-oncology agents, representing a new frontier for CRC treatment. While preclinical studies have shown remarkable promise, the journey to clinical approval remains challenging. The future success of ADCs in CRC hinges on a paradigm shift: moving beyond direct cytotoxicity to strategically harnessing their profound ability to modulate the TME and synergize with the host immune system. The true innovation in next-generation ADCs lies in the immunological consequences of their payload selection.

This immunotherapeutic lens also redefines what constitutes an optimal target. The focus is expanding from antigens on tumor cells (CEACAM5, HER2) to include those on critical TME components, such as cancer-associated fibroblasts (CEACAM6), or on immune checkpoints themselves (PD-L1, CD47). Targeting CSCs with markers like LGR5 or GPR56 using an ICD-inducing ADC is a particularly powerful strategy, as it aims to eradicate the root of relapse while simultaneously initiating an immune response from the most resilient tumor population. This dual-pronged attack-debulking the tumor while disabling its defenses-is central to the modern ADC concept.

Immune priming mechanisms position ADCs as ideal immuno-oncology partners. ADC-mediated ICD releases tumor antigens, activates cGAS-STING signaling, and recruits cytotoxic T-cells, converting immunologically "cold" MSS tumors to "hot" phenotypes (102). Immunostimulatory payloads exemplify this paradigm: photoimmunotherapy platforms induce dendritic cell maturation and amplify $CD8^+$ responses via localized ICD (103). This immune activation creates synergy with checkpoint inhibitors, as demonstrated in preclinical models where ADC pretreatment enhances anti-PD-1 efficacy (129). The dual capacity for direct cytotoxicity and immune engagement distinguishes ADCs from conventional targeted therapies. The antibody component further enables Fc-mediated ADCC and phagocytosis, creating synergistic immune engagement that maintains efficacy despite variable antigen expression.

Biomarker-driven patient selection and rational combination strategies remain critical. Current approaches relying on binary antigen expression are insufficient; integration of antigen density, spatial uniformity, and immune contexture (GSDME expression, cGAS-STING activity) is essential for optimizing patient selection. Payload selection must balance potency, membrane permeability for bystander killing, and hydrophilicity to minimize off-target toxicity while maintaining DAR and linker stability (103). Despite third/fourth-generation engineering advances (102), translational barriers persist, necessitating systematic evaluation of ADC-immunotherapy combinations in biomarker-stratified clinical trials to fully unlock their therapeutic potential in CRC.

To realize this vision, biomarker development must evolve beyond simple antigen expression. The selection of patients for ADC therapy should incorporate immuno-profiling to assess the TME, expression of key cell death mediators like GSDME, or activation of pathways such as cGAS-STING. In conclusion, ADCs offer a modular and mechanistically versatile platform with the potential to reshape the CRC treatment landscape. Their ultimate success will be driven by continued innovation in molecular engineering and, most critically, by their intelligent integration into biomarker-driven, immuno-oncology combination strategies designed to kill tumor cells and awaken the immune system in a single, coordinated assault.

Author contributions

YW: Writing – original draft, Writing – review & editing. KL: Writing – review & editing. YX: Writing – review & editing. SX: Writing – review & editing. HC: Writing – original draft, Writing – review & editing. XF: Writing – review & editing.

Funding

The author(s) declare that no financial support was received for the research, and/or publication of this article.

Conflict of interest

The authors declare that the research was conducted in the absence of any commercial or financial relationships that could be construed as a potential conflict of interest.

Generative AI statement

The author(s) declare that no Generative AI was used in the creation of this manuscript.

Any alternative text (alt text) provided alongside figures in this article has been generated by Frontiers with the support of artificial intelligence and reasonable efforts have been made to ensure accuracy, including review by the authors wherever possible. If you identify any issues, please contact us.

Publisher's note

All claims expressed in this article are solely those of the authors and do not necessarily represent those of their affiliated organizations, or those of the publisher, the editors and the reviewers. Any product that may be evaluated in this article, or claim that may be made by its manufacturer, is not guaranteed or endorsed by the publisher.

References

1. Keum N, Giovannucci E. Global burden of colorectal cancer: emerging trends, risk factors and prevention strategies. *Nat Rev Gastroenterol Hepatol*. (2019) 16:713–32. doi: 10.1038/s41575-019-0189-8

2. Morgan E, Arnold M, Gini A, Lorenzoni V, Cabasag CJ, Laversanne M, et al. Global burden of colorectal cancer in 2020 and 2040: incidence and mortality estimates from GLOBOCAN. *Gut*. (2023) 72:338–44. doi: 10.1136/gutjnl-2022-327736

3. Kotani D, Oki E, Nakamura Y, Yukami H, Mishima S, Bando H, et al. Molecular residual disease and efficacy of adjuvant chemotherapy in patients with colorectal cancer. *Nat Med*. (2023) 29:127–34. doi: 10.1038/s41591-022-02115-4

4. Grassi E, Vurchio V, Cresswell GD, Catalano I, Lupo B, Sassi F, et al. Heterogeneity and evolution of DNA mutation rates in microsatellite stable colorectal cancer. *Sci Transl Med*. (2025) 17:eado1641. doi: 10.1126/scitranslmed.ado1641

5. Bruun J, Kryeziu K, Eide PW, Moosavi SH, Eilertsen IA, Langerud J, et al. Patient-derived organoids from multiple colorectal cancer liver metastases reveal moderate intra-patient pharmacotranscriptomic heterogeneity. *Clin Cancer Res*. (2020) 26:4107–19. doi: 10.1158/1078-0432.CCR-19-3637

6. Ge M, Chen X-Y, Huang P, Fleishman JS, Yang D-H, Wu Z-X, et al. Understanding and overcoming multidrug resistance in cancer. *Nat Rev Clin Oncol*. (2025) 22:760–80. doi: 10.1038/s41571-025-01059-1

7. Tarantino P, Carmagnani Pestana R, Corti C, Modi S, Bardia A, Tolaney SM, et al. Antibody–drug conjugates: Smart chemotherapy delivery across tumor histologies. *CA: Cancer J Clin*. (2022) 72:165–82. doi: 10.3322/caac.21705

8. Drago JZ, Modi S, Chandarlapaty S. Unlocking the potential of antibody-drug conjugates for cancer therapy. *Nat Rev Clin Oncol*. (2021) 18:327–44. doi: 10.1038/s41571-021-00470-8

9. Narayan P, Osgood CL, Singh H, Chiu H-J, Ricks TK, Chiu Yuen Chow E, et al. FDA approval summary: fam-trastuzumab deruxtecan-nxki for the treatment of unresectable or metastatic HER2-positive breast cancer. *Clin Cancer Res*. (2021) 27:4478–85. doi: 10.1158/1078-0432.CCR-20-4557

10. Wahby S, Fashoyin-Aje L, Osgood CL, Cheng J, Fiero MH, Zhang L, et al. FDA approval summary: accelerated approval of sacituzumab govitecan-hziy for third-line treatment of metastatic triple-negative breast cancer. *Clin Cancer Res*. (2021) 27:1850–4. doi: 10.1158/1078-0432.CCR-20-3119

11. Chang E, Weinstock C, Zhang L, Charlab R, Dorff SE, Gong Y, et al. FDA approval summary: enfortumab vedotin for locally advanced or metastatic urothelial carcinoma. *Clin Cancer Res*. (2021) 27:922–7. doi: 10.1158/1078-0432.CCR-20-2275

12. Ritchie M, Tchistiakova L, Scott N. Implications of receptor-mediated endocytosis and intracellular trafficking dynamics in the development of antibody drug conjugates. *mAbs*. (2013) 5:13–21. doi: 10.4161/mabs.22854

13. Donaghy H. Effects of antibody, drug and linker on the preclinical and clinical toxicities of antibody-drug conjugates. *mAbs*. (2016) 8:659–71. doi: 10.1080/19420862.2016.1156829

14. Fu Z, Li S, Han S, Shi C, Zhang Y. Antibody drug conjugate: the "biological missile" for targeted cancer therapy. *Signal Transduct Target Ther*. (2022) 7:93. doi: 10.1038/s41392-022-00947-7

15. Redman JM, Hill EM, AlDeghaither D, Weiner LM. Mechanisms of action of therapeutic antibodies for cancer. *Mol Immunol*. (2015) 67:28–45. doi: 10.1016/j.molimm.2015.04.002

16. Tai YT, Mayes PA, Acharya C, Zhong MY, Cea M, Cagnetta A, et al. Novel anti-B-cell maturation antigen antibody-drug conjugate (GSK2857916) selectively induces killing of multiple myeloma. *Blood*. (2014) 123:3128–38. doi: 10.1182/blood-2013-10-535088

17. Herbener P, Schönfeld K, König M, Germer M, Przyborski JM, Bernöster K, et al. Functional relevance of *in vivo* half antibody exchange of an IgG4 therapeutic antibody-drug conjugate. *PloS One*. (2018) 13:e0195823. doi: 10.1371/journal.pone.0195823

18. Xu R, Zheng Y, Tai W. A single-chain fab derived drug conjugate for HER2 specific delivery. *Biomaterials*. (2025) 313:122798. doi: 10.1016/j.biomaterials.2024.122798

19. Balamkundu S, Liu C-F. Lysosomal-cleavable peptide linkers in antibody–drug conjugates. *J Biomedicines*. (2023) 11:3080. doi: 10.3390/biomedicines11113080

20. Hafeez U, Parakh S, Gan HK, Scott AM. Antibody–drug conjugates for cancer therapy. *Molecules (Basel Switzerland)*. (2020) 25:4764. doi: 10.3390/molecules25204764

21. Liang K, Mei S, Gao X, Peng S, Zhan J. Dynamics of endocytosis and degradation of antibody-drug conjugate T-DM1 in HER2 positive cancer cells. *Drug Des Devel Ther*. (2021) 15:5135–50. doi: 10.2147/DDDT.S344052

22. Staudacher AH, Brown MP. Antibody drug conjugates and bystander killing: is antigen-dependent internalisation required? *Br J Cancer*. (2017) 117:1736–42. doi: 10.1038/bjc.2017.367

23. Matsuda Y, Mendelsohn BA. An overview of process development for antibody-drug conjugates produced by chemical conjugation technology. *Expert Opin Biol Ther*. (2021) 21:963–75. doi: 10.1080/14712598.2021.1846714

24. Fukunaga A, Maeta S, Reema B, Nakakido M, Tsumoto K. Improvement of antibody affinity by introduction of basic amino acid residues into the framework region. *Biochem biophysics Rep*. (2018) 15:81–5. doi: 10.1016/j.bbrep.2018.07.005

25. Nadkarni DV. Conjugations to Endogenous Cysteine Residues, Methods in molecular biology. *(Clifton N.J.)*. (2020) 2078:37–49. doi: 10.1007/978-1-4939-9929-3_3

26. Levengood MR, Zhang X, Hunter JH, Emmerton KK, Miyamoto JB, Lewis TS, et al. Orthogonal cysteine protection enables homogeneous multi-drug antibody-drug conjugates. *Angew Chem Int Ed Engl*. (2017) 56:733–7. doi: 10.1002/anie.201608292

27. Hamblett KJ, Senter PD, Chace DF, Sun MM, Lenox J, Cerveny CG, et al. Effects of drug loading on the antitumor activity of a monoclonal antibody drug conjugate. *Clin Cancer Res*. (2004) 10:7063–70. doi: 10.1158/1078-0432.CCR-04-0789

28. Sun X, Ponte JF, Yoder NC, Laleau R, Coccia J, Lanieri L, et al. Effects of drug–antibody ratio on pharmacokinetics, biodistribution, efficacy, and tolerability of antibody–maytansinoid conjugates. *Bioconjugate Chem*. (2017) 28:1371–81. doi: 10.1021/acs.bioconjchem.7b00062

29. Chu H, Shan Y, Liu Z, Sun M, Zhao W, Xie X, et al. Rejuvenation of tumor-specific T cells via ultrahigh DAR antibody-polymeric imidazoquinoline complexes: coordinated targeting of PDL1 and efficient TLR7/8 activation in intratumoral dendritic cells. *Advanced materials (Deerfield Beach Fla.)*. (2025) 37:e2412974. doi: 10.1002/adma.202412974

30. Sutherland MS, Sanderson RJ, Gordon KA, Andreyka J, Cerveny CG, Yu C, et al. Lysosomal trafficking and cysteine protease metabolism confer target-specific cytotoxicity by peptide-linked anti-CD30-auristatin conjugates. *J Biol Chem*. (2006) 281:10540–7. doi: 10.1074/jbc.M510026200

31. Giugliano F, Corti C, Tarantino P, Michelini F, Curigliano G. Bystander effect of antibody-drug conjugates: fact or fiction? *Curr Oncol Rep*. (2022) 24:809–17. doi: 10.1007/s11912-022-01266-4

32. Tolaney SM, Cardillo TM, Chou CC, Dornan C, Faris M. The mode of action and clinical outcomes of sacituzumab govitecan in solid tumors. *Clin Cancer Res*. (2025) 31:1390–9. doi: 10.1158/1078-0432.CCR-24-1525

33. Gray E, Ulrich M, Epp A, Younan P, Sahetya D, Hensley K, et al. SGN-B7H4V, an investigational vedotin ADC directed to the immune checkpoint ligand B7-H4, shows promising activity in preclinical models. *J Immunother Cancer*. (2023) 11:e007572. doi: 10.1136/jitc-2023-007572

34. Kaina B. DNA damage-triggered apoptosis: critical role of DNA repair, double-strand breaks, cell proliferation and signaling. *Biochem Pharmacol*. (2003) 66:1547–54. doi: 10.1016/S0006-2952(03)00510-0

35. Iwata TN, Ishii C, Ishida S, Ogitani Y, Wada T, Agatsuma T. A HER2-targeting antibody-drug conjugate, trastuzumab deruxtecan (DS-8201a), enhances antitumor immunity in a mouse model. *Mol Cancer Ther*. (2018) 17:1494–503. doi: 10.1158/1535-7163.MCT-17-0749

36. Gerber HP, Sapra P, Loganzo F, May C. Combining antibody-drug conjugates and immune-mediated cancer therapy: What to expect? *Biochem Pharmacol*. (2016) 102:1–6. doi: 10.1016/j.bcp.2015.12.008

37. Strebhardt K, Ullrich A. Paul Ehrlich's magic bullet concept: 100 years of progress, Nature reviews. *Cancer*. (2008) 8:473–80. doi: 10.1038/nrc2394

38. Schlam I, Moges R, Morganti S, Tolaney SM, Tarantino P. Next-generation antibody-drug conjugates for breast cancer: Moving beyond HER2 and TROP2. *Crit Rev Oncol Hematol*. (2023) 190:104090. doi: 10.1016/j.critrevonc.2023.104090

39. Kovtun YV, Goldmacher VS. Cell killing by antibody-drug conjugates. *Cancer Lett*. (2007) 255:232–40. doi: 10.1016/j.canlet.2007.04.010

40. Leyton JV. The endosomal-lysosomal system in ADC design and cancer therapy. *Expert Opin Biol Ther*. (2023) 23:1067–76. doi: 10.1080/14712598.2023.2285996

41. Wang X, Gigant B, Zheng X, Chen Q. Microtubule-targeting agents for cancer treatment: Seven binding sites and three strategies. *MedComm-Oncology*. (2023) 2:e46. doi: 10.1002/mog2.46

42. Tsao L-C, Wang JS, Ma X, Sodhi S, Ragusa JV, Liu B, et al. Effective extracellular payload release and immunomodulatory interactions govern the therapeutic effect of trastuzumab deruxtecan (T-DXd). *Nat Commun*. (2025) 16:3167. doi: 10.1038/s41467-025-58266-8

43. Buyukgolcigezli I, Tenekeci AK, Sahin IH. Opportunities and challenges in antibody-drug conjugates for cancer therapy: A new era for cancer treatment. *Cancers (Basel)*. (2025) 17:958. doi: 10.3390/cancers17060958

44. Samantasinghar A, Sunildutt NP, Ahmed F, Soomro AM, Salih ARC, Parihar P, et al. A comprehensive review of key factors affecting the efficacy of antibody drug conjugate. *Biomedicine pharmacotherapy = Biomedecine pharmacotherapie*. (2023) 161:114408. doi: 10.1016/j.biopha.2023.114408

45. Lee HK, Kim B, Ko YG, Chung SW, Shim WS, Choi SY, et al. Enhancing the bystander effect of antibody-drug conjugate by using a novel caspase-3 cleavable peptide linker to overcome tumor heterogeneity. *J Control Release*. (2025) 382:113738. doi: 10.1016/j.jconrel.2025.113738

46. Chen DS, Mellman I. Oncology meets immunology: the cancer-immunity cycle. *Immunity*. (2013) 39:1–10. doi: 10.1016/j.immuni.2013.07.012

47. Müller P, Martin K, Theurich S, Schreiner J, Savic S, Terszowski G, et al. Microtubule-depolymerizing agents used in antibody-drug conjugates induce antitumor immunity by stimulation of dendritic cells. *Cancer Immunol Res*. (2014) 2:741–55. doi: 10.1158/2326-6066.CIR-13-0198

48. Nicolo E, Giugliano F, Ascione L, Tarantino P, Corti C, Tolaney SM, et al. Combining antibody-drug conjugates with immunotherapy in solid tumors: current landscape and future perspectives. *Cancer Treat Rev*. (2022) 106:102395. doi: 10.1016/j.ctrv.2022.102395

49. Advani RH, Moskowitz AJ, Bartlett NL, Vose JM, Ramchandren R, Feldman TA, et al. Brentuximab vedotin in combination with nivolumab in relapsed or refractory Hodgkin lymphoma: 3-year study results. *Blood*. (2021) 138:427–38. doi: 10.1182/blood.2020009178

50. Hamilton EP, Kaklamani V, Falkson C, Vidal GA, Ward PJ, Patre M, et al. Impact of anti-HER2 treatments combined with atezolizumab on the tumor immune microenvironment in early or metastatic breast cancer: results from a phase ib study. *Clin Breast Cancer*. (2021) 21:539–51. doi: 10.1016/j.clbc.2021.04.011

51. Torres ETR, Emens LA. Emerging combination immunotherapy strategies for breast cancer: dual immune checkpoint modulation, antibody-drug conjugates and bispecific antibodies. *Breast Cancer Res Treat*. (2022) 191:291–302. doi: 10.1007/s10549-021-06423-0

52. Haratani K, Yonesaka K, Takamura S, Maenishi O, Kato R, Takegawa N, et al. U3–1402 sensitizes HER3-expressing tumors to PD-1 blockade by immune activation. *J Clin Invest*. (2020) 130:374–88. doi: 10.1172/JCI126598

53. Hashimoto Y, Koyama K, Kamai Y, Hirotani K, Ogitani Y, Zembutsu A, et al. A novel HER3-targeting antibody-drug conjugate, U3-1402, exhibits potent therapeutic efficacy through the delivery of cytotoxic payload by efficient internalization. *Clin Cancer Res*. (2019) 25:7151–61. doi: 10.1158/1078-0432.CCR-19-1745

54. Nicoletti R, Lopez S, Bellone S, Cocco E, Schwab CL, Black JD, et al. T-DM1, a novel antibody-drug conjugate, is highly effective against uterine and ovarian carcinosarcomas overexpressing HER2. *Clin Exp metastasis*. (2015) 32:29–38. doi: 10.1007/s10585-014-9688-8

55. Zammarchi F, Havenith K, Bertelli F, Vijayakrishnan B, Chivers S, van Berkel PH. CD25-targeted antibody-drug conjugate depletes regulatory T cells and eliminates established syngeneic tumors via antitumor immunity. *J Immunother Cancer*. (2020) 8:e000860. doi: 10.1136/jitc-2020-000860

56. Xue D, Liu P, Chen W, Zhang C, Zhang L. An anti-CD103 antibody-drug conjugate prolongs the survival of pancreatic islet allografts in mice. *Cell Death Dis*. (2019) 10:735. doi: 10.1038/s41419-019-1980-8

57. Müller P, Kreuzaler M, Khan T, Thommen DS, Martin K, Glatz K, et al. Trastuzumab emtansine (T-DM1) renders HER2+ breast cancer highly susceptible to CTLA-4/PD-1 blockade. *Sci Transl Med*. (2015) 7:315ra188. doi: 10.1126/scitranslmed.aac4925

58. Kong X, Bian J, Wang M, Zuo W, Tang Q, Sun M, et al. HER2-positive, RAS-mutant, MSS colorectal cancer: a rare subtype report and novel insights into immunotherapy and ADC combinations. *Am J Cancer Res*. (2025) 15:3150–63. doi: 10.62347/GMRV6636

59. Alese OB, Wu C, Chapin WJ, Ulanja MB, Zheng-Lin B, Amankwah M, et al. Update on emerging therapies for advanced colorectal cancer. *ASCO Educ Book*. (2023) 43:e389574. doi: 10.1200/EDBK_389574

60. Liu H, Zhou D, Liu D, Xu X, Zhang K, Hu R, et al. Synergistic antitumor activity between HER2 antibody-drug conjugate and chemotherapy for treating advanced colorectal cancer. *Cell Death Dis*. (2024) 15:187. doi: 10.1038/s41419-024-06572-2

61. Wu X, Xu L, Li X, Zhou Y, Han X, Zhang W, et al. A HER2-targeting antibody-MMAE conjugate RC48 sensitizes immunotherapy in HER2-positive colon cancer by triggering the cGAS-STING pathway. *Cell Death Dis*. (2023) 14:550. doi: 10.1038/s41419-023-06073-8

62. Zhang J, Liu R, Gao S, Li W, Chen Y, Meng Y, et al. Phase I study of A166, an antibody–drug conjugate in advanced HER2-expressing solid tumours. *NPJ Breast Cancer*. (2023) 9:28. doi: 10.1038/s41523-023-00522-5

63. Dotan E, Cohen SJ, Starodub AN, Lieu CH, Messersmith WA, Simpson PS, et al. Phase I/II trial of labetuzumab govitecan (Anti-CEACAM5/SN-38 antibody-drug conjugate) in patients with refractory or relapsing metastatic colorectal cancer. *J Clin Oncol*. (2017) 35:3338–46. doi: 10.1200/JCO.2017.73.9011

64. Kopetz S, Boni V, Kato K, Raghav KPS, Vieito M, Pallis A, et al. Precemtabart tocentecan, an anti-CEACAM5 antibody–drug conjugate, in metastatic colorectal cancer: a phase 1 trial. *Nat Med*. (2025) 31:3504–13. doi: 10.1038/s41591-025-03843-z

65. Zhu XY, Li QX, Kong Y, Huang KK, Wang G, Wang YJ, et al. A novel human single-domain antibody-drug conjugate targeting CEACAM5 exhibits potent *in vitro* and *in vivo* antitumor activity. *Acta Pharmacol Sin*. (2024) 45:609–18. doi: 10.1038/s41401-023-01200-9

66. Cardenas KCA, Enos CW, Spear MR, Austin DE, Almofeez R, Kortchak S, et al. CT109-SN-38, a novel antibody-drug conjugate with dual specificity for CEACAM5 and 6, elicits potent killing of pancreatic cancer cells. *Curr Cancer Drug Targets*. (2024) 24:720–32. doi: 10.2174/0115680096260614231115192343

67. Lentz RW, Barnett M, Gerber M, Kaplan J, van Bokhoven A, Torkko KC. Abstract C001: Retrospective analysis of TROP2 expression in colorectal cancer (CRC) primary tumors and liver metastases (LM) and its correlation with clinical factors. *Mol Cancer Ther*. (2023) 22:C001–1. doi: 10.1158/1535-7163.TARG-23-C001

68. Foersch S, Schmitt M, Litmeyer AS, Tschurtschenthaler M, Gress T, Bartsch DK, et al. TROP2 in colorectal carcinoma: associations with histopathology, molecular phenotype, and patient prognosis, The journal of pathology. *Clin Res*. (2024) 10:e12394. doi: 10.1002/2056-4538.12394

69. Kogai H, Tsukamoto S, Koga M, Miyano M, Akagi T, Yamaguchi A, et al. Broad-spectrum efficacy of CEACAM6-targeted antibody-drug conjugate with BET protein degrader in colorectal. *Lung Breast Cancer Mouse Models Mol Cancer Ther*. (2025) 24:392–405. doi: 10.1158/1535-7163.MCT-24-0444

70. Koganemaru S, Kuboki Y, Koga Y, Kojima T, Yamauchi M, Maeda N, et al. U3-1402, a novel HER3-targeting antibody-drug conjugate, for the treatment of colorectal cancer. *Mol Cancer Ther*. (2019) 18:2043–50. doi: 10.1158/1535-7163.MCT-19-0452

71. Liu Z, Zhang H, Sun J, Zheng M, Cui L, Zhang Y, et al. Organic-solvent-free "Lego-like" Modular preparation of fab-nondestructive antibody-drug conjugates with ultrahigh drug-to-antibody ratio. *Advanced materials (Deerfield Beach Fla.)*. (2023) 35:e2300377. doi: 10.1002/adma.202300377

72. Zhang H, Sun J, Zhang Y, Zhang Z, Wang X, Liu Z, et al. Preparation of an Ultrahigh-DAR PDL1 monoclonal antibody-polymeric-SN38 conjugate for precise colon cancer therapy. *Biomaterials*. (2023) 301:122285. doi: 10.1016/j.biomaterials.2023.122285

73. Chiang ZC, Xu S, Zhao X, Liu M, Lin J, Chen Q. Generation and characterization of 7DC-DM1: a non-cleavable CD47-targeting antibody-drug conjugates with antitumor effects. *Int J Biol macromolecules*. (2025) 310:142844. doi: 10.1016/j.ijbiomac.2025.142844

74. Abu-Yousif AO, Cvet D, Gallery M, Bannerman BM, Ganno ML, Smith MD, et al. Preclinical antitumor activity and biodistribution of a novel anti-GCC antibody-drug conjugate in patient-derived xenografts. *Mol Cancer Ther*. (2020) 19:2079–88. doi: 10.1158/1535-7163.MCT-19-1102

75. Kim R, Leal AD, Parikh A, Ryan DP, Wang S, Bahamon B, et al. A phase I, first-in-human study of TAK-164, an antibody-drug conjugate, in patients with advanced gastrointestinal cancers expressing guanylyl cyclase C. *Cancer Chemother Pharmacol*. (2023) 91:291–300. doi: 10.1007/s00280-023-04507-w

76. Tao Y, Wang R, Lai Q, Wu M, Wang Y, Jiang X, et al. Targeting of DDR1 with antibody-drug conjugates has antitumor effects in a mouse model of colon carcinoma. *Mol Oncol*. (2019) 13:1855–73. doi: 10.1002/1878-0261.12520

77. Zhou D, Tang E, Wang W, Xiao Y, Huang J, Liu J, et al. Combined therapy with DR5-targeting antibody-drug conjugate and CDK inhibitors as a strategy for advanced colorectal cancer, Cell reports. *Medicine*. (2025) 6:102158. doi: 10.1016/j.xcrm.2025.102158

78. Scribner JA, Hicks SW, Sinkevicius KW, Yoder NC, Diedrich G, Brown JG, et al. Preclinical evaluation of IMGC936, a next-generation maytansinoid-based antibody-drug conjugate targeting ADAM9-expressing. *Tumors Mol Cancer Ther*. (2022) 21:1047–59. doi: 10.1158/1535-7163.MCT-21-0915

79. Wu Y, Li W, Chen X, Wang H, Su S, Xu Y, et al. DOG1 as a novel antibody-drug conjugate target for the treatment of multiple gastrointestinal tumors and liver metastasis. *Front Immunol*. (2023) 14:1051506. doi: 10.3389/fimmu.2023.1051506

80. Mazahreh R, Mason ML, Gosink JJ, Olson DJ, Thurman R, Hale C, et al. SGN-CD228A is an investigational CD228-directed antibody-drug conjugate with potent antitumor activity across a wide spectrum of preclinical solid tumor models. *Mol Cancer Ther*. (2023) 22:421–34. doi: 10.1158/1535-7163.MCT-22-0401

81. Jafary B, Akbarzadeh-Khiavi M, Farzi-Khajeh H, Safary A, Adibkia K. EGFR-targeting RNase A-cetuximab antibody-drug conjugate induces ROS-mediated apoptosis to overcome drug resistance in KRAS mutant cancer cells. *Sci Rep*. (2025) 15:1483. doi: 10.1038/s41598-025-85856-9

82. Pisheh L, Matis S, Taglieri M, Di Gregorio L, Benelli R, Poggi A. EGFR-targeted antibody-drug conjugate to different aminobisphosphonates: direct and indirect antitumor effects on colorectal carcinoma cells. *Cancers*. (2024) 16:1256. doi: 10.3390/cancers16071256

83. Bhattacharya S. Anti-EGFR-mAb and 5-fluorouracil conjugated polymeric nanoparticles for colorectal cancer. *Recent patents anti-cancer Drug Discov*. (2021) 16:84–100. doi: 10.2174/1574892815666201221121859

84. Junttila MR, Mao W, Wang X, Wang BE, Pham T, Flygare J, et al. Targeting LGR5+ cells with an antibody-drug conjugate for the treatment of colon cancer. *Sci Transl Med*. (2015) 7:314ra186. doi: 10.1126/scitranslmed.aac7433

85. Zhao H, Han R, Wang Z, Xian J, Bai X. Colorectal cancer stem cells and targeted agents. *Pharmaceutics*. (2023) 15:2763. doi: 10.3390/pharmaceutics15122763

86. Herpers B, Eppink B, James MI, Cortina C, Cañellas-Socias A, Boj SF, et al. Functional patient-derived organoid screenings identify MCLA-158 as a therapeutic EGFR × LGR5 bispecific antibody with efficacy in epithelial tumors. *Nat Cancer*. (2022) 3:418–36. doi: 10.1038/s43018-022-00359-0

87. Lundberg AS, Geuijen CAW, Hill S, Lammerts van Bueren JJ, Fumagalli A, de Kruif J, et al. Petosemtamab, a bispecific antibody targeting epidermal growth factor receptor (EGFR) and leucine-rich G repeat-containing protein-coupled receptor (LGR5) designed for broad clinical applications. *Cancers (Basel)*. (2025) 17:1665. doi: 10.3390/cancers17101665

88. Zumaya ALV, Rimpelová S, Štějdířová M, Ulbrich P, Vilčáková J, Hassouna F. Antibody conjugated PLGA nanocarriers and superparmagnetic nanoparticles for targeted delivery of oxaliplatin to cells from colorectal carcinoma. *Int J Mol Sci*. (2022) 23:1200. doi: 10.3390/ijms23031200

89. Mohd-Zahid MH, Zulkifli SN, Che Abdullah CA, Lim J, Fakurazi S, Wong KK, et al. Gold nanoparticles conjugated with anti-CD133 monoclonal antibody and 5-fluorouracil chemotherapeutic agent as nanocarriers for cancer cell targeting. *RSC Adv*. (2021) 11:16131–41. doi: 10.1039/D1RA01093J

90. Jacob J, Francisco LE, Chatterjee T, Liang Z, Subramanian S, Liu QJ, et al. An antibody-drug conjugate targeting GPR56 demonstrates efficacy in preclinical models of colorectal cancer. *Br J Cancer*. (2023) 128:1592–602. doi: 10.1038/s41416-023-02192-3

91. Fan Y, Yan XY, Guan W. GPR56, an adhesion GPCR with multiple roles in human diseases, current status and future perspective. *Curr Drug Targets*. (2024) 25:558–73. doi: 10.2174/0113894501298344240507080149

92. Zhang S, Chatterjee T, Godoy C, Wu L, Liu QJ, Carmon KS. GPR56 Drives Colorectal Tumor Growth and Promotes Drug Resistance through Upregulation of MDR1 Expression via a RhoA-Mediated Mechanism. *Mol Cancer Res*. (2019) 17:2196–207. doi: 10.1158/1541-7786.MCR-19-0436

93. Francisco LE, Chatterjee T, Liang Z, Zhang S, Carmon K. Abstract 6328: GPR56 as a therapeutic target for the development of antibody-drug conjugates for the treatment of colorectal cancer. *Cancer Res*. (2022) 82:6328–8. doi: 10.1158/1538-7445.AM2022-6328

94. Jacob J, Anami Y, High PC, Liang Z, Subramanian S, Ghosh SC, et al. Antibody-drug conjugates targeting the EGFR ligand epiregulin elicit robust antitumor activity in colorectal cancer. *Cancer Res*. (2025) 85:973–86. doi: 10.1158/0008-5472.CAN-24-0798

95. Jacob J, Liang Z, Carmon K. Abstract 4251: Development and characterization of an epiregulin antibody-drug conjugate for targeting colorectal cancer cell plasticity. *Cancer Res*. (2022) 82:4251–1. doi: 10.1158/1538-7445.AM2022-4251

96. Yang Y, Wang S, Ma P, Jiang Y, Cheng K, Yu Y, et al. Drug conjugate-based anticancer therapy - Current status and perspectives. *Cancer Lett*. (2023) 552:215969. doi: 10.1016/j.canlet.2022.215969

97. Sartore Bianchi A, Lonardi S, Amatu A, Bergamo F, Mauri G, Martino C. Trastuzumab-emtansine (T-DM1) in HER2-amplified metastatic colorectal cancer patients progressing to trastuzumab-lapatinib: the HERACLES RESCUE phase II trial. *Ann Oncol Off J Eur Soc Med Oncol*. (2022) 33:S705–S706. doi: 10.1016/j.annonc.2022.07.508

98. Benli Y, Arıkan H, Akbulut-Çalışkan Ö. HER2-targeted therapy in colorectal cancer: a comprehensive review. *Clin Trans Oncol Off Publ Fed Spanish Oncol Societies Natl Cancer Institute Mexico*. (2025) 27:3607–24. doi: 10.1007/s12094-025-03887-0

99. Gazzah A, Bedard PL, Hierro C, Kang YK, Abdul Razak A, Ryu MH, et al. Safety, pharmacokinetics, and antitumor activity of the anti-CEACAM5-DM4 antibody-drug conjugate tusamitamab ravtansine (SAR408701) in patients with advanced solid tumors: first-in-human dose-escalation study. *Ann Oncol Off J Eur Soc Med Oncol*. (2022) 33:416–25. doi: 10.1016/j.annonc.2021.12.012

100. Gonzalez-Exposito R, Semiannikova M, Griffiths B, Khan K, Barber LJ, Woolston A, et al. CEA expression heterogeneity and plasticity confer resistance to the CEA-targeting bispecific immunotherapy antibody cibisatamab (CEA-TCB) in patient-derived colorectal cancer organoids. *J Immunother Cancer*. (2019) 7:101. doi: 10.1186/s40425-019-0575-3

101. Nessler I, Rubahamya B, Kopp A, Hofsess S, Cardillo TM, Sathyanarayan N, et al. Improving intracellular delivery of an antibody–drug conjugate targeting carcinoembryonic antigen increases efficacy at clinically relevant doses *in vivo*. *Mol Cancer Ther*. (2024) 23:343–53. doi: 10.1158/1535-7163.MCT-23-0437

102. Wang R, Hu B, Pan Z, Mo C, Zhao X, Liu G, et al. Antibody-Drug Conjugates (ADCs): current and future biopharmaceuticals. *J Hematol Oncol*. (2025) 18:51. doi: 10.1186/s13045-025-01704-3

103. Wang Z, Li H, Gou L, Li W, Wang Y. Antibody-drug conjugates: Recent advances in payloads. *Acta Pharm Sinica. B*. (2023) 13:4025–59. doi: 10.1016/j.apsb.2023.06.015

104. Mahalingaiah PK, Ciurlionis R, Durbin KR, Yeager RL, Philip BK, Bawa B, et al. Potential mechanisms of target-independent uptake and toxicity of antibody-drug conjugates. *Pharmacol Ther*. (2019) 200:110–25. doi: 10.1016/j.pharmthera.2019.04.008

105. Ma Y, Yang Y, Huang Y, Fang W, Xue J, Meng X, et al. A B7H3-targeting antibody–drug conjugate in advanced solid tumors: a phase 1/1b trial. *Nat Med*. (2025) 31:1949–57. doi: 10.1038/s41591-025-03600-2

106. Lu G, Nishio N, van den Berg NS, Martin BA, Fakurnejad S, Keulen Sv, et al. Co-administered antibody improves penetration of antibody–dye conjugate into human cancers with implications for antibody–drug conjugates. *Nat Commun*. (2020) 11:5667. doi: 10.1038/s41467-020-19498-y

107. Xu S. Internalization, trafficking, intracellular processing and actions of antibody-drug conjugates. *Pharm Res*. (2015) 32:3577–83. doi: 10.1007/s11095-015-1729-8

108. Zhang Q, Zhang N, Xiao H, Wang C, He L. Small antibodies with big applications: nanobody-based cancer diagnostics and therapeutics. *Cancers*. (2023) 15:5639. doi: 10.3390/cancers15235639

109. Kleist B, Meurer T, Poetsch M. Mitochondrial DNA alteration in primary and metastatic colorectal cancer: Different frequency and association with selected clinicopathological and molecular markers. *Tumour biology: J Int Soc Oncodevelopmental Biol Med*. (2017) 39:1010428317692246. doi: 10.1177/1010428317692246

110. Müller MF, Ibrahim AE, Arends MJ. Molecular pathological classification of colorectal cancer. *Virchows Archiv: an Int J Pathol*. (2016) 469:125–34. doi: 10.1007/s00428-016-1956-3

111. Xie YH, Chen YX, Fang JY. Comprehensive review of targeted therapy for colorectal cancer. *Signal Transduct Target Ther*. (2020) 5:22. doi: 10.1038/s41392-020-0116-z

112. Xiao Y, Freeman GJ. The microsatellite instable subset of colorectal cancer is a particularly good candidate for checkpoint blockade immunotherapy. *Cancer Discov*. (2015) 5:16–8. doi: 10.1158/2159-8290.CD-14-1397

113. André T, Shiu KK, Kim TW, Jensen BV, Jensen LH, Punt C, et al. Pembrolizumab in microsatellite-instability-high advanced colorectal cancer. *New Engl J Med*. (2020) 383:2207–18. doi: 10.1056/NEJMoa2017699

114. Boland CR, Thibodeau SN, Hamilton SR, Sidransky D, Eshleman JR, Burt RW, et al. A National Cancer Institute Workshop on Microsatellite Instability for cancer detection and familial predisposition: development of international criteria for the determination of microsatellite instability in colorectal cancer. *Cancer Res*. (1998) 58:5248–57.

115. Lee V, Murphy A, Le DT, Diaz LA Jr. Mismatch repair deficiency and response to immune checkpoint blockade. *oncologist*. (2016) 21:1200–11. doi: 10.1634/theoncologist.2016-0046

116. van der Stok EP, Spaander MCW, Grünhagen DJ, Verhoef C, Kuipers EJ. Surveillance after curative treatment for colorectal cancer. *Nat Rev Clin Oncol*. (2017) 14:297–315. doi: 10.1038/nrclinonc.2016.199

117. Nielsen DL, Palshof JA, Brünner N, Stenvang J, Viuff BM. Implications of ABCG2 expression on irinotecan treatment of colorectal cancer patients: A review. *Int J Mol Sci*. (2017) 18:1926. doi: 10.3390/ijms18091926

118. Loo TW, Clarke DM. Recent progress in understanding the mechanism of P-glycoprotein-mediated drug efflux. *J membrane Biol*. (2005) 206:173–85. doi: 10.1007/s00232-005-0792-1

119. Goda K, Bacsó Z, Szabó G. Multidrug resistance through the spectacle of P-glycoprotein. *Curr Cancer Drug Targets*. (2009) 9:281–97. doi: 10.2174/156800909788166493

120. Hu WQ, Peng CW, Li Y. The expression and significance of P-glycoprotein, lung resistance protein and multidrug resistance-associated protein in gastric cancer. *J Exp Clin Cancer research: CR*. (2009) 28:144. doi: 10.1186/1756-9966-28-144

121. Xu HW, Xu L, Hao JH, Qin CY, Liu H. Expression of P-glycoprotein and multidrug resistance-associated protein is associated with multidrug resistance in gastric cancer. *J Int Med Res*. (2010) 38:34–42. doi: 10.1177/147323001003800104

122. Wang R, Fang P, Chen X, Ji J, Yu D, Mei F, et al. Overcoming multidrug resistance in gastrointestinal cancers with a CDH17-targeted ADC conjugated to a DNA topoisomerase inhibitor. *Cell Rep Med*. (2025) 6:102213. doi: 10.1016/j.xcrm.2025.102213

123. Yoshino T, Di Bartolomeo M, Raghav K, Masuishi T, Loupakis F, Kawakami H, et al. D.-C. investigators, Final results of DESTINY-CRC01 investigating trastuzumab deruxtecan in patients with HER2-expressing metastatic colorectal cancer. *Nat Commun*. (2023) 14:3332. doi: 10.1038/s41467-023-38032-4

124. Meric-Bernstam F, Hurwitz H, Raghav KPS, McWilliams RR, Fakih M, VanderWalde A, et al. Pertuzumab plus trastuzumab for HER2-amplified metastatic colorectal cancer (MyPathway): an updated report from a multicentre, open-label, phase 2a, multiple basket study, The Lancet. *Oncology*. (2019) 20:518–30. doi: 10.1016/S1470-2045(18)30904-5

125. Kumagai K, Aida T, Tsuchiya Y, Kishino Y, Kai K, Mori K. Interstitial pneumonitis related to trastuzumab deruxtecan, a human epidermal growth factor receptor 2-targeting Ab-drug conjugate, in monkeys. *Cancer Sci*. (2020) 111:4636–45. doi: 10.1111/cas.14686

126. Shitara K, Baba E, Fujitani K, Oki E, Fujii S, Yamaguchi K. Discovery and development of trastuzumab deruxtecan and safety management for patients with

HER2-positive gastric cancer. *Gastric Cancer*. (2021) 24:780–9. doi: 10.1007/s10120-021-01196-3

127. Raghav KPS, Siena S, Takashima A, Kato T, Van Den Eynde M, Di Bartolomeo M, et al. Trastuzumab deruxtecan (T-DXd) in patients (pts) with HER2-overexpressing/amplified (HER2+) metastatic colorectal cancer (mCRC): Primary results from the multicenter, randomized, phase 2 DESTINY-CRC02 study. *J Clin Oncol*. (2023) 41:3501–1. doi: 10.1200/JCO.2023.41.16_suppl.3501

128. D'Arienzo A, Verrazzo A, Pagliuca M, Napolitano F, Parola S, Viggiani M, et al. Toxicity profile of antibody-drug conjugates in breast cancer: practical considerations. *eClinicalMedicine*. (2023) 62:102113. doi: 10.1016/j.eclinm.2023.102113

129. Fong JY, Phuna Z, Chong DY, Heryanto CM, Low YS, Oh KC, et al. Advancements in antibody-drug conjugates as cancer therapeutics. *J Natl Cancer Center*. (2025) 5:362–78. doi: 10.1016/j.jncc.2025.01.007

Frontiers in Immunology

Explores novel approaches and diagnoses to treat immune disorders.

The official journal of the International Union of Immunological Societies (IUIS) and the most cited in its field, leading the way for research across basic, translational and clinical immunology.

Discover the latest Research Topics

See more →



Frontiers

Avenue du Tribunal-Fédéral 34
1005 Lausanne, Switzerland
frontiersin.org

Contact us

+41 (0)21 510 17 00
frontiersin.org/about/contact